Mediators of Inflammation

The MicroRNAs and Inflammation to Cardiovascular Diseases

Lead Guest Editor: Md Sayed Ali Sheikh
Guest Editors: Shanmughapriya Santhanam and Zhong-Bao Yang

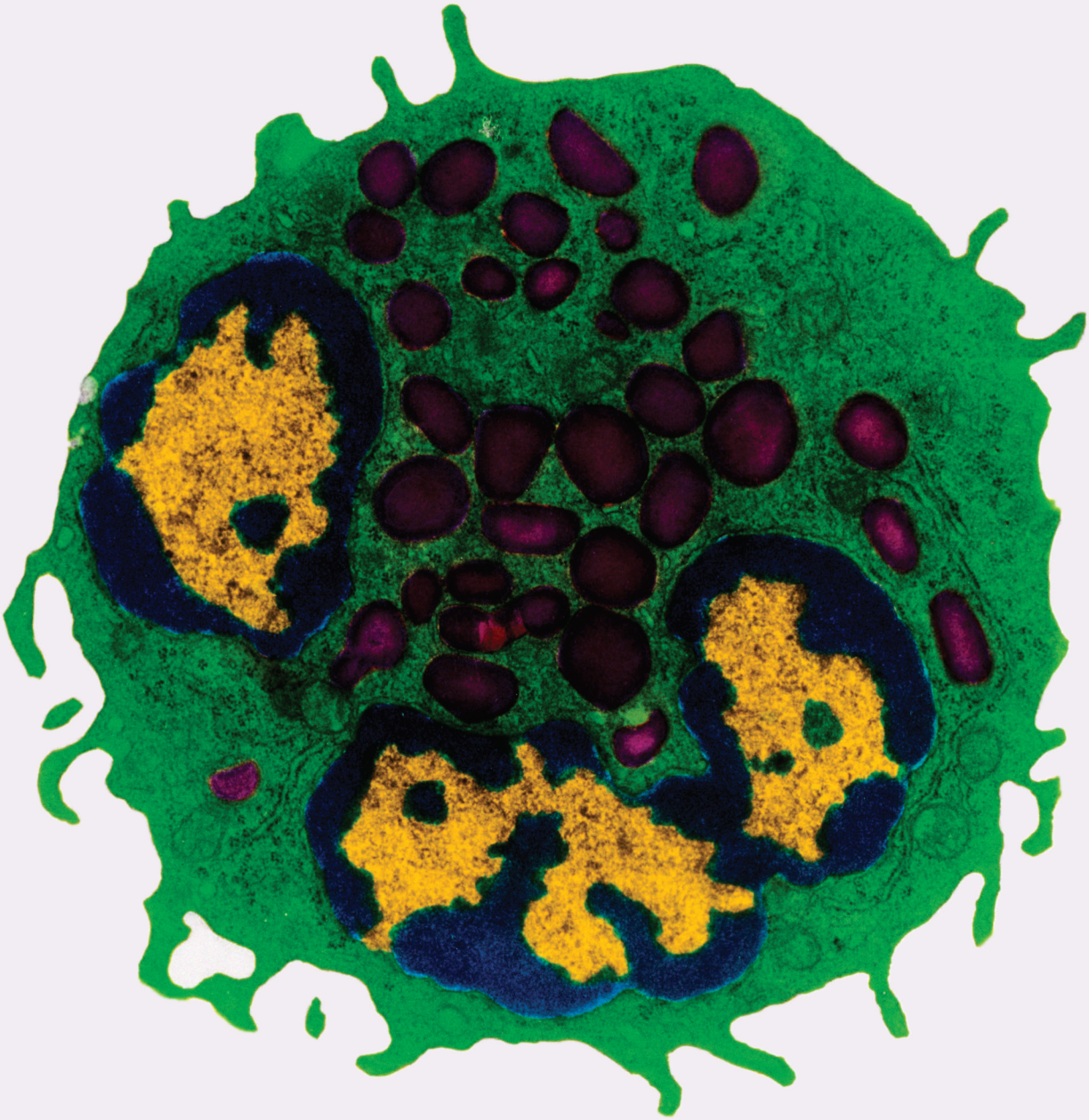

The MicroRNAs and Inflammation to Cardiovascular Diseases

The MicroRNAs and Inflammation to Cardiovascular Diseases

Lead Guest Editor: Md Sayed Ali Sheikh
Guest Editors: Shanmughapriya Santhanam and Zhong-Bao Yang

Contents

Hindawi
Mediators of Inflammation
Volume 2023, Article ID 4003618, 15 pages
https://doi.org/10.1155/2023/4003618

Research Article

lncRNA MIR503HG Targets miR-191-5p/PLCD1 Axis and Negatively Modulates Apoptosis, Extracellular Matrix Disruption, and Inflammation in Abdominal Aortic Aneurysm

Ye Tian,[1] Xinxi Li,[1] Chao Bai,[1] Zhenwei Yang,[1] Lei Zhang,[1] Jun Luo,[1] and Wenbin Zhang[2]

[1]*Department of Vascular and Thyroid Surgery, The First Affiliated Hospital of Xinjiang Medical University, Urumqi, 830000 Xinjiang Uygur Autonomous Region, China*
[2]*Department of Gastrointestinal Surgery, The First Affiliated Hospital of Xinjiang Medical University, Urumqi, 830000 Xinjiang Uygur Autonomous Region, China*

Correspondence should be addressed to Wenbin Zhang; youpin6995661668@163.com

Received 13 July 2022; Revised 9 November 2022; Accepted 5 April 2023; Published 16 May 2023

Academic Editor: Md Sayed Ali Sheikh

As the most prevalent subtype of aortic aneurysm, abdominal aortic aneurysm (AAA) features the apoptosis, extracellular matrix (ECM) disruption, and inflammation response of vascular smooth muscle cells (VSMCs). Noncoding RNAs (ncRNAs) are crucial factors in AAA progression, while the investigations have not been fully explained. miR-191-5p upregulation is found in aortic aneurysm. However, its role in AAA has not been addressed. This research purposed to excavate the possible and associated molecular axis of miR-191-5p in AAA. In our study, miR-191-5p level was detected to be high in the tissues from AAA patients in comparison with the control group. After miR-191-5p expression was enhanced, cell viability was repressed, cell apoptosis was boosted, and ECM disruption and the inflammation response were fortified. Furthermore, the relationship among MIR503HG, miR-191-5p, and phospholipase C delta 1 (PLCD1) in VSMCs was disclosed via mechanism assays. Decreased MIR503HG lacked the inhibition on miR-191-5p targeting PLCD1, resulting in downregulation of PLCD1, which facilitated the progression of AAA. Thus, targeting MIR503HG/miR-191-5p/PLCD1 pathway will provide an additional method for the cure of AAA patients.

1. Introduction

Focal dilatations of abdominal aorta with about 50% bigger than proximal normal segment or thickness more than 30 mm in diameter are defined as abdominal aortic aneurysm (AAA) [1, 2]. According to our knowledge, AAA is life-threatening due to its high morbidity and mortality among adults, especially among the older [3–5]. Unfortunately, the regulatory mechanisms underlying AAA pathogenesis are not well-illustrated, and therefore, effective therapeutic targets are lacking for AAA treatment. Increasing evidence has supported that vascular smooth muscle cells (VSMCs) are able to secrete elastin, an essential element of collagen synthesis and AAA wall remodeling [6, 7]. Therefore, the exploration of the cellular activities in VSMCs may be beneficial to the treatment of AAA.

Noncoding RNAs (ncRNAs) are transcripts that lack open reading frames (ORFs) and cannot encode proteins [8, 9]. Long ncRNAs (lncRNAs) with over 200 nucleotides (nt) and microRNAs (miRNAs) at about 22 nt are two subtypes of ncRNAs [10–12]. They can affect various biological processes in a molecular mechanism-dependent manner in diseases. For example, H19 activates AAA progression [13]. Interleukin 6 (IL-6) increases the level of NADPH oxidase 2 in human aortic endothelial cells with the assistance of MALAT1 [14]. miR-24 restricts inflammation of aortic vascular and murine abdominal aneurysm [15]. MicroRNA-712 and microRNA-205 prevent AAA in angiotensin II (Ang-II)-infused mice [16]. miR-191-5p is researched to be elevated and promote the development in multiple sclerosis and osteosarcoma [17, 18]. Importantly, miR-191 is reported to be highly expressed in AAA [19]. miR-191-5p of the miR-

Table 1: Primer sequences used in qRT-PCR were listed.

Gene name	Primer sequences used in qRT-PCR Primer sequence	Company name	Location
miR-191-5p	Reverse transcription stem loop primer: CTCAACTGGTGTCGTGGAGTCGGCAATTCAGTTGAGCcagctgct miRNA stem loop universal reverse primer: CTCAACTGGTGTCGTGGA F: GCCGAGtttgggattccgttg	NCBI	USA
AC079781.5	F: CGTGTCCAGAATTGGTGGGT R: GCACCCTGTCAAAACACACC	primer3plus	
RRN3P2	F: TCTGCTTGCGGTTGGATAGC R: TCTCCAGCAAACTGAGCCAC	NCBI	USA
XIST	F: TTAAAGCGCTGCAATTCGCT R: AGGGTGTTGGGGGACTAGAA	NCBI	USA
MIR503HG	F: TCCCGCCAAATGAGTCAGTC R: ACAGAGTTGTGACCACTGCC	NCBI	USA
PLCD1	F: GGACTTCCTGACCCTGCAC R: TTCGCACCTCCTGAATGTCC	NCBI	USA

191 family has also been demonstrated to affect senescence in ascending aortic aneurysm [20]. However, the specific function of miR-191-5p and relevant regulatory mechanism are unknown.

lncRNA MIR503HG is a newly identified repressor in several cancers [21–23]. In this study, we also aimed to figure out whether MIR503HG was involved in the regulatory network of miR-191-5p in AAA.

Herein, AAA patients' tissues and VSMCs were acquired for evaluating gene expressions. Cell viability, cell apoptosis, extracellular matrix (ECM) disruption, and inflammation responses were tested to analyze the functional influence of miR-191-5p. Additionally, mechanism assays were designed for detecting relations between genes.

2. Materials and Methods

2.1. Patients and Cell Lines. 43 AAA patients and controls were recruited for collecting AAA and normal aortic tissues which were resected and snap-frozen at -80°C in liquid nitrogen immediately. Clinical analysis was conducted with the ethical approval from the Research Ethics Committee of Henan Provincial People's Hospital. Informed consent was provided by all participants. Primary human aortic VSMCs were preserved in RPMI-1640 Glutamax with 1% antibiotic solution (10,000 U/mL streptomycin sulphate and 10,000 U/mL penicillin G) and 10% FBS. Additionally, HEK-293T cells were procured from Procell (Wuhan, China) and incubated in DMEM+10% FBS+1% penicillin/streptomycin. The environment was kept at 37°C with 5% CO_2.

2.2. Quantitative Real-Time PCR (qRT-PCR). TRIzol reagent (Life Technologies, Gaithersburg, MD, USA) was obtained for the extraction of total RNAs from VSMCs. TaqMan Reverse Transcription Kit (Applied Biosystems, Foster City, CA, USA) synthesized the first strand cDNA. Subsequent qPCR was completed using Applied Biosystems Prism 7900HT Fast Real-Time PCR system and SYBR-Green (Applied Biosystems). RNA expression was analyzed by the method of ΔΔCt [24] and normalized to U6 or GAPDH. Primer sequences are listed in Table 1.

2.3. Cell Transfection. The transfection procedures were in line with previous study [25]. VSMCs were cultivated until they reached 60-70% confluence. Subsequently, cells (80,000-120,000) in a 6-well culture plates with serum-free DMEM were subjected to transfection with various plasmids at the concentration of 10 nM using Lipofectamine 2000 reagent (Invitrogen, Carlsbad, CA, USA). The miR-191-5p mimics and miR-NC, pcDNA3.1/PLCD1 (PLCD1), and empty vector were provided by GenePharma (Shanghai, China). The miR-191-5p inhibitor and miR-NC, as well as the shRNAs specific to MIR503HG (shMIR503HG), PLCD1 (shPLCD1), and control shRNA (shNC), were also synthesized by GenePharma for gene silencing. 48 h later, VSMCs were harvested. The efficiency was measured by qRT-PCR.

2.4. CCK-8 Assay. VSMCs in 96-well plates (1×10^4/well) were transfected with plasmids and respective control. After 48 h, the samples were incubated with CCK-8 kit (Beyotime Institute of Biotechnology, Shanghai, China) for 2 h. The viability of VSMCs was monitored by measuring the OD value at 405 nm.

2.5. EdU Assay. EdU incorporation assay kit was procured from RiboBio (Guangzhou, China). Transfected cells were mixed with 100 μL of EdU medium diluent for 3 h in 96-well plates, followed by culture with 100 μL of 1x Apollo® 488 liquid in 4% paraformaldehyde for 30 min. Nuclei were counterstained with DAPI (Beyotime) for observation.

2.6. Flow Cytometry of Cell Apoptosis. VSMCs were transfected and collected to the 6-well plates (3×10^3/well), followed by double-stained with Annexin V/PI Kit (BD Biosciences, San Jose, CA, USA). Apoptosis of VSMCs was analyzed by FACSCalibur flow cytometer (BD Biosciences).

2.7. TUNEL Assay. Transfected VSMCs were fixed and permeabilized with 1% formaldehyde and 0.2% Triton X-100, respectively. After dUTP-end labeling (Clontech, Mountain View, CA, USA) and DAPI staining, VSMCs were visualized by TE200-U fluorescence microscope (Nikon, Tokyo, Japan).

2.8. Caspase-3 Activity Detection. Solarbio (Beijing, China) provided the caspase-3 activity kit for this assay. Protein extracts were cultivated with reaction buffer for 4 h, with the addition of caspase substrate in 96-well dishes. The environment was kept at 37°C. Caspase-3 activity was detected at 405 nm by a microplate reader.

2.9. Western Blot. VSMCs in RIPA lysis buffer were loaded onto 10% SDS-PAGE and transferred onto PVDF membranes (Millipore, Bedford, MA, USA) at 80 V, following treatment with 5% nonfat dry milk. The primary antibodies (1 : 1,000) against Ki67, Bcl-2, Bax, Total-caspase-3, Cleaved-caspase-3, MMP2, MMP9, TIMP-1, α-SMA, OPN, PLCD1, and GAPDH, as well as secondary antibodies conjugated with HRP (1 : 2,000), were all acquired from Abcam (Cambridge, MA, USA). The protein signals were analyzed by enhanced chemiluminescence (ECL) reagent (GE Healthcare, Milwaukee, MI, USA) following the guidelines.

2.10. ELISA Assay. VSMCs were transfected in 96-well plates (1×10^4/well) for 48 h. The culture medium was collected and maintained at -80°C. The cytokine TNF-α or IL-6 levels were assessed by Human TNF-α or IL-6 Quantikine ELISA Kit (R&D Systems, Minneapolis, MN, USA).

2.11. RNA Pull-Down Assay. The miR-191-5p and its antisense RNA (miR-191-5p AS) were in vitro biotin-labeled for obtaining the Bio-miR-191-5p sense and Bio-miR-191-5p AS. Cell lysates were incubated with biotinylated RNAs and Bio-NC. The pull-down complex was analyzed by qRT-PCR.

2.12. Dual-Luciferase Reporter Analysis. The wild-type (WT) or mutant (Mut) miR-191-5p binding sites to MIR503HG sequence were inserted into pmirGLO Dual-Luciferase Vector (Promega, Madison, WI, USA) and named as MIR503HG-WT/Mut. VSMCs and HEK-293T were transfected with MIR503HG-WT/Mut in the presence of miR-191-5p mimics and miR-NC for 48 h. The 3′UTRs of 13 possible mRNAs within predicted interacting sequences of miR-191-5p were separately cloned into pmirGLO Vectors and cotransfected with miR-191-5p mimics or miR-NC into VSMCs and HEK-293T. After transfection, Dual-Luciferase Reporter Assay System (Promega) was utilized for determination of luciferase activity.

2.13. Statistical Analyses. The data were shown as mean ± SD with at least three replications. Two-tailed Student's *t*-test or ANOVA by use of SPSS version 19.0 (SPSS, Chicago, IL, USA) was utilized for statistical analyses. A *P* value less than 0.05 was considered as the threshold value. Spearman's correlation analysis analyzed the correlation between every two genes.

3. Results

3.1. miR-191-5p Negatively Regulated the Apoptosis, ECM Degradation, and Inflammation in AAA. miR-191-5p is demonstrated to be elevated in aortic aneurysm, but its function is not explored in detail [20]. Therefore, we first detect the expression of miR-191-5p in clinical samples. As a result, miR-191-5p was significantly elevated in AAA tissues in comparison with controls (Figure 1(a)). For confirming the participation of miR-191-5p during AAA development, we carried out gain-of-function experiments with VSMCs. In preparation, miR-191-5p expression was elevated in VSMCs (Figure 1(b)). Then, we detected that when miR-191-5p was enhanced, cell viability and proliferation were dramatically reduced (Figures 1(c) and 1(d)). In addition, experimental results also demonstrated that cell apoptosis was induced under miR-191-5p increment (Figures 1(e)–1(g)). Subsequently, western blot affirmed that Ki67 and Bcl-2 proteins declined, but Total-caspase-3 protein was not changed, and the Bax and Cleaved-caspase-3 proteins were augmented, hinting that cell apoptosis was accelerated (Figure 1(h)). The impact of miR-191-5p elevation on ECM degradation was then analyzed. From western blot results, augmented miR-191-5p expression enhanced MMP2 and MMP9 protein expressions (enzymes able to degrade various components of ECM proteins [26]) but lessened the expression level of their inhibitor TIMP-1. The protein levels of α-SMA, a marker of contractile VSMCs, were downregulated. The protein levels of OPN, a marker of synthetic VSMCs, were upregulated (Figure 1(i)). Additionally, ELISA kit detected the augment of TNF-α and IL-6, two proinflammatory mediators (Figures 1(j) and 1(k)). Taken together, miR-191-5p elevation could cause the promotion of apoptosis, ECM degradation, and inflammation.

3.2. MIR503HG Bound with miR-191-5p in VSMCs. To figure out the lncRNA targeting miR-191-5p, starBase was applied for prediction. Four possible lncRNAs binding with miR-191-5p were found, namely, AC079781.5, RRN3P2, XIST, and MIR503HG. We noticed that MIR503HG exhibited the highest enrichment in the Bio-miR-191-5p sense group, compared to the control group and Bio-miR-191-5p antisense group (Figure 2(a)). Thus, MIR503HG was tentatively selected. Thereafter, we constructed pmirGLO Vectors containing wild-type and mutant miR-191-5p binding sequences in MIR503HG, which are shown in Figure 2(b). The luciferase activity of MIR503HG-WT was markedly impaired by the increment of miR-191-5p (Figure 2(c)). Then, low MIR503HG expression was found in AAA tissues, which could negatively modulate miR-191-5p expression, as measured by qRT-PCR and Spearman's correlation analysis (Figures 2(d) and 2(e)). Consistently, we found that in VSMCs, miR-191-5p expression was promoted by MIR503HG downregulation (Figures 2(f) and 2(g)). The impacts of MIR503HG on VSMCs were also explored. As a result, cell viability and proliferation were hampered when MIR503HG was silenced (Figures 2(h) and 2(i)). Additionally, experimental results also validated that MIR503HG inhibition enhanced the cell apoptosis (Figures 2(j)–2(m)).

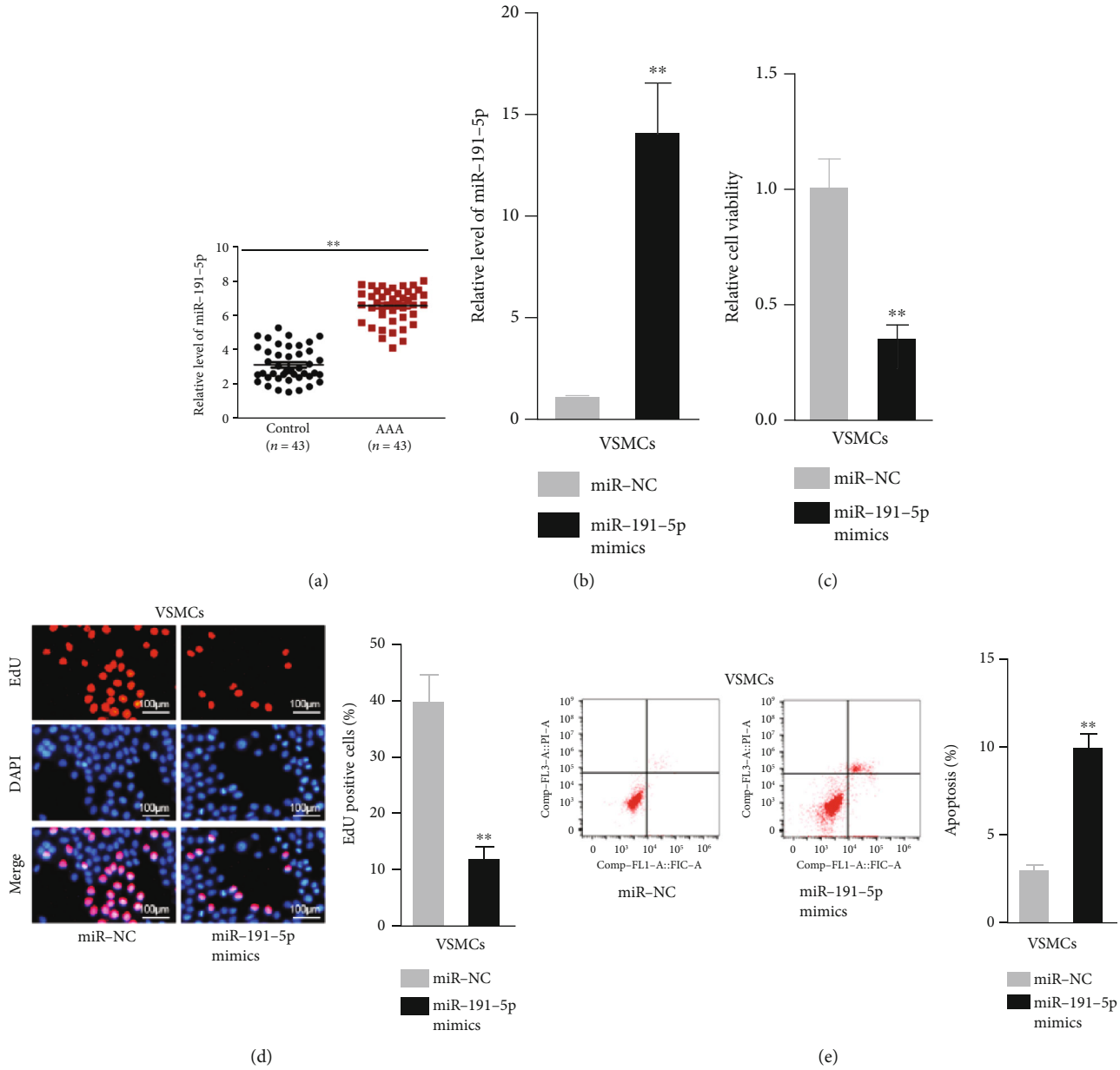

Figure 1: Continued.

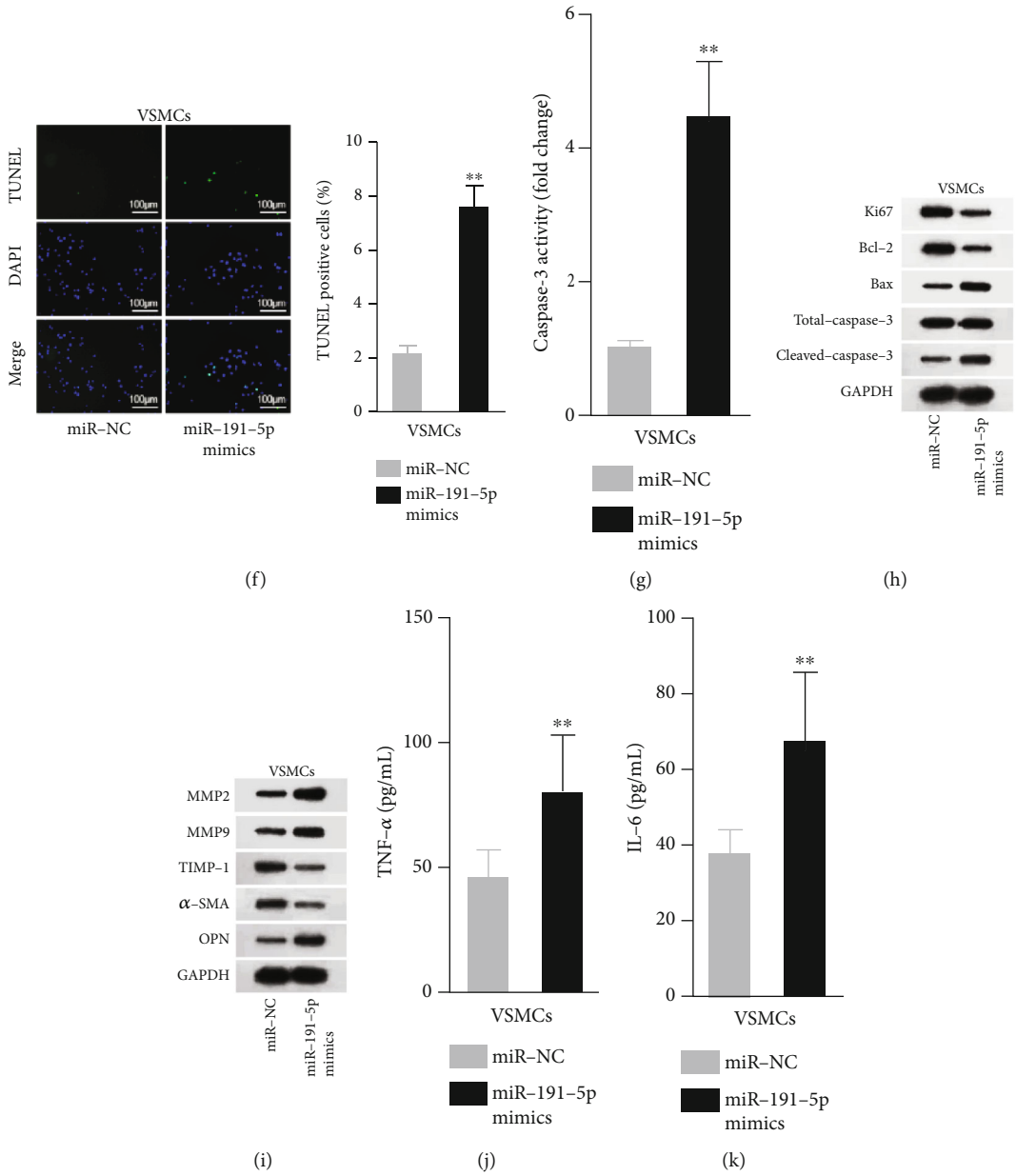

Figure 1: miR-191-5p augment influenced behaviors of VSMCs in AAA. (a) AAA tissues and control tissues were obtained for measurement of miR-191-5p level through qRT-PCR. (b) qRT-PCR data revealed the overexpression efficiency of miR-191-5p mimics in VSMCs. (c, d) CCK-8 and EdU staining assays were conducted for detecting the viability of VSMCs under miR-191-5p overexpression. (e–g) miR-191-5p mimic influence on VSMC apoptosis was assayed via flow cytometry, TUNEL staining, and caspase-3 activity detection assays. (h, i) Western blotting for the proliferation/apoptosis-associated proteins and proteins involved in ECM degradation after miR-191-5p mimic transfection. (j, k) Serum levels of the TNF-α and IL-6 were quantified by ELISA kits in VSMCs. Three biological replicates were involved for each experiment. $^{**}P < 0.01$.

ECM degradation and inflammation were also enhanced by the depletion of MIR503HG (Figures 2(n)–2(p)). Notably, MIR503HG interacted with miR-191-5p to promote the proliferation of VSMCs while impeding apoptosis, slowing down ECM degradation, and inhibiting inflammation.

3.3. PLCD1 Was the Downstream Target Underlying MIR503HG. To determine the downstream mRNA of miR-191-5p, after the prediction from microT, miRanda, miRmap, PicTar, PITA, and TargetScan, thirteen mRNAs were selected for further investigations (Figure 3(a)). Then, we found that the luciferase activity of PLCD1 3′UTR was most restrained by miR-191-5p elevation (Figure 3(b)). Moreover, PLCD1 was largely pulled down by Bio-miR-191-5p sense probe but not by Bio-NC or Bio-miR-191-5p antisense probe (Figure 3(c)). In addition, qRT-PCR analysis indicated that PLCD1 levels were relatively low in AAA tissues (Figure 3(d)). The negative association between PLCD1

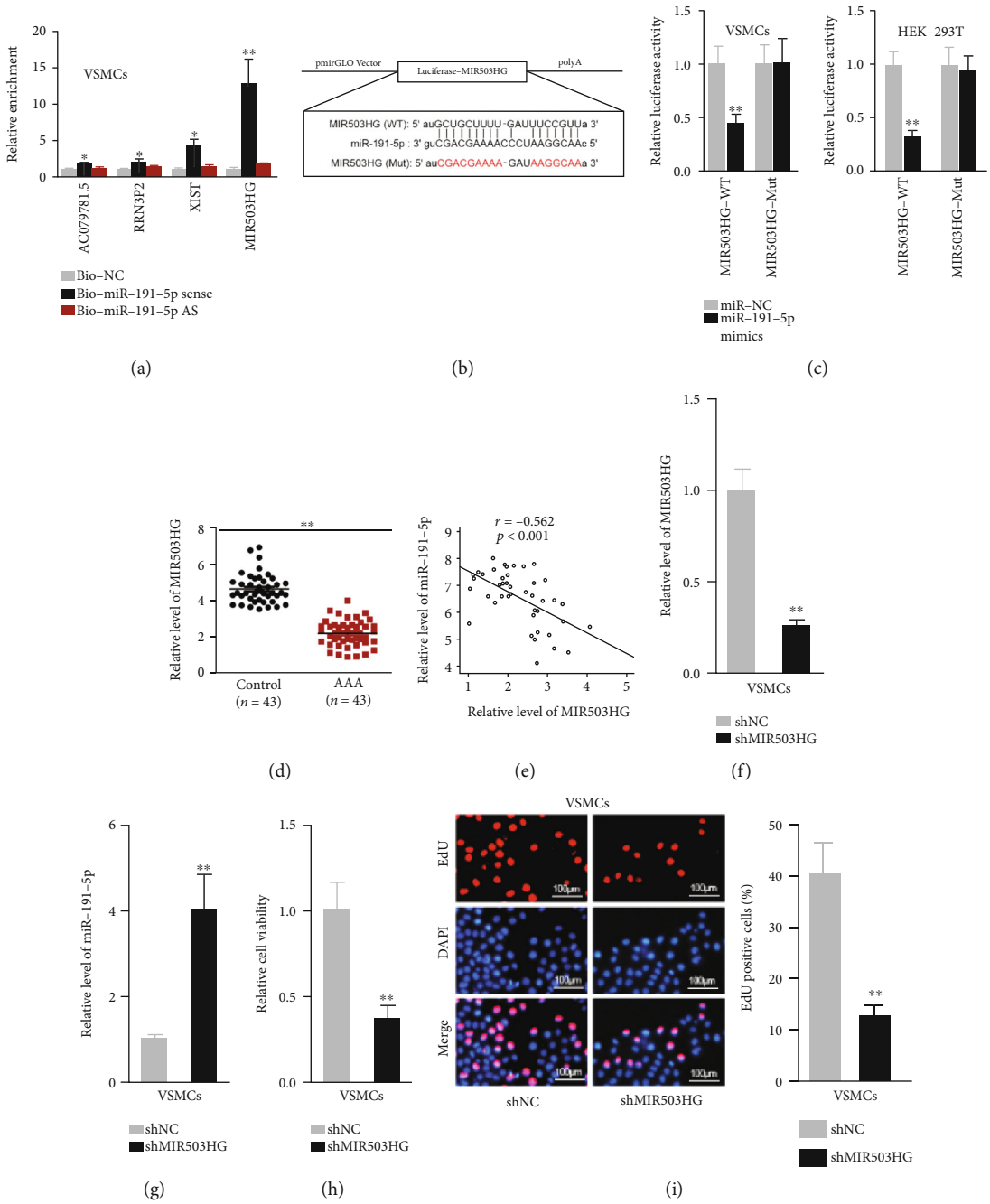

Figure 2: Continued.

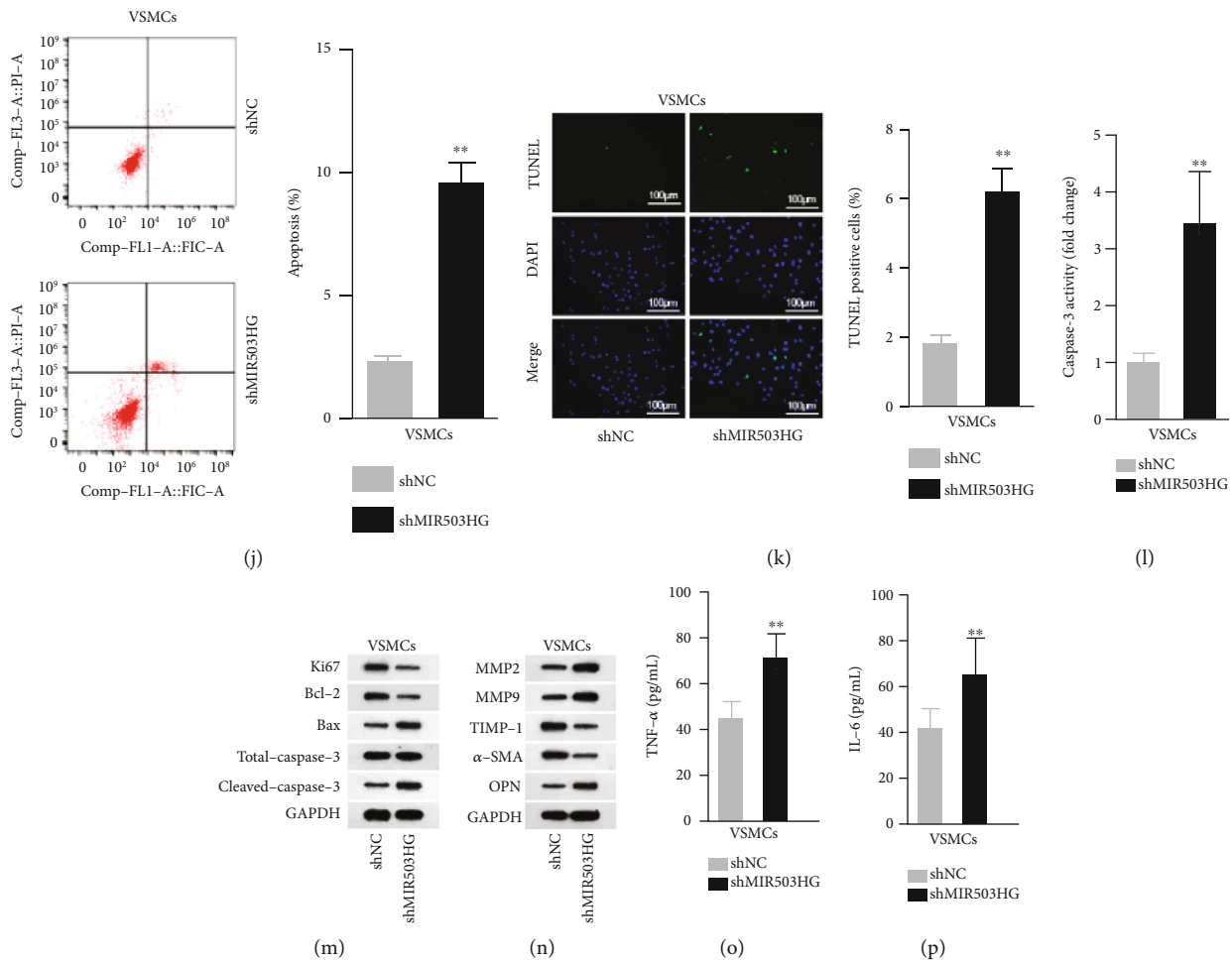

Figure 2: MIR503HG sponged miR-191-5p in VSMCs. (a) Pull-downs of biotinylated probes were quantified by qRT-PCR. (b, c) miR-191-5p binding sites on MIR503HG sequence (wild or mutant) were cloned into pmirGLO Vector for luciferase reporter assays. (d) MIR503HG expression in AAA tissues versus control samples was shown. (e) MIR503HG and miR-191-5p expression correlation was determined by Spearman's correlation analysis. (f) qRT-PCR was done for the silencing efficiency of shMIR503HG. (g) The miR-191-5p level in response to MIR503HG depletion was analyzed. (h, i) VSMC viability responding to shMIR503HG transfection was tested. (j–l) VSMC apoptosis after shMIR503HG transfection was analyzed. (m, n) The levels of proliferation/apoptosis-associated proteins and proteins involved in ECM degradation after silencing MIR503HG were evaluated. (o, p) Serum levels of inflammatory cytokines in shMIR503HG-regulated VSMCs were analyzed. Three biological replicates were involved for each experiment. $^{*}P < 0.05$ and $^{**}P < 0.01$.

and miR-191-5p, as well as the positive association between PLCD1 and MIR503HG, was demonstrated through Spearman's correlation analysis (Figure 3(e)). Thus, PLCD1 was confirmed as the mRNA target of miR-191-5p. PLCD1 expression was declined at both mRNA and protein levels by miR-191-5p elevation (Figure 3(f)). Subsequently, PLCD1 was knocked down via shPLCD1 transfection (Figure 3(g)). Inhibited PLCD1 refrained cell proliferation and facilitated cell apoptosis, ECM degradation, and inflammation in VSMCs (Figures 3(h)–3(p)). Collectively, miR-191-5p targeted PLCD1, which could enhance the proliferation but prevent the apoptosis, ECM degradation, and inflammation.

3.4. Upregulation of PLCD1 Countered the Impacts of miR-191-5p Increase on the Cellular Activities of VSMCs. To testify the regulatory function of miR-191-5p/PLCD1 axis in VSMCs, rescue assays were carried out. PLCD1 was overexpressed by PLCD1 overexpression vectors (Figure 4(a)). In CCK-8 and EdU assays, the miR-191-5p mimic-inhibited viability was rescued by upregulating PLCD1 (Figures 4(b) and 4(c)). As examined by flow cytometry, TUNEL, and caspase-3 activity kit, miR-191-5p promotion-accelerated apoptosis was reversed by elevation of PLCD1 (Figures 4(d)–4(f)). Western blot reconfirmed these results since the protein levels of Ki67 and Bcl-2 were lessened when miR-191-5p was elevated but reversed when PLCD1 was added. Bax and Cleaved-caspase-3 were augmented when miR-191-5p was overexpressed but recovered when PLCD1 was upregulated (Figure 4(g)). As for ECM, it was observed that miR-191-5p enhancement improved the protein levels of MMP2, MMP9, and OPN and lowered the protein levels of TIMP-1 and α-SMA, which was later neutralized by transfection of PLCD1 overexpression

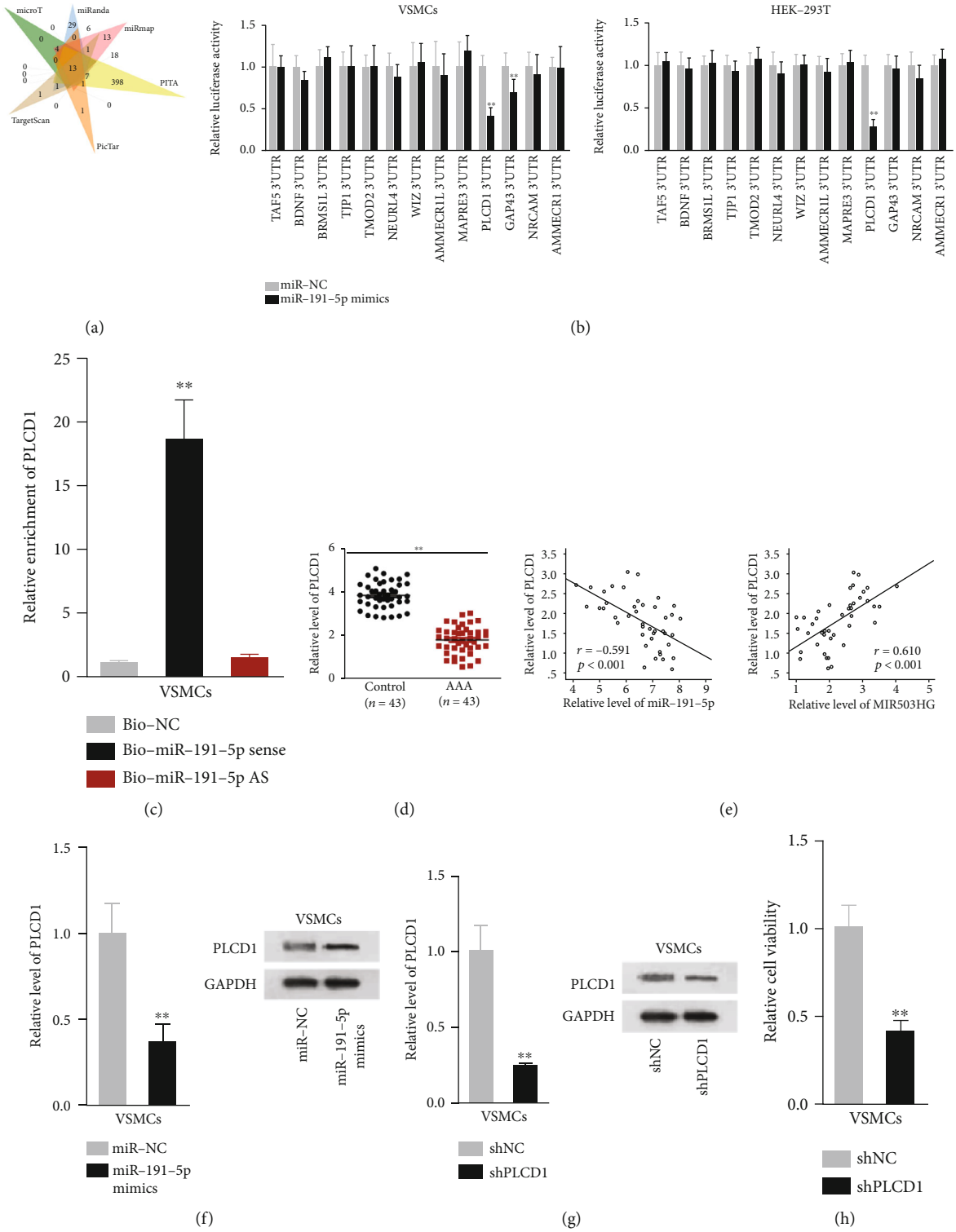

Figure 3: Continued.

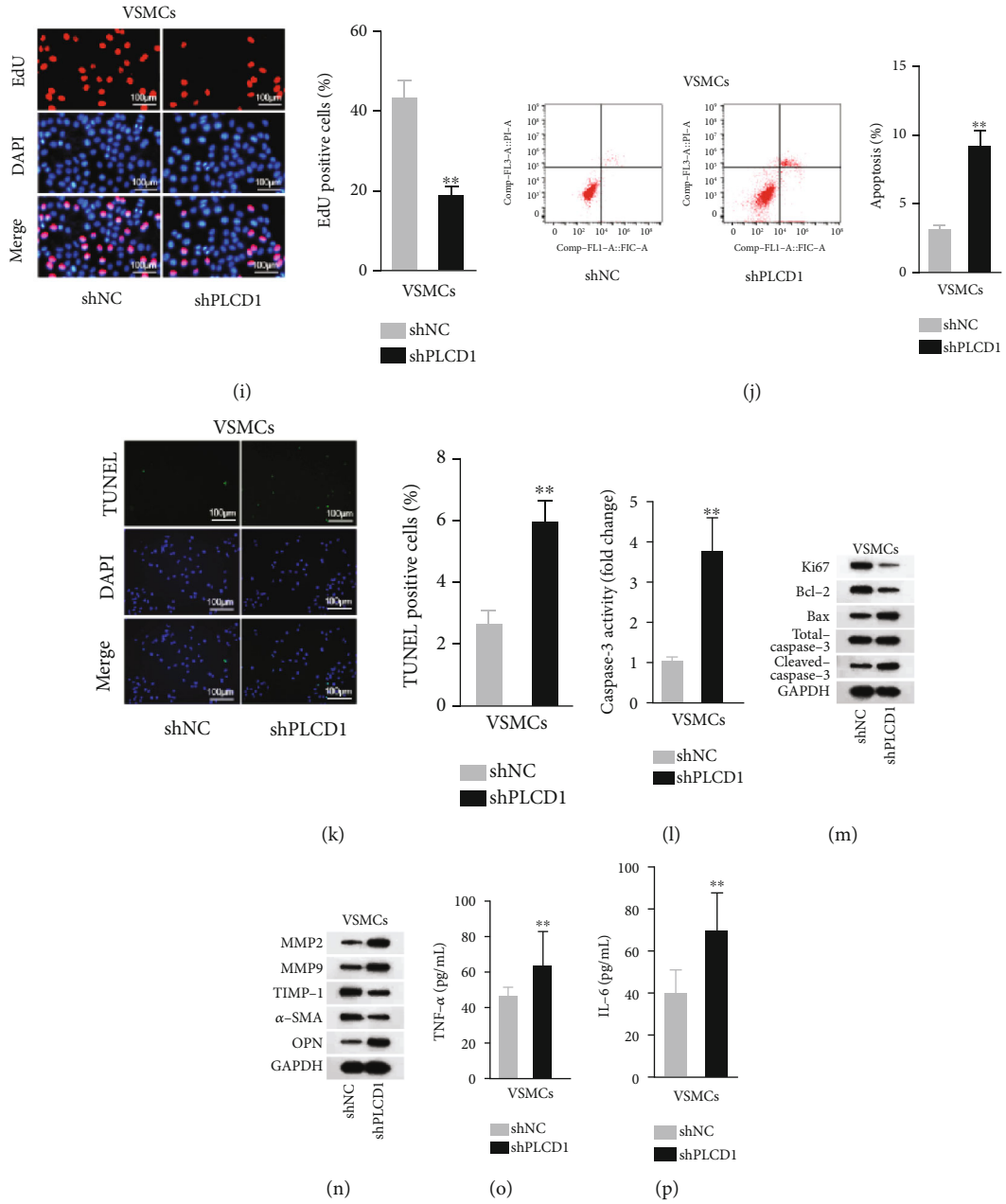

Figure 3: miR-191-5p targeted PLCD1 in VSMCs. (a) 13 possible mRNAs of miR-191-5p were screened out and presented as the Venn diagram. (b) Change in luciferase activity revealed the interplay of miR-191-5p and 13 possible mRNAs. (c) PLCD1 enrichment in pull-down complex by biotinylated miR-191-5p was measured. (d) PLCD1 levels in AAA tissues compared to the control group were measured. (e) Correlation between expressions of PLCD1 and miR-191-5p or MIR503HG was analyzed. (f, g) PLCD1 level in differentially transfected VSMCs was analyzed. (h–l) The regulation of PLCD1 knockdown on VSMC viability and apoptosis was assessed. (m, n) The levels of proliferation/apoptosis-associated proteins and proteins involved in ECM degradation under PLCD1 depletion were assessed. (o, p) Serum levels of inflammatory cytokines in shPLCD1-regulated VSMCs were measured. Three biological replicates were involved for each experiment. $^{**}P < 0.01$.

plasmids (Figure 4(h)). Besides, inflammation response facilitated by miR-191-5p increase was hindered by PLCD1 upregulation (Figures 4(i) and 4(j)). In conclusion, miR-191-5p exerted its function in VSMCs through PLCD1.

3.5. MIR503HG/miR-191-5p/PLCD1 Pathway Played an Important Part in the AAA Development. Subsequently, the function of MIR503HG/miR-191-5p/PLCD1 axis was validated. Before rescue experiments, miR-191-5p was silenced through transfection of miR-191-5p inhibitor (Figure 5(a)). After conducting a series of assays, we confirmed that cell viability weakened by MIR503HG knockdown was facilitated by miR-191-5p silence or PLCD1 enhancement (Figures 5(b) and 5(c)), while cell apoptosis activated due to MIR503HG repression was impaired with miR-191-5p depletion or PLCD1 increment, as determined by flow

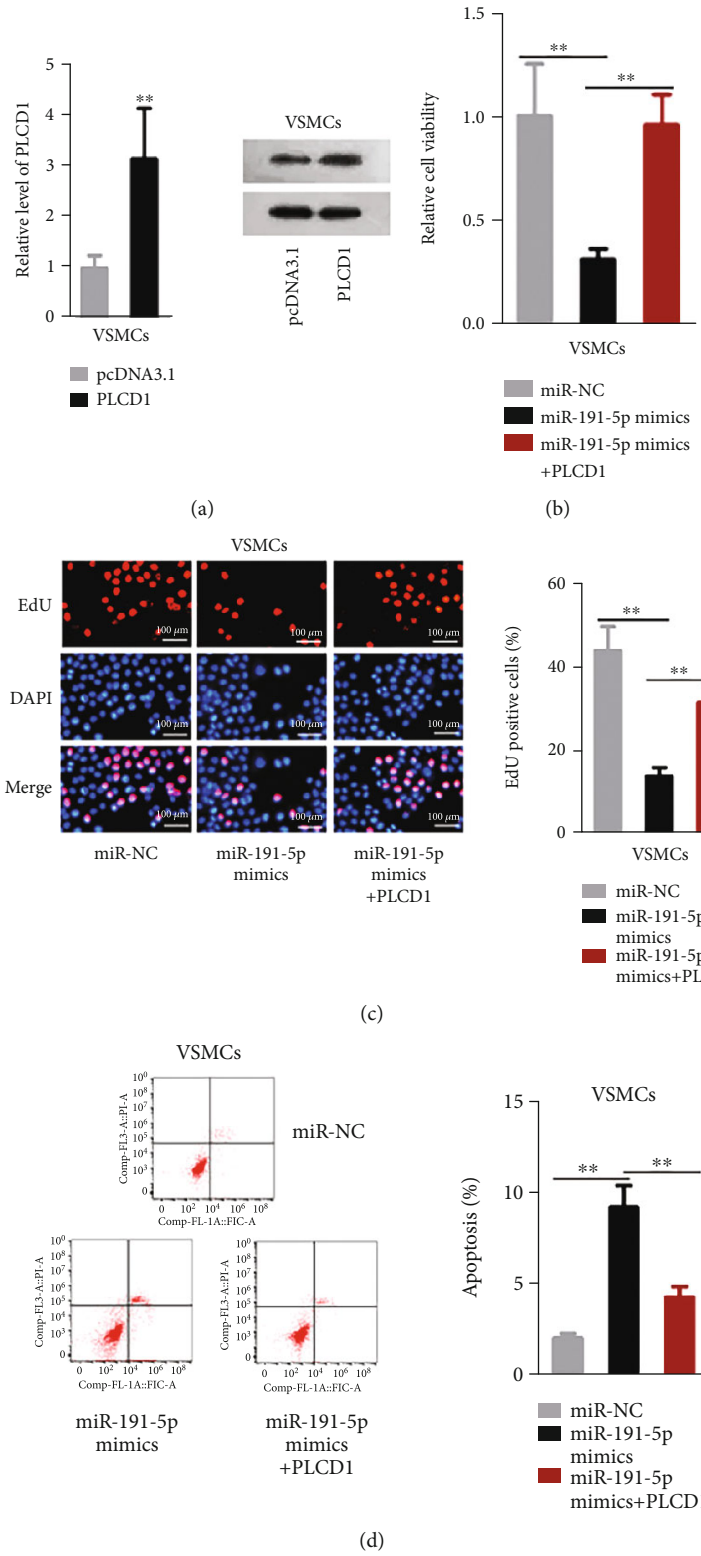

Figure 4: Continued.

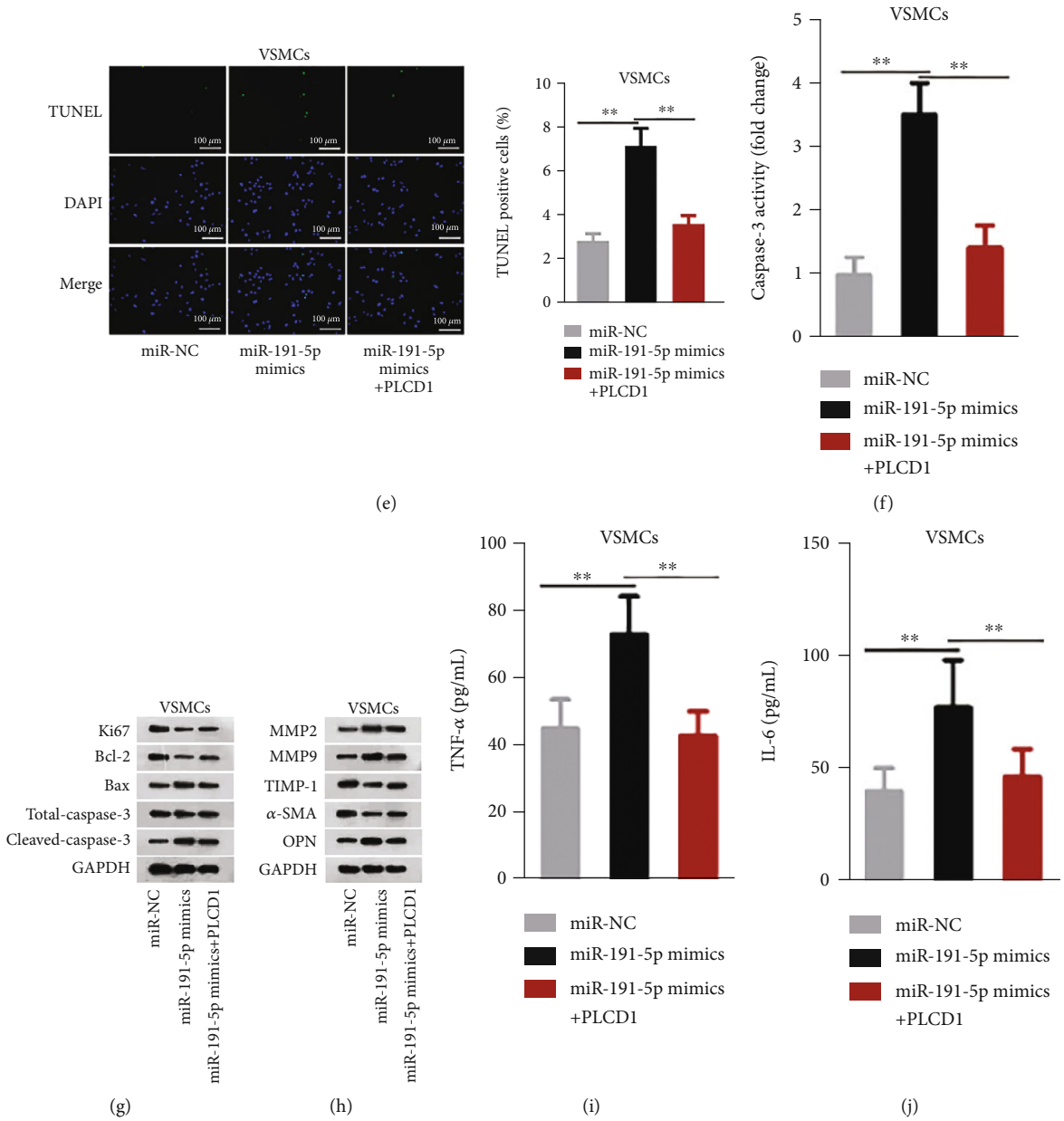

Figure 4: PLCD1 overexpression weakened miR-191-5p mimic-mediated AAA progression. (a) The overexpression efficiency of pcDNA3.1/PLCD1 (PLCD1) in VSMCs was evaluated. (b–f) The viability and apoptosis in three groups of differentially transfected VSMCs were analyzed. (g, h) The levels of proliferation/apoptosis-related proteins and proteins related to ECM degradation in each group were tested. (i, j) Serum levels of inflammatory cytokines in each sample. Three biological replicates were involved for each experiment. $^{**}P < 0.01$.

cytometry, TUNEL, and caspase-3 activity kit (Figures 5(d)–5(f)). We also detected that the reduction in Ki67 and Bcl-2 proteins and increase in Bax and Cleaved-caspase-3 proteins by MIR503HG silencing were abrogated by miR-191-5p inhibitor or PLCD1 (Figure 5(g)). Additionally, ECM degradation and inflammation boosted by depletion of MIR503HG were offset by knockdown of miR-191-5p or addition of PLCD1. In the shMIR503HG group, protein levels of MMP2, MMP9, and OPN as well as TNF-α and IL-6 levels were augmented, and protein levels of TIMP-1 and α-SMA were lowered compared with the control group. These phenomena were counteracted by cotransfection of miR-191-5p inhibitor or of PLCD1 (Figures 5(h)–5(j)). In summary, MIR503HG negatively mediated the apoptosis, ECM degradation, and inflammation in VSMCs via miR-191-5p/PLCD1.

4. Discussion

The apoptosis and phenotypic shift of VSMCs and inflammation response are noted features of AAA. More apoptotic and synthetic VSMCs as well as induced inflammation are

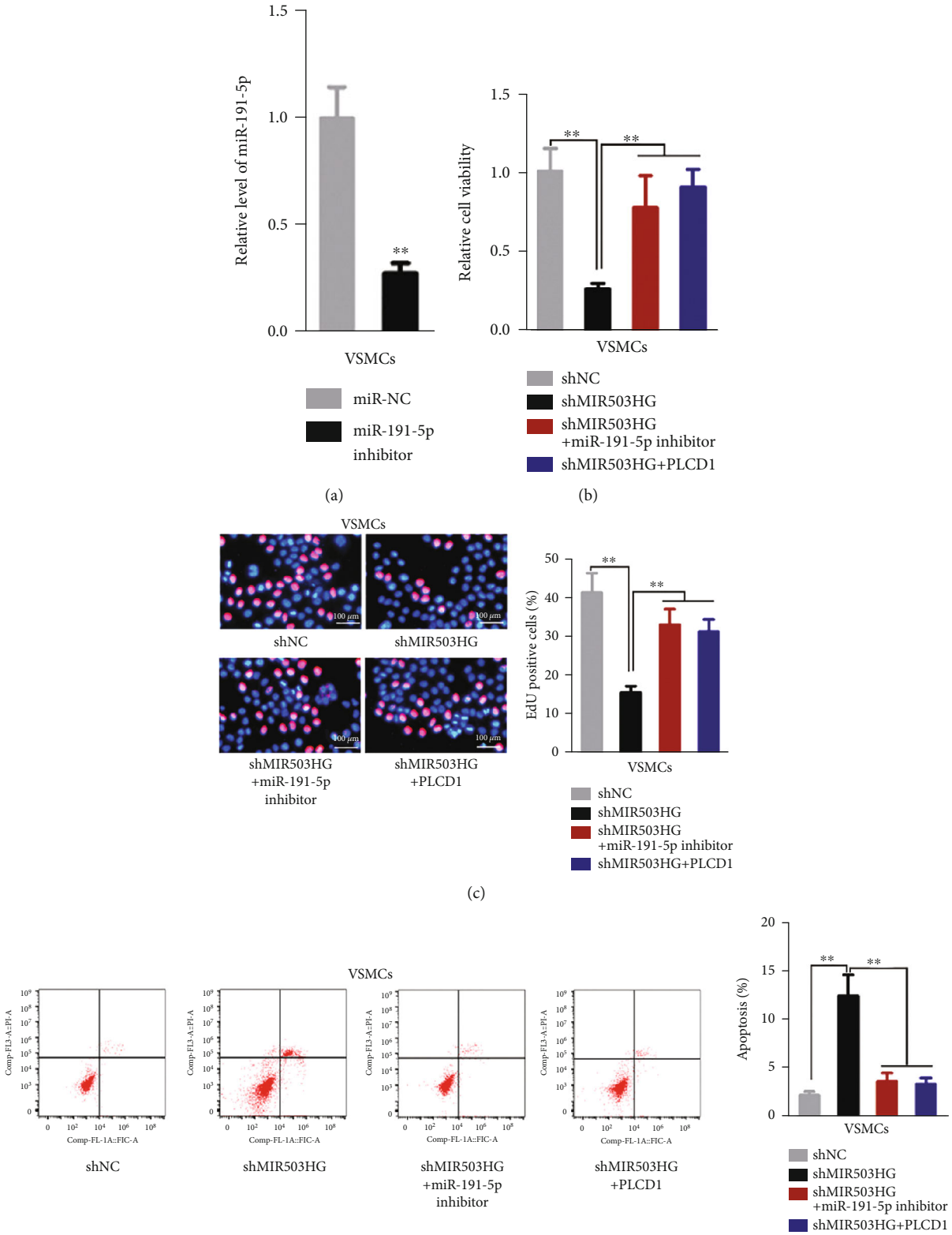

Figure 5: Continued.

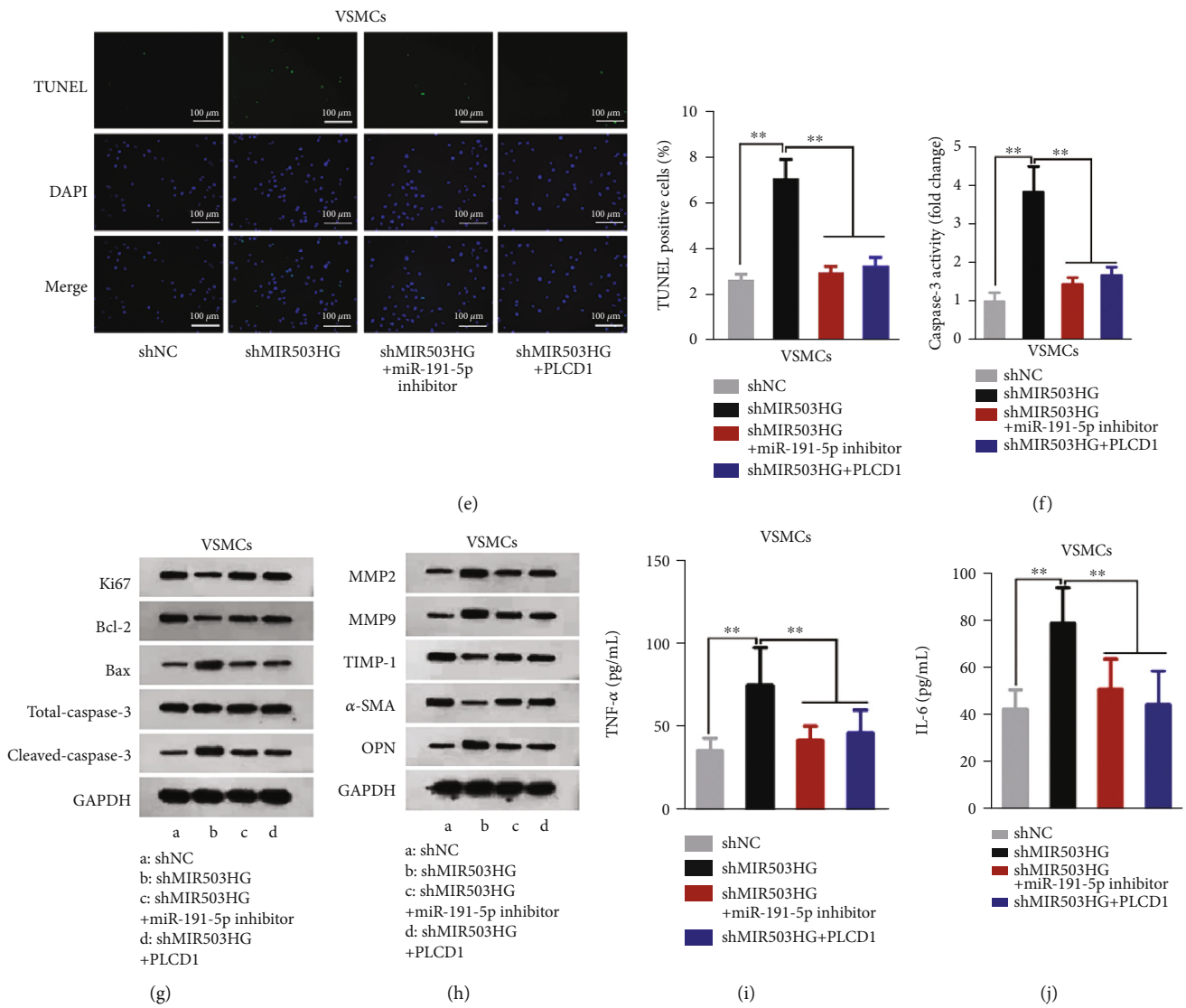

Figure 5: MIR503HG influenced AAA progression via miR-191-5p/PLCD1. (a) qRT-PCR assessed miR-191-5p inhibitor efficiency in VSMCs. (b–f) The viability and apoptotic capacities of VSMCs in four differently transfected groups were analyzed. (g, h) The levels of proliferation/apoptosis-correlated proteins and proteins associated with ECM degradation in each treatment group were detected. (i, j) Serum levels of the inflammatory cytokines in 4 groups were quantified. Three biological replicates were involved for each experiment. $^{**}P < 0.01$.

observed in AAA progression. The apoptotic VSMCs result in the numerous loss of contractile cells and thus promoting the expansion of the abdominal aortic wall [27]. Furthermore, it has been revealed that inflammation could secrete MMP, which can further degrade the components of the ECM and cause ECM disruption. The TIMP family has been documented to strictly regulate MMP family members [28]. Also, a synthetic phenotype of VSMCs occurs due to the imbalance of synthetic and contractile phenotype. α-SMA is a biomarker of contractile VSMCs, and OPN is a biomarker of synthetic VSMCs. In this study, all these factors were tested to reflect the functions of genes in AAA.

Past studies have excavated that miR-191-5p was elevated in aortic aneurysm, but its function role in AAA has never been explored [19, 20]. Hence, we attempted to explicitly figure out the role of miR-191-5p in AAA. In this paper, elevated miR-191-5p expression was discovered in AAA tissues. In addition, miR-191-5p promotion repressed cell viability, enhanced cell apoptosis, and enhanced ECM disruption and inflammation in VSMCs. This was the first time that miR-191-5p was demonstrated as a contributor for AAA. From starBase, we obtained four lncRNAs targeting miR-191-5p. MIR503HG was the most possible lncRNA binding to miR-191-5p in VSMCs, which was downregulated in AAA tissues and had negative regulation on miR-191-5p. In consistent with the antioncogenic role of MIR503HG played in tumors [21–23], the role of MIR503HG in VSMCs was proven to be suppressive. Then, we continued to probe into the downstream factor that MIR503HG/miR-191-5p axis targeted in VSMCs. Among

the thirteen targets gained from the Venn diagram, pPLCD1 was screened out for its significantly declined luciferase activity under the improvement of miR-191-5p. PLCD1 was previously disclosed to inhibit diseases, airway smooth muscle hypertrophy, colorectal cancer, and breast cancer contained [29–31]. PLCD1 as a target of miR-191-5p was affirmed through mechanism experiments. PLCD1 also exerted suppressive function in VSMCs. The functions of miR-191-5p/PLCD1 axis and MIR503HG/miR-191-5p/PLCD1 axis in VSMCs were verified via rescue assays.

Totally, in AAA progression, the sponge of miR-191-5p by MIR503HG was weakened, and therefore, PLCD1 expression was decreased, resulting in weakened viability, facilitated apoptosis, and enhanced ECM disruption and inflammation. Addition of MIR503HG might be a novel therapeutic strategy for patients with AAA.

Data Availability

The data used to support the research findings are included within this article.

Conflicts of Interest

The authors declare no conflict of interest.

Authors' Contributions

Ye Tian, Xinxi Li, and Chao Bai contributed equally to this work as co-first authors.

References

[1] J. Liu, S. Wei Zuo, Y. Li et al., "Hyperhomocysteinaemia is an independent risk factor of abdominal aortic aneurysm in a Chinese Han population," *Scientific Reports*, vol. 6, no. 1, p. 17966, 2016.

[2] J. H. Lindeman, H. Abdul-Hussien, J. H. van Bockel, R. Wolterbeek, and R. Kleemann, "Clinical trial of doxycycline for matrix metalloproteinase-9 inhibition in patients with an abdominal aneurysm: doxycycline selectively depletes aortic wall neutrophils and cytotoxic T cells," *Circulation*, vol. 119, no. 16, pp. 2209–2216, 2009.

[3] M. J. Bown, G. T. Jones, S. C. Harrison et al., "Abdominal aortic aneurysm is associated with a variant in low-density lipoprotein receptor-related protein 1," *American Journal of Human Genetics*, vol. 89, no. 5, pp. 619–627, 2011.

[4] J. Golledge, "Abdominal aortic aneurysm: update on pathogenesis and medical treatments," *Nature Reviews Cardiology*, vol. 16, no. 4, pp. 225–242, 2019.

[5] J. Raffort, F. Lareyre, M. Clément, R. Hassen-Khodja, G. Chinetti, and Z. Mallat, "Monocytes and macrophages in abdominal aortic aneurysm," *Nature Reviews. Cardiology*, vol. 14, no. 8, pp. 457–471, 2017.

[6] C. A. Lyon, H. Williams, R. Bianco et al., "Aneurysm severity is increased by combined Mmp-7 deletion and N-cadherin mimetic (EC4-Fc) over-expression," *Scientific Reports*, vol. 7, no. 1, p. 17342, 2017.

[7] H. Peng, K. Zhang, Z. Liu et al., "VPO1 modulates vascular smooth muscle cell phenotypic switch by activating extracellular signal-regulated kinase 1/2 (ERK 1/2) in abdominal aortic aneurysms," *Journal of the American Heart Association*, vol. 7, no. 17, article e010069, 2018.

[8] B. Bánfai, H. Jia, J. Khatun et al., "Long noncoding RNAs are rarely translated in two human cell lines," *Genome Research*, vol. 22, no. 9, pp. 1646–1657, 2012.

[9] T. T. Ho, N. Zhou, J. Huang et al., "Targeting non-coding RNAs with the CRISPR/Cas9 system in human cell lines," *Nucleic Acids Research*, vol. 43, no. 3, article e17, 2015.

[10] M. Mallardo, P. Poltronieri, and O. F. D'Urso, "Non-protein coding RNA biomarkers and differential expression in cancers: a review," *Journal of Experimental & Clinical Cancer Research*, vol. 27, no. 1, p. 19, 2008.

[11] L. Li, P. C. van Breugel, F. Loayza-Puch et al., "LncRNA-OIS1 regulates DPP4 activation to modulate senescence induced by RAS," *Nucleic Acids Research*, vol. 46, no. 8, pp. 4213–4227, 2018.

[12] Y. Kurihara and Y. Watanabe, "Arabidopsis micro-RNA biogenesis through Dicer-like 1 protein functions," *Proceedings. National Academy of Sciences. United States of America*, vol. 101, no. 34, pp. 12753–12758, 2004.

[13] D. Y. Li, A. Busch, H. Jin et al., "Abstract 314: H19 induces abdominal aortic aneurysm development and progression," *Circulation*, vol. 38, Supplement 1, 2018.

[14] Y. Wang, W. Nie, K. Yao, Z. Wang, and H. He, "Interleukin 6 induces expression of NADPH oxidase 2 in human aortic endothelial cells via long noncoding RNA MALAT1," *Pharmazie*, vol. 71, no. 10, pp. 592–597, 2016.

[15] L. Maegdefessel, J. M. Spin, U. Raaz et al., "miR-24 limits aortic vascular inflammation and murine abdominal aneurysm development," *Nature Communications*, vol. 5, no. 1, p. 5214, 2014.

[16] C. W. Kim, S. Kumar, D. J. Son, I. H. Jang, K. K. Griendling, and H. Jo, "Prevention of abdominal aortic aneurysm by anti-microRNA-712 or anti-microRNA-205 in angiotensin II-infused mice," *Arteriosclerosis, Thrombosis, and Vascular Biology*, vol. 34, no. 7, pp. 1412–1421, 2014.

[17] J. Vistbakka, M. L. Sumelahti, T. Lehtimäki, I. Elovaara, and S. Hagman, "Evaluation of serum miR-191-5p, miR-24-3p, miR-128-3p, and miR-376c-3 in multiple sclerosis patients," *Acta Neurologica Scandinavica*, vol. 138, no. 2, pp. 130–136, 2018.

[18] B. Chen, Z. Y. Zheng, J. Z. Yang, and X. G. Li, "MicroRNA-191-5p promotes the development of osteosarcoma via targeting EGR1 and activating the PI3K/AKT signaling pathway," *European Review for Medical and Pharmacological Sciences*, vol. 23, no. 9, pp. 3611–3620, 2019.

[19] E. J. R. Tenorio, A. F. F. Braga, D. P. D. C. Tirapelli, M. S. Ribeiro, C. E. Piccinato, and E. E. Joviliano, "Expression in whole blood samples of miRNA-191 and miRNA-455-3p in patients with AAA and their relationship to clinical outcomes after endovascular repair," *Annals of Vascular Surgery*, vol. 50, pp. 209–217, 2018.

[20] S. Licholai, M. Blaż, B. Kapelak, and M. Sanak, "Unbiased profile of microRNA expression in ascending aortic aneurysm tissue appoints molecular pathways contributing to the pathology," *The Annals of Thoracic Surgery*, vol. 102, no. 4, pp. 1245–1252, 2016.

[21] J. Fu, G. Dong, H. Shi et al., "LncRNA MIR503HG inhibits cell migration and invasion via miR-103/OLFM4 axis in triple negative breast cancer," *Journal of Cellular and Molecular Medicine*, vol. 23, no. 7, pp. 4738–4745, 2019.

[22] F. Qiu, M. R. Zhang, Z. Zhou, J. X. Pu, and X. J. Zhao, "lncRNA MIR503HG functioned as a tumor suppressor and inhibited cell proliferation, metastasis and epithelial-mesenchymal transition in bladder cancer," *Journal of Cellular Biochemistry*, vol. 120, no. 6, pp. 10821–10829, 2019.

[23] D. Chuo, F. Liu, Y. Chen, and M. Yin, "LncRNA MIR503HG is downregulated in Han Chinese with colorectal cancer and inhibits cell migration and invasion mediated by TGF-β2," *Gene*, vol. 713, article 143960, 2019.

[24] K. J. Livak and T. D. Schmittgen, "Analysis of relative gene expression data using real-time quantitative PCR and the $2^{-\Delta\Delta\_C\_}{}_{T}$ method," *Methods*, vol. 25, no. 4, pp. 402–408, 2001.

[25] X. Chen, R. Mao, W. Su et al., "Circular RNA circHIPK3 modulates autophagy via MIR124-3p-STAT3-PRKAA/AMPKα signaling in STK11 mutant lung cancer," *Autophagy*, vol. 16, no. 4, pp. 659–671, 2020.

[26] P. Pittayapruek, J. Meephansan, O. Prapapan, M. Komine, and M. Ohtsuki, "Role of matrix metalloproteinases in photoaging and photocarcinogenesis," *International Journal of Molecular Sciences*, vol. 17, no. 6, p. 868, 2016.

[27] J. H. Lee, S. T. Choi, and Y. J. Kang, "Kahweol, a diterpenoid molecule, inhibits CTGF-dependent synthetic phenotype switching and migration in vascular smooth muscle cells," *Molecules*, vol. 26, no. 3, p. 640, 2021.

[28] I. Porcellato, L. Menchetti, C. Brachelente et al., "Feline injection-site sarcoma," *Veterinary Pathology*, vol. 54, no. 2, pp. 204–211, 2017.

[29] S. K. Sasse, V. Kadiyala, T. Danhorn, R. A. Panettieri Jr., T. L. Phang, and A. N. Gerber, "Glucocorticoid receptor ChIP-seq identifies PLCD1 as a KLF15 target that represses airway smooth muscle hypertrophy," *American Journal of Respiratory Cell and Molecular Biology*, vol. 57, no. 2, pp. 226–237, 2017.

[30] Q. Xiang, X. He, J. Mu et al., "The phosphoinositide hydrolase phospholipase C delta1 inhibits epithelial- mesenchymal transition and is silenced in colorectal cancer," *Journal of Cellular Physiology*, vol. 234, no. 8, pp. 13906–13916, 2019.

[31] Q. Shao, X. Luo, D. Yang et al., "Phospholipase Cδ1 suppresses cell migration and invasion of breast cancer cells by modulating KIF3A-mediated ERK1/2/β- catenin/MMP7 signalling," *Oncotarget*, vol. 8, no. 17, pp. 29056–29066, 2017.

Hindawi
Mediators of Inflammation
Volume 2023, Article ID 1958046, 9 pages
https://doi.org/10.1155/2023/1958046

Research Article

Investigation of the Effects of Some Cardiovascular Drugs on Angiogenesis by Transgenic Zebrafish

Hui Lv,[1] **Bo Liu**,[2] **and Yongwen Qin**[3]

[1]*Department of Cardiovascular Disease, The Second Affiliated Hospital of Shanxi Medical University, Taiyuan, Shanxi 030001, China*
[2]*Department of Cardiovascular Disease, Xinhua Hospital Affiliated to Shanghai Jiaotong University School of Medicine, Shanghai 200433, China*
[3]*Department of Cardiovascular Disease, Changhai Hospital Affiliated to The Second Military Medical University, Shanghai 200433, China*

Correspondence should be addressed to Yongwen Qin; qyw2009@sina.cn

Received 20 June 2022; Revised 16 September 2022; Accepted 24 September 2022; Published 24 April 2023

Academic Editor: Md Sayed Ali Sheikh

Introduction. Angiogenesis contributes to the pathophysiology of cardiovascular disease (CVD). Some cardiovascular drugs used in the treatment of CVD have an effect on the process of angiogenesis. *Methods.* Transgenic Tg (flk1: EGFP) zebrafish embryos were used to identify the effects of some cardiovascular drugs on angiogenesis during vertebral development *in vivo*. Zebrafish embryos at a one-cell stage or two-cell stage were cultured with embryo medium containing cardiovascular drugs at a final solvent concentration of 0.5% (V/V) dimethyl sulfoxide (DMSO) for 24 hours in 24-well plates. *Results.* We found that 6 drugs including isosorbide mononitrate, amlodipine, bisoprolol fumarate, carvedilol, irbesartan, and rosuvastatin calcium may affect angiogenesis by vascular endothelial growth factor (VEGF) signaling pathway. *Conclusion.* These new findings of some cardiovascular drugs should improve the treatment of cardiovascular diseases.

1. Introduction

Angiogenesis is an important part of the pathophysiology of cardiovascular diseases (CVD) [1–3]. Among various cardiovascular drugs commonly used to treat CVD, some are known to affect the process of angiogenesis. For instance, statins [4], which are widely used in the treatment of hyperlipidemia and coronary heart disease (CHD), can inhibit angiogenesis and reduce the rate of revascularization. Nifedipine [5], a calcium antagonist used to control hypertension, can induce human coronary artery endothelial cells to form capillary-like tubes and increase the total capillary density of the hamster-dilated cardiomyopathic heart. Besides, angiotensin-converting enzyme inhibitor (ACEI) can induce angiogenesis through upregulating fibroblast growth factor-2 (FGF-2) in coronary endothelium [6]. Moreover, SH-containing ACEI zofenoprilat triggers angiogenesis by improving the availability of hydrogen sulfide [7]. However, whether other cardiovascular drugs have this angiogenic or antiangiogenic activity is unclear.

In order to study angiogenesis *in vivo*, zebrafish (*Danio rerio*) provides an excellent model for the transparency of its embryo, which can direct observe vertebral development [8]. Transgenic zebrafish, such as zebrafish with green fluorescence protein (GFP) gene, shows strong GFP expression in vascular endothelial cells which can visually screen vascular pattern defects and observe the changes of vasculogenesis [9]. In this study, we used transgenic zebrafish as a model to test the angiogenesis or antiangiogenesis effects of 6 cardiovascular drugs with known pharmacological activities in the human body (Table 1).

2. Materials and Methods

2.1. Embryo Collection. Transgenic zebrafish were raised following standard care and maintenance protocols of a 14 : 10

Table 1: Blood compound concentration in human.

Tested agents (CAS number)	Pharmacological class	Known pharmacological activities	Drug concentration range
Isosorbide mononitrate (16051-77-7)	Nitrate-class drug which can release nitric oxide and active cGMP in the endothelium cell.	Dilate the blood vessels to reduce blood pressure.	50-1000 μg/ml
Digoxin (20830-75-5)	Decrease the function of the Na^+/K^+ATPase pump so as to raise the calcium concentration in myocardiocytes.	Slightly increase myocardial contractility and decrease the heart rate and blood pressure.	30-2000 ng/ml
Nitroglycerin (55-63-0)	Nitrate-class drugs.	Vasodilation widening of the blood vessels.	3-100 ng/ml
Bisoprolol fumarate (104344-23-2)	Selective type β_1 adrenergic receptor blocker in the heart muscle cells and heart conduction tissue.	Less contractility of the heart muscle and lowered heart rate.	10-500 ng/ml
Metoprolol Tartrate (56392-17-7)	Selective β1 receptor blocker.	Decrease the heart rate and contraction.	0.05-100 μg/ml
Amiodarone hydrochloride (19774-82-4)	Class III antiarrhythmic agent and prolongs phase 3 of the cardiac action potential.	Slows intracardiac conduction of the cardiac action potential.	0.5-4 μg/ml
Lidocaine hydrochloride (137-58-6)	A common local anesthetic and antiarrhythmic drug.	Class 1B antiarrhythmic drug, decreases the ventricular rate.	1-100 μg/ml
Propafenone hydrochloride (34183-22-7)	Slowing the influx of sodium ions into the cardiac muscle cells.	Decrease in excitability of the cardiac muscle cells.	500-2000 ng/ml
Amlodipine (88150-42-9)	Dihydropyridine class, a long-acting calcium channel blocker.	Relax the smooth muscle in the arterial wall, decreasing total peripheral resistance and hence reducing blood pressure.	5-1000 ng/ml
Carvedilol (72956-09-3)	Beta blockers (β1, β2) and alpha blocker (α1).	Slow the heart rhythm and reduce the force of the heart's pumping. Lower blood pressure and reduce heart failure.	10-200 ng/ml
Dopamine hydrochloride (62-31-7)	Catecholamine neurotransmitter.	Increased heart rate and blood pressure.	5-100 μg/ml
Irbesartan (138402-11-6)	Angiotensin II receptor antagonists.	Modulate the renin–angiotensin-aldosterone system.	0.04-4 μg/ml
Spironolactone (52-01-7)	Synthetic steroid.	Inhibits the effect of aldosterone and decreases the reabsorption of sodium and water.	0.1-1000 μg/ml
Epinephrine hydrochloride (55-31-2)	A hormone and a neurotransmitter.	Increases heart rate and constricts blood vessels.	0.01-2 μg/ml
Rosuvastatin Calcium (147098-20-2)	A member of the drug class of statins.	A competitive inhibitor of the enzyme HMG-CoA reductase, reduce the level of LDL cholesterol.	10-2000 ng/ml
Clopidogrel (113665-84-2)	Thienopyridine class antiplatelet agent, irreversibly inhibiting a receptor called P2Y12, an adenosine diphosphate ADP chemoreceptor.	Inhibit blood clots.	15-1000 μg/ml
Ticlopidine (55142-85-3)	An antiplatelet drug in the thienopyridine family.	Inhibits platelet aggregation and prolongs bleeding time.	10-200 μg/ml

light : dark cycle [10]. Embryos were obtained by natural spawning, staged according to established criteria [11], and raised in the embryo culture medium E3M (containing 5 mM NaCl, 0.17 mM KCl, 0.33 mM $CaCl_2$, 0.33 mM Mg_2SO_4, 0.7 mM HEPES, and 10^{-5}% methylene blue (pH 7.2) with a conductivity of 672 μS and dissolved oxygen of 8.2 mg/l) in an incubator at 28.5°C. All the assays were performed at 25-28°C. Animal experiments were carried out in accordance with the guiding principles of the Animal Experimentation Ethics Committee of Second Military Medical University.

2.2. Drug Treatment. Seventeen cardiovascular drugs with known pharmacological activities in the human body were selected for the test (Table 1). The reagents were dissolved in DMSO and added to the embryo medium at a final DMSO concentration of 0.5%. One-cell stage or two-cell stage embryos were immersed in embryo medium

containing drugs in 0.5% (V/V) DMSO final solvent concentration for 24 hours in a 24-well plate. Each compound was tested at six concentrations according to human blood concentration (Table 1). We used 20 embryos in each group to obtain higher throughput and less variability.

2.3. Angiogenic Function Assessment. In order to improve the screening process and better demonstrate the blood vessels in embryos, we used a stable transgenic Tg (fli-1: EGFP) zebrafish embryo, in which GFP was expressed in all endothelial cells of the vasculature in the intersegmental blood vessels (ISVs). Embryos were exposed to a single concentration of reagent for 24 hours and then dechorionated and fixed in methylcellulose (0.5%, m/V). After fixation, the vascular development of embryos was examined by a LEICA 205FA microscope. Antiangiogenic and angiogenic effects are defined as significant inhibition or enhancement of mature ISV formation, which normally connects the dorsal aorta and dorsal longitudinal anastomotic vessel (DLAV) in living embryos. The length of ISVs was calculated by LEICA 205FA software through point-to-point distance. The number of ISVs was calculated from photos taken under a microscope. ISV length and number were used to quantify angiogenesis.

2.4. Cell Line and Cell Culture. Human Umbilical Vein Endothelial Cells (HUVECs) (ATCC, Manassas, USA) were cultured in DMEM media (Invitrogen) with 2% fetal bovine serum (FBS), 100 U/ml penicillin and 100 μg/ml streptomycin at 37°C with 5% CO_2. Then, HUVECs were passaged 3 times a week.

2.5. Quantitative Reverse Transcriptase-Polymerase Chain Reaction (qRT-PCR). The VEGF expression level in HUVECs was determined by qRT-PCR. Briefly, total RNA was extracted from 1×10^5 HUVECs from passages 3 using TRIzol reagent (Takara Biotechnology, Dalian, China). Besides, NanoDrop 2000 (Thermo Fisher Scientific, Waltham, MA, USA) was utilized to analyze the quality and integrity of RNA. Next, 2 μg RNA of each sample was reverse transcribed into cDNA by the PrimeScript™ 1st Strand cDNA Synthesis Kit (Takara Biotechnology). Subsequently, the amount of target RNA was normalized to that of internal control (GAPDH) and given by $2^{-\triangle\triangle Ct}$ relative to the control sample. Primers used in qRT-PCR were listed as follows (shown 5′-3′): VEGF F: TGGACCCTGGCTTT ACTGCTG and R: GGCAATAGCTGCGCTGGTAGA; GAPDH F: GAEAACTTTGGCATCGTGGA and R: TGCA GGGATGATGTTCTGG.

2.6. Statistical Analysis. The data of the current study were analyzed using a mixed design analysis of variance between-subject factors of drugs, drug dose, and timing of drug administration. All experiments were repeated for at least three times. Next, the values were presented as mean ± standard definition (SD). And statistical analysis was performed with Microsoft Excel software. Statistical significance was assessed using Student's t-test to compare the vehicle control group with a drug-treated group. All the statistical tests were two-tailed. A P value less than 0.05 was considered to indicate a statistical significance.

3. Results

3.1. Effect of 0.5% DMSO on Angiogenesis in Zebrafish. To maximize drug dissolution, we used 0.5% DMSO as the drug carrier control. First, we test the effect of DMSO to angiogenesis in zebrafish. As shown in Figure 1, there was no significant difference in the length and number of ISVs in embryos treated with egg water and 0.5% DMSO.

3.2. Identification of Three Angiogenic Agents. To determine the proangiogenic properties of the drug, we used a transgenic Tg (fli1: EGFP) zebrafish as an animal model and 0.5% DMSO as the solvent of the drug. At the same time, VEGF, a known angiogenic compound, was used as a positive control. As a control, VEGF (200 ng/ml) was conducive to the formation of ISVs (Figure 2(a)). Then, as shown in Figure 2(b), 500 μg/ml isosorbide mononitrate, 100 ng/ml amlodipine, and 500 ng/ml bisoprolol fumarate significantly promoted the growth of angiogenic ISVs in embryos ($P < 0.05$). The bar graph in Figure 2(c) showed the accurate length and number of ISVs after treatments with 3 drugs. These data strongly suggested that isosorbide mononitrate, amlodipine, and bisoprolol fumarate had angiogenic properties, depending on the concentrations.

3.3. Identification of Three Antiangiogenic Drugs. In the process of drug screening, we also found that the other 3 drugs could inhibit the formation of ISVs. First, we used an antiangiogenic compound PD173074 as a positive control, which suppresses angiogenesis through inhibiting fibroblast growth factor receptor 1 (FGFR1) [12, 13]. PD173074 (3 μg/ml) could significantly decrease the number and length of ISVs (Figure 3(a)). Figure 3(b) showed the inhibitory effects of carvedilol, irbesartan, and rosuvastatin calcium on angiogenesis in Tg (flk1: EGFP) zebrafish embryo. In addition, the average length and number of ISV were significantly reduced after treatments with 100 ng/ml carvedilol, 100 ng/ml irbesartan, and 200 ng/ml rosuvastatin calcium compared to those in the control group (Figure 3(c), $P < 0.05$), suggesting that carvedilol, irbesartan, and rosuvastatin calcium could suppress the formation of capillary under similar experimental conditions.

3.4. Expression of VEGF in HUVEC Model In Vitro. Due to the potent pro- and antiangiogenic activities of drugs, its mechanism is worthy of further investigation. Among the known angiogenic factors, VEGF is the most important factor in the process of angiogenesis [14]. To further explore the involvement of VEGF in drug-induced angiogenesis, an *in vitro* HUVEC model was established using drug incubation for 24 hours. The expression of VEGF mRNA was detected by qRT-PCR. Results showed that the expression of VEGF was dramatically increased in HUVEC exposure to 50 μg/ml isosorbide mononitrate, 10 ng/ml amlodipine, and 50 ng/ml bisoprolol fumarate (Figure 4(a), $P < 0.05$). However, compared with the control group, the expression of VEGF was decreased in HUVECs incubated with 10 ng/ml

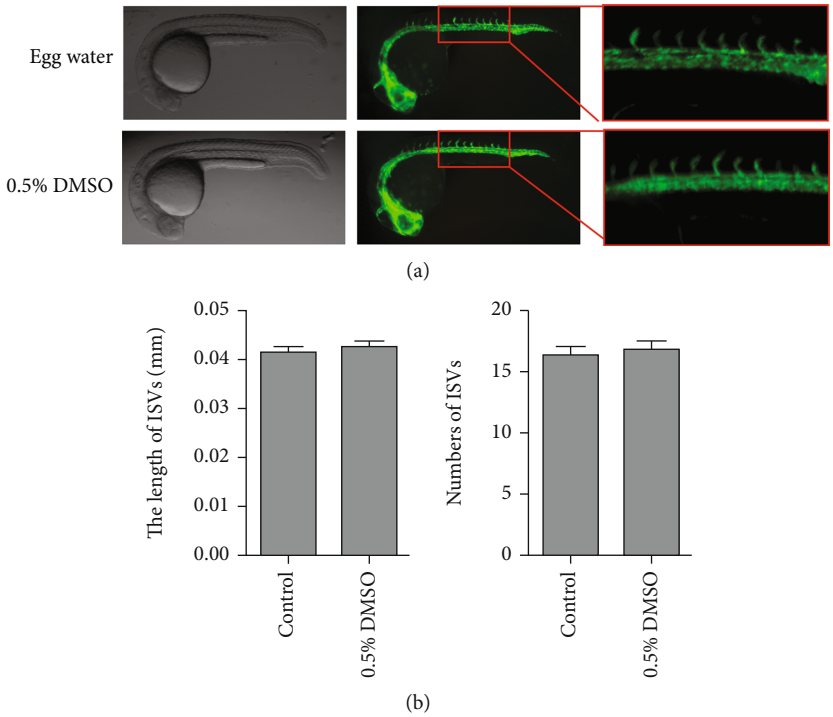

Figure 1: Effect of 0.5% DMSO on the growth of intersegmental vessels (ISVs) in the zebrafish model. (a) Bright-field and fluorescent images of zebrafish embryos at 24 h postfertilization (hpf) treated with egg water and 0.5% DMSO. (b) Average length and number of ISVs in zebrafish treated with different solvents.

carvedilol, 10 ng/ml irbesartan, and 20 ng/ml rosuvastatin calcium (Figure 4(b), $P < 0.05$). These data indicated that the above drugs may play a role in promoting angiogenesis and antiangiogenesis through the VEGF signal pathway.

4. Discussion

Results of this study indicated that isosorbide mononitrate, amlodipine, and bisoprolol fumarate exerted angiogenic effects, whereas carvedilol, irbesartan, and rosuvastatin calcium inhibited angiogenesis. Besides, these drugs might regulate angiogenesis through the VEGF pathway.

Zebrafish has become a novel preclinical model that can support rapid decision-making in the early phases of the drug discovery process [15]. Our study demonstrated that zebrafish can high-throughput screen the effects of cardiovascular on vascular development by analyzing the phenotypic changes of zebrafish embryos after drug treatment. This model may be valuable for drug discovery when the pharmacological targets are unknown [16]. However, a stable zebrafish model for chemical screening is still under development. To fully validate the zebrafish model, more efforts need to be made [8].

In the transgenic zebrafish model, we found that isosorbide mononitrate, amlodipine, and bisoprolol fumarate might exert angiogenic effects through upregulating VEGF expression (Figures 2(b) and 4). As an organic nitrate vasodilator, isosorbide mononitrate can relax the peripheral vascular muscles by increasing nitric oxide (NO) release, thereby reducing systolic blood pressure [17]. Besides, NO could enhance angiogenesis through inducing VEGF expression by cyclic guanosine monophosphate pathway- (cGMP-) dependent pathway [18]. Furthermore, NO can promote cGMP production in HUVECs [19]. Thus, isosorbide mononitrate might stimulate angiogenesis through activating the NO-cGMP-VEGF pathway.

Amlodipine, a dihydropyridine calcium (Ca^{2+}) channel blocker used for treatment of hypertension, also shows angiogenic activity in human coronary artery endothelial cells *in vitro* [20]. Moreover, amlodipine inhibitor suppresses angiogenesis in EA.hy926 endothelial cells [21]. However, the correlation between amlodipine and VEGF has not been reported. Therefore, this study revealed that amlodipine might induce angiogenesis by regulating VEGF for the first time.

Bisoprolol fumarate is a beta-selective blocker and an effective drug for the treatment of heart failure and hypertension. A previous study has demonstrated that bisoprolol fumarate displays angiogenic activity in mouse aortic ring assay [22]. Our results confirmed the effect of bisoprolol fumarate on angiogenesis in zebrafish model, suggesting that the zebrafish model could be used for the high-throughput screen of cardiovascular drugs. Besides, VEGF blockade prevents the effect of bisoprolol fumarate on angiogenesis [23], which is consistent with our results.

Furthermore, we also identified the antiangiogenic activity of carvedilol, irbesartan, and rosuvastatin calcium in the zebrafish model. Carvedilol is a pharmacological antioxidant

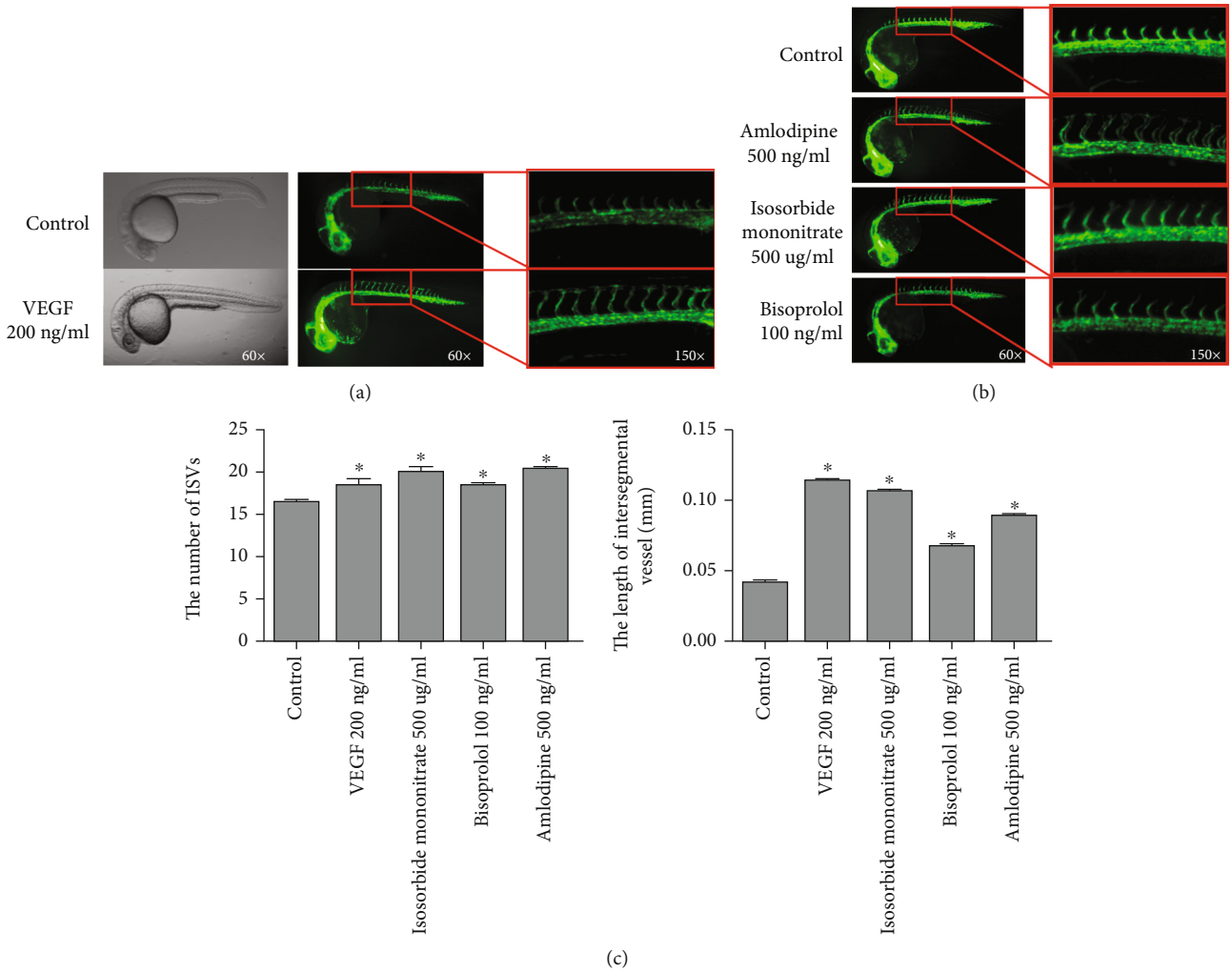

Figure 2: Chemical screen to identify angiogenic drugs in cardiovascular medicine. (a) Bright-field and fluorescent images of zebrafish embryos in 24 hpf treated with 0.5% DMSO (control) and 200 ng/ml VEGF (positive control) for 24 h. (b) Amlodipine-, isosorbide mononitrate-, and bisoprolol-treated embryos are shown. (c) Average ISV numbers and lengths in the control and drug-treated zebrafish embryos. Values for the average ISV numbers and lengths are present as mean ± SD. $^{*}P < 0.05$ vs. control group.

with α1- and nonselective β-adrenoceptor antagonist activity, which is widely used in hypertension and heart failure [24]. However, previous studies only revealed the antiangiogenic activity of carvedilol in intrahepatic angiogenesis through the VEGF pathway [25, 26]. Thus, this study indicated the antiangiogenic activity of carvedilol in cardiovascular by zebrafish model.

Irbesartan is an angiotensin II receptor blocker. Recent research has shown that irbesartan may reduce angiogenesis by decreasing the number of infiltrating cells expressing VEGF in cancer [27]. Besides, irbesartan also inhibits coronary angiogenesis in rats [28]. Therefore, these studies further suggest that the zebrafish model could be used for the high-throughput screen of cardiovascular drugs.

Rosuvastatin calcium is a member of the statins family. Currently, the effect of statins on angiogenesis remains controversial. Weis et al. concluded that statins have a biphasic dose-dependent effect on angiogenesis [29]. In the zebrafish model, rosuvastatin calcium displayed the antiangiogenic effect at 10-200 ng/ml, which was similar to that reported by Wang et al. [12]. The discrepancy in currently available data can be attributed to differences in statins concentrations and applied animal models. In addition, rosuvastatin calcium regulates angiogenesis by modifying VEGF expression in rats [30, 31], which is consistent with our study. Thus, rosuvastatin calcium (10-200 ng/ml) might induce angiogenesis by regulating VEGF expression.

However, there were several limitations in this study. We did not address the problem of the potential effects of hydrophilicity that may affect drug absorption and lead to possible false negative results. In addition, like any other animal models, the zebrafish model does not reliably predict the human outcome; nevertheless, it provides valuable insights into the "new" pharmacological effects of the drugs tested. The evidence obtained from this model may enrich our understanding of the pharmacological profiles of the currently used cardiovascular drugs.

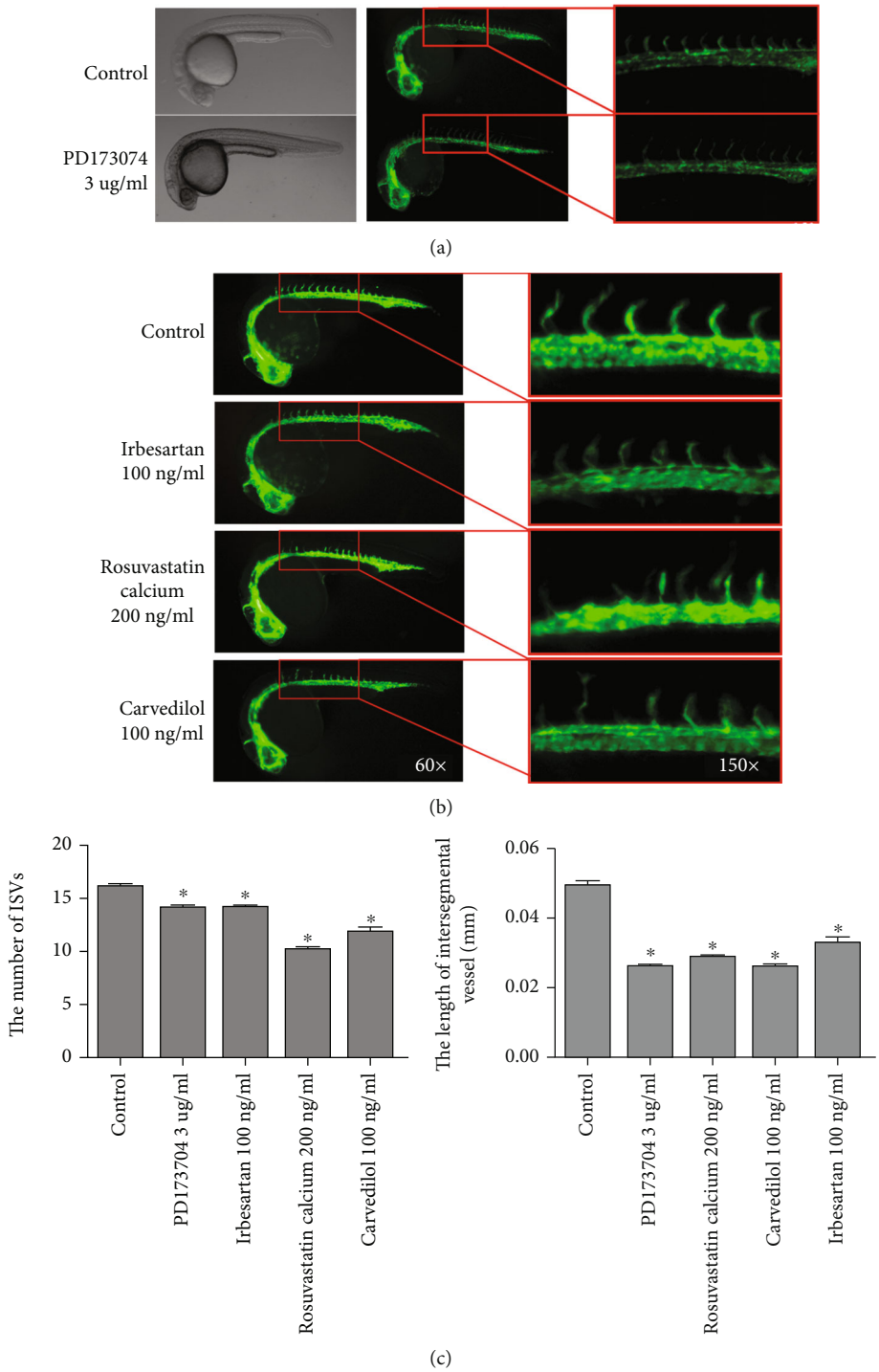

Figure 3: Effects of antiangiogenic drugs on ISV formation in Tg (flk1: EGFP) zebrafish embryos. (a) Bright-field and fluorescent images of zebrafish embryos at 24 hpf treated with 0.5% DMSO (control) and 3 μg/ml PD173074 (positive control) for 24 h. (b) Fluorescent images of zebrafish embryos treated for 24 h with the antiangiogenic agents identified. Control: embryo treated with 0.5% DMSO. (c) Average number and length of ISVs was significantly inhibited, compared with the control, by the drugs at their optimal concentrations. Columns represent the mean of three independent experiments ($n = 20$). $^*P < 0.05$ vs. control group.

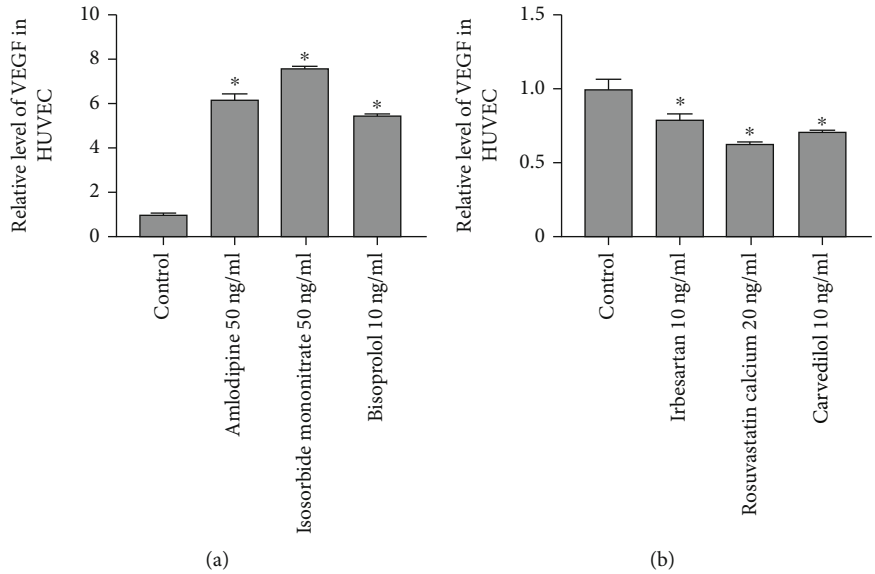

Figure 4: Expression of VEGF in HUVECs treated with different drugs which have an effect on the growth of ISV in zebrafish. VEGF expression level was detected by qRT-PCR. (a) Angiogenic agents significantly increased the expression level of VEGF in HUVECs. (b) The expression level of VEGF was significantly downregulated in HUVECs treated with an angiogenic agents. $^{*}P < 0.05$ vs. control group.

5. Conclusion

Results of this study indicated that isosorbide mononitrate, amlodipine, and bisoprolol fumarate exerted angiogenic effects, whereas carvedilol, irbesartan, and rosuvastatin calcium inhibited angiogenesis. Besides, these drugs might regulate angiogenesis through the VEGF pathway. The new functions of these drugs should improve the treatment of cardiovascular diseases.

Abbreviations

ARB: Angiotensin II receptor blocker
Ca^{2+}: Calcium
cGMP: Cyclic guanosine monophosphate pathway
CHD: Coronary heart diseases
CVD: Cardiovascular disease
GFP: Green fluorescence protein
DLAV: Dorsal longitudinal anastomotic vessel
DMSO: Dimethyl sulfoxide
HUVEC: Human umbilical vein endothelial cell
ISV: Intersegmental blood vessel
NO: Nitric oxide
qRT-PCR: Quantitative reverse transcriptase-polymerase chain reaction
VEGF: Vascular endothelial growth factor.

Data Availability

All data generated or analyzed during this study are included in this article. Further inquiries can be directed to the corresponding author.

Ethical Approval

The animal experiments were performed in line with the guidelines of the Animal Experimentation Ethics Committee of Second Military Medical University.

Conflicts of Interest

The authors have no conflicts of interest to declare.

Authors' Contributions

The conception or design of the work was carried out by Hui Lv; the drafting the work or revising it critically for important intellectual content was carried out by Bo Liu; and the final approval of the version to be published was carried out by Yongwen Qin.

Acknowledgments

This work was financially supported by the Department of Cardiovascular Diseases of Changhai Hospital in Shanghai, China. The authors are grateful to the staff in the Department of Cardiology.

References

[1] E. J. Battegay, L. S. de Miguel, M. Petrimpol, and R. Humar, "Effects of anti-hypertensive drugs on vessel rarefaction," *Current Opinion in Pharmacology*, vol. 7, no. 2, pp. 151–157, 2007.

[2] Y. Wang, Y. Zheng, W. Zhang et al., "Polymorphisms of *KDR* gene are associated with coronary heart disease," *Journal of the American College of Cardiology*, vol. 50, no. 8, pp. 760–767, 2007.

[3] D. Hilfiker-Kleiner, U. Landmesser, and H. Drexler, "Molecular mechanisms in heart failure: focus on cardiac hypertrophy, inflammation, angiogenesis, and apoptosis," *Journal of the American College of Cardiology*, vol. 48, no. 9, pp. A56–A66, 2006.

[4] K. I. Paraskevas, "Applications of statins in cardiothoracic surgery: more than just lipid-lowering," *European Journal of Cardio-Thoracic Surgery*, vol. 33, no. 3, pp. 377–390, 2008.

[5] S. Miura, M. Fujino, Y. Matsuo, H. Tanigawa, and K. Saku, "Nifedipine-induced vascular endothelial growth factor secretion from coronary smooth muscle cells promotes endothelial tube formation _via_ the kinase insert domain-containing receptor/fetal liver kinase-1/NO pathway," *Hypertension Research*, vol. 28, no. 2, pp. 147–153, 2005.

[6] S. Donnini, R. Solito, A. Giachetti, H. J. Granger, M. Ziche, and L. Morbidelli, "Fibroblast growth factor-2 mediates angiotensin-converting enzyme inhibitor-induced angiogenesis in coronary endothelium," *The Journal of Pharmacology and Experimental Therapeutics*, vol. 319, no. 2, pp. 515–522, 2006.

[7] E. Terzuoli, M. Monti, V. Vellecco et al., "Characterization of zofenoprilat as an inducer of functional angiogenesis through increased H2S availability," *British Journal of Pharmacology*, vol. 172, no. 12, pp. 2961–2973, 2015.

[8] K. L. Taylor, N. J. Grant, N. D. Temperley, and E. E. Patton, "Small molecule screening in zebrafish: an in vivo approach to identifying new chemical tools and drug leads," *Cell Communication and Signaling: CCS*, vol. 8, no. 1, p. 11, 2010.

[9] M. Melani, M. Fujita, D. Castranova et al., "A mutagenesis genetic screen to identify zebrafish embryos with defects in vasculature development," *Developmental Biology*, vol. 331, no. 2, p. 493, 2009.

[10] D. J. Milan, I. L. Jones, P. T. Ellinor, and C. A. Mac Rae, "In vivo recording of adult zebrafish electrocardiogram and assessment of drug-induced QT prolongation," *American Journal of Physiology. Heart and Circulatory Physiology*, vol. 291, no. 1, pp. H269–H273, 2006.

[11] D. J. Milan, T. A. Peterson, J. N. Ruskin, R. T. Peterson, and C. A. Mac Rae, "Drugs that induce repolarization abnormalities cause bradycardia in zebrafish," *Circulation*, vol. 107, no. 10, pp. 1355–1358, 2003.

[12] C. Wang, W. Tao, Y. Wang et al., "Rosuvastatin, identified from a zebrafish chemical genetic screen for antiangiogenic compounds, suppresses the growth of prostate cancer," *European Urology*, vol. 58, no. 3, pp. 418–426, 2010.

[13] Y. Zhao, X. Wang, S. Yang et al., "Kanglexin accelerates diabetic wound healing by promoting angiogenesis via FGFR1/ERK signaling," *Biomedicine & Pharmacotherapy*, vol. 132, article 110933, 2020.

[14] A. Paramasivam, M. Kalaimangai, S. Sambantham, B. Anandan, and G. Jayaraman, "Anti-angiogenic activity of thymoquinone by the down-regulation of VEGF using zebrafish (*Danio rerio*) model," *Biomedicine & Preventive Nutrition*, vol. 2, no. 3, pp. 169–173, 2012.

[15] P. Goldsmith, "Zebrafish as a pharmacological tool: the how, why and when," *Curropinpharm*, vol. 4, no. 5, pp. 504–512, 2004.

[16] T. C. Farrell, C. L. Cario, C. Milanese, A. Vogt, J. H. Jeong, and E. A. Burton, "Evaluation of spontaneous propulsive movement as a screening tool to detect rescue of Parkinsonism phenotypes in zebrafish models," *Neurobiology of Disease*, vol. 44, no. 1, pp. 9–18, 2011.

[17] A. Stockis, S. D. Bruyn, X. Deroubaix, B. Jeanbaptiste, and D. Acerbi, "Pharmacokinetic profile of a new controlled-release isosorbide-5-mononitrate 60 mg scored tablet (Monoket Multitab®)," *European Journal of Pharmaceutics & Biopharmaceutics*, vol. 53, no. 1, pp. 49–56, 2002.

[18] G. de Almeida, B. Schirmer, M. Crucet et al., "The NO-donor MPC-1011 stimulates angiogenesis and arteriogenesis and improves hindlimb ischemia via a cGMP-dependent pathway involving VEGF and SDF-1 _α_," *Atherosclerosis*, vol. 304, pp. 30–38, 2020.

[19] M. Feelisch, F. Brands, and M. Kelm, "Human endothelial cells bioactivate organic nitrates to nitric oxide: implications for the reinforcement of endothelial defence mechanisms," *European Journal of Clinical Investigation*, vol. 25, no. 10, pp. 737–745, 1995.

[20] R. K. Verma, A. M. Kaushal, and S. Garg, "Development and evaluation of extended release formulations of isosorbide mononitrate based on osmotic technology," *International Journal of Pharmaceutics*, vol. 263, no. 1-2, pp. 9–24, 2003.

[21] R. E. Maltaneri, A. Schiappacasse, M. E. Chamorro, A. B. Nesse, and D. C. Vittori, "Participation of membrane calcium channels in erythropoietin-induced endothelial cell migration," *European Journal of Cell Biology*, vol. 97, no. 6, pp. 411–421, 2018.

[22] T. Stati, M. Musumeci, S. Maccari et al., "β-Blockers promote angiogenesis in the mouse aortic ring assay," *Journal of Cardiovascular Pharmacology*, vol. 64, no. 1, pp. 21–27, 2014.

[23] G. Rengo, A. Cannavo, D. Liccardo et al., "Vascular endothelial growth factor blockade prevents the beneficial effects of β-blocker therapy on cardiac function, angiogenesis, and remodeling in heart failure," *Circulation Heart Failure*, vol. 6, no. 6, pp. 1259–1267, 2013.

[24] P. Dandona, R. Karne, H. Ghanim, W. Hamouda, A. Aljada, and C. H. Magsino Jr., "Carvedilol inhibits reactive oxygen species generation by leukocytes and oxidative damage to amino acids," *Circulation*, vol. 101, no. 2, pp. 122–124, 2000.

[25] Q. Ding, X. G. Tian, Y. Li, Q. Z. Wang, and C. Q. Zhang, "Carvedilol may attenuate liver cirrhosis by inhibiting angiogenesis through the VEGF-Src-ERK signaling pathway," *World Journal of Gastroenterology*, vol. 21, no. 32, pp. 9566–9576, 2015.

[26] L. Ling, G. Li, D. Meng, S. Wang, and C. Zhang, "Carvedilol ameliorates intrahepatic angiogenesis, sinusoidal remodeling and portal pressure in cirrhotic rats," *Medical Science Monitor*, vol. 24, pp. 8290–8297, 2018.

[27] E. I. Ager, S. W. Wen, J. Chan, W. W. Chong, J. H. Neo, and C. Christophi, "Altered efficacy of AT1R-targeted treatment after spontaneous cancer cell-AT1R upregulation," *BMC Cancer*, vol. 11, no. 1, p. 274, 2011.

[28] K. Rakusan, Z. Chvojkova, P. Oliviero et al., "ANG II type 1 receptor antagonist irbesartan inhibits coronary angiogenesis stimulated by chronic intermittent hypoxia in neonatal rats," *American Journal of Physiology Heart and Circulatory Physiology*, vol. 292, no. 3, pp. H1237–H1244, 2007.

[29] M. Weis, C. Heeschen, A. J. Glassford, and J. P. Cooke, "Statins have biphasic effects on angiogenesis," *Circulation*, vol. 105, no. 6, pp. 739–745, 2002.

[30] D. Huang, F. B. Wang, M. Guo et al., "Effect of combined treatment with rosuvastatin and protein kinase Cβ2 inhibitor on angiogenesis following myocardial infarction in diabetic rats," *International Journal of Molecular Medicine*, vol. 35, no. 3, pp. 829–838, 2015.

[31] S. A. Zaitone and N. M. Abo-Gresha, "Rosuvastatin promotes angiogenesis and reverses isoproterenol-induced acute myocardial infarction in rats: role of iNOS and VEGF," *European Journal of Pharmacology*, vol. 691, no. 1-3, pp. 134–142, 2012.

Hindawi
Mediators of Inflammation
Volume 2023, Article ID 9335166, 9 pages
https://doi.org/10.1155/2023/9335166

Research Article

TLR4 Enhances Cerebral Ischemia/Reperfusion Injury via Regulating NLRP3 Inflammasome and Autophagy

Li Mao,[1] **Da-Hua Wu**,[2] **Guo-Huang Hu**,[3] **and Jian-Hu Fan**[2]

[1]*Department of Basic Medicine, Changsha Health Vocational College, Changsha, 410600 Hunan, China*
[2]*Department of Neurology, Affiliated Hospital of Hunan Academy of Traditional Chinese Medicine, Changsha, 410006 Hunan, China*
[3]*The Affiliated Changsha Hospital of Hunan Normal University, Changsha, 410006 Hunan, China*

Correspondence should be addressed to Jian-Hu Fan; jianhufan@qq.com

Received 1 June 2022; Revised 23 September 2022; Accepted 17 October 2022; Published 25 February 2023

Academic Editor: Calogero Caruso

Ischemic stroke is a kind of central nervous disease characterized by high morbidity, high mortality, and high disability. Inflammation and autophagy play important roles in cerebral ischemia/reperfusion (CI/R) injury. The present study characterizes the effects of TLR4 activation on inflammation and autophagy in CI/R injury. An in vivo CI/R rat injury model and an in vitro hypoxia/reoxygenation (H/R) SH-SY5Y cell model were established. Brain infarction size, neurological function, cell apoptosis, inflammatory mediators' levels, and gene expression were measured. Infarction, neurological dysfunction, and neural cell apoptosis were induced in CI/R rats or in H/R-induced cells. The expression levels of NLRP3, TLR4, LC3, TNF-α, interleukin-1 (IL-1), interleukin-6 (IL-6), and interleukin-18 (IL-18) clearly increased in I/R rats or in H/R-induced cells, while TLR4 knockdown significantly suppressed NLRP3, TLR4, LC3, TNF-α, and interleukin-1/6/18 (IL-1/6/18) in H/R-induced cells, as well as cell apoptosis. These data indicate that TLR4 upregulation induced CI/R injury via stimulating NLRP3 inflammasome and autophagy. Therefore, TLR4, is a potential therapeutic target to improve management of ischemic stroke.

1. Introduction

Ischemic stroke (IS) is a common disease in the clinic, which has high morbidity, high mortality, and high disability. It imposes heavy economic and emotional burdens on society [1]. Ischemia is an aging-related disease that results from cardiac insufficiency and brain vascular occlusion. Its occurrence increases with age and is aggravated by a sedentary lifestyle. Circulatory dysfunction causes both glucose and oxygen insufficiencies which are the main causes of ischemic stroke [2, 3] of the blood supplied by either thrombolysis or thrombectomy which is the main therapeutic regimen for reversal of the declines in glucose and oxygenation. However, blood flow restoration will rapidly result in cerebral ischemia/reperfusion (CI/R) injury [4]. Recently, studies have demonstrated that during the process of CI/R injury, the insulted brain tissues undergo severe oxidative stress, excitotoxicity, inflammatory reaction, autophagy, and edema [2, 3, 5]. Among these responses, inflammation and autophagy have received extensive attention, but the cellular mechanisms are unclear that mediate these responses to CI/R injury. Therefore, improved therapeutic management of ischemic stroke awaits clarification of the mechanisms that mediate CI/R [6].

Inflammation and autophagy are key players in mediating the neurological deficits that develop following a CI/R accident [6]. During the process of ischemia-reperfusion, inflammation develops in the brain tissue due to increases in infiltration of inflammatory cells such as macrophages and microglia, and they release many proinflammatory factors, such as TNF-α and interleukin-1β/18 (IL-1β/18), ultimately inducing brain tissue damage [7–9]. This inflammatory process is mediated through the formation and activation of NLRP3 inflammasomes in MCAO (middle cerebral artery occlusion) mouse models [9]. Evidence for their activation stems from NLRP3-induced rises in IL-1β release [9]. In addition, it was shown

that crosstalk exists between the mediators controlling NLRP3 inflammasome formation and autophagy in CI/R injury [6]. Autophagy activation coexists with NLRP3 inflammasome induction in neuronal apoptosis or death in different models of CI/R injury (global ischemia, ischemia, or hypoxic ischemia). However, the molecular mechanisms are unclear that underlie these pathological responses and they need clarification.

Recent studies showed that Toll-like receptor 4 (TLR4) activation in stress-induced hypoxia of neuronal cells induces an inflammatory response. TLR4 involvement is evident since they undergo upregulation during an ischemic insult, whereas this response is suppressed in TLR4-deficient/knockout mice [10, 11]. These effects suggest that CI/R injury-induced TLR4 upregulation is an inadvertent injurious side effect to such stress. However, it is still unclear whether TLR4 expression and activation directly contribute to the side effects of Cl/R-induced injury through upregulating and stimulating NLRP3 inflammasomes and autophagy in brain tissues.

We show here that hypoxia-induced TLR4 upregulation and activation during reperfusion contribute to mediating through NLRP3 inflammasomes which increase in inflammation and autophagy in brain neuronal tissue in vivo and in vitro. These results provide novel insight into the pathogenesis and treatment of ischemic stroke.

2. Materials and Methods

2.1. Animal Experiments. SD male rats ($n = 16$; 8 weeks old, 250 g in weight) were provided by Hunan SJA Laboratory Animal Co., Ltd. The rats were maintained at 25°C, 65% humidity on a cycle of 12 h light/12 h dark. This investigation was approved by the Ethics Committee of the Affiliated Changsha Hospital of Hunan Normal University, and the performed experiments comply with the guidelines of National Institutes of Health (NIH).

A SD rat CI/R model was created following the method established by Mao et al. [12] or Zuo et al. [4]. The rats were lightly anesthetized by intraperitoneal injection with pentobarbital sodium. The occlusion of rat's anterior cerebral artery was performed using a nylon monofilament. After 2 h of occlusion, the rats underwent 24 h of reperfusion. The sham group only received a skin incision without internal carotid artery occlusion. Neurological function was assessed following the 24 h reperfusion, and brain tissue was sampled for TTC (2,3,5-tripenyltetrazolium chloride) staining or other relevant analysis, such as gene expression.

2.2. Cell Culture. The SH-SY5Y cell line was obtained from the CTCC of Chinese Academy of Sciences and authenticated using STR (short tandem repeat) profiling. Cells were cultured at 37°C, 95% air, and 5% CO_2 in a compound medium containing DMEM, 10% fetal bovine serum, and antibiotics.

2.3. In Vitro Model In Vitro Model of Ischemic Stroke (IS). To mimic ischemic stroke in vitro, an H/R (hypoxia/reoxygenation) model was used. SH-SY5Y cells were subjected to 4 h of hypoxia followed by 20 h reoxygenation. During hypoxia, the SH-SY5Y cells were only induced using DPBS (Dulbecco's phosphate-buffered saline), while during the reoxygenation, the DPBS was replaced with normal medium (DMEM medium containing 10% FBS).

2.4. Neurological Function Evaluation. The neurological function assessment followed a 5-point rating scale [4]. According to the rating scale, 0 means normal, 1 means the left forepaw cannot be straightened, 2 represents a decrease in the grip strength of the forepaw, 3 means turning to the left when pulling the tail, and 4 means spontaneous rotation.

2.5. Infarct Size Measurement. TTC (2,3,5-tripenyltetrazolium chloride) staining was performed for brain infarction size measurement following previous described methods [4]. Briefly, brain sections (0.2-0.3 cm in thickness) were incubated with 2% TTC solution for half an hour at 25°C in the dark and then imaged. The total infarction size (cm^3) of sections was calculated by the equation: total infarction size = infarction area (cm^2) of each section* section thickness.

2.6. Cell Apoptosis Characterization. TUNEL/Hoechst double-labelling was used for assaying the apoptosis of brain tissues [13]. Brain sections were handled as follows: immersed in 4% w/v paraformaldehyde (25°C, 10 min) for fixing, immersed in paraformaldehyde plus acetic acid (4°C, 5 min) for postfixing, and immersed in reaction solutions containing equilibration buffer and working strength deoxynucleotide transferase (TdT) (35°C, 1 h) and blotting off, followed by incubation with Hoechst 33342 (25°C, 5 min). At the end, images were captured using epifluorescence microscopy (×200 amplifications), and the number of TUNEL-positive cells was counted.

The cell apoptosis analysis was performed as previously described [4]. SH-SY5Y cell suspension (100 cells/ml) was mixed with FITC-conjugated Annexin V and propidium iodide and maintained in the dark at 25°C for 15 min. Subsequently, the cells apoptosis was detected using a flow cytometer.

2.7. Gene Expression Knockdown. Loss of TLR4 function was obtained with the following transfection procedure in SH-SY5Y cells. Mixtures were prepared by mixing siRNA having the TLR4 (R: UGUUCUAGAAUUAAUAAGCCC sequence directed against R: GCUUAUUAAUUCUAGAACAAA) and Lipofectamine 2000. SH-SY5Y cells were transfected for 24 h.

2.8. Determination of Inflammatory Mediators. An ELISA kit was used for determining the levels of TNF-α (Beyotime), L-1β (Beyotime), IL-6 (Beyotime), or IL-18(Beyotime) according to the manufacturer instructions. Briefly, SH-SY5Y cell supernatants were collected, and the optical absorbance at 540 nm was determined using a microplate reader.

2.9. Real-Time PCR. Real-time PCR was conducted following described methods [4]. Briefly, total RNA extracted

using a TRizol Reagent kit (TakaRa) both its purity and concentration was determined spectrophotometrically. A reverse transcription system and a real-time PCR reaction system were established to quantitatively determine the expression levels of TLR4, NLRP3, and LC3 according to the instructions of a transcription kit (DRR037A; TaKaRa) and a SYBR Premix Ex Taq kit (TaKaRa). The amplification reaction was conducted using the ABI 7300 Real-Time PCR System. PCR primers used as follows: TLR4 (F: 5′-CCGCTC TGGCATCATCTTCA-3′; R: 5′-TCCCACTCGAGGTAGG TGTT-3′), NLRP3 (F: 5′-CTGCAGAGCCTACAGTTGGG-3′; R: 5′-GTCCTGCTTCCACACCTACC-3′), and β-actin (F: 5′-CCCATCTATGAGGGTTACGC-3′; R: 5′-TTTAAT GTCACGCACGATTTC-3′).

2.10. Western Blotting. Total protein was extracted using an extracting solution containing 1% PMSF, and its concentration was determined. SDS-PAGE (on 10% gel) was used for target protein isolation, and they were electrotransfered to PVDF membranes. Membranes were incubated with primary antibodies (4°C, 16 h) and secondary antibodies (25°C, 2 h) successively. The intensity of band signals was detected using enhanced chemiluminescence and ChemiDoc XRS System (Bio-Rad). The primary antibodies include rabbit anti-TLR4, -NLRP3, LC3-I, and LC3-II. β-Actin was used to establish protein loading equivalence. All primary antibodies were provided by Santa Cruz.

2.11. Statistical Analysis. SPSS 21 was used for statistical analysis. Data are presented as mean ± SD. One-way analysis of variance and independent sample t-test were used to calculate differences between groups. P values <0.05 were considered significant.

3. Results

3.1. Severe Damage Occurs in CI/R Injury Rat. Figures 1(a) and 1(b) compare the effects of exposure to the I/R stress on neuronal histology with that in the sham group. The results clearly show that imposing the I/R stress induced a brain infarct, whereas the sham group histology was unchanged. Figure 1(c) shows the results of the neurological function assay, and they indicate that in the I/R group, the I/R stress induced neurological dysfunction (Figure 1(c)). Figures 1(d) and 1(e) show that the brain tissues in the I/R rats had more TUNEL-positive cells, which suggest that they underwent apoptosis. These data confirm that that this I/R regimen induced severe neuronal structural and functional damage.

3.2. CI/R Injury Upregulates Proinflammatory Cytokine Release. Since inflammation is the leading cause of CI/R injury, we determined if increases in proinflammatory mediator release accompanies this response. The results in Figures 2(a)–2(d) show that the levels of TNF-α and interleukin-1β/6/18 (1L-1β/6/18) significantly increased in the I/R rat group compared to their corresponding levels in the sham group.

3.3. CI/R Injury Upregulates NLRP3, TLR4, and LC3 Expression Levels. The effects were determined of CI/R injury on relevant inflammation gene expression levels. The results shown in Figures 3(a) and 3(b) indicate that such stress increased the TLR4 expression level relative to its sustained level in the sham group. Consistently, the NLRP3 gene expression level also underwent upregulation in the I/R stressed rats (c.f. Figures 3(a) and 3(c)). This agreement suggested that TLR4 and NLRP3 upregulation are closely associated with the inflammation response in the I/R rat. Considering that there is an interplay between inflammation and autophagy, we then measured the expression level of LC3 (a biomarker of apoptosis) [6]. The results shown in Figures 3(a) and 3(d) clearly show that the ratio of LC3-II to LC3-I increased in the I/R rats. This correspondence between the increases in the LC3-II/LC3-1(biomarker of apoptosis) [6] ratio and NLRP3 inflammasome upregulation suggests that these responses are linked to one another in CI/R injury.

3.4. Correspondence between the Effects of TLR4 Knockdown on NLRP3 and LC3 in H/R-Induced SH-SY5Y Cells and Those in the CI/R Rat Group. We determined if there is a correspondence between in vivo H/R-induced upregulation of TLR4, NLRP3, and LC3 expression levels in vivo and those induced by exposing SH-SY5Y cells to this stress (Figures 4(a)–4(g)). The results shown in Figures 4(a)–4(g) confirm that H/R exposure under both conditions upregulates these mediators through stimulating TLR4 activity. The results in Figure 4(a) show that transfection with the TLR4 gene silencing siRNA significantly inhibited the expression of TLR4 in SH-SY5Y cells that underwent H/R, but the NC physiologically irrelevant siRNA had no effect. Figures 4(d) and 4(e) show that transfection of this TLR4 siRNA inhibited the TLR4 protein expression level in H/R-induced SH-SY5Y cells. In addition, TLR4 knockdown inhibited the expression levels of NLRP3 and LC3 in H/R-induced SH-SY5Y cells, while the NC siRNA had no inhibitory effect on any of their expression levels (c.f. Figures 4(b)–4(d), 4(f), and 4(g)). These data confirm that H/R upregulates NLRP3 inflammasome and autophagy through increases in TLR4 activity.

3.5. TLR4 Knockdown Suppresses Inflammatory Mediator Release in H/R-Induced SH-SY5Y Cells. To determine if exposure of SH-SY5Y cells to the H/R stress mediates increases in proinflammatory cytokine release through stimulating the TLR4 receptor, the effects of TLR4 knockdown were evaluated on these rises in H/R stressed SH-SY5Y cells. Consistent with the animal results, the release of TNF-α and interleukin -1β/6/18 (1L-1β/6/18) significantly increased in H/R-induced SH-SY5Y cells, while TLR4 knockdown obviously reduced their release (Figures 5(a)–5(d)). These results confirm TLR4 involvement in mediating H/R-induced increases on proinflammatory cytokine expression levels underlying inflammation in neurons.

3.6. TLR4 Knockdown Suppresses H/R-Induced SH-SY5Y Apoptosis. The association was determined between H/R-induced TLR4 activation and apoptosis in SH-SY5Y cells.

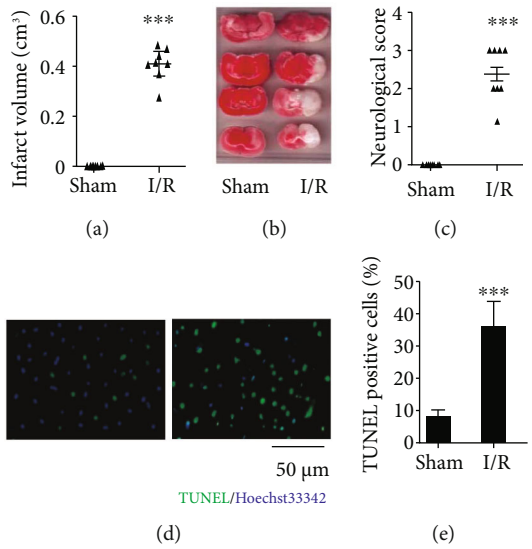

Figure 1: Neuronal histological changes induced in CI/R injury rat. (a) Infarction size. (b) Representative images of TTC staining. (c) Neurological function analysis. (d) Representative images of TUNEL/Hoechst double staining. (e) TUNEL-positive cell numbers. The data expressed as *mean* ± *SD* ($n = 8$). $^{***}P < 0.001$ vs. sham.

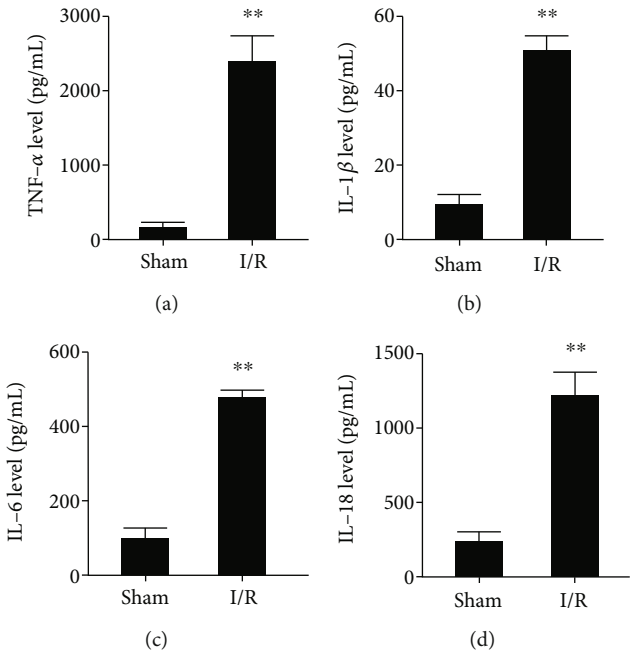

Figure 2: CI/R injury enhances inflammatory mediator release. (a) TNF-α level. (b) IL-1β level. (c) IL-6 level. (d) IL-18 level. The data expressed as *mean* ± *SD*. $^{**}P < 0.01$ vs. sham.

The results shown in Figures 6(a) and 6(b) indicate that H/R treatment obviously induced increases in SH-SY5Y while TLR4 knockdown obviously inhibited this response. Therefore, H/R induces neuronal apoptosis through upregulating and stimulating TLR4 expression levels.

4. Discussion

Inflammation exerts key roles in CI/R injury. The present study revealed that the high expression of TLR4 led to CI/R injury via regulating NLRP3 and LC3 upregulation and stimulation. The results indicate that the expression level of TLR4 positively correlates with the expression level of NLRP3 and LC3. The cell apoptosis and the release of inflammatory mediators rose in brain tissues subjected to CI/R or in SH-SY5Y cells. TLR4 knockdown significantly suppressed the expression of TLR4, NLRP3, and LC3 and inhibited apoptosis of SH-SY5Y cells that underwent H/R. These results indicate that TLR4 induces CI/R injury via regulating NLRP3 inflammasome and autophagy. These findings suggest that NLRP3 inhibition is a potential target for ischemic stroke treatment.

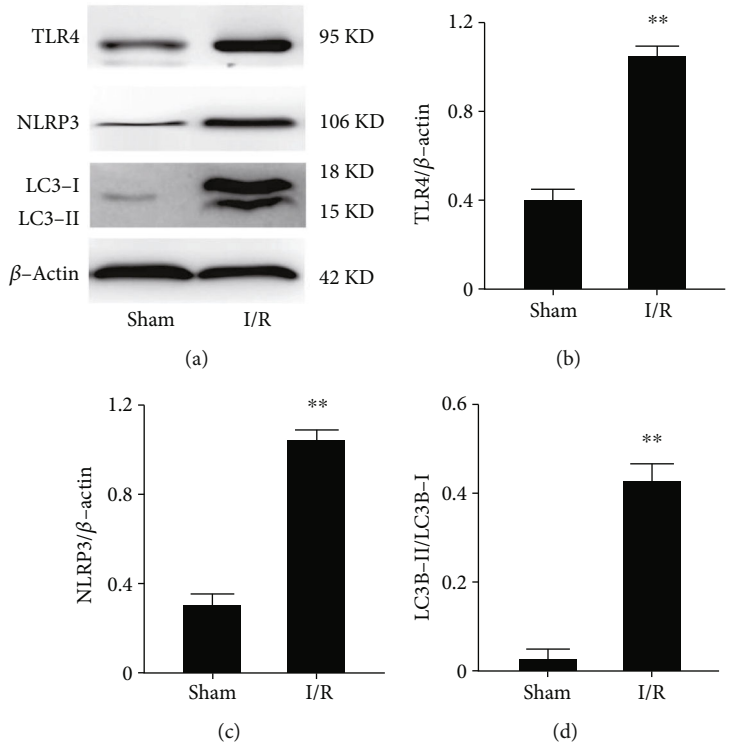

Figure 3: CI/R injury increases the expression of NLRP3, TLR4, and LC3. (a) Protein expression level. (b) The ratio of TLR4 to β-actin. (c) The ratio of NLRP3 to β-actin. (d) The ratio of LC3-I to LC3-II. The data expressed as *mean* ± *SD*. $^{**}P < 0.01$ vs. control vs. sham.

Inflammation is activated in response to ischemia/reperfusion in brain tissues. This effect is due to increases in inflammatory cells (macrophages) and the microglia infiltration which release many proinflammatory factors, such as TNF-α and interleukin -1β/18(1 L-1β/18) [14]. During this process, the formation and activation of the NLRP3 inflammasome are critical to the initiation of the inflammatory response. Accordingly, the role of NLRP3 inflammasome in CI/R injury is very widely studied [7, 8]. For example, NLRP3 upregulation was found to be upregulated in MCAO mouse models as well as Bruton's Ttrosine kinase (BTK) which induces responses through regulating the expression level of NLRP3 [9, 15]. Increases in the release of IL-1β are a marker of NLRP3 inflammasome activation, which was identified in the brain tissues of MCAO mouse [9]. We found that CI/R- and H/R-induced neuronal injury in vitro and in vivo is associated with increases in the release of TNF-α and interleukin-1β/18 (1L-1β/18), which confirms that NLRP3 activation contributes to mediating these effects. This mimicry confirms the relevance of TLR4-induced increases in inflammation in which H/R and cerebral artery occlusion both upregulated TNF-α and interleukin-1β/18 (1L-1β/18) [9] through NLRP3 inflammasome upregulation and activation. In addition, He et al. recently found that resveratrol can reduce cerebral infarction area and improve neurobiological function of rats that underwent CI/R injury, and its mechanism involves inhibition of NLRP3 inflammasome [16]. These data provide additional proof that exposure to CI/R induces neuronal injury through NLRP3 inflammasome activation. Thus, clarifying the mechanisms that underlie the control of NLRP3 function is very relevant for identifying novel therapeutic approaches to lessen CI/R injury.

Autophagy is a conserved, controlled, and lysosomal-dependent biological process formed during the evolution of eukaryotes and participates in the pathogenesis of many diseases in mammals, such as CI/R injury [7, 17]. In the process of CI/R injury, it was found that autophagy may be a double-edged sword (beneficial or harmful), such as in the ischemic preconditioning model. In this condition, autophagy activation is neuroprotective, while in the CI/R injury model (complete cerebral ischemia and ischemia or hypoxia ischemia model), autophagy activation is instead associated with nerve cell apoptosis or death [18–20]. This suggested that the mechanism of autophagy in CI/R injury is very complex. Therefore, clarifying the mechanism of autophagy in CI/R injury is critical for ischemic stroke therapy, and there is an urgent need warranting extensive basic or clinical research to solve this complex question. Previous studies showed that autophagy accompanies infarction and apoptosis in neuronal brain tissues of CI/R injury rats, while inhibition of autophagy provides protection against neuronal brain damage [20, 21]. For example, Zhang et al. found that deltonin can inhibit autophagy to alleviate cerebral ischemia-reperfusion injury [21]. Consistently, we found that LC3 was obviously upregulated in CI/R injury rats. There was an association between increases in the expression level of LC3 (a biomarker of autophagy) [18] and brain infarction size and TUNEL-positive cell number. These results suggest that there is an association between CI/R injury and autophagy.

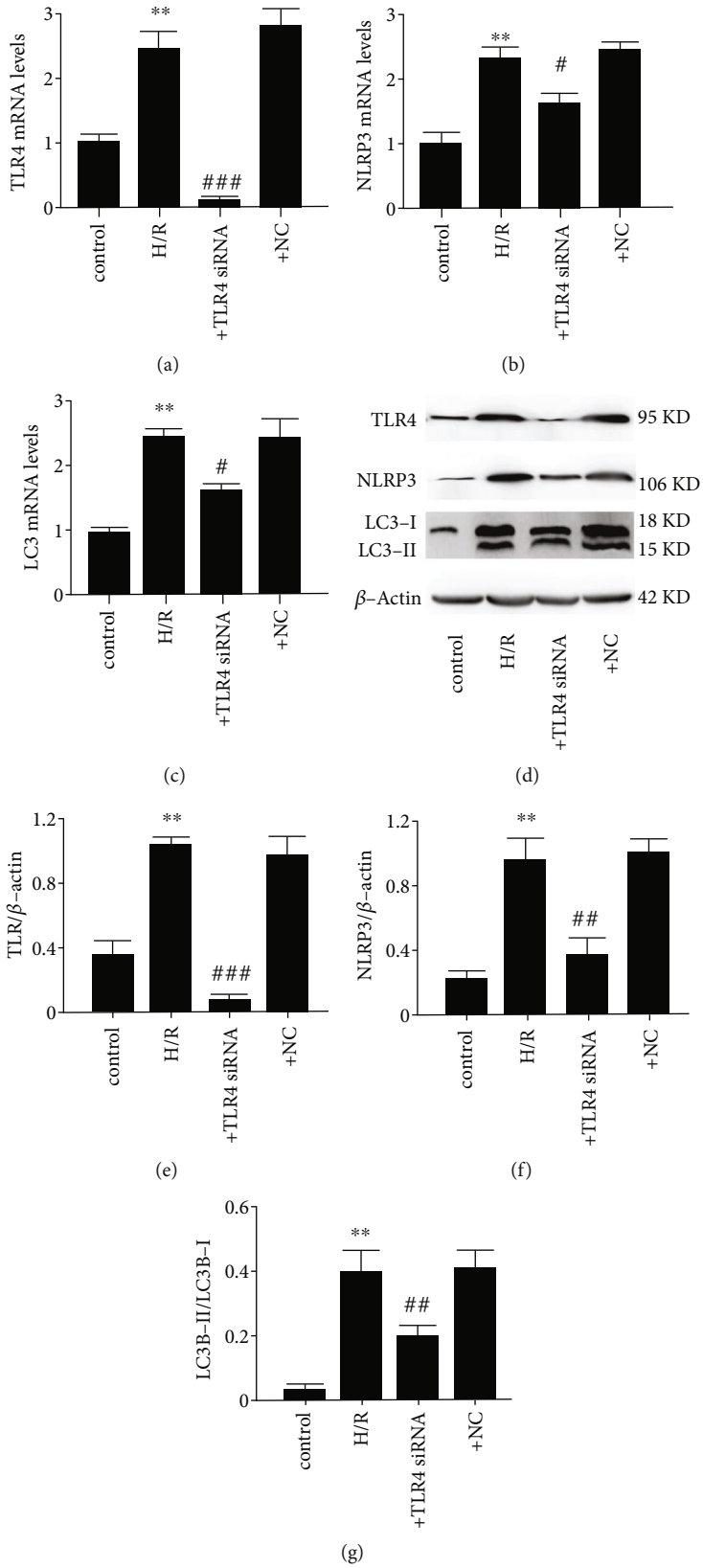

Figure 4: TLR4 knockdown suppresses rises in NLRP3 and LC3 in H/R-induced SH-SY5Y cells. (a) TLR4 mRNA level. (b) NLRP3 mRNA level. (c) LC3 mRNA level. (d) protein expression level. (e) The ratio of TLR4 to β-actin. (f) The ratio of NLRP3 to β-actin. (g) The ratio of LC3-I to LC3-II. The data expressed as *mean* ± *SD*. +TLR4 siRNA: cells treated with siRNA against TLR4 (100 nm); +NC siRNA: cells with negative control siRNA (100 nm). $^{**}P < 0.05$ vs. control; $^{\#}P < 0.05$ vs. H/R; $^{\#\#}P < 0.01$ vs. H/R; $^{\#\#\#}P < 0.001$ vs. H/R.

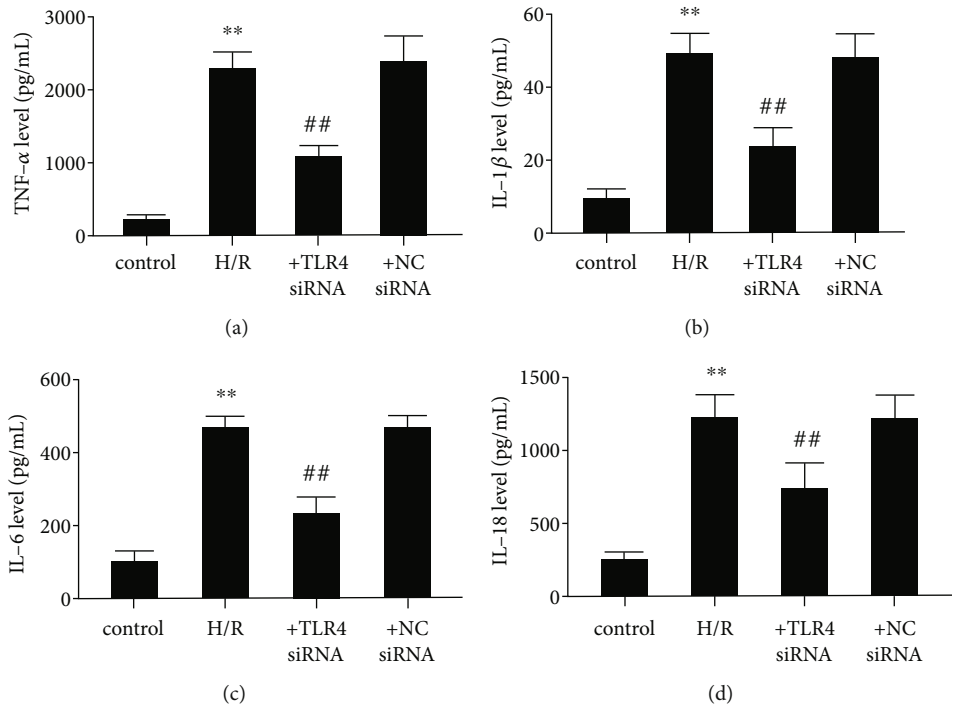

Figure 5: TLR4 knockdown inhibits inflammatory mediator release in H/R treated SH-SY5Y cells. (a) TNF-α level. (b) IL-1β level. (c) IL-6 level. (d) IL-18 level. The data expressed as *mean* ± *SD*. $^{**}P < 0.01$ vs. control; $^{\#\#}P < 0.01$ vs. H/R.

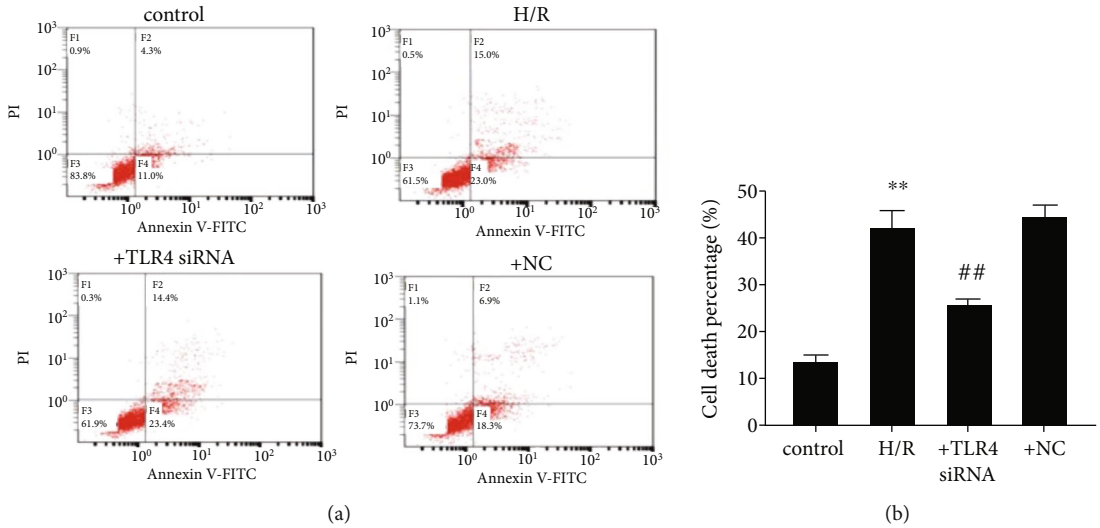

Figure 6: (a) TLR4 knockdown reduces increases in cell apoptosis in H/R-induced SH-SY5Y cells. Representative images of flow cytometry. (b) Cell death percentage. The data expressed as *mean* ± *SD*. $^{**}P < 0.01$ vs. control; $^{\#\#}P < 0.01$ vs. H/R.

It is apparent that the mechanism of autophagy in CI/R injury is very complex, which is mediated by signaling pathways, such as AMPK-mTOR pathway, PI3K/Akt/mTOR pathway, and TLR4/p38/MAPK [19, 21–23]. Among them, the PI3K/Akt/mTOR pathway and the TLR4/P38/MAPK pathway-mediated apoptosis of neurons is recently the focus of numerous reports. Many studies have described that CI/R injury is associated with a disrupted TLR4/P38/MAPK signaling pathway which suggests it is an important target for the treatment of CI/R injury. For example, Huang et al. found that curcumin can alleviate CI/R injury through inhibition of the TLR4/P38/MAPK signaling pathway [24]. Consistently, we found that there is a positive correlation between TLR4 expression levels and autophagy, cell apoptosis in I/R rats, or in H/R-induced SH-SY5Y cells. This suggests that there is an internal relationship between CI/R-induced inflammation and autophagy.

Recent studies demonstrated that TLR4 has an important role in mediating inflammation and autophagy in many CNS diseases, such as stroke and sclerosis [25]. Inhibition of

TLR4 protects experimental stroke animals from injury [10, 11]. Recently, it is reported that TLR4-dependent autophagy is critical for macrophage-induced inflammation [25]. This result is consistent with our finding that TLR4 is upregulated in the CI/R injury rat or in the H/R-induced SH-SY5Y cells. This response is associated with increases in the expression levels of NLRP3 and LC3. These results demonstrate that CI/R-induced TLR4 upregulation is critical for activating inflammation and autophagy. This dependence is consistent with our finding showing that in the TLR4-deficient/knockout mice, an ischemic insult was associated with a smaller inflammatory response [10]. In addition, a previous study reported that TLR4-knockdown attenuates brain damage via inhibiting inflammation and autophagy in traumatic brain injury rats [26]. Considering the cause-and-effect relationship between ischemic stroke and traumatic brain injury, it is apparent that TLR4 is a potential therapeutic target for CI/R injury treatment.

However, considering the complexity of an interaction between inflammation and autophagy, there is no definitive mechanism that describes the role of TLR4 in CI/R injury. For example, the mechanism is unknown that accounts for how TLR4 regulates NLRP3 inflammasome and autophagy. It is still not clear if TLR4-mediated inflammation promotes autophagy or TLR4-mediated autophagy promotes inflammation in CI/R injury. Thus, much effort is still required to fully elucidate the role of TLR4 in inducing inflammation and autophagy in cerebral ischemia/reperfusion injury.

In summary, TLR4 plays an important role in inducing inflammation and autophagy in CI/R injury. We show here that brain CI/R injury induced-TLR4 activation promotes inflammation and autophagy via upregulating NLRP3 inflammasome expression and activity. This finding may lead to the development of novel approaches to improve therapeutic management of ischemic episodes in a clinical setting.

Data Availability

The dataset can be available from the corresponding author if reasonably requested.

Ethical Approval

This study was approved by the Ethics Committee of Affiliated Hospital of Hunan Academy of Traditional Chinese Medicine.

Conflicts of Interest

The authors declare that they have no conflicts of interest.

Authors' Contributions

Li Mao, Da-Hua Wu, and Guo-Huang Hu contributed to Figures 1–6. Jian-Hu Fan drafted the manuscript.

Acknowledgments

This work was supported by Science and Health Joint Project of Hunan Natural Science Foundation (No. 2020JJ8017) and the Changsha Science & Technology Bureau (No. kq2004154 to Guo-Huang Hu).

References

[1] B. Juan, S. Shi, H.-Q. Wang et al., "Acacetin protects against cerebral ischemia-reperfusion injury via the NLRP3 signaling pathway," *Neural Regeneration Research*, vol. 14, no. 4, pp. 605–612, 2019.

[2] S. E. Khoshnam, W. Winlow, M. Farzaneh, Y. Farbood, and H. F. Moghaddam, "Pathogenic mechanisms following ischemic stroke," *Neurological Sciences*, vol. 38, no. 7, pp. 1167–1186, 2017.

[3] G. Enzmann, S. Kargaran, and B. Engelhardt, "Ischemia–reperfusion injury in stroke: impact of the brain barriers and brain immune privilege on neutrophil function," *Therapeutic Advances in Neurological Disorders*, vol. 11, 2018.

[4] M. L. Zuo, A. P. Wang, G. L. Song, and Z. B. Yang, "miR-652 protects rats from cerebral ischemia/reperfusion oxidative stress injury by directly targeting NOX2," *Biomedicine & Pharmacotherapy*, vol. 124, article 109860, 2020.

[5] M. Franke, M. Bieber, P. Kraft, A. N. R. Weber, G. Stoll, and M. K. Schuhmann, "The NLRP3 inflammasome drives inflammation in ischemia/reperfusion injury after transient middle cerebral artery occlusion in mice," *Brain, Behavior, and Immunity*, vol. 92, pp. 223–233, 2021.

[6] M. Biasizzo and N. Kopitar-Jerala, "Interplay between NLRP3 inflammasome and autophagy," *Frontiers in Immunology*, vol. 11, article 591803, 2020.

[7] S. Zhao, X. Li, J. Wang, and H. Wang, "The role of the effects of autophagy on NLRP3 inflammasome in inflammatory nervous system diseases," *Frontiers in Cell and Development Biology*, vol. 9, article 657478, 2021.

[8] N. Kelley, D. Jeltema, Y. Duan, and Y. He, "The NLRP3 inflammasome: an overview of mechanisms of activation and regulation," *International Journal of Molecular Sciences*, vol. 20, no. 13, p. 3328, 2019.

[9] K. L. Lambertsen, K. Biber, and B. Finsen, "Inflammatory cytokines in experimental and human stroke," *Journal of Cerebral Blood Flow & Metabolism*, vol. 32, no. 9, pp. 1677–1698, 2012.

[10] J. R. Caso, J. M. Pradillo, O. Hurtado, P. Lorenzo, M. A. Moro, and I. Lizasoain, "Toll-like receptor 4 is involved in brain damage and inflammation after experimental stroke," *Circulation*, vol. 115, no. 12, pp. 1599–1608, 2007.

[11] K. Hyakkoku, J. Hamanaka, K. Tsuruma et al., "Toll-like receptor 4 (TLR4), but not TLR3 or TLR9, knock-out mice have neuroprotective effects against focal cerebral ischemia," *Neuroscience*, vol. 171, no. 1, pp. 258–267, 2010.

[12] L. Mao, M. L. Zuo, G. H. Hu, X. M. Duan, and Z. B. Yang, "Mir-193 targets ALDH2 and contributes to toxic aldehyde accumulation and tyrosine hydroxylase dysfunction in cerebral ischemia/reperfusion injury," *Oncotarget*, vol. 8, no. 59, pp. 99681–99692, 2017.

[13] G. Whiteside, N. Cougnon, S. P. Hunt, and R. Munglani, "An improved method for detection of apoptosis in tissue sections and cell culture, using the TUNEL technique combined with Hoechst stain," *Brain Research Protocols*, vol. 2, no. 2, pp. 160–164, 1998.

[14] Ł. Przykaza, "Understanding the connection between common stroke comorbidities, their associated inflammation, and the course of the cerebral ischemia/reperfusion cascade," *Frontiers in Immunology*, vol. 12, article 782569, 2021.

[15] Y. Ye, T. Jin, X. Zhang et al., "Meisoindigo protects against focal cerebral ischemia-reperfusion injury by inhibiting NLRP3 inflammasome activation and regulating microglia/macrophage polarization via TLR4/NF-κB signaling pathway," *Frontiers in Cellular Neuroscience*, vol. 13, p. 553, 2019.

[16] Q. He, Z. Li, Y. Wang, Y. Hou, L. Li, and J. Zhao, "reperfusion injury in rats by inhibiting /reperfusion injury in rats by inhibiting NLRP3 inflammasome activation through Sirt1-dependent autophagy induction," *International Immunopharmacology*, vol. 50, pp. 208–215, 2017.

[17] S. Saha, D. P. Panigrahi, S. Patil, and S. K. Bhutia, "Autophagy in health and disease: a comprehensive review," *Biomedicine & Pharmacotherapy*, vol. 104, pp. 485–495, 2018.

[18] X. Zhang, H. Yan, Y. Yuan et al., "Cerebral ischemia-reperfusion-induced autophagy protects against neuronal injury by mitochondrial clearance," *Autophagy*, vol. 9, no. 9, pp. 1321–1333, 2013.

[19] K. Wei, P. Wang, and C. Y. Miao, "A double-edged sword with therapeutic potential: an updated role of autophagy in ischemic cerebral injury," *CNS neuroscience & therapeutics*, vol. 18, no. 11, pp. 879–886, 2012.

[20] X.-X. Wang, B. Zhang, R. Xia, and Q.-Y. Jia, "Inflammation, apoptosis, and autophagy as critical players in vascular dementia," *European Review for Medical and Pharmacological Sciences*, vol. 24, no. 18, pp. 9601–9614, 2020.

[21] Y. Zhang, Z. Tian, H. Wan, W. Liu, F. Kong, and G. Ma, "Deltonin ameliorates cerebral ischemia/reperfusion injury in correlation with modulation of autophagy and inflammation," *Neuropsychiatric Disease and Treatment*, vol. 16, pp. 871–879, 2020.

[22] L. Shen, Q. Gan, Y. Yang et al., "Mitophagy in cerebral ischemia and ischemia/reperfusion injury," *Frontiers in Aging Neuroscience*, vol. 13, article 687246, 2021.

[23] Z. Q. Shao, S. S. Dou, J. G. Zhu et al., "Apelin-13 inhibits apoptosis and excessive autophagy in cerebral ischemia/reperfusion injury," *Neural Regeneration Research*, vol. 16, no. 6, pp. 1044–1051, 2021.

[24] L. Huang, C. Chen, X. Zhang et al., "Neuroprotective effect of curcumin against cerebral ischemia-reperfusion via mediating autophagy and inflammation," *Journal of Molecular Neuroscience*, vol. 64, no. 1, pp. 129–139, 2018.

[25] C. Qin, Q. Liu, Z. W. Hu et al., "Microglial TLR4-dependent autophagy induces ischemic white matter damage via STAT1/6 pathway," *Theranostics*, vol. 8, no. 19, pp. 5434–5451, 2018.

[26] H. Jiang, Y. Wang, X. Liang, X. Xing, X. Xu, and C. Zhou, "Toll-like receptor 4 knockdown attenuates brain damage and neuroinflammation after traumatic brain injury via inhibiting neuronal autophagy and astrocyte activation," *Cellular and Molecular Neurobiology*, vol. 38, no. 5, pp. 1009–1019, 2018.

Hindawi
Mediators of Inflammation
Volume 2023, Article ID 9380398, 11 pages
https://doi.org/10.1155/2023/9380398

Research Article

lncRNA DLX6-AS1 Promotes Myocardial Ischemia-Reperfusion Injury through Mediating the miR-204-5p/FBXW7 Axis

Fanshun Wang[1] and Yuan Wu[2]

[1]*Department of Cardiac Surgery, Zhongshan Hospital of Fudan University, Shanghai 200032, China*
[2]*Department of Cardiovascular Medicine, People's Hospital of Ningxia Hui Autonomous Region, The First Clinical College of Northwest University for Nationalities, Yinchuan, Ningxia Hui Autonomous Region 750002, China*

Correspondence should be addressed to Yuan Wu; wuyuan1971@163.com

Received 23 June 2022; Accepted 26 August 2022; Published 10 January 2023

Academic Editor: Md Sayed Ali Sheikh

Myocardial ischemia-reperfusion (IR) injury is the restoration of blood flow post ischemia, which threatens the human life. Long noncoding RNA distal-less homeobox 6 antisense 1 (DLX6-AS1) has been found to take part in the IR-induced cerebral injury. Here, we determined the functional role of DLX6-AS1 in IR-induced myocardial injury. We ligated the left anterior descending coronary artery of rats to induce IR injury. IR injury rats exhibited severe tissue damage and increase of infraction size. The levels of lactate dehydrogenase (LDH), creatine kinase (CK), proinflammatory factors including MCP-1, IL-6, and IL-1β, and cell apoptosis were also enhanced in IR rats, indicating that IR induced significant myocardial injury in rats. DLX6-AS1 expression was elevated in the myocardial tissues of IR injury rats, while DLX6-AS1 deficiency alleviated IR-induced myocardial injury in rats by reducing inflammatory response and cell apoptosis. Moreover, rat embryonic cardiomyocyte cell line H9c2 was subjected to hypoxia reoxygenation (HR). DLX6-AS1 was upregulated in the HR-treated H9c2 cells, and DLX6-AS1 enhanced the expression of F-box and WD40 repeat domain-containing 7 (FBXW7) by sponging miR-204-5p. Inhibition of DLX6-AS1 inhibited inflammatory response and cell apoptosis in H9c2 cells via miR-204-5p/FBXW7 axis. In conclusion, this work demonstrates that DLX6-AS1 accelerates myocardial IR injury through regulating miR-204-5p/FBXW7 axis. Thus, this work provides a novel ceRNA DLX6-AS1/miR-204-5p/FBXW7 axis in myocardial IR injury, and DLX6-AS1 may be a potential target for the treatment of myocardial IR injury.

1. Introduction

Acute myocardial infarction (AMI) is a common and frequently occurring disease in the cardiovascular system [1]. Timely reperfusion therapy is the most effective treatment for AMI patients, which can save more cardiomyocytes that are on the verge of necrosis [2, 3]. However, a lot of cardiomyocytes died owing to reperfusion injury after revascularization. Although AMI patients survived form myocardial ischemic necrosis, they still have severe cardiac dysfunction, which affects the long-term prognosis of AMI patients [4]. This kind of reperfusion therapy after ischemia restores the blood supply but aggravates the tissues injury, which is called ischemia-reperfusion (IR) injury [5]. The main feature of IR is the severe mucosal and submucosal osmotic inflammation, which leads to the necrosis of endothelial cells [6].

Long noncoding RNA (lncRNA) has been proposed as a key regulator of various biological processes [7]. Recent evidences indicate that lncRNA regulates various physiological processes such as cell differentiation, proliferation, apoptosis, and inflammation [8–10]. lncRNA distal-less homeobox 6 antisense 1 (DLX6-AS1) plays a carcinogenic role in lung adenocarcinoma, ovarian cancer, and other cancers [11, 12]. Moreover, DLX6-AS1 is upregulated in cerebral IR injury, and inhibition of

DLX6-AS1 significantly reduces apoptosis in neuronal cells [13]. However, little is known about DLX6-AS1 in myocardial IR injury.

lncRNA and microRNA (miRNA) are widely involved in competitive endogenous RNA (ceRNA) model. lncRNA relieves the inhibitory effect of miRNA on the downstream target mRNA by sponging miRNA [14]. Many miRNAs have become important regulators in the physiological and pathological processes of cardiovascular diseases and participate in regulating cardiac functions, such as contraction, cardiac growth, and morphogenesis [15, 16]. Previous study has revealed that the expression of miR-204-5p is lower in the myocardial tissue of the myocardial IR injury mouse model. KCNQ1OT1 binds to miR-204-5p and aggravates myocardial IR injury in mice by upregulating LGALS3, which provides a new idea for the treatment of myocardial IR injury [17]. Whether miR-204-5p has a functional role in IR-induced myocardial injury remains unclear. Additionally, Bioinformatical analysis (Starbase) revealed that miR-204-5p may be a downstream target of DLX6-AS1, and there may be binding sites between miR-204-5p and oxidized low-density lipoprotein receptor-1 (FBXW7). A previous study has uncovered that FBXW7 expression was elevated in myocardial IR injury. Inhibition of FBXW7 significantly alleviated inflammatory response, cell apoptosis, and IR-induced myocardial injury in mice [18, 19]. Thus, we speculated that DLX6-AS1 may alleviate myocardial IR injury by regulating miR-204-5p/FBXW7 axis.

In this work, we constructed a rat model of IR injury and determined the impact of DLX6-AS1 inhibition on IR injury in rats. Next, we further verified the mechanism of action of DLX6-AS1/miR-204-5p/FBXW7 axis in myocardial IR injury *in vitro*.

2. Materials and Methods

2.1. IR Injury Rat Model. Wistar male rats with 14 weeks were purchased from the Shanghai SLAC Laboratory Animal Co., Ltd (China). All protocols were carried out under the authorization of the Ethics Committee of Zhongshan Hospital of Fudan University.

IR injury rat model was established by ligation of the left anterior descending (LAD) coronary artery as previously described [20]. Briefly, rats were anesthetized with intraperitoneal injection of 45 mg/kg pentobarbitone. Subsequently, the trachea of rats was carefully exposed. Then, a rodent ventilator TOPO Dual Mode Ventilator (Kent Scientific Corporation, Torrington, CT, USA) was connected to the trachea for establishment of mechanical ventilation. The left ventricle was exposed from the chest under the rats with steady breathing. The LAD coronary artery was ligated with a 6-0 suture to induce ischemia for 30 min. Subsequently, the ligature was cut to mimic reperfusion. After that, the chest was sutured utilizing 6-0 Prolene sutures. In sham-operated rats, the procedure was the same except for artery ligation. The rats were sacrificed 6 h after the LAD ligation-reperfusion intervention. After the rats were sacrificed, tissues about 5 mm around the infarct area were selected for subsequent experiments.

For induce knockdown of DLX6-AS1, rats were injected with 1×10^{12} vg/mL of AAV9-sh-DLX6-AS1 at multiple sites of myocardium (basal anterior, midanterior, midlateral, anterior apical, and lateral apical) using a microsyringe. Rats were injected with AAV9-sh-Scramble as control. The LAD coronary artery of rats was ligated after 24 hours post the injection. The AAV9-adenovirus particles containing short hairpin RNA (shRNA) specifically targeting DLX6-AS1 (AAV9-sh-DLX6-AS1) and scrambled RNA (AAV9-sh-Scramble) were obtained from GenePharma (Shanghai, China).

2.2. Histological Analysis. Paraffin sections (5 μm) of myocardial tissues were subjected to dewaxing and hydration. Then, the sections were stained with hematoxylin and eosin sequentially using Hematoxylin-Eosin (HE) Staining Kit (Beyotime, Shanghai, China). For detection of apoptotic cells in myocardial tissues, the paraffin sections were stained with TUNEL Apoptosis Assay Kit (Beyotime, Shanghai, China). The nucleus was stained with DAPI (Beyotime, Shanghai, China). Finally, the pathological changes and apoptotic cells in myocardial tissues were observed under optical or fluorescence microscope.

2.3. 2,3,5-Triphenyte-Trazoliumchloride (TTC) Staining. The infarction size of myocardial tissues was determined as previously reported [20]. The hearts were separated form rats, and the left ventricle was sliced into sections with 2 mm perpendicular to the long axis of heart. The sections were incubated with 1% TTC (Solarbio, Beijing, China) at 37°C for 60 min. The sections were sealed in closed freezer bag containing PBS to avoid oxidation of samples. The red part with TTC staining was ischemic but viable tissue, and the unstained area indicated the infarction area of myocardial tissues. The infarction size of myocardial tissues was analyzed using Image Pro Plus 6.0.

2.4. Enzyme-Linked Immunosorbent Assay (ELISA). The levels of lactate dehydrogenase (LDH), creatine kinase (CK), monocyte chemoattractant protein-1 (MCP-1), IL-6, and IL-1β in the serum of rats were assessed utilizing Rat ELISA Kit (Jianglaibio, Shanghai, China) following the protocol of kit. The absorbance was examined on a microplate reader (Tecan, San Jose, CA, USA).

2.5. Cell Culture. The rat embryonic cardiomyocyte cell line H9c2 (CCTCC, Wuhan, China) was cultured in Dulbecco's Modified Eagle Medium (DMEM; Gibco BRL, Grand Island, NY, USA) containing 10% fetal bovine serum (FBS; Gibco) and 100 μg/mL penicillin/streptomycin at 37°C and 5% CO_2. For inducing IR through hypoxia reoxygenation (HR) treatment, H9c2 cells were cultured in serum- and glucose-free DMEM in a hypoxic chamber for 6 h, followed by incubation in DMEM containing 10% FBS in normal oxygen environments.

2.6. Cell Transfection. The pcDNA3.1 carrying DLX6-AS1 (pc-DLX6-AS1) and small interfering RNA specially targeting DLX6-AS1 (si-DLX6-AS1) were used for overexpressing or knocking down DLX6-AS1. The oligonucleotides miR-204-5p mimic and miR-204-5p inhibitor were used to upregulate

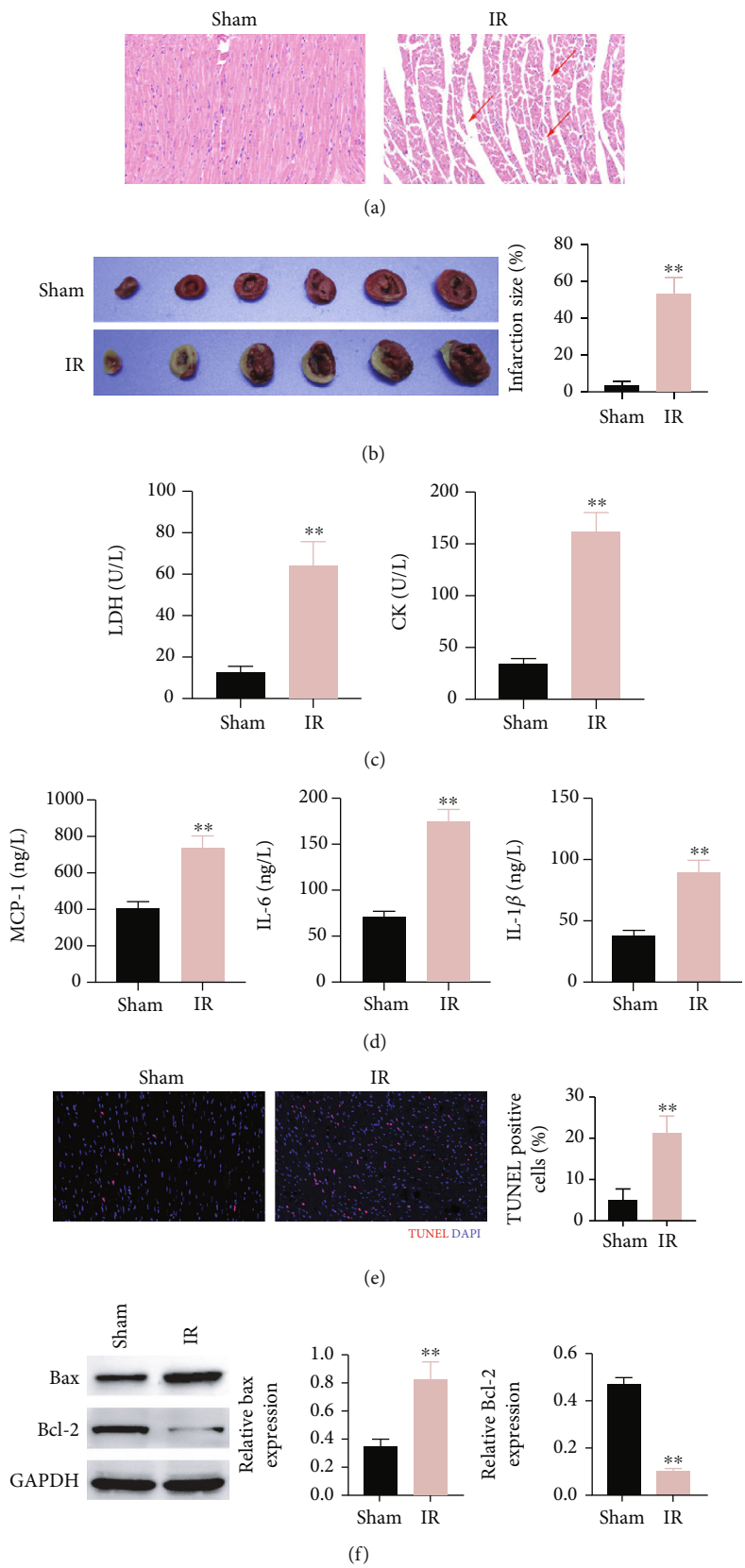

Figure 1: Continued.

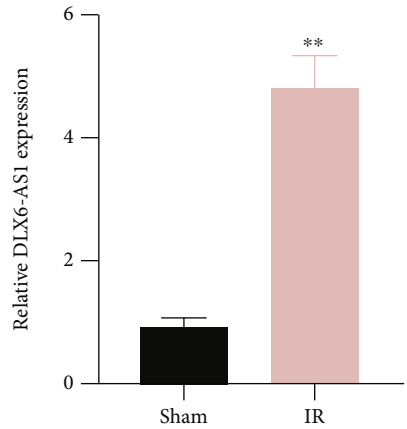

(g)

Figure 1: DLX6-AS1 expression was increased in the myocardial tissues of IR injury rats. IR rats were established by LAD ligation. Sham-operated rats were served as control. (a) The pathological changes of myocardial tissues were analyzed by HE staining. (b) Infarction size of myocardial tissues was examined by TTC staining. (c) The levels of LDH and CK in the serum were detected by ELISA. (d) The levels of MCP-1, IL-6, and IL-1β in the serum were detected by ELISA. (e) Apoptosis in myocardial tissues was detected by TUNEL staining. (f) The expression of Bax and Bcl-2 in myocardial tissues was analyzed by WB. (g) The DLX6-AS1 mRNA expression was examined through qRT-PCR. $^{**}P$ vs. Sham.

and downregulate miR-204-5p. The plasmids pc-DNA, NC-mimic, and inh-NC were served as control. All the plasmids were obtained from the GenePharma. H9c2 cells were transfected with the plasmids utilizing Lipofectamine 2000 Transfection Reagent (Invitrogen, Carlsbad, CA, USA).

2.7. Quantitative Real-Time PCR (qRT-PCR). Myocardial tissues and H9c2 cells were treated with TRIzol reagent (Invitrogen) to extract total RNA. PrimeScript RT Master Mix (TaKaRa, Tokyo Japan) was utilized to synthesize complementary DNA from total RNA. The relative expression of mRNAs was assessed by using TB Green Premix Ex Taq II (TaKaRa). The primer sequence (5′-3′) was shown as follows: DLX6-AS1-forward: CCA CCC ACT GAG AGA AGA GG, DLX6-AS1-reverse: CCT CCA AGC AAT TGT CCA GT; FBXW7-forward: GTT CCG CTG CCT AAT CTT CCT, FBXW7-reverse: CCC TTC AGG GAT TCT GTG CC; miR-204-5p-forward: TCC GTA TCC TAC TGT T, miR-204-5p-reverse: GCA GGG TCC GAG GTA TTC; MCP-1-forward: TCT GGG CCT GTT GTT CAC AGT, MCP-1-reverse: TGC TGC TGG TGA TTC TCT TGT AGT; IL-6-forward: CTC TCC GCA AGA GAC TTC CAG, IL-6-reverse: TTC TGA CAG TGC ATC ATC GCT; IL-1β-forward: ACA GAT GAA GTG CTC CT; IL-1β-reverse: AAG ATA GGT TCT TCT TCA; GAPDH-forward: GTC AGC CGC ATC TTC TTT TG, GAPDH-reverse: GCG CCC AAT ACG ACC AAA TC; U6-forward: CTC GCT TCG GCA GCA CA, U6-reverse: AAC GCT TCA CGA ATT TGC GT. The relative expression of lncRNA and mRNA was normalized to GAPDH, and miRNA expression was normalized to U6. The results were analyzed using $2^{-\Delta\Delta CT}$ method for quantification.

2.8. Western Blot (WB). Total Protein Extraction Kit (Solarbio, Beijing, China) and BCA Protein Assay Kit (Solarbio, Beijing, China) were utilized to extract proteins from myocardial tissues or H9c2 cells and measure protein concentration. Proteins from each sample were separated by SDS-PAGE gel electrophoresis and then transferred onto the PVDF membranes. The membranes were stained with the primary antibody, Bax (Cat: ab32503; 1 : 1000 dilution), Bcl-2 (Cat: ab194583; 1 : 1000 dilution), FBXW7 (Cat: ab109617; 1 μg/mL dilution), or GAPDH (Cat: ab181602; 1 : 1000 dilution) 4°C for 12 h and then incubated with goat antirabbit HRP-IgG (Cat: ab6721; 1 : 2000 dilution) at 37°C for 1 h. These antibodies were obtained from Abcam (Cambridge, MA, USA). The data was analyzed by Image J software. The expression of protein was normalized to the internal reference gene GAPDH.

2.9. Luciferase Reporter Assay. Starbase online tool uncovered that there may be binding sites between DLX6-AS1 and miR-204-5p or betweenmiR-204-5p and FBXW7. To verify this speculation, the luciferase reporter vectors pmirGLO containing wild type (WT) or mutant type (Mut) of DLX6-AS1 and FBXW7 were constructed by GenePharma. H9c2 cells were transfected with WT/Mut of luciferase reporter vectors and miR-204-5p mimic or NC-mimic using Lipofectamine 2000 Transfection Reagent. Finally, Luciferase Assay System (Ambion, Austin, TX, USA) was used to assess the relative luciferase activity of H9c2 cells.

2.10. RNA-Binding Protein Immunoprecipitation (RIP). RIP assay was carried out to determine whether DLX6-AS1 and miR-204-5p interacted with Ago-2 to form a RNA-induced silencing complex (RISC) according to reported work [21]. H9c2 cells transfected with pc-DLX6-AS1 were incubated with polysome lysis buffer on ice for 5 min. The cell lysates were incubated with 10 μg anti-pan-Ago IgG 2A8 (Cat: MABE56; Merck Millipore, Billerica, MA, USA) and conjugated with Dynabeads Protein G (Thermo Fisher Scientific,

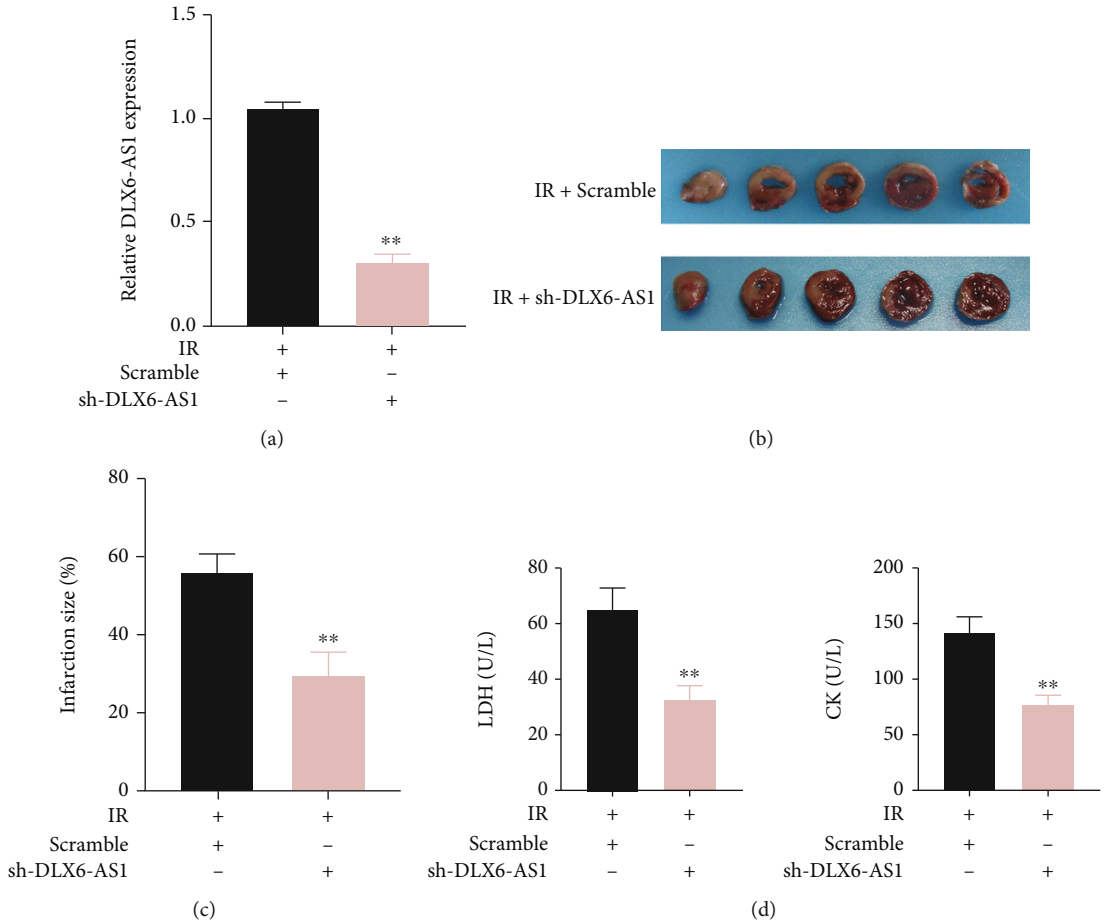

Figure 2: DLX6-AS1 downregulation alleviated myocardial infarction and myocardial damage in IR rats. IR rats were established by LAD ligation, which were then transfected with sh-DLX6-AS1 or Scramble. (a) The expression of DLX6-AS1 in the myocardial tissues was examined by qRT-PCR. (b and c) Infarction size of myocardial tissues was examined by TTC staining. (d) The levels of LDH and CK in the serum were assessed by ELISA. $^{**}P$ vs. IR + Scramble.

Waltham, MA, USA) at overnight rotating at 4°C. IgG1 isotype control (Cat: 21275511; ImmunoTools, Friesoythe, Germany) coated with Dynabeads Protein G was used as control. Subsequently, the cell lysates were incubated with 50 μL glycine (pH 2.3) at room temperature for 15 min to elute protein-RNA complexes from the beads. The protein-RNA complexes were lysed with proteinase K. Finally, miRNeasy Mini Kit (Qiagen, Düesseldorf, Germany) was used to purify RNA following the manufacturer's recommendations. The purified RNA was served as template to detect DLX6-AS1 and miR-204-5p expression by performing qRT-PCR. Cell lysates were served as Input group.

2.11. Flow Cytometry. Flow cytometry was done to measure apoptotic cells in H9c2 cells utilizing Annexin V-FITC Apoptosis Detection Kit (Beyotime, Shanghai, China) on a BD FACSCalibur (BD Bioscience, San Jose, USA). H9c2 cells were cultured for 24 h. After washing with PBS for 3 times, cells were stained with Annexin V-FITC and PI in the dark. Finally, the apoptotic cells were detected by flow cytometry analysis.

2.12. Statistical Analysis. Each assay was performed for 3 times. The representative data were presented and expressed as mean ± standard deviation. Statistical analysis was carried out utilizing SPSS 22.0 statistical software (IBM, Armonk, NY, USA). Two-tailed Student's t-test (between two groups) and one-way ANOVA (among multiple groups) were utilized to analyze the statistical differences. $P < 0.05$ indicates significant differences.

3. Results

3.1. The Expression of DLX6-AS1 Was Decreased in IR Injury Rats. In order to determine the function of DLX6-AS1 in IR injury, a rat model of IR injury was constructed by LAD ligation. HE and TTC staining revealed that IR rats exhibited a severe damage and an increase of infarction size in the myocardial tissues compared with sham-operated rats (Figures 1(a) and 1(b)). Moreover, we detected the level of myocardial enzyme spectrum in the serum by ELISA, showing that LDH and CK were increased in IR rats (Figure 1(c)). The proinflammatory factors such as MCP-1, IL-6, and IL-

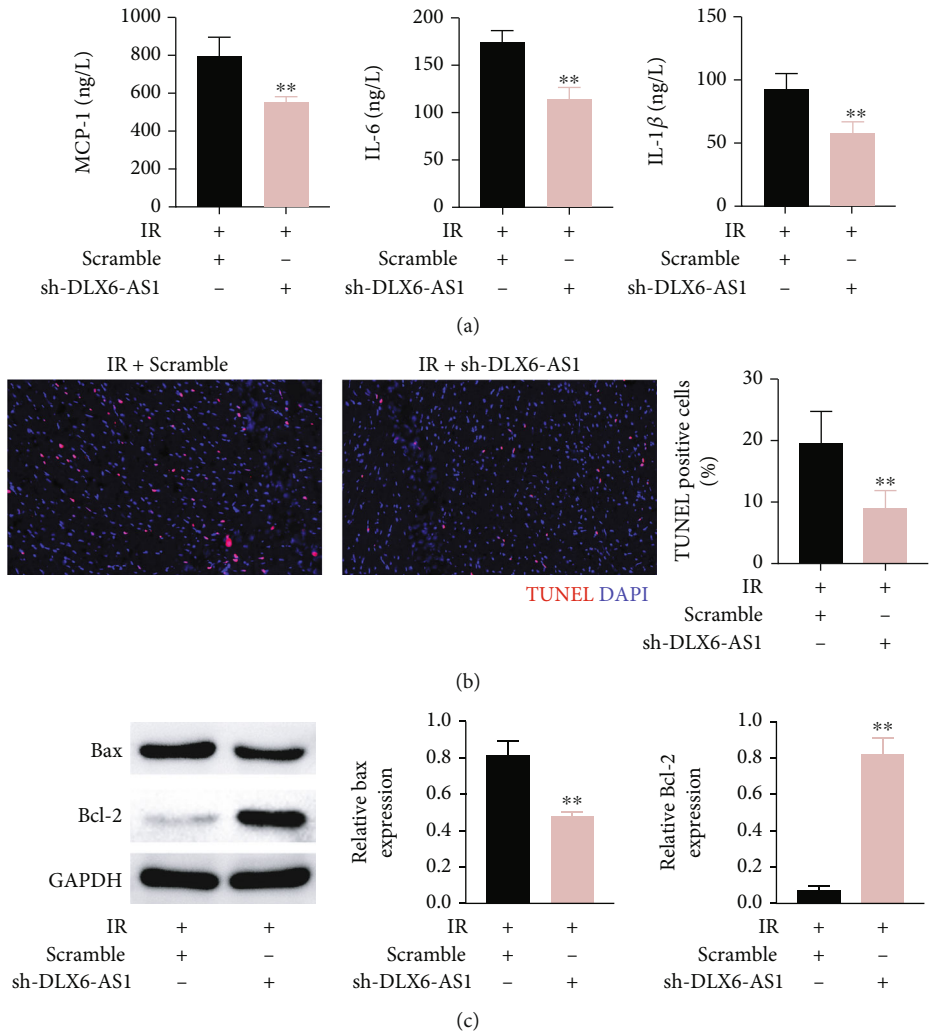

Figure 3: DLX6-AS1 downregulation repressed inflammatory response and cell apoptosis in IR rats. IR rats were established by LAD ligation, which were then transfected with sh-DLX6-AS1 or Scramble. (a) The levels of MCP-1, IL-6, and IL-1β in the serum were detected by ELISA. (b) Apoptosis in myocardial tissues was detected by TUNEL staining. (c) The expression of Bax and Bcl-2 in myocardial tissues was analyzed by WB. $^{**}P$ vs. IR + Scramble.

1β were also enhanced in the serum of IR rats as compared with sham-operated rats (Figure 1(d)). Furthermore, cell apoptosis in the myocardial tissues of rats was measured by TUNEL staining, revealing that the apoptotic cells were increased in IR rats (Figure 1(e)). Compared with that in sham-operated rats, Bax protein was upregulated, while Bcl-2 protein was downregulated in myocardial tissues of IR rats (Figure 1(f)). Interestingly, DLX6-AS1 expression was upregulated in the myocardial tissues of IR rats (Figure 1(g)). Thus, these data indicated that the upregulation of DLX6-AS1 may be associated with myocardial IR injury.

3.2. Inhibition of DLX6-AS1 Attenuated IR-Induced Myocardial Injury. Next, we investigated whether inhibition of DLX6-AS1 can attenuate IR injury in rats. DLX6-AS1 was silenced in IR rats, and the results showed that DLX6-AS1 was severely downregulated in the myocardial tissues of IR rats following injection of sh-DLX6-AS1 (Figure 2(a)). Then, the myocardial infarction of IR rats was examined by TTC staining. As shown in Figures 2(b) and 2(c), the infarction size in myocardial tissues of IR rats was severely decreased. We also found that silencing DLX6-AS1 caused a decrease in the levels of LDH and CK in the serum of IR rats (Figure 2(d)).

Additionally, ELISA results revealed that the inflammatory cytokines including MCP-1, IL-6, and IL-1β in the serum of IR rats were decreased by DLX6-AS1 deficiency (Figure 3(a)). TUNEL staining and WB assays were carried out to assess apoptotic cells and the expression of apoptosis-related proteins in myocardial tissues of IR rats. Silence of DLX6-AS1 reduced the number of apoptotic cells through downregulating Bax and upregulating Bcl-2 in IR rats (Figures 3(b) and 3(c)).

Taken together, DLX6-AS1 deficiency reduced myocardial infarction, inflammatory response, and cell apoptosis in IR rats.

3.3. DLX6-AS1 Promoted FBXW7 Expression by Competitively Binding to miR-204-5p. Bioinformatics software Starbase revealed that there may be binding sites between DLX6-AS1

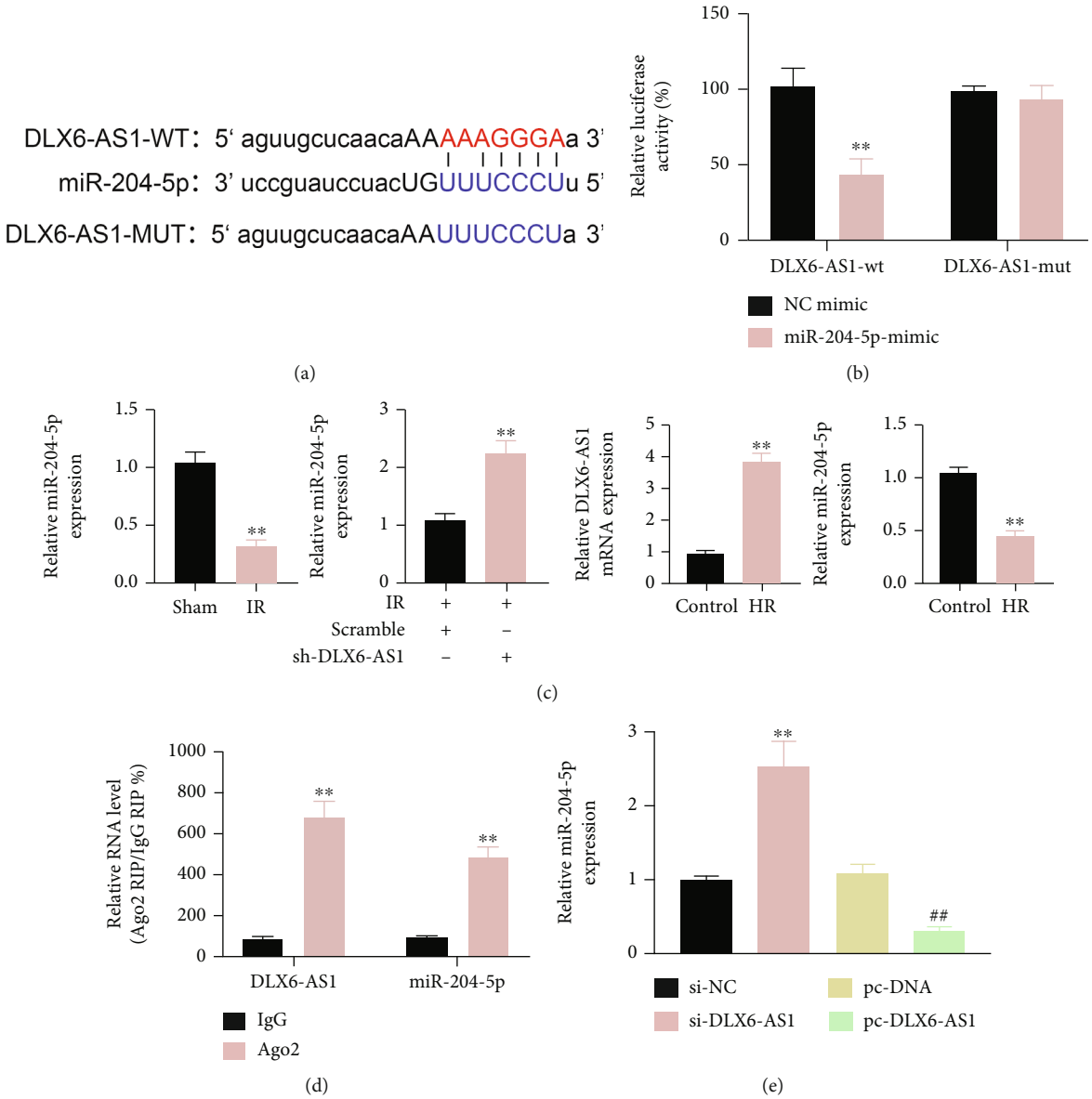

Figure 4: DLX6-AS1 interacted with miR-204-5p and repressed miR-204-5p expression. (a) The predicted binding sites between DLX6-AS1 and miR-204-5p were presented. (b) The interaction between DLX6-AS1 and miR-204-5p in H9c2 cells was verified by luciferase reporter assay. (c) IR rats were established by LAD. Sham-operated rats were served as control. H9c2 cells were subjected to HR. Normal H9c2 cells were served as control. The expression of miR-204-5p and DLX6-AS1 in the myocardial tissues and H9c2 cells was examined by qRT-PCR. (d) RIP assay was carried out utilizing an anti-Ago2 antibody in H9c2 cells transfected with pc-DLX6-AS1 to detect the expression of DLX6-AS1 and miR-204-5p through qRT-PCR. (e) The qRT-PCR was carried out to assess the expression of miR-204-5p in H9c2 cells transfected with si-NC, si-DLX6-AS1, pc-DNA, or pc-DLX6-AS1. $^{**}P$ vs. NC-mimic, Sham, Control, IgG, si-NC; $^{\#\#}P$ vs. pc-DNA.

and miR-204-5p (Figure 4(a)). Luciferase reporter assay confirmed that DLX6-AS1 interacted with miR-204-5p in H9c2 cells (Figure 4(b)). Furthermore, the expression of miR-204-5p and DLX6-AS1 in IR rats and HR-treated H9c2 cells was examined by qRT-PCR. Compared with sham-operated rats, miR-204-5p expression was decreased in IR rats and HR-treated H9c2 cells. DLX6-AS1 was upregulated in HR-treated H9c2 cells. Furthermore, miR-204-5p expression was increased after silencing DLX6-AS1 (Figure 4(c)). In addition, both DLX6-AS1 and miR-204-5p interacted with Ago-2 to form a RISC (Figure 4(d)). The mRNA expression of miR-204-5p was significantly enhanced in H9c2 cells transfected with si-DLX6-AS1, while miR-204-5p expression was severely decreased in H9c2 cells transfected with pc-DLX6-AS1 (Figure 4(e)).

Subsequently, bioinformatics analysis uncovered that FBXW7 may be a downstream target of miR-204-5p, which was verified by luciferase reporter assay (Figures 5(a) and 5(b)). Moreover, FBXW7 expression was repressed by miR-204-5p overexpression and increased by DLX6-AS1 upregulation in H9c2 cells. DLX6-AS1 upregulation reversed miR-204-5p mimic-mediated inhibitory effect on FBXW7 expression (Figure 5(c)).

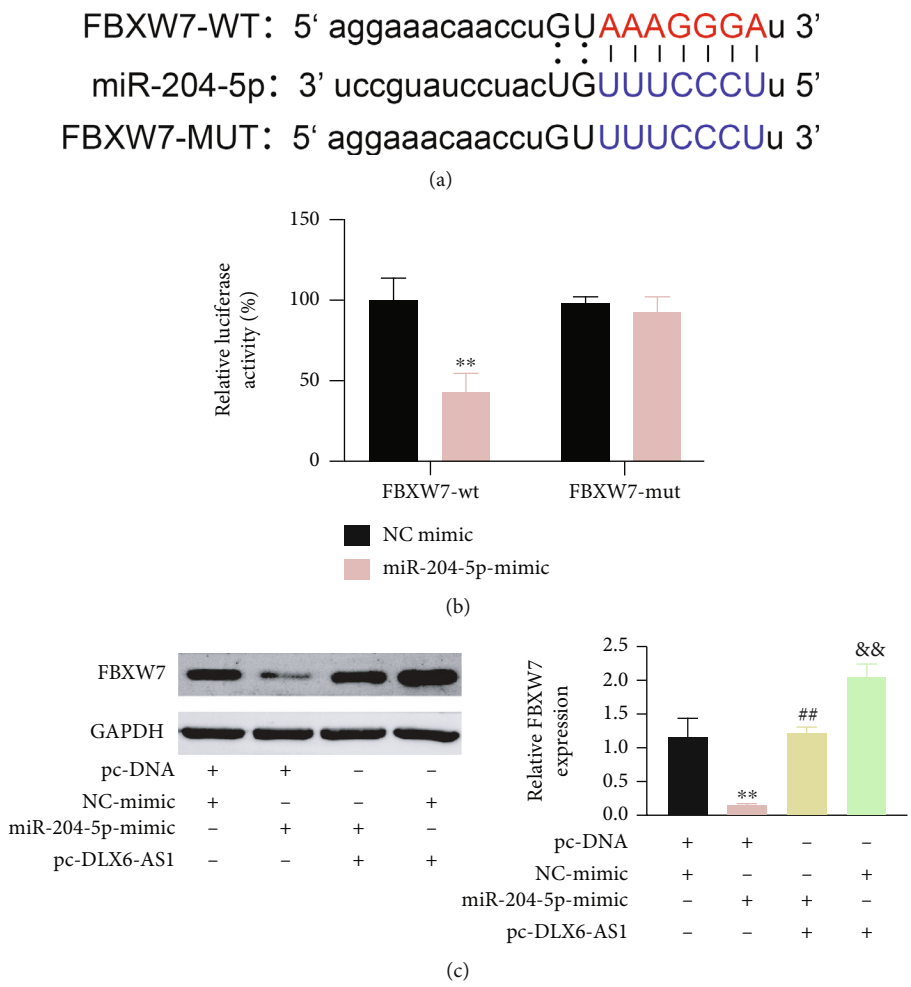

Figure 5: DLX6-AS1 promoted FBXW7 expression by sponging miR-204-5p. (a) The predicted binding sites between miR-204-5p and FBXW7 were presented. (b) The interaction between miR-204-5p and FBXW7 in H9c2 cells was verified by luciferase reporter assay. (c) H9c2 cells were transfected with pc-DLX6-AS1 or pc-DNA and miR-204-5p-mimic or NC-mimic. FBXW7 expression in the H9c2 cells was examined by WB. $^{**}P$ vs. NC-mimic, pc-DNA + NC-mimic; $^{\#\#}P$ vs. pc-DNA + miR-204-5p-mimic; $^{\&\&}P$ vs. miR-204-5p-mimic + pc-DLX6-AS1.

In a word, DLX6-AS1 functioned as a ceRNA to interact with miR-204-5p, which contributed to regulate the expression of its down-stream target FBXW7.

3.4. DLX6-AS1 Deficiency Alleviated IR-Induced Myocardial Injury by Regulating miR-204-5p. Finally, the functional role of DLX6-AS1 was verified *in vitro*. Both DLX6-AS1 and miR-204-5p were silenced in H9c2 cells, which were then treated with HR. Inhibition of miR-204-5p significantly enhanced MCP-1, IL-6, and IL-1β expression in HR-treated H9c2 cells. In contrast, DLX6-AS1 silencing led a decrease of these inflammatory factors in HR-treated H9c2 cells. Inhibition of miR-204-5p reversed si-DLX6-AS1-mediated anti-inflammatory effect in HR-treated H9c2 cells (Figure 6(a)). Moreover, the influence of knocking down DLX6-AS1 on apoptosis was investigated in HR-treated H9c2 cells by WB and flow cytometry. Knockdown of miR-204-5p enhanced Bax expression and repressed Bcl-2 expression in HR-treated H9c2 cells. Upregulation of DLX6-AS1 exerted an opposite effect on these apoptosis-related proteins, which was rescued by silencing DLX6-AS1 (Figure 6(b)). Apoptosis of HR-treated H9c2 cells was accelerated by miR-204-5p deficiency and decreased by DLX6-AS1 inhibition. However, knockdown of DLX6-AS1-mediated inhibition of apoptosis was abrogated by miR-204-5p inhibitor (Figure 6(c)). Thus, inhibition of DLX6-AS1 repressed inflammatory response and cell apoptosis in HR-treated H9c2 cells by regulating miR-204-5p.

It is also important that we discovered that the infraction size was reduced after silencing DLX6-AS1, but this effect could be reversed by overexpressing FBXW7 (Figure Supplementary A). Additionally, the decreased LDH and CK levels of mediated DLX6-AS1 knockdown were rescued by FBXW7 overexpression (Figure Supplementary B).

4. Discussion

Myocardial IR injury is a complex process, and many factors are involved in the damage of myocardial tissues [22]. In the past few decades, scholars attempt to clarify the molecular mechanism of myocardial IR injury and find the effective treatment to reduce the scope and extent of myocardial injury caused by IR [22].

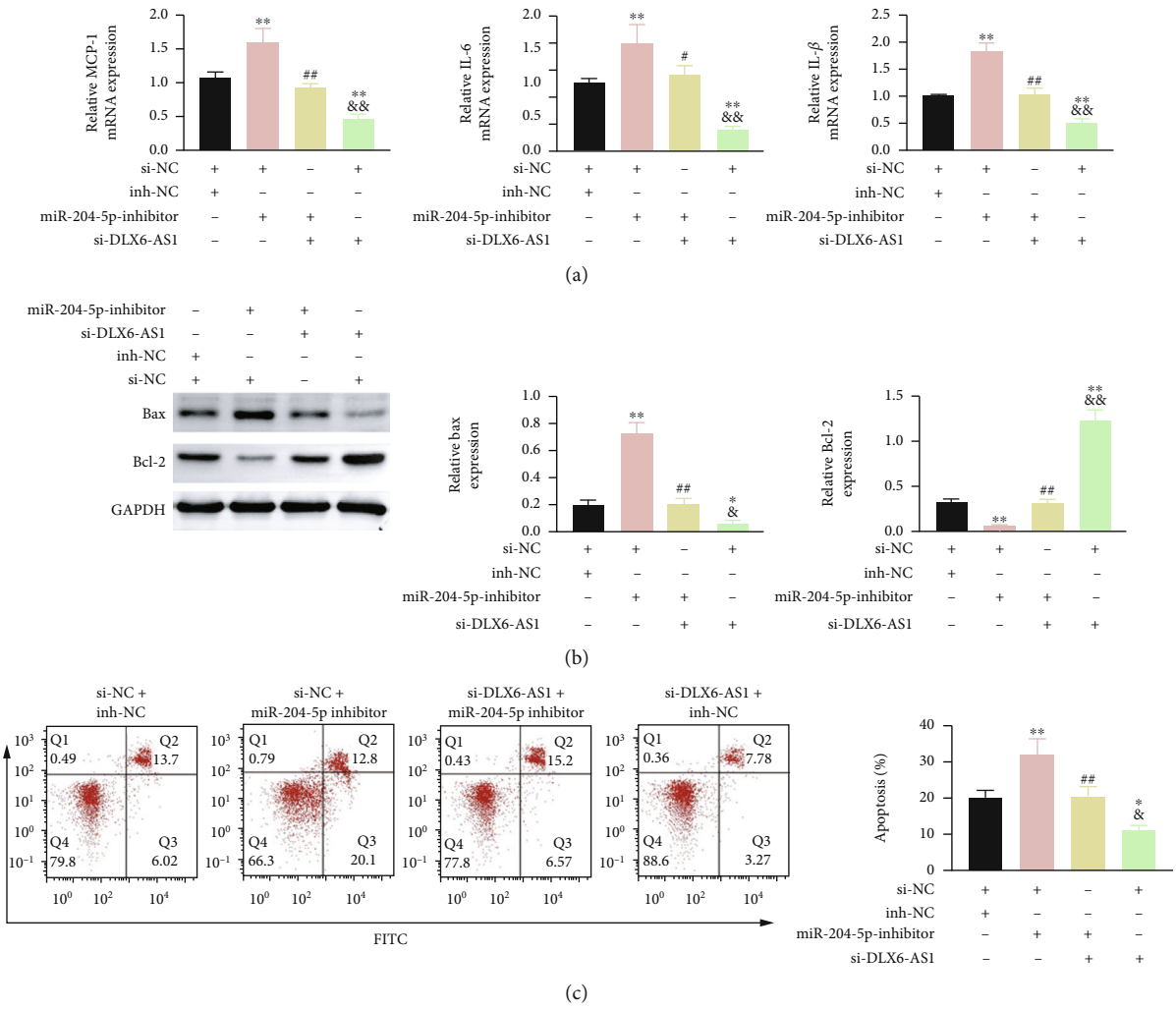

Figure 6: DLX6-AS1 deficiency repressed inflammatory response and cell apoptosis in HR-treated H9c2 cells by regulating miR-204-5p. H9c2 cells were transfected with si-DLX6-AS1 or si-NC and miR-204-5p inhibitor or inh-NC, followed by HR treatment. (a) The expression of MCP-1, IL-6, and IL-1β in the H9c2 cells was detected by qRT-PCR. (b) The expression of Bax and Bcl-2 in the H9c2 cells was assessed by WB. (c) Apoptosis of H9c2 cells was measured through flow cytometry. $^{**}P$ vs. si-NC + inh-NC; $^{\#\#}P$ vs. si-NC + miR-204-5p inhibitor; $^{\&\&}P$ vs. miR-204-5p inhibitor + si-DLX6-AS1.

DLX6-AS1 participates in various diseases. For instance, Liu et al. have revealed that DLX6-AS1 expression was elevated in the placenta tissues of preeclampsia [23]. DLX6-AS1 functions as ceRNA to regulate miR-149-5p/ERP44 axis, which contributes to aggravate preeclampsia progression. DLX6-AS1 is rich in the serum exosomes of cervical cancer patients, whose upregulation is positively related to the poor prognosis of cervical cancer [24]. DLX6-AS1 inhibits ANXA10 expression through ubiquitination-mediated degradation to accelerate hepatocellular carcinoma development, which can be attributed to the regulation on miR-513c/Cul4A axis [25]. Hu et al. have confirmed that DLX6-AS1 promoted I/R-induced cerebral neuron impairments by regulating miR-149-3p/BOK axis [13]. In the present work, the IR injury rats displayed a severe tissue damage and significant increase of the myocardial infarction size and cell apoptosis. The levels of serum myocardial enzyme spectrum LDH and CK and proinflammatory factors MCP-1, IL-6, and IL-1β were significantly increased in the myocardial tissues of IR injury rats. These data showed that IR injury rats had a significant myocardial damage, which was rescued by inhibition of DLX6-AS1 expression. Thus, DLX6-AS1 played a crucial role in the development of myocardial IR injury.

The miR-204-5p expression is lower in the myocardial tissue, and KCNQ1OT1/miR-204-5p/LGALS3 axis was involved in the myocardial IR injury in mice [17]. In this work, it was verified that DLX6-AS1 repressed miR-204-5p expression by targeting miR-204-5p. The expression of miR-204-5p was decreased in IR rats and HR-treated H9c2 cells. Both DLX6-AS1 and miR-204-5p interacted with Ago-2 to form a RISC. The assembly of RISC is the central link of RNAi and miRNA pathways, which has the activity of silencing the target mRNA [26]. Ago-2 is the core protein in RISC and has the ability to shear mRNA [27]. Moreover, miR-204-5p interacted with FBXW7, and inhibited FBXW7 expression. DLX6-AS1 rescued the miR-204-5p-mediated inhibition on FBXW7 expression.

Thus, DLX6-AS1 elevated FBXW7 expression by inhibiting miR-204-5p expression, thereby can act as a ceRNA.

FBXW7 is a F-box WD40 protein and serves as a substrate recognition subunit of the SCF (SKP1/CUL1/F-box protein) E3 ubiquitin ligase complex. In recent years, a lot of work has found that miR-223-3p targets FBXW7 to regulate myocardial inflammation and apoptosis after myocardial infarction [18]. Additionally, miR322 modulates the FBXW7/notch pathway to affect cardioprotection against IR injury [19]. FBXW7 regulates EZH2-SIX1 signaling to accelerate pathological cardiac hypertrophy [28]. Moreover, miR-211-5p/FBXW7 axis relieves the myocardial ischemia injury stimulated by IR treatment [29]. Besides, miR-195-5p affects MFN2 and FBXW7 to facilitate cardiomyocyte hypertrophy [30]. Consistently, the role of FBXW7 in IR injury was also confirmed in this study. DLX6-AS1 deficiency repressed inflammatory response and cell apoptosis in HR-treated H9c2 cells through regulating miR-204-5p/FBXW7 axis.

5. Conclusion

This work demonstrated that lncRNA DLX6-AS1 promoted FBXW7 expression by sponging miR-204-5p, which contributed to accelerating myocardial IR injury. Thus, this work provides a novel ceRNA DLX6-AS1/miR-204-5p/FBXW7 axis in myocardial IR injury, and DLX6-AS1 may be a potential target for myocardial IR injury treatment.

Data Availability

All data generated or analyzed during this study are included in this published article.

Ethical Approval

Ethical approval was obtained from the Ethics Committee of Zhongshan Hospital of Fudan University.

Conflicts of Interest

The authors state that there are no conflicts of interest to disclose.

Authors' Contributions

Fanshun Wang and Yuan Wu designed the study and supervised the data collection; Fanshun Wang analyzed the data and interpreted the data; Yuan Wu prepared the manuscript for publication and reviewed the draft of the manuscript. All authors have read and approved the manuscript. Fanshun Wang and Yuan Wu are contributed equally to the work and are co-first author.

Supplementary Materials

Figure Supplementary. (A) Infarction size of myocardial tissues was examined by TTC staining. (B) The levels of LDH and CK in the serum were detected by ELISA. $^{**}P$ vs. IR + AAV-scramble+empty; $^{\#\#}P$ vs. IR + AAV-sh-DLX6-AS1 + empty. *(Supplementary Materials)*

References

[1] D. Mozaffarian, E. J. Benjamin, A. S. Go et al., "Heart disease and stroke statistics-2016 update: a report from the American Heart Association," *Circulation*, vol. 133, no. 4, pp. e38–360, 2016.

[2] S. Kristensen, K. G. Laut, J. Fajadet et al., "Reperfusion therapy for ST elevation acute myocardial infarction 2010/2011: current status in 37 ESC countries," *European Heart Journal*, vol. 35, no. 29, pp. 1957–1970, 2014.

[3] K. Rentrop and F. Feit, "Reperfusion therapy for acute myocardial infarction: concepts and controversies from inception to acceptance," *American Heart Journal*, vol. 170, no. 5, pp. 971–980, 2015.

[4] D. Hausenloy and D. Yellon, "Ischaemic conditioning and reperfusion injury," *Nature Reviews Cardiology*, vol. 13, no. 4, pp. 193–209, 2016.

[5] R. Jennings, H. M. Sommers, G. A. Smyth, H. A. Flack, and H. Linn, "Myocardial necrosis induced by temporary occlusion of a coronary artery in the dog," *Archives of Pathology*, vol. 70, pp. 68–78, 1960.

[6] M. Wu, G. T. Yiang, W. T. Liao et al., "Current mechanistic concepts in ischemia and reperfusion injury," *Cellular Physiology and Biochemistry: International Journal of Experimental Cellular Physiology, Biochemistry, and Pharmacology*, vol. 46, no. 4, pp. 1650–1667, 2018.

[7] S. Jathar, V. Kumar, J. Srivastava, and V. Tripathi, "Technological developments in lncRNA biology," *Advances in Experimental Medicine and Biology*, vol. 1008, pp. 283–323, 2017.

[8] D. Fu, S. Yang, J. Lu, H. Lian, and K. Qin, "LncRNA NORAD promotes bone marrow stem cell differentiation and proliferation by targeting miR-26a-5p in steroid-induced osteonecrosis of the femoral head," *Stem Cell Research & Therapy*, vol. 12, no. 1, p. 18, 2021.

[9] V. Simion, H. Zhou, S. Haemmig et al., "A macrophage-specific lncRNA regulates apoptosis and atherosclerosis by tethering HuR in the nucleus," *Nature Communications*, vol. 11, no. 1, p. 6135, 2020.

[10] Y. Zhao and Y. Ai, "Overexpression of lncRNA Gm15621 alleviates apoptosis and inflammation response resulting from sevoflurane treatment through inhibiting miR-133a/Sox4," *Journal of Cellular Physiology*, vol. 235, no. 2, pp. 957–965, 2020.

[11] J. Li, P. Li, W. Zhao et al., "Expression of long non-coding RNA DLX6-AS1 in lung adenocarcinoma," *Cancer Cell International*, vol. 15, no. 1, p. 48, 2015.

[12] L. Kong and C. Zhang, "LncRNA DLX6-AS1 aggravates the development of ovarian cancer via modulating FHL2 by sponging miR-195-5p," *Cancer Cell International*, vol. 20, no. 1, p. 370, 2020.

[13] X. Hu, Z. Xiang, W. Zhang et al., "Protective effect of DLX6-AS1 silencing against cerebral ischemia/reperfusion induced impairments," *Aging*, vol. 12, no. 22, pp. 23096–23113, 2020.

[14] Y. Huang, "The novel regulatory role of lncRNA-miRNA-mRNA axis in cardiovascular diseases," *Journal of Cellular and Molecular Medicine*, vol. 22, no. 12, pp. 5768–5775, 2018.

[15] I. Díaz, E. Calderón-Sánchez, R. D. Toro et al., "miR-125a, miR-139 and miR-324 contribute to Urocortin protection against myocardial ischemia-reperfusion injury," *Scientific Reports*, vol. 7, no. 1, p. 8898, 2017.

[16] A. Wojciechowska, A. Braniewska, and K. Kozar-Kamińska, "MicroRNA in cardiovascular biology and disease," *Advances in clinical and experimental medicine: official organ Wroclaw Medical University*, vol. 26, no. 5, pp. 865–874, 2017.

[17] J. Rong, H. Pan, J. He et al., "Long non-coding RNA KCNQ1OT1/microRNA-204-5p/LGALS3 axis regulates myocardial ischemia/reperfusion injury in mice," *Cellular Signalling*, vol. 66, article 109441, 2020.

[18] L. Zhang, J. Yang, M. Guo, and M. Hao, "MiR-223-3p affects myocardial inflammation and apoptosis following myocardial infarction via targeting FBXW7," *Journal of Thoracic Disease*, vol. 14, no. 4, pp. 1146–1156, 2022.

[19] Z. Chen, X. Su, Y. Shen et al., "MiR322 mediates cardioprotection against ischemia/reperfusion injury via FBXW7/notch pathway," *Journal of Molecular and Cellular Cardiology*, vol. 133, pp. 67–74, 2019.

[20] Z. Liu, J. Liu, Y. Wei et al., "LncRNA MALAT1 prevents the protective effects of miR-125b-5p against acute myocardial infarction through positive regulation of NLRC5," *Experimental and Therapeutic Medicine*, vol. 19, no. 2, pp. 990–998, 2020.

[21] A. Frank, S. Ebersberger, A. F. Fink et al., "Apoptotic tumor cell-derived microRNA-375 uses CD36 to alter the tumor-associated macrophage phenotype," *Nature Communications*, vol. 10, no. 1, p. 1135, 2019.

[22] N. Papageorgiou, A. Briasoulis, and D. Tousoulis, "Ischemia-reperfusion injury: complex pathophysiology with elusive treatment," *HJC = Hellenike kardiologike epitheorese*, vol. 59, no. 6, pp. 329-330, 2018.

[23] R. Liu, X. Wang, and Q. Yan, "The regulatory network of lncRNA DLX6-AS1/miR-149-5p/ERP44 is possibly related to the progression of preeclampsia," *Placenta*, vol. 93, pp. 34–42, 2020.

[24] X. Ding, S. Q. Zhang, X. L. Deng, and J. H. Qiang, "Serum exosomal lncRNA DLX6-AS1 is a promising biomarker for prognosis prediction of cervical cancer," *Technology in Cancer Research & Treatment*, vol. 20, article 1533033821990060, 2021.

[25] X. Liu, D. Peng, Y. Cao et al., "Upregulated lncRNA DLX6-AS1 underpins hepatocellular carcinoma progression via the miR-513c/Cul4A/ANXA10 axis," *Cancer Gene Therapy*, vol. 28, no. 5, pp. 486–501, 2021.

[26] Z. Paroo, Q. Liu, and X. Wang, "Biochemical mechanisms of the RNA-induced silencing complex," *Cell Research*, vol. 17, no. 3, pp. 187–194, 2007.

[27] G. Meister, M. Landthaler, A. Patkaniowska, Y. Dorsett, G. Teng, and T. Tuschl, "Human Argonaute2 mediates RNA cleavage targeted by miRNAs and siRNAs," *Molecular Cell*, vol. 15, no. 2, pp. 185–197, 2004.

[28] W. Gao, N. Guo, S. Zhao et al., "FBXW7 promotes pathological cardiac hypertrophy by targeting EZH2-SIX1 signaling," *Experimental Cell Research*, vol. 393, no. 1, article 112059, 2020.

[29] Y. Liu, J. Meng, H. Di, L. Zheng, and Z. Meng, "miR-211-5p alleviates the myocardial ischemia injury induced by ischemic reperfusion treatment via targeting FBXW7," *BioMed Research International*, vol. 2022, Article ID 5423929, 7 pages, 2022.

[30] L. Wang, D. Qin, H. Shi, Y. Zhang, H. Li, and Q. Han, "MiR-195-5p promotes cardiomyocyte hypertrophy by targeting MFN2 and FBXW7," *BioMed Research International*, vol. 2019, Article ID 1580982, 10 pages, 2019.

Hindawi
Mediators of Inflammation
Volume 2022, Article ID 4007469, 15 pages
https://doi.org/10.1155/2022/4007469

Research Article

Identification and Analysis of Senescence-Related Genes in Head and Neck Squamous Cell Carcinoma by a Comprehensive Bioinformatics Approach

Lin Deng,[1,2] Jinglin Mi,[1] Xiaolan Ruan,[2] Guozhen Zhang,[2] Yufei Pan,[2] and Rensheng Wang[1]

[1]*Department of Oncology, The First Affiliated Hospital of Guangxi Medical University, Nanning 530021, China*
[2]*Department of Radiation Oncology, Nanxishan Hospital of Guangxi Zhuang Autonomous Region, Guilin 541004, China*

Correspondence should be addressed to Yufei Pan; 23865934@qq.com and Rensheng Wang; 13807806008@163.com

Lin Deng and Jinglin Mi contributed equally to this work.

Received 12 July 2022; Accepted 10 September 2022; Published 17 October 2022

Academic Editor: Md Sayed Ali Sheikh

Head and neck cancer is the sixth most frequent cancer all over the world, with the majority of subtypes of head and neck squamous cell carcinoma (HNSCC). Cellular senescence-associated genes have been confirmed to play a critical role in cancer and have the potential to be prognostic biomarkers for cancer. Clinical information of HNSCC samples and expression data were acquired from public databases. Expression profiles of genes related to cellular senescence were used to identify molecular subtypes by consensus clustering. To screen differentially expressed genes (DEGs) between different subtypes, differential analysis was performed. We used the univariate Cox regression to identify prognostic DEGs and performed least absolute shrinkage and selection operator (LASSO) to optimize and construct a prognostic model. CIBERSORT, ESTIMATE, and TIDE tools were applied to estimate immune characteristics. Four molecular subtypes were established based on cellular senescence-associated genes. Differential prognosis was observed among different subtypes with C4 having the longest overall survival and C1 having the worst prognosis. C4 subtype also showed the highest immune infiltration. We screened a total of eight cellular senescence prognosis-related genes and established a cellular senescence-related signature score (CSRS.Score) that could stratify samples into high-CSRS.Score and low-CSRS.Score groups. The high-CSRS.Score group had worse prognosis, lower immune infiltration, and lower response to immunotherapy. We further improved the prognostic model and survival prediction by combining CSRS.Score with clinicopathological features using a decision tree model, which had high predictive accuracy and survival prediction. This study demonstrated an important role of cellular senescence in HNSCC. The identified eight cellular senescence-associated genes have the potential to provide ideas for adjuvant treatment and personalized treatment of HNSCC patients.

1. Introduction

Head and neck cancer (HNC) is the sixth most frequently diagnosed cancer type that causes 500,000 affected individuals per year worldwide [1]. Head and neck squamous cell carcinoma (HNSCC) accounts for the majority HNC patients, and more than half of the patients with HNSCC are initially diagnosed with locally advanced disease [2, 3]. Lymph node (LN) metastasis is a negative signal of head and neck cancer prognosis. However, it is challengeable to identify metastatic LN within the fibroadipose tissue [4]. The prognosis for HNSCC remains poor even with the use of combination therapy including surgery, radiation, chemotherapy, and immunotherapy [5]. Although no tumor LN is detected from clinical and radiographic estimation, there is still a high possibility over than 30% to observe nodal metastasis in the surgery

[6]. Therefore, there is an urgent need to provide effective biomarkers for early diagnosis, personalized treatment, and prognostic evaluation.

Senescence is a nearly unavoidable feature in all creatures, which is marked by a descending function of multiple cells and tissues. In spite of that degeneration is the most common age-related phenotype, aging allows to generate gain-of-function changes that lead to abnormal cell proliferation [7]. Moreover, these changes can result in genomic instability that enable to provide an advantage for the abnormal cells in proliferation, migration, and escape from immune surveillance [8]. Obviously, these phenotypes are the hallmarks of malignant cancers. Senescence plays a two-sided role in cancer development, preventing tumorigenesis by cell growth arrest in precancerous cells, but also facilitating malignant transformation of adjacent cells through protumorigenic drivers [9, 10]. Senescent cells can alter epigenetic modifications in neighboring cells by releasing senescence-associated signals [11–13]. A number of genes have been demonstrated to regulate senescence in cancer cells, such as p53 [14], Raf1 [14], MAP2K6/p38 [15], and PTEN [16]. Therapy-induced senescence has been observed in cancer cells after radiotherapy or chemotherapy [17]. When exposed to various conventional and targeted anticancer drugs, tumor cell senescence is induced, resulting in a positive effect on patient treatment [18, 19]. Thus, senescence is considered as a therapeutic target for clinical cancer treatment [20].

Senescence-associated genes also have the great potential to predict cancer prognosis. Althubiti et al. identified 10 plasma membrane-associated proteins expressed in senescent cells to be prognostic biomarkers especially in breast cancer [21]. Coppola et al. discovered a series of senescence-associated genes that correlated with age, overall survival, and grade of glioblastoma [22]. Yang et al. identified seven age-related genes by analyzing the expression profiles of HNSCC and adjacent cancer samples [23]. The risk score based on the seven age-related genes was significantly related to prognosis and immune response. But none of the studies have explored a molecular subtyping system based on senescence-associated genes in HNSCC. Senescence-associated molecular subtypes may help to further understand the role of cellular senescence in the tumor progression.

Therefore, in this study, we used cellular senescence-associated genes to identify molecular subtypes. Differential pathways and immune features were observed among different subtypes. Differential expressed genes (DEGs) were screened between different subtypes, and least absolute shrinkage and selection operator (LASSO) regression analysis was used to develop a cellular senescence-related signature scoring (CSRS) system. The CSRS system could define CSRS.Score for each HNSCC sample and classify them into high-CSRS.Score and low-CSRS.Score groups. Importantly, CSRS.Score had the potential to guide immunotherapy and chemotherapy for HNSCC patients. A decision tree and a nomogram based on CSRS.Score were constructed to more accurately predict prognosis than CSRS.Score only.

2. Materials and Methods

2.1. Data Source and Preprocessing. From The Cancer Genome Atlas (TCGA) database (named as TCGA cohort), we downloaded RNA-seq data of HNSCC samples and removed samples that did not have survival time, clinical follow-up information, or status of patients' survival. Ensembl ID was transformed into gene symbol. The median value of gene expression was selected for the genes with multiple gene symbols. GSE65858 and GSE41613 cohorts including gene expression profiles of HNSCC samples were obtained from Gene Expression Omnibus (GEO) database and were used as validation cohorts. We downloaded the annotation information of the corresponding microarray platform and mapped the probes to genes based on the annotation information to remove the probes that match one probe to multiple genes. If certain number probes matched to one gene, the median value was taken as the expression value of that gene. Finally, 499, 253, and 97 samples were remained in TCGA, GSE65858, and GSE41613 cohorts, respectively.

From CellAge database (https://genomics.senescence.info/cells/), we obtained 279 cellular senescence-associated genes.

2.2. Molecular Typing Based on Cellular Senescence-Associated Genes. We next constructed a consistency matrix by ConsensusClusterPlus to cluster HNSCC samples [24]. The expression data of genes associated with cellular senescence was used as a basis to obtain the molecular subtypes of the samples. "Pam" algorithm and "1 - Spearman correlation" were determined as a metric distance to perform 500 bootstraps, with each bootstrap consisting of 80% patients in the training set. Cluster numbers were set from 2 to 10, and the optimal cluster was determined by cumulative distribution function (CDF) and consensus matrix. Finally, the confirmed clusters were the molecular subtypes.

2.3. Construction of a CSRS.Score Scoring System. We identified differentially expressed cellular senescence genes between subtypes using limma R package [25] and selected prognostically significant differentially expressed genes through the univariate Cox regression analysis ($P < 0.05$). LASSO regression using the glmnet R package [26] and stepwise Akaike information criterion (stepAIC) [27] were performed to compress and reduce the differential genes to obtain prognostic genes associated with cellular senescence. The CSRS.Score for each sample was shown as follows: CSRS.Score = $\Sigma\, \beta i \times$ Expi, where Expi indicates the gene expression level of prognostic genes and βi is Cox regression coefficients of the corresponding genes. CSRS.Score was normalized using z-score, and the threshold "0" was determined to classify samples into low-risk and high-risk groups. The Kaplan-Meier (KM) survival analysis was conducted to assess the overall survival of different molecular subtypes. Significant differences were determined using the log-rank test.

2.4. Assessment of Immune Infiltration. CIBERSORT algorithm was employed to estimate the proportion of 22 immune cell types [28]. ESTIMATE algorithm was used to

calculate stromal score and immune score for evaluating stromal and immune infiltration [29].

2.5. Prediction of Immunotherapy Responsiveness. We used the TIDE algorithm to validate predicted treatment responsiveness. The TIDE algorithm is a computational method for predicting immune checkpoint blockade responsiveness using gene expression profiles [30]. TIDE can use gene expression information to predict cancer sensitivity to immune checkpoint therapy. The TIDE algorithm evaluates three immunosuppressive cell types that limit T cell infiltration in tumors, including M2 tumor-associated macrophages (TAMs), tumor-associated fibroblasts (CAFs), and myeloid-derived suppressor cells (MDSCs). The dysfunction score of tumor-infiltrating cytotoxic T lymphocytes (CTLs) (T cell dysfunction) and the exclusion score of CTLs by immunosuppressive factors (T cell exclusion) can be calculated by TIDE analysis.

2.6. Gene Set Enrichment Analysis (GSEA). GSEA allows to calculate the enrichment score of a gene set for annotating biological function [31]. We used GSEA for Kyoto Encyclopedia of Genes and Genomes (KEGG) pathway analysis in different molecular subtypes. Gene sets of KEGG pathways were accessed from the Molecular Signature Database (MSigDB) [32]. The enrichment scores of aneuploidy, homologous recombination defect number of segments, and fraction altered were calculated using GSEA.

2.7. Statistical Analysis. R software (v4.1) was applied to conduct all statistical analysis. The Kruskal-Wallis test was performed in testing the significance among four subtypes. Between high- and low-risk groups, the Wilcoxon test was performed to test the significance. Log-rank test was conducted in the Cox regression analysis and survival analysis. ANOVA was conducted in comparing different groups containing multiple subgroups. $P < 0.05$ was considered as significant.

3. Results

3.1. Molecular Typing Based on Cellular Senescence-Associated Genes. First, we extracted the expression of cellular senescence-associated genes from TCGA cohort. Then, the univariate Cox regression analysis was performed, and we obtained 28 genes associated with prognosis (Table S1) ($P < 0.01$). Then, based on the expression data of 28 prognosis-related cellular senescence-associated genes, we clustered 499 HNSCC samples into four clusters (molecular subtypes) through the determination of the CDF and the CDF delta area (Figures 1(a) and 1(b)). The consensus matrix showed that four clusters were independently distributed for most samples (Figure 1(c)). KM survival curves displayed that four molecular subtypes had significant differences of overall survival ($P < 0.01$, Figure 1(d)), with C4 having the most favorable prognosis and C1 having the highest proportion of dead samples ($P < 0.05$, Figure 1(e)). In addition, C1 also had a higher proportion of advanced stages of T stage, N stage, and AJCC stage (Figure S1).

3.2. Genomic Characteristics and Enriched Pathways of Molecular Subtypes. We explored the differences of genomic alterations in the TCGA cohort (acquired from previous research, [33]) among the four molecular subtypes. C1 subtype showed higher score of aneuploidy, homologous recombination defects, number of segments, and fraction altered (Figure 2(a)). However, no significant difference was shown in tumor mutation burden. In addition, we also analyzed the frequency of gene mutations among molecular subtypes (Figure 2(b)). TP53 had the highest mutation frequency of 81.3% and over a half samples had TP53 mutation. Missense mutation contributed the majority of gene mutation, while nonsense mutation was the most in CDKN2A.

Next, we analyzed whether differential enriched pathways exist in the different molecular subtypes by GSEA. 37 pathways were identified to be significantly enriched in the C1 subtype in the TCGA cohort. The enriched pathways mainly include cancer-related pathways, such as small cell lung cancer, ECM receptor interaction, and Wnt signaling pathway (Figure S2). The results suggested that cellular senescence-associated genes were possibly involved in cancer-related pathways and inflammatory pathways.

3.3. Immunological Characteristics and Immunotherapy/Chemotherapy Responses in Different Molecular Subtypes. We used immune cell signatures to assess immune cell infiltration in different subtypes to evaluate their immune characteristics. CIBERSORT revealed that 16 of 22 immune cells had a significant difference among four subtypes, such as regulatory T cells, CD8 T cells, resting memory CD4 T cells, and M0 macrophages ($P < 0.05$, Figure 3(a)). C1 had the lowest stromal score and immune score, while C4 had the highest scores ($P < 0.0001$, Figure 3(b)), indicating higher immune infiltration in C4. We considered that differential immune characteristics of four subtypes may result in different immune responses to immunotherapy.

Therefore, we assessed the expression of immune checkpoint genes in different molecular subtypes. We could see that the majority immune checkpoints were differentially expressed among four subtypes (Figure 3(c)), suggesting that the different subtypes may differentially response to immune checkpoint blockade. Not surprisingly, TIDE analysis revealed different responses of four subtypes to immune checkpoint inhibitors. As shown in Figure 3(d), the highest TIDE score was shown in C1, indicating that C1 was more probably to escape from immunotherapy. A higher proportion of MDSCs and CAFs may result in a higher T cell exclusion and unsatisfied immune response (Figure 3(d)). In addition, we also analyzed the predicted response of different molecular subtypes to four chemotherapeutic drugs (paclitaxel, docetaxel, cisplatin, and 5-fluorouracil). C1 and C2 subtypes are more sensitive to paclitaxel, docetaxel, and cisplatin drugs (Figure 3(e)).

3.4. Identification of Key Cellular Senescence-Associated Genes. We then used limma package to screen differentially expressed cellular senescence-associated genes between C1 and non-C1, C2 and non-C2, C3 and non-C3, and C4 and non-C4 molecular subtypes based on the conditions of false

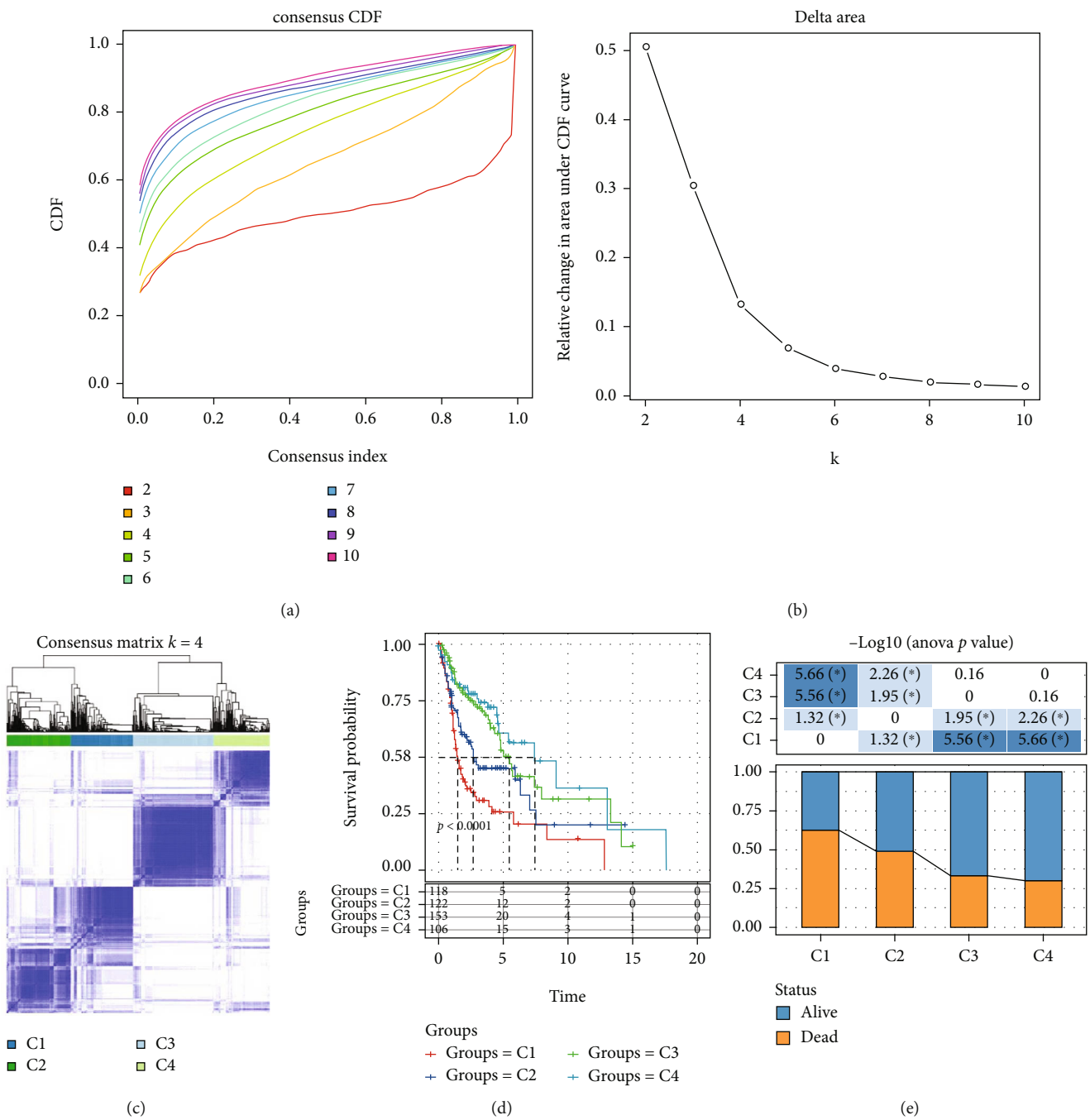

Figure 1: The TCGA cohort molecular typing based on cellular senescence-associated genes. (a) CDF curve for TCGA cohort samples. (b) CDF delta area curve for TCGA cohort samples. The vertical axis represents the relative change in area under CDF curve, and the horizontal axis represents the category number k. (c) At consensus $k = 4$, heat map of sample clustering. (d) KM curve of the four subtypes. (e) Survival status differences in different subtypes. $^{*}P < 0.05$.

discovery rate (FDR) < 0.05 and $|\log 2(\text{fold change})| > 1$. 232 DEGs were identified by the above intersection. And 77 prognostic genes were confirmed by the univariate Cox regression analysis including 31 "risk" and 46 "protective" genes (Figure 4(a)). Next, LASSO regression was conducted to compress the 77 prognostic genes. As shown in Figure 4(b), the coefficients of the prognostic genes tended to zero as lambda increased, and the optimal model was confirmed when lambda = 0.0275 (Figure 4(c)). StepAIC was further performed to optimize the model with the least number of prognostic genes. Finally, we identified eight key cellular senescence-associated genes related to prognosis (Figure 4(c)), including PYGL, KRT8, AREG, MAGEA4, DES, EPHX3, CDKN2A, and SPINK6.

3.5. Validation of the Eight-Gene Prognostic Model. We calculated and normalized the cellular senescence-related signature score (CSRS.Score) for each sample according to the

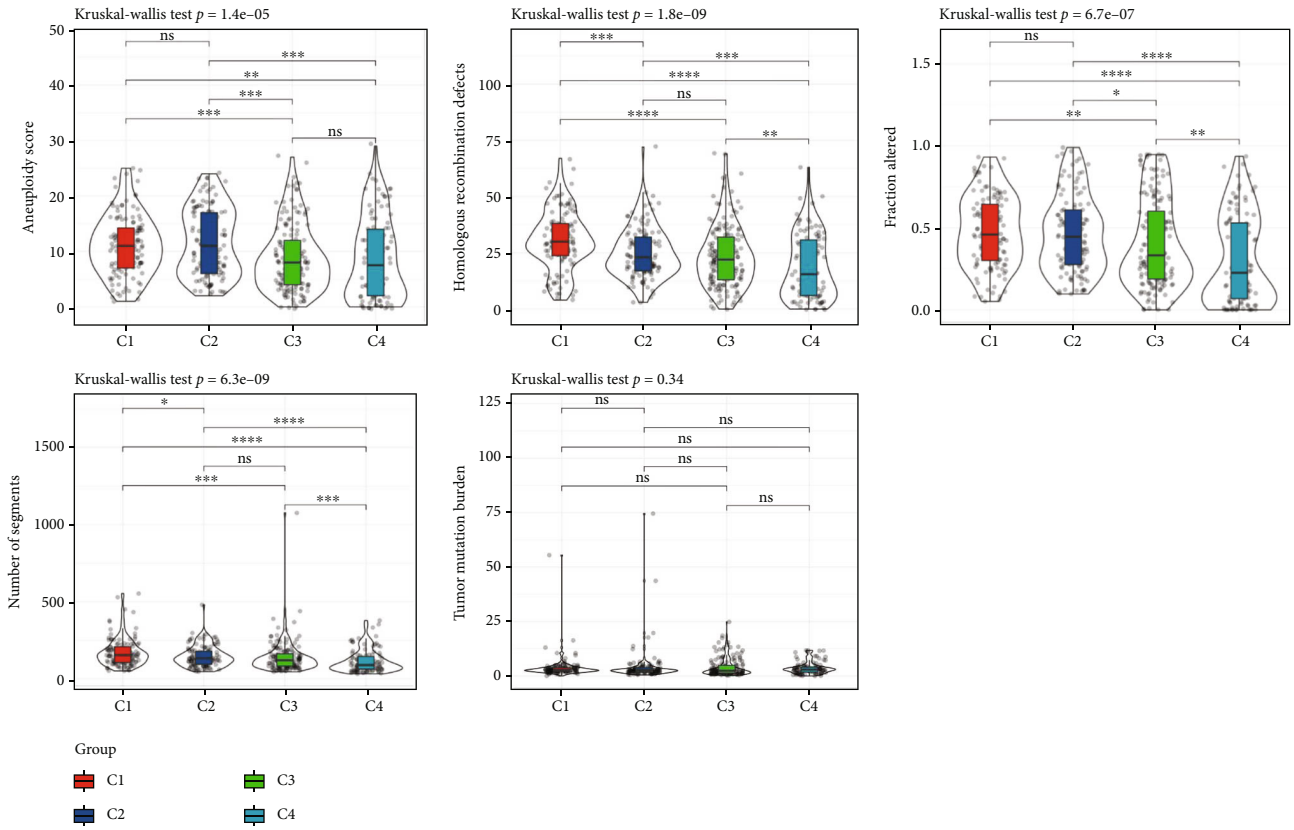

(a)

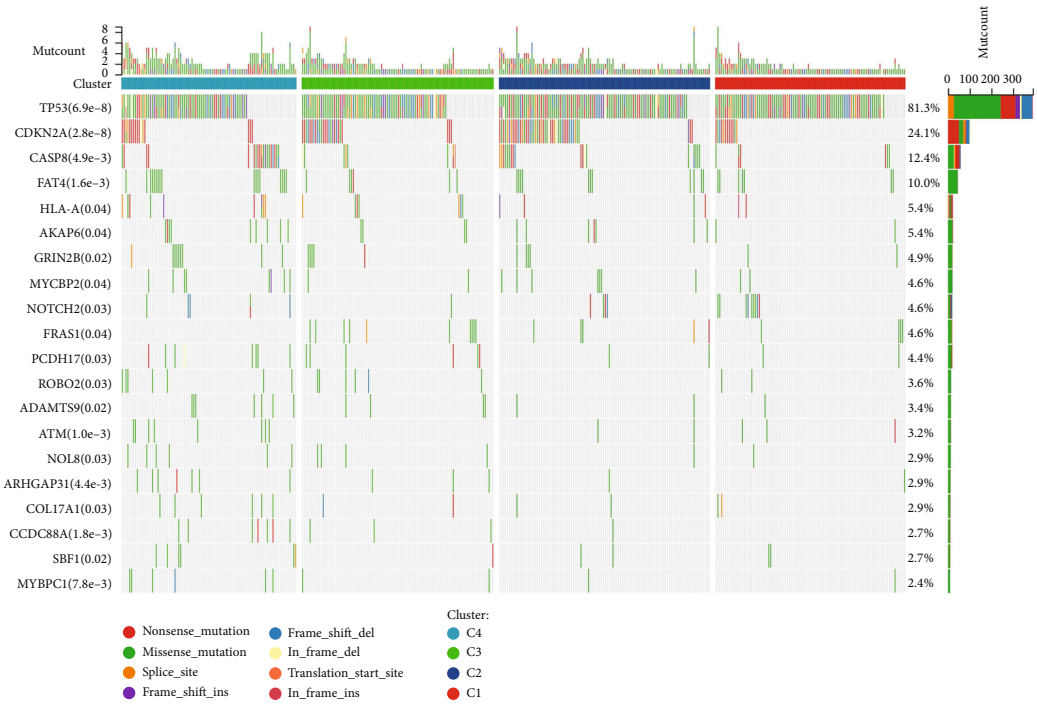

(b)

Figure 2: Genomic alterations in the molecular subtypes of the TCGA cohort. (a) Comparison of tumor mutation burden differences, aneuploidy score, homologous recombination defects, number of segments, and fraction altered. (b) Somatic mutations in the four molecular subtypes (chi-square test). $^{*}P < 0.05$, $^{**}P < 0.01$, $^{***}P < 0.001$, and $^{****}P < 0.0001$.

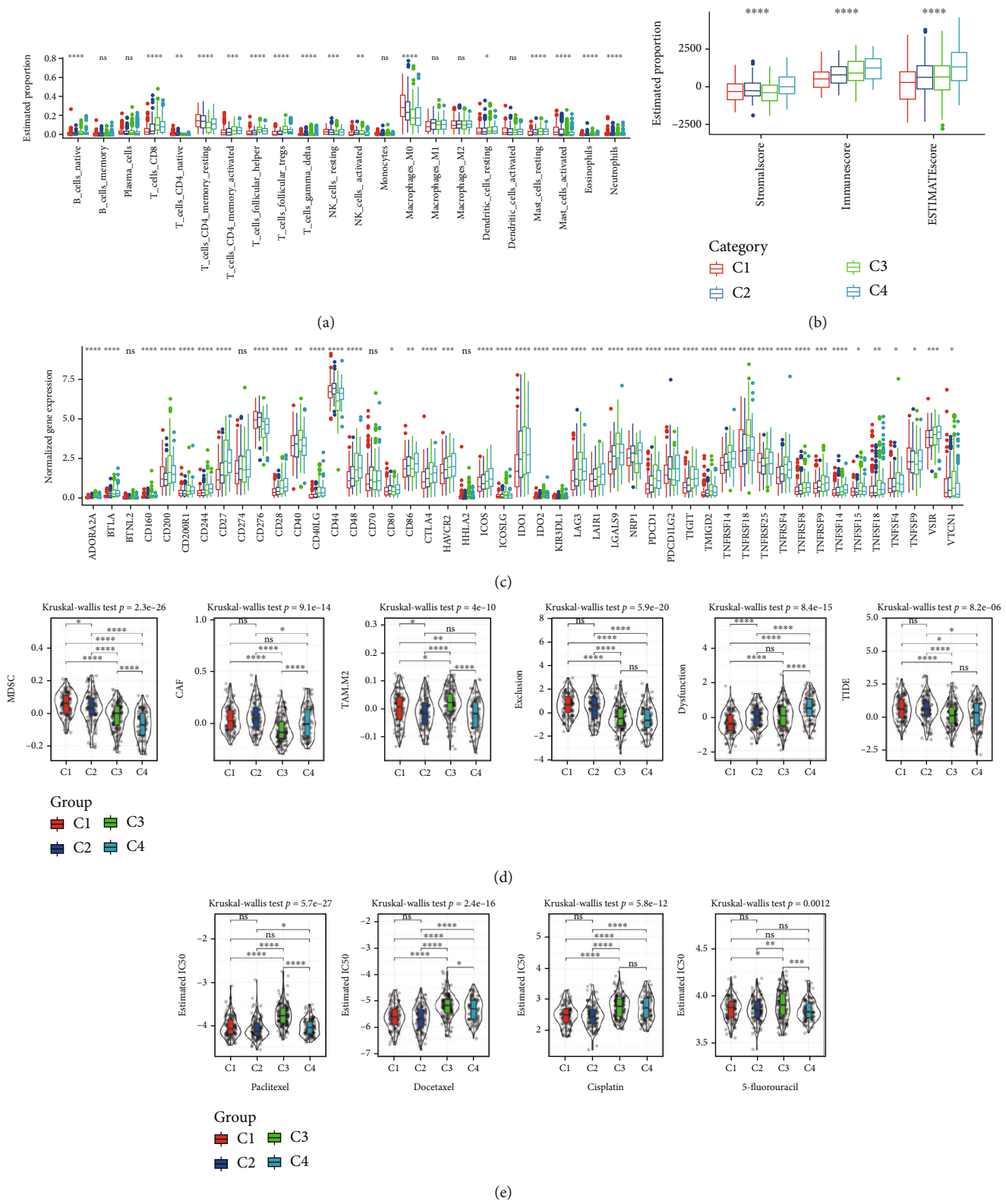

Figure 3: Immune characteristics and immunotherapy/chemotherapy differences between molecular subtypes. (a) The TCGA cohort differences in 22 immune cell scores between molecular subtypes. (b) Differences in ESTIMATE immune infiltration between molecular subtypes in the TCGA cohort. (c) Differentially expressed immune checkpoints between subtypes in the TCGA cohort. (d) Differences in TIDE analysis results between different subgroups in the TCGA cohort. (e) The box plots of the estimated IC50 for paclitaxel, docetaxel, cisplatin, and 5-fluorouracil in the TCGA cohort.

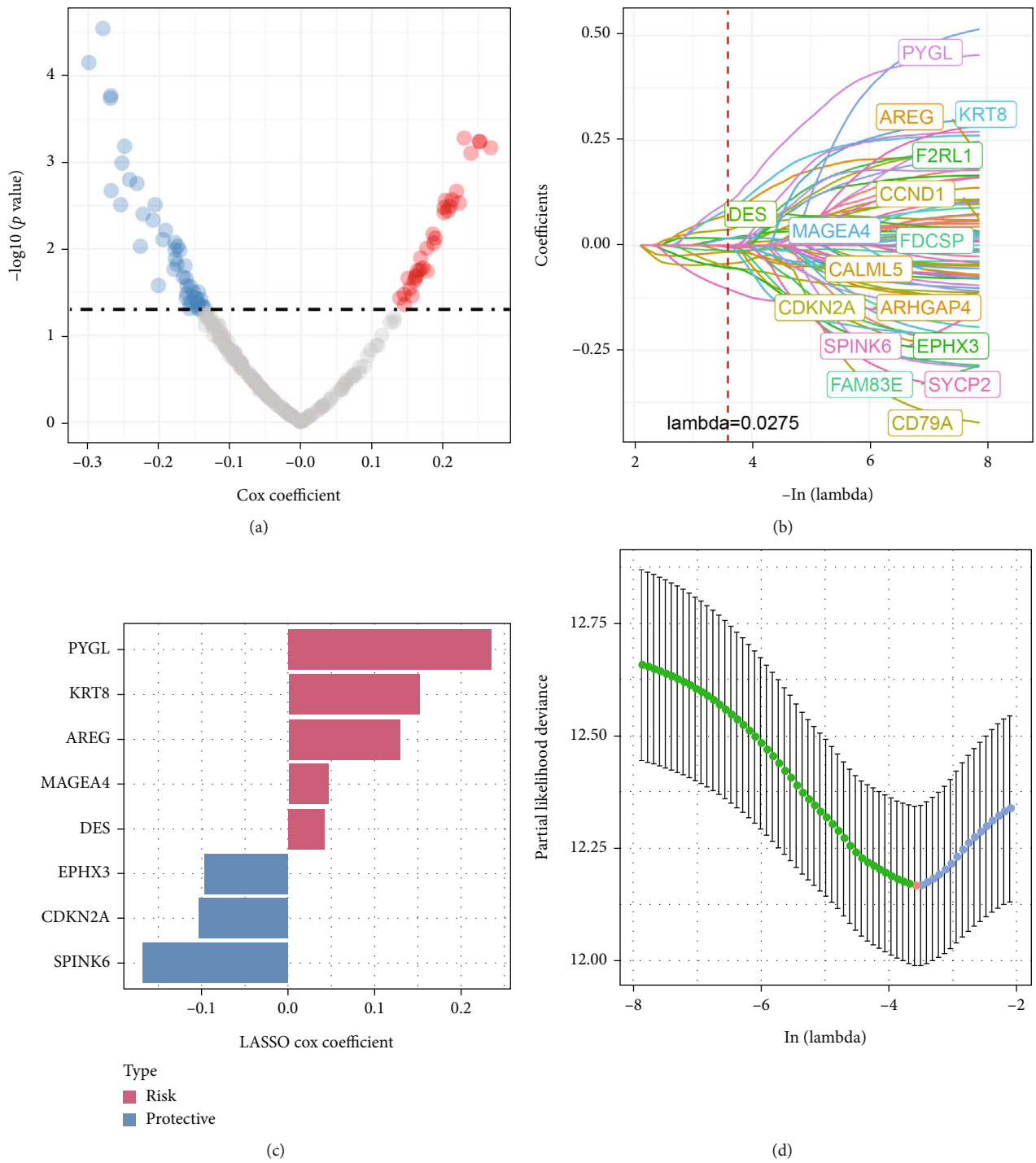

Figure 4: Identification of key cellular senescence-associated genes. (a) A total of 77 promising candidates were identified among the DEGs. (b) Trajectory of each independent variable with lambda. (c) Confidence interval under lambda. (d) LASSO coefficient distribution of gene signature correlated with the senescence.

eight-gene model. We classified the samples as the high-risk group if the score was greater than 0 and as the low-risk group if the score was less than 0. The distribution of CSRS.Score for samples in the training set (TCGA cohort) is shown in Figure 5(a). The high-risk group had an obviously higher proportion of dead samples and had a significantly short overall survival. We analyzed the prognostic predictive classification efficiency for 1 year (AUC = 0.72), 3 years (AUC = 0.72), and 5 years (AUC = 0.72), as shown in Figure 5(b). The KM survival curve showed that the overall survival of two risk groups was significantly different ($P < 0.0001$), and higher CSRS.Score had worse overall survival in the training cohort (Figure 5(c)). We further validated the robustness of the eight-gene model in two validation cohorts (GSE65858 and GSE41613), and the similar results were observed (Figures 5(d)–5(g)). For the

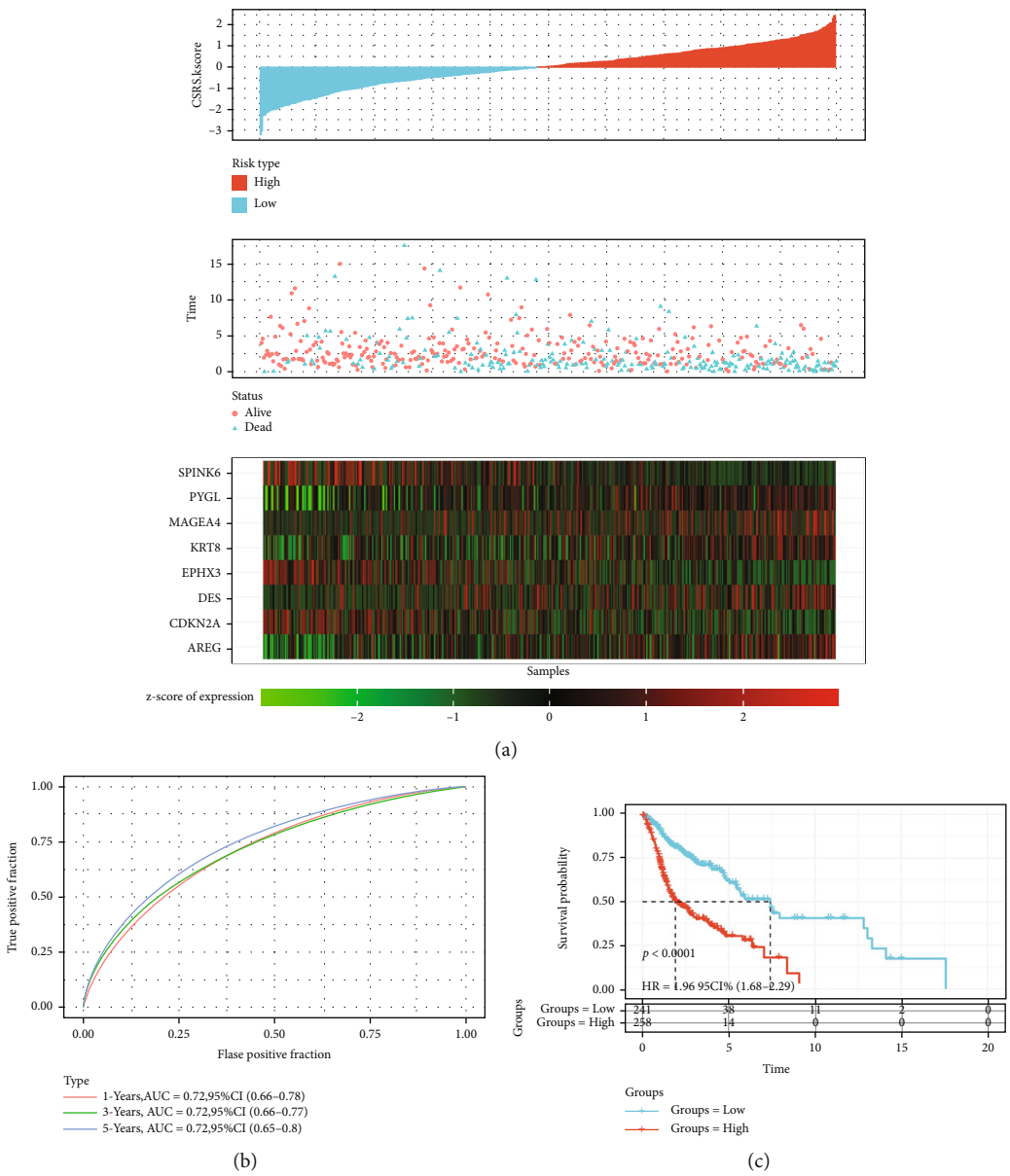

Figure 5: Continued.

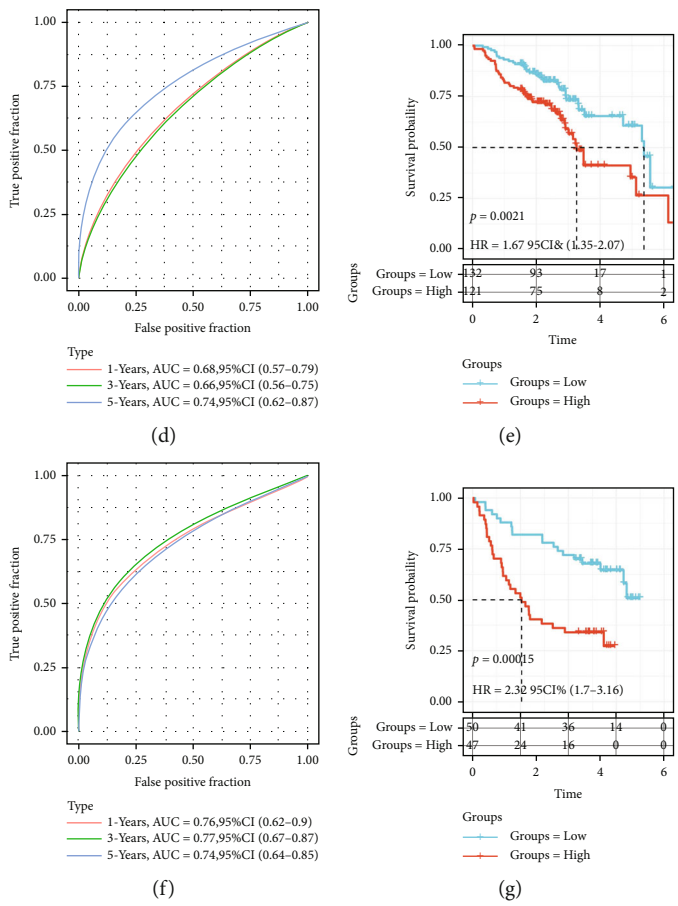

Figure 5: Clinical prognostic modeling and validation. (a) The distribution of survival status, CSRS.Score, and survival time corresponding to senescence-related genes expression in the TCGA cohort. (b) ROC curve with AUC for CSRS.Score classification in the TCGA cohort. (c) KM survival curves of two risk groups in the TCGA cohort. (d, e) ROC curves and KM survival curves of CSRS.Score in the GSE65858 cohort. (f, g) ROC curves and KM survival curves of CSRS.Score in the GSE41613 cohort.

performance of CSRS.Score in different clinical features, samples were also clearly divided into two risk groups with differential overall survival ($P < 0.0001$, Figure S3).

3.6. CSRS.Score Was Correlated with Immune Infiltration and Immunotherapy/Chemotherapy Responses. To further explore the immune characteristics between two risk groups, we analyzed the estimated proportion of 22 immune cells in high- and low-risk groups in the TCGA cohort (Figure 6(a)). Some immune cells were differently enriched in high- and low-CSRS.Score subgroups, such as M1 macrophages, activated CD4 memory T cells, and CD8 T cells. Overall, the high-risk group had lower immune infiltration than the low-risk group according to ESTIMATE analysis (Figure 6(b)). The correlation analysis between CSRS.Score and 22 immune cells demonstrated that CSRS.Score was significantly correlated with resting CD4 memory T cells, M0 macrophages, mast cells, CD8 T cells, follicular helper T cells, and regulatory T cells ($P < 0.001$, Figure 6(c)).

We further explored the immune response of two risk groups to immunotherapy. The expression of most immune checkpoints was differential between high- and low-risk groups (Figure 6(d)). TIDE prediction showed that the high-risk group had higher scores of two immunosuppressive cells (MDSC and CAF) probably contributing to higher T cell exclusion score and TIDE score (Figure 6(e) and Figure S4A-B), indicating that the high-risk group was more liable to escape from immunotherapy. In addition to immunotherapeutic response, we also assessed the response of two risk groups to chemotherapeutic drugs (paclitaxel, docetaxel, cisplatin, and 5-fluorouracil). The results showed that the high-risk group was more sensitive to paclitaxel, docetaxel, cisplatin, and 5-fluorouracil (Figure S4C-E).

3.7. CSRS.Score Incorporates Clinicopathological Features to Further Improve Survival Prediction. We constructed a decision tree based on clinical information and CSRS.Score, and only stage, gender, and CSRS.Score were remained in the decision tree (Figure 7(a)). Four subgroups including low, median, high, and highest were determined with differential overall survival (Figure 7(b)). Only highest subgroup consisted of high-risk samples (Figure 7(c)) and highest subgroup had the most proportions of C1 and C2 subtypes (Figure 7(d)). Univariate and multifactorial Cox regression analyses illustrated that CSRS.Score was the most significant prognostic factor and age and stage were also independent risk factors (Figures 7(e) and 7(f)). Then, we established a

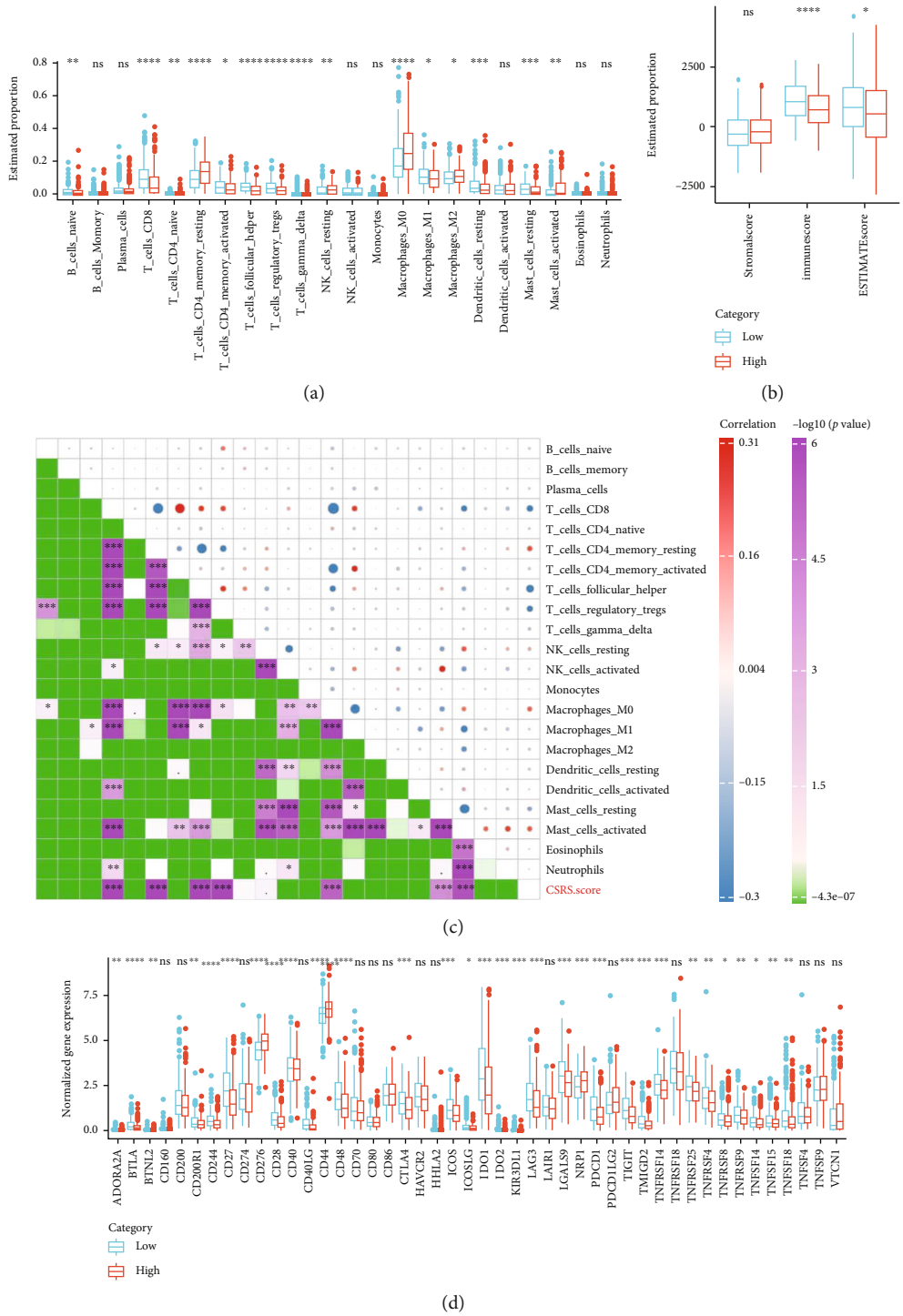

Figure 6: Continued.

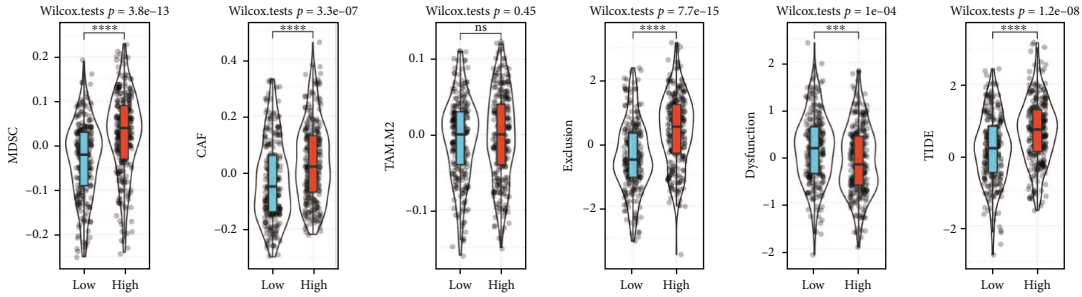

(e)

Figure 6: Immune characteristics between two risk groups in the TCGA cohort. (a) The quantity of 22 immune cells analyzed by CIBERSORT. (b) The TCGA cohort immune score and stromal score evaluated by ESTIMATE software. (c) Correlation analysis on CSRS. Score and 22 immune cells in the TCGA cohort. (d) The level of immune checkpoint genes in two risk groups. (e) TIDE analysis for predicting immune response to immune checkpoint blockade. ns: no significance. $^{****}P < 0.0001$, $^{***}P < 0.001$, $^{**}P < 0.01$, and $^{*}P < 0.05$.

nomogram based on the three independent risk factors for predicting 1-year, 3-year, and 5-year survival (Figure 7(g)). The predictive accuracy of the nomogram was validated by calibration curve (Figure 7(h)). The predicted overall survival of 1 year, 3 years, and 5 years fitted with the observed overall survival, indicating the reliability of the nomogram. Decision curve analysis showed that the nomogram reached relatively high net benefit compared with others (Figure 7(i)). Both nomogram and CSRS.Score had a higher AUC than other clinical features (Figure 7(j)), proving a favorable performance for predicting prognosis in HNSCC patients.

4. Discussion

A number of evidences prove that senescence-dependent changes are associated with proinflammatory properties and are involved in the chronic inflammatory microenvironment. Increased levels of inflammation and immune cell infiltration with senescence-dependent changes may lead to tumor formation and malignancy, and their function in HNC is unknown [34]. Exploring the molecular mechanisms of cellular senescence-associated genes is important to determine the role of senescence-dependent changes in HNC. To date, few studies have systematically investigated the molecular mechanisms of cellular senescence-associated genes in HNC and the association between cellular senescence-associated genes and HNC prognosis. We used cellular senescence-associated genes to identify four molecular subtypes by consensus clustering, and these four molecular subtypes differed significantly in prognosis and several clinical features.

Senescence and tumor microenvironment are closely related in tumor progression and invasion. There is an obvious difference of immunity between elder patients and younger patients, where younger patients have more abundant T cells in tumor tissue than elder patients. Senescence leads to a declining immune system which is referred to as immune senescence [35]. It is suggested that tumor-infiltrating CD4+ and CD8+ T cells are reduced in old mice compared to young mice and old mice are more infiltrated with neutrophils and macrophages [36]. Our results showed that CD8 T cells and activated memory CD4 T cells were lower enriched in C1 subtype, while M0 macrophages were extremely higher enriched. C1 also performed a lower stromal and immune infiltration than other subtypes. GSEA results revealed that the immune-related pathways were suppressed in the C1 subtype, which was consistent with its immune features. Therefore, we inferred that cellular senescence-associated genes may play a large role in immune-related pathways and tumor infiltration.

Based on the DEGs among different subtypes, we confirmed a total of eight key cellular senescence prognosis-related genes including CDKN2A, PYGL, KRT8, AREG, MAGEA4, DES, EPHX3, and SPINK6. CDKN2A has been shown to mediate the antitumor effects in HNSCC through cell cycle arrest [37]. Low CDKN2A expression predicts unfavorable prognosis in HPV-negative HNSCC independent of other clinical factors [38], which is accordant with our result that CDKN2A is lower expressed in high-risk group. PYGL is significantly associated with overall survival in HNC patients and may be an independent risk factor for HNSCC prognosis [39]. Keratin 8 (KRT8) overexpression enhanced cell proliferation and migration in gastric cancer and lung cancer, while its decreased expression markedly inhibited cell proliferation, migration, and EMT process [40, 41]. A multiscale integrated analysis figured out KRT8 as a pan-cancer early biomarker [42]. Amphiregulin (AREG) is a ligand of epidermal growth factor receptor (EGFR), which is underlined to function in several aspects of cancerogenesis including cancer cell growth, invasion, metastasis, angiogenesis, and resistance to apoptosis [43].

Additionally, the correlation of molecular subtypes with gene mutations was analyzed, and a significant correlation between the two was detected. The common TP53 and CDKN2A were mutated at a high frequency in the four subtypes. We further evaluated the degree of clinical response of conventional chemotherapeutic drugs paclitaxel, docetaxel, cisplatin, and 5-fluorouracil to CSRS.Score subgroups, and the results showed that high-CSRS.Score to paclitaxel, docetaxel, cisplatin, and 5-fluorouracil was more sensitive. The results suggest that different subgroups have different degrees corresponding to different chemotherapeutic drugs, and perhaps our screened aging-related genes can be used as biomarkers of clinical drug treatment response.

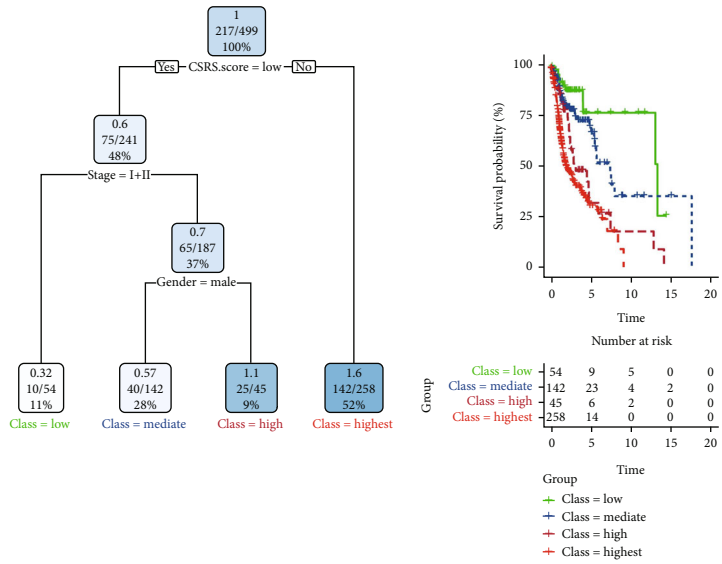

(a) (b)

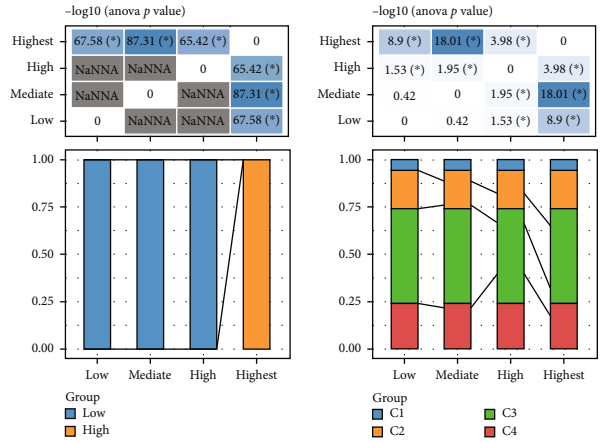

(c) (d)

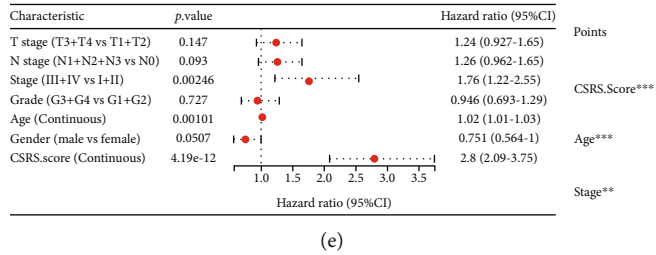

(e)

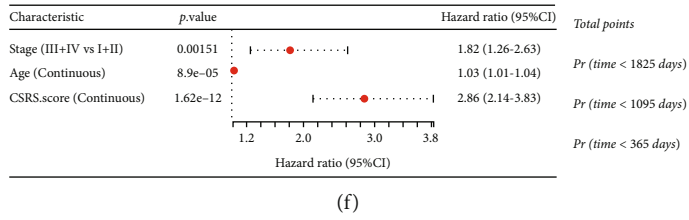

(f)

Figure 7: Continued.

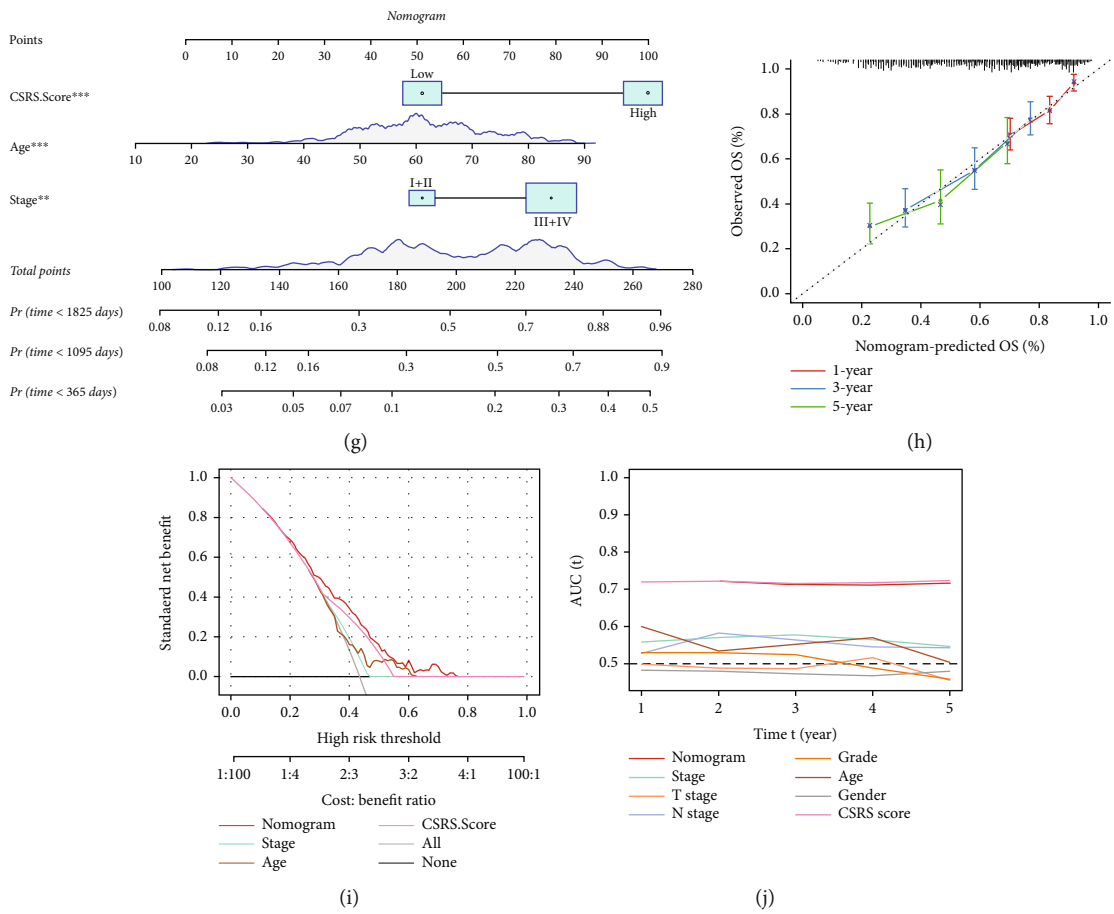

Figure 7: CSRS.Score combined with clinicopathological characteristics to further improve prognostic models and survival prediction. (a) Full-scale annotations of patients including gender, CSRS.Score, age, grade, and TNM stage were applied to develop a survival decision tree for optimizing the risk stratification. (b) Among the four subgroups, significant differences in overall survival could be found. (c, d) Comparative analysis between different subgroups. (e, f) Univariate (e) and multivariate (f) Cox analysis of CSRS.Score and clinicopathological features. (g) A nomogram was developed based on age, CSRS.Score, and stage. (h) Calibration curves for 1, 3, and 5 years for the columnar graph. (i) Decision curve analysis of the nomogram, CSRS.Score, and other clinical features. (j) Compared with other clinicopathological features, the nomogram exhibited the most powerful capacity for survival prediction.

Although the prognostic risk model based senescence-associated genes was illustrated to have robust performance in several independent cohorts, this study did not validate the model in the wet experiments. More clinical HNSCC samples should be included to support the reliability and accuracy of the eight prognostic biomarkers in the future.

5. Conclusion

In this study, we developed a prognostic risk model with cellular senescence-associated genes that has great potential as a biomarker for HNSCC patients and provides insights into individualized immunotherapy for head and neck cancer patients.

Data Availability

The datasets analyzed in this study could be found in GSE65858 at https://www.ncbi.nlm.nih.gov/geo/query/acc.cgi?acc=GSE65858 and GSE41613 at https://www.ncbi.nlm.nih.gov/geo/query/acc.cgi?acc=GSE41613.

Conflicts of Interest

The authors declare that they have no conflicts of interest.

Authors' Contributions

Rensheng Wang and Lin Deng conceived and designed the research. Jinglin Mi and Guozhen Zhang acquired the data. Xiaolan Ruan and Lin Deng analyzed and interpreted the data. Yufei Pan carried out statistical analysis. Yufei Pan drafted the manuscript. Rensheng Wang revised the manuscript for important intellectual content. Lin Deng and Jinglin Mi are equal contributors and co-first authors.

Supplementary Materials

Figure S1: clinicopathological characteristics between molecular subtypes. (A–I) Clinicopathological characteristics of molecular subtypes in the TCGA-HNSC cohort, where the lower half is the proportion and the upper half is the statistical significance of the difference in distribution between the

two-log10 (*P* value). Figure S2: results of GSEA analysis of pathways between different molecular subtypes in the TCGA cohort. Figure S3: KM curves between high- and low-risk groups of CSRS.Score in different clinical features in the TCGA cohort. Figure S4: response differences to immunotherapy/chemotherapy in two risk groups. (A, B) TIDE analysis results between two risk groups in the GSE65858 (A) and GSE41613 (B) cohorts. (C–E) The box plots of the estimated IC50 for paclitaxel, docetaxel, cisplatin, and 5-fluorouracil in the TCGA cohort, GSE65858, and GSE41613 cohorts. Table S1: a list of 28 prognostic cellular senescence-associated genes used for molecular subtyping. *(Supplementary Materials)*

References

[1] D. M. Shin, S. Nannapaneni, M. R. Patel et al., "Phase Ib study of chemoprevention with green tea polyphenon E and erlotinib in patients with advanced premalignant lesions (APL) of the head and neck," *Clinical Cancer Research*, vol. 26, no. 22, pp. 5860–5868, 2020.

[2] S. Marur and A. A. Forastiere, "Head and neck cancer: changing epidemiology, diagnosis, and treatment," *Mayo Clinic Proceedings*, vol. 83, no. 4, pp. 489–501, 2008.

[3] F. Bray, J. Ferlay, I. Soerjomataram, R. L. Siegel, L. A. Torre, and A. Jemal, "Global cancer statistics 2018: GLOBOCAN estimates of incidence and mortality worldwide for 36 cancers in 185 countries," *CA: a Cancer Journal for Clinicians*, vol. 68, no. 6, pp. 394–424, 2018.

[4] N. Nishio, N. S. van den Berg, S. van Keulen et al., "Optical molecular imaging can differentiate metastatic from benign lymph nodes in head and neck cancer," *Nature Communications*, vol. 10, no. 1, p. 5044, 2019.

[5] T. Nakashima, R. Yasumatsu, K. Asai, H. Uryu, R. Kogo, and T. Nakagawa, "Single-cycle induction chemotherapy for resectable advanced hypopharyngeal cancer," *International Journal of Clinical Oncology*, vol. 22, no. 3, pp. 442–447, 2017.

[6] F. J. Civantos, R. P. Zitsch, D. E. Schuller et al., "Sentinel lymph node biopsy accurately stages the regional lymph nodes for T1-T2 oral squamous cell carcinomas: results of a prospective multi-institutional trial," *Journal of Clinical Oncology*, vol. 28, no. 8, pp. 1395–1400, 2010.

[7] J. Campisi, "Aging, cellular senescence, and cancer," *Annual Review of Physiology*, vol. 75, no. 1, pp. 685–705, 2013.

[8] P. A. Pérez-Mancera, A. R. Young, and M. Narita, "Inside and out: the activities of senescence in cancer," *Nature Reviews Cancer*, vol. 14, no. 8, pp. 547–558, 2014.

[9] M. K. Ruhland, A. J. Loza, A. H. Capietto et al., "Stromal senescence establishes an immunosuppressive microenvironment that drives tumorigenesis," *Nature Communications*, vol. 7, no. 1, article 11762, 2016.

[10] L. Yuan, L. Zhai, L. Qian et al., "Switching off IMMP2L signaling drives senescence via simultaneous metabolic alteration and blockage of cell death," *Cell Research*, vol. 28, no. 6, pp. 625–643, 2018.

[11] M. Xu, T. Pirtskhalava, J. N. Farr et al., "Senolytics improve physical function and increase lifespan in old age," *Nature Medicine*, vol. 24, no. 8, pp. 1246–1256, 2018.

[12] N. Tasdemir, A. Banito, J. S. Roe et al., "BRD4 connects enhancer remodeling to senescence immune surveillance," *Cancer Discovery*, vol. 6, no. 6, pp. 612–629, 2016.

[13] W. Xie, I. Kagiampakis, L. Pan et al., "DNA methylation patterns separate senescence from transformation potential and indicate cancer risk," *Cancer Cell*, vol. 33, no. 2, pp. 309–321.e5, 2018.

[14] M. M. Sugrue, D. Y. Shin, S. W. Lee, and S. A. Aaronson, "Wild-type p 53 triggers a rapid senescence program in human tumor cells lacking functional p 53," *Proceedings of the National Academy of Sciences of the United States of America*, vol. 94, no. 18, pp. 9648–9653, 1997.

[15] R. Haq, J. D. Brenton, M. Takahashi et al., "Constitutive p38HOG mitogen-activated protein kinase activation induces permanent cell cycle arrest and senescence," *Cancer Research*, vol. 62, no. 17, pp. 5076–5082, 2002.

[16] A. Alimonti, C. Nardella, Z. Chen et al., "A novel type of cellular senescence that can be enhanced in mouse models and human tumor xenografts to suppress prostate tumorigenesis," *The Journal of Clinical Investigation*, vol. 120, no. 3, pp. 681–693, 2010.

[17] D. A. Gewirtz, S. E. Holt, and L. W. Elmore, "Accelerated senescence: an emerging role in tumor cell response to chemotherapy and radiation," *Biochemical Pharmacology*, vol. 76, no. 8, pp. 947–957, 2008.

[18] P. Hari, F. R. Millar, N. Tarrats et al., "The innate immune sensor Toll-like receptor 2 controls the senescence-associated secretory phenotype," *Science Advances*, vol. 5, no. 6, p. -eaaw0254, 2019.

[19] B. Zhao, P. Liu, T. Fukumoto et al., "Topoisomerase 1 cleavage complex enables pattern recognition and inflammation during senescence," *Nature Communications*, vol. 11, no. 1, p. 908, 2020.

[20] J. A. Ewald, J. A. Desotelle, G. Wilding, and D. F. Jarrard, "Therapy-induced senescence in cancer," *Journal of the National Cancer Institute*, vol. 102, no. 20, pp. 1536–1546, 2010.

[21] M. Althubiti, L. Lezina, S. Carrera et al., "Characterization of novel markers of senescence and their prognostic potential in cancer," *Cell Death & Disease*, vol. 5, no. 11, p. e1528, 2014.

[22] D. Coppola, L. Balducci, D. T. Chen et al., "Senescence-associated-gene signature identifies genes linked to age, prognosis, and progression of human gliomas," *Journal of Geriatric Oncology*, vol. 5, no. 4, pp. 389–399, 2014.

[23] J. Yang, Q. Jiang, L. Liu et al., "Identification of prognostic aging-related genes associated with immunosuppression and inflammation in head and neck squamous cell carcinoma," *Aging*, vol. 12, no. 24, pp. 25778–25804, 2020.

[24] M. D. Wilkerson and D. N. Hayes, "ConsensusClusterPlus: a class discovery tool with confidence assessments and item tracking," *Bioinformatics*, vol. 26, no. 12, pp. 1572-1573, 2010.

[25] M. E. Ritchie, B. Phipson, D. Wu et al., "limma powers differential expression analyses for RNA-sequencing and microarray studies," *Nucleic Acids Research*, vol. 43, no. 7, article e47, 2015.

[26] J. Friedman, T. Hastie, and R. Tibshirani, "Regularization paths for generalized linear models via coordinate descent," *Journal of Statistical Software*, vol. 33, no. 1, pp. 1–22, 2010.

[27] Z. Zhang, "Variable selection with stepwise and best subset approaches," *Annals of Translational Medicine*, vol. 4, no. 7, p. 136, 2016.

[28] B. Chen, M. S. Khodadoust, C. L. Liu, A. M. Newman, and A. A. Alizadeh, "Profiling tumor infiltrating immune cells with

CIBERSORT," *Methods in Molecular Biology*, vol. 1711, pp. 243–259, 2018.

[29] K. Yoshihara, M. Shahmoradgoli, E. Martínez et al., "Inferring tumour purity and stromal and immune cell admixture from expression data," *Nature Communications*, vol. 4, no. 1, p. 2612, 2013.

[30] P. Jiang, S. Gu, D. Pan et al., "Signatures of T cell dysfunction and exclusion predict cancer immunotherapy response," *Nature Medicine*, vol. 24, no. 10, pp. 1550–1558, 2018.

[31] A. Subramanian, P. Tamayo, V. K. Mootha et al., "Gene set enrichment analysis: a knowledge-based approach for interpreting genome-wide expression profiles," *Proceedings of the National Academy of Sciences of the United States of America*, vol. 102, no. 43, pp. 15545–15550, 2005.

[32] A. Liberzon, C. Birger, H. Thorvaldsdóttir, M. Ghandi, J. P. Mesirov, and P. Tamayo, "The Molecular Signatures Database (MSigDB) hallmark gene set collection," *Cell Systems*, vol. 1, no. 6, pp. 417–425, 2015.

[33] V. Thorsson, D. L. Gibbs, S. D. Brown et al., "The immune landscape of cancer," *Immunity*, vol. 48, no. 4, pp. 812–30.e14, 2018.

[34] T. Kuilman, C. Michaloglou, L. C. Vredeveld et al., "Oncogene-induced senescence relayed by an interleukin-dependent inflammatory network," *Cell*, vol. 133, no. 6, pp. 1019–1031, 2008.

[35] R. M. Gorczynski and E. Terzioglu, "Aging and the immune system," *International Urology and Nephrology*, vol. 40, no. 4, pp. 1117–1125, 2008.

[36] M. Provinciali, K. Argentati, and A. Tibaldi, "Efficacy of cancer gene therapy in aging: adenocarcinoma cells engineered to release IL-2 are rejected but do not induce tumor specific immune memory in old mice," *Gene Therapy*, vol. 7, no. 7, pp. 624–632, 2000.

[37] S. Bhattacharyya, V. Sekar, B. Majumder et al., "CDKN2A-p53 mediated antitumor effect of lupeol in head and neck cancer," *Cellular Oncology*, vol. 40, no. 2, pp. 145–155, 2017.

[38] W. S. Chen, R. S. Bindra, A. Mo et al., "CDKN2A copy number loss is an independent prognostic factor in HPV-negative head and neck squamous cell carcinoma," *Frontiers in Oncology*, vol. 8, p. 95, 2018.

[39] L. Chen, X. He, S. Yi, G. Liu, Y. Liu, and Y. Ling, "Six glycolysis-related genes as prognostic risk markers can predict the prognosis of patients with head and neck squamous cell carcinoma," *BioMed Research International*, vol. 2021, Article ID 8824195, 13 pages, 2021.

[40] H. Chen, X. Chen, B. Pan, C. Zheng, L. Hong, and W. Han, "KRT8 serves as a novel biomarker for LUAD and promotes metastasis and EMT via NF-κB signaling," *Frontiers in Oncology*, vol. 12, article 875146, 2022.

[41] J. Fang, H. Wang, Y. Liu, F. Ding, Y. Ni, and S. Shao, "High KRT8 expression promotes tumor progression and metastasis of gastric cancer," *Cancer Science*, vol. 108, no. 2, pp. 178–186, 2017.

[42] M. K. D. Scott, M. Limaye, S. Schaffert et al., "A multi-scale integrated analysis identifies KRT8 as a pan-cancer early biomarker," *Pacific Symposium on Biocomputing*, vol. 26, pp. 297–308, 2021.

[43] B. Busser, L. Sancey, E. Brambilla, J. L. Coll, and A. Hurbin, "The multiple roles of amphiregulin in human cancer," *Biochimica et Biophysica Acta*, vol. 1816, no. 2, pp. 119–131, 2011.

Hindawi
Mediators of Inflammation
Volume 2022, Article ID 9652169, 21 pages
https://doi.org/10.1155/2022/9652169

Research Article

Mining Potential Drug Targets and Constructing Diagnostic Models for Heart Failure Based on miRNA-mRNA Networks

Xiangming Fang,[1] Rensheng Song,[2] Jiaxing Wei,[1] Qin Liao,[1] and Zhenhong Zeng[1]

[1]*Key Laboratory of Biological Targeting Diagnosis, Therapy and Rehabilitation of Guangdong Higher Education Institutes, The Fifth Affiliated Hospital of Guangzhou Medical University Intensive Care Unit, Guangzhou, China 510700*
[2]*Key Laboratory of Biological Targeting Diagnosis, Therapy and Rehabilitation of Guangdong Higher Education Institutes, The Fifth Affiliated Hospital of Guangzhou Medical University Cardiovascular Medicine Department, Guangzhou, China 510700*

Correspondence should be addressed to Xiangming Fang; 2015687042@gzhmu.edu.cn

Xiangming Fang and Rensheng Song contributed equally to this work.

Received 15 July 2022; Revised 18 August 2022; Accepted 26 August 2022; Published 27 September 2022

Academic Editor: Md Sayed Ali Sheikh

Heart failure (HF) is a globally prevalent cardiovascular disease, but effective drug targets and diagnostic models are still lacking. This study was designed to investigate effective drug targets and diagnostic models for HF in terms of miRNA targets, hoping to contribute to the understanding and treatment of HF. Using HF miRNA and gene expression profile data from the GEO database, we analyzed differentially expressed miRNAs/gene identification in HF using Limma and predicted miRNA targets by the online TargetScan database. Subsequently, gene set enrichment analysis and annotation were performed using WebGestaltR package. Protein-protein interactions were identified using the STRING database. The proximity of drugs to treat HF was also calculated and predicted for potential target therapeutic drug. In addition, further drug identification was performed by molecular docking. Finally, diagnostic models were constructed based on differential miRNAs. The GEO dataset was used to screen 66 differentially expressed miRNAs, incorporating 56 downregulated miRNAs and 10 upregulated miRNAs. The JAK-STAT signaling pathway, MAPK signaling pathway, p53 signaling pathway, Prolactin signaling pathway, and TGF-beta signaling pathway were enriched, as shown by KEGG enrichment analysis on the target genes. In addition, we found that 83 genes were upregulated and 92 genes were downregulated in HF patients vs. healthy individuals. Based on the inflammation-related score, hypoxia-related score, and energy metabolism-related score, we identified key miRNA-mRNA pairs and constructed an interaction network. Following that, TAP1, which had the highest expression and network connectivity in acute HF with crystal and molecular docking studies, was selected as a key candidate gene in the network. And the compound DB04847 was selected to produce a large number of favorable interactions with TAP1 protein. Finally, we constructed two diagnostic models based on the differential miRNAs hsa-miR-6785-5p and hsa-miR-4443. In conclusion, we identified TAP1, a key candidate gene in the diagnosis and treatment of HF, and determined that compound DB04847 is highly likely to be a potential inhibitor of TAP1. The TAP1 gene was also found to be regulated by hsa-miR-6785-5p and hsa-miR-4443, and a diagnostic model was constructed. This provides a new promising direction to improve the diagnosis, prognosis, and treatment outcome and guide more effective immunotherapy strategies of HF.

1. Introduction

Heart failure (HF) results from the dysfunction of diastolic and/or the systolic function of the heart; insufficient blood perfusion and blood stasis in the venous system in the arterial system would occur if the venous return blood could not be fully discharged from the heart, thereby causing cardiac circulatory disorder syndrome [1, 2]. Instead of an independent disease, HF is a terminal stage in heart disease development. A great number of HF begins with left HF, which first

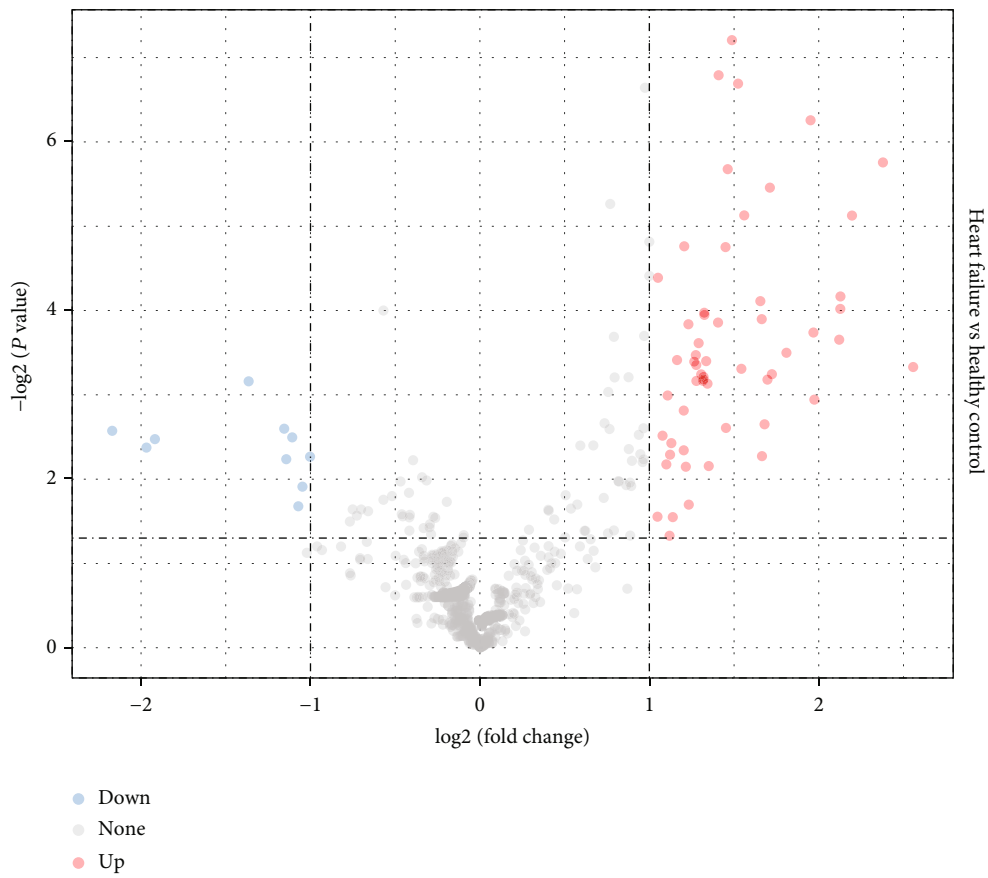

(a)

Figure 1: Continued.

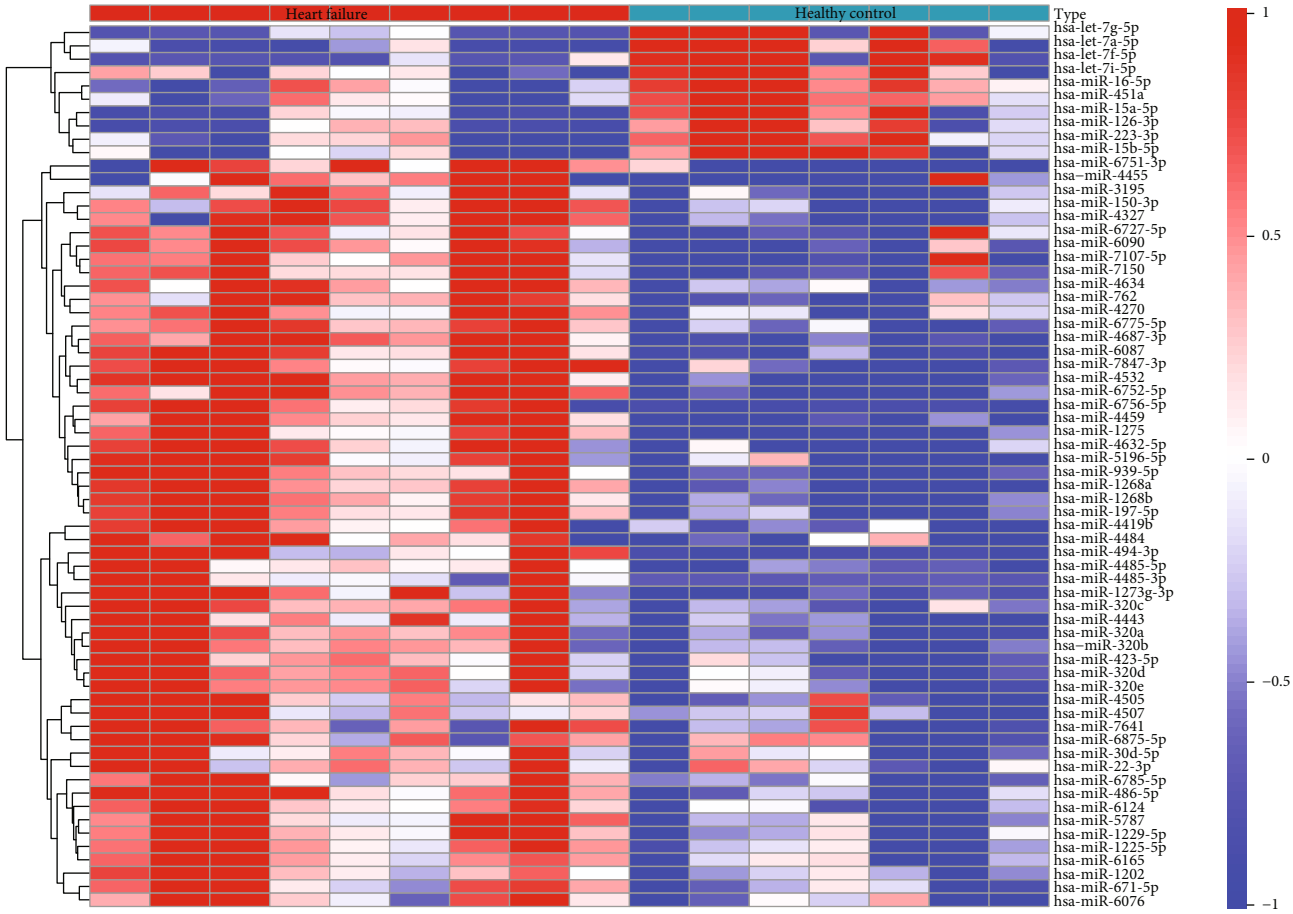

(b)

Figure 1: Differentially expressed miRNA analysis on the GSE104150 dataset: (a) volcano plot of miRNA differential analysis; (b) heat map of differential miRNA expression.

manifests as pulmonary circulation congestion. Advanced interventions such as drug therapy, cardiac synchronization therapy, and heart transplantation mainly focus on the control of heart failure-related symptoms [3] Mortality in HF could be reduced to some extent through these interventions [4]. Nevertheless, the discovery of new drugs and new diagnostic strategies is still necessary to further reduce mortality and improve quality of life in the process of HF. Therefore, further research and in-depth understanding of the biological mechanisms of HF are urgently needed.

In a healthy heart, 90% of ATP production is produced via mitochondrial oxidative phosphorylation, and 60–70% of the energy was derived from lipid oxidation [5]. Therefore, the heart is greatly dependent on the continuous supply of fatty acids and oxygen. Moreover, under diverse and non-optimal physiological conditions, the heart has great metabolic plasticity and could maintain ATP production, using other substrates such as amino acids, glucose, ketone bodies, and lactate [6]. However, a combination of oxidative and substrate level phosphorylation more evenly produces skeletal muscle ATP, allowing a relatively more flexibility in terms of oxygen demand and substrate use [7]. A heart deprived of oxygen shows a decreased ATP production and mitochondrial respiration [8]. Under hypoxia, a significant loss of mitochondrial density and skeletal muscle mass [9] could be seen as an adaptive modification that lowers reactive oxygen species (ROS) and reduces tissue's demand for low O_2 [9].

At the posttranscriptional level, microRNAs (miRNAs) with approximately 22 nucleotides regulate expression of genes [10, 11]. Such a process involves binding to the complementary sequence of messenger RNA (mRNA), subsequently resulting in degradation of the mRNA or translational inhibition [12]. Study showed that miRNAs play a role in multiple pathophysiological mechanisms, including in HF development [13]. In the circulation, extracellular miRNAs are measurable, and they have now been increasingly regarded as prognostic and diagnostic biomarkers in various diseases [14]. As a new category of biomarkers, studies have shown the potential of miRNAs in HF [15], which are critical drivers of cardiac tissue remodeling and can be used as therapeutic targets. For example, in cardiac hypertrophic remodeling, miR-132 has been previously verified as a master switch [16] and is markedly increased in the early hypertrophic phase of HF [17], and in genetic or pharmacological studies, inhibition of miR-132 has the effect of reversing or preventing the progression of HF [18]. Transcription factor 3 (ATF3) expression was increased in

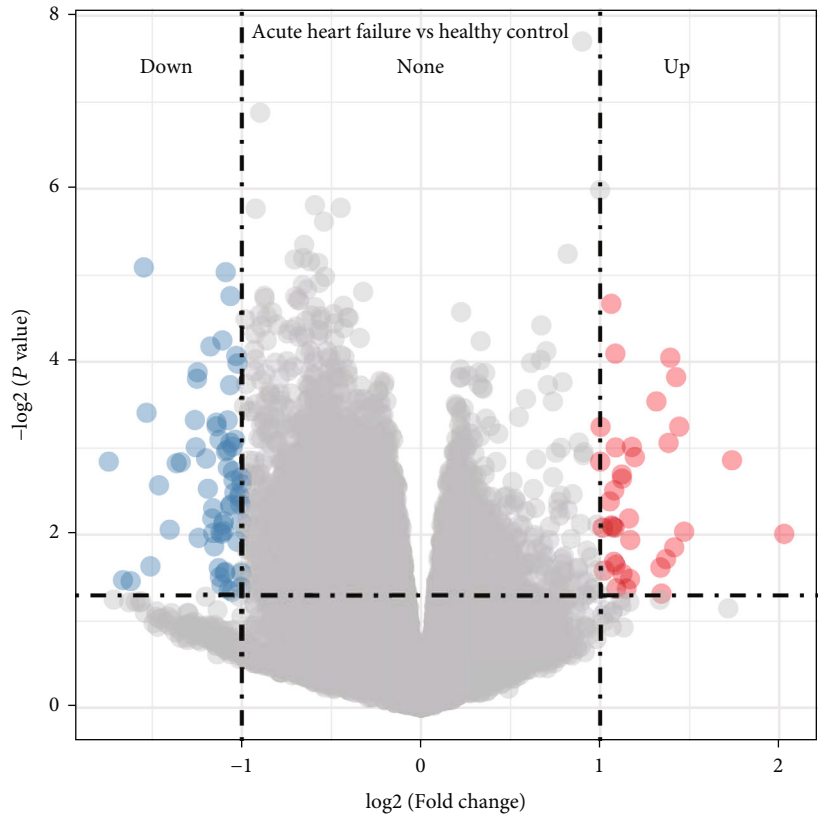

(a)

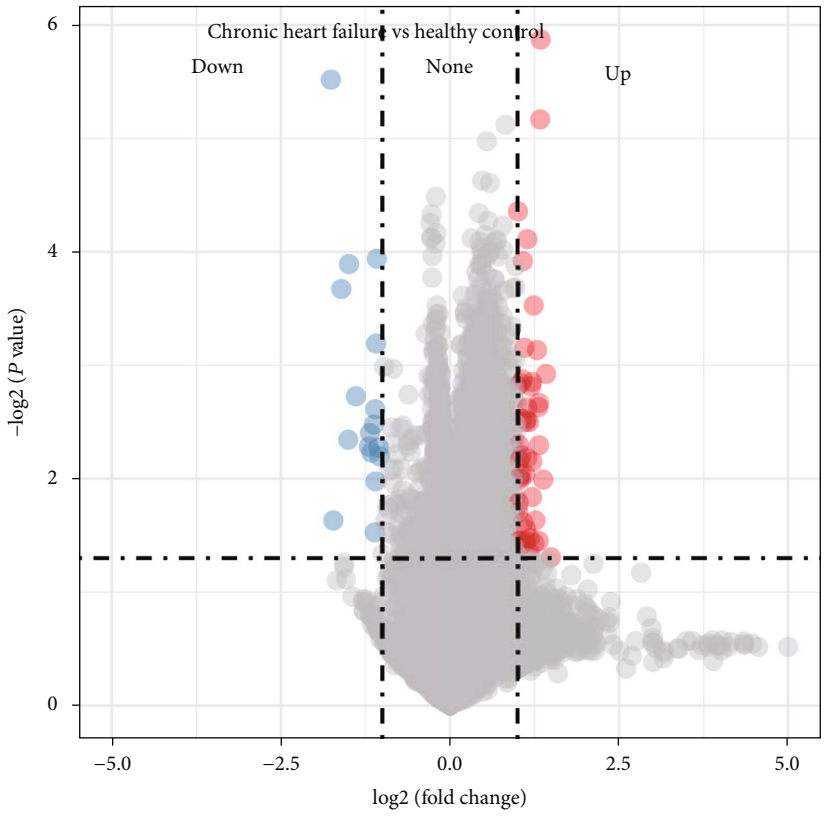

(b)

Figure 2: Continued.

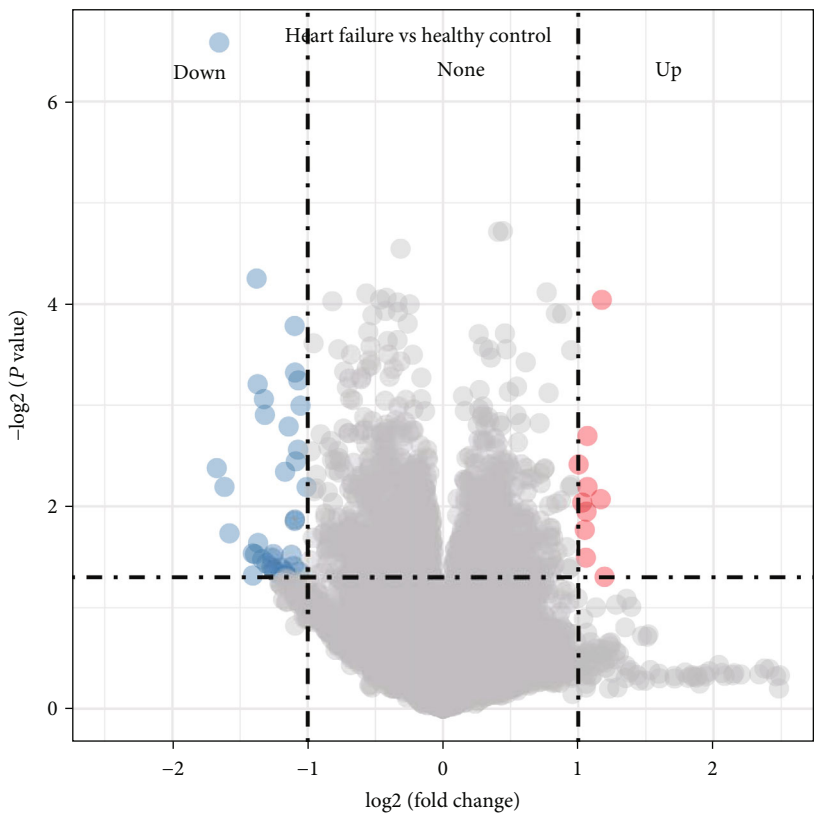

(c)

Figure 2: Differentially expressed gene analysis on the GSE21125 dataset: (a) volcano plot of differential analysis of acute heart failure patients vs. healthy individuals; (b) volcano plot of differential analysis of chronic heart failure patients vs. healthy individuals; (c) volcano plot of differential analysis of heart failure patients vs. healthy individuals.

human hypertrophic heart; ATF3 upregulation protects the heart by suppressing Map2K3 expression and subsequent p38-transforming growth factor-β signaling [19]. Therefore, analysis and exploration of miRNAs-mRNA as potential drug targets for the treatment of HF have great potential.

The heart, as a vital tissue that maintains blood circulation, ensures the metabolic needs. And it is too hard to obtain the tissue, especially in a healthy body. Based on the above statements, this study is aimed at mining key drug targets in HF using the NCBI Gene Expression Omnibus (GEO) dataset, including expression profiles of mRNAs and miRNAs. Differential miRNA and differential gene expression profiles of healthy controls and HF subjects were analyzed with the "Limma" package in R software. After that, we detected the key target gene of key miRNA, namely, TAP1. Finally, a diagnostic model was constructed based on the differential miRNAs. The current findings contributed to the development of understanding novel molecular mechanisms of HF pathogenesis, particularly the possible association of dysregulated pathways of the TAP1 gene with HF pathological processes, and ultimately predicted a new therapeutic target drug DB04847 for HF patients.

2. Methods

2.1. Data Collection and Preprocessing. Expression profile data were downloaded from the NCBI GEO database [20] for miRNA number GSE104150, which contained a total of 2549 miRNAs from 7 healthy controls and 9 patients with HF. mRNA expression profile data were downloaded from the NCBI GEO database for mRNA number GSE21125, which contained 9 patients with acute HF, 9 patients with chronic HF, 9 patients at risk of HF, 9 patients with left ventricular dysfunction, and 9 healthy controls. In this analysis, we kept only 9 patients with acute HF, 9 patients with chronic HF, and 9 healthy controls, for a total of 18 HF patients, 9 healthy controls, and 20,295 genes.

HF with other diseases was excluded, and HF with survival information was retained.

2.2. Analysis of Differentially Expressed miRNAs/Genes and Functional Enrichment. Differentially expressed miRNAs were analyzed using Limma [21] and filtered using the criteria of $|\log 2(\text{fold change})| > 1$ and FDR (false discovery rate) < 0.05. Similarly, differentially expressed genes were analyzed using Limma and filtered using the criteria of $|\log 2(\text{fold change})| > 1$ and $P < 0.05$. We performed Kyoto Encyclopedia of Genes and Genomes (KEGG) enrichment analysis on miRNA target genes by the R software package clusterProfiler, filtered at P value < 0.05.

We downloaded energy metabolism-related pathways from the Gene Set Enrichment Analysis (GSEA) [22] website for subsequent enrichment analysis and downloaded genes related to Toll-like receptor signaling pathway, NF-kappa B

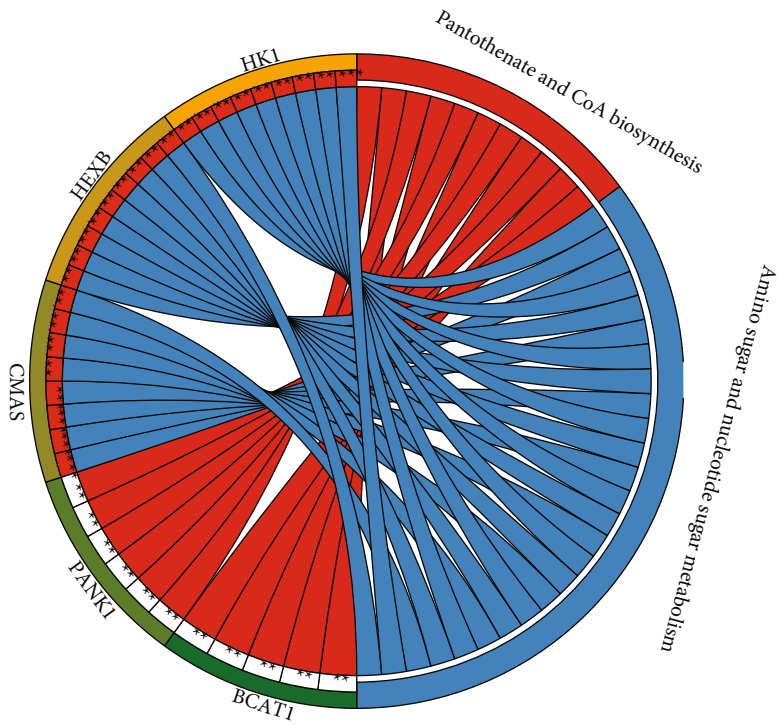

(a)

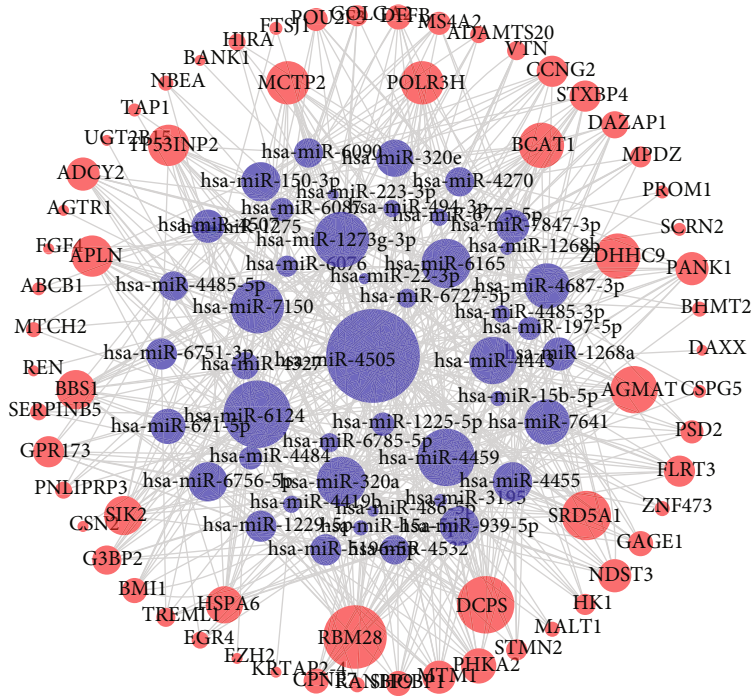

(b)

Figure 3: Functional enrichment analysis: (a) KEGG enrichment analysis of differential genes; (b) network plot of miRNA interactions with differential target genes, where blue is miRNA, red is gene, and the size of the dot is degree, where the larger the dot, the closer the connectivity with other nodes at that point, and the more important the dot is.

signaling pathway, JAK-STAT signaling pathway, T-cell receptor signaling pathway, INFLAMMATORY_RESPONSE, B-cell receptor signaling pathway, and other associated pathways. KEGG enrichment analysis of differential genes was performed by WebGestaltR package. The enrichment scores of each pathway in the KEGG pathway regarding the samples were calculated by the GSVA package, and the correlation between genes and pathways was calculated by the rcorr function of the Hmisc package; here, we used $P < 0.05$ and $\text{cor} > 0.4$ as the threshold. In addition,

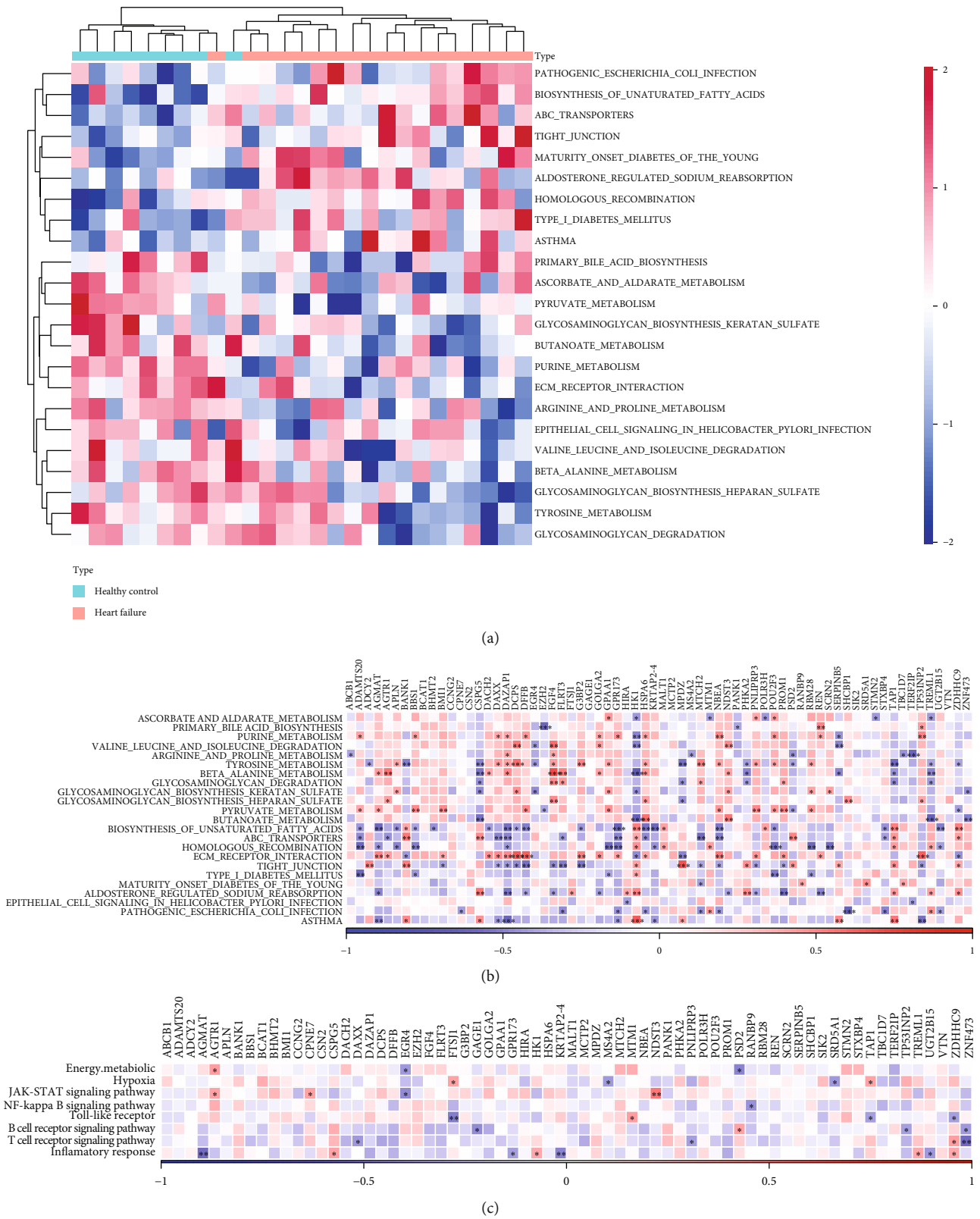

Figure 4: Characterization of pathways abnormally regulated in heart failure: (a) heat map of enrichment scores of pathways significantly different in heart failure patients and healthy group by GSVA ($P < 0.05$); (b) heat map of correlation analysis between related pathways and differentially miRNA-regulated differential target genes; (c) heat map of correlation between energy metabolism, hypoxia score, and inflammation-related pathways and differentially miRNA-regulated; (d) heat map of correlation analysis between energy metabolism, hypoxia score, and inflammation-related pathways and differential miRNA-regulated target genes.

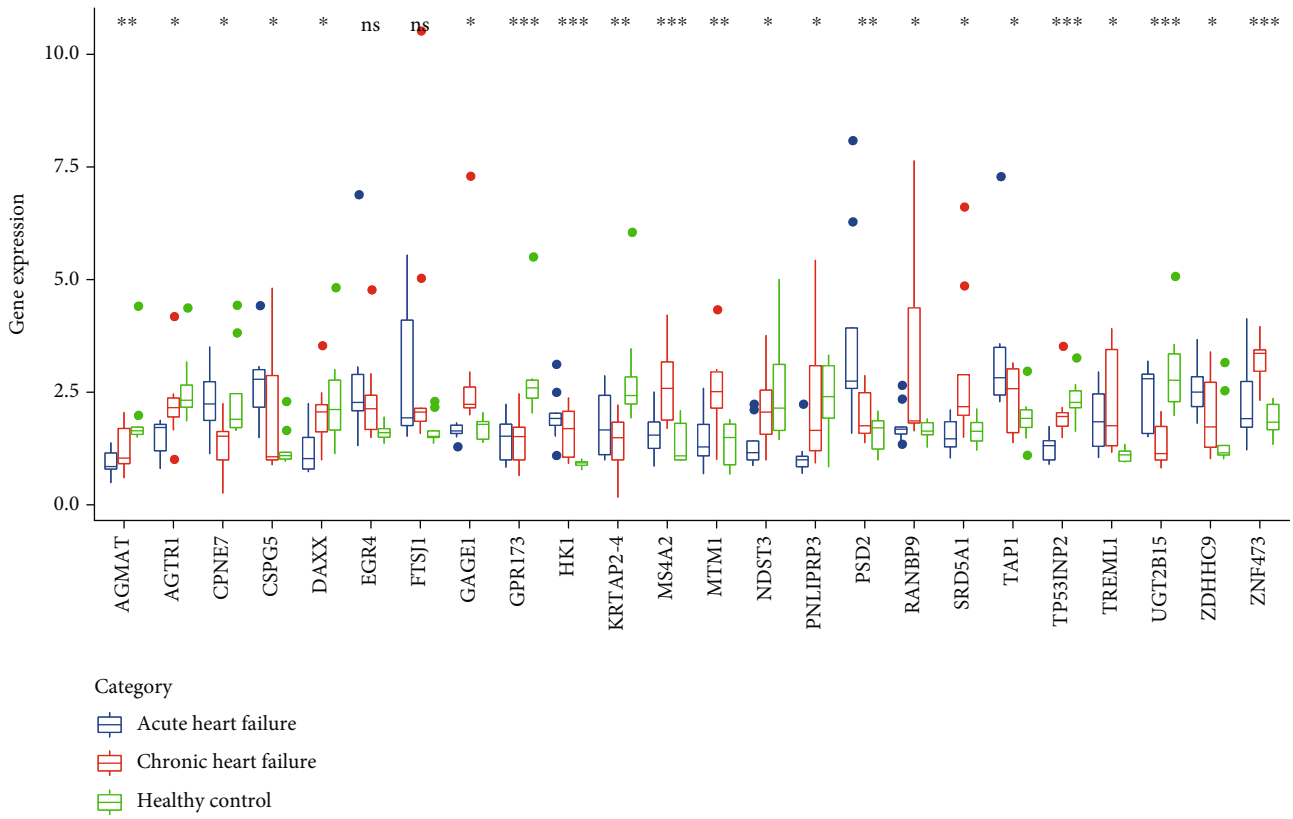

(a)

Figure 5: Continued.

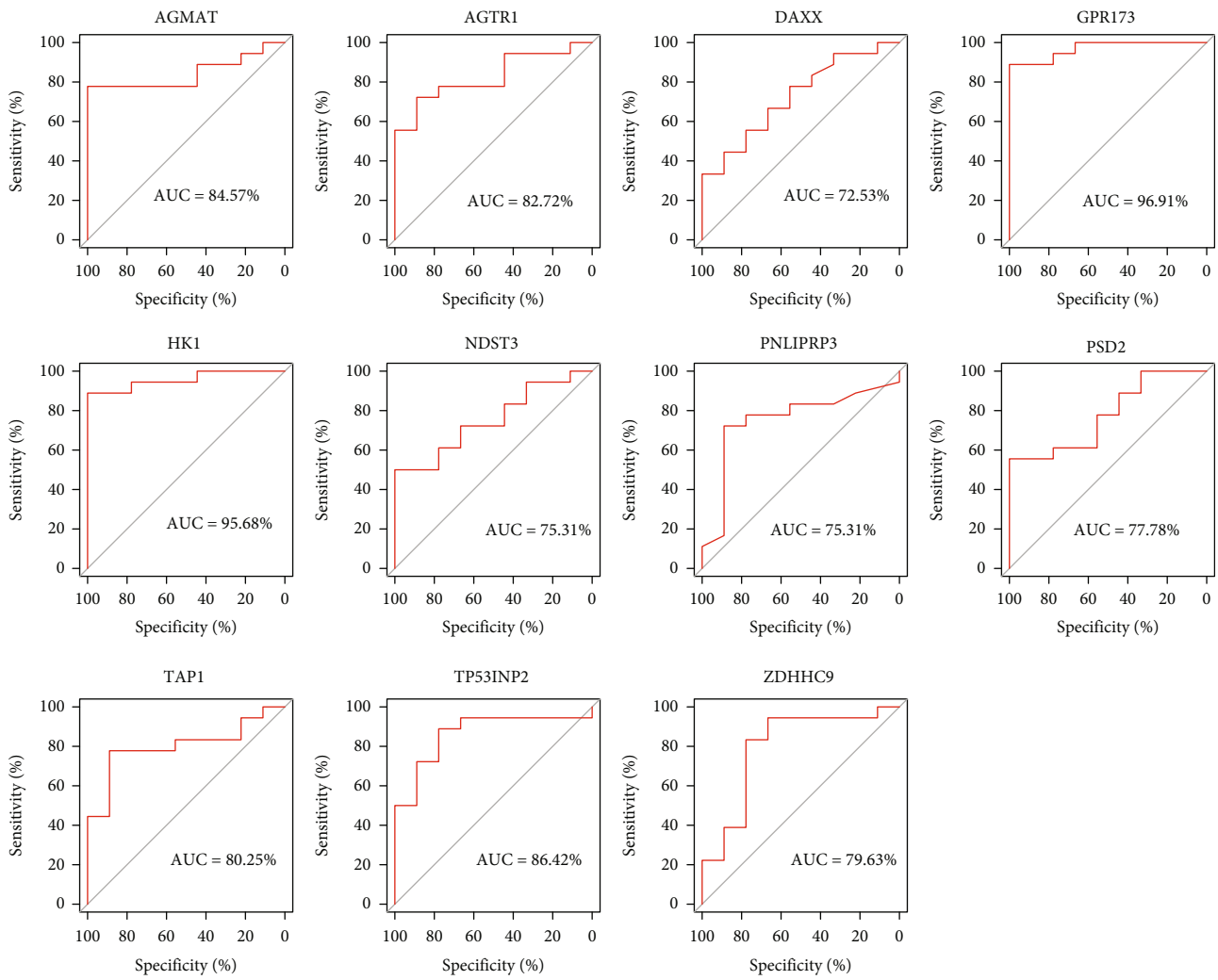

(b)

Figure 5: Screening analysis of correlated target genes: (a) box line plot of 24 genes expressed in acute, chronic heart failure and healthy groups (ANOVA, $^{*}P < 0.05$; $^{**}P < 0.01$; $^{***}P < 0.001$; and $^{****}P < 0.0001$); (b) construction of diagnostic models for 11 key genes.

we also performed single-sample gene set enrichment analysis (ssGSEA) of KEGG-related pathways by the R language GSVA package and analyzed pathways that were statistically significant in HF patients and healthy individuals by t-test ($P < 0.05$).

2.3. miRNA Target Analysis. The miRNA regulatory relationships were predicted from the online TargetScan [23] (https://www.targetscan.org/vert_72/) regulatory database. TargetScan is a software for predicting miRNA binding sites in mammals. Before prediction of miRNA target genes, the 3′UTR region of the transcript needs to be determined first. The TargetScan database identifies the corresponding 3′ UTR region of the transcript by a sequencing technique called 3P-seq (miRNAs in mammals bind the 3′UTR region of the transcript sequence to exert posttranscriptional regulation) and provides a comprehensive sequence of the 3′ UTR region by combining the analysis results of this technique with the available 3′UTR annotations in NCBI.

2.4. Protein-Protein Interaction Network Construction. The STRING (https://string-db.org/) database [24] supports the search for known protein-protein interactions and predicted protein-protein interactions (PPI). The PPI database can be applied to 2031 species and contains 9.6 million proteins and 13.8 million types of protein. In addition to results predicted using bioinformatics methods, it stores results of text mining from PubMed abstracts and synthesis of data from other databases as well as experimental data. Exploring interaction networks among proteins helps to mine the core regulatory genes. Though already many protein interaction databases are available to us, STRING is one of them covering the most species with the largest interaction information. We used STRING web version (version v11.0, https://string-db.org/) in this study, and based on the STRING database of protein interaction relationships, we filtered the interaction score ≧ 400, that is, medium confidence.

2.5. Prediction of Potential Target Therapeutic Agents. We calculated the proximity of drugs and its effect on treating

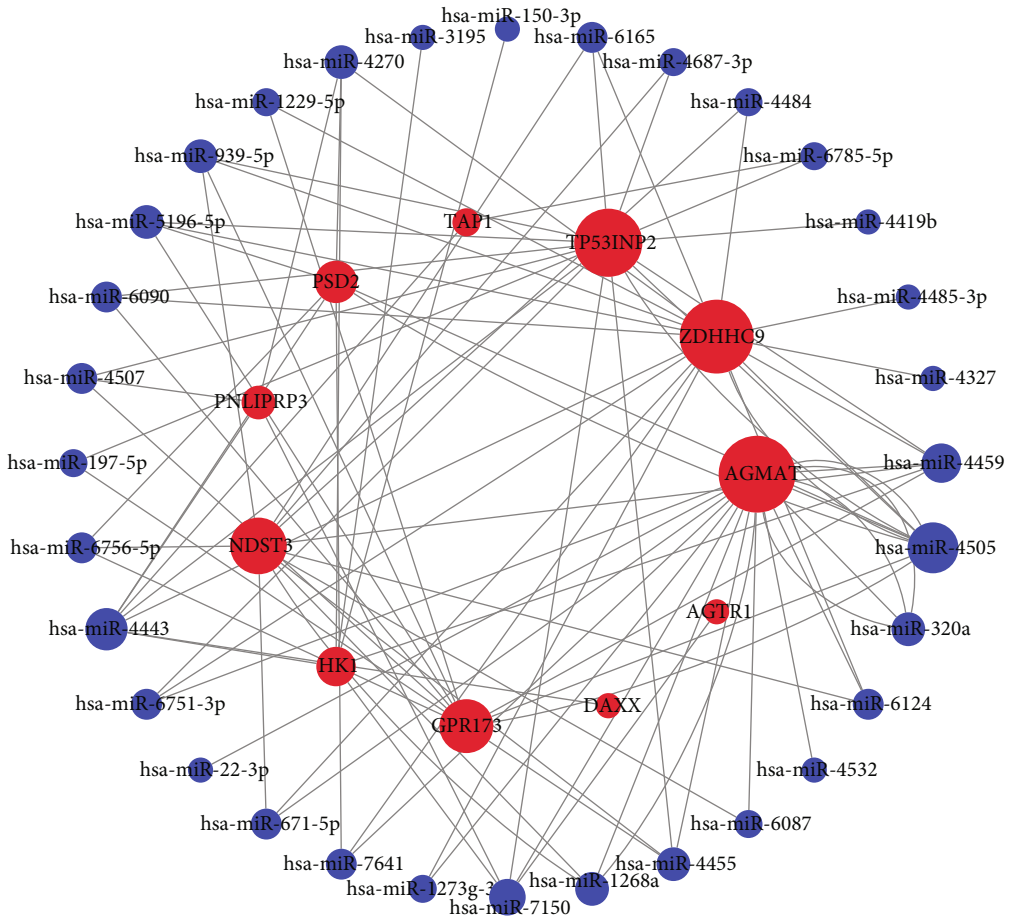

(a)

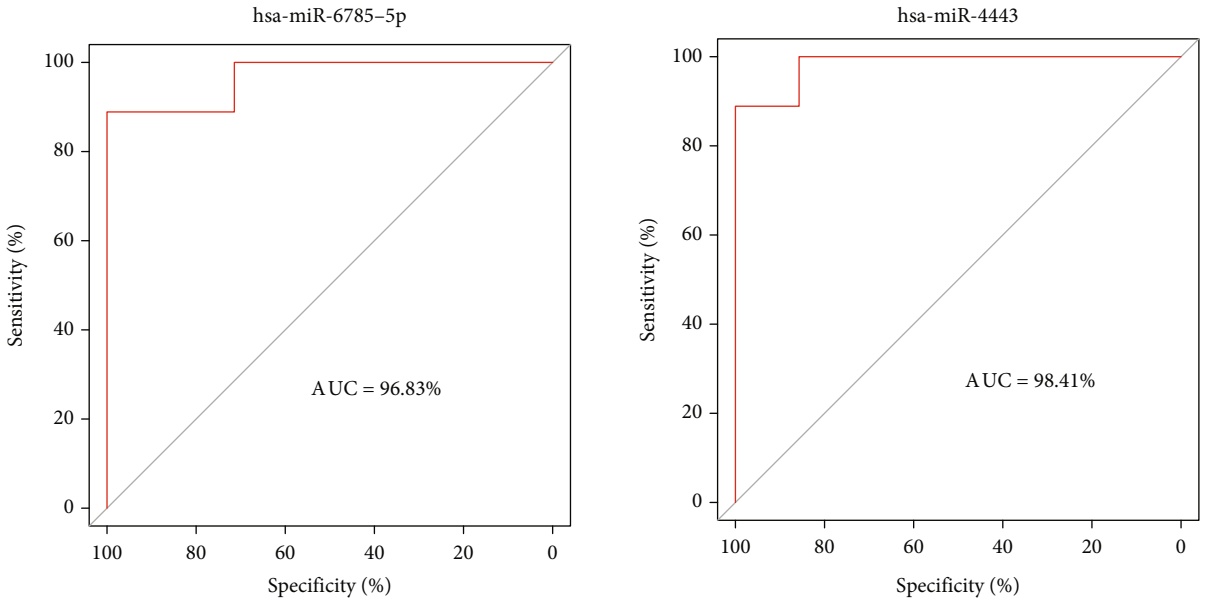

(b)

Figure 6: Continued.

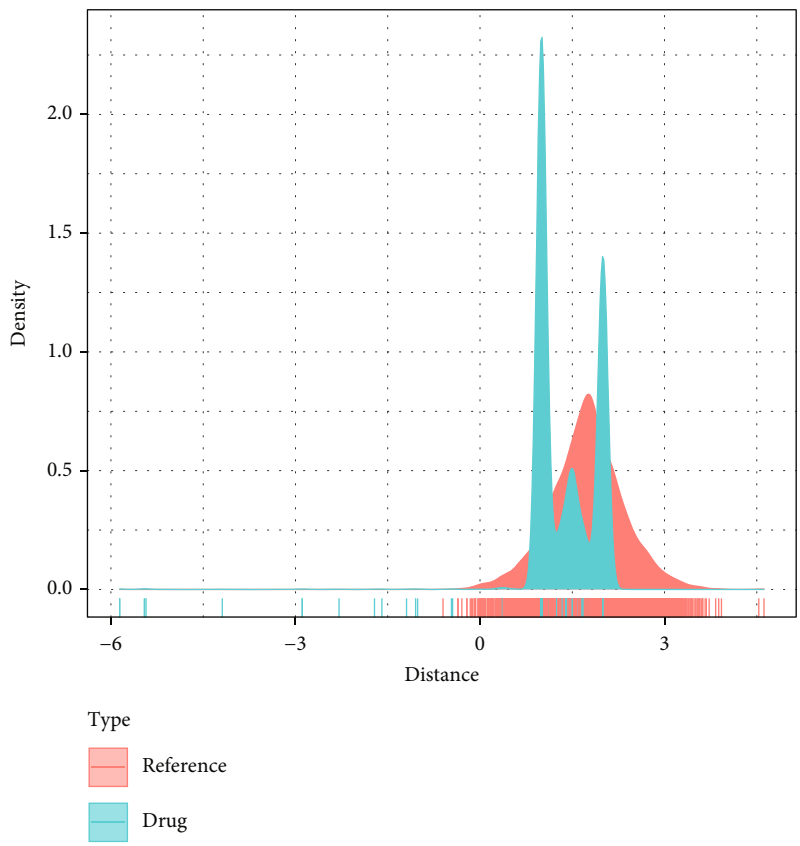

(c)

Figure 6: miRNA-mRNA relationship analysis: (a) miRNA-mRNA interaction relationship network; (b) diagnostic model of miRNA; (c) distance density fractionation plot of drug to TAP1-related gene set.

Table 1: Molecular docking scores of compounds with TAP1 proteins and generated important interactions.

Compound	AutoDock Vina score	H-bond interactions	Hydrophobic interactions
DB04847	-9.8	GLN195, SER344, GLN347	ALA229, TRP232, ALA302, ILE306, PHE343
DB01116	-8.7	GLN990	ALA229, TRP232, ILE306, LEU339, ILE340, PHE343
DB06412	-8.1	ASN721, GLN838	PHE303, TYR307, ALA987, VAL991
DB00480	-7.9	GLN990	TRP232, PHE343
DB08378	-7.6	TRP232, ASN721, GLY722, SER766, ASN842	PHE303, VAL991

HF. Here, we can give S (the gene set related to the treatment of heart failure), T (the set of drug target genes), D (the degree of the node of the related gene set in the PPI), and the distance $d(s,t)$, which indicated the shortest path between node t and node s (where $s \in S$, HF-related genes; $t \in T$, drug target genes). The calculation was as shown below:

$$d(S,T) = \frac{1}{|T|}\sum_{t\in T}\min_{s\in S}(d(s,t)+\omega), \quad (1)$$

where ω is the weight of the target gene. The calculation method is $\omega = -\ln\ (D+1)$, otherwise if the target gene is a gene in the HF-related gene set, $\omega = 0$.

We calculated simulated reference distance distribution corresponding to the drug. Protein nodes were randomly seen as the simulated drug target in the network, with the number of nodes keeping the same as the target scale (denoted as R). The distance $d(S,R)$ between these simulated drug targets (representing simulated drugs) and the TAP1-related gene set was then calculated, and after 10,000 random repetitions, a simulated reference distribution was calculated. Using both $\mu d\,(S,R)$ and $\sigma d(S,R)$, the mean and standard deviation of the corresponding actual observation distance and the reference distribution were converted into a standardized score, that is, the degree of proximity z:

$$z(S,T) = \frac{d(S,T) - \mu_{d(S,R)}}{\sigma_{d(S,R)}}. \quad (2)$$

We found that whether we took the TAP1-related gene set as the sample or our randomly selected gene set as the

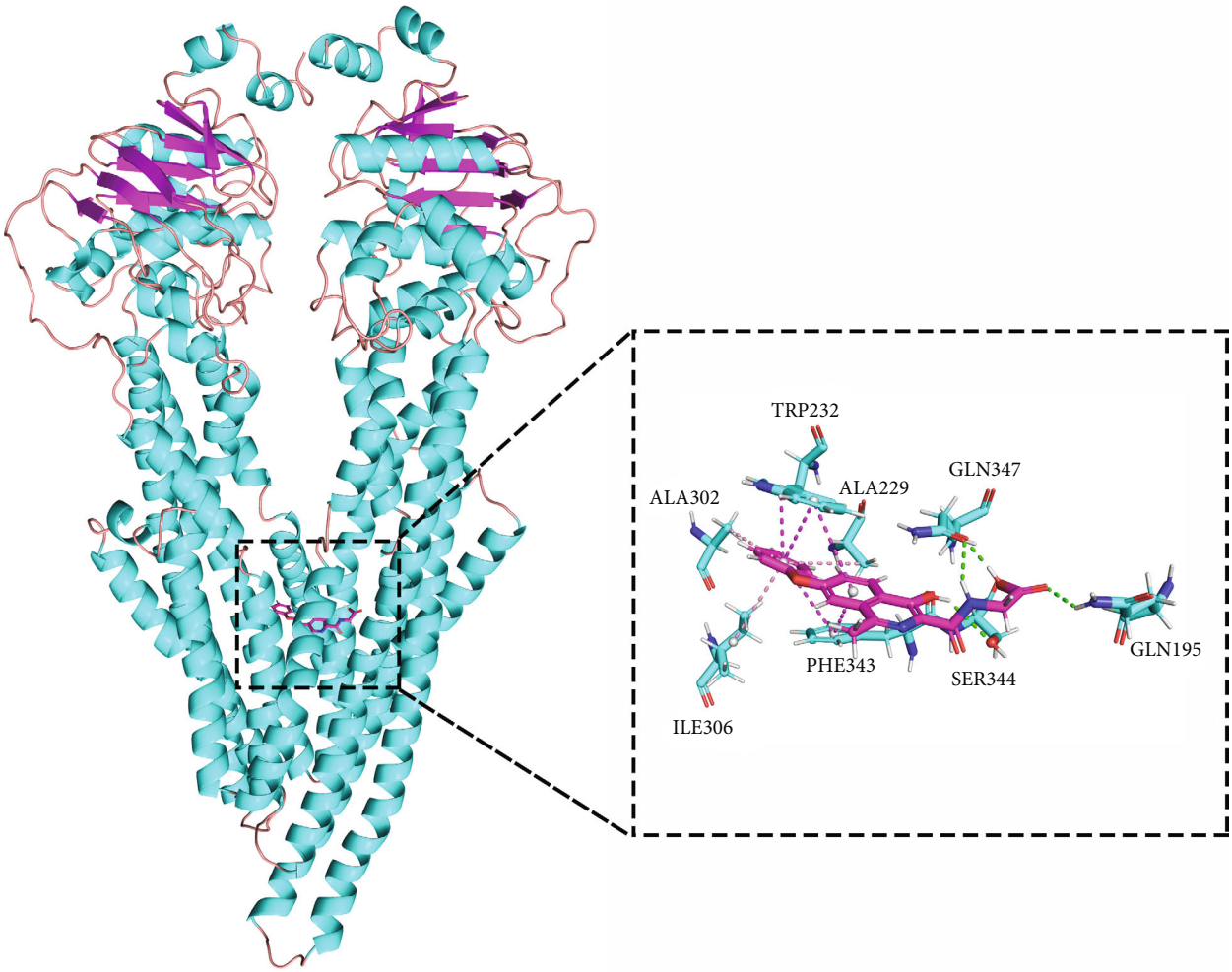

(a)

Figure 7: Continued.

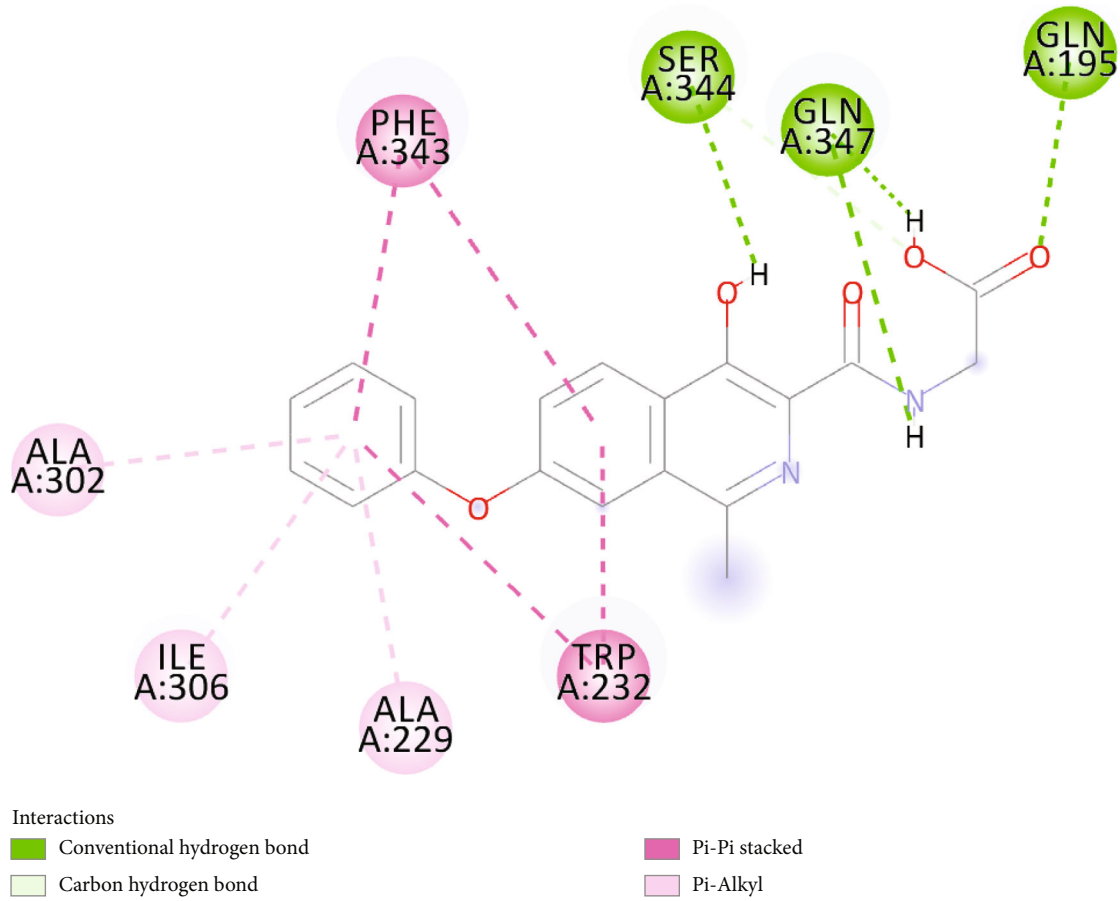

(b)

Figure 7: Binding pattern map of TAP1 protein with compound DB04847: (a) 3D binding pattern map of compound DB04847 with TAP1 protein; (b) 2D analysis map of detailed interaction generated by compound DB04847 with TAP1 protein, in which the α-helix of the protein backbone is shown as a cyan band and the β-fold is shown as a magenta band. Compound DB04847 is shown as a plum-red stick, the amino acid residues that produce the interaction are shown as cyan sticks, and the colors of the heteroatoms in the compound and amino acid residues are shown by element type. Hydrogen bonds are shown as green dashed lines, π-π stacked interactions are shown as magenta dashed lines, and π-Alkyl interactions are shown as pink dashed lines.

sample, in the location of central distribution of the drug distance, we performed multiple hypothesis tests with the random data obtained in the reference and selected drug with short distance and FDR < 0.001; a candidate drug set related to the TAP1-related gene set was obtained as an analysis.

2.6. Molecular Docking. AutoDock Vina software [25] was used for molecular docking. Firstly, to prepare all the input files, AutoDockTools 1.5.6 was used. The PDB files of the proteins were downloaded from the Protein Data Bank (PDB ID: 6SUK). All protein B chains, water molecules, and potassium ions were removed, and polar hydrogens were added to the system. The charge of the zinc ion in the PDBQT file of the receptor protein was changed to +2.0. The coordinates of the grid in each *XYZ* direction during molecular docking were 20.2 Å, -46.5 Å, and 15.2 Å. The lengths in each *XYZ* direction were 20 Å. To identify the most binding mode of the ligand molecule, the Lamarckian algorithm was introduced. The maximum number of conformations of output was set to 10, the exhaustiveness was set to 8, and the maximum energy range allowed was set to 3 kcal/mol. The processing of the result maps was performed using PyMOL.

The following are used for conditional screening: (1) Homo sapiens, (2) resolution: 1.75 Å, (3) ligand: dual inhibitor of omapatrilat metalloproteinases ACE and NEP with Ki values of 0.64 nM and 0.45 nM, respectively, and (4) omapatrilat is a relatively mature NEP inhibitor, and the resolution of the crystal is 1.75, which is relatively low.

2.7. Statistical Analysis. ANOVA was conducted in comparing different groups containing multiple subgroups. $P < 0.05$ was considered as significant.

3. Results

3.1. Identification of Key miRNAs. First, we identified 66 differentially expressed miRNAs, of which 10 miRNA expressions were downregulated and 56 miRNA expressions were

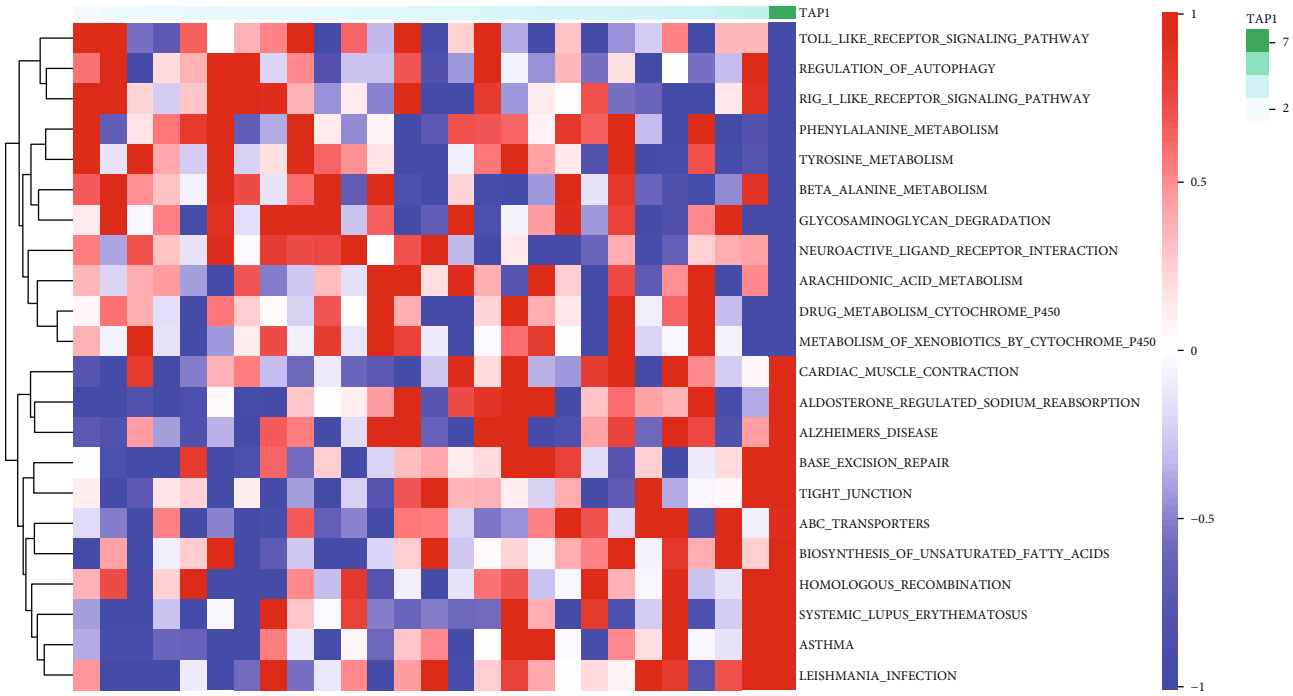

(a)

Figure 8: Continued.

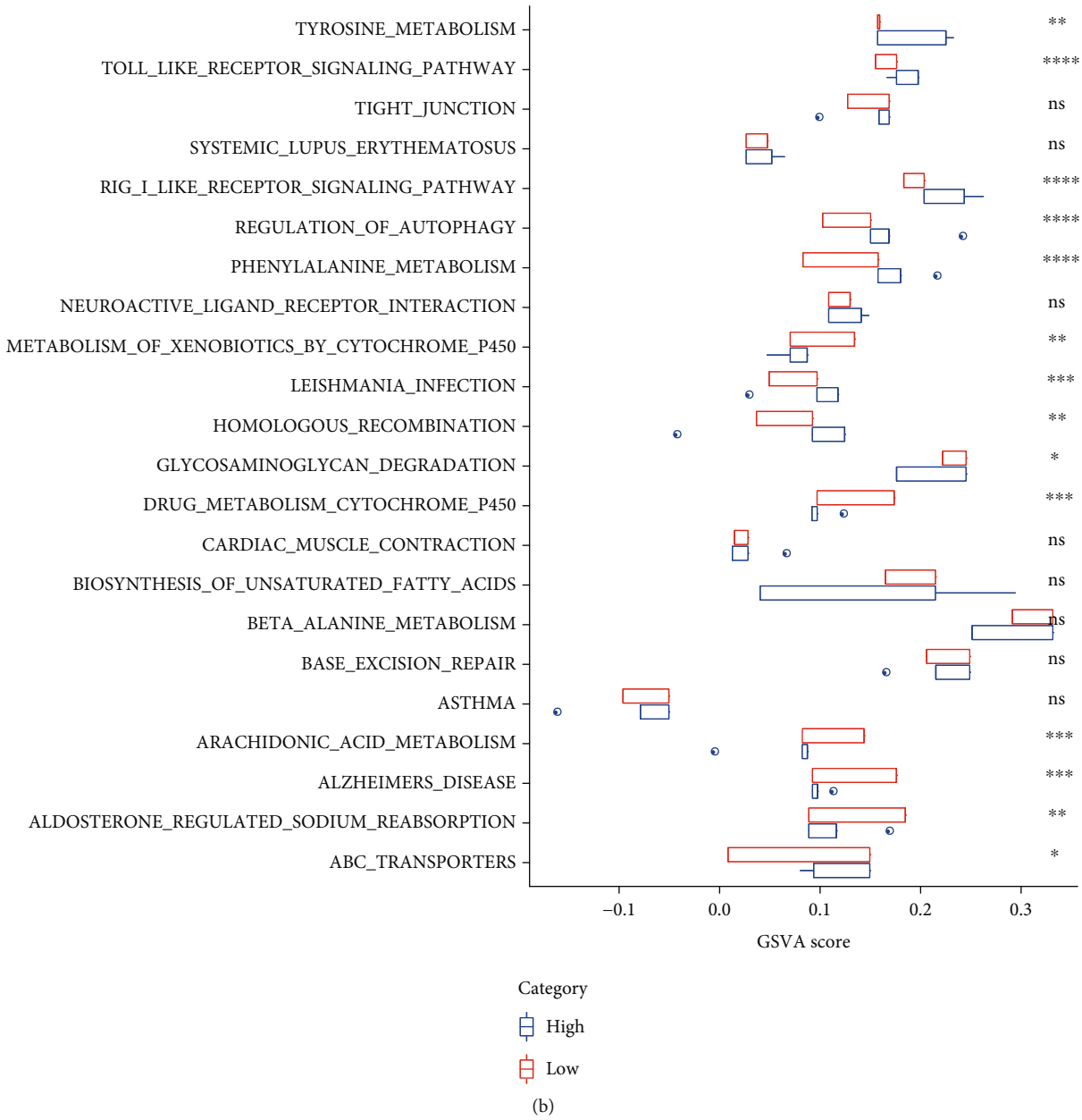

(b)

Figure 8: Continued.

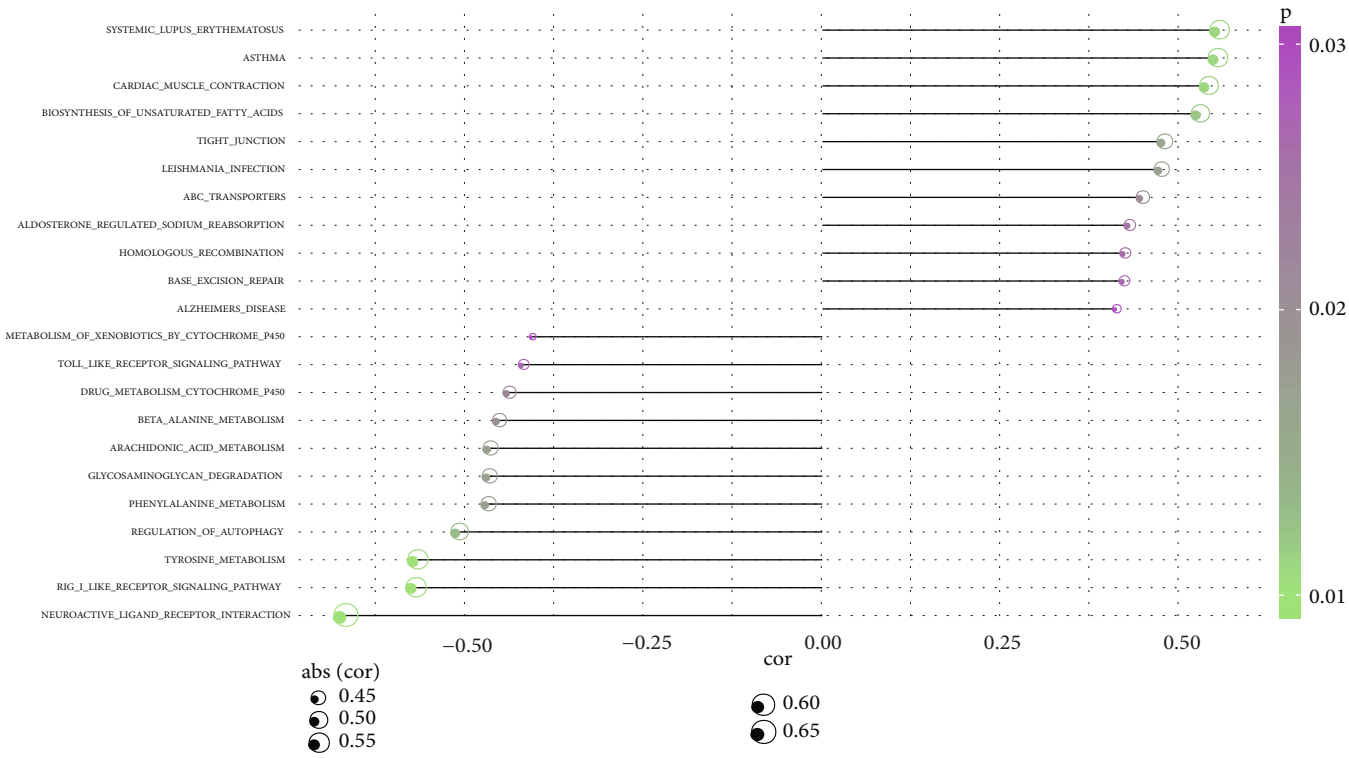

(c)

Figure 8: Continued.

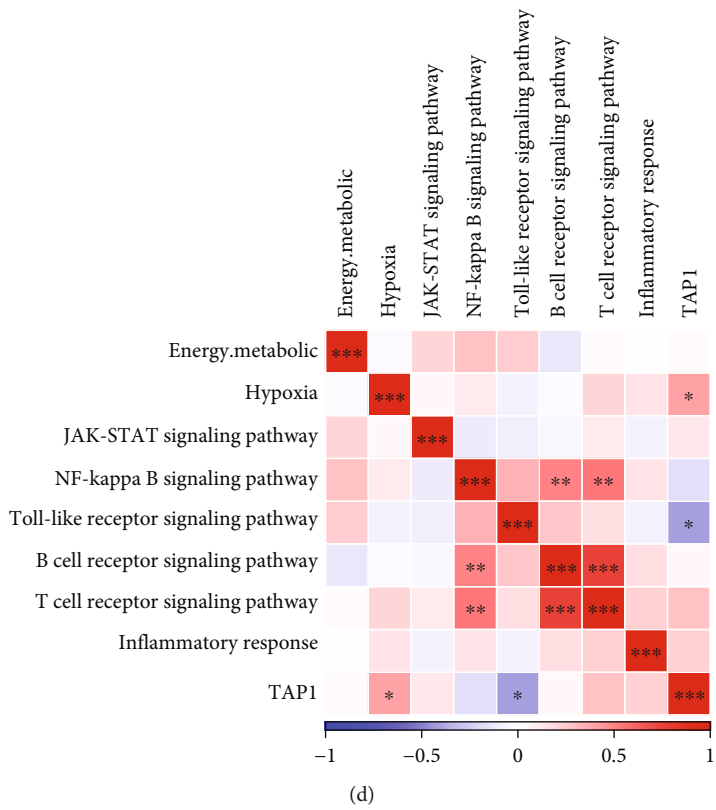

Figure 8: Pathway analysis of aberrant regulation of TAP1 gene: (a) heat map of aberrantly regulated pathway enrichment scores; (b) difference in aberrantly regulated pathway enrichment scores between the high- and low-expression groups of the TAP1 gene; (c) point bar graph of correlation between aberrantly regulated pathway enrichment scores and TAP1 gene expression, where color is significance and size of point is strength of correlation; (d) correlation between TAP1 expression and hypoxia, energy metabolism, and inflammation-related pathways in a correlation heat map.

upregulated (Figure 1(a)). Then, we looked at the clustering of the 66 differentially expressed miRNAs and found that the HF group showed significantly different miRNA expression patterns than the control group (Figure 1(b)). To further investigate the functions of the 66 differential miRNAs, we obtained 66 miRNA key target genes, among which hsa-miR-126-3p did not have a corresponding target gene. KEGG enrichment analysis on the target genes showed that the target genes were enriched to the MAPK signaling pathway, TGF-beta signaling pathway, p53 signaling pathway, Prolactin signaling pathway, and JAK-STAT signaling pathway (Supplementary Figure 1).

3.2. Identification of Key Target Genes of Key miRNAs. To identify key genes associated with HF, we performed differential analysis of mRNA expression profile data (HF patients vs. healthy individuals). First, the differential analysis was performed for acute HF patients/chronic HF patients/HF patients vs. healthy individuals, respectively, and we found that 64 genes with downregulated expression and 36 genes with upregulated expression were obtained from the acute HF patients vs. the healthy group (Figure 2(a)); 17 genes with downregulated expression and 48 genes with upregulated expression were obtained from the chronic HF patients vs. the healthy group (Figure 2(b)). After combining chronic HF/acute HF patients with the healthy group for differential analysis, 38 genes with downregulated expression and 10 genes with upregulated expression were finally screened (Figure 2(c)). By combining these differential genes of three groups, we finally found 83 genes upregulated and 92 genes downregulated in HF patients vs. healthy individuals. Next, we performed KEGG enrichment analysis on 175 differential genes ($P < 0.05$). These genes were enriched to a total of two pathways (Figure 3(a)), including amino sugar and nucleotide sugar metabolism, pantothenate, and CoA biosynthesis. Combined with the 66 key differentially expressed miRNAs screened in the above analysis, we found that only 68 of these 175 differential genes were the target genes of these key miRNAs, and subsequently, we constructed a miRNA-mRNA regulatory network, which included 46 miRNAs such as hsa-miR-4505, hsa-miR-6124, and hsa-miR-4459 and 64 miRNAs such as RBM28, DCPS, SRD5A1, and HSPA6 mRNAs (Figure 3(b)).

3.3. Pathway Characteristics of Abnormal HF Regulation. To further understand the abnormal regulatory pathways in the organism triggered by HF, we performed ssGSEA of KEGG-related pathways and found that 23 pathway scores were

significantly different between HF patients and healthy groups (Figure 4(a)), including TIGHT_JUNCTION, PATHOGENIC_ESCHERICHIA_COLI_ INFECTION, ABC_TRANSPORTERS, BIOSYNTHESIS_OF_UNSATURATED_FATTY_ACIDS, and MATURITY_ONSET_DIABETES_OF_THE_YOUNG. To further investigate the pathways potentially regulated by the differential target genes of these differential miRNAs, we performed Pearson correlation analysis using the rcorr function of Hmisc package on the expression of these target genes and the 23 pathways (Figure 4(b)). We found that most of the target genes were significantly associated with ECM_RECEPTOR_ INTERACTION, ABC_ TRANSPORTERS, HOMOLOGOUS_RECOMBINATION, and BETA_ALANINE_ METABOLISM.

HF leads to hypoxia [26, 27]; therefore, we calculated the hypoxic score of each sample in the GSE21125 dataset by the ssGSEA method using genes in the HALLMARK_HYPOXIA pathway as hypoxic key genes, and the correlation between target genes and hypoxic score was determined by Pearson's method. The results revealed that the FTSJ1 gene and TBC1D7 gene were significantly and positively correlated with hypoxia score and that MS4A2 and SRD5A1 genes were significantly and negatively correlated with hypoxia score.

HF not only leads to hypoxia but also may affect the process of energy metabolism of the body. The corresponding scores of genes in these pathways SULFUR_METABOLISM, OXIDATIVE_PHOSPHORYLATION, and NITROGEN_ METABOLISM were calculated by ssGSEA, the mean of which was taken as the score to indicate energy metabolism. We found a significant positive correlation between AGTR1 and energy metabolism and a significant negative correlation between EGR4 and PSD2 genes and energy metabolism by the correlation analysis.

Further, we analyzed HF and inflammation [28]. Inflammation-related pathways are Toll-like receptor (TLR) pathway, T cell receptor signaling, NF-κB signaling, Jak/Stat signaling, B cell receptor signaling, and IL-6 receptor family. For the genes in the above related pathways, we calculated their related pathway scores by the ssGSEA method and found that a total of 24 genes were significantly associated with inflammation-related scores, hypoxia-related scores, and energy metabolism-related scores by correlation analysis (Figure 4(c)). These 24 genes were AGMAT, AGTR1, CPNE7, CSPG5, DAXX, EGR4, FTSJ1, GAGE1, GPR173, HK1, KRTAP2-4, MS4A2, MTM1, NDST3, PNLIPRP3, PSD2, RANBP9, SRD5A1, TAP1 TP53INP2, TREML1, UGT2B15, ZDHHC9, and ZNF473.

Through the previous analysis, we found a total of 24 genes significantly associated with inflammation-related scores, hypoxia-related scores, and energy metabolism-related scores. First, we looked at the expression of these 24 genes in HF and healthy groups. The expression of 11 genes, AGMAT, AGTR1, DAXX, GPR173, HK1, NDST3, PNLIPRP3, PSD2, TAP1, TP53INP2, and ZDHHC9, was significantly different between the acute and chronic and healthy groups, while their expression was significantly different in acute-chronic-normal with gradual increase/decrease (Figure 5(a)). We then constructed diagnostic models for these 11 genes and found that the AUC of all the 11 genes reached above 0.7 (Figure 5(b)).

3.4. Identification of Key miRNA-mRNA. We constructed miRNA-mRNA interaction network based on the 11 key target genes, and through using Cytoscape software [29], it has been found that these 11 target genes had closely related interactions with 32 miRNAs in the miRNA-mRNA network (Figure 6(a)). Among them, four genes were highly expressed in the disease group, namely, ZDHHC9, PSD2, HK1, and TAP1. Next, we explored the crystal structures of the proteins corresponding to these four genes, among which ZDHHC9 and PSD2 showed no crystal structures, HK1 had complete crystals but no one has performed molecular docking on this protein with small molecules so far, and TAP1 had crystals [30, 31], and there are articles on its molecular docking [32]. Therefore, we selected the TAP1 gene as a candidate gene, which had the highest expression in acute HF, followed by chronic HF, and the lowest expression in the healthy group.

Then, based on the miRNA-mRNA interaction network analyzed above, it could be seen that the TAP1 gene was regulated by two miRNAs, hsa-miR-6785-5p and hsa-miR-4443. Next, we constructed diagnostic models for these two miRNAs based on the pROC package and found that the AUC of these two miRNAs reached above 0.9 (Figure 6(b)).

3.5. Prediction of TAP1-Related Gene Set and Potential Target Therapeutic Agents. We performed correlation analysis of the genes in the GSE21125 dataset by the rcorr function of the Hmisc package and obtained a total of 119 genes that were highly significantly associated with the TAP1 gene after screening the genes with a correlation greater than 0.4 ($P < 0.001$). We concluded that the above TAP1-related gene sets were important genes for the treatment of HF and that drugs targeting these genes could have a greater impact on HF treatment development. Based on the drug target pairs in DrugBank and the predicted PPI interactions, we calculated the proximity of drugs and the effect on treating HF (Figure 6(c)) and then analyzed the obtained TAP1-related gene set of relevant drug candidates.

We analyzed the potential target compounds by molecular docking and observed that five compounds with TAP1 scored high molecular docking (Table 1) and generated more favorable interactions. Notably, DB04847 had the highest molecular docking score of -9.8 kcal/mol. DB04847 bound in the active site of the TAP1 protein and produced hydrogen bonding interactions with GLN195, SER344, and GLN347 in the binding pocket and generated π-Alkyl interactions with ALA229, ALA302, and ILE306 and π-π stacked interactions with TRP232 and PHE343 (Figures 7(a) and 7(b)). The relatively high molecular docking score and the ability of compound DB04847 to produce so many favorable interactions with TAP1 protein suggested that this compound was highly likely to be a potential inhibitor of TAP1.

3.6. Pathways Abnormally Regulated by the TAP1 Gene. To better investigate the pathways potentially regulated by the

TAP1 gene, we screened a total of 22 TAP1 aberrantly regulated pathways by enrichment score and TAP1-pathway correlation (Figure 8(a)), and we also divided the TAP1 gene into high- and low-expression groups by median value. It has been found that 14 of these 22 aberrantly regulated pathways (64%) were significantly different in the high- and low-expression groups (t-test. Figure 8(b)). We further looked at the correlation of these 22 aberrantly regulated enrichment scores with TAP1 expression (Figure 8(c)). SYSTEMIC_LUPUS_ERYTHEMATOSUS, ASTHMA, CARDIAC_MUSCLE_CONTRACTION and BIOSYNTHESIS_OF_UNSATURATED_ FATTY_ACIDS, LEISHMANIA_INFECTION, and ABC_TRANSPORTERS pathways had enrichment scores positively correlated with TAP1 expression, and NEUROACTIVE_LIGAND_RECEPTOR_INTERACTION, RIG_LIKE_RECEPTOR_SIGNALING, and TYROSINE_METABOLISH had enrichment scores negatively correlated with TAP1 expression. In addition, correlation analysis of energy metabolism, hypoxia, and inflammation-related pathways with TAP1 expression showed a significant positive correlation between TAP1 and hypoxia pathway and a significant negative correlation with Toll-like receptor signaling pathway (Figure 8(d)). The above data indicated that TAP1 was closely correlated with classic cell growth pathways.

4. Discussion

HF is a globally common clinical syndrome characterized by structural damage to the heart and/or cardiac dysfunction leading to fatigue at rest and dyspnea [33]. HF is a multifactorial disease, the development of which is associated with complex regulation. Despite numerous studies [34, 35], the exact mechanisms of HF remain to be elucidated in order to facilitate the discovery of key drug targets in HF [36]. In this study, we screened miRNAs associated with HF by differential analysis and obtained miRNA-regulated mRNAs (genes) and explored the pathway characteristics of abnormal regulation of HF by enrichment analysis of miRNA target genes.

Our analysis revealed a significant positive correlation between TAP1 and hypoxia score, which is closely associated with HF [26, 27]. TAP1 belongs to the ATP binding cassette (ABC) transporter protein superfamily [37]. The existence of ABC_TRANSPORTERS in the regulatory pathways involved in the differential target genes of HF-related miRNAs is consistent with the above results. Moreover, TAP1 is mainly involved in transporting antigen from the cytoplasm to the endoplasmic reticulum, binding to major histocompatibility complex (MHC) class I molecules, and acting as a molecular scaffold for the final stage of MHC class I folding, that is, peptide binding [38]. Thus, TAP1 can perform antigen-presenting functions and regulate adaptive immunity [39]. TAP1 has been reported to be associated with tumor immune escape, and high-expressed TAP1 has been seen as a poor prognostic factor in stage I/II colorectal cancer patients [40]. In the present study, TAP1 was highly expressed in HF patients, which also suggests that high TAP1 expression is an unfavorable factor in the disease of HF. There is no reported association of TAP1 with the mechanism or prognosis of HF other than the present study, much less a study reporting TAP1 as an important gene for HF treatment. Therefore, for the first time, this study revealed the important function of TAP1 in HF management, and molecular docking verified that DB04847 was a potential inhibitor of TAP1.

Two key miRNAs, hsa-miR-4443 and hsa-miR-6785-5p, were recruited into the diagnostic model of miRNAs regulating TAP1 gene constructed in this study. hsa-miR-6785-5p was reported to be a novel target for diagnosis of advanced bladder cancer and its prognosis. It has been reported that LINC01929, which is highly expressed in advanced bladder cancer, upregulates the expression level of ADAMTS12 through competitive adsorption of miR-6875-5p, and based on this molecular mechanism, overexpressed miR-6875-5p inhibits the progression of bladder cancer [41]. However, there are no reports on hsa-miR-6785-5p in HF. Some other studies showed that miR-4443 can inhibit metastasis and energy metabolism of papillary thyroid cancer through targeting TRIM14 [42]. Most importantly, it has been reported that hsa-miR-4443 is implicated in atrial fibrillation regulation; that is, in atrial fibrillation, hsa-miR-4443 regulates TGF-β1/α-SMA/collagen signaling via targeting THBS1, thereby inhibiting cardiac fibroblast proliferation [43]. This study supported the involvement of hsa-miR-4443 as a potentially important miRNA in HF and as a potential target for HF therapy.

Although many adequate analyses have been conducted earlier in this paper, our study still has several limitations. First, the sample size of the current work was small; therefore, a larger cohort to further validate these results is required. Secondly, the specific biological functions of miRNAs in diagnostic models are still unclear, and whether these miRNAs could exert regulatory effects on pathways implicated in HF requires future exploration. Because HF is a heterogeneous syndrome that mainly affects patients suffering from multiple comorbidities, it is not uncommon that there are some overlaps in the mechanisms of other diseases; thus, the pathways identified in this study could be as well important in associated comorbidities. For further overcoming the limitations of this study, we are planning to re-collect and expand the clinical sample in subsequent work and will validate the accuracy of this drug target and model through additional external experiments.

Our analysis of the GEO dataset provided drug targets and diagnostic models for HF management. The drug target and model provide a comprehensive perspective to study the prognostic features and treatment of HF, and the newly discovered TAP1-mediated miRNA-regulated diagnostic model may provide new insights into the current knowledge of the mechanisms of HF initiation and progression as well as a new idea and basis for further study of HF treatment options.

5. Conclusion

In the treatment of HF, we identified TAP1 as a potential target and predicted that DB04847 drug is highly likely to

be a potential inhibitor of TAP1. In addition, two miRNAs (hsa-miR-6785-5p and hsa-miR-4443) that regulate TAP1 targets have a potential diagnostic value.

Data Availability

The data used to support the findings of this study are included within the article.

Conflicts of Interest

The authors declare that they have no competing interest.

Authors' Contributions

Xiangming Fang and Rensheng Song contributed equally to this work.

Acknowledgments

This study was funded by the Key Laboratory of Guangdong Higher Institute (2021KSY009).

Supplementary Materials

Supplementary Figure 1: functional enrichment of differential miRNAs. *(Supplementary Materials)*

References

[1] J. J. McMurray and M. A. Pfeffer, "Heart failure," *Lancet (London, England)*, vol. 365, no. 9474, pp. 1877–1889, 2005.

[2] E. Tanai and S. Frantz, "Pathophysiology of heart failure," *Comprehensive Physiology*, vol. 6, no. 1, pp. 187–214, 2015.

[3] D. Dobre, J. S. Borer, K. Fox et al., "Heart rate: a prognostic factor and therapeutic target in chronic heart failure. The distinct roles of drugs with heart rate-lowering properties," *European Journal of Heart Failure*, vol. 16, no. 1, pp. 76–85, 2014.

[4] S. J. Shah, T. Feldman, M. J. Ricciardi et al., "One-year safety and clinical outcomes of a transcatheter interatrial shunt device for the treatment of heart failure with preserved ejection fraction in the reduce elevated left atrial pressure in patients with heart failure (REDUCE LAP-HF I) trial," *JAMA Cardiology*, vol. 3, no. 10, pp. 968–977, 2018.

[5] J. R. Neely, M. J. Rovetto, and J. F. Oram, "Myocardial utilization of carbohydrate and lipids," *Progress in Cardiovascular Diseases*, vol. 15, no. 3, pp. 289–329, 1972.

[6] H. Taegtmeyer, L. Golfman, S. Sharma, P. Razeghi, and M. van Arsdall, "Linking gene expression to function: metabolic flexibility in the normal and diseased heart," *Annals of the New York Academy of Sciences*, vol. 1015, no. 1, pp. 202–213, 2004.

[7] D. A. Hood, I. Irrcher, V. Ljubicic, and A. M. Joseph, "Coordination of metabolic plasticity in skeletal muscle," *The Journal of Experimental Biology*, vol. 209, no. 12, pp. 2265–2275, 2006.

[8] M. F. Essop, P. Razeghi, C. McLeod, M. E. Young, H. Taegtmeyer, and M. N. Sack, "Hypoxia-induced decrease of UCP3 gene expression in rat heart parallels metabolic gene switching but fails to affect mitochondrial respiratory coupling," *Biochemical and Biophysical Research Communications*, vol. 314, no. 2, pp. 561–564, 2004.

[9] L. M. Edwards, A. J. Murray, D. J. Tyler et al., "The effect of high-altitude on human skeletal muscle energetics: P-MRS results from the Caudwell Xtreme Everest expedition," *PloS One*, vol. 5, no. 5, article e10681, 2010.

[10] V. Ambros, "The functions of animal microRNAs," *Nature*, vol. 431, no. 7006, pp. 350–355, 2004.

[11] D. P. Bartel, "MicroRNAs: genomics, biogenesis, mechanism, and function," *Cell*, vol. 116, no. 2, pp. 281–297, 2004.

[12] V. Ambros, "microRNAs: tiny regulators with great potential," *Cell*, vol. 107, no. 7, pp. 823–826, 2001.

[13] Y. F. Melman, R. Shah, and S. Das, "MicroRNAs in heart failure," *Circulation Heart Failure*, vol. 7, no. 1, pp. 203–214, 2014.

[14] X. Chen, Y. Ba, L. Ma et al., "Characterization of microRNAs in serum: a novel class of biomarkers for diagnosis of cancer and other diseases," *Cell Research*, vol. 18, no. 10, pp. 997–1006, 2008.

[15] Y. Goren, M. Kushnir, B. Zafrir, S. Tabak, B. S. Lewis, and O. Amir, "Serum levels of microRNAs in patients with heart failure," *European Journal of Heart Failure*, vol. 14, no. 2, pp. 147–154, 2012.

[16] J. Täubel, W. Hauke, S. Rump et al., "Novel antisense therapy targeting microRNA-132 in patients with heart failure: results of a first-in-human phase 1b randomized, double-blind, placebo-controlled study," *European Heart Journal*, vol. 42, no. 2, pp. 178–188, 2021.

[17] T. Thum, P. Galuppo, C. Wolf et al., "MicroRNAs in the human heart," *Circulation*, vol. 116, no. 3, pp. 258–267, 2007.

[18] A. Ucar, S. K. Gupta, J. Fiedler et al., "The miRNA-212/132 family regulates both cardiac hypertrophy and cardiomyocyte autophagy," *Nature Communications*, vol. 3, no. 1, p. 1078, 2012.

[19] Y. Li, Z. Li, C. Zhang et al., "Cardiac fibroblast-specific activating transcription factor 3 protects against heart failure by suppressing MAP2K3-p38 signaling," *Circulation*, vol. 135, no. 21, pp. 2041–2057, 2017.

[20] T. Barrett, S. E. Wilhite, P. Ledoux et al., "NCBI GEO: archive for functional genomics data sets–update," *Nucleic Acids Research*, vol. 41, pp. D991–D995, 2013.

[21] M. E. Ritchie, B. Phipson, D. Wu et al., "limma powers differential expression analyses for RNA-sequencing and microarray studies," *Nucleic Acids Research*, vol. 43, no. 7, article e47, 2015.

[22] A. Subramanian, P. Tamayo, V. K. Mootha et al., "Gene set enrichment analysis: a knowledge-based approach for interpreting genome-wide expression profiles," *Proceedings of the National Academy of Sciences of the United States of America*, vol. 102, no. 43, pp. 15545–15550, 2005.

[23] B. P. Lewis, C. B. Burge, and D. P. Bartel, "Conserved seed pairing, often flanked by adenosines, indicates that thousands of human genes are microRNA targets," *Cell*, vol. 120, no. 1, pp. 15–20, 2005.

[24] D. Szklarczyk, A. L. Gable, K. C. Nastou et al., "The STRING database in 2021: customizable protein-protein networks, and functional characterization of user-uploaded gene/measurement sets," *Nucleic Acids Research*, vol. 49, no. D1, pp. D605–D612, 2021.

[25] O. Trott and A. J. Olson, "AutoDock Vina: improving the speed and accuracy of docking with a new scoring function, efficient optimization, and multithreading," *Journal of Computational Chemistry*, vol. 31, no. 2, pp. 455–461, 2010.

[26] K. Yamashita, K. Ito, J. Endo et al., "Adrenal cortex hypoxia modulates aldosterone production in heart failure," *Biochemical and Biophysical Research Communications*, vol. 524, no. 1, pp. 184–189, 2020.

[27] J. E. Sanderson, F. Fang, M. Lu, C. Y. Ma, and Y. X. Wei, "Obstructive sleep apnoea, intermittent hypoxia and heart failure with a preserved ejection fraction," *Heart (British Cardiac Society).*, vol. 107, no. 3, pp. 190–194, 2021.

[28] E. Pena, J. Brito, S. El Alam, and P. Siques, "Oxidative stress, kinase activity and inflammatory implications in right ventricular hypertrophy and heart failure under hypobaric hypoxia," *International Journal of Molecular Sciences*, vol. 21, no. 17, p. 6421, 2020.

[29] P. Shannon, A. Markiel, O. Ozier et al., "Cytoscape: a software environment for integrated models of biomolecular interaction networks," *Genome Research*, vol. 13, no. 11, pp. 2498–2504, 2003.

[30] A. Hinz, J. Jedamzick, V. Herbring et al., "Assembly and function of the major histocompatibility complex (MHC) I peptide- loading complex are conserved across higher vertebrates∗," *The Journal of Biological Chemistry*, vol. 289, no. 48, pp. 33109–33117, 2014.

[31] F. Seyffer and R. Tampé, "ABC transporters in adaptive immunity," *Biochimica et Biophysica Acta*, vol. 1850, no. 3, pp. 449–460, 2015.

[32] R. Badhan and J. Penny, "In silico modelling of the interaction of flavonoids with human P-glycoprotein nucleotide-binding domain," *European Journal of Medicinal Chemistry*, vol. 41, no. 3, pp. 285–295, 2006.

[33] G. S. Francis and W. H. Tang, "Pathophysiology of congestive heart failure," *Reviews in Cardiovascular Medicine*, vol. 4, Supplement 2, pp. S14–S20, 2003.

[34] N. F. Marrouche, J. Brachmann, D. Andresen et al., "Catheter ablation for atrial fibrillation with heart failure," *The New England Journal of Medicine*, vol. 378, no. 5, pp. 417–427, 2018.

[35] E. J. Velazquez, D. A. Morrow, A. D. DeVore et al., "Angiotensin-neprilysin inhibition in acute decompensated heart failure," *The New England Journal of Medicine*, vol. 380, no. 6, pp. 539–548, 2019.

[36] B. Ziaeian and G. C. Fonarow, "Epidemiology and aetiology of heart failure," *Nature Reviews Cardiology*, vol. 13, no. 6, pp. 368–378, 2016.

[37] R. Abele and R. Tampé, "The ABCs of immunology: structure and function of TAP, the transporter associated with antigen processing," *Physiology*, vol. 19, no. 4, pp. 216–224, 2004.

[38] P. Leone, E. C. Shin, F. Perosa, A. Vacca, F. Dammacco, and V. Racanelli, "MHC class I antigen processing and presenting machinery: organization, function, and defects in tumor cells," *Journal of the National Cancer Institute*, vol. 105, no. 16, pp. 1172–1187, 2013.

[39] D. Parcej and R. Tampé, "ABC proteins in antigen translocation and viral inhibition," *Nature Chemical Biology*, vol. 6, no. 8, pp. 572–580, 2010.

[40] A. Ling, A. Löfgren-Burström, P. Larsson et al., "TAP1 downregulation elicits immune escape and poor prognosis in colorectal cancer," *Oncoimmunology*, vol. 6, no. 11, article e1356143, 2017.

[41] Y. Xiong, M. Pang, Y. Du et al., "The LINC01929/miR-6875-5p/ADAMTS12 Axis in the ceRNA network regulates the development of advanced bladder cancer," *Frontiers in Oncology*, vol. 12, article 856560, 2022.

[42] X. M. Zuo, H. W. Sun, H. Fang, Y. Wu, Q. Shi, and Y. F. Yu, "miR-4443 targets TRIM14 to suppress metastasis and energy metabolism of papillary thyroid carcinoma (PTC) in vitro," *Cell Biology International*, vol. 45, no. 9, pp. 1917–1925, 2021.

[43] J. Xiao, Y. Zhang, Y. Tang et al., "hsa-miR-4443 inhibits myocardial fibroblast proliferation by targeting THBS1 to regulate TGF-β1/α-SMA/collagen signaling in atrial fibrillation," *Brazilian Journal of Medical and Biological Research*, vol. 54, no. 4, article e10692, 2021.

Hindawi
Mediators of Inflammation
Volume 2022, Article ID 6830635, 10 pages
https://doi.org/10.1155/2022/6830635

Research Article

Identification of Diagnostic Genes and Effective Drugs Associated with Osteoporosis Treatment by Single-Cell RNA-Seq Analysis and Network Pharmacology

Zhanyue Zhang,[1,2,3] **Tingbao Zhang**,[1,2,3] **Liangshuang Zhou**,[1,2,3] **and Jianzhong Guan**[1,2,3]

[1]*Department of Orthopaedics, The First Affiliated Hospital of Bengbu Medical College, Bengbu 233004, China*
[2]*Anhui Provincial Key Laboratory of Tissue Transplantation, Bengbu Medical College, Bengbu 233030, China*
[3]*Bengbu Medical College, Bengbu 233000, China*

Correspondence should be addressed to Jianzhong Guan; jzguan2002@163.com

Received 21 July 2022; Revised 25 August 2022; Accepted 1 September 2022; Published 25 September 2022

Academic Editor: Md Sayed Ali Sheikh

Background. Osteoporosis is a common bone metabolic disease with increased bone fragility and fracture rate. Effective diagnosis and treatment of osteoporosis still need to be explored due to the increasing incidence of disease. *Methods*. Single-cell RNA-seq was acquired from GSE147287 dataset. Osteoporosis-related genes were obtained from chEMBL. Cell subpopulations were identified and characterized by scRNA-seq, t-SNE, clusterProfiler, and other computational methods. "limma" R packages were used to identify all differentially expressed genes. A diagnosis model was build using rms R packages. Key drugs were determined by proteins-proteins interaction and molecular docking. *Results*. Firstly, 15,577 cells were obtained, and 12 cell subpopulations were identified by clustering, among which 6 cell subpopulations belong to CD45+ BM-MSCs and the other subpopulations were CD45-BM-MSCs. CD45- BM-MSCs_6 and CD45+ BM-MSCs_5 were consider as key subpopulations. Furthermore, we found 7 genes were correlated with above two subpopulations, and F9 gene had highest AUC. Finally, five compounds were identified, among which DB03742 bound well to F9 protein. *Conclusions*. This work discovered that 7 genes were correlated with CD45-BM-MSCs_6 and CD45+ BM-MSCs_5 subpopulations in osteoporosis, among which F9 gene had better research value. Moreover, compound DB03742 was a potential inhibitor of F9 protein.

1. Introduction

Osteoporosis is a common bone metabolic disease, which is characterized by the loss of bone mass and the disorder of bone structure caused by the imbalance between bone formation and bone resorption. Therefore, patients with osteoporosis are often accompanied by increased bone fragility and fracture rate [1, 2]. Older people and postmenopausal women are particularly susceptible to the disease, which is strongly associated with decreased levels of sex hormones [3, 4]. Among the many clinical adverse consequences of osteoporosis, hip fracture and vertebral fracture are the most serious, and the mortality rate can be as high as 20% after one year of onset. Patients often need hospitalization, and the accompanying complications of other organs are significantly increased, such as pneumonia and pulmonary thrombosis induced by long-term repose [5]. Therefore, effective diagnosis and treatment of osteoporosis are particularly important.

With the proposal of the concept of "precision therapy," clinical treatment based on sequencing technology has become one of the most important methods to treat cancer [6–8]. The most widely used field of single-cell sequencing technology is tumor research. So far, the analysis of single-cell sequencing data has provided us with a new understanding of the heterogeneity, origin of tumor

cells, and occurrence and development of most tumors. In colorectal cancer, Zhang et al. studied the transcriptional map of infiltrating T cell immune receptors; elaborated the subgroup distribution of these cells, tissue distribution characteristics, and tumor heterogeneity; and identified potential drug targets [9]. Bian et al. used this technology to study single cell copy number variation during the occurrence and metastasis of human colorectal cancer and analyzed abnormal DNA methylation and differential expression [10]. In breast cancer, researchers discovered and identified the polyclonal origin of breast cancer by means of cell trajectory inference and tumor heterogeneity analysis, providing a new theoretical basis for the early diagnosis of breast cancer [11]. By single-cell sequencing of microenvironment cells, the researchers mapped a variety of immune cells infiltrated in the breast cancer microenvironment [12–14]. However, the heterogeneity, diagnosis, and treatment of osteoporosis are rarely studied by single cell sequencing.

In view of the powerful function of single-cell sequencing technology in tumor research, this study will use this technology to explore osteoporosis and provide new ideas for early diagnosis and treatment of osteoporosis through single-cell sequencing analysis.

2. Materials and Methods

2.1. Data Acquisition. Single-cell sequencing data GSE147287 [15], downloaded from the Gene Expression Omnibus (GEO) dataset, includes two samples (osteoporosis patients and osteoarthritis patients). First of all, from the PubChem database (https://pubchem.ncbi.nlm.nih.gov/) [16], to download 3D/2D structure of osteoporosis drugs, mainly including of glucocorticoid hormones and calcineurin inhibitors, chEMBL (http://www.ebi.ac.uk/chembl/) [17] was used to download these drugs active site-related genes.

2.2. Data Control. The R Package Seurat function [18] was used to set the expression of each gene in at least 3 cells, and each cell expressed at least 250 genes to filter a single cell. Mitochondria and rRNA quantities were further calculated by PercentageFeatureSet function. Genes expressed in each cell were less than 5,000, the percentage of mitochondria was less than 25%, and the UMI of each cell was at least greater than 100. The FindVariableFeatures function was employed to detect highly variable genes, followed by scaling and PCA dimensionality reduction for all genes using the ScaleData function.

2.3. Cell Type Annotation. We used FindNeighbors and FindClusters [19] (Dim = 20, Resolution = 0.1) here for cell clustering. The FindAllMarkers function was conducted to select the marker gene. Kyoto Encyclopedia of Genes and Genomes (KEGG) pathway annotation was performed using R Package ClusterProfiler [20].

2.4. Compared Patient with and without Osteoporosis. Differential gene expression analysis was performed in patients with and without osteoporosis in the GSE35959 dataset [21] by limma package [22] with $|\log 2(\text{Fold Change})| > 1$ and $p < 0.05$.

2.5. Classification Algorithms. In GSE35959 dataset, RMS was used to construct diagnostic model [23]. We combined multiple genes model as well as single gene model to identify osteoporosis.

2.6. Computation of Estimate Score, Stromal Score, and Immune Score. R software estimation of stromal and immune cells in malignant tumors using expression data (ESTIMATE) arithmetic [24] was utilized to compute overall stroma level (stromal score), the immunocyte infiltration (immune score), and the combination (ESTIMATE score).

2.7. ssGSEA. For analyzing the infiltration level of 28 immune cells, we used the single-sample gene set enrichment analysis (ssGSEA) method of R software gene set variation analysis (GSVA) [25] package [26].

2.8. Molecular Docking Simulation. In this experiment, Autodock Vina software [27] was used for molecular docking simulation. AutoDockTools 1.5.6 [28] is used to prepare all input files. PDB-IDs of target genes were obtained from Protein Data Bank (PDB) [29] database. To identify the most binding mode for ligand molecules, the Lamarckian algorithm [30] was used with exhaustiveness being set to 8, the maximum number of conformations output being set to 10, and the maximum allowable energy range being set to 3 kcal/mol. The results were processed by Pymol [31]. 100 ns molecular dynamics simulations were performed using Gromacs2019 software package [32] to assess the binding stability of the receptor-ligand complex.

3. Results

3.1. Single-Cell RNA-Seq Profiling and Clustering. First, the single-cell data was filtered by setting each gene to be expressed in at least three cells, with at least 250 genes per cell, yielding 17,669 cells. The quality control diagram of samples before and after filtration is shown in Figure S1A-B, which requires that the detected cells express less than 5,000 genes, the mitochondrial content is less than 25%, and the UMI of each cell is at least more than 100. Therefore, 15,577 cells are finally obtained. In addition, a significant positive relationship was observed between UMI and the number of detected genes (Pearson's $r = 0.73$), and there was a significant negative correlation between UMI and mitochondrial content (Pearson's $R = -0.16$), gene number, and mitochondrial content (Pearson's $R = -0.16$) (Figure S1C). The cells were mapped to two dimensions based on PC_2 and PC_1 groups. It has been found that the two cell subpopulations were not significantly separated (Figure S1D).

Furthermore, t-distributed stochastic neighbor embedding (t-SNE) algorithm, which is commonly in visualizing high dimensional data, was applied here for cell population clustering. Figure 1(a) is the t-SNE diagram of two samples, and Figure 1(b) is t-SNE of 12 cell subpopulations. Next, we detected the expression of CD45 in 12 subpopulations and found that 6 subpopulations were CD45+ BM-MSCs and 6 subpopulations were CD45-BM-MSCs (Figure 1(c), Figure S1E).

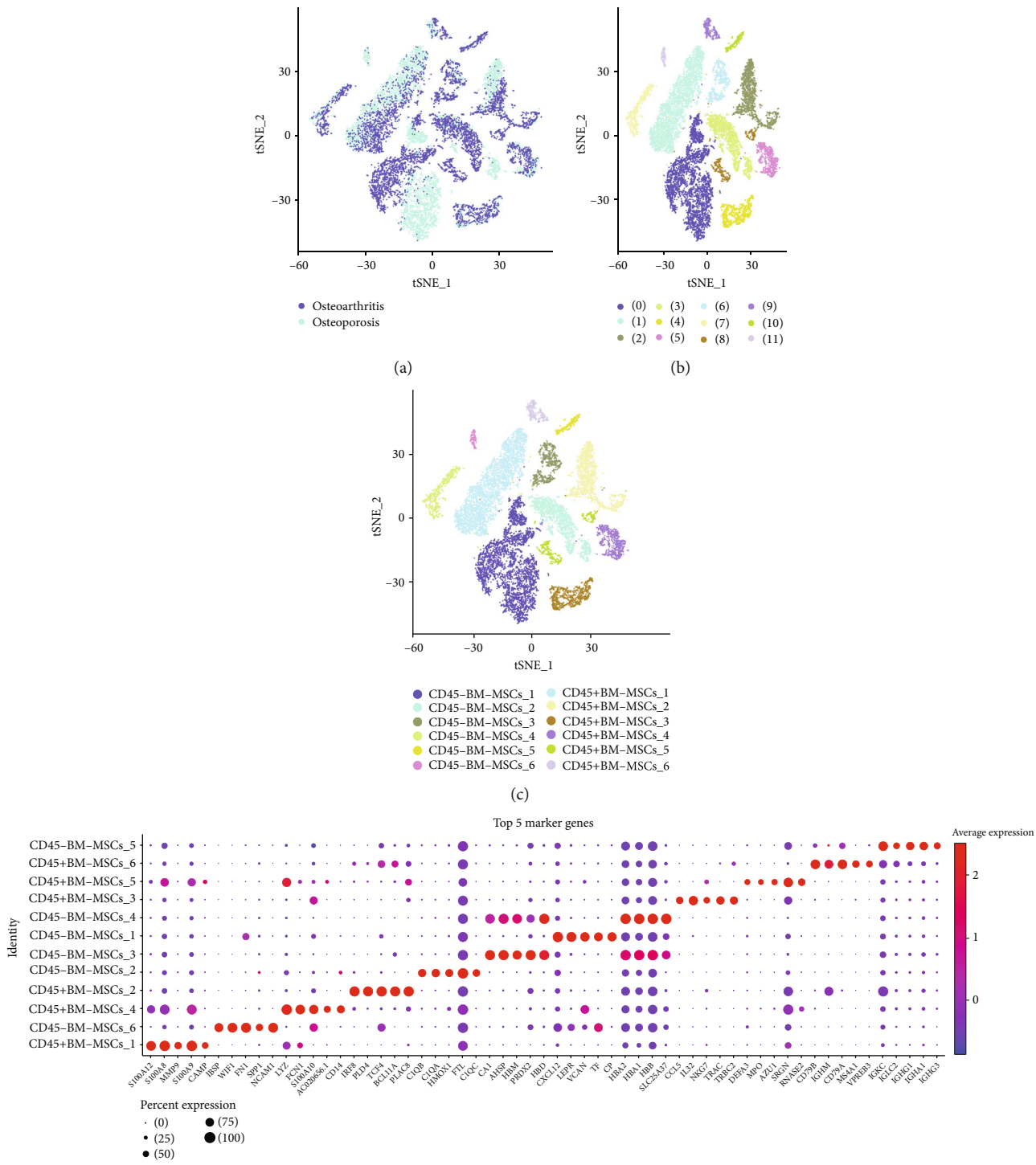

Figure 1: Continued.

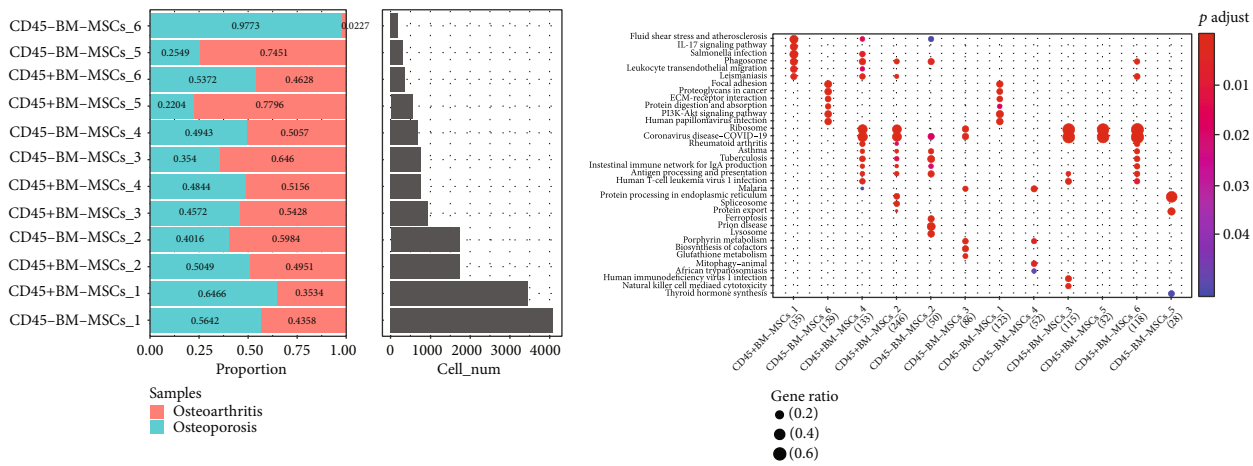

Figure 1: Single-cell RNA analysis of osteoporosis patients and osteoarthritis patients. (a) t-Distributed stochastic neighbor embedding of two samples. (b) t-Distributed stochastic neighbor embedding of 12 subpopulations. (c) t-Distributed stochastic neighbor embedding of 12 subpopulations after BM-MSCs cell annotation. (d) The proportion and cell numbers of 12 subpopulations in two samples. (f) Kyoto Encyclopedia of Genes and Genomes enrichment analysis of 12 subpopulations.

Table 1: Differential analysis of cell types.

	Osteoporosis/osteoarthritis	
cell_name	*p*.val	fc
CD45+ BM-MSCs_1	1.03E-64	1.952078384
CD45- BM-MSCs_6	1.29E-43	40.55324249
CD45+ BM-MSCs_4	0.045726035	0.861342268
CD45+ BM-MSCs_2	0.185992587	0.934653196
CD45- BM-MSCs_2	1.50E-25	0.584120062
CD45- BM-MSCs_3	5.45E-21	0.489261845
CD45- BM-MSCs_1	3.69E-11	1.274037866
CD45- BM-MSCs_4	0.175479663	0.898346627
CD45+ BM-MSCs_3	8.77E-05	0.765464953
CD45+ BM-MSCs_5	1.89E-48	0.249892213
CD45+ BM-MSCs_6	0.52377383	1.073767195
CD45- BM-MSCs_5	1.76E-21	0.309302402

Accordingly, we performed differential analysis using the FindAllMarkers function with logfc = 0.5, Minpct = 0.5, and adjPval < 0.05. The top 5 differential genes of 12 cell subpopulations in the heat map plot are illustrated in Figure 1(d). The distribution of 12 cell subpopulations in two samples is shown in Figure 1(e). KEGG analysis indicated that 35 pathways were significantly enriched on 12 cell subpopulations, and many of them were related to tumorigenesis (Figure 1(f)).

3.2. Identification of Hub Genes. Fisher test was adopted to analyze the distribution variation of 12 cell subpopulations between osteoporosis and osteoarthritis, as the cutoff of FC>4 or FC<0.25 and $p < 0.05$, and subpopulations of CD45- BM-MSCs_6 and CD45+ BM-MSCs_5 were selected as vital for next analysis (Table 1).

Next, limma package was used to identified differentially expressed gene between osteoporosis and no-osteoporosis; as a result, 191 downregulated genes and 1,717 upregulated genes were screened (Figures 2(a) and 2(b)). Venn analysis between 1,908 differentially expressed gene and 135 genes, which from chEMBL, showed that only 17 genes were targets for the treatment of osteoporosis (Figure 2(c)).

Based on the above marker genes of subpopulations, ssGSEA analysis was used to calculate score of the two hub subpopulations, and variance analysis of subpopulations score between osteoporosis and no-osteoporosis indicated that CD45+ BM-MSCs_5 subpopulation had significant difference (Figures 2(d) and 2(e)). The correlation analysis of the 17 genes with the two hub subpopulations score demonstrated that 7 genes (HSD17B2, ACHE, CCR4, F9, ADRA1D, MC5R, and GRM2) were negatively correlated with CD45+ BM-MSCs_5 subpopulation (Figure 2(f)).

3.3. Construction of Diagnostic Model Base on 7 Genes. The diagnostic models were separately constructed for these 7 genes. The results showed that the AUC values calculated by these 7 genes alone were not well (Figure 3). Due to the poor diagnosis of single genes, rms was used to construct diagnostic model based on 7 genes, and the AUC values in GSE35959 dataset, GSE7158 dataset, GSE13850 dataset, and GSE7429 dataset, were, respectively, 1, 0.762, 0.798, and 0.91 (Figure 4), which are better than the AUC values of singles genes. This data indicated that the combination of these 7 genes is of great significance in diagnosing osteoporosis patients.

3.4. Analysis of Hub Genes and Immune. First, stromal score, immune score, and ESTIMATE score were calculated by ESTIMATE, and the results showed that three genes (CCR4, F9, and GRM2) were positively correlated with the immune score (Figure 5(a)). Then, 28 characteristic genes of immune cells obtained from previous study were used to calculate the score of immune cells by ssGSEA method. Pearson correlation analysis showed that CCR4, F9, and

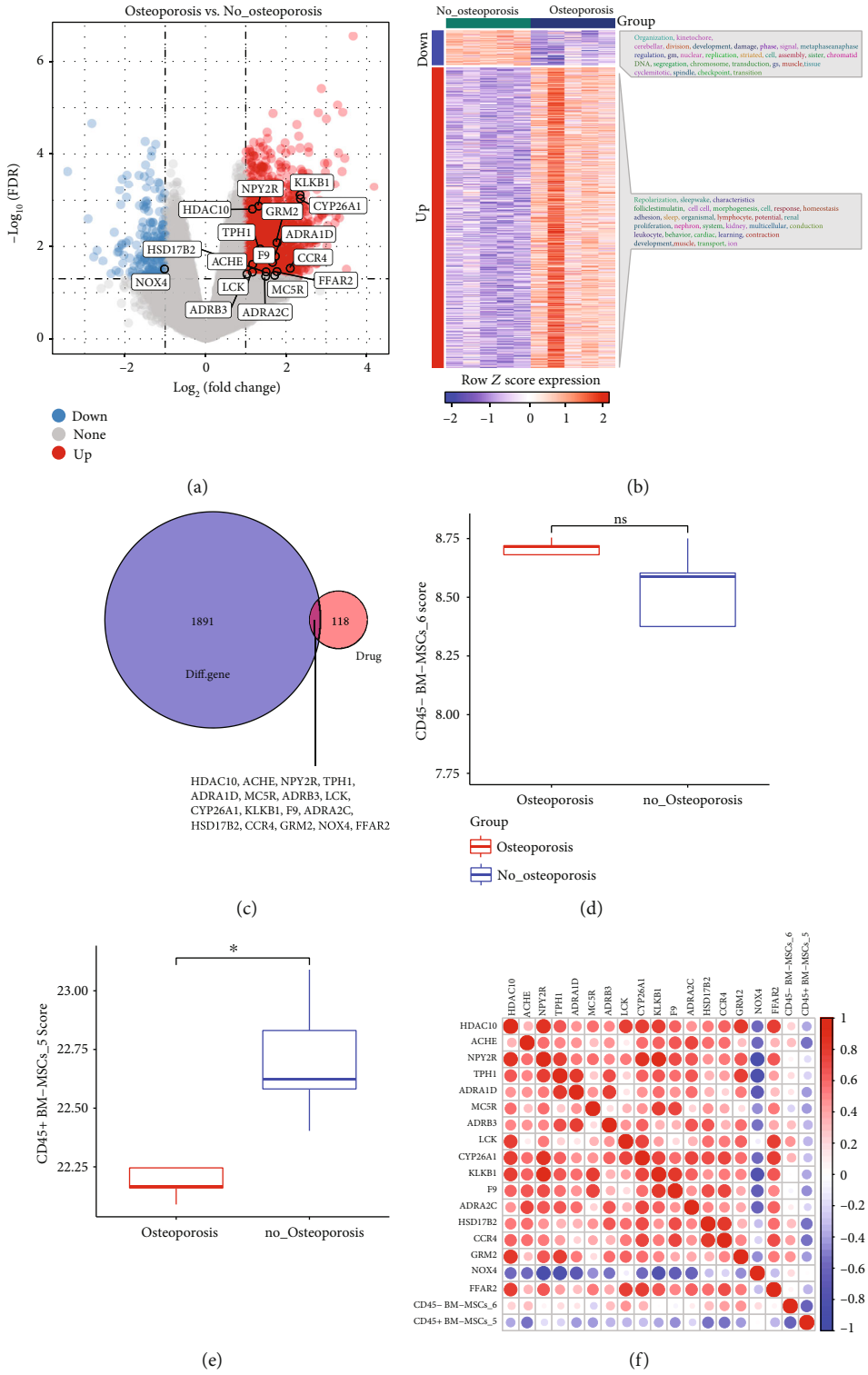

Figure 2: Identification of hub genes. (a) Volcano plot of differentially expressed genes between osteoporosis and nonosteoporosis. (b) Heatmap of differentially expressed genes between osteoporosis and nonosteoporosis. (c) Venn of differentially expressed genes and target genes for osteoporosis drugs. (d) CD45-BM-MSCs score differences analysis between osteoporosis and nonosteoporosis. (e) CD45 +BM-MSCs score differences analysis between osteoporosis and nonosteoporosis. (f) The correlation analysis between 17 hub genes and CD45-BM-MSCs subpopulation or CD45+BM-MSCs subpopulation.

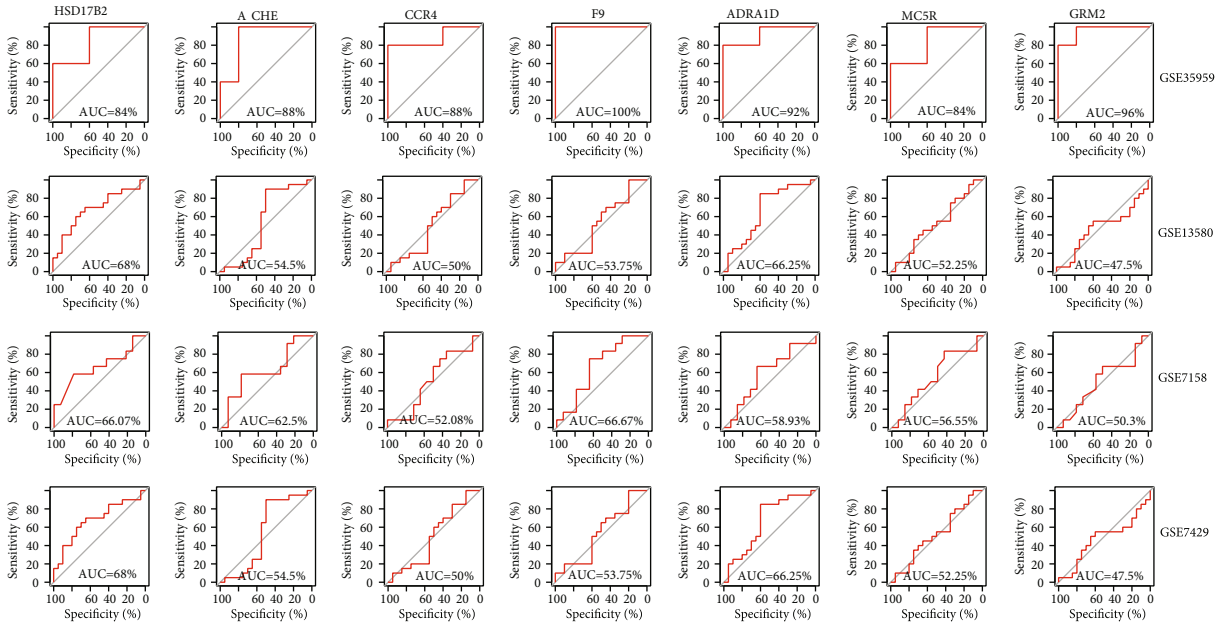

Figure 3: Individual ROC curves for 7 genes in GSE35959, GSE13580, GSE7158, and GSE7429 dataset.

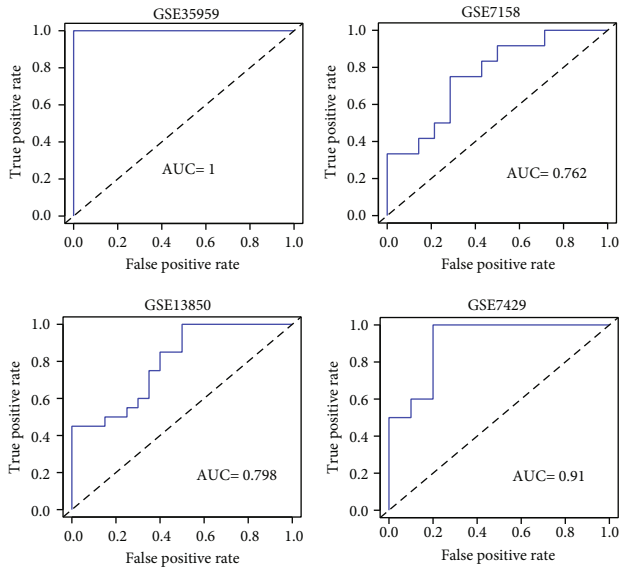

Figure 4: Construction of 7 key gene diagnostic models.

GRM2 were significantly associated with some immune cells (Figure 5(b)). Enrichment analysis was conducted by GSVA package, and the correlation between three genes and pathways was calculated by Pearson's method. The results indicated that these three genes were correlated with multiple pathways (Figure 5(c)).

3.5. Prediction of Therapeutic Drugs. Since the area under the curve (AUC) values of F9 gene were higher than those of the other two genes in multiple data sets, we believed that the role of F9 gene in osteoporosis patients has more potential to be studied. The RCORR function of Hmisc package was used for correlation analysis of osteoporosis patients in GSE35959 data set, and a total of 1377 genes were highly significantly correlated with F9 gene. The distance density plot of drug to F9-related gene set is shown in Figure 6.

Molecular docking was conducted to verify whether the top 5 compounds closest to F9 gene set (Table 2) had significant regulatory effects on F9 protein. The results showed that all the key compounds in the network, especially DB03742, had strong affinity for F9 protein (-8.2 kcal/mol) (Figure 7(a)). In addition, DB03742 could form a stable complex with F9 by hydrogen bonding with SER190 of F9 protein and hydrophobic interaction with ALA95, LYS98, TYR99, CYS191, and TRP215 (Figures 7(b) and 7(c)).

Molecular dynamics simulations at 100 ns showed that the F9 protein concept was stable (Figures 7(d) and 7(f)). In addition, the RMSF value of compound DB03742 was basically stable at about 3 Å (Figure 7(e)). In general, compound DB03742 binds to the active site of F9 protein relatively stable, suggesting that compound DB03742 has a high potential as an inhibitor of F9 protein.

4. Discussion

ScRNA-seq is a highly useful tool in transcriptional classification of various disease cell types [33–36]. Herein, osteoporosis scRNA-seq data from GEO database was collected to distinguish cell subpopulations, and here, we determined 12 subgroups, among which 6 cell subpopulations belong to CD45-BM-MSCs. In a large set of samples, specifically expressed gene markers could be utilized as specific markers in cell subgroup identification. Furthermore, 7 key genes associated with osteoporosis treatment drugs were screened and found to be negatively correlated with CD45+ BM-MSCs_5 subgroup score, and they showed excellent diagnosis efficiency, especially F9 gene.

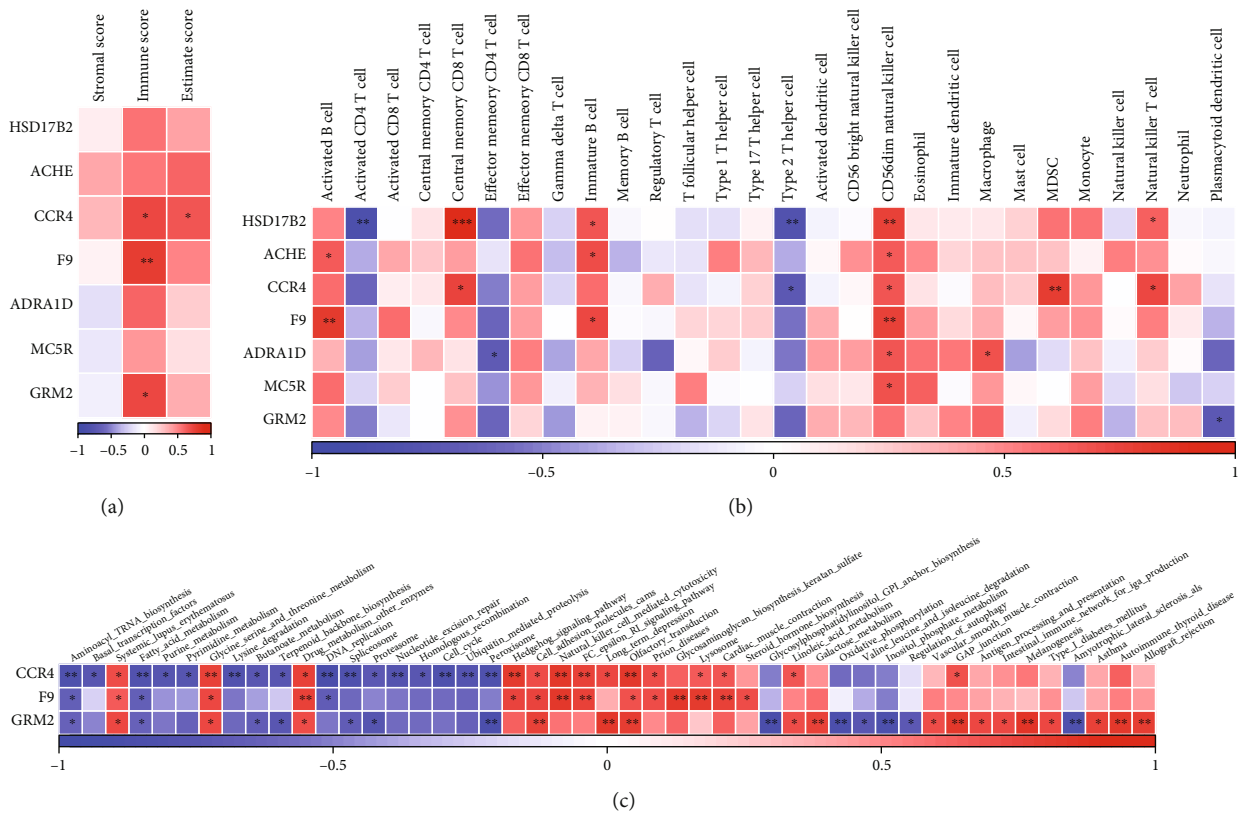

Figure 5: The correlation analysis between hub genes and immune. (a) The correlation analysis between 7 hub genes and immune scores. (b) The correlation analysis between 7 hub genes and 28 immune cells scores. (c) Heatmaps of potentially regulated pathways of 3 genes associated with immune.

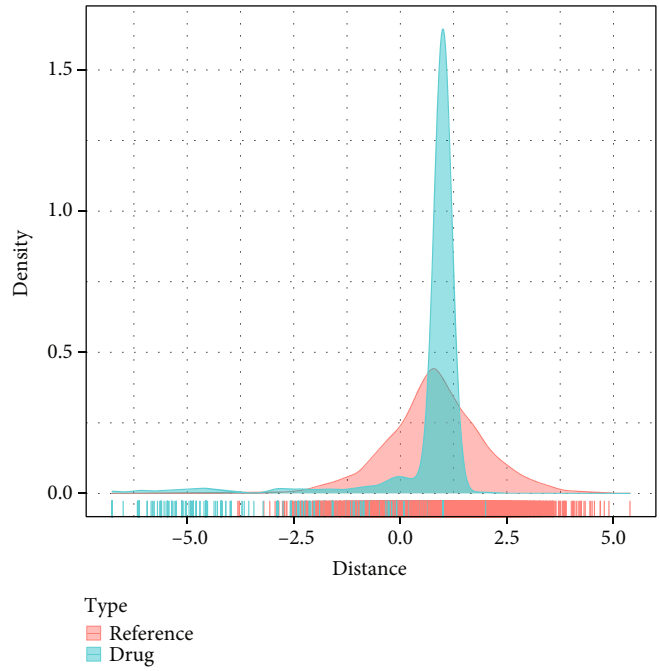

Figure 6: Distance density scaling diagram of drug to F9-related gene sets.

Table 2: Molecular docking of drugs to F9 protein.

Compound	Autodock Vina score	H-bond interactions	Hydrophobic interactions
DB00269	-6.4	LYS98, SER195	TYR99
DB00947	-7.7	LYS98, SER190	LYS98, TYR99, SER190, CYS191, SER214, TRP215, CYS220
DB01357	-7.3	SER190	SER190, CYS191, TRP215, CYS220
DB02715	-8.0	SER190	TYR99, CYS191, TRP215,
DB03742	-8.2	SER190	ALA95, LYS98, TYR99, CYS191, TRP215

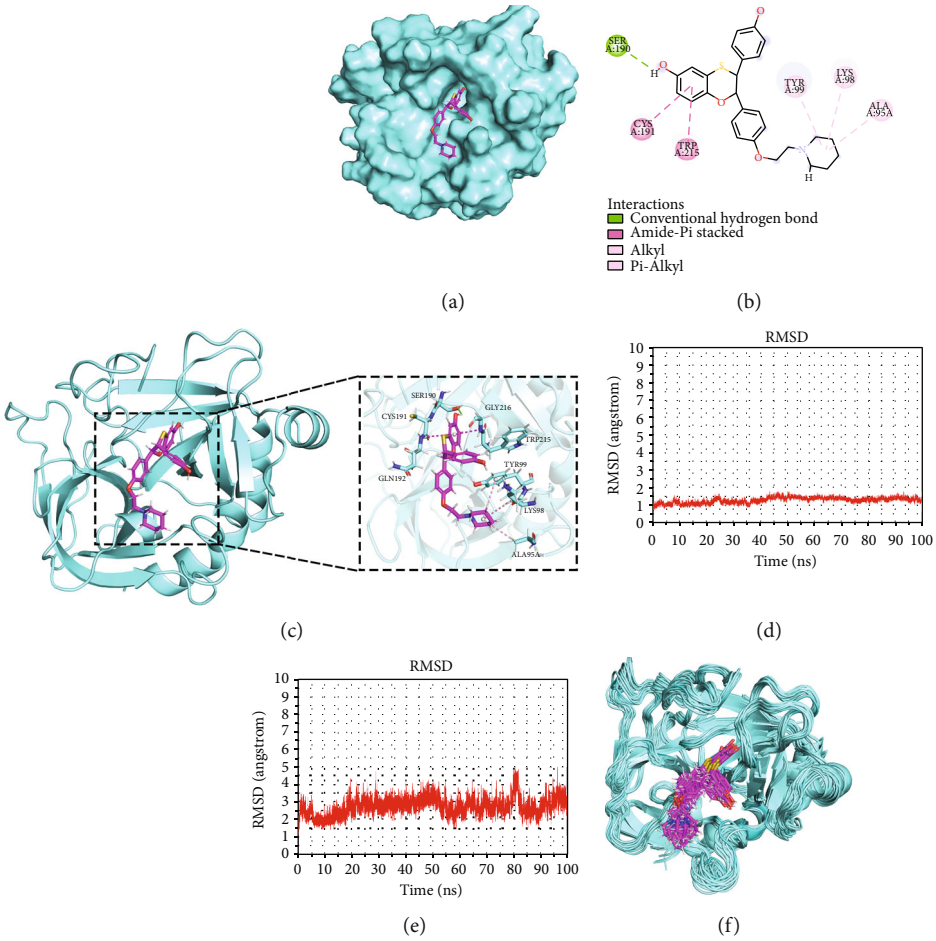

Figure 7: Molecular docking and dynamics simulation. (a) Surface binding of compound DB03742 to F9 protein. (b) 2D diagram of interaction between compound DB03742 and F9 protein. (c) 3D diagram of interaction between compound DB03742 and F9 protein. (d) RMSD of F9 protein skeleton during 100 ns molecular dynamics simulation. (e) RMSF of F9 protein skeleton during 100 ns molecular dynamics simulation. (f) Binding diagram of compound DB03742 to F9 protein during 100 ns molecular dynamics simulation.

Through network pharmacology, we found that DB03742 is highly bound to F9 protein, which is a potential F9 protein inhibitor, and speculated that DB03742 may be effective in the treatment of osteoporosis. In previous research, Liang et al. reported the heterogeneity of tumor immune cells analyzed by scRNA-seq, and a risk model was constructed to predict the survival of ovarian cancer samples [37]. Juan Lu *et al.* analyzed the heterogeneity of the TIME at the single-cell level and determined a 3-gene model that could accurately evaluate the survival outcome and immunotherapy response of HCC samples [38]. This work was the first to identify the heterogeneity of osteoporosis at the single-cell level and to identify key genes and therapeutics for the diagnosis of osteoporosis.

Here, we performed differential analysis on gene expression data from the GSE35959 database. 7 genes were vital for diagnosis of osteoporosis, among which 17β-hydroxysteroid dehydrogenase type 2 (17β-HSD2) is an enzyme that catalyzes the conversion of estradiol (E2) and testosterone (T) to estrone (E1) and androstenedione, respectively. Blockade of 17β-HSD2 increases intracellular E2 and T, inhibits further bone resorption by osteoclasts, and stimulates osteoblast osteogenesis by estrogen and androgen receptor stimulation, respectively [39, 40]. A minor reduction in

Th2 cells was detected from the mice with CCR4 knock-out in parallel with major Treg migration impairment. Study showed that such a phenomenon was related to higher pro-inflammatory and osteoclastogenic cytokine levels and increased inflammatory bone loss [41]. At present, most genes have not been reported to play a role in osteoporosis. Moreover, the prediction performance of 7 genes model was not very good, probably because of the sample size. These results suggested that these genes may play an important role in the development of osteoporosis and provided evidences for further research.

In this work, we analyzed the gene expression profile of the scRNA-seq data, the results of which improved our understanding of the heterogeneity of osteoporosis at the single-cell level and provided a 7-gene-based diagnostic model and therapeutic agent. However, there are some limitations to this study. First, the sample size was relatively small. Secondly, functional experiments and potential molecular mechanisms of these 7 genes need to be studied.

By the analysis of scRNA-seq, we analyzed the heterogeneity of osteoporosis at the single-cell level and determined a 7-gene diagnostic model that could accurately diagnostic patients with osteoporosis.

Data Availability

The datasets analyzed in this study could be found in GSE35959 at [https://www.ncbi.nlm.nih.gov/geo/query/acc.cgi?acc=GSE35959], GSE7158 dataset at [https://www.ncbi.nlm.nih.gov/geo/query/acc.cgi?acc=GSE7158], GSE13850 dataset at [https://www.ncbi.nlm.nih.gov/geo/query/acc.cgi?acc=GSE13850], and GSE7429 dataset at [https://www.ncbi.nlm.nih.gov/geo/query/acc.cgi?acc=GSE7429].

Conflicts of Interest

The authors declare that they have no interest.

Supplementary Materials

Figure S1. Clustering and dimension reduction analysis of single cell data. A: Correlation analysis of UMI and number of mRNA, Mitochondrial gene. B: MRNA/UMI/mitochondrial content/rRNA content of samples before filtration. C: MRNA/UMI/mitochondrial content/rRNA content of samples after filtration. D: The sample distribution of PCA dimension reduction and the anchor point diagram of PCA. E: CD45 expression of 12 subpopulations. *(Supplementary Materials)*

References

[1] P. D. Delmas, "Treatment of postmenopausal osteoporosis," *Lancet*, vol. 359, no. 9322, pp. 2018–2026, 2002.

[2] R. M. Neer, C. D. Arnaud, J. R. Zanchetta et al., "Effect of parathyroid hormone (1-34) on fractures and bone mineral density in postmenopausal women with osteoporosis," *The New England Journal of Medicine*, vol. 344, no. 19, pp. 1434–1441, 2001.

[3] K. E. Ensrud and C. J. Crandall, "Osteoporosis," *Annals of Internal Medicine*, vol. 167, no. 3, pp. Itc17–itc32, 2017.

[4] J. Blake, F. A. Cosman, E. M. Lewiecki, M. R. McClung, J. Pinkerton, and M. Shapiro, "Management of osteoporosis in postmenopausal women: the 2021 position statement of the North American Menopause Society," *Menopause*, vol. 28, no. 9, pp. 973–997, 2021.

[5] J. R. Center, T. V. Nguyen, D. Schneider, P. N. Sambrook, and J. A. Eisman, "Mortality after all major types of osteoporotic fracture in men and women: an observational study," *Lancet*, vol. 353, no. 9156, pp. 878–882, 1999.

[6] A. M. Tsimberidou, E. Fountzilas, M. Nikanjam, and R. Kurzrock, "Review of precision cancer medicine: evolution of the treatment paradigm," *Cancer Treatment Reviews*, vol. 86, p. 102019, 2020.

[7] S. Morganti, P. Tarantino, E. Ferraro, P. D'Amico, B. A. Duso, and G. Curigliano, "Next generation sequencing (NGS): a revolutionary technology in pharmacogenomics and personalized medicine in cancer," *Advances in Experimental Medicine and Biology*, vol. 1168, pp. 9–30, 2019.

[8] Y. Zhong, F. Xu, J. Wu, J. Schubert, and M. M. Li, "Application of next generation sequencing in laboratory medicine," *Annals of Laboratory Medicine*, vol. 41, no. 1, pp. 25–43, 2021.

[9] L. Zhang, X. Yu, L. Zheng et al., "Lineage tracking reveals dynamic relationships of T cells in colorectal cancer," *Nature*, vol. 564, no. 7735, pp. 268–272, 2018.

[10] S. Bian, Y. Hou, X. Zhou et al., "Single-cell multiomics sequencing and analyses of human colorectal cancer," *Science*, vol. 362, no. 6418, pp. 1060–1063, 2018.

[11] A. K. Casasent, A. Schalck, R. Gao et al., "Multiclonal invasion in breast tumors identified by topographic single cell sequencing," *Cell*, vol. 172, no. 1-2, pp. 205–17.e12, 2018.

[12] E. Azizi, A. J. Carr, G. Plitas et al., "Single-cell map of diverse immune phenotypes in the breast tumor microenvironment," *Cell*, vol. 174, no. 5, pp. 1293–308.e36, 2018.

[13] J. Wagner, M. A. Rapsomaniki, S. Chevrier et al., "A single-cell atlas of the tumor and immune ecosystem of human breast cancer," *Cell*, vol. 177, no. 5, pp. 1330–45.e18, 2019.

[14] W. Chung, H. H. Eum, H. O. Lee et al., "Single-cell RNA-seq enables comprehensive tumour and immune cell profiling in primary breast cancer," *Nature Communications*, vol. 8, no. 1, p. 15081, 2017.

[15] Z. Wang, X. Li, J. Yang et al., "Single-cell RNA sequencing deconvolutes the in vivo heterogeneity of human bone marrow-derived mesenchymal stem cells," *International Journal of Biological Sciences*, vol. 17, no. 15, pp. 4192–4206, 2021.

[16] S. Kim, J. Chen, T. Cheng et al., "PubChem in 2021: new data content and improved web interfaces," *Nucleic Acids Research*, vol. 49, no. D1, pp. D1388–D1395, 2021.

[17] S. Bühlmann and J. L. Reymond, "ChEMBL-likeness score and database GDBChEMBL," *Frontiers in Chemistry*, vol. 8, p. 46, 2020.

[18] Y. Zhai, G. Li, R. Li et al., "Single-cell RNA-sequencing shift in the interaction pattern between glioma stem cells and immune cells during tumorigenesis," *Frontiers in Immunology*, vol. 11, p. 581209, 2020.

[19] A. Rodriguez and A. Laio, "Machine learning. Clustering by fast search and find of density peaks," *Science*, vol. 344, no. 6191, pp. 1492–1496, 2014.

[20] G. Yu, L. G. Wang, Y. Han, and Q. Y. He, "clusterProfiler: an R package for comparing biological themes among gene clusters," *OMICS*, vol. 16, no. 5, pp. 284–287, 2012.

[21] Y. Chen, L. Zou, J. Lu, M. Hu, Z. Yang, and C. Sun, "Identification and validation of novel gene markers of osteoporosis by weighted co expression analysis," *Annals of Translational Medicine*, vol. 10, no. 4, p. 210, 2022.

[22] M. E. Ritchie, B. Phipson, D. Wu et al., "Limma powers differential expression analyses for RNA-sequencing and microarray studies," *Nucleic Acids Research*, vol. 43, no. 7, article e47, 2015.

[23] X. Zhang, S. Wang, E. R. Rudzinski et al., "Deep learning of rhabdomyosarcoma pathology images for classification and survival outcome prediction," *The American Journal of Pathology*, vol. 192, no. 6, pp. 917–925, 2022.

[24] P. Yang, W. Chen, H. Xu et al., "Correlation of CCL8 expression with immune cell infiltration of skin cutaneous melanoma: potential as a prognostic indicator and therapeutic pathway," *Cancer Cell International*, vol. 21, no. 1, p. 635, 2021.

[25] B. Xiao, L. Liu, A. Li et al., "Identification and verification of immune-related gene prognostic signature based on ssGSEA for osteosarcoma," *Frontiers in Oncology*, vol. 10, article 607622, 2020.

[26] P. Charoentong, F. Finotello, M. Angelova et al., "Pan-cancer immunogenomic analyses reveal genotype-immunophenotype relationships and predictors of response to checkpoint blockade," *Cell Reports*, vol. 18, no. 1, pp. 248–262, 2017.

[27] O. Trott and A. J. Olson, "AutoDock Vina: improving the speed and accuracy of docking with a new scoring function, efficient optimization, and multithreading," *Journal of Computational Chemistry*, vol. 31, no. 2, pp. 455–461, 2010.

[28] D. D. Mukherjee, N. M. Kumar, M. P. Tantak et al., "NMK-BH2, a novel microtubule-depolymerising bis (indolyl)-hydrazide-hydrazone, induces apoptotic and autophagic cell death in cervical cancer cells by binding to tubulin at colchicine - site," *Biochimica et Biophysica Acta, Molecular Cell Research*, vol. 1867, no. 10, p. 118762, 2020.

[29] H. M. Berman, J. Westbrook, Z. Feng et al., "The protein data bank," *Nucleic Acids Research*, vol. 28, no. 1, pp. 235–242, 2000.

[30] A. Kerstjens and H. De Winter, "LEADD: Lamarckian evolutionary algorithm for de novo drug design," *Journal of Cheminformatics*, vol. 14, no. 1, p. 3, 2022.

[31] B. H. M. Mooers and M. E. Brown, "Templates for writing PyMOL scripts," *Protein Science*, vol. 30, no. 1, pp. 262–269, 2021.

[32] H. Rakhshani, E. Dehghanian, and A. Rahati, "Enhanced GROMACS: toward a better numerical simulation framework," *Journal of Molecular Modeling*, vol. 25, no. 12, p. 355, 2019.

[33] M. G. Filbin, I. Tirosh, V. Hovestadt et al., "Developmental and oncogenic programs in H3K27M gliomas dissected by single-cell RNA-seq," *Science*, vol. 360, no. 6386, pp. 331–335, 2018.

[34] N. E. Navin, "The first five years of single-cell cancer genomics and beyond," *Genome Research*, vol. 25, no. 10, pp. 1499–1507, 2015.

[35] A. Tanay and A. Regev, "Scaling single-cell genomics from phenomenology to mechanism," *Nature*, vol. 541, no. 7637, pp. 331–338, 2017.

[36] M. D. Young, T. J. Mitchell, F. A. Vieira Braga et al., "Single-cell transcriptomes from human kidneys reveal the cellular identity of renal tumors," *Science*, vol. 361, no. 6402, pp. 594–599, 2018.

[37] L. Liang, J. Yu, J. Li et al., "Integration of scRNA-Seq and bulk RNA-Seq to analyse the heterogeneity of ovarian cancer immune cells and establish a molecular risk model," *Frontiers in Oncology*, vol. 11, article 711020, 2021.

[38] J. Lu, Y. Chen, X. Zhang, J. Guo, K. Xu, and L. Li, "A novel prognostic model based on single-cell RNA sequencing data for hepatocellular carcinoma," *Cancer Cell International*, vol. 22, no. 1, p. 38, 2022.

[39] L. Wu, M. Einstein, W. M. Geissler, H. K. Chan, K. O. Elliston, and S. Andersson, "Expression cloning and characterization of human 17 beta-hydroxysteroid dehydrogenase type 2, a microsomal enzyme possessing 20 alpha-hydroxysteroid dehydrogenase activity," *The Journal of Biological Chemistry*, vol. 268, no. 17, pp. 12964–12969, 1993.

[40] M. L. Lu, Y. W. Huang, and S. X. Lin, "Purification, reconstitution, and steady-state kinetics of the trans-membrane 17 beta-hydroxysteroid dehydrogenase 2," *The Journal of Biological Chemistry*, vol. 277, no. 25, pp. 22123–22130, 2002.

[41] A. C. Araujo-Pires, A. E. Vieira, C. F. Francisconi et al., "IL-4/CCL22/CCR4 axis controls regulatory T-cell migration that suppresses inflammatory bone loss in murine experimental periodontitis," *Journal of Bone and Mineral Research*, vol. 30, no. 3, pp. 412–422, 2015.

Hindawi
Mediators of Inflammation
Volume 2022, Article ID 2689918, 9 pages
https://doi.org/10.1155/2022/2689918

Research Article

Connexin 37 Regulates the Kv1.3 Pathway and Promotes the Development of Atherosclerosis

Minqi Liao, Lihua Chen, Jiongbin Lu, Guangzhu Liang, Yongzhao Yao, Shumin Ouyang, Yanhua Yang, Zhengwei Jian, and Suxia Guo

Department of Cardiology, Affiliated Dongguan Hospital, Southern Medical University, 523000, China

Correspondence should be addressed to Suxia Guo; guo7771812@163.com

Received 9 July 2022; Accepted 6 August 2022; Published 23 September 2022

Academic Editor: Md Sayed Ali Sheikh

Objective. To investigate the mechanism of Connexin 37 (Cx37) and Kv1.3 pathways in atherosclerosis (AS). *Methods*. ApoE$^{-/-}$ mice were given a high-fat diet to establish atherosclerosis (AS) model, and macrophages in mice were isolated and extracted to transfect Cx37 vectors with silencing or overexpressing, and Kv1.3 pathway blockers were used to inhibit the pathway activity. The indexes of body weight, blood glucose, and blood lipid of mice were collected. The protein and mRNA expression levels of Cx37 and Kv1.3 were detected by reverse transcription-PCR (RT-PCR), Western blot, and immunofluorescence technique. Oil red O staining was used to observe plaque area. Masson staining was used to detect collagen content. The concentrations of chemokine CCL7 were quantified using the ELISA kits. CCK8 was used to detect cell proliferation. *Results*. Cx37 and Kv1.3 were highly expressed in macrophages of AS mice, and the expression of Kv1.3 and CCL7 decreased after Cx37 was silenced, and the proliferation of macrophages was also decreased. Wild-type mice and AS model mice were treated with Cx37 overexpression vectors and Kv1.3 pathway blocking, and it was found that Cx37 overexpression could improve the blood lipid and blood glucose levels and increase the area of AS in AS mice. However, blocking the activity of Kv1.3 pathway can reduce the levels of blood lipid and blood glucose, increase the body weight of mice, and reduce the area of AS mice. Blocking the activity of Kv1.3 pathway can slow down the plaque development of AS mice and make its indexes close to wild-type mice. And the use of Kv1.3 pathway blockers on the basis of overexpression of Cx37 indicated that inhibition of Kv1.3 pathway activity did not affect the expression of Cx37, but could inhibit the collagen content in the plaque area of AS mice, inhibit the expression of chemokine CCL7, and reverse the effect of Cx37 overexpression. *Conclusion*. Cx37 can improve the activity of macrophages by regulating the expression of chemokines and the activity of Kv1.3 pathway in AS mice, and enrich macrophages in inflammatory tissues and expand the area of plaque formation.

1. Background

Atherosclerosis (AS) is a chronic inflammatory disease characterized by immune activity, which is prone to plaque rupture and thrombosis, causing a series of cardiovascular events and seriously harming human health [1]. Anticoagulant, antiplatelet, control of blood pressure, blood lipid and blood sugar are the main methods to prevent and treat atherosclerosis. [2]. The use of the above-mentioned treatments can significantly reduce the occurrence of cardiovascular events, but atherosclerosis is still the primary cause of coronary heart disease and stroke, it accounting for half of the death causes in western countries [3]. It is still a great challenge for cardiovascular therapy to clarify its mechanism and seek more effective treatment measures.

The unstable development of atherosclerotic plaque forms vulnerable plaque, and then, the rupture of vulnerable plaque leads to platelet aggregation and thrombosis, and the infiltration of a large number of inflammatory cells inside plaque is the main cause of plaque rupture, resulting in myocardial ischemia and infarction [4, 5]. With the further study of vulnerable plaques, we found that mononuclear/macrophages are one of the main inflammatory cells in plaque, which not only exist inside of the plaque but also infiltrate the vascular bed outside the artery in large numbers [6]. Under the stimulation of

ox LDL, monocyte-derived macrophages are activated to aggregate, adhere, and migrate to vascular walls through endothelial cells and secrete cytokines, chemokines, metalloproteinases, and other proteolytic enzymes to accelerate the activation of inflammatory responses. At the same time, as the inflammatory response worsens, macrophages continue to activate and trigger further inflammatory response, which amplifies the inflammatory response [7]. Therefore, macrophage activation plays an important role in the pathogenesis of emergency of geriatric cardiology.

Connexin 37 (Cx37) is an important protein that mediates inflammatory response which is mainly expressed in vascular endothelial cells. Cx37 expression can also be detected on the surface of foam cells and smooth muscle cells in atherosclerotic plaques [8]. Recent studies have shown that Cx37 is also expressed on the surface of free mononuclear/macrophages in blood. Previous studies have found that Cx37 gene expression is strongly correlated with the incidence of coronary heart disease [9]. In order to further clarify the role of Cx37 in AS, the researchers selected miniature pigs with AS plaque properties highly similar to those of humans for in vivo experiments and found that interference of Cx37 gene expression with siRNA Cx37 transfection resulted in the reduction of AS plaque volume and thickening of fibrous cap, reversing the formation of unstable plaques [10]. These results suggest that Cx37 may play an important role in the development of AS vulnerable plaques, and inhibition of its expression can reverse vulnerable plaques. In the follow-up study, the researcher further observed the effect of siRNA Cx37 transfection on the fractional fow reserve (FFR) of porcine myocardium, and the results showed that after Cx37 siRNA interference, FFR was significantly improved [11], suggesting that inhibition of Cx37 expression can inhibit the progression of AS and improve overall cardiac function. Therefore, the correlation between Cx37 and AS has been confirmed from clinical disease genetics detection and animal experiments, and Cx37 is expected to become a potential target to curb the occurrence and development of AS.

In recent years, great progress has been made in the study of potassium ion channels in macrophages, and it has been found that the potassium ion channels on the surface of macrophages have an extremely important relationship with cell activation. The opening of voltage-dependent potassium channels causes hyperactivation of the cell membrane, promotes Ca^{2+} influx, and indirectly regulates cell proliferation and cytokine secretion [12]. Meanwhile, Kv channel plays a key role in regulating cell volume, electrolyte transport, cell excitation and contraction, enzyme activation, and other life activities [13]. After the activation of macrophages, the potassium channel kv1.3 on the membrane of macrophages affects the activation and function of macrophages by regulating the membrane potential pathway. Activation of macrophages runs throughout atherosclerosis [14–16]. Therefore, there are many studies on affect the activity of macrophages by blocking the Kvl.3 potassium channel.

Therefore, based on the results of previous studies, we hypothesized that Cx37 may regulate the development of AS by regulating the kv1.3 channel. In this study, $ApoE^{-/-}$ mice were used to establish AS model, change the expression of Cx37, and explore the role of Cx37 and KVL.3 channels in AS mice.

2. Materials and Methods

2.1. Construction of Cx37 Expression Vector. The target DNA fragments were collected, and the Cx37 silenced expression vector (shRNA-1/2/3) was constructed using pLVX-shRNA2-PURO vector plasmid (Hunan Fenghui Biotechnology Co., Ltd.). Meanwhile, the Cx37 overexpression vector (pre-CX37) was constructed using rAAV2/8 vector (Brain Case Biotechnology Co., Ltd., Shenzhen). The silenced expression vector was transfected into 293T cells, and the stably transfected cell lines were constructed by subculture. Subsequently, the protein was extracted, and Western blot was performed to detect the expression efficiency of Cx37. The sequence of Cx37 silenced expression vector is as follows: mCx37-1 sequence: 5′-GCCATCCAAGG ACCTACATGT-3′; mCx37-2 sequence: 5′-GCTCATGGG TACCTATGTGGT-3′; mCx37-3 sequence: 5′-GCTCTC ATCCACTGAGCAGAA-3′.

2.2. Experimental Animal. Eight-week-old $ApoE^{-/-}$ mice were purchased from Beijing Weitong Lihua Company, and C57BL/6 wild-type mice were purchased from Experimental Animal Center of Southern Medical University. All laboratory animals were approved by the Laboratory Animal Ethics Committee of Dongguan People's Hospital and in accordance with the guidelines of the National Institutes of Health for the care and use of laboratory animals.

Before the experiment, all animals were fed standard diet with ambient temperature of 20-25°C, humidity of 30-70%, and light/dark for 12 h each. Before administration, all C57BL/6 mice were given a normal diet for 4 weeks, and all $ApoE^{-/-}$ mice were given a high-fat diet for 4 weeks to establish AS model. From week 4, C57BL/6 wild-type mice were fed a normal diet and given an intraperitoneal injection of equal volume of normal saline. $ApoE^{-/-}$ control mice were given high-fat diet and given an intraperitoneal injection of equal volume of normal saline. $ApoE^{-/-}$ mice in pre-CX37 group were given high-fat diet and tail vein injection of Cx37 overexpression vector (pre-CX37) solution. $ApoE^{-/-}$ mice in ShK(L5) group were given high-fat diet and subcutaneous injection of Kv1.3 blocker ShK(L5). During the feeding period, the changes of body weight, blood lipid, and blood glucose of mice in each group were recorded. After 8 weeks of drug feeding, mice in each group were anesthetized and sacrificed, and blood samples and aorta samples of mice were quickly separated and preserved. Experimental operation is shown in Figure 1.

2.3. Handling of Experimental Specimens. The mice were sacrificed after blood collection, and aorta was immediately separated. Vascular rings about 0.5 cm long were cut from thoracic aorta, fixed with 4% paraformaldehyde, embedded with paraffin, and finally sected. 50~100 mg of other aortic tissues were selected and frozen in liquid nitrogen. Mouse

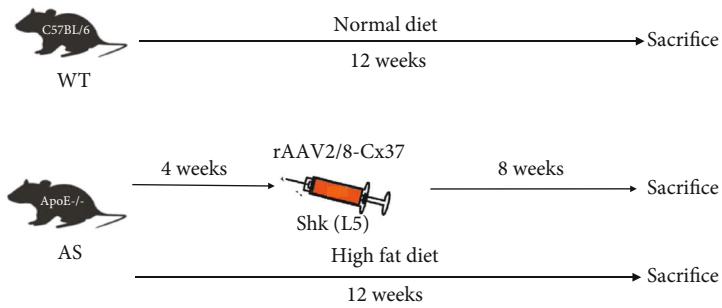

Figure 1: Experimental mouse operation flowchart.

Table 1: Primer sequences of RT-PCR.

Gene	Gene ID	Primer sequence (5′-3′)		DALP (bp)
M-actb	NM_007393.5	Forward:	GAGGTATCCTGACCCTGAAGTA	104
		Reverse:	CACACGCAGCTCATTGTAGA	
M-Cx37	NM_008120.3	Forward:	CACTGGCTGCTTACCAGAAT	87
		Reverse:	CGAGGGTTCACAGAACACTTAG	
M-Kv1.3	NM_008418.2	Forward:	GTGACCATAGGAGGCAAGATT	111
		Reverse:	CCGGTGGTAGAAGTAGTTGAAG	

arterial blood was collected, and monocytes were isolated from mouse peripheral blood by density gradient centrifugation and wall adhesion method [17]. The isolated monocytes were cultured in complete medium and differentiated into macrophages after 5 days of culture.

2.4. Western Blot. Cells were collected, and total protein was extracted. BCA solution (FUDE Biology, Hangzhou) was prepared to detect protein concentration of the samples to be tested. The prepared protein samples were taken out, dissolved on the ice box, and then, added into the electrophoresis tank for 40 min. The PVDF membrane of corresponding size was cut, and the separation glue was closely attached to the PVDF membrane, and the protein was transferred to the PVDF membrane in Bio-Rad Trans-Blot. After membrane transfer, remove PVDF membrane, wash it for 3 times, and add an appropriate amount of 5% skim milk powder for 1 h. The membrane was washed with TBS-T for 3 times, and the corresponding strip was added into the primary antibody solution and incubated overnight at 4°C. The next day, the strips were washed with TBS-T for 3 times and then added with corresponding secondary antibodies and incubated at 4°C for 4 h. ECL luminescent solution (Omiget Pharmaceutical Technology Co., Ltd., Beijing) was prepared and uniformly dropped on PVDF membrane, and the reaction was carried out in the darkroom for several seconds. The cut film is completely covered on PVDF membrane, exposed for 5-10 seconds, then put into the prepared developer, using IPP6.0 software for gray value analysis of the film.

2.5. Reverse Transcription-PCR. Total RNA of macrophages was extracted with TRIzol reagent (Tiangen Company, Beijing), and cDNA was synthesized by reverse transcription using PrimeScript RT Reagent Kit (TAKARA Company). RT-PCR was then performed using SYBR Premix Ex Taq Kit (TAKARA Company). The primers used are shown in Table 1.

2.6. Oil Red O Staining. First, 0.5% oil red O stock solution (Sigma) was prepared, diluted with distilled water (dilution ratio 3 : 2), and stood at room temperature for 10 min. The blood vessel tissue were fixed in 10% neutral formaldehyde solution for 30 min, then removed and bathed in water for 15 min. Tissue samples were added to oil red O solution and stained for 1~2 h. The tissue samples were rinsed with 70% ethanol until the patches were red and the background was white. Finally, the specimen was washed with distilled water, and the staining was observed using a microscope (Shanghai Caikon Optical Instrument Co., Ltd.).

2.7. Masson Staining. Paraffin sections of aortic tissue were taken for dewaxing and hydration. Then, the slices were stained with hematoxylin solution for 5-10 min. The sections were then rinsed with running water and stained in ponceau acid fuchsin for 5-10 min. Sections were rinsed again and treated with 1% phosphomolybdic acid aqueous solution for 5 minutes, followed by aniline blue for 5 minutes. Finally, the tissue sections were treated with 1% glacial acetic acid for 1 minute, dehydrated repeatedly with 95% alcohol, and sealed with xylene and neutral gum. The staining was observed using a microscope.

2.8. Enzyme-Linked Immunosorbent Assay (ELISA). Mouse MCP3 ELISA Kit (CCL7) (Abcam) was used to perform the experiment according to the instructions. CCL7 antibody was diluted with carbonate buffer and added to the culture plate for overnight culture at 4°C. The next day, the

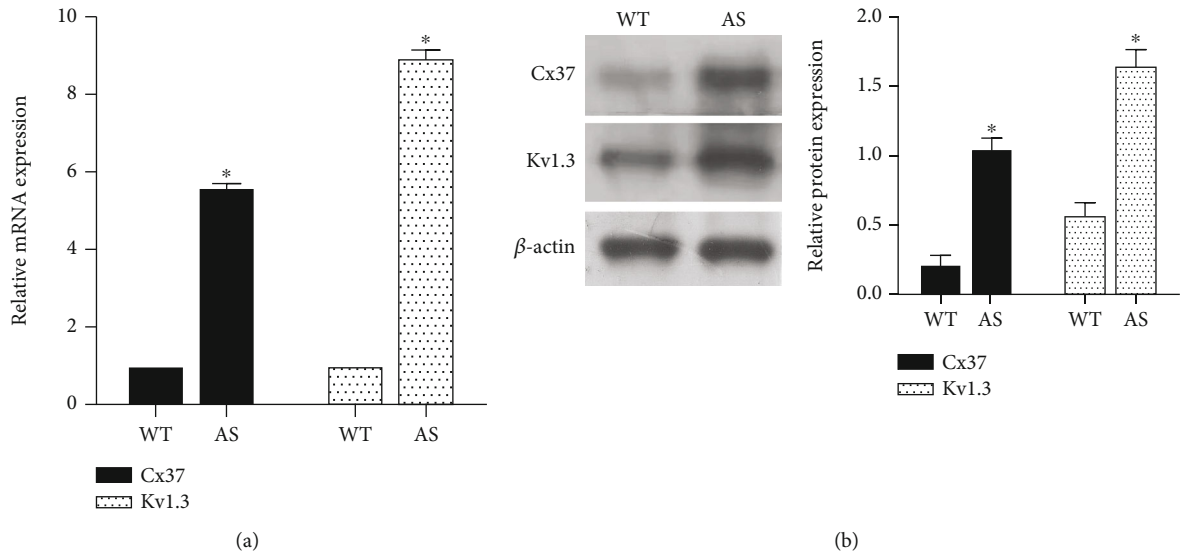

Figure 2: Expression of Cx37 and Kv1.3 in atherosclerosis. (a) The expression of Cx37 and Kv1.3 in macrophages was detected by RT-PCR. (b) The expressions of Cx37 and Kv1.3 proteins were detected by Western blot. $^{*}P < 0.05$, compared with WT group.

solution in the culture wells was discarded and washed with PBS solution three times, and the cell samples to be tested were added to the culture wells. The cells were incubated at 37°C for 1 hour. Biotinylated antibody working solution and enzyme conjugate were added to the reaction well, and the reaction well was cleaned after incubation for 30 min. Add color substrate TMB 100 μL to each well, and incubate in a dark room for 15 min. Add stop solution 100 μL to each well, measure OD_{450} value after mixing, and draw standard curve to calculate the concentration.

2.9. CCK8. Logarithmic growth stage cells were collected and counted, cell density was adjusted, and cells were inoculated on 96-well plates and incubated overnight at 37°C. 0.1 mL complete culture medium containing 10% CCK8 (Beyotime Institute of Biotechnology, Beijing) was added to each well, and incubated at 37°C and 5% CO_2 for 2-3 h. OD450 was determined using a microplate reader (Beijing Pulang New Technology Co., Ltd.).

2.10. Immunofluorescence Technique. The blood vessel rings to be measured were fixed with methanol for 20 min, and the tissues were dried at room temperature for 10 min. The vascular tissues were cleaned 3 times with PBS solution and treated with 1% Triton solution for 25-30 min. The tissue was then placed in goat serum and sealed at 37°C for 20 min. The tissues were then placed into primary antibody solutions such as Cx37 antibody and Kv1.3 antibody (Abcam) and incubated at 4°C overnight. Then, the tissue was added into a fluorescence-labeled secondary antibody solution (Abcam) for 1 h reaction. After washing the tissue with PBS solution for 3 times, the slides were dried and sealed, and the staining results were observed by fluorescence microscope.

2.11. Statistical Analysis. SPSS 20.0 software was used for data analysis. All experiments were set up with three double wells and repeated at least three times. Measurement data were expressed as mean ± standard deviation ($\bar{x} \pm s$). Continuous variables between the two groups were analyzed by independent sample t test, and the mean values between multiple groups were compared by ANOVA analysis. $P \leq 0.05$ was considered statistically significant.

3. Results

3.1. Expression of Cx37 and Kv1.3 in Atherosclerosis. $ApoE^{-/-}$ mice were given a high-fat diet to establish AS mouse model, and macrophages were isolated from WT mice and AS mice to detect the expressions of Cx37 and Kv1.3. The detection results showed that Cx37 and Kv1.3 were highly expressed in macrophages of AS mice (Figure 2(a)). Protein detection also showed that Cx37 and Kv1.3 proteins were highly expressed in AS mice (Figure 2(b)).

3.2. Effect of Cx37 Gene on Proliferation and Chemotactic Function of Mononuclear Macrophages. It has been known from previous studies that Cx37 is highly expressed in AS mononuclear macrophages, and the expression of Cx37 is closely related to the development of AS. Therefore, we silenced the expression of Cx37 in macrophages, constructed Cx37 silenced expression vector, and detected its expression efficiency by WB. It was found that all three expression vectors could effectively inhibit the expression of Cx37, and shRNA-2 had the highest inhibition efficiency (Figure 3(a)). Therefore, we transfected macrophages with shRNA-2 silencing expression vector. RT-PCR results showed that Cx37 expression decreased in sh-CX37 group, and transfection was successful (Figure 3(b)). Subsequently, we detected that reduced Cx37 expression in macrophages resulted in decreased Kv1.3 protein expression and decreased chemokine CCL7 concentration (Figures 3(c) and 3(d)). Meanwhile, silencing Cx37 expression can also inhibit the proliferation activity of macrophages

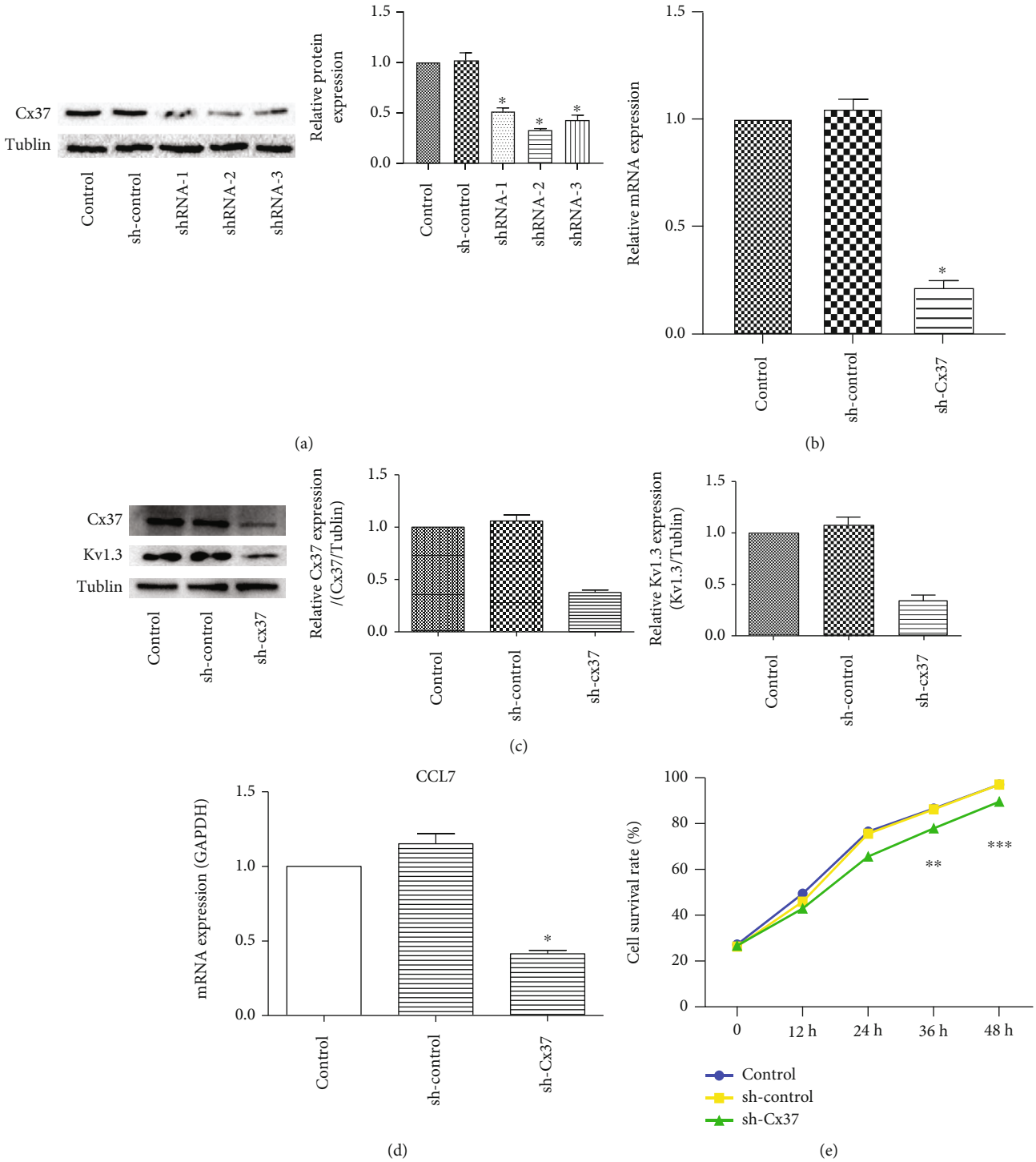

Figure 3: Effect of Cx37 silencing expression on physiological function of mononuclear macrophages. (a) Western blot was used to detect the expression efficiency of Cx37 silenced expression vector. (b) The expression efficiency of Cx37 in macrophages was detected by RT-PCR. (c) The expressions of Cx37 and Kv1.3 proteins were detected by Western blot. (d) The expression of CCL7 was detected by RT-PCR. (e) CCK8 was used to detect cell proliferation. $^{*}P < 0.05$, $^{**}P < 0.01$, $^{***}P < 0.001$, compared with control group.

(Figure 3(e)). The expression of Cx37 can promote macrophage activity.

3.3. Effect of Cx37 Gene and Kv1.3 Channel on Vein Atherosclerosis in Mice. ApoE$^{-/-}$ mice were given a high-fat diet, followed by a tail vein injection of Cx37 overexpression vector (pre-CX37) or subcutaneous injection of Kv1.3 blocker ShK (L5). The weight of mice and other indicators were detected, and it was found that there was no significant difference in the weight of mice in the 4 groups in the first 4 weeks. From the 4th week of administration, the rate of weight gain of all AS mice decreased, and the body weight

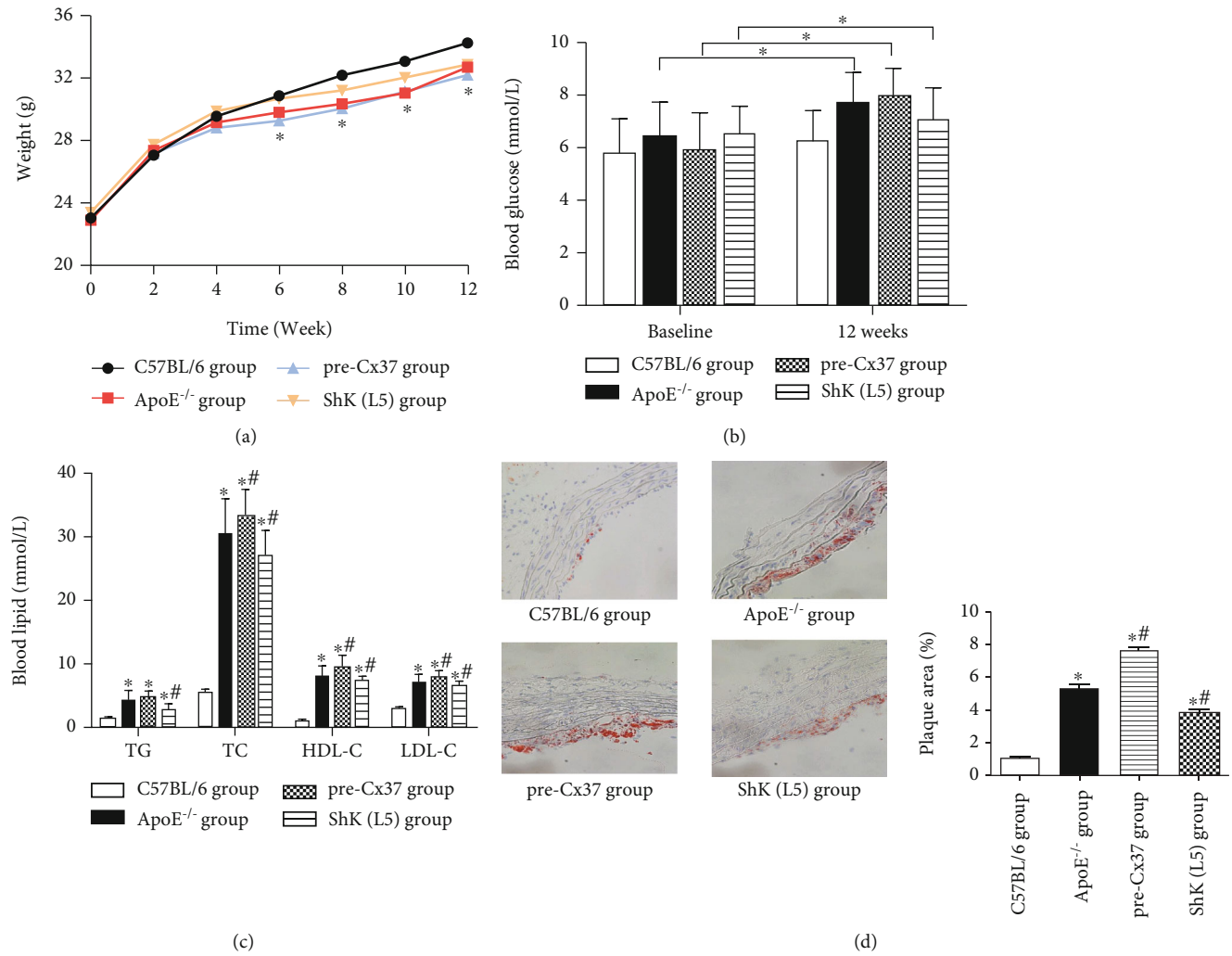

Figure 4: Effect of Cx37 and Kv1.3 expression on atherosclerosis. (a) Body weight statistics of mice. (b) Blood glucose index statistics of mice. (c) Four statistics of blood lipid in mice. (d) The atherosclerotic plaque area was detected by oil red O staining. $^{*}P < 0.05$, compared with C57BL/6 group; $^{\#}P < 0.05$, compared with ApoE$^{-/-}$ group.

of mice was smaller than that of wild-type mice. There was no significant difference in the weight growth trend between the pre-CX37 group and the ApoE$^{-/-}$ group, and the weight gain of the ShK (L5) group was slightly higher than that of the ApoE$^{-/-}$ group, which was closer to that of the C57BL/6 group (Figure 4(a)).

After 12 weeks, the blood glucose indexes of ApoE$^{-/-}$ mice in three groups were all higher than before. After 12 weeks, the blood glucose index of mice in the pre-CX37 group was higher than that in the ApoE$^{-/-}$ group, and the blood glucose concentration of mice in the ShK(L5) group was lower and close to that of wild-type mice (Figure 4(b)). The four tests of blood lipid in mice showed that the concentrations of TG (triglyceride), TC (total cholesterol), HDL-C (high-density lipoprotein cholesterol), and LDL-C (low-density lipoprotein cholesterol) of AS mice in the three groups were significantly higher than those of wild-type mice, while the four indexes of ShK(L5) group were lower than those of ApoE$^{-/-}$ group and pre-CX37 (Figure 4(c)). Cx37 overexpression has no significant effect on body weight of AS mice, but blocking the activity of Kv1.3 pathway in mice can effectively reduce the increase of blood lipid and blood glucose of AS mice. Oil red O staining results showed that Cx37 overexpression increased the atherosclerotic plaque area, while ShK(L5) decreased the atherosclerotic plaque area (Figure 4(d)). These results suggest that Cx37 overexpression in AS mice can promote the formation of AS plaques, while blocking the activity of Kv1.3 pathway can inhibit the formation of AS plaques.

3.4. Study on the Mechanism of Cx37 Gene Promoting the Development of Atherosclerosis by Promoting Kv1.3 Opening. In order to detect the relationship between Cx37 and Kv1.3 pathway, we selected to add Kv1.3 blocker to culture mice based on Cx37 overexpression. Firstly, we detected that both Kv1.3 and Cx37 were highly expressed in AS mice. After the expression of Cx37 was increased, the expression of Kv1.3 was also increased; however, when the expression of Kv1.3 was inhibited, the expression of Cx37 was not significantly changed (Figure 5(a)). Immunofluorescence detection also showed the same results as RT-PCR: Cx37 overexpression could increase Kv1.3 expression, but

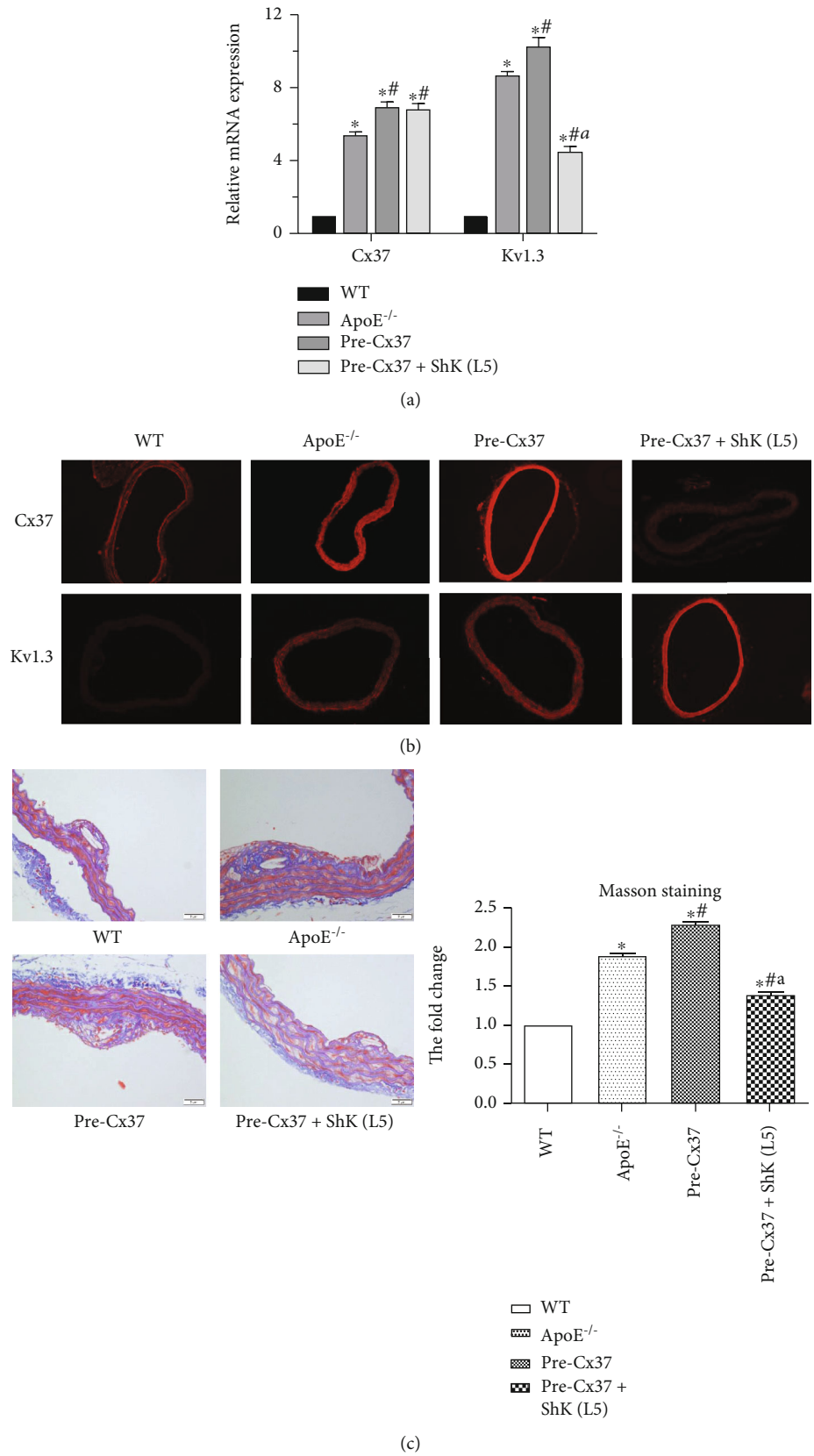

Figure 5: Study on the mechanism of Cx37 gene regulating atherosclerosis. (a) The expression efficiency of Cx37 and Kv1.3 was detected by RT-PCR. (b) The expression of Cx37 and Kv1.3 in mouse aorta was detected by immunofluorescence. (c) The expression of plaque collagen content was detected by Masson staining. $^{*}P < 0.05$, compared with WT group; $^{\#}P < 0.05$, compared with ApoE$^{-/-}$ group; $^{a}P < 0.05$, compared with Pre-Cx37 group.

decreased Kv1.3 expression could not affect Cx37 expression (Figure 5(b)). Masson staining showed that plaque collagen content in the ApoE$^{-/-}$ group was increased compared with that in the wild-type group. Compared with ApoE$^{-/-}$ group, Cx37 overexpression increased plaque collagen content, and the addition of Kv1.3 blocker on the basis of Cx37 overexpression decreased plaque collagen content (Figure 5(c)). Cx37 overexpression can promote the expression of chemokine CCL7, and the expression of CCL7 decreased after the addition of Kv1.3 blocker (Figure 5(d)).

4. Discussion

Atherosclerosis (AS) is a chronic disease with continuous progression of large arteries, and its formation mechanism is characterized by the accumulation of vascular smooth cells, macrophages, and lipids under the intima of arteries in the early stage, followed by the formation of fibrous caps with distinct characteristics by the hyperplasia of connective tissues such collagen, elastic fibers, and proteoglycan [18]. Gap junction is a membrane channel structure between adjacent cells, and its basic constituent unit is connexin (Cx). In the early stage of atherosclerotic lesions, monocytes and vascular endothelial cells regulate each other by secreting or expressing various adhesion molecules and chemokines [19]. A large number of studies in recent years have shown that gap junction intercellular communication (GJIC) dysfunction caused by Cx expression changes is closely related to AS vascular lesions [20]. Kwak et al. [21] detected AS plaques in mice and humans and found that with the progression of AS, Cx37 expression was gradually lost in endothelial cells, gradually increased in smooth muscle, and increased in monocytes. In situ hybridization revealed abundant Cx37 expression in macrophages and foam cells in the AS region [22]. In this study, Cx37 was detected to be highly expressed in macrophages of AS mice, which was consistent with literature results.

Chemokines are secreted by endothelial cells or activated monocytes and can mediate migration and infiltration of a large number of monocytes into intima [23]. In recent years, studies have found that chemokines not only play a role in cell recruitment but also affect cell homeostasis and activation [24]. CCL7 (Chemokine C-C Motif Ligand 7) plays an important role in the recruitment of monocytes, calcium influx, tumor metastasis, and other biological effects [25]. In AS, the high expression of CCL7 can promote the recruitment and infiltration of inflammatory cells, which is directly related to the accumulation of macrophages at plaque lesions and the formation range of AS lesions and even directly related to the incidence of coronary heart disease or myocardial infarction [26, 27]. Therefore, reducing the secretion of CCL7 in monocytes can reduce the aggregation of macrophages and slow down the area of plaque formation.

In this study, we detected that Cx37 and Kv1.3 were overexpressed in macrophages of AS mice, and after Cx37 expression was silenced, the expressions of Kv1.3 and CCL7 were decreased, and the proliferation of macrophages were decreased. Wild-type mice and AS model mice were treated with Cx37 overexpression and Kv1.3 pathway blocking, and it was found that Cx37 overexpression could improve the blood lipid and blood glucose levels and increase the area of AS in AS mice. However, blocking the activity of Kv1.3 pathway can reduce the levels of blood lipid and blood glucose, increase the body weight of mice, and reduce the area of AS plaque. Blocking the activity of Kv1.3 pathway can slow down the plaque development of AS mice and make its indexes close to wild-type mice. And the use of Kv1.3 pathway blockers on the basis of overexpression of Cx37 indicated that inhibition of Kv1.3 pathway activity did not affect the expression of Cx37, but could inhibit the collagen content in the plaque area of AS mice, inhibit the expression of CCL7, and reverse the effect of Cx37 overexpression. Therefore, Cx37 can improve the activity of macrophages in AS mice by regulating the expression of chemokines and the activity of the Kv1.3 pathway and enrich macrophages in inflammatory tissues to expand the area of plaque formation.

Relevant clinical studies have shown that increasing the expression of Cx37 and the activity of chemokine CCL7 can accelerate the inflammatory reaction and promote the process of AS [10, 27], which is consistent with the conclusion of this study. To explore the inhibition of Cx37 and CCL7 expression has important significance for the treatment of atherosclerosis and provides a new therapeutic target for the treatment of atherosclerosis. At the same time, because atherosclerosis exists in a variety of diseases such as Coronary heart disease, cerebral infarction, peripheral vascular disease, targeting Cx37, Kv1.3, and other genes may have therapeutic effects on coronary heart disease and other diseases. This study proved that the expression of Cx37 can regulate the activity of Kv1.3 pathway. However, the mechanism of Cx37 regulating Kv1.3 pathway is still unclear, and further research is needed to explore the regulatory mechanism in the future.

Data Availability

The data used to support the findings of this study are included within the article.

Conflicts of Interest

There are no conflicts to declare.

Acknowledgments

This study was supported by the Key Projects of Dongguan Science and Technology Bureau (202050715001179) and Scientific Research and Development Fund of Dongguan People's Hospital (k201906).

References

[1] J. Frostegård, "Immunity, atherosclerosis and cardiovascular disease," *BMC Medicine*, vol. 11, no. 1, p. 117, 2013.

[2] A. V. Poznyak, D. Zhang, V. Orekhova, A. V. Grechko, R. Wetzker, and A. N. Orekhov, "A brief overview of currently used atherosclerosis treatment approaches targeting lipid

metabolism alterations," *American Journal of Cardiovascular Disease*, vol. 10, no. 2, pp. 62–71, 2020.

[3] J. Zhou, M. Chew, H. B. Ravn, and E. Falk, "Plaque pathology and coronary thrombosis in the pathogenesis of acute coronary syndromes," *Scandinavian Journal of Clinical and Laboratory Investigation. Supplementum*, vol. 230, pp. 3–11, 1999.

[4] T. Thim, M. K. Hagensen, J. F. Bentzon, and E. Falk, "From vulnerable plaque to atherothrombosis," *Journal of Internal Medicine*, vol. 263, no. 5, pp. 506–516, 2008.

[5] M. L. Grønholdt, S. Dalager-Pedersen, and E. Falk, "Coronary atherosclerosis: determinants of plaque rupture," *European Heart Journal*, vol. 19 Suppl C, pp. C24–C29, 1998.

[6] G. R. Geovanini and P. Libby, "Atherosclerosis and inflammation: overview and updates," *Clinical Science*, vol. 132, no. 12, pp. 1243–1252, 2018.

[7] A. Viola, F. Munari, R. Sánchez-Rodríguez, T. Scolaro, and A. Castegna, "The metabolic signature of macrophage responses," *Frontiers in Immunology*, vol. 10, no. 10, p. 1462, 2019.

[8] A. Pfenniger, M. Chanson, and B. R. Kwak, "Connexins in atherosclerosis," *Biochimica et Biophysica Acta*, vol. 1828, no. 1, pp. 157–166, 2013.

[9] D. Wen, X. Du, S. P. Nie, J. Z. Dong, and C. S. Ma, "Association of Connexin37 C1019T with myocardial infarction and coronary artery disease: a meta-analysis," *Experimental Gerontology*, vol. 58, pp. 203–207, 2014.

[10] S. Guo, J. Zhu, Z. Yang et al., "Reduction of connexin 37 expression by RNA interference decreases atherosclerotic plaque formation," *Molecular Medicine Reports*, vol. 11, no. 4, pp. 2664–2670, 2015.

[11] S. Guo, Y. Yang, Z. Yang et al., "Improving myocardial fractional flow reserve in coronary atherosclerosis via CX37 gene silence: a preclinical validation study in pigs," *Interactive Cardiovascular and Thoracic Surgery*, vol. 26, no. 1, pp. 139–145, 2018.

[12] O. Scheel, M. Papavlassopoulos, R. Blunck et al., "Cell activation by ligands of the toll-like receptor and interleukin-1 receptor family depends on the function of the large-conductance potassium channel MaxiK in human macrophages," *Infection and Immunity*, vol. 74, no. 7, pp. 4354–4356, 2006.

[13] R. Hasan and J. H. Jaggar, "KVchannel trafficking and control of vascular tone," *Microcirculation*, vol. 25, no. 1, article e12418, 2018.

[14] X. H. Kan, H. Q. Gao, Z. Y. Ma, L. Liu, M. Y. Ling, and Y. Y. Wang, "Kv1.3 potassium channel mediates macrophage migration in atherosclerosis by regulating ERK activity," *Archives of Biochemistry and Biophysics*, vol. 591, pp. 150–156, 2016.

[15] Y. Yuan, H. Zhai, Z. Guo et al., "Effects of Mahuang (*Herba Ephedra Sinica*) and Wuweizi (*Fructus Schisandrae Chinensis*) medicated serum on chemotactic migration of alveolar macrophages and inters regions macrophages in rats," *Journal of Traditional Chinese Medicine*, vol. 37, no. 5, pp. 607–615, 2017.

[16] Y. C. Chen, J. Rivera, M. Fitzgerald et al., "Preimplantation factor prevents atherosclerosis via its immunomodulatory effects without affecting serum lipids," *Thrombosis and Haemostasis*, vol. 115, no. 5, pp. 1010–1024, 2016.

[17] Y. Luo, S. Lu, Y. Gao et al., "Araloside C attenuates atherosclerosis by modulating macrophage polarization via Sirt1-mediated autophagy," *Aging*, vol. 12, no. 2, pp. 1704–1724, 2020.

[18] G. K. Hansson and A. Hermansson, "The immune system in atherosclerosis," *Nature Immunology*, vol. 12, no. 3, pp. 204–212, 2011.

[19] R. Ramadan, S. Baatout, A. Aerts, and L. Leybaert, "The role of connexin proteins and their channels in radiation-induced atherosclerosis," *Cellular and Molecular Life Sciences*, vol. 78, no. 7, pp. 3087–3103, 2021.

[20] L. Burnier, P. Fontana, A. Angelillo-Scherrer, and B. R. Kwak, "Intercellular communication in atherosclerosis," *Physiology*, vol. 24, no. 1, pp. 36–44, 2009.

[21] B. R. Kwak, F. Mulhaupt, N. Veillard, D. B. Gros, and F. Mach, "Altered pattern of vascular connexin expression in atherosclerotic plaques," *Arteriosclerosis, Thrombosis, and Vascular Biology*, vol. 22, no. 2, pp. 225–230, 2002.

[22] M. Chanson and B. R. Kwak, "Connexin37: a potential modifier gene of inflammatory disease," *Journal of Molecular Medicine*, vol. 85, no. 8, pp. 787–795, 2007.

[23] M. C. Miller and K. H. Mayo, "Chemokines from a structural perspective," *International Journal of Molecular Sciences*, vol. 18, no. 10, p. 2088, 2017.

[24] A. E. Vilgelm and A. Richmond, "Chemokines modulate immune surveillance in tumorigenesis, metastasis, and response to immunotherapy," *Frontiers in Immunology*, vol. 10, p. 333, 2019.

[25] Y. S. Lee and Y. B. Cho, "CCL7 signaling in the tumor microenvironment," *Advances in Experimental Medicine and Biology*, vol. 1231, pp. 33–43, 2020.

[26] Q. N. Dinh, S. Chrissobolis, H. Diep et al., "Advanced atherosclerosis is associated with inflammation, vascular dysfunction and oxidative stress, but not hypertension," *Pharmacological Research*, vol. 116, pp. 70–76, 2017.

[27] S. Li, W. Sun, H. Zheng, and F. Tian, "Microrna-145 accelerates the inflammatory reaction through activation of NF-κB signaling in atherosclerosis cells and mice," *Biomedicine & Pharmacotherapy*, vol. 103, pp. 851–857, 2018.

Hindawi
Mediators of Inflammation
Volume 2022, Article ID 1878766, 24 pages
https://doi.org/10.1155/2022/1878766

Research Article

FAM171B as a Novel Biomarker Mediates Tissue Immune Microenvironment in Pulmonary Arterial Hypertension

Lai-Hao Qu,[1,2] Wen-Juan Luo,[3] Zhi-Guo Yan,[1] and Wen-Pan Liu[1]

[1]*Cardiothoracic Surgery, The First People's Hospital of Kunming City & Ganmei Affiliated Hospital of Kunming Medical University, Kunming, 650000 Yunnan Province, China*
[2]*Department of Thoracic Surgery, Kunming Yan'an Hospital Affiliated to Kunming Medical University, Kunming, 650000 Yunnan Province, China*
[3]*Department of Cardiology, The First People's Hospital of Kunming City & Ganmei Affiliated Hospital of Kunming Medical University, Kunming, 650000 Yunnan Province, China*

Correspondence should be addressed to Wen-Pan Liu; 15001020348@xs.hnit.edu.cn

Received 22 July 2022; Revised 22 August 2022; Accepted 5 September 2022; Published 22 September 2022

Academic Editor: Md Sayed Ali Sheikh

The purpose of this study was to uncover potential diagnostic indicators of pulmonary arterial hypertension (PAH), evaluate the function of immune cells in the pathogenesis of the disease, and find innovative treatment targets and medicines with the potential to enhance prognosis. Gene Expression Omnibus was utilized to acquire the PAH datasets. We recognized differentially expressed genes (DEGs) and investigated their functions utilizing R software. Weighted gene coexpression network analysis, least absolute shrinkage and selection operators, and support vector machines were used to identify biomarkers. The extent of immune cell infiltration in the normal and PAH tissues was determined using CIBERSORT. Additionally, the association between diagnostic markers and immune cells was analyzed. In this study, 258DEGs were used to analyze the disease ontology. Most DEGs were linked with atherosclerosis, arteriosclerotic cardiovascular disease, and lung disease, including obstructive lung disease. Gene set enrichment analysis revealed that compared to normal samples, results from PAH patients were mostly associated with ECM-receptor interaction, arrhythmogenic right ventricular cardiomyopathy, the Wnt signaling pathway, and focal adhesion. FAM171B was identified as a biomarker for PAH (area under the curve = 0.873). The mechanism underlying PAH may be mediated by nave CD4 T cells, resting memory CD4 T cells, resting NK cells, monocytes, activated dendritic cells, resting mast cells, and neutrophils, according to an investigation of immune cell infiltration. FAM171B expression was also associated with resting mast cells, monocytes, and CD8 T cells. The results suggest that PAH may be closely related to FAM171B with high diagnostic performance and associated with immune cell infiltration, suggesting that FAM171B may promote the progression of PAH by stimulating immune infiltration and immune response. This study provides valuable insights into the pathogenesis and treatment of PAH.

1. Introduction

Abnormally high blood pressure in the pulmonary arteries is the hallmark of pulmonary arterial hypertension (PAH), a disease or physiological condition with multiple known and unidentified factors [1]. It is characterized by thickening of the intima of the pulmonary artery wall, resulting in abnormal hemodynamics and increased pulmonary resistance [2]. In addition, PAH is a life-threatening cardiovascular illness that can lead to impaired heart function and increased mortality [3]. Over the past few decades, the prevalence of PAH has been reported to range from 15 to 60 cases per million people per year. Significant progress has been made in uncovering the pathophysiology of PAH, as well as identifying prognostic biomarkers and alternative treatments [4]. However, the molecular mechanism underlying PAH has not been elucidated. Angiotropic and hyperplastic drugs, such as PDE-5 inhibitors, endothelin receptor antagonists (ERAs), and prostacyclin receptor agonists can increase exercise endurance and heart function in PAH patients [5–7]. However, the efficacy of the

treatment of PAH still needs to be improved for a better prognosis for patients [8]. Thus, it is important to identify effective biomarkers for PAH, study its pathogenesis, and develop targeted therapies.

With the rapid development of gene sequencing technology and bioinformatics research methods, it is now possible to investigate the underlying causes of numerous diseases by carefully assessing the potential changes in gene expression between aberrant and paired normal tissues [4]. However, only a few studies have used machine learning approaches to uncover biomarkers for PAH [9, 10]. These techniques include least absolute shrinkage and selection operator (LASSO) logistic regression, support vector machine-recursive feature elimination (SVM-RFE), random forest (RF), and weighted gene coexpression network analysis (WGCNA). As a regression analysis technique, LASSO analysis sets the coefficients of less significant variables to zero by applying an L1-penalty (lambda) to screen for significant variables and construct the best classification model [11]. The SVM-RFE analysis is a supervised machine learning technique for classifying data points by maximizing the margin between distinct classes in a high-dimensional space [12]. The RF analysis is a nonparametric approach for carrying out classification under supervision [13]. RF encompasses decision trees derived from subdivided datasets. In this study, a single RF classification model was trained and analyzed to identify descriptors capable of discriminating PAH samples from general samples. In addition, this method, represented as WGCNA, is used to investigate gene expression patterns within samples. Genes with consistent expressing modes were subjected to the clustering process, and the relationship between the module and a specific characteristic or phenotype was determined [14]. Consequently, these four machine learning techniques are widely used to identify diagnostic markers and forecast models with high precision and understandability.

In this study, we aimed to reanalyze the datasets previously published by Mura et al. [15], Stearman et al. [16], and Zhao et al. [17], which included the GSE113439, GSE117261, and GSE53408 datasets, respectively. In addition, two sets of microarray mRNA expression data were combined to find genes that were expressed differently. We used differentially expressed genes (DEGs) for functional enrichment analysis and different machine learning approaches for biomarker identification and investigated the diagnostic value of biomarker expression in PAH patients. Finally, we determined the proportion of immune cell infiltration in PAH using the CIBERSORT tool. In the future, we intend to use PAH patient data in the GEO database to conduct bioinformatics research for the determination of biomarkers and specific immune cells associated with PAH, with an ultimate goal to develop drugs that target these biomarkers and immune cells to delay or reverse PAH and improve patient outcomes.

2. Materials and Methods

2.1. Data Selection. The GSE113439, GSE117261, and GSE53408 microarray datasets were retrieved from the Gene Expression Omnibus (GEO) database (http://www.ncbi.nlm.nih.gov/geo/), containing data for lung tissues collected from 11 normal subjects and 15 PAH patients; 25 normal subjects and 58 PAH patients; and 11 normal subjects and 12 PAH patients, respectively. The GSE113439, GSE117261, and GSE53408 datasets were derived from the GPL6244 platform. We validated our results using GSE53408 expression profiling. Table 1 provides a complete summary of these datasets.

2.2. Data Preprocessing and DEGs Screening. The probes were converted into gene symbols by making use of the probe annotation files that were given by the researchers. Based on the annotated file of each dataset, unmapped probes were eliminated. Multiple probes correspond to the same gene, and the average of this gene in all samples was used for subsequent analyses.

Batch effects were removed from the GSE113439 and GSE117261 datasets using the "sva" function in R [18]. As these datasets contain similar platforms, data can be merged. Principal component analysis (PCA) plots were used on the training matrices to highlight the influence of between-sample rectification. These plots were created before and after the "PCA" function was used to eliminate the inter-batch effect [19]. The "limma" function [20] was used to filter DEGs and the "ggplot2" function [21] to show differential gene expression. DEGs were considered statistically significant when adjusted $P < 0.05$ and |log2FC| was >0.5.

2.3. Functional Enrichment Analysis. Using the "clusterProfiler" function in R, we investigated DEG enrichment in Disease Ontology (DO), Kyoto Encyclopedia of Genes and Genomes (KEGG), and Gene Ontology (GO) terms (22). In a previous study, researchers used Metascape (http://metascape.org) to conduct pathway enrichment analyses and annotate biological processes to explain the information included in each gene [22]. This study analyzed the DEGs from the training dataset using Metascape's GO and pathway enrichment methods to determine the most important functional biological keywords and signaling pathways. Statistical significance was determined based on the number of enriched genes being ≥3 and $P < 0.01$. Additionally, all the important phrases were categorized according to their membership similarity, and the most enriched term from each cluster was chosen as the representative term. By using the ClusterProfiler function and the "c5.go.v7.4.symbols.gmt" and "c2.cp.kegg.v7.0.symbols.gmt." datasets, a gene set enrichment analysis (GSEA) of the genomic array was carried out.

2.4. Feature Selection Using the Random Forest Model. The DEGs obtained were analyzed using the randomForest function in R [23]. First, the average rate of model miscalculation across all genes was determined. The optimal number of variables for the binary tree in the node was 3, and the best random forest tree count was 500. Random forest models were developed, and the dimensional importance value was computed using the decreasing accuracy method (Gini

Table 1: Characteristics of three datasets.

Datasets	PAH	Tissue source	Normal	Tissue source	Platform
GSE113439	15	6 patients with idiopathic PAH, 4 patients with PAH secondary to connective tissue disease, 4 patients with PAH secondary to congenital heart disease, and 1 patient with chronic thromboembolic pulmonary hypertension	11	Tissue flanking lung cancer resections	GPL6244
GSE117261	58	Patients with PAH at transplant	25	Patients who do not have an appropriate recipient but still meet physiologic standards	GPL6244
GSE53408	12	The recipient's lung at the time of lung transplantation	11	Normal tissue of cancer patients undergoing surgery	GPL6244

PAH: pulmonary arterial hypertension.

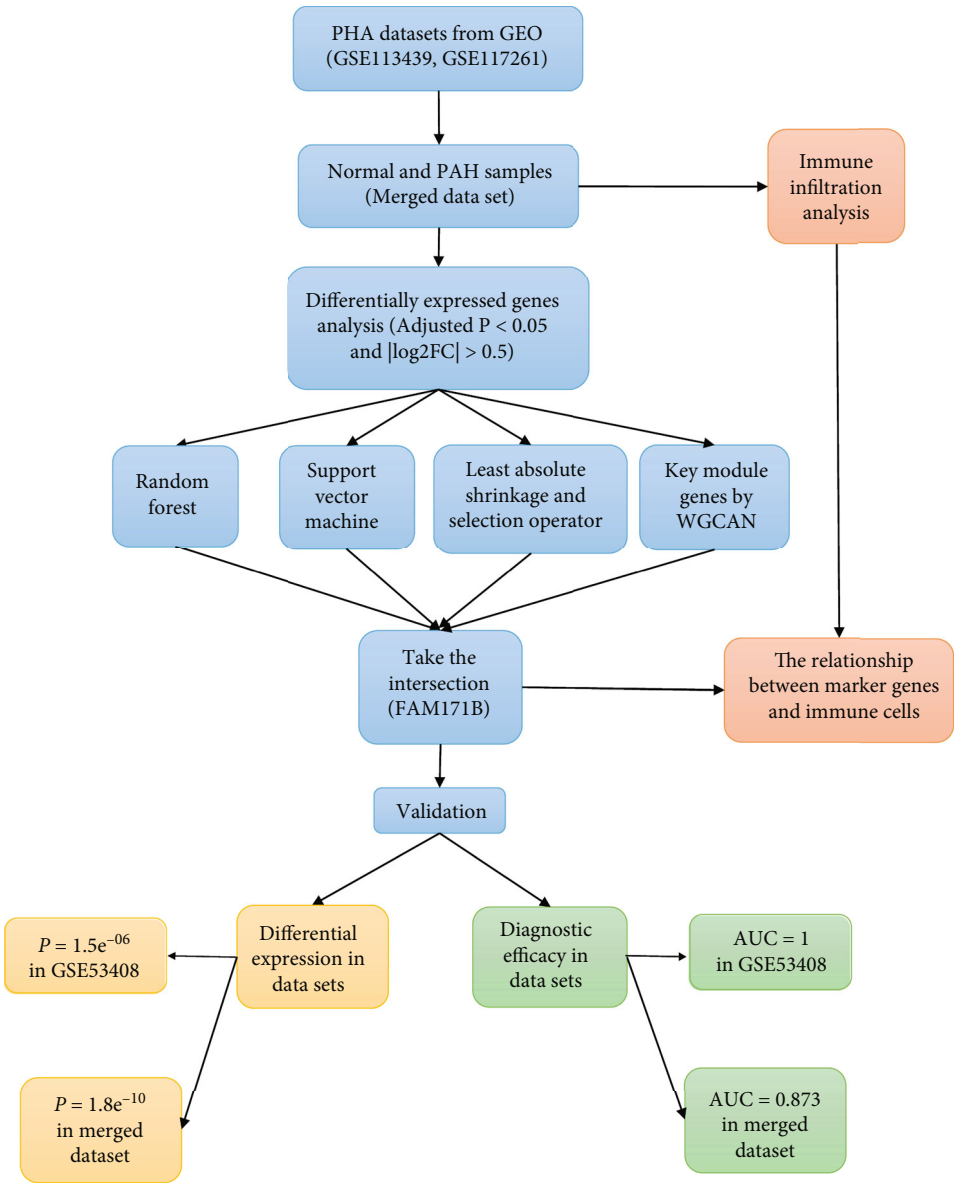

Figure 1: Workflow for the study.

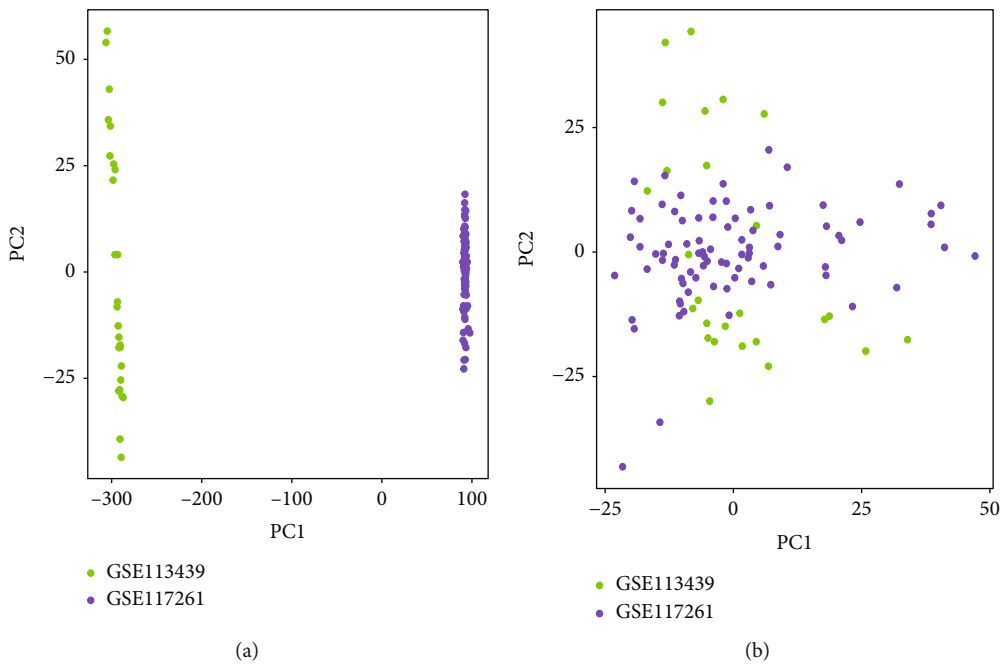

Figure 2: Principal component analysis (PCA) analysis of gene expression datasets. The scatter plots' points depict samples based on the top two principal components (PC1 and PC2) of gene expression profiles without and with batch effect removal. (a) PCA cluster plot of GSE113439 and GSE117261 before sample correction and batch effect removal. (b) PCA cluster plot of GSE113439 and GSE117261 after sample correction and batch effect removal. The colors denote samples from two distinct datasets, respectively. Each dot represents a sample; green represents a sample from GSE113439; purple represents a sample from GSE117261.

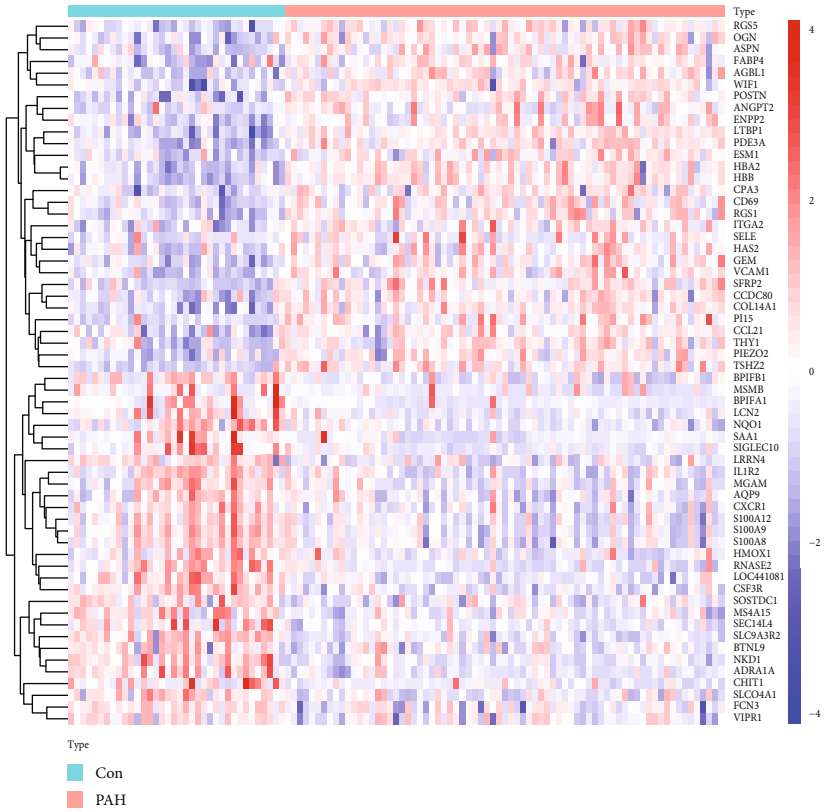

(a)

Figure 3: Continued.

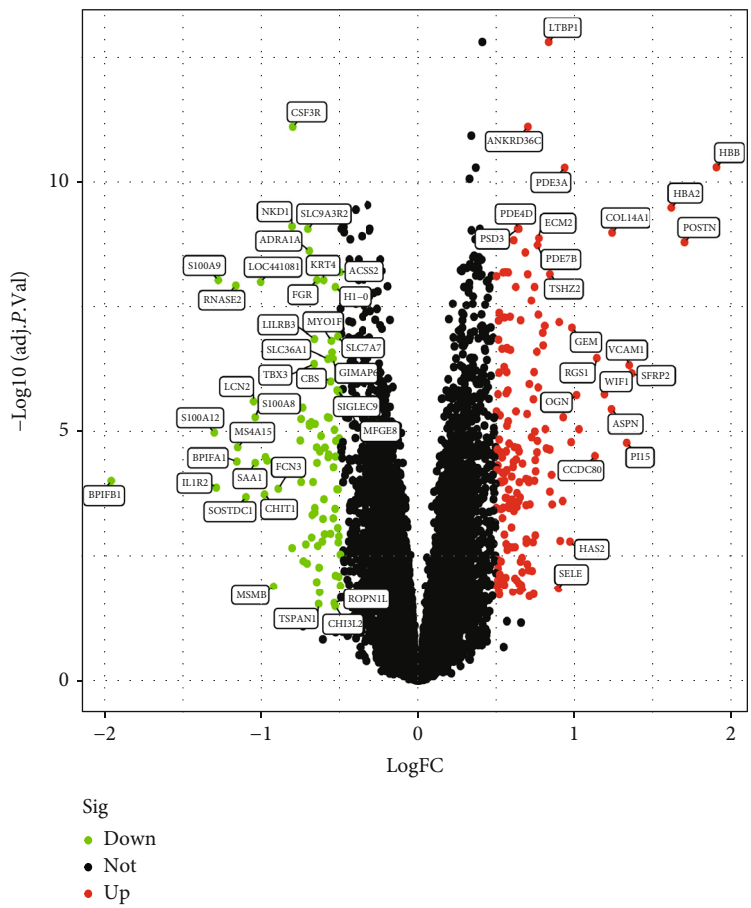

(b)

Figure 3: Visualizing the results of differential genes. (a) Clustering heat map of the genes exhibiting significantly differential expression PAH versus normal samples. Statistically significant DEGs were defined as |log2Foldchange| > 0.5 and adjusted P value<0.05. Cyan represents PAH samples; reddish-orange represents normal samples. (b) Volcano map of DEGs; red represents upregulated differential genes, black represents no significant difference in genes, and the green represents downregulated differential genes. DEGs: differentially expressed genes; PAH: pulmonary arterial hypertension.

coefficient method). Disease-specific genes were determined as those with a significance value greater than 2 and ranked among the top three.

2.5. Feature Selection Using the LASSO Regression Model. LASSO is a method used to carry out gene selection and classification through regression analysis. The glmnet function in the R package [24] was used to establish a logistic LASSO regression model using 258 DEGs to identify significant prospective gene combinations consistently related to PAH. Ten-fold cross-validation was employed in this study to define tuning parameters, and the partial likelihood of deviance fulfilled the minimal criterion.

2.6. Feature Selection Using the SVM Classifier Model. The feature selection approach is an effective method for extracting useful data from available gene datasets [25]. SVM is a supervised learning model used to accurately categorize data points by optimizing the distance between two hyperplanes [26]. SVM-RFE is a well-known feature selection approach that has shown significant and increasing applicability in a high-dimensional data analysis. Feature selection methods are superior to many other feature selection algorithms in terms of data overfitting and classification accuracy and are useful in a variety of fields, including microarray gene expression [27, 28].

2.7. Key Module Identification Using WGCNA. The system biology approach, WGCNA, was used to generate gene coexpression networks to investigate gene-gene relationships [29]. First, genes with a variance of over 25% across samples in the integrated dataset were entered into the WGCNA platform. Second, outlier samples were eliminated to confirm the reliability of the network construction outcomes. Third, adjacency was determined using the pick-SoftThreshold function obtained using the soft thresholding power, which was generated through coexpression similarity. After transforming the adjacency matrix into a topological overlap matrix (TOM), the associated dissimilarity (1-TOM) was measured. Fourth, modules were identified using a combination of hierarchical clustering and a dynamic tree-cut algorithm. We employed average connection

Table 2: The top 20 up- and downregulated DEGs in PAH and normal samples.

Genes	Log2FC	AveExpr	*T*	*P* value	Adj. *P* value	*B*
Upregulated						
HBB	1.905556883	9.856392202	8.817638633	2.05E-14	5.16E-11	22.29719033
POSTN	1.706056477	9.004745628	7.883631545	2.56E-12	1.65E-09	17.65365235
HBA2	1.623246487	9.995273661	8.395393375	1.84E-13	3.35E-10	20.18546164
SFRP2	1.364599703	6.835061904	6.259692192	7.73E-09	6.77E-07	9.956619921
VCAM1	1.348484359	6.33270595	6.359079782	4.83E-09	4.68E-07	10.40761494
PI15	1.332181179	5.338197295	5.364027131	4.59E-07	1.68E-05	6.054507121
COL14A1	1.239026153	7.436785148	8.01864568	1.28E-12	1.03E-09	18.31809232
ASPN	1.234775416	7.13255928	5.807955926	6.29E-08	3.53E-06	7.949732975
WIF1	1.190095167	9.744898457	5.996873555	2.64E-08	1.78E-06	8.780077328
RGS1	1.141220379	7.504991123	6.443957755	3.22E-09	3.37E-07	10.79526605
CCDC80	1.12913297	8.080546692	5.183353767	1.01E-06	3.04E-05	5.30766633
ENPP2	1.028785935	9.494957558	5.544595076	2.06E-07	8.96E-06	6.815449702
OGN	1.012257941	7.501144893	5.987771459	2.75E-08	1.84E-06	8.739767044
GEM	0.983757223	7.038971522	6.81826404	5.28E-10	8.31E-08	12.53033356
ESM1	0.978601315	5.94799635	5.374557277	4.38E-07	1.63E-05	6.098491469
HAS2	0.971047451	6.507270998	3.905308804	0.000163209	0.001579558	0.510130208
PDE3A	0.937415523	7.215983585	8.816355258	2.07E-14	5.16E-11	22.29074747
AGBL1	0.928098439	6.426958445	5.706068912	1.00E-07	5.14E-06	7.507594521
FABP4	0.924223274	8.40626485	4.525883107	1.54E-05	0.000241578	2.725479162
ANGPT2	0.907969049	5.841628396	3.918091772	0.000155808	0.001526427	0.553359741
Downregulated						
CSF3R	-0.802339405	7.69132216	-9.322132247	1.46E-15	7.90E-12	24.83851182
AQP9	-0.806618791	7.940157165	-3.800645776	0.000237754	0.002124247	0.160190529
NKD1	-0.807008288	6.232544998	-8.187270593	5.40E-13	7.70E-10	19.15162494
FCN3	-0.894325549	10.56417571	-4.710864558	7.29E-06	0.000136457	3.42917004
MSMB	-0.923641782	4.535954481	-3.117142176	0.002333392	0.012605115	-1.939453915
MGAM	-0.963945588	5.678217693	-5.117611008	1.33E-06	3.74E-05	5.039674765
SLCO4A1	-0.975611085	7.118272517	-5.164935589	1.09E-06	3.21E-05	5.232380522
CHIT1	-0.981420709	5.221009621	-4.628773964	1.02E-05	0.000177714	3.114574322
LOC441081	-1.005779498	7.09466789	-7.367729041	3.48E-11	9.93E-09	15.14314687
S100A8	-1.041186811	10.0442234	-5.703814773	1.01E-07	5.14E-06	7.497859186
SAA1	-1.041252274	4.232431929	-5.085585452	1.53E-06	4.18E-05	4.909874548
LCN2	-1.051025788	6.391003715	-5.901638768	4.10E-08	2.48E-06	8.35982061
SOSTDC1	-1.098927062	6.477777826	-4.589229089	1.19E-05	0.000201156	2.964336963
MS4A15	-1.151439894	6.595835828	-5.303669318	5.97E-07	2.05E-05	5.803351239
BPIFA1	-1.157491285	4.694038015	-5.103986002	1.41E-06	3.91E-05	4.984392023
RNASE2	-1.163968826	5.60043777	-7.328408686	4.24E-11	1.18E-08	14.95389119
S100A9	-1.275518557	7.549020869	-7.393186829	3.07E-11	9.17E-09	15.26585058
IL1R2	-1.287495193	7.121522058	-4.727398557	6.82E-06	0.000129741	3.492972276
S100A12	-1.300940357	7.131519115	-5.502100612	2.49E-07	1.04E-05	6.635105221
BPIFB1	-1.955118819	6.8396727	-4.829346556	4.48E-06	9.46E-05	3.889569936

hierarchical clustering by minimum genome size (50) to identify genes with similar expression patterns in gene modules [30]. Fifth, for modules related to clinical features, module membership (MM) and gene significance (GS) were calculated. Finally, the correlation between MM and GS of important modules is shown. Furthermore, genes in the modules were evaluated using the information included in the modules. We identified the most important key module associated with PAH by assessing the *P* value and Pearson's correlation coefficient of module eigengenes (MEs) and the

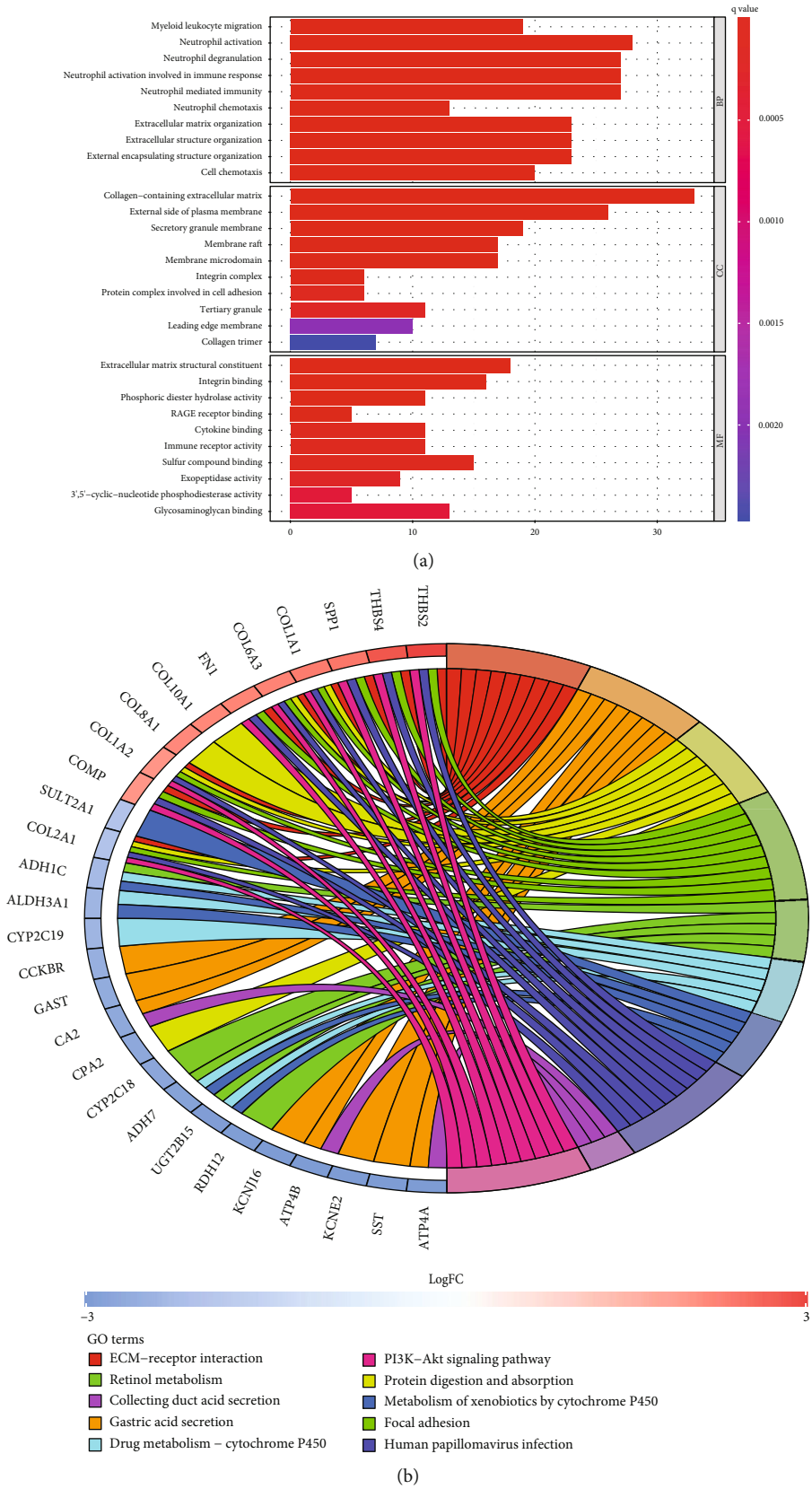

Figure 4: Functional enrichment analyses of DEGs. (a) Gene Ontology (GO) enrichment analyses of DEGs. The x-axis shows the number of genes enriched on the terms, and the y-axis shows the pathway terms. The q-value of each term is colored according to the legend. BP: biological process; CC: cellular component; MF: molecular function; (b) Kyoto Encyclopedia of Genes and Genomes (KEGG) enrichment analyses of DEGs. The q value of each term is colored according to the legend. The different colors represent different pathway terms.

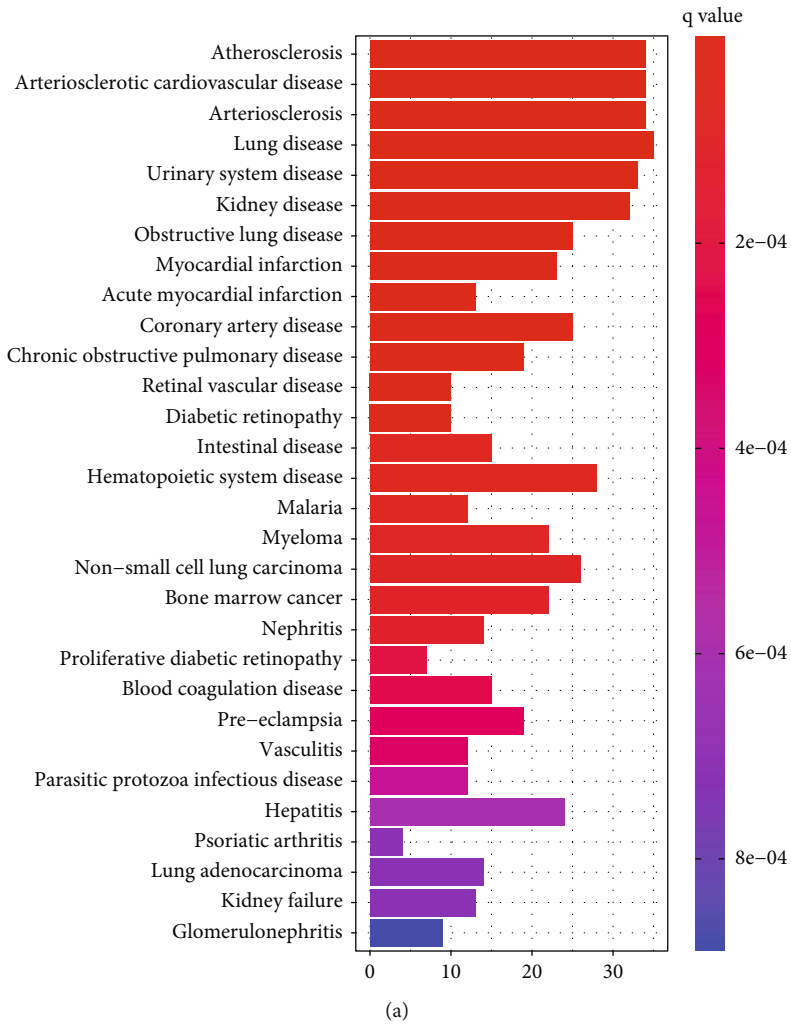

(a)

Figure 5: Continued.

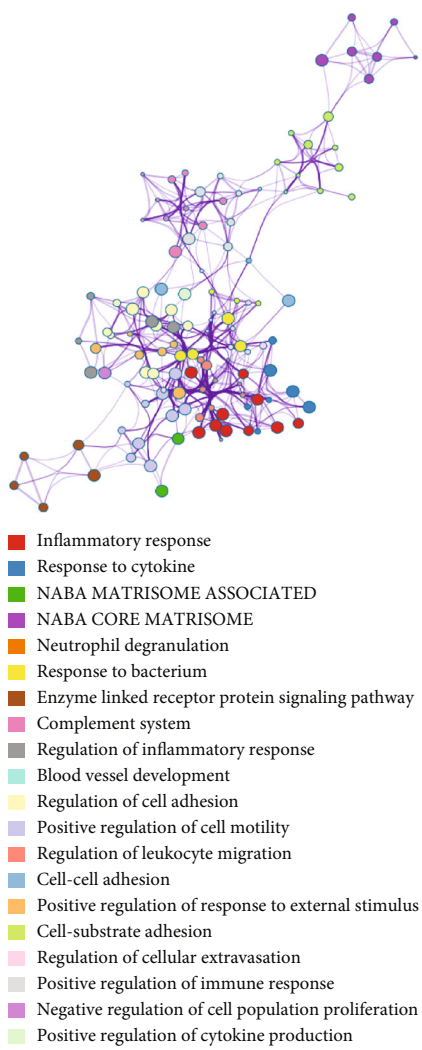

(b)

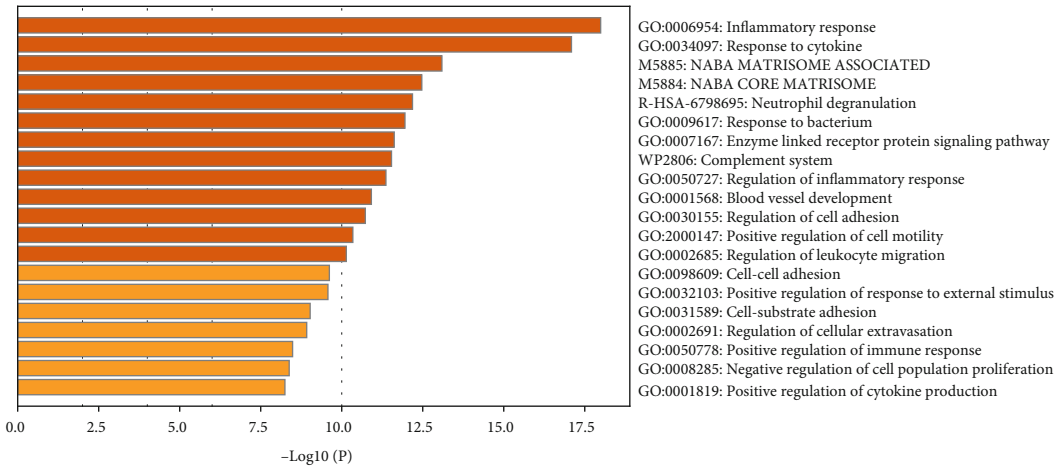

(c)

Figure 5: Disease Ontology (DO) and Metascape analyses of DEGs. (a) DO enrichment analysis was performed on DEGs. The x-axis shows the number of genes enriched on the terms, and the y-axis shows the pathway terms. The q value of each term is colored according to the legend. DEGs are differentially expressed genes. (b) The network of the top 20 enriched term clusters. The color indicates cluster identification, the thickness of the edge indicates the similarity score, and terms with a similarity score> 0.3 are connected by an edge. (c) The top 20 clusters are shown in a heat map. Color is used to indicate cluster identification: the lower the P value, the darker the color.

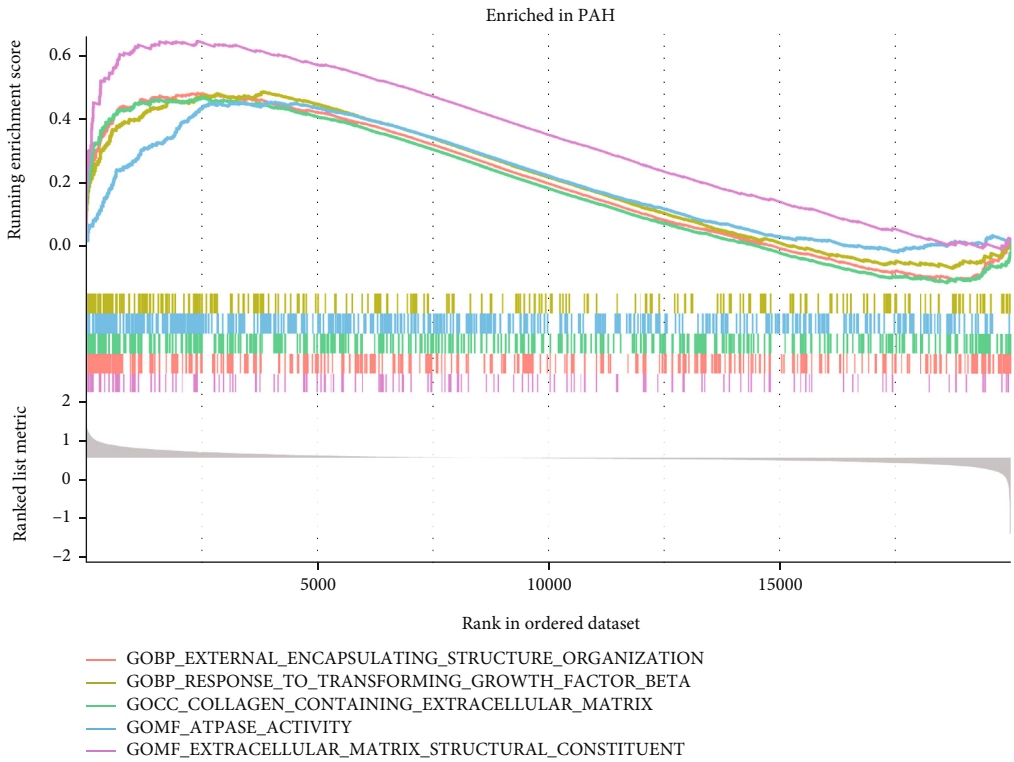

(a)

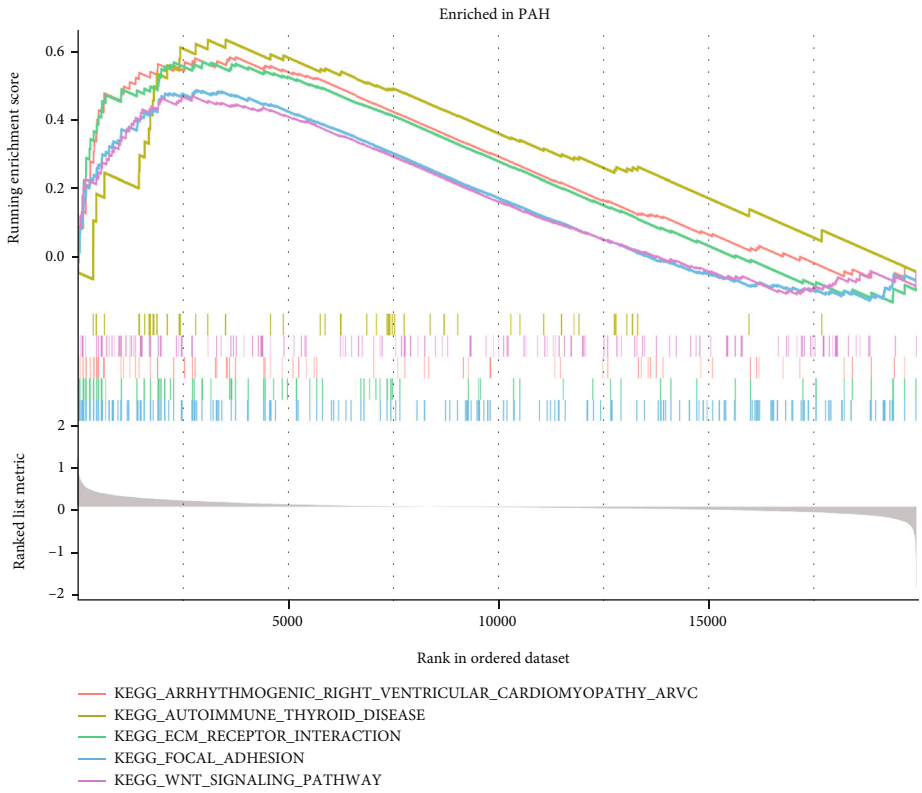

(b)

Figure 6: LogFC values were calculated for all genes, and gene set enrichment analysis (GSEA) analysis was performed based on logFC using "c2.cp.kegg.v7.4.symbols.gmt" and "c5.go.v7.4.symbols.gmt" in the PAH samples. (a) Analysis of the GO pathway terms for all genes enriched in the PAH samples using GSEA. (b) Analysis of the KEGG pathway terms for all genes enriched in the PAH samples using GSEA. PAH: pulmonary arterial hypertension.

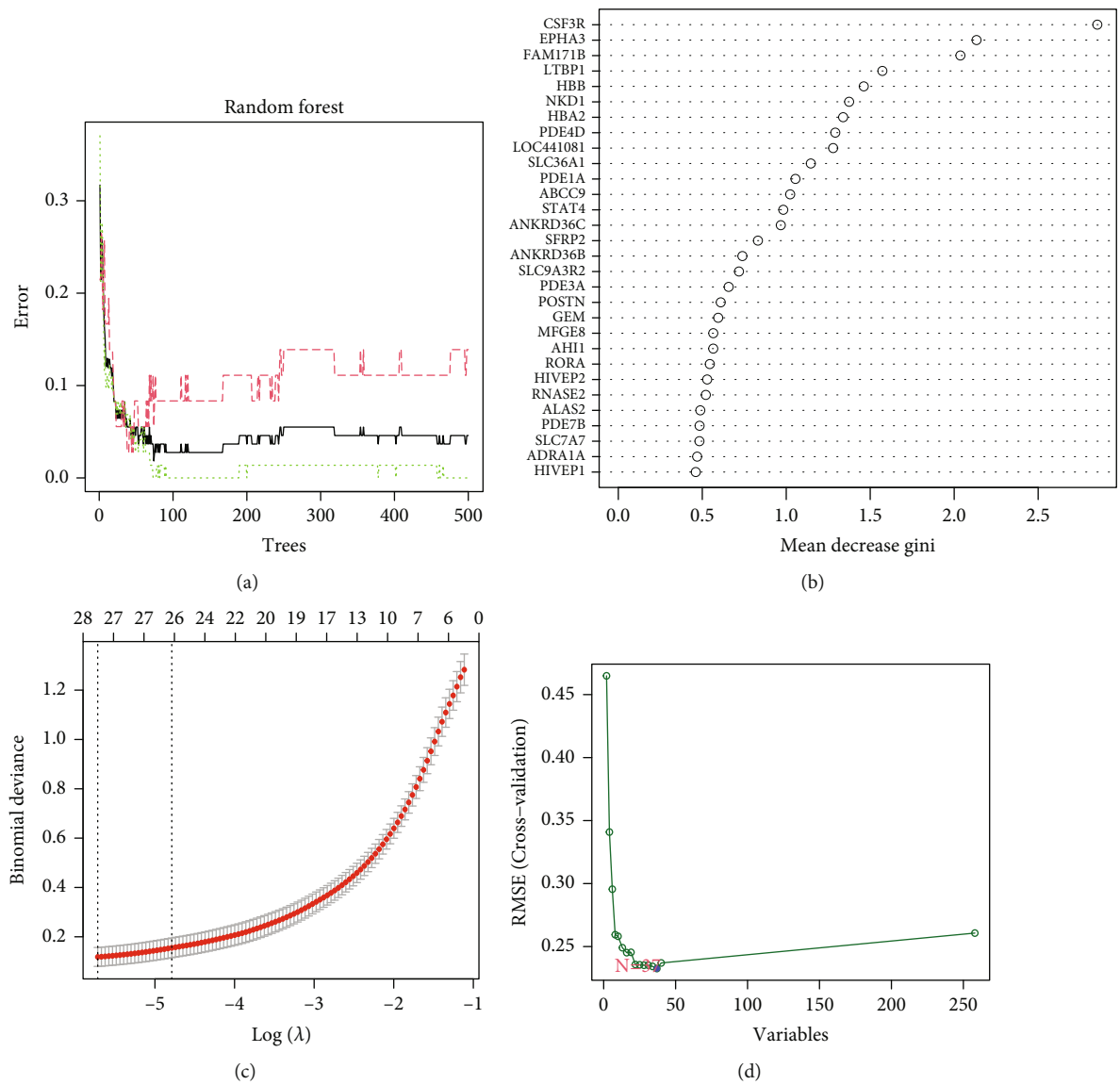

Figure 7: Construct multiple machine learning models based expression of DEGs. (a) The effect of the decision tree number on the error rate. The x-axis denotes the number of decision trees, while the y-axis shows the error rate. When approximately 100 decision trees are used, the error rate is generally steady. (b) The results of Gini coefficient method in a random forest classifier. The x-axis displays the genetic variable, and the y-axis the significance index. (c) Fine-tuning the least absolute shrinkage and selection operator (LASSO) model's feature selection. LASSO regression was used to narrow down the DEGs, resulting in the discovery of 28 variables as potential markers for PAH. The ordinate represents the value of the coefficient, the lower abscissa represents log(λ), and the upper abscissa represents the current number of nonzero coefficients in the model. (d) A plot illustrating the process of selecting biomarkers using the support vector machine-recursive feature elimination (SVM-RFE) technique. The SVM-RFE technique was used to identify a subset of 37 characteristics from the DEGs. DEGs: differentially expressed genes; PAH: pulmonary arterial hypertension.

disease feature associated with each module. MM denoted the association between MEs and gene expression profiles. Then, the GS of the modules, which represents the association between genetic markers and disease characteristics, was determined. Genes with high MM and GS values in the critical module were significantly associated with disease characteristics. We set MM>0.55 and GS>0.55 as the filter criteria for selecting important genes in the critical module after its selection.

2.8. Screening and Verification of Biomarkers. Next, intersecting genes identified using the four different methods were chosen for subsequent analyses. The GSE53408 was used as validation sets for the comprehensive assessment of the efficacy of critical diagnostic markers. The datasets mentioned above were employed to validate differences in diagnostic markers expression between samples collected from normal subjects and PAH patients. Diagnostic effectiveness was then assessed by calculating the receiver operating

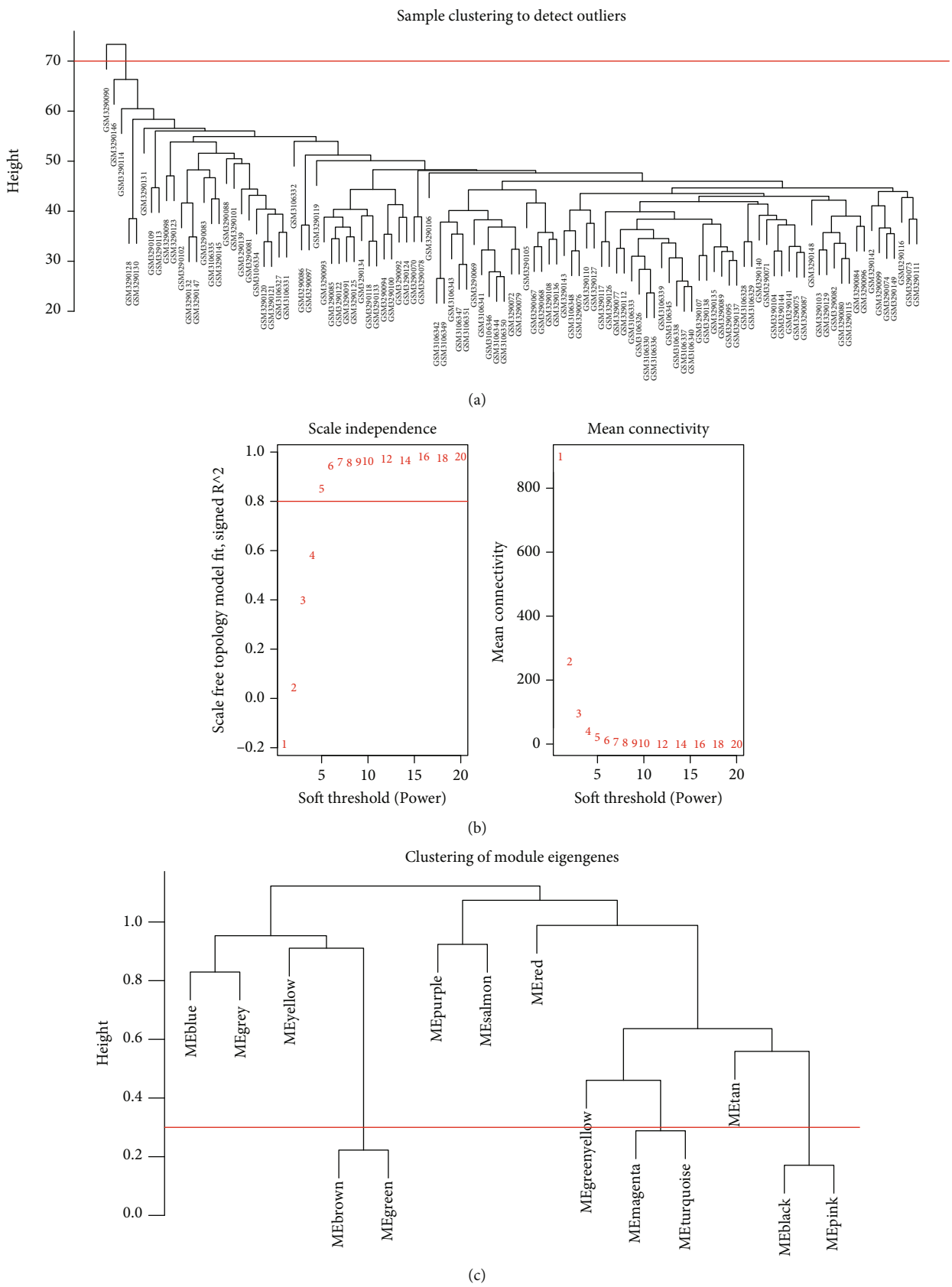

Figure 8: Continued.

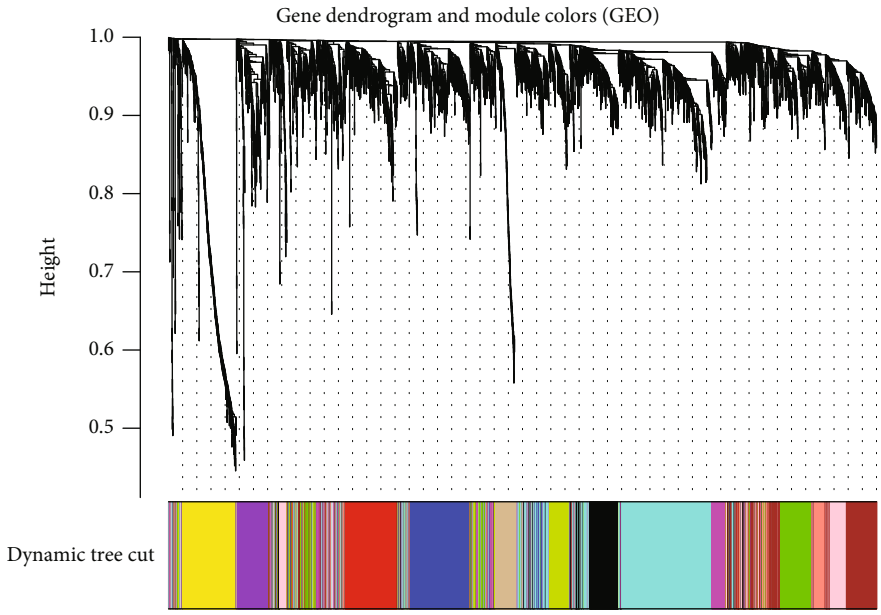

(d)

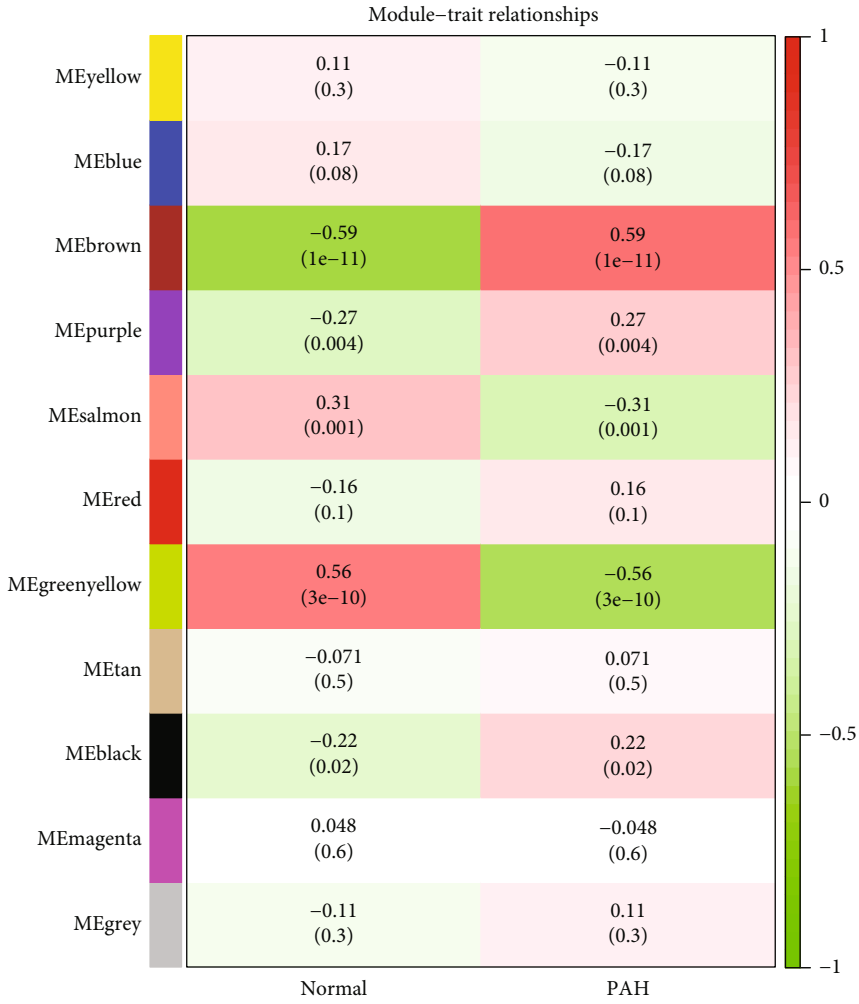

(e)

Figure 8: Continued.

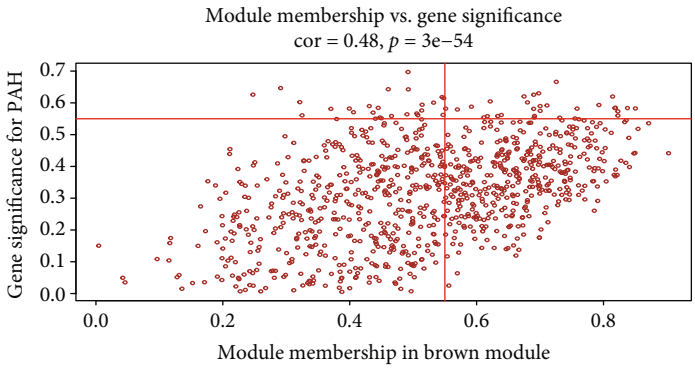

(f)

Figure 8: Analysis of the weighted coexpression network in merged dataset. (a) Sample clustering of merged data set. The samples were classified into two clusters that were significantly distinct. Cluster 1 was chosen for further analysis. (b) Selection of optimal thresholds. The threshold is 5. (c) The threshold was set to 0.3 and minimum number of genes per module to 50 to merge modules that are similar in the cluster tree. (d) Different modules are produced and shown in different colors by aggregating genes with strong correlations into a same module. (e) Analysis of correlations between modules and PAH. The brown module was significantly correlated with PAH ($r = 0.59$; $P = 1e-11$) and with normal samples ($r = -0.59$; $P = 1e-11$). (f) Correlation plot between MM (x-axis) and GS (y-axis) of genes contained in the brown module. PAH: pulmonary arterial hypertension.

characteristic (ROC) according to the area under the curve (AUC), which provided insight into the algorithm's predictive potential. A value of $P < 0.05$ indicated two-sided statistical significance.

2.9. Immune Cell Infiltration Analysis. Using CIBERSORT with the merged matrix, we evaluated immune cell infiltration. Afterwards, PCA was performed on the results using the ggplot2 function in R and a 2D PCA map was produced. The "corrplot" function was used to plot correlated data. Correlations between 22 distinct infiltrating immune cell types were determined using the "corrplot" function [31]. We constructed violin plots using the "ggplot2" function to illustrate variations in immune cell infiltration.

2.10. Interaction between Immune Cells and Biomarkers. The Spearman's rank correlation test, performed with the help of the R program, was used to investigate the potential significance of a link between infiltrating immune cells and newly discovered biomarkers. Correlations were shown through a chart approach using the "ggplot2" function.

2.11. Statistical Analysis. The moderate t -test was performed to filter DEGs, while Fisher's exact test was used to evaluate GO and KEGG annotation enrichments. Wilcoxon's test was conducted to determine immune cell counts. The statistical analysis was done in the R program (version 4.1.1).

3. Results

3.1. Analysis Process. The workflow of this study is shown in Figure 1.

3.2. Data Processing and DEG Selection. Expression matrices for the GSE113439 and GSE117261 datasets were merged, which included 27 normal samples and 22 PAH samples. Next, normalization and batch effect removal were performed, and a 2D PCA plot was used to represent the dataset before and after batch effect removal (Figures 2(a) and 2(b)). After data preparation, using the R software, we identified 258 DEGs in the normalized data, as illustrated by the heat and volcano maps shown in Figures 3(a) and 3(b). DEGs obtained by differential analysis of PAH and normal samples, which included 169 upregulated and 89 downregulated genes are shown in Supplementary Table 1. Table 2 displays the top 20 most upregulated and downregulated genes.

3.3. Functional Correlation Analysis. The results of the GO enrichment analysis of DEGs are mainly presented in the following aspects: biological process (BP): ribosome biogenesis, mitotic nuclear division regulation, and mitotic cytokinesis; cellular component (CC): preribosome and centriole; and molecular function (MF): DNA-dependent ATPase and DNA helicase activity (Figure 4(a); Supplementary Table 2). DEGs were abundant in eukaryotes, melanoma, hypertrophic cardiomyopathy, and dilated cardiomyopathy, according to the KEGG analysis (Figure 4(b); Supplementary Table 3). Figure 5(a) illustrates the findings of the DO analysis (Supplementary Table 4). DEGs were most related to osteoarthritis, lung disorders including chronic obstructive pulmonary disease and obstructive lung disease, and cardiovascular diseases including arteriosclerosis, atherosclerosis, myocardial infarction, and coronary artery disease. To further comprehend the functional and metabolic pathways connected with these DEGs, an enrichment analysis was conducted utilizing Metascape to uncover the top 20 clusters with the highest significant enrichment (Figures 5(b) and 5(c); Supplementary Table 5). The results of Metascape enrichment are mainly manifested in the inflammatory response, response to cytokines, and response to bacteria. GSEA results suggested that in PAH samples, immune response inactivation and adaptive immune responses dominated GO biological processes (Figure 6(a); Supplementary Table 6). And the enrichment pathway in

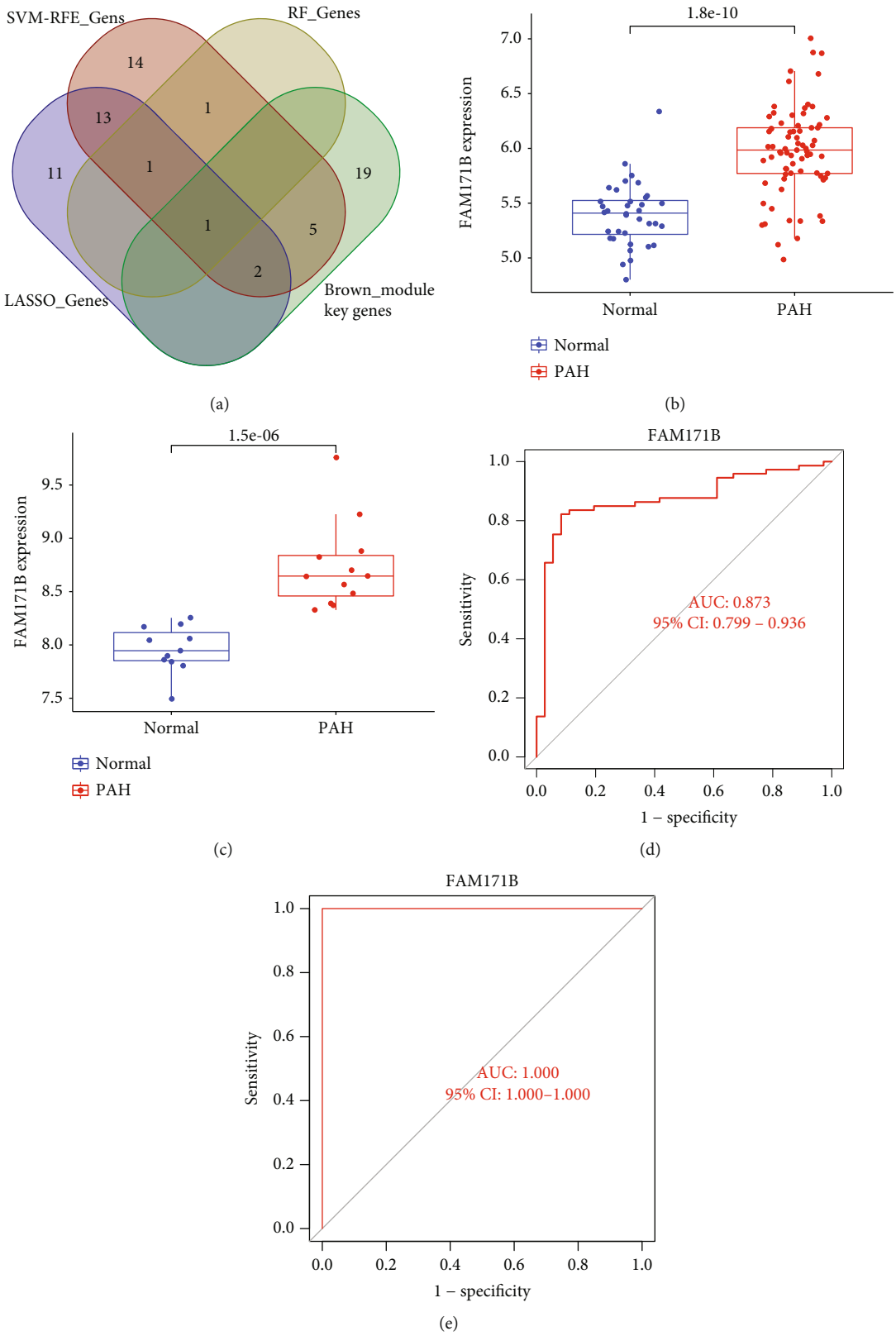

Figure 9: Screening and verification of diagnostic markers. (a) Venn diagram showing overlapping marker with RF, Lasso, SVM-RFE, and WGCNA. FAM171B mRNA expression is significantly higher in PAH samples than in normal samples, (b) the combined dataset ($P = 1.8e-10$) and (c) the GSE53408 ($P = 1.5e-06$). ROC curves were constructed using publicly available data to assess the diagnostic accuracy of FAM171B for PAH. (d) The combined dataset had an AUC of 0.873. (e) GSE53408 had an AUC of 1. ROC: receiver operating characteristic; AUC: area under the ROC curve; PAH: pulmonary arterial hypertension.

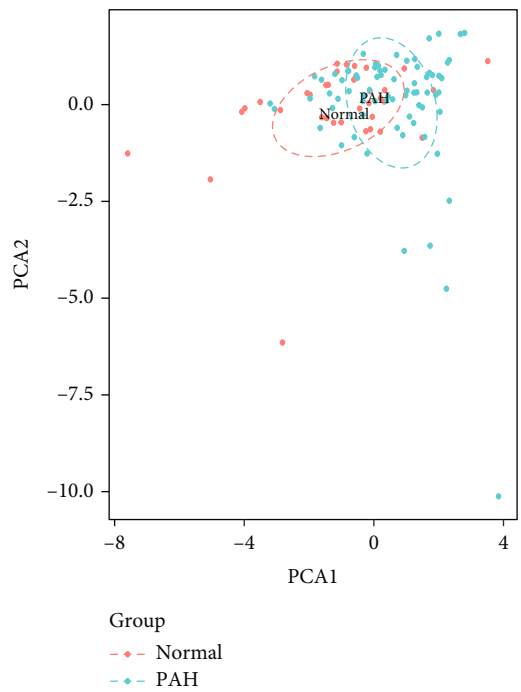

(a)

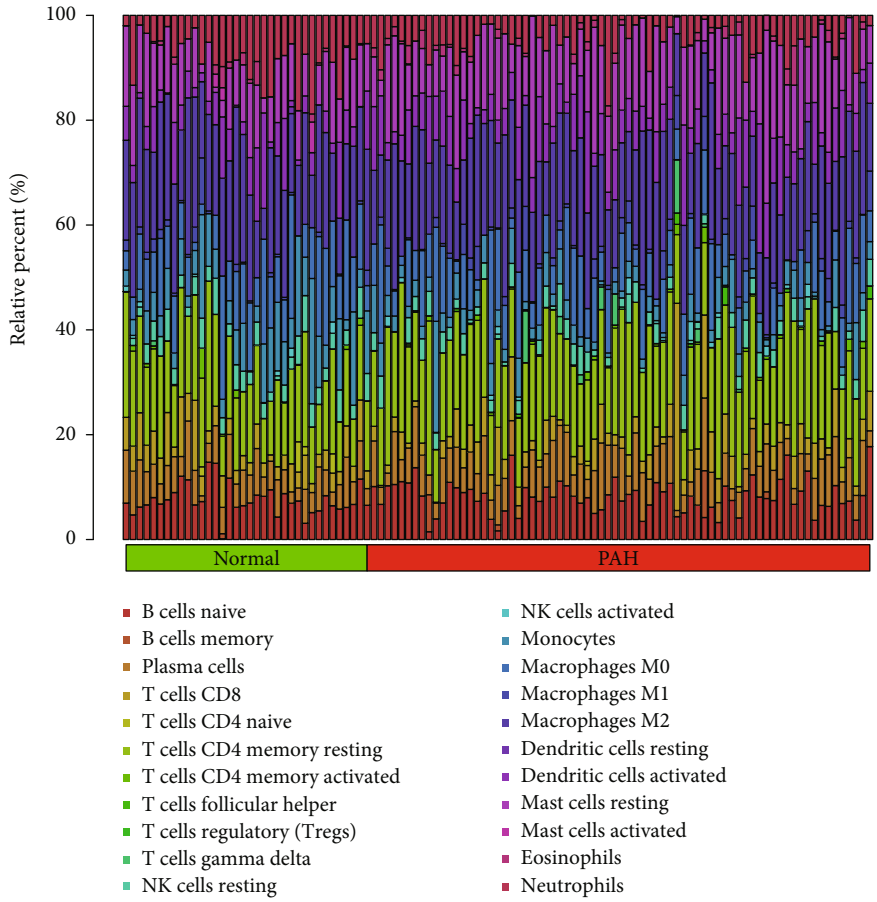

(b)

Figure 10: Continued.

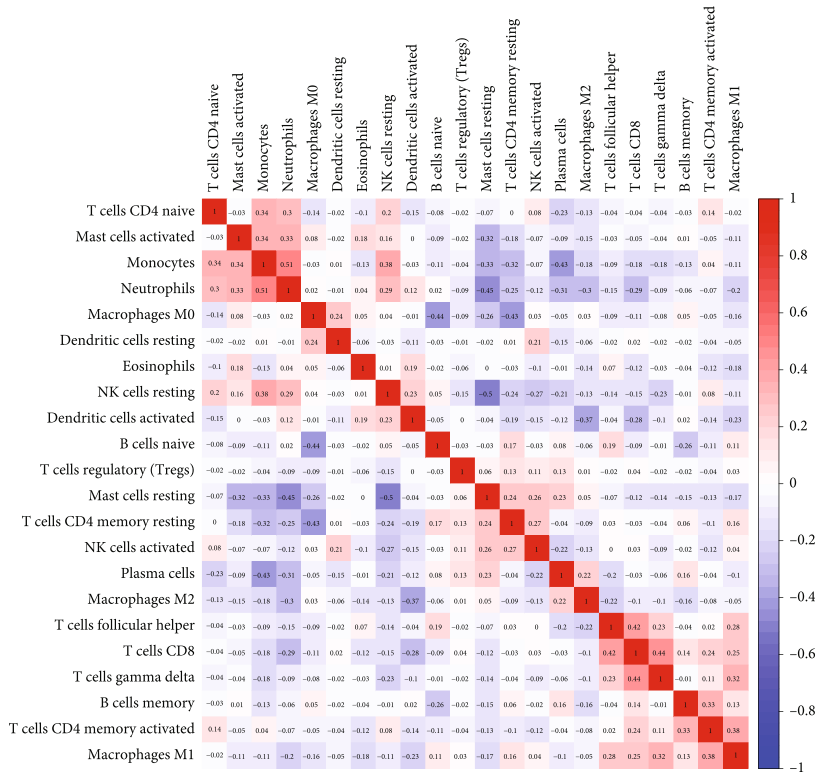

(c)

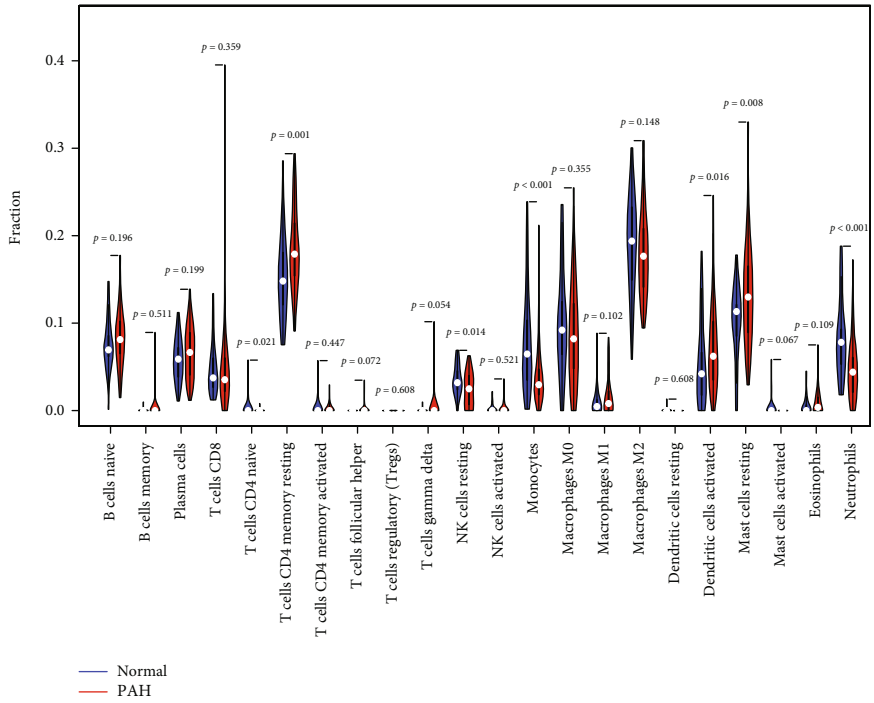

(d)

Figure 10: Comparing the composition of immune cell infiltration in the normal and PAH samples by using the combined data matrix of GSE113439 and GSE117261 and visualized the results. (a) PCA cluster plot of immune cell infiltration between normal and PAH samples. (b) The heat map of the 22 subpopulations of immune cells. (c) Correlation heat map of 22 types of immune cells. The size of the colored squares represents the strength of the correlation: red represents a positive correlation; blue represents a negative correlation. The redder the color, the stronger the correlation. (d) Violin diagram of the proportion of 22 types of immune cells. (The normal samples are marked as blue color and PAH samples marked as red color. P values <0.05 were considered as statistically significant.) PAH: pulmonary arterial hypertension; PCA: principal component analysis.

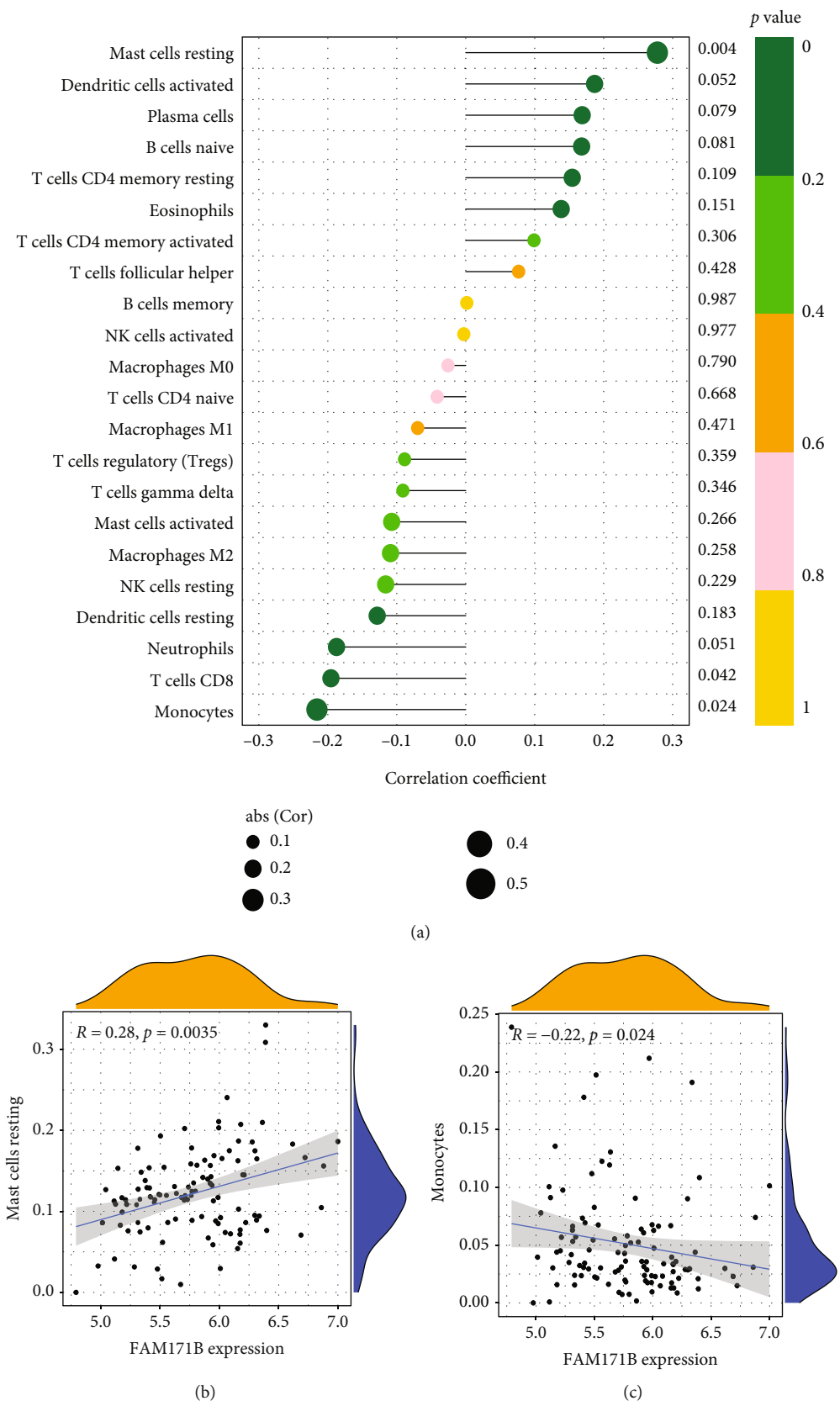

Figure 11: Continued.

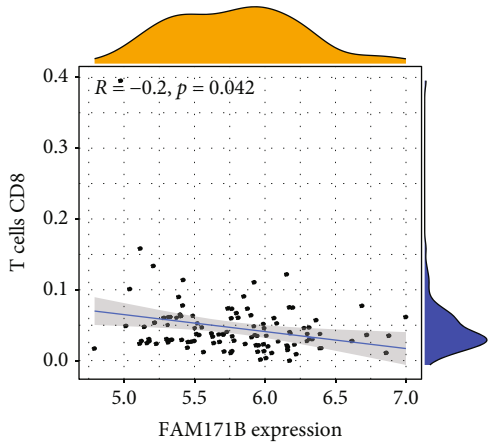

(d)

Figure 11: Visualization of the results of immune cell infiltration and FAM171B correlation analysis based on the combined data matrix of GSE113439 and GSE117261. (a) Correlation between FAM171B and infiltrating immune cells. The size of the dots represents the strength of the correlation between genes and immune cells: the larger the dots, the stronger the correlation and vice versa. The color of the dots represents the P value: the greener the color, the lower the P value, and the yellower the color, the larger the P value. ($P < 0.05$ was considered statistically significant.) The correlation analysis in the expression of FAM171B and mast cells resting (b), monocytes(c), and CD8 T cells (d).

KEGG mainly includes the chemokine signaling pathway, cytokine–cytokine receptor interaction pathways, and hematopoietic cell pathways (Figure 6(b); Supplemental Table 6). These findings suggest that the immune response significantly influences the development of PAH.

3.4. Random Forest-Identified Key Genes. A random forest filter was then used to narrow down the 258 DEGs. After determining the optimal parameter, mtry (the optimal number of variables in the binary tree in a node), we performed recurrent random forest classification on all possible values of 1–258 variables and evaluated the average error rate of the model. The average error rate when all variables were chosen is shown in Figure 7(a). Then, we chose 3 as the variable number parameter. The number of variables, as well as the out-of-band error, was kept to a minimum. Finally, we determined the relationship between the model error and the number of decision trees using 500 trees as the model's parameters (Figures 7(a) and 7(b)), which showed a steady error in the model. After that, we calculated the variable significance of the output results (Gini coefficient approach) throughout the random forest model building process in terms of decreasing accuracy and decreasing mean square error. Next, we selected three genes with importance greater than 2 (*CSF3R*, *EPHA3*, and *FAM171B*) as prospective genes for subsequent investigations.

3.5. Selection of Significant Genes by Using the LASSO Regression Model. To construct a LASSO regression model, 258 DEGs between the two groups were chosen. Next, the best suitable log (λ) (=28) values were determined through 10-fold cross-validation (Figure 7(c)). Finally, 28 genes with nonzero coefficients were identified (*LTBP1*, *CSF3R*, *ANKRD36C*, *HBB*, *HBA2*, *NKD1*, *PDE4D*, *HIVEP1*, *POSTN*, *ADRA1A*, *FAM171B*, *BICC1*, *H1-0*, *RGS5*, *AHCYL2*, *FZD7*, *RGS1*, *WIF1*, *LRRN4*, *PI15*, *CD14*, *ACE2*, *C5*, *BPIFB1*, *SOSTDC1*, *IL13RA2*, *FAM107A*, and *TFPI2*) and used for subsequent analyses.

3.6. Selection of Significant Genes by Using the SVM-RFE Model. A total of 37 genes (*LTBP1*, *FAM171B*, *TSHZ2*, *CSF3R*, *NT5E*, *EPHA3*, *HBB*, *HBA2*, *STAT4*, *ANKRD36C*, *PDE7B*, *ADRA1A*, *PDE3A*, *ECM2*, *AHCYL2*, *NKD1*, *SLC9A3R2*, *WIF1*, *HIVEP2*, *PSD3*, *ALAS2*, *LOC441081*, *KRT4*, *H1-0*, *FGR*, *ABCC9*, *AHI1*, *GEM*, *SFRP2*, *C5*, *RORA*, *BICC1*, *IL13RA2*, *PDE4D*, *FZD7*, *POSTN*, and *COL14A1*) with the lowest root mean square error were fitted into the SVM classifier by the SVM-RFE method (Figure 7(d)).

3.7. Gene Coexpression Network and Module Identification. First, genes were ordered from the largest to smallest in terms of variance, and the top 25% (4992) of these genes were selected for subsequent investigations. Second, the flashClust function in R was used to carry out a cluster analysis, with a threshold of 65 and one outlier sample identified and eliminated (Figure 8(a)). Cluster 1 contained 108 samples, which we intended to maintain. Third, the "pickSoftThreshold" mechanism of the WGCNA software package was used to filter values from the power parameter range of 1-20. In this research, we created a scale-free network with a soft threshold of a power of 5 (scale − free R2 = 0.85) (Figure 8(b)). The threshold was set at 0.3, and the minimum gene number per module was set at 50, enabling the merging of similar modules in the cluster tree (Figure 8(c)). As shown in Figure 8(d), we found 11 modules containing genes with similar coexpression characteristics. The colors used to differentiate the modules were chosen at random. As compared to the other modules, the module eigengene (ME) of the brown model showed the most significant positive correlation and relationship with PAH

($r = 0.59$; $P = 1e - 11$) (Figure 8(e); Supplementary Table 7). Thus, the brown module comprised 921 genes. In addition, we evaluated the correlation between gene MMs and GSs in the brown module. As expected, significant positive correlations were discovered between the MMs and GSs of brown module genes (cor = 0.48, $P = 3e - 54$) (Figure 8(f) and Supplementary Table 8). In the brown module, 27 essential genes (*ABCC9*, *AHI1*, *ANKRD36*, *ANKRD36B*, *ANKRD36C*, *ARHGAP21*, *CACNA2D1*, *ECM2*, *FAM171B*, *FRMD4B*, *GLT8D2*, *JMY*, *KLF12*, *LUC7L3*, *MACF1*, *N4BP2*, *NBEAL1*, *NT5E*, *PHIP*, *PNISR*, *RORA*, *RPS6KA5*, *RUFY3*, *SHPRH*, *WIF1*, ZNF483, and *ZNF711*) were identified for subsequent analyses.

3.8. Biomarker Screening and Verification. A diagnosis-related gene was generated by merging the genes identified using the four approaches (Figure 9(a)). The difference in FAM171B expression between normal and PAH samples in the combined dataset and GSE53408 dataset were $P = 1.8e - 10$ (Figure 9(b)) and $P = 1.5e - 06$ (Figure 9(c)), respectively. We generated ROC curves for the combined dataset, and the GSE53408 dataset found that their ROC AUCs were 0.873 (Figure 9(d)) and 1 (Figure 9(e)), respectively. Although the small sample quantity may have influenced the ROC values, these results demonstrate that FAM171B helps to distinguish PAH samples from normal samples.

3.9. Immune Cell Infiltration Analysis Findings. The combined data matrices of the GSE113439 and GSE117261 datasets were analyzed using CIBERSORT, and the findings of this analysis are shown in Supplementary Table 9.

PCA analysis was used to determine the difference between PAH and healthy samples. The PCA cluster analysis revealed a statistical difference between the two groups' immune cell infiltration (Figure 10(a)). Using the data matrix derived from the combined GSE113439 and GSE117261 datasets, we assessed the infiltrating immune cell composition in PAH and healthy samples (Figure 10(b)). According to our results, the percentage of CD4 naïve T cells ($P < 0.05$), resting NK cells ($P < 0.05$), monocytes ($P < 0.05$), and neutrophils ($P < 0.05$) was substantially higher in healthy samples than in PAH samples. In PAH tissues, however, the fraction of resting CD4 memory T cells ($P < 0.05$), activated dendritic cells ($P < 0.05$), and resting mast cells ($P < 0.05$) was considerably greater than in healthy samples (Figure 10(c)). In addition, the interaction across 22 immune cells was studied (Figure 10(d)). Naïve CD4 T cells showed significant association with monocytes ($r = 0.34$), neutrophils ($r = 0.3$), and resting NK cells ($r = 0.2$) and a significantly inverse relationship with activated dendritic cells ($r = -0.15$) and resting mast cells ($r = -0.07$). Monocytes showed significant association with neutrophils ($r = 0.51$) and resting NK cells ($r = 0.38$) and a significantly inverse relationship with resting mast cells ($r = -0.33$), activated dendritic cells ($r = -0.03$), and resting memory CD4 T cells ($r = -0.32$). Neutrophils showed significant association with resting NK cells ($r = 0.29$) and activated dendritic cells ($r = 0.12$) and a significantly inverse relationship with resting mast cells ($r = -0.45$) and resting memory CD4 T cells ($r = -0.25$). Resting NK cells showed significant association with activated dendritic cells ($r = 0.23$) and a significantly inverse relationship with resting mast cells ($r = -0.5$) and resting memory CD4 T cells ($r = -0.24$). Activated dendritic cells showed significant association with resting mast cells ($r = -0.04$) and resting memory CD4 T cells ($r = -0.19$). Resting mast cells are significantly associated with resting memory CD4 T cells ($r = 0.24$).

3.10. Correlation between FAM171B and Infiltrating Immune Cells. We evaluated the relationship between the immune infiltration outcomes and FAM171B. As shown in Figure 11(a), FAM171B was strongly connected with resting mast cells ($r = 0.28$, $P = 0.0035$; Figure 11(b)) and negatively associated with CD8 T cells ($r = -0.2$, $P = 0.042$; Figure 11(c)) and monocytes ($r = -0.22$, $P = 0.024$; Figure 11(d)). Supplementary Table 10 shows the relationship between FAM171B and immune cells.

4. Discussion

PAH causes shear stress, endothelial damage in the artery wall, and unfavorable pulmonary vascular reconstruction over time. A distinctive feature of PAH is pulmonary artery remodeling caused by an imbalance of vascular wall proliferation and apoptosis; however, the precise mechanism by which PAH occurs remains unknown [32]. Consequently, it is essential to explore the biological processes underlying the incidence and progression of PAH to allow earlier identification and treatment of the disease, improve the prognosis of the condition, and develop effective strategies for reversing the disease process [33].

By comparing gene expression between PAH and normal samples, we identified 258 significant DEGs, including 169 upregulated and 89 downregulated DEGs. These DEGs were subsequently analyzed by GO and Metascape function-related enrichment analyses. These genes exhibited significant correlations with immune responses and inflammatory signals (e.g., neutrophil activation during the immune response, myeloid leukocyte migration, and neutrophil activation). KEGG analysis revealed that genes involved in the coagulation cascades and complement, NF-κB signaling, chemokine signaling, and ECM–receptor interactions were enriched. The functional enrichment analysis results confirmed further that inflammation and immunity play a role in the occurrence and progression of PAH. Irrespective of the etiology or type of PAH, inflammation usually occurs in the lungs of patients suffering from the disease, with immune cell infiltration [34]. Recruited immune cells produce localized and circulating cytokines, which cause alterations in the pulmonary vascular system; these include interleukin (IL)-1, IL-2, IL-4, IL-8, and IL-12p70, tumor necrosis factor (TNF)-α, macrophage inflammatory protein-1α, and the chemokines, CXC3L1 (fractalkine), CCL5 (RANTES), and CCL2 [35, 36]. In patients with PAH, a rise in the levels of serum inflammatory markers is a prognostic indicator of disease severity and patient survival [35]. Inflammatory indicators, such as CCL2, CCL5, and

fractalkine, have been associated with severe PAH [37]. In the context of PAH, IL-6 is an indicator of right ventricular failure, and investigations on humans and animals have revealed an elevation in IL-6 levels during PAH [38]. In addition, alterations in immunological processes significantly contribute to PAH by inducing inflammatory cell recruitment, pulmonary vasculature remodeling, and autoimmune reactions [39]. In the PAH model, NF-κB signaling is activated, and sevoflurane can modulate NF-κB signaling by inhibiting p-IκB, p-p65, and p65 levels, reducing pulmonary fibrosis, and preventing PAH [40]. TLR/NF-κB pathway inhibition may also benefit PAH patients, reducing inflammatory and immune responses and pulmonary vascular remodeling [41]. Cytokines IL-1β, IL-6, and TNF-α are involved in PAH-related modifications of the pulmonary artery wall [42]. The TLR family is pattern recognition receptors that recognize microbial fragments and activate the NF-κB pathway. Decreased TLR3 expression is associated with endothelial cell death and changes in the pulmonary artery wall [43]. These data support the notion that inflammation and immune responses play a role in PAH development.

In the last 20 years, several different machine learning strategies and feature extraction algorithms have been widely applied for diagnosing and predicting diseases [44–49]. Most of these studies apply machine learning methods to simulate the progression of malignancy and find significant characteristics that are then used in a categorization scheme. According to the results of our study and those of other researchers [50–56], this was the first study in which analytical methods for identifying PAH biomarkers use many machine learning approaches, including RF, Lasso, SVM-RFE, and WGCNA. Akter et al. [57] suggest that merging different machine learning algorithms may boost prediction performance and construct highly accurate diagnostic models. Thus, using the four machine learning approaches enabled us to identify potentially significant biomarkers critical for the evaluation of PAH. Finally, in this study, FAM171B was selected and shown to be accurate for in-depth verification, confirming our prediction and proving its feasibility through the integration approach.

FAM171B is a protein yet to be identified, and its function is unknown. A group of researchers reported on a mutant mouse with gastroschisis that had a mutation in *Slit3*, as well as an extra point mutation in Fam171A1, a related family member that has 35% amino acid identity with FAM171B [58]. In addition to gastroschisis, this mutant mouse was found to have a double-outlet right ventricle with an atrioventricular septal defect, atrioventricular septal defect, and ventricular noncompaction [59]. Furthermore, FAM171B is a member of the Fam171b protein family, a family of secreted proteins with high and selective expression levels in the brain; however, its function has not yet been determined. Owing to these traits, *Fam171b* is one of 106 genes known as the "core brain ignorome" [60]. Only a few studies have demonstrated that this gene is involved in developing congenital heart disease; however, its precise function in the illness's progression remains unknown. Since the cardiopulmonary vascular system is closely related to PAH, it is likely to become a potential therapeutic target for reversing or delaying PAH progression.

We utilized CIBERSORT to evaluate immune cellular components in PAH and normal samples and discovered that PAH-associated biological processes are strongly connected to several immune cell types. This investigation showed that resting memory CD4 T cells, activated dendritic cells, and resting mast cells are considerably expressed in PAH samples. However, resting NK cells, monocytes, and neutrophils are significantly expressed in normal samples. In addition, it was discovered that *FAM171B* is substantially expressed in PAH tissues. The correlation analysis revealed that resting mast cells were significantly associated with *FAM171B*, whereas CD8 T cells and monocytes were negatively associated with *FAM171B*, indicating that high *FAM171B* expression was closely associated with the extent of infiltration of resting mast cells and CD8 T cells. These results prove that the high resting mast cell counts reported in PAH tissues and the high monocyte counts observed in normal tissues may be connected to FAM171B. Therefore, the results of this analysis indicate that FAM171B and many inflammatory cell types are involved in the process of PAH; this supports the need for further research into PAH molecular pathways.

IL-5, IL-4, and IL-13, as well as antibodies (particularly IgE), are produced by $CD4^+$ T_H2 cells [61]. Several studies using animal models have investigated T_H2 immune responses as causative factors for PAH. For instance, T_H2 responses, which include antigen sensitization and subsequent antigen challenge, may result in smaller pulmonary artery muscularization due to interactions between $CD4^+$ cells and IL-13 [62]. Hypoxia induces the resistin-like alpha protein, which is associated with vascular remodeling [63]. The T_H2 immune response also induces this protein. Dendritic cells (DCs) essential for activating naïve T cells are crucial antigen-presenting cells in the immune function. The ability of DCs to develop into many cell types, including endothelial cells (ECs), may play a significant function in the pathophysiology of vascular diseases [64]. The accumulation of immature DCs in altered pulmonary arteries in experimental and clinical PAH tissue samples suggests that they may play a role in the immunopathology of PAH [65]. Antibodies in the serum of patients with PAH and collagen vascular disease directed against fibroblasts and endothelial cells, in addition to nuclear antigens, may be a contributing factor in the formation of these antigen-presenting cells [66]. Wang et al. [67] found that PAH patients had a lower proportion of monocyte-derived DCs in their peripheral blood, suggesting the involvement of the T_H1 immune response in the pathogenesis of PAH. During PAH, mast cells secrete the vascular endothelial growth factor, which may induce dysfunction in angiogenesis [68]. In addition, during PAH, perivascular mast cells produce chymase [69]. As chymase can induce localized angiotensin II production, endothelin activation, and matrix metalloprotease activation, it may be involved in vascular remodeling and vasomotor tone regulation. In PAH-associated fibrosis, mast cell chymase may be a significant target for the therapy of immune cell- and autoantibody-associated pulmonary hypertension [70]. The

levels of total serum tryptase in PAH samples were significantly greater than those in control samples [71], indicating high mast cell counts or enhanced mast cell activation. Thus, multiple studies have identified the important role of immune cell infiltration in PAH.

There were a few problems with this research. First, increasing the number of individuals represented in the sample and filling out all genetic data will make the illness analysis and prediction more reliable. Second, to give reliable evidence for the development of targeted therapeutic medicines, the potential marker genes and pathways discovered in this study need to be confirmed in additional research. In the end, investigating the protein expression levels of marker genes may provide more proof of the possible roles that marker genes play in PAH. Additional research is necessary to validate the biological function for our results.

5. Conclusions

Overall, FAM171B has strong diagnostic utility and is associated with immune cell infiltration for PAH. We also discovered that resting memory CD4 T cells, activated dendritic cells, and resting mast cells may all play a role in the development and progression of PAH. Furthermore, FAM171B was significantly associated with resting mast cells and negatively associated with CD8 T cells and monocytes. These immune cells possibly affect PAH development, and further research into their action may help identify immunotherapeutic targets and improve immunomodulation-based PAH treatment.

Data Availability

The datasets used and analyzed during the current study are all available from the corresponding author.

Conflicts of Interest

The authors state that the publication of this work does not involve any conflicts of interest.

Authors' Contributions

L.H.Q and W.J.L were engaged to come up with the concept; L.H.Q was responsible for the R code. W.J.L. was responsible for the methodology; Z.G.Y is responsible for the interpretation of the results; L.H.Q. and W.J.L. was in charge of the writing—original draft production; and W.P.L. was responsible for reviewing and editing. The final, published version of the work has been reviewed and approved by all authors. Lai-Hao Qu and Wen-Juan Luo contributed equally to this work, and are the co-first authors.

Acknowledgments

This project was made easier to finish because of GEO's assistance. We would like to use this opportunity to thank the GEO network for the kind way in which it shares vast volumes of data.

Supplementary Materials

Supplementary Table 1: The results of differentially expressed genes (DEGs). Supplementary Table 2: Gene Ontology (GO) enrichment analysis results of differentially expressed genes (DEGs). Supplementary Table 3: Kyoto Encyclopedia of Genes and Genomes (KEGG) enrichment analysis results of differentially expressed genes (DEGs). Supplementary Table 4: Disease Ontology (DO) enrichment analysis results of differentially expressed genes (DEGs). Supplementary Table 5: Metascape function analysis results of differentially expressed genes (DEGs). Supplementary Table 6: results of Gene Set Enrichment Analysis (GSEA) of gene expression matrix. Supplementary Table 7: results of all genes in brown module. Supplementary Table 8: results of key genes in brown module. Supplementary Table 9: results of analyzing the combined data matrix of GSE113439 and GSE117261 using CIBERSORT. Supplementary Table 10: results of the correlation of FAM171B with immune cells. *(Supplementary Materials)*

References

[1] J. J. Ryan and S. L. Archer, "The right ventricle in pulmonary arterial hypertension: disorders of metabolism, angiogenesis and adrenergic signaling in right ventricular failure," *Circulation Research*, vol. 115, no. 1, pp. 176–188, 2014.

[2] G. G. Pietra, F. Capron, S. Stewart et al., "Pathologic assessment of vasculopathies in pulmonary hypertension," *Journal of the American College of Cardiology*, vol. 43, no. 12, pp. 25S–32S, 2004.

[3] R. Zolty, "Pulmonary arterial hypertension specific therapy: the old and the new," *Pharmacology & Therapeutics*, vol. 214, p. 107576, 2020.

[4] T. Wang, X. Zheng, R. Li et al., "Integrated bioinformatic analysis reveals YWHAB as a novel diagnostic biomarker for idiopathic pulmonary arterial hypertension," *Journal of Cellular Physiology*, vol. 234, no. 5, pp. 6449–6462, 2019.

[5] S. Bhogal, O. Khraisha, M. Al Madani, J. Treece, S. J. Baumrucker, and T. K. Paul, "Sildenafil for pulmonary arterial hypertension," *American Journal of Therapeutics*, vol. 26, no. 4, pp. e520–e526, 2019.

[6] A. Keshavarz, H. Kadry, A. Alobaida, and F. Ahsan, "Newer approaches and novel drugs for inhalational therapy for pulmonary arterial hypertension," *Expert Opinion on Drug Delivery*, vol. 17, no. 4, pp. 439–461, 2020.

[7] A. K. Toxvig, M. Wehland, D. Grimm, M. Infanger, and M. Kruger, "A focus on riociguat in the treatment of pulmonary arterial hypertension," *Basic & Clinical Pharmacology & Toxicology*, vol. 125, no. 3, pp. 202–214, 2019.

[8] T. Thenappan, M. L. Ormiston, J. J. Ryan, and S. L. Archer, "Pulmonary arterial hypertension: pathogenesis and clinical management," *BMJ*, vol. 360, p. 5492, 2018.

[9] T. Xiong, S. Han, L. Pu et al., "Bioinformatics and machine learning methods to identify FN1 as a novel biomarker of aortic valve calcification," *Frontiers in Cardiovascular Medicine*, vol. 9, p. 832591, 2022.

[10] R. Yu, J. Zhang, Y. Zhuo et al., "Identification of diagnostic signatures and immune cell infiltration characteristics in rheumatoid arthritis by integrating bioinformatic analysis and

machine-learning strategies," *Frontiers in Immunology*, vol. 12, p. 724934, 2021.

[11] M. A. S. Mullah, J. A. Hanley, and A. Benedetti, "LASSO type penalized spline regression for binary data," *BMC Medical Research Methodology*, vol. 21, no. 1, p. 83, 2021.

[12] L. Gutierrez-Gomez, J. Vohryzek, B. Chiem et al., "Stable biomarker identification for predicting schizophrenia in the human connectome," *NeuroImage: Clinical*, vol. 27, p. 102316, 2020.

[13] H. Wang, F. Yang, and Z. Luo, "An experimental study of the intrinsic stability of random forest variable importance measures," *BMC Bioinformatics*, vol. 17, no. 1, p. 60, 2016.

[14] B. Zhang and S. Horvath, "A general framework for weighted gene co-expression network analysisStatistical applications in genetics and molecular biology," vol. 4, 2005.

[15] M. Mura, M. J. Cecchini, M. Joseph, and J. T. Granton, "Osteopontin lung gene expression is a marker of disease severity in pulmonary arterial hypertension," *Respirology*, vol. 24, no. 11, pp. 1104–1110, 2019.

[16] R. S. Stearman, Q. M. Bui, G. Speyer et al., "Systems analysis of the human pulmonary arterial hypertension lung transcriptome," *American Journal of Respiratory Cell and Molecular Biology*, vol. 60, no. 6, pp. 637–649, 2019.

[17] Y. D. Zhao, H. Z. H. Yun, J. Peng et al., "De novo synthesize of bile acids in pulmonary arterial hypertension lung," *Metabolomics*, vol. 10, no. 6, pp. 1169–1175, 2014.

[18] J. T. Leek, W. E. Johnson, H. S. Parker, A. E. Jaffe, and J. D. Storey, "The sva package for removing batch effects and other unwanted variation in high-throughput experiments," *Bioinformatics*, vol. 28, no. 6, pp. 882-883, 2012.

[19] G. Sharma, C. Colantuoni, L. A. Goff, E. J. Fertig, and G. Stein-O'Brien, "ProjectR: an R/Bioconductor package for transfer learning via PCA, NMF, correlation and clustering," *Bioinformatics*, vol. 36, no. 11, pp. 3592-3593, 2020.

[20] M. E. Ritchie, B. Phipson, D. Wu et al., "Limma powers differential expression analyses for RNA-sequencing and microarray studies," *Nucleic Acids Research*, vol. 43, no. 7, p. e47, 2015.

[21] K. Ito and D. Murphy, "Application of ggplot2 to pharmacometric graphics," *CPT: Pharmacometrics & Systems Pharmacology*, vol. 2, no. 10, p. e79, 2013.

[22] Y. Zhou, B. Zhou, L. Pache et al., "Metascape provides a biologist-oriented resource for the analysis of systems-level datasets," *Nature Communications*, vol. 10, no. 1, p. 1523, 2019.

[23] H. Ishwaran and M. Lu, "Standard errors and confidence intervals for variable importance in random forest regression, classification, and survival," *Statistics in Medicine*, vol. 38, no. 4, pp. 558–582, 2019.

[24] J. Friedman, T. Hastie, and R. Tibshirani, "Regularization paths for generalized linear models via coordinate descent," *Journal of Statistical Software*, vol. 33, no. 1, pp. 1–22, 2010.

[25] X. Lin, F. Yang, L. Zhou et al., "A support vector machine-recursive feature elimination feature selection method based on artificial contrast variables and mutual information," *Journal of Chromatography. B, Analytical Technologies in the Biomedical and Life Sciences*, vol. 910, pp. 149–155, 2012.

[26] V. Cherkassky, "The nature of statistical learning theory~," *IEEE Transactions on Neural Networks*, vol. 8, no. 6, p. 1564, 1997.

[27] S. Huang, N. Cai, P. P. Pacheco, S. Narrandes, Y. Wang, and W. Xu, "Applications of support vector machine (SVM) learning in cancer genomics," *Cancer Genomics Proteomics*, vol. 15, no. 1, pp. 41–51, 2018.

[28] M. Pirooznia, J. Y. Yang, M. Q. Yang, and Y. Deng, "A comparative study of different machine learning methods on microarray gene expression data," vol. 9, no. BMC Genomics, Supplement 1, p. S13, 2008.

[29] P. Langfelder and S. Horvath, "WGCNA: an R package for weighted correlation network analysis," *BMC Bioinformatics*, vol. 9, no. 1, p. 559, 2008.

[30] E. Ravasz, A. L. Somera, D. A. Mongru, Z. N. Oltvai, and A. L. Barabasi, "Hierarchical organization of modularity in metabolic networks," *Science*, vol. 297, no. 5586, pp. 1551–1555, 2002.

[31] P. A. Salome and S. S. Merchant, "Co-expression networks in Chlamydomonas reveal significant rhythmicity in batch cultures and empower gene function discovery," *Plant Cell*, vol. 33, no. 4, pp. 1058–1082, 2021.

[32] E. Spiekerkoetter, S. M. Kawut, and V. A. de Jesus Perez, "New and emerging therapies for pulmonary arterial hypertension," *Annual Review of Medicine*, vol. 70, no. 1, pp. 45–59, 2019.

[33] M. Vaillancourt, G. Ruffenach, J. Meloche, and S. Bonnet, "Adaptation and remodelling of the pulmonary circulation in pulmonary hypertension," *The Canadian Journal of Cardiology*, vol. 31, no. 4, pp. 407–415, 2015.

[34] E. Stacher, B. B. Graham, J. M. Hunt et al., "Modern age pathology of pulmonary arterial hypertension," *American Journal of Respiratory and Critical Care Medicine*, vol. 186, no. 3, pp. 261–272, 2012.

[35] S. Jafri and M. L. Ormiston, "Immune regulation of systemic hypertension, pulmonary arterial hypertension, and pre-eclampsia: shared disease mechanisms and translational opportunities," *American Journal of Physiology. Regulatory, Integrative and Comparative Physiology*, vol. 313, no. 6, pp. R693–R705, 2017.

[36] A. Mamazhakypov, G. Viswanathan, A. Lawrie, R. T. Schermuly, and S. Rajagopal, "The role of chemokines and chemokine receptors in pulmonary arterial hypertension," *British Journal of Pharmacology*, vol. 178, no. 1, pp. 72–89, 2021.

[37] R. Savai, S. S. Pullamsetti, J. Kolbe et al., "Immune and inflammatory cell involvement in the pathology of idiopathic pulmonary arterial hypertension," *American Journal of Respiratory and Critical Care Medicine*, vol. 186, no. 9, pp. 897–908, 2012.

[38] K. W. Prins, S. L. Archer, M. Pritzker et al., "Interleukin-6 is independently associated with right ventricular function in pulmonary arterial hypertension," *The Journal of Heart and Lung Transplantation*, vol. 37, no. 3, pp. 376–384, 2018.

[39] P. M. Hassoun, L. Mouthon, J. A. Barbera et al., "Inflammation, growth factors, and pulmonary vascular remodeling," *Journal of the American College of Cardiology*, vol. 54, no. 1, pp. S10–S19, 2009.

[40] X. Zhao, X. Bai, J. L. Li, S. M. Li, and J. Xi, "Sevoflurane improves circulatory function and pulmonary fibrosis in rats with pulmonary arterial hypertension through inhibiting NF-κB signaling pathway," *European Review for Medical and Pharmacological Sciences*, vol. 23, no. 23, pp. 10532–10540, 2019.

[41] G. Xiao, W. Zhuang, T. Wang et al., "Transcriptomic analysis identifies toll-like and nod-like pathways and necroptosis in pulmonary arterial hypertension," *Journal of Cellular and Molecular Medicine*, vol. 24, no. 19, pp. 11409–11421, 2020.

[42] M. Rabinovitch, C. Guignabert, M. Humbert, and M. R. Nicolls, "Inflammation and immunity in the pathogenesis of pulmonary arterial hypertension," *Circulation Research*, vol. 115, no. 1, pp. 165–175, 2014.

[43] D. Farkas, A. A. R. Thompson, A. R. Bhagwani et al., "Toll-like receptor 3 is a therapeutic target for pulmonary hypertension," *American Journal of Respiratory and Critical Care Medicine*, vol. 199, no. 2, pp. 199–210, 2019.

[44] J. A. Cruz and D. S. Wishart, "Applications of machine learning in cancer prediction and prognosis," *Cancer Informatics*, vol. 2, pp. 59–77, 2007.

[45] D. V. Cicchetti, "Neural networks and diagnosis in the clinical laboratory: state of the art," *Clinical Chemistry*, vol. 38, no. 1, pp. 9-10, 1992.

[46] A. J. Cochran, "Prediction of outcome for patients with cutaneous melanoma," *Pigment Cell Research*, vol. 10, no. 3, pp. 162–167, 1997.

[47] K. Kourou, T. P. Exarchos, K. P. Exarchos, M. V. Karamouzis, and D. I. Fotiadis, "Machine learning applications in cancer prognosis and prediction," *Computational and Structural Biotechnology Journal*, vol. 13, pp. 8–17, 2015.

[48] K. P. Exarchos, Y. Goletsis, and D. I. Fotiadis, "Multiparametric decision support system for the prediction of oral cancer reoccurrence," *IEEE Transactions on Information Technology in Biomedicine*, vol. 16, no. 6, pp. 1127–1134, 2012.

[49] I. Kononenko, "Machine learning for medical diagnosis: history, state of the art and perspective," *Artificial Intelligence in Medicine*, vol. 23, no. 1, pp. 89–109, 2001.

[50] Y. Ma, S. S. Chen, Y. Y. Feng, and H. L. Wang, "Identification of novel biomarkers involved in pulmonary arterial hypertension based on multiple-microarray analysis," *Bioscience Reports*, vol. 40, no. 9, 2020.

[51] Y. Zeng, N. Li, Z. Zheng et al., "Screening of key biomarkers and immune infiltration in pulmonary arterial hypertension via integrated bioinformatics analysis," *Bioengineered*, vol. 12, no. 1, pp. 2576–2591, 2021.

[52] Q. Li, L. Meng, and D. Liu, "Screening and identification of therapeutic targets for pulmonary arterial hypertension through microarray technology," *Frontiers in Genetics*, vol. 11, p. 782, 2020.

[53] Y. Zeng, N. Li, Z. Zheng et al., "Screening of hub genes associated with pulmonary arterial hypertension by integrated bioinformatic analysis," *BioMed Research International*, vol. 2021, Article ID 6626094, 16 pages, 2021.

[54] A. Li, J. He, Z. Zhang et al., "Integrated bioinformatics analysis reveals marker genes and potential therapeutic targets for pulmonary arterial hypertension," *Genes (Basel)*, vol. 12, no. 9, 2021.

[55] Z. Bai, L. Xu, Y. Dai, Q. Yuan, and Z. Zhou, "ECM2 and GLT8D2 in human pulmonary artery hypertension: fruits from weighted gene co-expression network analysis," *Journal of Thoracic Disease*, vol. 13, no. 4, pp. 2242–2254, 2021.

[56] H. Dong, X. Li, M. Cai et al., "Integrated bioinformatic analysis reveals the underlying molecular mechanism of and potential drugs for pulmonary arterial hypertension," *Aging (Albany NY)*, vol. 13, no. 10, pp. 14234–14257, 2021.

[57] S. Akter, D. Xu, S. C. Nagel et al., "Machine learning classifiers for endometriosis using transcriptomics and methylomics data," *Frontiers in Genetics*, vol. 10, p. 766, 2019.

[58] Y. Li, N. T. Klena, G. C. Gabriel et al., "Global genetic analysis in mice unveils central role for cilia in congenital heart disease," *Nature*, vol. 521, no. 7553, pp. 520–524, 2015.

[59] J. S. Hauptman, R. Bollo, R. Damerla et al., "Coincident myelomeningocele and gastroschisis: report of 2 cases," *Journal of Neurosurgery. Pediatrics*, vol. 21, no. 6, pp. 574–577, 2018.

[60] Y. Tom Tang, P. Emtage, W. D. Funk et al., "TAFA: a novel secreted family with conserved cysteine residues and restricted expression in the brain," *Genomics*, vol. 83, no. 4, pp. 727–734, 2004.

[61] F. Annunziato and S. Romagnani, "Heterogeneity of human effector CD4+ T cells," *Arthritis Research & Therapy*, vol. 11, no. 6, p. 257, 2009.

[62] T. Skaria, J. Burgener, E. Bachli, and G. Schoedon, "IL-4 causes hyperpermeability of vascular endothelial cells through Wnt5A signaling," *PLoS One*, vol. 11, no. 5, p. e0156002, 2016.

[63] R. A. Johns, "Th2 inflammation, hypoxia-induced mitogenic factor/FIZZ1, and pulmonary hypertension and vascular remodeling in schistosomiasis," *American Journal of Respiratory and Critical Care Medicine*, vol. 181, no. 3, pp. 203–205, 2010.

[64] J. R. Conejo-Garcia, F. Benencia, M. C. Courreges et al., "Tumor-infiltrating dendritic cell precursors recruited by a β-defensin contribute to vasculogenesis under the influence of Vegf-A," *Nature Medicine*, vol. 10, no. 9, pp. 950–958, 2004.

[65] F. Perros, P. Dorfmuller, R. Souza et al., "Dendritic cell recruitment in lesions of human and experimental pulmonary hypertension," *The European Respiratory Journal*, vol. 29, no. 3, pp. 462–468, 2007.

[66] A. Anwar, M. Li, M. G. Frid et al., "Osteopontin is an endogenous modulator of the constitutively activated phenotype of pulmonary adventitial fibroblasts in hypoxic pulmonary hypertension," *American Journal of Physiology. Lung Cellular and Molecular Physiology*, vol. 303, no. 1, pp. L1–L11, 2012.

[67] W. Wang, H. Yan, W. Zhu et al., "Impairment of monocyte-derived dendritic cells in idiopathic pulmonary arterial hypertension," *Journal of Clinical Immunology*, vol. 29, no. 6, pp. 705–713, 2009.

[68] V. Shlyonsky, R. Naeije, and F. Mies, "Possible role of lysophosphatidic acid in rat model of hypoxic pulmonary vascular remodeling," *Pulmonary Circulation*, vol. 4, no. 3, pp. 471–481, 2014.

[69] S. Farha, J. Sharp, K. Asosingh et al., "Mast cell number, phenotype, and function in human pulmonary arterial hypertension," *Pulmonary Circulation*, vol. 2, no. 2, pp. 220–228, 2012.

[70] D. Kosanovic, H. Luitel, B. K. Dahal et al., "Chymase: a multifunctional player in pulmonary hypertension associated with lung fibrosis," *The European Respiratory Journal*, vol. 46, no. 4, pp. 1084–1094, 2015.

[71] T. Novotny, J. Krejci, J. Malikova et al., "Mast cell stabilization with sodium cromoglycate modulates pulmonary vessel wall remodeling during four-day hypoxia in rats," *Experimental Lung Research*, vol. 41, no. 5, pp. 283–292, 2015.

Hindawi
Mediators of Inflammation
Volume 2022, Article ID 3121492, 9 pages
https://doi.org/10.1155/2022/3121492

Research Article

miR-559 Inhibits Proliferation, Autophagy, and Angiogenesis of Hepatocellular Carcinoma Cells by Targeting PARD3

Chunjing Wang,[1] **Chengcheng Li**,[2] **and Rui Hao**[3]

[1]*Department of Gastroenterology, Affiliated Hospital of Beihua University, Jilin, Jilin Province 132000, China*
[2]*Department of Graduate Student, Affiliated Hospital of Beihua University, Jilin, Jilin Province 132000, China*
[3]*Department of Infectious Liver Disease, Affiliated Hospital of Beihua University, Jilin, Jilin Province 132000, China*

Correspondence should be addressed to Rui Hao; ruihaodkl@163.com

Received 20 July 2022; Revised 15 August 2022; Accepted 20 August 2022; Published 5 September 2022

Academic Editor: Md Sayed Ali Sheikh

Hepatocellular carcinoma (HCC) is one of the most common cancers in the world and has a high mortality rate. Although prevention and treatment of HCC has improved, it still faces poor prognosis and high mortality. miRNAs play a critical role in the tumorigenesis of HCC, but the underlying mechanism has not been well investigated. Here, the functions and interaction between miR-559 and PARD3 were investigated in HCC cells. Increased PARD3 and decreased miR-559 expression were observed in HCC cells compared with those in normal liver cells, especially in Huh-7 cells. Studies further demonstrated that PARD3 silencing or miR-559 overexpression impaired the proliferation, autophagy, and angiogenesis in Huh-7 cells. Mechanistically, PARD3 represents a target of miR-559. Furthermore, investigations revealed that miR-559 inhibition induced the expression of PARD3, thereby enhancing cell proliferation, autophagy, and angiogenesis in Huh-7 cells. These results reveal the interaction between miR-559 and PARD3 in HCC cells and provide new insights into their potential targets as therapeutic treatment against HCC.

1. Introduction

Hepatocellular carcinoma (HCC) is one of the most common malignancies in the world [1]. Although increasing studies are focusing on HCC, the underlying mechanisms about its tumorigenesis and development are still unclear. Since the proliferation and metastasis of tumor cells depend upon the formation of angiogenesis, the progress of neovascularization is actually important for cell proliferation, invasion, and metastasis in solid tumors [2]. Currently, a large number of drugs targeting angiogenesis have been approved for the first- and second-line treatment of HCC [3].

Autophagy is a highly regulated catabolic process in cells. Under normal or stress conditions, autophagy participates in the removal of damaged organelles and the transformation of intracellular substances to maintain homeostasis [4, 5]. Dysregulation of autophagy has serious consequences and is related to the development and progression of various diseases, such as infectious neurodegenerative and metabolic diseases, as well as cancer [6]. Moreover, studies have shown that autophagy may be involved in maintaining the occurrence of HCC [7]. In the early stage in the development of HCC, autophagy is against tumor formation by inhibiting inflammation and maintaining genomic stability. Once cancer develops, autophagy may act as a prosurvival mechanism to protect HCC cells from death induced by different types of stimulation, including oxidative stress, and thus maintain cancer progression [8].

miRNAs are short noncoding RNAs of 19-25 nucleotides in length that inhibit target gene expression by specifically binding in a sequence-specific manner to the 3′-UTR regions of the target gene [9]. Abnormal expression of miRNAs is associated with the development of most tumors, such as HCC, and involved in the regulation of tumor cell growth, autophagy, and angiogenesis [10]. miR-559 is one of these miRNAs, which has been demonstrated to be involved in the inhibition of cell proliferation and invasion in HCC cells [11]. PARD3 (zonal defect 3

Table 1: The information of primers.

Gene name	Forward (5′-3′)	Reverse (3′-5′)
miR-559	CCTGGGACCCCATTATCCTT	TGCTGTCCACAGTGTGTTTG
Pard3	CAGACAGAACTACTAACTTCGCC	ATGCCTCGGATGAAGAGTCCT
U6	CTCGCTTCGGCAGCACA	AACGCTTCACGAATTTGCGT
Gapdh	TCAAGATCATCAGCAATGCC	CGATACCAAAGTTGTCATGGA

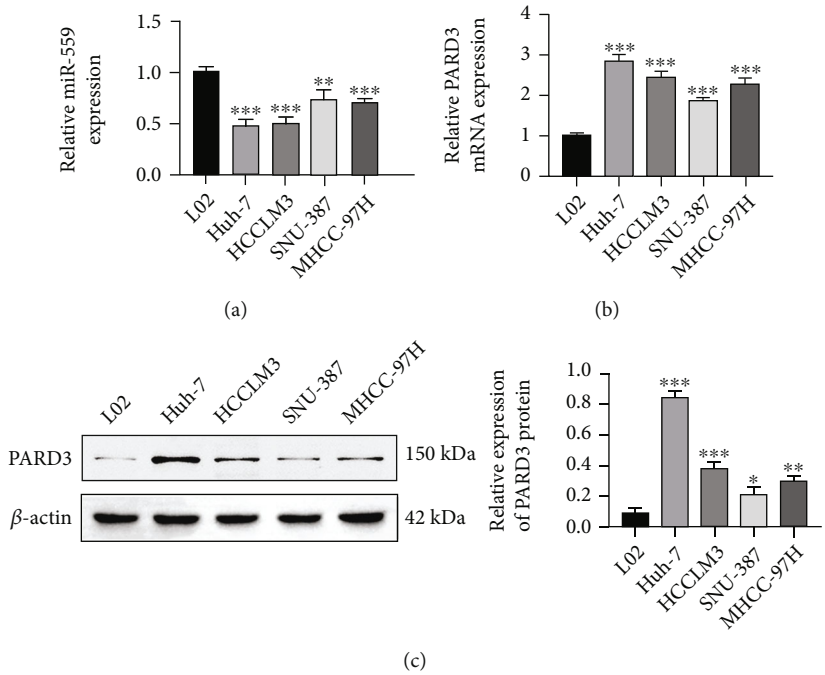

Figure 1: miR-559 was downregulated, and PARD3 was upregulated in HCC cells. (a) The expression level of miR-559 in HCC cells. (b) The mRNA expression of PARD3 in HCC cells. (c) The protein level of PARD3 in HCC cells. The values were obtained from three independent experiments and shown as mean ± SD. $^{*}p < 0.05$, $^{**}p < 0.01$, and $^{***}p < 0.001$, compared with L02 cells.

homolog) is a scaffold protein consisting of an N-terminal structural domain, a C-terminal structural domain, and three PDZ structural domains [12]. PARD3 regulates cell proliferation, migration, and invasion in most cancers, including lung cancer and bladder cancer [13, 14]. Also, activation of PARD3 signaling was associated with the increased autophagy activity and colorectal cancer cell proliferation [15]. It was found that PARD3 was overexpressed in HCC and associated with poor prognosis [16]. However, its role in HCC has not been reported. Bioinformatics analysis revealed that PARD3 is a target gene of miR-559. Thus, in the present study, a series of experiments were performed to investigate the effect of miR-559 and PARD3 on HCC cells, as well as to further clarify the relationship between miR-559 and PARD3.

2. Materials and Methods

2.1. Cell Lines and Cell Culture. The HCC cell lines (SNU-387, Huh-7, HCCLM3, and MHCC-97H cells) and the normal human liver cell line L02 were provided by ATCC (Manassas, VA, USA). Cells were cultured in high-glucose DMEM (Gibco BRL, USA), with the supplements of fetal bovine serum (10%, FBS) and penicillin/streptomycin (1%; Sigma-Aldrich, St. Louis, MO, USA) at 37°C with 5% CO_2.

2.2. CCK8 Assay. Cell viability was detected by the CCK8 assay. $1 * 10^5$ cells were inoculated in 96-well plates for 6 h. Then, cells were transfected with si-RNA or miRNA mimics/inhibitor for 24 h. The medium was removed and replaced with fresh medium containing 10% CCK8 solutions (Meilunbio; China) and cultured for another 1 hour. The optical density at 450 nm was measured with a microplate reader (Biotek, Inc., Woburn, MA, USA).

2.3. Cell Transfection. si-RNA for PARD3, miR-559 mimics, or miR-559 inhibitor was obtained from GenePharma (Shanghai, China). Cells were seeded in 6-well plates to 50-60% and transfected for si-RNA or miRNA mimics/inhibitor using RiboFECT™ CP transfection Reagent (Ribobio, Guangzhou, China) as per instructions.

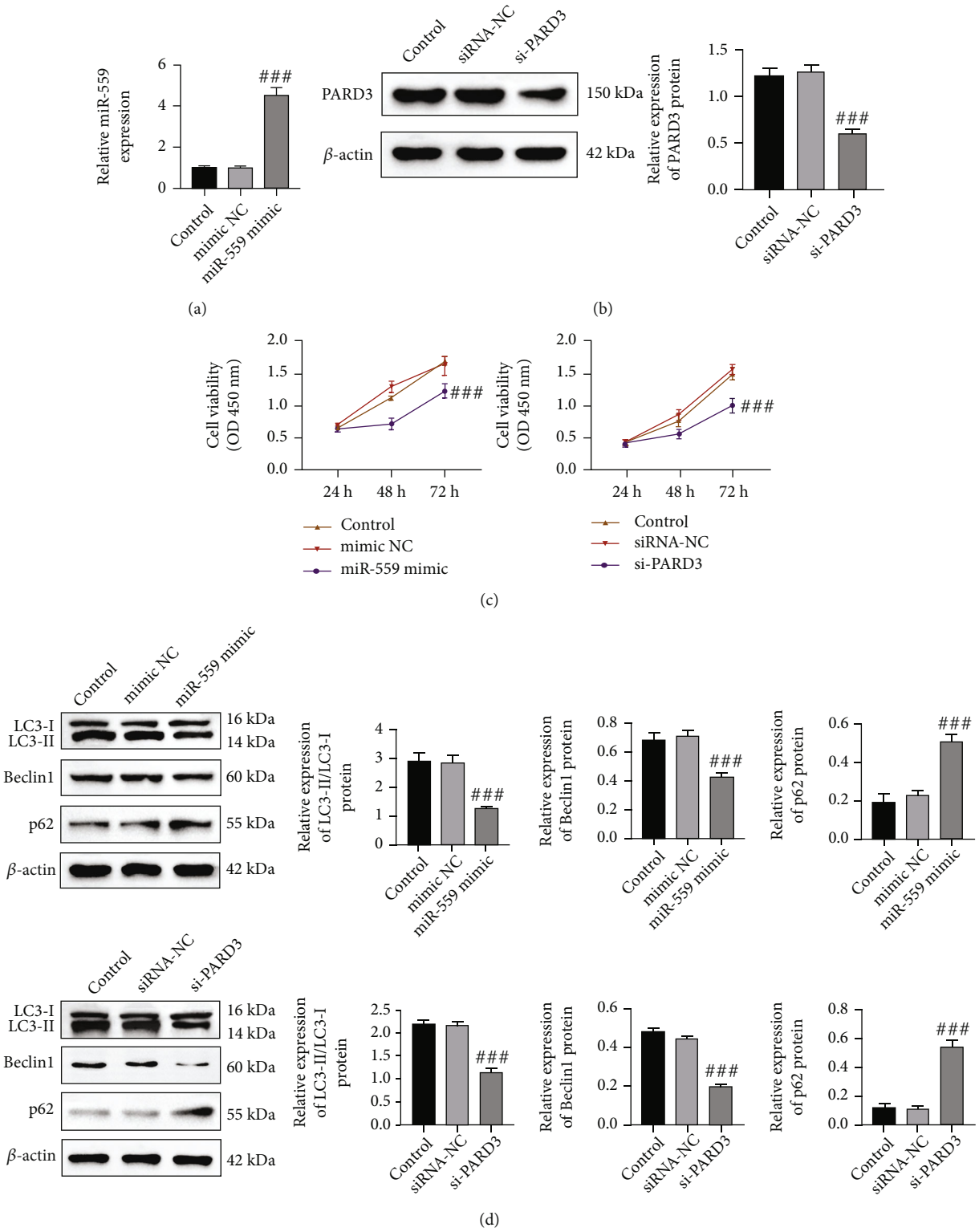

Figure 2: miR-559 overexpression or PARD3 silencing inhibited the proliferation and autophagy of Huh-7 cells. Huh-7 cells were transfected with miR-559 NC/mimics or si-RNA NC/PARD3 for 24 h. (a) The relative expression of miR-559. (b) The relative protein expression of PARD3. (c) Cell viability was detected by the CCK8 assay. (d) The relative protein levels of LC3-II/I, Beclin1, and p62. The values were obtained from three independent experiments and shown as mean ± SD. $^{###}p < 0.001$, compared with mimic NC or siRNA-NC.

2.4. RT-PCR Assay. The TRIzol reagent (Invitrogen, Carlsbad, CA, USA) was used to extract total RNA as per instructions. A Mir-X™ miRNA qRT-PCR TB Green kit (Takara, Japan) and PrimeScript RT reagent kit (Takara) were used for miRNA and total RNA reverse transcription, respectively. Relative level of miR-559 was normalized to U6 expression. RT-PCR

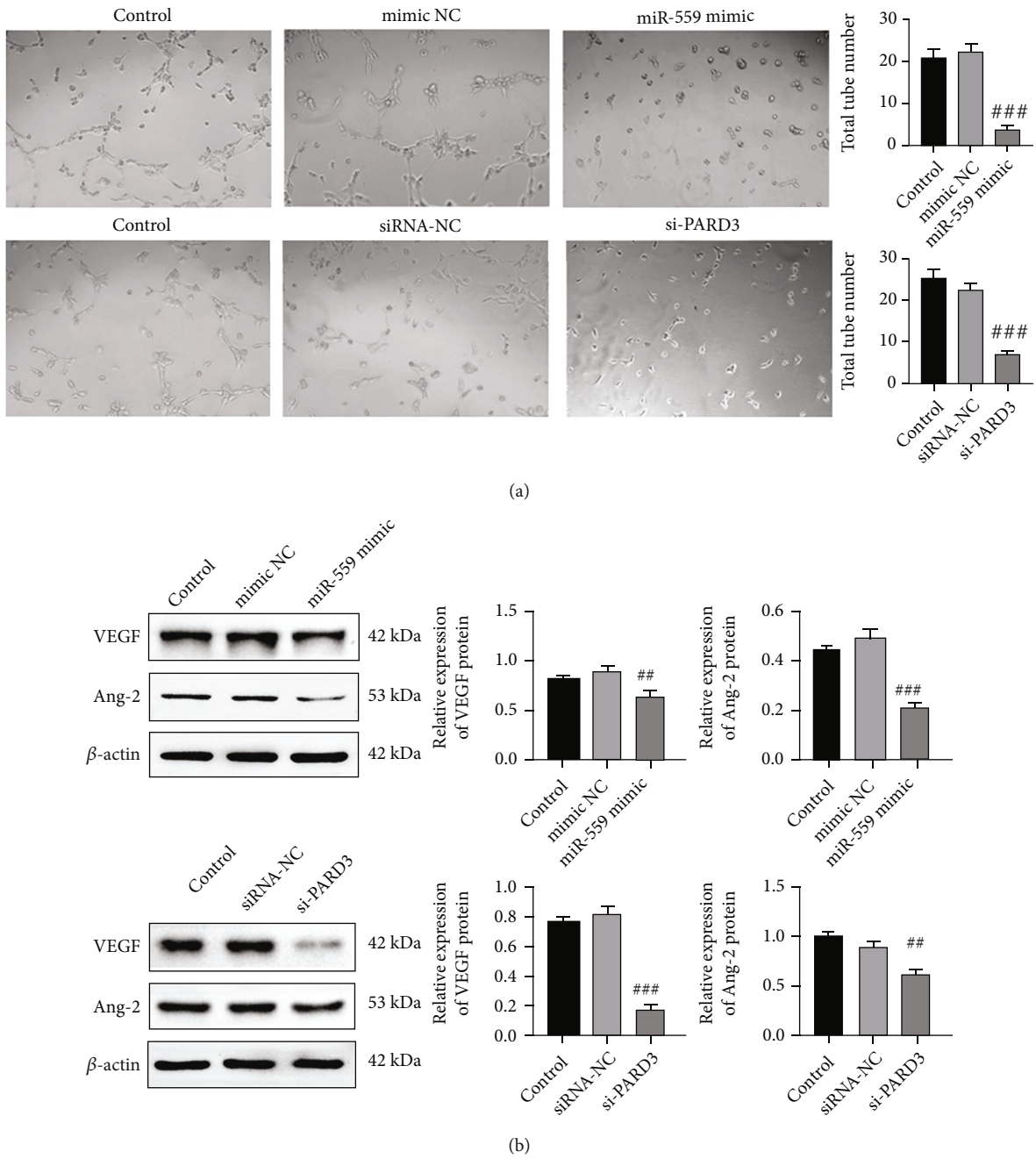

Figure 3: Overexpression of miR-559 or inhibition of PARD3 reduced the angiogenesis of Huh-7 cells. Huh-7 cells were transfected with miR-559 NC/mimics or si-RNA NC/PARD3 for 24 h. (a) *In vitro* HUVEC tube formation assay using conditioned medium and the quantification of tube length in each group. (b) Western blot analysis on the protein expressions of VEGF and Ang-2. The values were obtained from three independent experiments and shown as mean ± SD. $^{###}p < 0.001$, compared with mimic NC or siRNA-NC.

was performed using TB Green Premix Ex Taq (Takara) on StepOne Plus Real-Time PCR System (Applied Biosystems, CA, USA). Relative gene levels were normalized to GAPDH expression. The primer sequence is presented in Table 1.

2.5. Western Blot Assay. HCC cells were collected and dealt with RIPM lysed buffer to obtain total protein. The protein concentration was measured by using a BCA protein quantification kit (Kerui, Wuhan, China). Then, the proteins were divided by SDS-PAGE and shifted to PVDF (0.45 μm) membranes. Next, the membranes were soaked in nonfat milk (5%). After blocking, the blots were incubated with antibodies against PARD3 (BioVision, Palo Alto, USA; 1 : 1000), LC3-I/II (Cell Signaling Technology (CST), Beverly, MA, USA; 1 : 1000), Beclin1 (Absin, Shanghai, China; 1 : 1000), p62 (Absin, 1 : 1000), VEGF (CST, 1 : 1000), Ang-2 (Santa Cruz, CA, USA; 1 : 1000), and β-actin (Absin, 1 : 1000) overnight at 4°C. Finally, bands were incubated with an HRP-conjugated secondary antibody (1 : 2500) (at room temperature, 1 h) and quantitated using bioimaging.

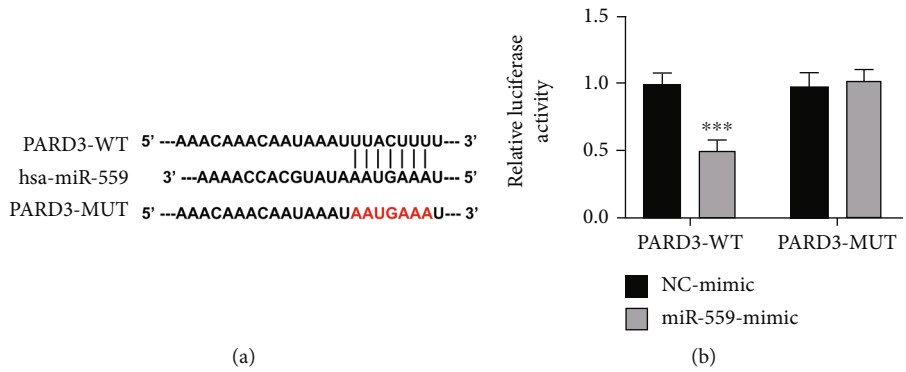

Figure 4: PARD3 was a target gene of miR-559. (a) Target prediction between PARD3 and miR-559. (b) Luciferase reporter constructs containing wild-type or mutated miR-559 paring sites of PARD3 were cotransfected with the miR-559 mimic or mimic NC into Huh-7 cells. The values were obtained from three independent experiments and shown as mean ± SD. $^{***}p < 0.001$, compared with mimic NC.

The protein level was valued using β-actin as a loading control.

2.6. HUVEC Tube Formation Assays. In tumor cell-conditioned medium (TCM) preparation, stably transfected Huh-7 cells were cultured in DMEM supplemented with 10% FBS (37°C, 24 h). Then, the medium was changed to DMEM containing FBS (1%) and cultured (48 h). Then, the medium was collected and centrifuged (600 g, 5 min). The detached cells were removed, and the TCM supernatant was then concentrated by using the Millipore 3 kDa Centricon column. The TCM should be used immediately or stored in aliquots at -20°C until use.

In tube formation assays *in vitro*, $5 * 10^4$ cells of HUVECs were cultured with TCM for 12 h until tube-like structures formed, at 37°C in 24-well plates coated with Matrigel. Use a light microscope to capture the formation of tubes. Four images were obtained at nonoverlapping locations, and the number of tubes was measured using ImageJ software.

2.7. Dual-Luciferase Reporter Assay. Wild-type and mutant luciferase vectors were constructed according to the predicted binding sites of PARD3 and miR-559. Then, cells were cotransfected with miR-559 mimics or NC mimics for 24 h. After transfection, cells were collected and lysed and centrifuged (10,000 g, 5 min). The upper supernatant was collected, and the luciferase activity was detected using the Dual-Luciferase Reporter Assay System (Promega Corporation, Madison, WI, USA).

2.8. Target Prediction. The prediction of miRNAs binding with PARD3 was performed using the TargetScan database (http://www.targetscan.org/vert_72/).

2.9. Statistical Analysis. Data was analyzed statistically using GraphPad 8.0 and expressed as mean ± SD. The differences between two groups were performed by two-tailed Student's *t*-test or one-way ANOVA followed by post hoc Dunnett's test. $p < 0.05$ was considered statistically significant.

3. Results

3.1. miR-559 Was Downregulated and PARD3 Was Upregulated in HCC Cells. The expression levels of miR-559 and PARD3 were detected in HCC cell lines (Huh-7, HCCLM3, SNU-387, and MHCC-97H) and the normal liver cell line (L02) by the RT-PCR assay. As shown in Figures 1(a) and 1(b), miR-559 was markedly downregulated, while PARD3 was obviously upregulated in HCC cells. Analysis on protein expression showed consistent results (Figure 1(c)). The Huh-7 cell line showed the lowest expression of miR-559 and the highest expression of PARD3, which was used in the following study to explore the role of PARD3 in HCC and its interaction between miR-559.

3.2. miR-559 Overexpression or PARD3 Silencing Inhibited the Proliferation and Autophagy of Huh-7 Cells. To further investigate the effects of miR-559 and PARD3 in Huh-7 cells, Huh-7 cells were transfected with miR-559 mimics or si-PARD3, respectively. The results are presented in Figures 2(a) and 2(b); the mRNA expression of miR-559 and protein expression of PARD3 were, respectively, increased and decreased in Huh-7 cells after being transfected with miR-559 mimics and si-PARD3, validating the successful transfection. Then, the cell viability was measured by the CCK8 assay. Overexpression of miR-559 significantly reduced cell viability, and the similar investigation was found in cells with si-PARD3 (Figure 2(c)). PARD3 overexpression enhanced autophagy and promoted the development of colorectal cancer [15]. The level of LC3-II/I is known as an autophagosomal marker [17]. It has been reported that autophagic overexpression of LC3-II contributes to malignant progression and predicts poor prognosis in HCC [18]. Beclin1 is a key regulator of autophagy, and Beclin1-dependent autophagy has been shown to be associated with the development of HCC [17]. As an important autophagy receptor, P62 participates in the autophagy process. When autophagy activity is weakened or the autophagy system is damaged, P62 protein accumulates in the cytoplasm, and therefore, P62 is

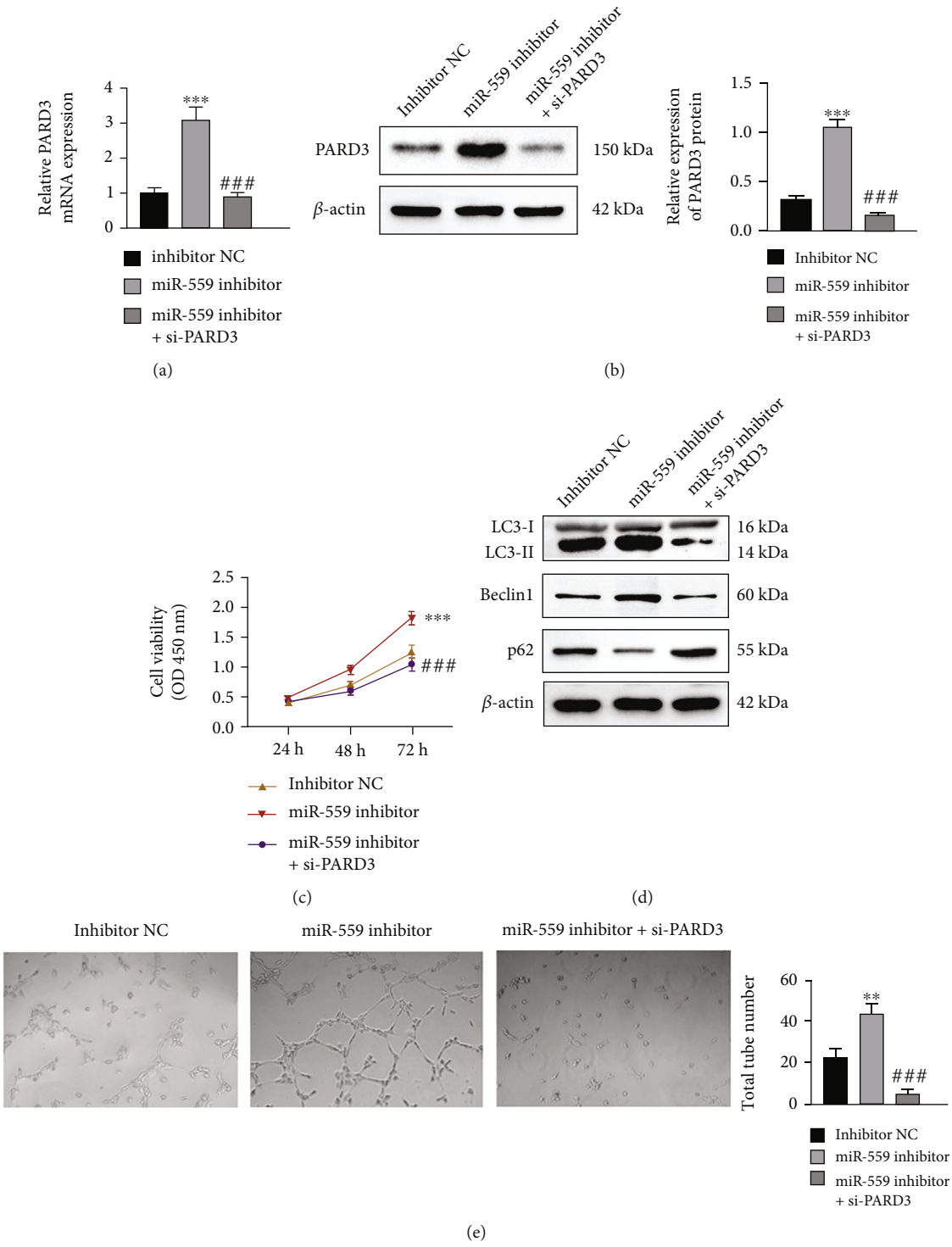

Figure 5: Continued.

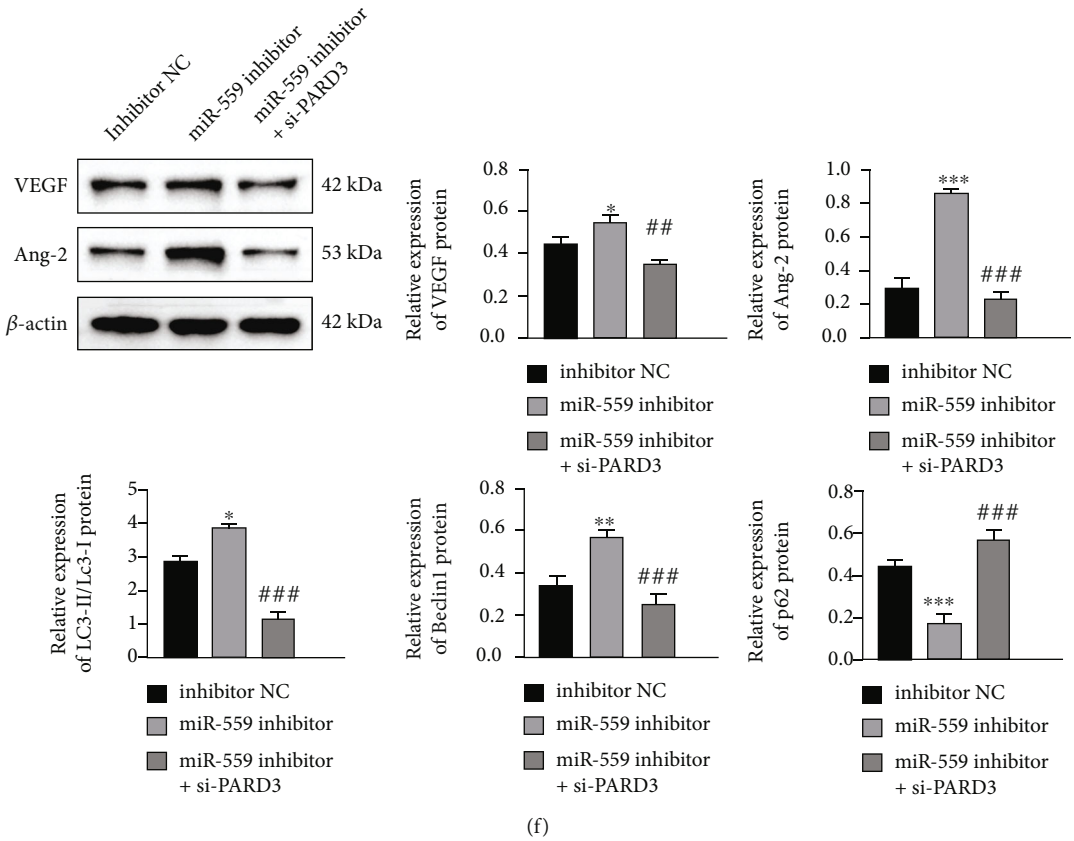

Figure 5: PARD3 silencing reversed the effects of the miR-559 inhibitor on Huh-7 cells. Huh-7 cells were cotransfected with the miR-559 inhibitor and si-PARD3 for 24 h. The mRNA (a) and protein (b) levels of PARD3 in Huh-7 cells. (c) Using the CCK8 assay to detect cell viability. (d) The expression levels of LC3-II/I, Beclin1, and p62 were measured by the western blot assay. (e) HUVEC tube formation assay was proposed using conditioned medium *in vitro*. (f) The protein levels of VEGF and Ang-2 were detected by western blotting in Huh-7 cells. The values were obtained from three independent experiments and shown as mean ± SD. $^{*}p < 0.05$, $^{**}p < 0.01$, and $^{***}p < 0.001$, compared with inhibitor NC; $^{\#\#}p < 0.001$ and $^{\#\#\#}p < 0.001$, compared with the miR-559 inhibitor.

considered to be one of the important marker proteins reflecting autophagy activity [19]. In this study, upregulation of miR-559 decreased the expression of LC3-II/I and Beclin1 and increased the expression of p62. PARD3 silencing showed the similar results (Figure 2(d)). These results suggested that miR-559 overexpression or PARD3 downregulation might inhibit the proliferation and autophagy in Huh-7 cells.

3.3. Overexpression of miR-559 or Inhibition of PARD3 Reduced the Angiogenesis of Huh-7 Cells. Increasing studies have shown that abnormal angiogenesis is a key process in the development of cancer [20]. Thus, the role of miR-559 or PARD3 was evaluated in the angiogenesis in Huh-7 cells by using the *in vitro* tube formation assay. As shown in Figure 3, HUVECs cultured with TCM from miR-559 mimics or si-PARD3-treated cells developed less capacity for angiogenesis. Studies reported that proangiogenic molecules including VEGF and Ang-2 were involved in cancer development [21]. The results showed that the protein levels of VEGF and Ang-2 were also markedly reduced in HUVECs cultured with TCM treated with miR-559 mimics and si-PARD3. Collectively, these above results suggest that overexpression of miR-559 or downregulation of PARD3 may inhibit the progression of HCC.

3.4. PARD3 Was a Target Gene of miR-559. To further explore the correlation between miR-559 and PARD3, TargetScan software was used to analyze the interaction between miRNAs and PARD3. Seven conserved binding sites for miR-559 were identified in the 3′-UTR region of the PARD3 gene. To elucidate whether PARD3 was a direct target of miR-559, a luciferase reporter plasmid containing the 3′-UTR of PARD3 was established. As shown in Figure 4, the luciferase activity was similar in cells cotransfected with miR-559 mimics or negative control mimics in the mutant-type 3′-UTR group. However, the relative luciferase activity with wild-type 3′-UTR was markedly reduced by miR-559 mimics. These results indicated that PARD3 was directly regulated by miR-559.

3.5. PARD3 Silencing Reversed the Effect of the miR-559 Inhibitor on Huh-7 Cells. To further validate whether the effects of miR-559 on Huh-7 cells are related to the direct regulation of PARD3, Huh-7 cells were treated with si-PARD3 and miR-559 inhibitor, and the protein level of

PARD3, cell viability, autophagy, and angiogenesis were, respectively, evaluated. Inhibition of miR-559 obviously induced the mRNA and protein expression of PARD3, while si-PARD3 totally blocked this phenomenon (Figures 5(a) and 5(b)). In addition, inhibition of miR-559 enhanced cell proliferation, autophagy, and angiogenesis, but the inhibitory effect of miR-559 on Huh-7 cells was reversed by PARD3 silencing (Figures 5(c)–5(f)). These results suggested that miR-559 regulates cell proliferation, autophagy, and angiogenesis by negatively regulating PARD3.

4. Discussion

HCC is a common type of liver cancers, comprising more than 90% of all primary malignant liver cancers [3]. Although HCC has been extensively studied, the underlying mechanisms about its tumorigenesis and progression are still poorly understood due to its complexity. In recent years, accumulating evidence showed that most miRNAs are closely related to the occurrence, metastasis, and poor prognosis of HCC [22]. Moreover, advancements in exploring the molecular mechanism of miRNAs hold the promise of these molecules as attractive targets for the diagnosis and management of HCC [23]. Our study found that miR-559 was downregulated in various HCC cells, while PARD3 was upregulated in HCC cells (Figure 1). In addition, overexpression of miR-559 or knockdown of PARD3 decreased the proliferation of HCC cells (Figure 2(c)). These results suggested that a relationship between miR-559 and PARD3 might be involved in the development of HCC cells.

Autophagy is thought to act as a tumor suppressor to maintain the stability of the intracellular environment. However, after tumorigenesis, autophagy enables cancer cells to survive in the tumor microenvironment and promote tumor growth and development [6, 24]. Therefore, blocking autophagy may be an ideal target for HCC treatment. Our results demonstrated that upregulation of miR-559 or PARD3 silencing inhibited autophagy to restrain HCC growth. The expression of autophagy activation-related proteins was significantly decreased, such as LC3-II/I and Beclin1 [17]. In contrast, the expression of autophagy inhibition-related proteins was significantly increased, such as p62 [25] (Figure 2(d)).

In HCC, the angiogenic pathway is dysregulated, suggesting the involvement of angiogenesis in the development and pathogenesis of HCC [2]. Many vascular growth factors can promote tumor angiogenesis, and the tumor itself can induce the secretion of these vascular growth factors through a variety of ways [26, 27]. In particular, vascular endothelial growth factor (VEGF) mainly regulates the growth and survival of endothelial cells, which promotes tumor angiogenesis and accelerates tumor development since it induces dormant tumor cells to rejuvenate the cell cycle process [28]. This study showed that overexpression of miR-559 or PARD3 knockdown inhibited tumor angiogenesis by decreasing the expression of VEGF and Ang-2 (Figure 3), two representative angiogenic factors.

Since the main function of miRNAs is to inhibit the expression of target genes by interfering with their transcription via binding to the 3′-UTR region of target genes [29]. In combination with bioinformatics prediction and dual luciferin reporting experiments, PARD3 was identified as a target gene for miR-559 (Figure 4). Therefore, the high expression of PARD3 in HCC cells was related to the downregulation of miR-559. Meanwhile, it is demonstrated that miR-559 inhibition induced the protein level of PARD3, while cell viability, autophagy, and angiogenesis were promoted in HCC cells by miR-559 inhibition. However, knockout of PARD3 reversed these phenomena. Thus, the role of miR-559 on cell viability, autophagy, and angiogenesis might be through the regulation of PARD3 expression.

In conclusion, all these results suggested that PARD3 is a target gene of miR-559. Overexpression of miR-559 inhibits the proliferation, autophagy, and angiogenesis in HCC cells via reducing the expression of PARD3, thus contributing to the development of HCC resistance. Therefore, miR-559 can serve as a novel therapeutic target for HCC.

Data Availability

All data generated or analyzed during this study are included in this published article.

Conflicts of Interest

The authors state that there are no conflicts of interest to disclose.

Authors' Contributions

Chunjing Wang designed the experiments and carried them out. Chengcheng Li analyzed and interpreted the data. Rui Hao prepared the manuscript with contributions from all coauthors.

Acknowledgments

This work was supported by the Education Department of Jilin Province "13th Five-Year" Science and Technology Research Planning Project (Grant No. JJKH20200054KJ).

References

[1] B. F. Torre LA, R. L. Siegel, J. Ferlay, J. Lortet-Tieulent, and A. Jemal, "Global cancer statistics," *CA: a Cancer Journal for Clinicians*, vol. 65, no. 2, pp. 87–108, 2015.

[2] M. A. S. W. Morse, R. Kim, A. R. He, P. B. Abada, M. Mynderse, and R. S. Finn, "The role of angiogenesis in hepatocellular carcinoma," *Clinical Cancer Research*, vol. 25, no. 3, pp. 912–920, 2019.

[3] D. D. J. Semela and J. F. Dufour, "Angiogenesis and hepatocellular carcinoma," *Journal of Hepatology*, vol. 41, no. 5, pp. 864–880, 2004.

[4] G. M. G. Kroemer and B. Levine, "Autophagy and the integrated stress response," *Molecular Cell*, vol. 40, no. 2, pp. 280–293, 2010.

[5] D. B. S. Glick and K. F. Macleod, "Autophagy: cellular and molecular mechanisms," *The Journal of Pathology*, vol. 221, no. 1, pp. 3–12, 2010.

[6] A. M. R. S. Choi and B. Levine, "Autophagy in human health and disease," *The New England Journal of Medicine*, vol. 368, no. 7, pp. 651–662, 2013.

[7] L. Jaime and A. M. C. Schneider, "Liver autophagy: much more than just taking out the trash," *Nature Reviews. Gastroenterology & Hepatology*, vol. 11, no. 3, pp. 187–200, 2014.

[8] K. D. Desirée Bartolini, P. Torquato, M. Piroddi, and F. Galli, "Nrf2-p62 autophagy pathway and its response to oxidative stress in hepatocellular carcinoma," *Translational Research*, vol. 193, pp. 54–71, 2018.

[9] F. Vasuri, M. Visani, G. Acquaviva et al., "Role of microRNAs in the main molecular pathways of hepatocellular carcinoma," *World Journal of Gastroenterology*, vol. 24, no. 25, pp. 2647–2660, 2018.

[10] I. A. S. G. Ziogas, K. S. Mylonas, and G. Tsoulfas, "Role of microRNA in the diagnosis and management of hepatocellular carcinoma," *MicroRNA*, vol. 9, no. 1, pp. 25–40, 2020.

[11] X. S. Zheng, H. J. Liu, L. L. Zhang et al., "MiR-559 targets GP73 to suppress proliferation and invasion of hepatocellular carcinoma in vitro," *Medical Science*, vol. 36, no. 10, pp. 793–798, 2020.

[12] F. E. S. Atashrazm and S. Ellis, "The polarity protein PARD3 and cancer," *Oncogene*, vol. 40, no. 25, pp. 4245–4262, 2021.

[13] E. Bonastre, S. Verdura, I. Zondervan et al., "PARD3 inactivation in lung squamous cell carcinomas impairs STAT3 and promotes malignant invasion," *Cancer Research*, vol. 75, no. 7, pp. 1287–1297, 2015.

[14] S. C. J. Wang, S. Zhang, M. Dong et al., "Loss of polarity protein Par3, via transcription factor Snail, promotes bladder cancer metastasis," *Cancer Science*, vol. 112, no. 7, pp. 2625–2641, 2021.

[15] Z. J. J. Wang and J. Jin, "LncRNA SLCO4A1-AS1 promotes colorectal cancer cell proliferation by enhancing autophagy via miR-508-3p/PARD3 axis," *Aging*, vol. 11, no. 14, pp. 4876–4889, 2019.

[16] S. H. J. Li, F. Yang, H. Zeng, Y. Tong, and K. Li, "High expression of PARD3 predicts poor prognosis in hepatocellular carcinoma," *Scientific Reports*, vol. 11, no. 1, p. 11078, 2021.

[17] J. Q. Sheng, M. R. Wang, D. Fang et al., "LncRNA NBR2 inhibits tumorigenesis by regulating autophagy in hepatocellular carcinoma," *Biomedicine & Pharmacotherapy*, vol. 133, article 111023, 2021.

[18] D. H. J. C. Wu, J. Chen, Z. X. Lin et al., "Autophagic LC3B overexpression correlates with malignant progression and predicts a poor prognosis in hepatocellular carcinoma," *Tumour Biology*, vol. 35, no. 12, pp. 12225–12233, 2014.

[19] M. L. T. Tao, Q. You, and Z. Jiang, "p62 as a therapeutic target for tumor," *European Journal of Medicinal Chemistry*, vol. 193, article 112231, 2020.

[20] T. K. G. Li, T. Wang, and H. Huang, "Tumor angiogenesis and anti-angiogenic gene therapy for cancer," *Oncology Letters*, vol. 16, no. 1, pp. 687–702, 2018.

[21] J. L. S. Welti, S. Dimmeler, and P. Carmeliet, "Recent molecular discoveries in angiogenesis and antiangiogenic therapies in cancer," *The Journal of Clinical Investigation*, vol. 123, no. 8, pp. 3190–3200, 2013.

[22] J. L. J. Xu, T. H. Zheng, L. Bai, and Z. J. Liu, "MicroRNAs in the occurrence and development of primary hepatocellular carcinoma," *Advances in Clinical and Experimental Medicine*, vol. 25, no. 5, pp. 971–975, 2016.

[23] K. Oura, A. Morishita, and T. Masaki, "Molecular and Functional Roles of MicroRNAs in the Progression of Hepatocellular Carcinoma-A Review," *International Journal of Molecular Sciences*, vol. 21, no. 21, p. 8362, 2020.

[24] F. W. B. Huang, Y. G. Wang, and Y. G. Wang, "Role of autophagy in tumorigenesis, metastasis, targeted therapy and drug resistance of hepatocellular carcinoma," *World Journal of Gastroenterology*, vol. 24, no. 41, pp. 4643–4651, 2018.

[25] S. Lu, Y. Yao, G. Xu et al., "CD24 regulates sorafenib resistance via activating autophagy in hepatocellular carcinoma," *Cell Death & Disease*, vol. 9, no. 6, p. 646, 2018.

[26] L. J. M. I. Gay and I. Malanchi, "The sleeping ugly: tumour microenvironment's act to make or break the spell of dormancy," *Biochimica Et Biophysica Acta. Reviews on Cancer*, vol. 1868, no. 1, pp. 231–238, 2017.

[27] X. Wang, T. Chen, Z. Deng et al., "Melatonin promotes bone marrow mesenchymal stem cell osteogenic differentiation and prevents osteoporosis development through modulating circ_0003865 that sponges miR-3653-3p," *Stem Cell Research & Therapy*, vol. 12, no. 1, p. 150, 2021, PMID: 33632317.

[28] C. S. Melincovici, A. B. Boşca, S. Şuşman et al., "Vascular endothelial growth factor (VEGF) - key factor in normal and pathological angiogenesis," *Romanian Journal of Morphology and Embryology*, vol. 59, no. 2, pp. 455–467, 2018.

[29] X. Q. Shengping Song, "LncRNA miR503HG inhibits epithelial-mesenchymal transition and angiogenesis in hepatocellular carcinoma by enhancing PDCD4 via regulation of miR-15b," *Digestive and Liver Disease*, vol. 53, no. 1, pp. 107–116, 2021.

Hindawi
Mediators of Inflammation
Volume 2022, Article ID 7911033, 8 pages
https://doi.org/10.1155/2022/7911033

Research Article

The Role of the Monocyte-to-Lymphocyte Ratio in Acute Ischemic Stroke Patients with Acute Kidney Injury

Fen Jiang,[1] Zhen Shi,[1,2] Xiangyang Liu,[3] Jiaxuan Xiang,[1] Jie Lei,[1] Bo Yang,[1] XiangLi Lei,[4] and Xuewei Li[5]

[1]*The First Affiliated Hospital, Department of Nephrology, Hengyang Medical School, University of South China, Hengyang, Hunan 421001, China*
[2]*Division of Nephrology, Huayuan People's Hospital, Xiangxi, Hunan 416400, China*
[3]*Department of Clinical Medicine, Xiangnan University, Chenzhou, 423000 Hunan Province, China*
[4]*Affiliated Nanhua Hospital, Department of Nephrology, Hengyang Medical School, University of South China, No. 336 Dongfeng Road, Hengyang, Hunan 421001, China*
[5]*The First Affiliated Hospital, Department of Neurology, Hengyang Medical School, University of South China, Hengyang, Hunan 421001, China*

Correspondence should be addressed to XiangLi Lei; leixiangli.happy@163.com and Xuewei Li; 2021000010@usc.edu.cn

Received 11 June 2022; Revised 11 July 2022; Accepted 26 July 2022; Published 28 August 2022

Academic Editor: Md Sayed Ali Sheikh

Objective. The objective of the study was to determine if acute kidney injury (AKI) in patients with acute ischemic stroke was associated with the monocyte-to-lymphocyte ratio (MLR) assessed upon admission to the neurology intensive care unit (NICU) (AIS). We also looked into the MLR's function in predicting hospital mortality in AIS patients. *Methods*. This retrospective analysis included 595 adult patients with AIS who were hospitalized to the NICU of the First Affiliated Hospital of South China between January 2017 and December 2019. Clinical signs and imaging studies were used to diagnose AIS. KDIGO criteria were used to define AKI. The ratio of monocytes to lymphocytes was used to compute MLR, the ratio of neutrophils to lymphocytes was used to calculate NLR, and the ratio of platelets to lymphocytes was used to calculate PLR. *Result*. 361 males and 234 women between the ages of 66.27 ± 12.05 years took part in the study. The individuals' MLR was 0.4729 ± 0.3461 and their neutrophil-to-lymphocyte ratio (NLR) was 8.18 ± 5.45. There were notable disparities in MLR and NLR between the AKI and non-AKI groups ($p < 0.001$). The link between MLR and AKI development risk was enhanced after adjustment, with respective cutoff values of 0.4581 and 9.26. For the MLR-based prediction of AKI incidence, the areas under the receiver-operating characteristic curves (AUCs) were 0.711 (95% CI: 0.663-0.758). And NLR-based prediction of AKI incidence the AUCs was (95% CI: 0.742-0826). Additionally, MLR was associated with a higher rate of in-hospital mortality (2.825, 95% confidence interval: 1.058, 7.545), whereas NLR was associated with a risk of in-hospital mortality of 1.085. (95 percent CI: 1.022, 1.151). An AUC of 0.745 (95% CI: 0.601-0.889, $p = 0.026$) was obtained for in-hospital mortality based on the MLR, whereas an AUC of 0.724 (95% CI: 0.531-0.916, $p = 0.042$) was obtained for in-hospital mortality based on the NLR. *Conclusion*. MLR and neutrophil-to-lymphocyte ratio (NLR) were associated with a higher risk of AKI and in-hospital death in AIS patients.

1. Introduction

The leading cause of mortality and disability in the world, acute ischemic stroke (AIS), has a large economic impact [1, 2]. Stroke is frequently accompanied by a number of side effects, including thrombosis, infection, and starvation. Acute kidney damage (AKI) following stroke has received more attention in recent years. It has been noted that the incidence of AKI following a stroke might range from 2.2 to 28.4 percent [3–6]. AKI also raises the likelihood of severe disability and in-hospital mortality after a stroke. Early detection and early development of AKI have important

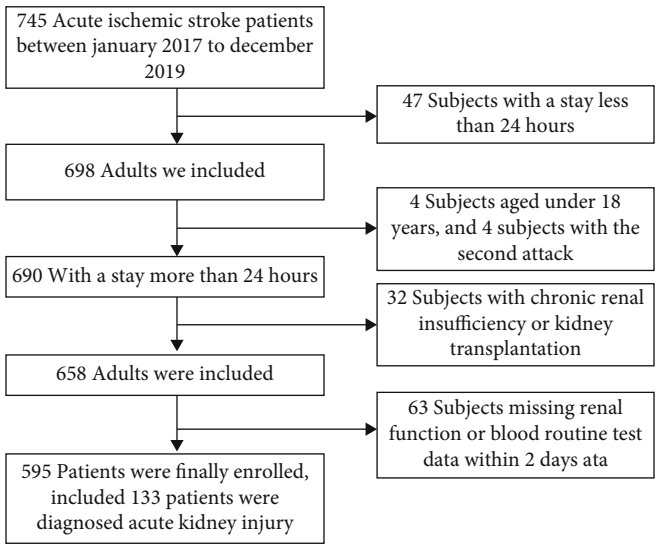

Figure 1: Flowchart of participant screening.

practical significance, which may lead to better clinical outcomes and reduce financial burdens. Currently, changes in serum creation (Scr) levels and urine volume are used to diagnose AKI. But previous studies have suggested that Scr is changed by many nonrenal factors and only increases after a substantial portion of nephrons has already been injured [7, 8]. Although new markers like kidney injury molecule-1 (KIM-1) and cystatin C (Cyst C) have been developed in numerous studies to help diagnose AKI early on, few have been used in clinical settings [9–11].

Inflammation has a profound impact on the development of AIS. After the stroke, a robust inflammatory response is triggered [12, 13], neutrophils and monocyte are upregulated, and lymphocytes are reduced, which are immediately induced in the peripheral blood [14]. In the meantime, AKI development involves inflammation heavily. AKI patients exhibit changes in the morphology or/and functionality of their tubular epithelium and/or vascular endothelial cells [15, 16].

A new systemic inflammatory response biomarker called the monocyte-to-lymphocyte ratio (MLR) is obtained by dividing the frequency of monocytes by the number of lymphocytes. MLR has been linked to poststroke depression (PSD) after three months and may have a role in the inflammatory process, according to previous research [17]. Cheng et al. discovered that a high MLR increased the risk of stroke-associated pneumonia (SAP), which can assist clinicians to diagnose patients with high-risk SAP earlier [18]. However, it is unclear if MLR has any clinical benefit in foretelling the emergence of AKI in acute ischemic stroke.

Given the potential role of inflammation in AIS and AKI, we proposed exploring the potential MLR role in AKI after AIS.

2. Material and Methods

2.1. Study Population. From January 2017 to December 2019, we included all patients (aged 18 or older) with AIS in the Department of Neurology Intensive Care Unit (NICU) at the University of South China's First Affiliated Hospital. The exclusion criteria included the following: ① presence of AKI before admission; ② preexisting chronic renal insufficiency or renal dysfunction requiring renal replacement therapy (RRT) before admission; ③ kidney transplantation; ④ admission to the NICU for less than 24 hours; ⑤ missing renal function or regular blood test results within two days of NICU admission; second AIS attack. Clinical symptoms and imaging exams were used to define AIS.

The primary outcome is the onset of AKI, while the secondary outcomes are in-hospital mortality, renal replacement therapy, ventilation, and hospital stay. This study, which was carried out in accordance with the Declaration of Helsinki, was approved by the First Affiliated Hospital of the University of South China.

2.2. Clinical Assessment and Data Collection. Sex, age, preexisting clinical conditions, complete blood count, blood biochemistry, inflammatory markers, and the National Institutes of Health Stroke Scale (NIHSS) score for neurological severity and Glasgow coma score (GCS) were all collected [19].

2.3. Acute Renal Damage Diagnosis. AKI was identified, according to the Kidney Damage: Enhancing Global Outcomes report (KDIGO) [20]. The minimum amount of serum creatinine found in the emergency hospital or general ward before admission to the NICU was used to calculate the benchmark creatinine level. When this value could not be acquired, the modifying of diet in renal disease (MDRD) approach was used to determine it, assuming a normal glomerular filtration rate of $75\,\mathrm{ml}\cdot\mathrm{min}^{-1}\cdot 1.73\,\mathrm{m}^{-2}$ [21]. The estimated baseline glomerular filtration rate was calculated using the Chronic Kidney Disease Epidemiology Collaboration algorithm (eGFR) [22]. Utilizing the KDIGO recommendations, cases of AKI were identified: (a) a rise in

Table 1: Subjects' initial features and outcomes.

Variables	ALL ($n = 595$)	Patients with AKI ($n = 133$)	Patients without AKI ($n = 462$)	p value
Male (%)	361 (60.7%)	91 (68.4%)	270 (58.4%)	0.000
Age (years)	66.27 ± 12.05	68.17 ± 12.32	65.72 ± 11.93	0.823
Comorbidities				
Hypertension	436 (73.4%)	107 (80.5%)	329 (71.4%)	0.037*
Diabetes	136 (22.9%)	43 (32.3%)	93 (20.2%)	0.003*
Coronary artery disease	148 (24.9%)	41 (30.8%)	107 (23.2%)	0.071
COPD	13 (2.2%)	7 (5.3%)	6 (1.3%)	0.016
eGFR (ml/min/1.73m^2)	76.58 ± 18.93	71.55 ± 22.82	78.03 ± 17.41	0.000
Laboratory index at NICU admission				
Baseline Scr (umol/l)	86.27 ± 35.76	99.21 ± 60.37	82.55 ± 23.29	0.000*
BUN (mmol/l)	5.97 ± 3.65	8.11 ± 6.03	5.35 ± 2.24	0.000
Albumin (g/l)	40.14 ± 4.79	39.35 ± 5.59	40.36 ± 4.52	0.364
Triglyceride (mmol/l)	1.57 ± 1.42	1.38 ± 1.08	1.63 ± 1.50	0.087
PCT (ng/ml)	0.24 (0.07, 0.55)	0.54 (0.80, 0.72)	0.08 (0.05, 0.16)	0.001*
White blood count/mm^3	9.57 ± 3.77	10.61 ± 3.40	9.27 ± 3.66	0.314
CRP	11.29 (2.10,18.87)	25.78 (17.02,131.59)	8.47 (4.6, 56.08)	0.002*
Haemoglobin	128.70 ± 20.68	124.49 ± 25.23	129.98 ± 19.01	0.005
NIHSS score	12.13 ± 6.61	14.51 ± 6.37	11.44 ± 6.52	<0.001*
GCS score	11.26 ± 2.99	10.18 ± 3.18	11.57 ± 2.92	0.000
PLR	192.46 ± 105.31	230.71 ± 109.99	181.45 ± 101.40	<0.001*
MLR	0.4729 ± 0.3461	0.6401 ± 0.4170	0.4248 ± 0.3069	<0.001*
NLR	8.18 ± 5.45	11.65 ± 5.27	7.19 ± 5.08	<0.001*
Neutrophils	7.77 ± 3.61	8.89 ± 3.82	7.44 ± 3.69	0.356
Lymphocytes	1.25 ± 0.63	1.12 ± 0.57	1.68 ± 0.63	0.092
Monocytes	0.49 ± 0.29	0.54 ± 0.33	0.48 ± 0.28	0.006
Platelets	201.91 ± 73.65	195.13 ± 72.47	203.87 ± 73.95	0.228
Outcome				
In-hospital mortality	11	4 (3.0%)	7 (1.5%)	0.026*
RRT	2	2 (1.5%)	0	0.000*
Ventilation	43 (7.23%)	17 (12.8%)	26 (5.6%)	0.005*
Hospital stay	12.20 ± 10.12	13.96 ± 12.86	11.70 ± 9.22	0.024*

MLR: monocyte-to-lymphocyte ratio; PLR: platelet-to-lymphocyte ratio; NIHSS: National Institutes of Health Stroke Scale score; GCS: Glasgow coma score; Scr: serum creatinine; RRT: renal replacement treatment; COPD: chronic obstructive pulmonary disease; CRP: C-reactive protein; PCT: procalcitonin; NLR: neutrophil-to-lymphocyte ratio; HGB: haemoglobin.

serum creatinine (sCr) of 0.3 mg/dL (26.5 mol/l) within the previous 48 hours; (b) an increase in Scr to 1.5 times baseline within the previous 7 days; and (c) a urine flow rate of 0.5 ml/kg/h for six hours.

2.4. Neutrophil to Lymphocyte Ratio, Platelet to Lymphocyte Ratio, and Monocyte to Lymphocyte Ratio. The ratio of monocytes to lymphocytes was used to compute MLR, the ratio of neutrophils to lymphocytes was used to calculate NLR, and the ratio of platelets to lymphocytes was used to calculate PLR. MLR, NLR, and PLR were obtained from a standard blood test, and Roche's automatic analyzer identified the blood test as routine. MLR illustrates the interaction between innate (monocyte) and adaptive (lymphocyte) immune responses, including lymphocyte depletion and increase of monocytes.

2.5. Statistical Analysis. Continuous data showed variables as medians with interquartile ranges, while categorical data showed variables as frequency counts (percent). The chi-square test was used to compare groups in both categorical and continuous data. Spearman's correlation was used to look into how the MLR related to other variables. Using multivariable logistic regression, the MLR and NLR were examined for associations with the course of AKI and prognosis. The outcomes are shown as odds ratios (ORs). Using

Table 2: The relationship between baseline MLR and other variables.

Variable	OR (95% CI)	p value
Age	-0.133	0.001*
Baseline Scr (umol/l)	0.047	0.249
Triglyceride (mmol/l)	-0.085	0.045*
CRP	0.297	<0.001*
PCT (ng/ml)	0.120	0.008*
ALB (g/l)	-0.091	0.026*
NLR	0.562	<0.001*
PLR	0.302	<0.001*
HGB (g/dl)	-0.073	0.077
Neutrophils (count/mm^3)	0.284	0.000*
Lymphocytes (count/mm^3)	-0.367	0.000*
Platelets (count/mm^3)	-0.05	0.021*
NIHSS score	0.097	0.019*
GCS score	-0.102	0.013*
Monocytes (count/mm^3)	0.575	0.000*

MLR: monocyte-to-lymphocyte ratio; CRP: C-reactive protein; PCT: procalcitonin; NLR: neutrophil-to-lymphocyte ratio; PLR: platelet-to-lymphocyte ratio; NIHSS: National Institutes of Health Stroke Scale score; GCS: Glasgow coma score; HGB: haemoglobin; Scr: serum creatinine; ALB: albumin.

receiver-operating characteristic (ROC) curves, the predictive value of the MLR and NLR for the emergence of AKI and in-hospital mortality was assessed. Cut-off values, as well as the sensitivity and specificity for parameters, were computed using the Youden index. A two-tailed $p < 0.05$ indicated statistical significance for each study. The complete data analysis was carried out using SPSS 16. (Chicago, IL, USA).

3. Results

3.1. Basic Characteristics of Patients. 150 participants were eliminated from the research due to the baseline characteristics of the 745 patients who were screened for inclusion (Figure 1). In the end, 595 patients were recruited for the research analysis.

The baseline characteristics and results of the patients are summarised in Table 1. Participants included 361 (60.7%) men and 238 (39.3%) women, representing 66.27 ± 12.05 years of age. The eGFR was 76.58 ± 18.93, and the mean ± SD was 0.4729 ± 0.3461 for the MLR, 8.18 ± 5.45 for the NLR, and 192.46 ± 105.31 for the PLR. According to the KDIGO criteria, 133 patients (22.35%) were diagnosed with AKI, 104 were at stage 1, 24 were at stage 2, and 5 were at stage 3. There were remarkable differences flanked by the AKI set and nongroup in hypertension and diabetes, COPD, eGFR, baseline Scr, BUN, PCT, CRP, HGB, monocyte, MLR, NLR, and PLR. Additionally, individuals who possess AKI had a superior NIHSS and GCS than the non-AKI group. Moreover, patients who experienced AKI had a higher rate of CRRT and ventilation and a longer hospital stay. No significant differences were observed in age, coronary artery disease, albumin, triglycerides, white blood count, neutrophils, lymphocytes, or platelets between the two groups. The AKI group saw worse outcomes in comparison to the non-AKI group, including higher death rates and longer hospital stays (13.96 ± 12.86 vs. 11.70 ± 9.22, $p = 0.024$) and higher ventilation (12.8% vs. 5.6%, $p = 0.005$).

3.2. Association between MLR and Other Parameters. To investigate the relationship between the MLR and clinical factors, Spearman correlation coefficients were generated. Initial MLR was favourably correlated with CRP, PCT, NLR, PLR, NIHSS score, and monocytes at baseline ($p < 0.05$). In addition, age, triglycerides, ALB, HGB, lymphocytes, platelets, and GCS score were all linked negatively with baseline MLR ($p < 0.05$). However, there was no relationship between the baseline Scr and the MLR (Table 2).

3.3. By Logistic Regression, MLR and NLR for the Development of AKI. After correcting for sex, age, sepsis, hypertension, diabetes, COPD, baseline Scr, and eGFR, logistic regression was used to examine relationships between MLR and NLR with AKI after admission to the NICU. MLR and NLR were linked to the incidence of AKI in AIS patients, according to the analyses, with ORs of 3.652 and 1.163 (p0.001), respectively (Table 3). Meanwhile, the ORs of CRP and HGB for AKI incidence were 1.005 (1.00-1.010) and 0.986 (0.975, 0.997), respectively. However, PCT, triglycerides, and albumin levels also were not proposed as potential risk variables for AKI.

Age, sex, sepsis, hypertension, diabetes, coronary artery disease, COPD, Scr, and eGFR are all considered after adjusting for sex. Diabetes (DM) is denoted by the letters MLR (monocyte-to-lymphocyte ratio), CRP (c-reactive protein), PCT (procalcitonin), NLR (neutrophil-to-lymphocyte ratio), PLR (platelet-to-lymphocyte ratio), NIHSS (National Institutes of Health Stroke Scale score), and GCS (Glasgow Coma Score). ALB stands for albumin, HGB for haemoglobin, and Scr for serum creatinine. Diabetes is indicated by DM. The disorder that affects the lungs is called chronic obstructive pulmonary disease (COPD).

3.4. The ROC Curve of MLR and NLR with AKI Incidence. To assess the MLR and NLR's capacity for discrimination in the diagnosis of AKI, ROC curves were developed. AUCs for the MLR and NLR were 0.711. (95 percent CI: 0.663-0.758, $p < 0.001$) and 0.784 (95 percent CI: 0.742-0826, $p < 0.001$) for AKI prediction, respectively. MLR has the best ROC cut-off value of 0.4581, with 69.2% sensitivity and 65.4 percent specificity. The NLR has a cut-off value of 9.46 on the ROC curve, with 73.7 percent sensitivity and 76.6 percent specificity (Figure 2).

3.5. Multivariable Logistic Regression Predicts the Risk of In-Hospital Death. The in-hospital mortality-adjusted odds ratios based on MLR and NLR were 2.825 (1.058-7.545) and 1.085 (1.022, 1.151), respectively, after adjusting for sex, age, hypertension, COPD, or baseline Scr. In-hospital

Table 3: values of the multivariable logistic regression analysis' MLR and NLR for AKI.

Variable	Unadjusted OR (95% CI)	*p* value	Adjusted OR (95% CI)	*p* value
MLR	6.135 (3.1797-11.772)	0.000	6.261 (3.142,12.477)	0.000
PCT (ng/ml)	1.005 (0.979-1.127)	0.174	1.035 (0.988-1.084)	0.151
CRP	1.006 (1.002-1.010)	0.005	1.005 (1.00-1.010)	0.036
WBC (count/mm^3)	1.092 (1.040-1.146)	0.000	1.083 (1.028-1.140)	0.003
Albumin (g/l)	0.957 (0.920-0.996)	0.032	0.983 (0.951-1.026)	0.425
HGB (g/dl)	0.987 (0.978-0.996)	0.006	0.986 (0.975-0.997)	0.010
NLR	1.168 (1.119-1.218)	0.000	1.164 (1.114-1.215)	0.000
Triglyceride (mmol/l)	0.837 (0.682-1.029)	0.092	0.822 (0.621-1.021)	0.077
NIHSS	1.074 (1.042-1.108)	0.000	1.080 (1.045-1.115)	0.000
GCS	0.861 (0.809-0.918)	0.000		
Baseline Scr (umol/l)	1.012 (1.006-1.018)	0.000		
Sex	1.541 (1.023-2.321)	0.039		
Age (year)	1.018 (1.001-1.035)	0.040		
Sepsis	3.485 (0.217-56.091)	0.379		
Hypertension	1.651 (1.028, 2.652)	0.038		
DM	1.891 (1.231-2.902)	0.004		
Coronary artery disease	1.479 (0.965-2.266)	0.073		
COPD	4.222 (1.394-12.788)	0.011		

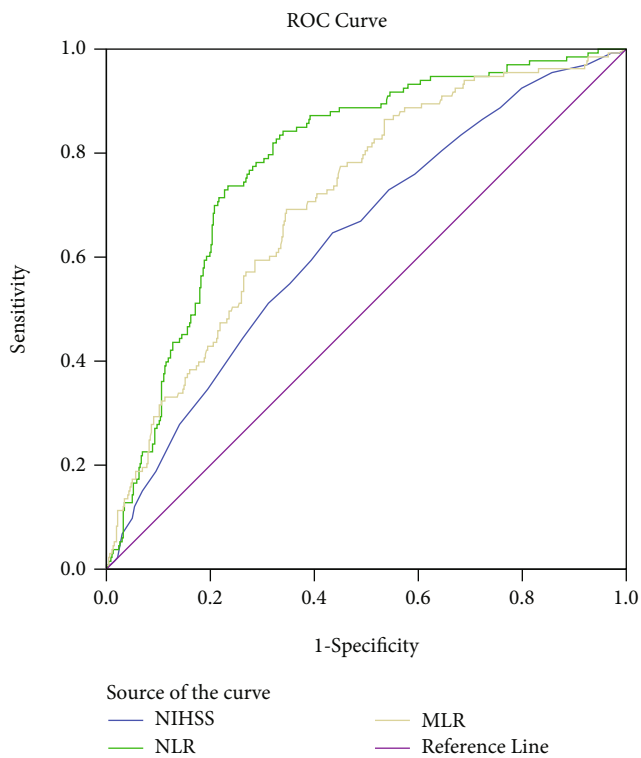

Figure 2: Receiver-operating characteristic curves for MLR, NLR, and NIHSS for predicting AKI. MLR: monocyte-to-lymphocyte ratio; NLR: neutrophil-to-lymphocyte ratio; PLR: platelet-to-lymphocyte ratio.

mortality risk for NIHSS was 1.199 (1.062, 1.354). There was no link between CRP and PCT and mortality at clinic (Table 4).

3.6. The ROC Analysis of MLR for In-Hospital Death. With an ideal cut-off of 0.4731, 85.7 percent sensitivity, and 61.6 percent specificity, MLR produced an AUC of 0.745 (95 percent CI: 0.601-0.889, $p = 0.026$) for in-hospital mortality. For in-hospital mortality, NLR had an AUC of 0.724 (95 percent CI: 0.531-0.916, $p = 0.042$), with the optimal cut-off of 19.35, 57.1 percent sensitivity, and 96.1 percent specificity. With the optimal cut-off of 19.5, 71.4 percent sensitivity, and 89.89 percent specificity, 95 percent confidence interval for the AUC of NIHSS for in-hospital mortality was 0.587-0.976, $p = 0.010$ (Figure 3).

4. Discussion

The results of this study showed a relationship between the initial MLR and NLR evaluated at admission and the emergence of AKI in AIS patients. MLR and NLR both were higher in AKI patients than in non-AKI patients, with cutoff values of 0.4581 and 9.46, respectively. Furthermore, both the MLR and the NLR were found to be strongly linked to in-hospital death in patients admitted. NLR is an available, low-cost, and reproducible indicator of inflammation. It is also a marker of extensive secondary damage caused by neutrophils and their products. Therefore, NLR has been used to predict the prognosis of patients with sepsis with inconsistent results.

This is the first investigation examining the relationship between MLR and AKI in the setting of AIS. AKI was diagnosed in 133 (22.35 percent) of the patients in this study, which was higher than in a previous study [6]. This could be due to changes in the NICU patient demographic or the severity of the sickness. Male sex, hypertension, diabetes, and decreased eGFR have all been linked to an increased risk

Table 4: The markers that predict in-hospital mortality.

Variable	Unadjusted		After adjustment	
	OR (95% CI)	p value	OR (95% CI)	p value
MLR	2.930 (1.118, 7.677)	0.029	2.825 (1.058, 7.545)	0.038
NLR	1.082 (1.021, 1.147)	0.008	1.085 (1.022, 1.151)	0.007
CRP	1.005 (0.993, 1.018)	0.397	1.005 (0.993, 1.018)	0.422
PCT	0.976 (0.672, 1.417)	0.898	0.979 (0.694, 1.382)	0.905
NIHSS	1.201 (1.065, 1.355)	0.003	1.199 (1.062, 1.354)	0.003
GCS	0.733 (0.584, 0.92)	0.007	0.728 (0.580, 0.914)	0.006

Adjusted by sex, hypertension, COPD, and Scr. MLR: monocyte-to-lymphocyte ratio; CRP: C-reactive protein; PCT: procalcitonin; NLR: neutrophil-to-lymphocyte ratio; PLR: platelet-to-lymphocyte ratio; NIHSS: National Institutes of Health Stroke Scale score; GCS: Glasgow coma score; HGB: haemoglobin.

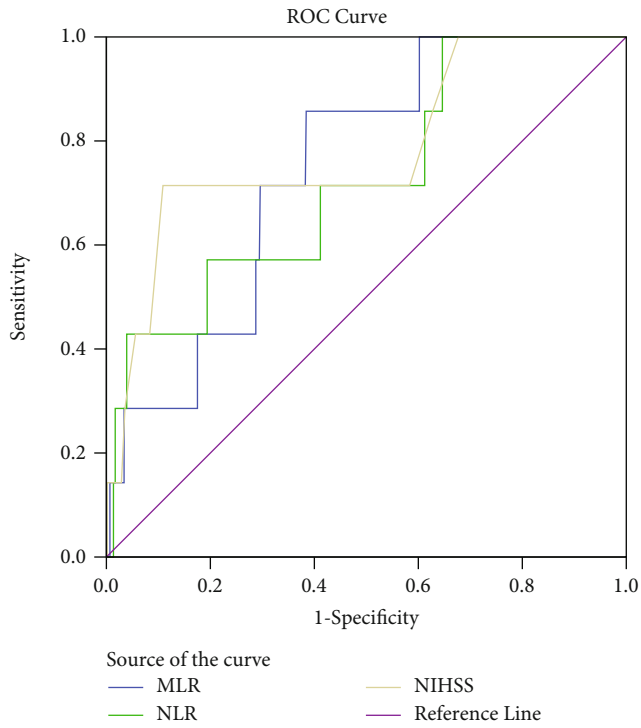

Figure 3: In-hospital mortality receiver-operating characteristic curves for MLR, NLR, and NIHSS. MLR stands for monocyte-to-lymphocyte ratio, while NLR stands for neutrophil-to-lymphocyte ratio, and PLR is for platelet-to-lymphocyte ratio.

of acute kidney damage. An eGFR of less than 30 ml/min and having high blood pressure were identified to be risk factors for acute renal injury in AIS patients in a related study by Chusiri et al. [23].

Increasing evidence suggests that inflammatory and oxidative stress mechanisms initiated by inflammatory cells play a critical role in the pathological processes of ischemic stroke and its subtypes [24, 25]. Monocytes and activated macrophages can enter and adhere to the inner surface of the arterial wall by secreting various proinflammatory and prooxidant mediators [26].

Ischemia-reperfusion and inflammation may be key players in the aetiology of AKI, according to several experimental and clinical investigations [15, 27, 28]. The MLR has been hypothesised as a potential peripheral marker and an independent risk factor for ischemic stroke patients [29]. In this investigation, we discovered that in AIS patients, the MLR and NLR enhanced the likelihood of severe kidney damage. MLR and NLR may therefore be simple, practical, and affordable techniques in clinical practice for the prediction of AKI. There have been few studies on the MLR mechanism in AIS, and inflammation may be a crucial factor.

The AUC of the MLR for in-clinical death was 0.745 (95 percent CI: 0.601-0.889, $p = 0.026$), with the optimal cut-off value being 0.4731. In this study, we further examined the association between the MLR and NLR and in-hospital mortality. The 95 percent confidence interval for the AUC of the NLR for in-hospital mortality was 0.531-0.916, $p = 0.042$. A risk factor for hospital death is both MLR and NLR. The MLR and NLR also showed clear value for in-hospital mortality.

We also looked at RRT and ventilation as a secondary endpoint and discovered that there was a substantial difference in-hospital stay, ventilation, and RRT between AKI and non-AKI teams ($p < 0.05$), which was similar to Nadkarni et al.'s study [30].

The advantage of this study was to show that MLR and NLR were associated with a higher risk of AKI and in-hospital death in AIS patients. However, there are certain restrictions on this study that must be recognized. The first reason is that our investigation was a retrospective observational study carried out in a single facility. It was difficult to adjust for control variables and selective biases to prevent selection bias brought on by other factors; patients who spent less than 48 hours in the hospital or who had just one or two blood tests were excluded. As a result, the findings of this study can still be used to describe the epidemiological features of AKI in AIS patients. The diagnosis of AKI based on the Scr level and urine output, as well as histologic confirmation, was not accessible since diuretics might affect urine production, and histologic confirmation was not employed in the clinic. This could lead to an underestimation of the true occurrence of AKI. Finally, the study only looked at short-term prognoses; it neglected to look at long-term prognoses, which calls for long-term surveillance of AKI patients.

5. Conclusion

Our research supports the use of a single MLR and NLR measurement in the admission of AIS patients, and it may

be a useful tool for the early detection of individuals who are at high risk of AKI. The MLR and NLR, meanwhile, help estimate in-hospital mortality.

Abbreviations

AIS: Acute ischemic stroke
MLR: Monocyte-to-lymphocyte ratio
PLR: Platelet-to-lymphocyte ratio
NLR: Neutrophil-to-lymphocyte ratio
NICU: Neurology intensive care unit
PSD: Poststroke depression
AKI: Acute kidney injury
PCT: Procalcitonin
CRP: C-reactive protein
CystC: Cystatin C
Scr: Serum creation
WBC: White blood cell
HGB: Haemoglobin
COPD: Chronic obstructive pulmonary disease
DM: Diabetes mellitus
KDIGO: Kidney Disease: Improving Global Outcomes
KIM-1: Kidney injury molecule-1
ROC: Receiver-operating characteristic
BUN: Blood urea nitrogen
GFR: Glomerular filtration rate
NIHSS: National Institutes of Health Stroke Scale score
GCS: Glasgow coma score
AUC: Areas under the receiver-operating characteristic curve.

Data Availability

The raw data used to support the study's findings is given in the article's tables and figures.

Ethical Approval

The first associated hospital of South China's ethics committee accepted the study, which was constructed in accordance with the Declaration of Helsinki's ethical principles (certification number 20201211LL012). Additionally, the first associated hospital of South China's ethics committee approved a study exemption from the requirement for informed consent.

Disclosure

This manuscript was submitted as a preprint in the link "https://assets.researchsquare.com/files/rs-1006561/v1/e5cd4c2e-4e2c-4987-a6cd-6f7bcb091b83.pdf?c=1639493061."

Conflicts of Interest

For the purpose of this paper's publication, the authors declare no conflicts of interest.

Authors' Contributions

The concept, design, and draught of the manuscript were worked on by FJ, XL, and XL. All patient data were gathered by ZS, JX, XL, and JL. FJ ,BY and XL participated in data interpretation, critical paper revision for significant intellectual content, funding acquisition, and resource acquisition. The final version that will be published has the consent of all authors.

Acknowledgments

This study was supported by grants of the Hunan Provincial Health Commission Technology Foundation (202103050110 and 202103052372) and Hunan Provincial Science Technology Foundation (2020JJ4550).

References

[1] N. Zhang, F. Chen, X. Xie et al., "Application of quantitative EEG in acute ischemic stroke patients who underwent thrombectomy: a comparison with CT perfusion," *Clinical Neurophysiology*, vol. 141, pp. 24–33, 2022.

[2] G. A. Donnan, M. Fisher, M. Macleod, and S. M. Davis, "Stroke," *Lancet*, vol. 371, no. 9624, pp. 1612–1623, 2008.

[3] M. Khatri, J. Himmelfarb, D. Adams, K. Becker, W. T. Longstreth, and D. L. Tirschwell, "Acute kidney injury is associated with increased hospital mortality after stroke," *Journal of Stroke and Cerebrovascular Diseases*, vol. 23, no. 1, pp. 25–30, 2014.

[4] K. Stamatellopoulos, A. Laggouranis, M. Alevizaki, E. Manios, and K. Stamatellopoulos, "Renal dysfunction in acute stroke: an independent predictor of long-term all combined vascular events and overall mortality," *Nephrology Dialysis Transplantation*, vol. 24, no. 1, pp. 194–200, 2014.

[5] A. Covic, A. Schiller, N. Mardare, L. Petrica, M. Petrica, and A. Mihaescu, "The impact of acute kidney injury on short-term survival in an Eastern European population with stroke," *Nephrology Dialysis Transplantation*, vol. 23, no. 7, pp. 2228–2234, 2008.

[6] A. Zorrilla, W. Ziai, E. Sander Connolly Jr., R. Geocadin, R. Thompson, and L. Rivera-Lara, "Acute kidney injury following acute ischemic stroke and intracerebral hemorrhage: a meta-analysis of prevalence rate and mortality risk," *Cerebrovascular Diseases*, vol. 45, no. 1–2, pp. 1–9, 2018.

[7] J. Cerda, "A biomarker able to predict acute kidney injury before it occurs," *Lancet*, vol. 394, no. 10197, pp. 448–450, 2019.

[8] B. D. De Oliveira, K. Xu, T. H. Shen et al., "Molecular nephrology: types of acute tubular injury," *Nature Reviews Nephrology*, vol. 15, no. 10, pp. 99–612, 2019.

[9] D. M. Tanase, E. M. Gosav, S. Radu, C. F. Costea, M. Ciocoiu, and A. Carauleanu, "The predictive role of the biomarker kidney molecule-1 in acute kidney injury cisplatin-induced nephrotoxicity," *International Journal of Molecular Sciences*, vol. 20, no. 20, p. 5238, 2019.

[10] W. K. Han, V. Bailly, R. Abichandani, R. Thadhani, and J. V. Bonventre, "Kidney injury molecule-1: a novel biomarker for human renal proximal tubule injury," *Kidney International*, vol. 62, no. 1, pp. 237–244, 2002.

[11] X. Wang, X. Lin, B. Xie et al., "Early serum cystatin C-enhanced risk prediction for acute kidney injury post cardiac surgery: a prospective, observational, cohort study," *Biomarkers*, vol. 25, no. 1, pp. 20–26, 2020.

[12] S. Kaibin, D. Tian, Z. Guo Li, A. F. Ducruet, M. T. Lawton, and F. D. Shi, "Global brain inflammation in stroke," *The Lancet Neurology*, vol. 18, no. 11, pp. 1058–1066, 2019.

[13] S. E. Khoshnam, W. Winlow, M. Farzaneh, Y. Farbood, and H. F. Moghaddam, "Pathogenic mechanisms following ischemic stroke," *Neurological Sciences*, vol. 38, no. 7, pp. 1167–1186, 2017.

[14] E. Kim and S. Cho, "Microglia and monocyte-derived macrophages in stroke," *Neurotherapeutics*, vol. 13, no. 4, pp. 702–718, 2016.

[15] I. Mami, Q. Tavernier, N. Bouvier et al., "A novel extrinsic pathway for the unfolded protein response in the kidney," *Journal of the American Society of Nephrology*, vol. 27, no. 9, pp. 2670–2683, 2016.

[16] H. Rabb, M. D. Griffin, D. McKay et al., "Inflammation in AKI: current understanding, key questions, and knowledge gaps," *Journal of the American Society of Nephrology*, vol. 27, no. 2, pp. 371–379, 2016.

[17] K. Ding, Z. Hua Lai, Y. Zhang, G. Yang, J. He, and L. Zeng, "Monocyte-to-lymphocyte ratio is associated with depression 3 months after stroke," *Neuropsychiatric Disease and Treatment*, vol. 17, pp. 835–845, 2021.

[18] H. R. Cheng, J. Y. Song, Y. N. Zhang et al., "High monocyte-to-lymphocyte ratio is associated with stroke-associated pneumonia," *Frontiers in Neurology*, vol. 11, pp. 575–580, 2020.

[19] T. Brott, H. P. Adams Jr., C. P. Olinger et al., "Measurements of acute cerebral infarction: a clinical examination scale," *Stroke*, vol. 20, no. 7, pp. 864–870, 1989.

[20] J. A. Kellum, N. Lameire, P. Aspelin et al., "Kidney Disease: Improving Global Outcomes (KDIGO) acute kidney injury work group KDIGO clinical practice guideline for acute kidney injury," *Kidney International*, vol. 2, no. 1, pp. 1–38, 2012.

[21] R. Bellomo, C. Ronco, J. A. Kellum, and R. L. Mehta, "Acute Dialysis Quality Initiative workgroup. Acute renal failure-definition, outcome measures, animal models, fluid therapy and information technology needs: the Second International Consensus Conference of the Acute Dialysis Quality Initiative (ADQI) Group," *Critical Care*, vol. 8, no. 4, pp. 1–9, 2004.

[22] A. S. Levey, L. A. Stevens, C. H. Schmid, Y. Zhang, H. I. Feldman, and CKD-EPI (Chronic Kidney Disease Epidemiology Collaboration), "A new equation to estimate glomerular filtration rate," *Annals of Internal Medicine*, vol. 150, no. 9, pp. 604–612, 2009.

[23] S. Chusiri, A. Chutinet, N. C. Suwanwela, and C. Puttilerpong, "Incidence and risk factors of postcontrast acute kidney injury in patients with acute ischemic stroke," *Stroke Research and Treatment*, vol. 2020, Article ID 7182826, 6 pages, 2020.

[24] R. Jin, G. Yang, and G. Li, "Inflammatory mechanisms in ischemic stroke: role of inflammatory cells," *Journal of Leukocyte Biology*, vol. 87, no. 5, pp. 779–789, 2010.

[25] A. Bonaventura, L. Liberale, A. Vecchié et al., "Update on inflammatory biomarkers and treatments in ischemic stroke," *International Journal of Molecular Sciences*, vol. 17, no. 12, p. 1967, 2016.

[26] A. S. Jaipersad, G. Y. Lip, S. Silverman, and E. Shantsila, "The role of monocytes in angiogenesis and atherosclerosis," *Journal of the American College of Cardiology*, vol. 63, no. 1, pp. 1–11, 2014.

[27] H. Rabb, M. D. Griffin, D. B. Mckay et al., "Acute dialysis quality initiative consensus XIII work group inflammation in AKI: current understanding, key questions, and knowledge gaps," *Journal of the American Society of Nephrology*, vol. 27, no. 2, pp. 371–379, 2016.

[28] M. Jansen, D. Emal, G. J. Teske, C. Mark, F. Sandrine, and J. Joris, "Release of extracellular DNA influences renal ischemia reperfusion injury by platelet activation and formation of neutrophil extracellular traps," *Kidney International*, vol. 91, no. 2, pp. 352–364, 2017.

[29] T. Wu, K. Chien, and H. Lin, "Total white blood cell count or neutrophil count predict ischemic stroke events among adult Taiwanese: report from a community-based cohort study," *BMC Neurology*, vol. 13, no. 1, pp. 1–8, 2013.

[30] G. Nadkarni, A. Patel, I. Konstantinidis et al., "Dialysis requiring acute kidney injury in acute cerebrovascular accident hospitalizations," *Stroke*, vol. 46, no. 11, pp. 3226–3231, 2015.

Hindawi
Mediators of Inflammation
Volume 2022, Article ID 5187218, 10 pages
https://doi.org/10.1155/2022/5187218

Research Article

miR-212 Promotes Cardiomyocyte Hypertrophy through Regulating Transcription Factor 7 Like 2

Jinxia Yuan and Guoliang Yuan

Department of Cardiology, Shuyang Hospital of Traditional Chinese Medicine, Yangzhou University, Shuyang, Jiangsu, China

Correspondence should be addressed to Guoliang Yuan; yuanguoliang0815@126.com

Received 3 July 2022; Accepted 6 August 2022; Published 24 August 2022

Academic Editor: Md Sayed Ali Sheikh

To explore the role and possible mechanism of miRNA-212 in heart failure (HF). The rat model of abdominal aortic constriction was constructed, the changes of myocardial morphology were observed by hematoxylin-eosin (HE) staining, and the hypertrophy-related marker molecules were detected by quantitative real-time polymerase chain reaction (qRT-PCR). At the cellular level, phenylephrine and angiotensin II were added to induce cardiomyocyte hypertrophy. The overexpression of miR-212 adenovirus was constructed, and the expression of miR-212 was overexpressed, and its effect on cardiac hypertrophy (CH) was detected by immunofluorescence and qRT-PCR. Then, the mechanism of miR-212 regulating CH was verified by website prediction, luciferase reporter gene assay, qRT-PCR, and western blotting assay. In the successfully constructed rat model of abdominal aortic constriction and cardiomyocyte hypertrophy, ANP and myh7 were dramatically increased, myh6 expression was decreased, and miRNA-212 expression was increased. Overexpression of miRNA-212 in cardiomyocytes can promote cardiomyocyte hypertrophy, while knocking down miR-212 in cardiomyocytes can partially reverse cell hypertrophy. In addition, miR-212 targets TCF7L2 and inhibits the expression of this gene. miRNA-212 targets TCF7L2 and inhibits the expression of this gene, possibly through this pathway to promote cardiomyocyte hypertrophy.

1. Introduction

Cardiovascular disease, especially heart failure (HF), has always been a serious threat to human health [1]. HF is a syndrome of cardiac structure and function disorder caused by a variety of physiological factors, which is manifested as ventricular systolic ejection or diastolic filling dysfunction, which can lead to clinical symptoms such as sitting breathing, nocturnal paroxysmal dyspnea, lower limb pitting edema, and fatigue [2]. Despite advances in the treatment of HF, its high morbidity and mortality remain important issues affecting public health and socioeconomic development [3]. According to the analysis, HF is one of the main causes of hospitalization in the elderly over 65 years old, and it is one of the primary medical problems to be solved [4]. Of various cardiovascular diseases, it will eventually lead to HF, including myocardial infarction, after pressure overload (aortic stenosis and poor control of high blood pressure), inflammation (myocarditis) and overload capacity of hypertrophic cardiomyopathy (valvular regurgitation), genes inherited cardiomyopathy, and drug factors (such as alcohol and drugs such as cocaine, with heart damage side-effects adriamycin) [5]. The mechanism of HF is a complex signal cascade reaction between cell and molecular physiology change regulation of disease: myocardial cells, myocardial hypertrophy (MH), electrophysiological changes, contraction dysfunction, oxidative stress, metabolic disorders, extracellular matrix remodeling, apoptosis, and necrosis. Finally, it leads to the rational reconstruction of cardiomyopathy, with reduced cardiac output, blood stasis, increased capacity load, increased chronic filling pressure, hypoxia, and edema. With the deepening of the research on the pathogenesis of HF, the regulation of cellular and molecular signals has attracted more and more attention [6].

Noncoding RNA (ncRNA) in the RNA family is an important regulatory RNA, including a variety of different subgroups, such as small sequence microRNA (miRNA, tRNA, snRNA, and snoRNA), large sequence long

noncoding RNA (lncRNA), and circularRNA (circRNA), which can participate in the HF process as important regulatory factors [7]. miRNA genes are highly conserved in evolution and can be transcribed as independent transcription units in the intergenic or intron and exon regions of protein-coding genes [8]. Studies have shown that miRNAs play a crucial regulatory role in every link of the occurrence and development of heart diseases, participating in and regulating angiogenesis, MH, myocardial cell and interstitial fibrosis, inflammatory response, apoptosis, and necrosis [9].

The pathologic process of HF involves CH. MH in cell volume increases; protein secretion increased as the characteristics of the pathological process of sarcomere organization; its potential triggers for hemodynamics, ischemic injury and nerve endocrine imbalance, a variety of pathological conditions, such as its internal mechanism for fetal gene expression, excitation contraction coupling changes, energy metabolism, balance, molecular mechanisms involved in Ca^{2+} depend on the way, and PI3K/Akt pathway [10]. Studies have shown that many miRNAs function in a positive or negative way to regulate the molecular mechanisms of CH. For example, the expressions of miR-23a, miR-27b, miR-125b, and miR-195 were upregulated in the early stage of CH caused by aortic stenosis [11], while the expressions of miR-23a, miR-23b, miR-24, miR-125b, miR-195, miR-199a, and miR-214 were upregulated in the later stage, while the expressions of miR-93, miR-133a, miR-150, and miR-181b were downregulated [12], while miR-34a, miR-28, miR-148a, and miR-93 were upregulated and miR-126 and other miRNAs were downregulated in right HF hypertrophy caused by pulmonary artery stenosis [13]. Current studies have shown that miR-1, miR-18, miR-19, miR-133, miR-378, miR-185, and miR-155 can inhibit various types of CH, while miR-208 family, miR-100, miR-125b, miR-214, miR-212, miR-23, miR-24, miR-195, and miR-199a can promote CH [14].

Currently known diagnostic markers of HF are BNP and NT-proBNP, which have high sensitivity but low specificity. With the in-depth study of miRNA, miRNA may become a new marker of HF. Most miRNAs exist in cardiomyocytes but can also be detected in body fluids (serum, plasma, and urine), which are specifically associated with the physiological process of HF and have high specificity [14]. Fukushima et al. found that plasma expression of miR-126 in patients with chronic HF with low expression of NT-proBNP was elevated, suggesting that it might be used as a marker of HF [15]. Other studies found that the expression levels of miR-18a-5p, miR-26b-5p, and miR-30b were decreased in acute HF, while miR-499 was highly expressed [14]. However, due to limited factors such as small sample size and lack of standardization of detection methods, the diagnostic role of miRNA still needs to be further explored. miRNA plays an important regulatory role in posttranscriptional level and is therefore a potential therapeutic target.

Studies have shown that miR-212 plays a role in promoting CH, but its mechanism has not been fully revealed [16, 17]. This research selects miR-212 as the research object to explore the function and mechanism of miRNA-212 in the process of MH.

2. Materials and Methods

2.1. Animal Experiment. The SD rats, weighing about 200-220 g, were purchased from Weitonglihua Company (Beijing, China) and fed in the animal center of our hospital. Rats were fasted and watered for 12 hours after adapting to the environment after 3 days of regular feeding. The abdominal cavity was opened in a sterile environment, and the abdominal aorta was obtuse separated from the fascia with forceps. The separated abdominal aorta was bound and tied with 0.6 mm needle tube (Jiancheng, Nanjing, China) with silk thread, the needle tube was removed, and the abdominal posterior suture skin was closed. The abdominal aorta was not ligated in the sham group, and the rest of the operations were the same. After feeding the rats for 4 weeks, the cardiac function of the rats was examined by echocardiography (Philips, Eindhoven, The Netherlands) before the rats were sacrificed. After anesthesia, the rat heart was quickly removed and isolated from the left ventricle. The blood was thoroughly washed with phosphate-buffered saline (PBS) solution (Beyotime, Shanghai, China) to remove the blood and stored in the -80°C refrigerator for later use. This study was approved by the Animal Ethics Committee of Shuyang Hospital of Traditional Chinese Medicine Animal Center.

2.2. Cell Culture. Newborn suckled rats were sterilized with 75% alcohol (Jiancheng, Nanjing, China) on the skin surface of the suckled rats for 1-3 days. The skin under the costal margin of the suckled rats was cut off in the super clean table, the heart was exposed, and the forceps were removed. It was quickly placed in the precooled D-Hanks solution (Elabscience, Wuhan, China), the atria were removed, the blood in the heart was washed, and the ventricles were cut into small pieces with the size of <1 mm^3 by ophthalmic scissors (Belevo (Beijing) Medical Technology Co., Ltd., Beijing, China), and the blood was further washed. The obtained myocardial tissue was placed in a petri dish with a diameter of 6 cm, diluted with 1% collagenase (Elabscience, Wuhan, China) and 1x D-Hanks solution (Elabscience, Wuhan, China) in a ratio of 1 : 4, and placed in a refrigerator at 4°C. After 15 hours, the tissue block was blown into turbid suspension with a pipette. The obtained suspension was added to a 15 mL centrifuge tube, followed by a complete Dulbecco's Modified Eagle's Medium (DMEM; Life Technology, Wuhan, China) culture solution to terminate digestion. The suspension was centrifuged at a speed of 1000 rpm for 5 min, and the supernatant was removed. The cells were added with a complete DMEM culture solution of 10 mL and transferred to a 10 cm culture dish. After 1 hour, the culture medium was removed and gently knocked and shaken. The culture medium was transferred to another 10 cm culture dish. The previous process was repeated. After 24 hours, Brdu (Elabscience, Wuhan, China) was added at a concentration of 1% to inhibit the proliferation of nonmyocardial cells, and the culture was continued in a CO_2 thermostatic incubator. 48 hours after the replacement of DMEM solution (excluding serum and streptomycin), further ensure consistency of myocardial cells. Under the condition of

myocardial cells in serum-free culture after 12 hours, the concentration of 100 microns to join phenylephrine (PE, Tianpu Biochemical Pharmaceutical, Guangzhou, China) and final concentration tendency for 1/L Ang II (Tianpu Biochemical Pharmaceutical, Guangzhou, China) stimulate myocyte; after 48 hours in fluorescence microscope cell morphology, extract RNA and save for experiment in -20°C refrigerator.

2.3. Western Blotting Technology. The cultured plate cells were washed with PBS, 50-70 μL radioimmunoprecipitation assay (RIPA; Thermo Fisher Scientific, Waltham, MA, USA) lysate was added to each well, and the ice abrasive rod was ground for 20 s for 3 times, followed by 30 s of vortex homogenate. The cells were left on the ice for 5 min and then centrifuged for 3 times at 4°C for 30 min at 14000 × g. The supernatant was taken, and the total protein concentration was determined by the bicinchoninic acid (BCA) protein concentration measurement kit (Jiancheng, Nanjing, China). Total protein loading of 20~50 μg was separated by sodium dodecyl sulphate-polyacrylamide gel electrophoresis (SDS-PAGE), and the separated protein was transferred to a polyvinylidene difluoride (PVDF; Thermo Fisher Scientific, Waltham, MA, USA) membrane. After 5% of the skim milk powder was sealed for 1 hour, it was incubated overnight with the corresponding primary antibody (TCF7L2, Abcam, Cambridge, MA, USA, Rabbit, 1 : 2000; GAPDH, Proteintech, Rosemont, IL, USA, 1 : 2000) at 4°C, washed with 0.1% PBST solution, and coincubated with the secondary antibody (goat anti-rabbit IgG antibody, Yifei Xue Biotechnology, Nanjing, China, 1 : 2000), and the enhanced chemiluminescence (ECL) technology was used to develop western blot bands, and the grayscale analysis software was used for quantitative analysis.

2.4. Quantitative Real-Time Polymerase Chain Reaction (qRT-PCR). The specific reverse transcription primers of miRNAs were combined with corresponding miRNAs, which were reverse-transcribed into cDNA in the presence of reverse transcriptase reaction system, and the template fragments were amplified. The reaction process was: 16°C, 30 min, 42°C 90 min. After the reverse transcription product was diluted by 40 times, PCR was performed according to the instructions (Thermo Fisher Scientific, Waltham, MA, USA). The reaction process was as follows: 95°C, 20 s; 58°C, 15 s; and 72°C, 20 s, 40 cycles. The reaction system used GAPDH as an internal reference, and the results were analyzed by qRT-PCR. The results were expressed in relative multiples to compare the relative contents of the target molecules in each group. Primers used are shown in Table 1.

2.5. Hematoxylin-Eosin (HE) Staining. The removed heart was washed three times with PBS solution and fixed in 4% paraformaldehyde (Sinopharm Chemical Reagent, Shanghai, China) to maintain the original shape of the cells. The tissues were washed with PBS and dehydrated successively with low concentration of alcohol to high concentration of alcohol to gradually remove the water in the myocardial tissue. The alcohol in the myocardial tissue was removed with xylene (Sinopharm Chemical Reagent, Shanghai, China). The tissues were immersed in the melted paraffin wax (Sinopharm Chemical Reagent, Shanghai, China) for about 2–3 hours and then solidified into blocks. Then, we used a slicer to cut the package into thin slices. The sections were soaked in xylene (Sinopharm Chemical Reagent, Shanghai, China) for about 5 min, and then, the sections were soaked in gradient ethanol for many times, each time for about 5 min. After dyeing with hematoxylin (Sinopharm Chemical Reagent, Shanghai, China) for about 10 min, rinsed with hematoxylin, then added acid alcohol for about 10 s for color separation, rinsed with PBS, then dyed with 1% eosin (Sinopharm Chemical Reagent, Shanghai, China) for 10 min, and then washed with distilled water to remove eosin. The pure alcohol was dehydrated again, and the section was made transparent by xylene. Add gum to the transparent slice, cover with the cover glass, and seal the slice with the corresponding label.

2.6. Immunofluorescence. After routine isolation, rat cardiomyocytes were inoculated with a density of 1×10^5/ml in a 24-well cell culture dish, in which those stimulated by PE and Ang II were the experimental group and those not stimulated were the control group. DMEM was absorbed and washed with PBS solution for 3 times. Then, 4% paraformaldehyde was added to fix the cardiomyocytes, which were fixed at room temperature for about 30 min. Then, PBS was added to soak them for cleaning, and they were placed in a shaking table for about 15 min. 10% BSA (bovine serum albumin, Thermo Fisher Scientific, Waltham, MA, USA) was sealed at room temperature for 10 min, washed once with PBS solution, and incubated overnight with antibody a-actinin (Abcam, Cambridge, MA, USA, Rabbit, 1 : 1000) at room temperature. Wash with PBS containing 0.1% twain for 3 times, each time for about 10 min. Incubate with fluorescently labeled secondary antibody against light for 2 min. The above steps for cleaning were repeated.

2.7. Double-Luciferase Reporter Gene Assay. Complete DMEM was used to culture 293T cells (ATCC, Manassas, VA, USA), Lipofectamine^{2000} (1 UI/hole; R&D Systems, Minneapolis, MN, USA) and opti medium (50 UI/hole) thoroughly incorporated, miR-212 overexpressed plasmid (400 ng/hole; R&D Systems, Minneapolis, MN, USA), opti medium (50 UI/hole) thoroughly incorporated, pGL3 recombinant plasmid (200 ng/hole; R&D Systems, Minneapolis, MN, USA) and opti medium (50 UI/hole) thoroughly incorporated, and let stood for 5 min. The three mixing systems were then thoroughly mixed and left to rest at room temperature for 20 min. Then, they were uniformly added to the cell culture dishes and continued to be routinely cultured in the cell culture box for 24 hours. 293T cells were fully lysed by cell lysate. 10 μL cell lysate was taken, and 40 μL luciferase detection reagent (R&D Systems, Minneapolis, MN, USA) was added to generate firefly fluorescence signal. For fluorescence detector measurement value of firefly luciferase report gene, we finally added 40 μL sea kidney in sample luciferase substrates, blended after 10 s,

Table 1: Real-time PCR primers.

Gene name	Forward (5′>3′)	Reverse (5′>3′)
miR-212	AGCGTAACAGTCTCCAGTC	TCCTCCTCTCCTTCCTTCTC
ANP	GCTTCCAGGCCATATTGGAG	GGGGGCATGACCTCATCTT
myh7	ACTGTCAACACTAAGAGGGTCA	TTGGATGATTTGATCTTCCAGGG
myh6	GCCCAGTACCTCCGAAAGTC	GCCTTAACATACTCCTCCTTGTC
TCF7L2	AACGAACACAGCGAATGTTTCC	GACCTTGCCATCCTAGCGG
U6	GCTTCGGCAGCACATATACTAAAAT	CGCTTCACGAATTTGCGTGTCAT
GAPDH	ACAACTTTGGTATCGTGGAAGG	GCCATCACGCCACAGTTTC

RT-PCR: quantitative reverse-transcription polymerase chain reaction.

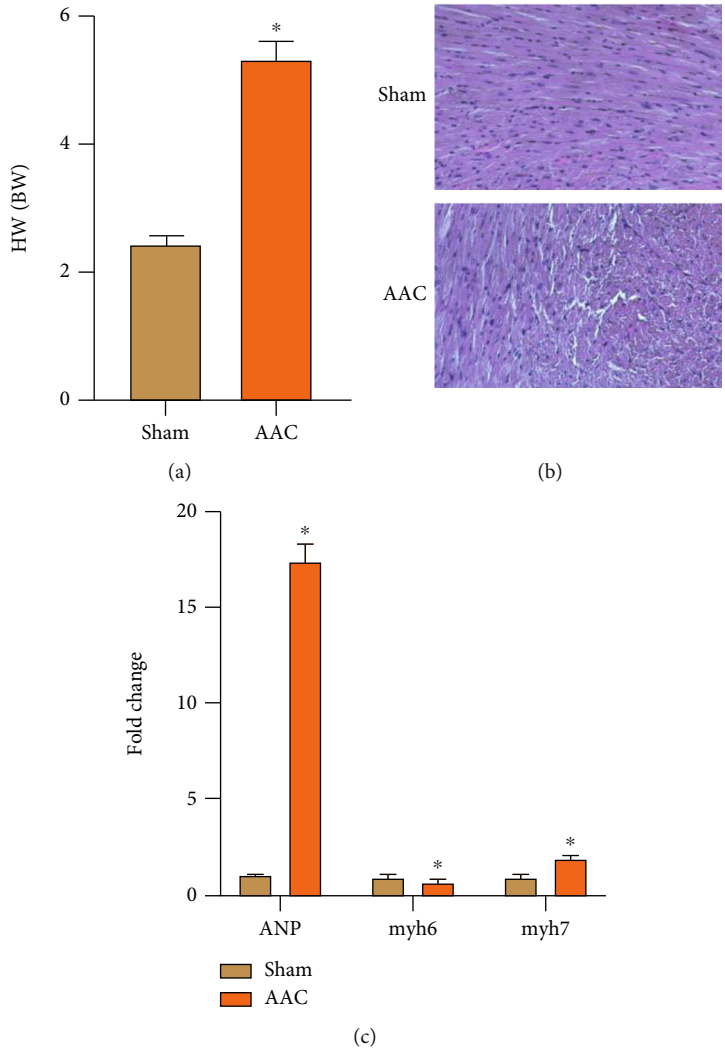

Figure 1: Identification of rat model of abdominal aortic coarctation and hypertrophy. (a) The rate of HW/BW in sham and AAC groups ("∗" indicates statistical difference from the sham group $P < 0.05$). (b) HE staining of renal tissues in sham and AAC groups (200x). (c) The expression of ANP, myh6, and myh7 in the sham and AAC groups ("∗" indicates statistical difference from the sham group $P < 0.05$).

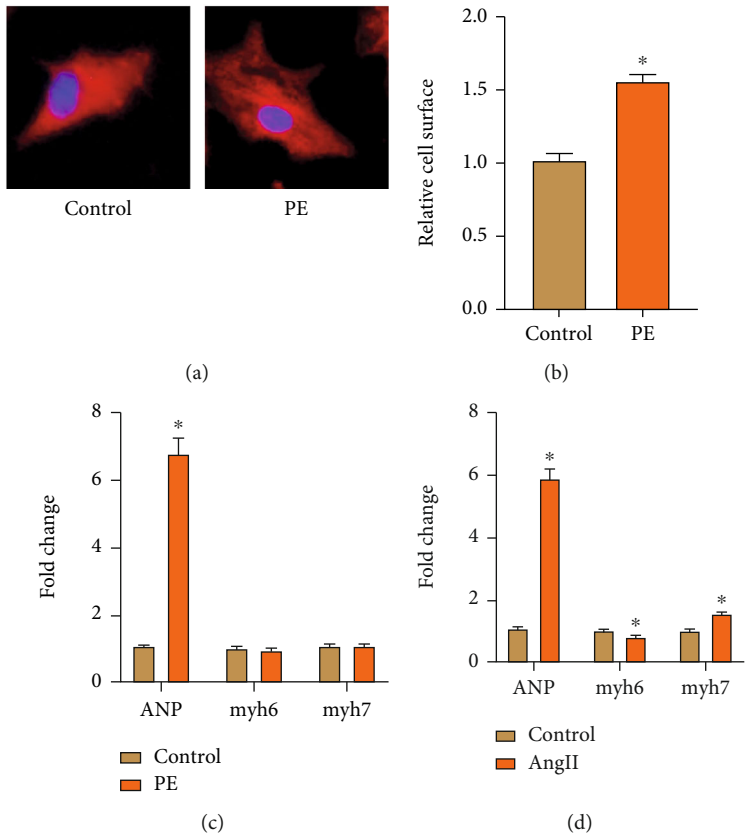

Figure 2: Identification of primary MH model. (a) Cell immunofluorescence staining α-actinin in control and PE groups. (b) Analysis of cardiomyocyte surface area ("$*$" indicates statistical difference from the control group $P < 0.05$). (c) The expression of ANP, myh6, and myh7 in the control and PE groups ("$*$" indicates statistical difference from the control group $P < 0.05$). (d) The expression of ANP, myh6, and myh7 in the control and Ang II groups ("$*$" indicates statistical difference from the control group $P < 0.05$).

terminated the above reaction, and started the sea renal luciferase reaction. Finally, we measured the fluorescence signal.

2.8. Statistical Analysis. The data were expressed as mean $\pm$ standard error. All the experimental results were repeated 3 times. t-test was used for comparison between the two groups. We default $P < 0.05$, which is a significant difference.

3. Results

3.1. Identification of Rat Model of Abdominal Aortic Coarctation and Hypertrophy. After abdominal aorta ligation, SD rats had increased cardiac afterload, in order to maintain normal blood supply, at the same time, RAAS system was activated, due to increased cardiac systolic protein synthesis, compensatory hypertrophy occurred, and cardiac weight/body weight (mg/g) increased (Figure 1(a)). HE staining of the left ventricle of the heart showed that the appearance of the heart increased dramatically 4 weeks after abdominal aortic ligation. At the same time, the longitudinal section of HE staining showed that, compared with sham group, the left ventricular wall of the hypertrophy group was dramatically thickened, and the left ventricular cavity was reduced, presenting centripetal hypertrophy (Figure 1(b)). During the process of CH remodeling, some fetal genes are expressed again. The commonly used marker molecules in the literature include atrial natriuretic peptide (ANP), myosin heavy chain 6 (myh6), and myosin heavy chain 7 (myh7). The expression level of these molecules can usually reflect the degree of CH or HF. Therefore, in this experiment, we will detect the expression levels of these marker molecules by qRT-PCR. qRT-PCR results showed that compared with the sham group, ANP expression increased dramatically, myh6 decreased, and myh7 increased after 4 w of ligation, which may be related to the compensatory mechanism of the heart (Figure 1(c)). Overall, the results show that the model is successful.

3.2. Identification of Primary MH Model. In this study, we used classical phenylephrine (PE) and Ang II to induce cardiomyocyte hypertrophy. After 2 days of induction by PE and Ang II, the cardiomyocytes beat well. After specificity of a-actinin tags parallel cell immunofluorescence staining, we can see Figure 2(a): stick wall myocardial cell was triangular or fusiform, control cells were relatively flat, PE group of myocardial cells in full and obviously increase the surface area, and in the control group and the PE induced CH group, 100 cells in 10 visual fields were randomly selected and their surface area was measured. In the PE group, the cell surface area was increased compared with the control group (Figure 2(b)). Myocytes were stimulated with

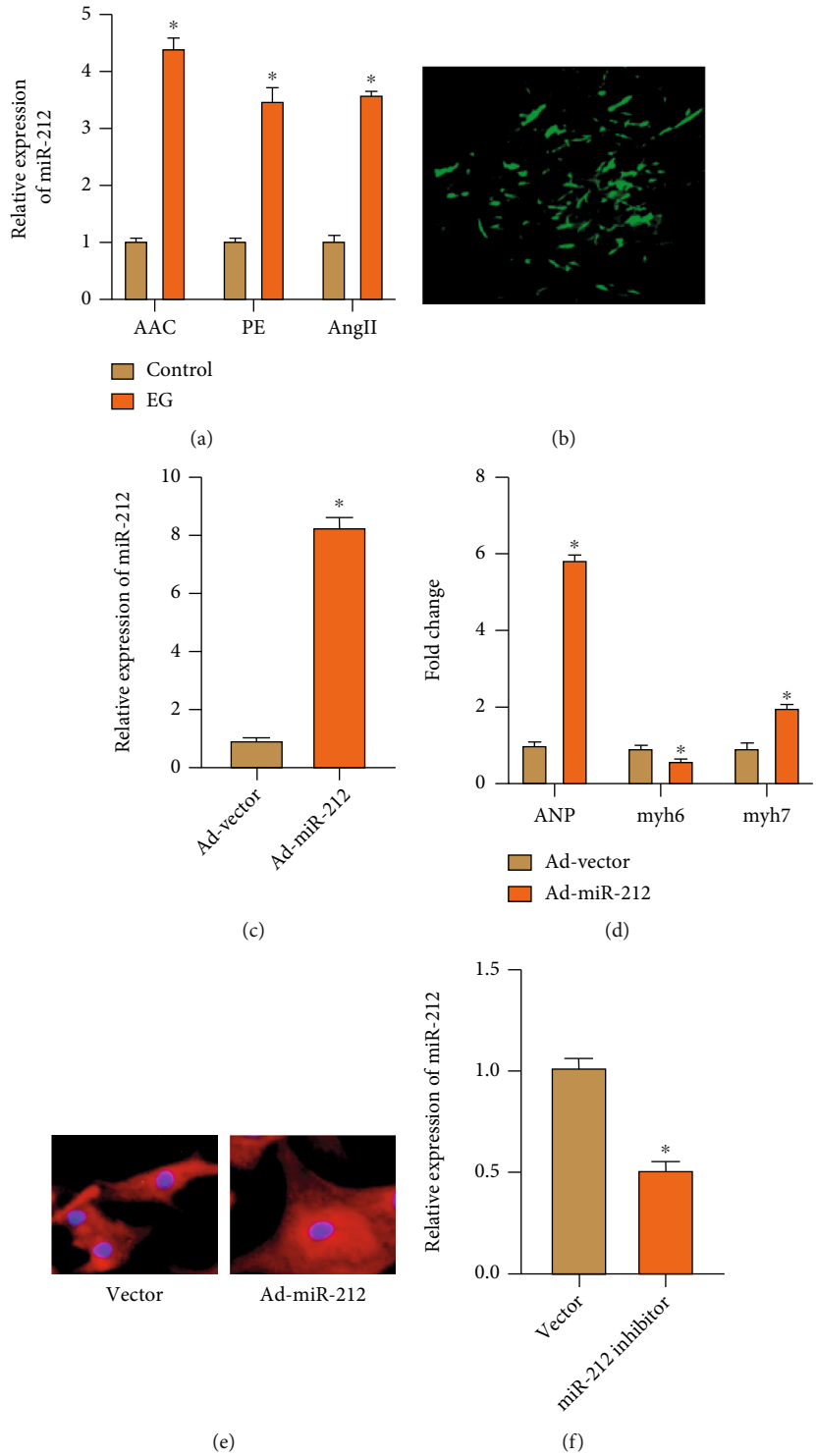

Figure 3: Continued.

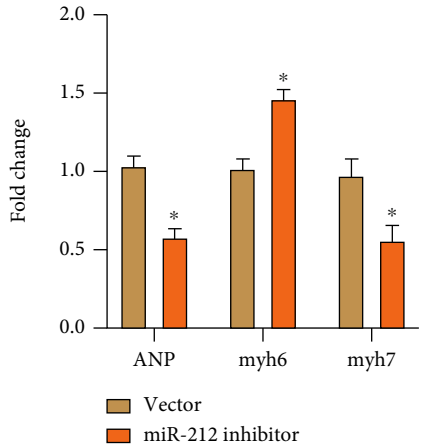

(g)

Figure 3: miR-212 promotes CH. (a) The expression of miR-212 in the control and EG groups ("∗" indicates statistical difference from the control group $P < 0.05$). (b) Effect of primary cardiac myocytes transfected with Ad-miR-212 adenovirus. (c) The expression of miR-212 in the Ad-vector and Ad-miR-212 groups ("∗" indicates statistical difference from the Ad-vector group $P < 0.05$). (d) The expression of ANP, myh6, and myh7 in the Ad-vector and Ad-miR-212 groups ("∗" indicates statistical difference from the Ad-vector group $P < 0.05$). (e) Cell immunofluorescence staining α-actinin in the Ad-vector and Ad-miR-212 group. (f) The expression of miR-212 in the vector and miR-212 inhibitor groups ("∗" indicates statistical difference from the vector group $P < 0.05$). (g) The expression of ANP, myh6, and myh7 in the vector and miR-212-inhibitor groups ("∗" indicates statistical difference from the vector group $P < 0.05$).

100 μM PE and 10 μM Ang II for 12 h after starvation induction, and RNA was extracted for 48 hours after conventional culture to detect the mRNA expression levels of ANP, myh6, and myh7, respectively. The results showed that the expressions of ANP in PE group and Ang II group were dramatically increased, while the expressions of myh6 and myh7 were not dramatically changed in the PE group (Figure 2(c)), and the expression levels of myh7 were increased in the Ang II group, with statistical differences (Figure 2(d)). Overall, the results indicate successful cell modeling.

3.3. miR-212 Promotes CH. miRNA with a high specific richness expressed in the heart often plays a crucial biological function in the occurrence and development of HF. The expression level of miR-212 was detected in the hypertrophy model, and it was found that the expression of miR-212 was increased in the rat model with abdominal aortic constriction for 4 weeks, and the expression of miR-212 was also dramatically increased in the model of mast cardiomyocytes induced by PE and Ang II (Figure 3(a)), suggesting that miR-212 may be involved in the regulation of CH. Then, adenovirus blank Vector (Ad-vector) was used as the control group, and miR-212 overexpressed adenovirus was transfected into cardiac muscle cells as the experimental group. Under the fluorescence microscope, we observed that most cardiomyocytes could emit strong green fluorescence, which proved that adenovirus transfection was effective (Figure 3(b)). We detected the expression level of miR-212 in the transfected primary cardiac myocytes by qRT-PCR, and the results showed that the expression level of miR-212 increased after the transfection of ad-miR-212 (Figure 3(c)), which proved that the construction of overexpressed adenovirus was successful. First, qRT-PCR was used to detect the changes in the expression of ANP, myh6, and myh7 in myocytes of the two groups. The results showed that after the same hunger stress, the myocytes transfected with Ad-miR-212 were dramatically higher in ANP and myh7 and decreased in myh6 compared with the control group (Figure 3(d)). Therefore, we hypothesized that miR-212 overexpression promoted primary CH. In addition, in the detection of cellular immunofluorescence, overexpression of miR-212 in primary cardiomyocytes promoted cardiomyocyte hypertrophy (Figure 3(e)). Compared with the PE-induced CH group, miR-212 expression was dramatically downregulated after PE-induced transfection with miR-212 inhibitor (Figure 3(f)). Moreover, ANP level was also reduced (Figure 3(g)), suggesting that knockdown of miR-212a expression in hypertrophic cardiomyocytes could effectively reverse the hypertrophy level of cardiomyocytes.

3.4. miR-212 Regulates CH by Targeting TCF7L2. We used the Targetscan website (https://www.targetscan.org/vert_80/) to predict the potential target genes of miR-212. Through retrieval, we found that rat TCF7L2 had the possible action sites of miR-148a in the 3′UTR region, and the matching situation is shown in the figure (Figure 4(a)). As a member of the T cell factor/lymphocyte enhancer factor (TCF/LEF) family, TCF7L2 is one of the downstream nuclear transcription factors of the classical Wnt/β-catenin signaling pathway and is involved in the regulation of cell proliferation and differentiation [18]. Recent studies have found a significant association between TCF7L2 gene polymorphism and diabetes mellitus. TCF7L2 is involved in the regulation of secretion, proliferation, and apoptosis of islet cells [19]. Then, the sequence of miR-212 interacting with TCF7L2 was inserted into the 3′UTR region of the reporter

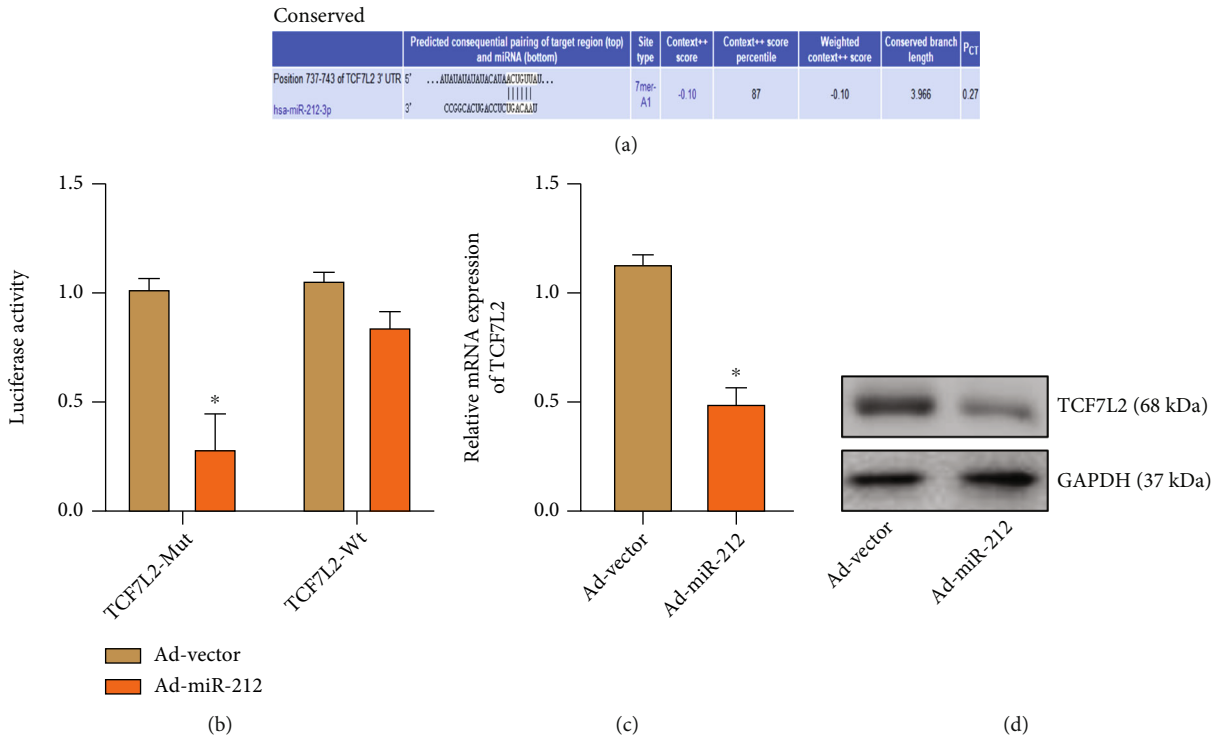

Figure 4: miR-212 regulates CH by targeting TCF7L2. (a) Results of site prediction. (b) Double-luciferase reporter gene assay ("∗" indicates statistical difference from the Ad-vector+TCF7L2-WT group $P < 0.05$). (c) The expression of miR-212 in the Ad-vector and Ad-miR-212 groups ("∗" indicates statistical difference from the Ad-vector group $P < 0.05$). (d) The band of TCF7L2 in the Ad-vector and Ad-miR-212 groups.

plasmid. After transfection with Ad-miRNA-212, 293T cells dramatically inhibited the luciferase expression at the TCF7L2 action site (Figure 4(b)). Next, we overexpressed miR-212 in primary cardiac myocytes and detected the expression changes of TCF7L2 by qRT-PCR and western blot. It was found that after overexpression of miRNA-212, the expression of TCF7L2 decreased (Figures 4(c) and 4(d)). Further evidence suggests that miR-212 may regulate CH by targeting TCF7L2 (Figure 5).

4. Discussion

We constructed a model of MH from the tissue to the cell level. The results verified each other and confirmed the success of the model construction; it can provide a good experimental basis and platform for further research on the expression and function of miRNA-212 in MH. At the same time, we further determined that the expression level of miR-212 was upregulated in the HF model. Then, the expression of miR-212 in cardiac myocytes was artificially interfered with by transfection with overexpressed adenovirus and inhibitor. However, knockdown of miR-212 can reverse the cell hypertrophy induced by PE to a certain extent. Then, we predicted the downstream target genes of miRNA-212 through the website and verified the regulation of miR-212 by targeting TCF7L2 on CH by luciferase gene reporting experiment, qRT-PCR, and WB.

Ventricular remodeling is the pathological basis of chronic HF. According to the results of this experiment, the rat heart showed obvious left ventricular hypertrophy and ventricular enlargement after 4 weeks of modeling. HE staining showed the characteristics of hypertrophy and disordered arrangement of cardiomyocytes, myocardial interstitial fibrosis, nuclear thickening, and increased myocardial sarcomere. In addition, the symptoms of HF in rats all indicated that the abdominal aortic model was a mature and reliable method. There are many causes of HF, and the choice of model is often decided according to the cause of the disease. Abdominal aortic constriction is due to CH caused by excessive pressure load, and the heart gradually goes from the compensatory stage to the decompensated stage. Therefore, the clinical diseases corresponding to this model are more similar to HF caused by hypertensive cardiomyopathy [20].

Myosin is an important part of the physiological structure of myocardium and also plays a crucial biological function; myosin heavy chain (MYHC) plays a vital role in cardiac contractile function. The encoded proteins corresponding to myh6 and myh7 are, respectively, a-MYHC and p-MYHC. Although these two genes are located on the same chromosome, their expression regulation is independent of each other. When cardiomyocytes age, due to changes in fetal gene expression, diastolic and contractile functions are reduced compared to normal cardiomyocytes. At the gene level, the expression of SERCA2 is reduced, myh6 is converted to myh7, and the expression level of

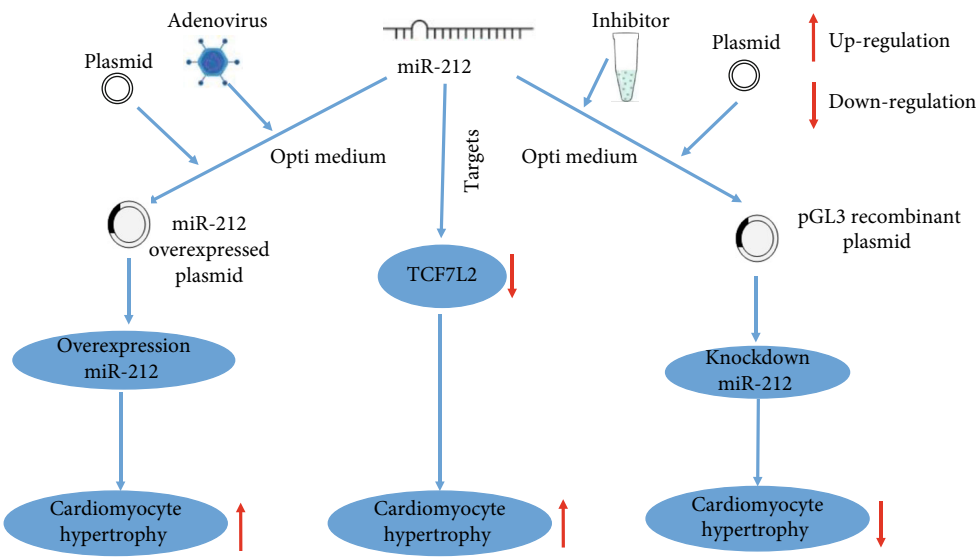

Figure 5: Schematic diagram of the molecular mechanism of miR-212 regulating CH by targeting TCF7L2.

ACTA1 is increased [21]. Since HF is often accompanied by changes in myocardial structure, the expression levels of myh6 and myh7 changes can also be a good representative of the changes in heart function.

Studies have shown that in the process of HF, a large number of miRNA expression is dysregulated, which plays a crucial role in regulating the process of myocardial remodeling. Correcting the expression of miRNA will have a significant reversal effect on MH. The use of miRNA as a diagnostic marker for HF in clinic has been widely reported [22]. Sinfield et al. proposed that miR-423-5p can be used as a diagnostic marker for HF [23]. In addition, miR-1, miR-133, miR-499, and miR-208 in acute myocardial infarction were all proved to be dramatically elevated, and further meta-analysis was performed to verify the role of miRNA [24]. The impaired cardiac contractility caused by the imbalance of calcium pump is an important sign in the process of HF. Studies have found that miR-765 is overexpressed in HF samples and can increase the activity of protein phosphatase PP-1 and increase the dephosphorylation of calcium circulating protein by inhibiting endogenous inhibitor-1. miR-25 is also believed to inhibit the calcium pump SERCA2a in HF and lead to HF [25]. Inhibiting the expression of miR-25 can effectively restore cardiac contractile function and improve survival rate of HF patients. Also, in the process of MH, miRNA may be used as a new biomarker for predicting and diagnosing HF. In this sense, the functional study of miR-212 is also important in clinical work. However, there are still some limitations in the present study. For example, we did not test whether knockdown or overexpression of miR-212 had an effect on myocardial hypertrophy in animal models. What is more, after we predicted TCF7L2 as a possible target gene of miR-212, we did not further verify the accuracy of the target gene by interfering with the expression of TCF7L2. In the future, our research group will further carry out the above unfinished experiments under the premise of sufficient funds, so as to better illustrate the clinical value of this research.

5. Conclusion

miRNA-212 targets TCF7L2 and inhibits the expression of this gene, possibly through this pathway to promote cardiomyocyte hypertrophy. The results of the current study may provide new insights for the treatment of cardiomyocyte hypertrophy.

Abbreviations

HF:	Heart failure
HE:	Hematoxylin-eosin
qRT-PCR:	Quantitative real-time polymerase chain reaction
CH:	Cardiac hypertrophy
MH:	Myocardial hypertrophy
ncRNA:	Noncoding RNA
lncRNA:	Long noncoding RNA
circRNA:	CircularRNA
miRNA:	microRNA
AKT:	Phosphatidylinositol 3 kinase (PI3K)/protein kinase B
BNP:	Brain natriuretic peptide
SD:	Sprague-Dawley
PBS:	Phosphate-buffered saline
DMEM:	Dulbecco's Modified Eagle's Medium
PE:	Phenylephrine
RIPA:	Radioimmunoprecipitation assay
BCA:	Bicinchoninic acid
SDS-PAGE:	Sodium dodecyl sulphate-polyacrylamide gel electrophoresis
PVDF:	Polyvinylidene difluoride
GAPDH:	Glyceraldehyde-3-phosphate dehydrogenase
ECL:	Enhanced chemiluminescence
PBST:	Phosphate-buffered saline-tween
cDNA:	Complementary DNA
BSA:	Bovine serum albumin
ATCC:	American Type Culture Collection

RAAS: Renin-angiotensin-aldosterone system
ANP: Atrial natriuretic peptide
myh6: Myosin heavy chain 6
myh7: Myosin heavy chain 7
TCF/LEF: T cell factor/lymphocyte enhancer factor
MYHC: Myosin heavy chain.

Data Availability

The datasets used and analyzed during the current study are available from the corresponding author on reasonable request.

Conflicts of Interest

The authors declare that they have no competing interests.

References

[1] R. J. Trupp and W. T. Abraham, "American College of Cardiology/American Heart Association 2009 clinical guidelines for the diagnosis and management of heart failure in adults: update and clinical implications," *Polskie Archiwum Medycyny Wewnętrznej*, vol. 119, no. 7-8, pp. 436–438, 2009.

[2] J. A. Hill and E. N. Olson, "Cardiac plasticity," *The New England Journal of Medicine*, vol. 358, no. 13, pp. 1370–1380, 2008.

[3] S. Stewart, K. MacIntyre, D. J. Hole, S. Capewell, and J. J. McMurray, "More 'malignant' than cancer? Five-year survival following a first admission for heart failure," *European Journal of Heart Failure*, vol. 3, no. 3, pp. 315–322, 2001.

[4] F. Alla, F. Zannad, and G. Filippatos, "Epidemiology of acute heart failure syndromes," *Heart Failure Reviews*, vol. 12, no. 2, pp. 91–95, 2007.

[5] F. L. Johnson, "Pathophysiology and etiology of heart failure," *Cardiology Clinics*, vol. 32, no. 1, pp. 9–19, 2014.

[6] H. Wang and J. Cai, "The role of microRNAs in heart failure," *Biochimica et Biophysica Acta - Molecular Basis of Disease*, vol. 1863, no. 8, pp. 2019–2030, 2017.

[7] J. Beermann, M. T. Piccoli, J. Viereck, and T. Thum, "Non-coding RNAs in development and disease: background, mechanisms, and therapeutic approaches," *Physiological Reviews*, vol. 96, no. 4, pp. 1297–1325, 2016.

[8] F. Wahid, A. Shehzad, T. Khan, and Y. Y. Kim, "MicroRNAs: synthesis, mechanism, function, and recent clinical trials," *Biochimica et Biophysica Acta*, vol. 1803, no. 11, pp. 1231–1243, 2010.

[9] G. Condorelli, M. V. Latronico, and E. Cavarretta, "microRNAs in cardiovascular diseases: current knowledge and the road ahead," *Journal of the American College of Cardiology*, vol. 63, no. 21, pp. 2177–2187, 2014.

[10] M. Ha and V. N. Kim, "Regulation of microRNA biogenesis," *Nature Reviews. Molecular Cell Biology*, vol. 15, no. 8, pp. 509–524, 2014.

[11] P. K. Busk and S. Cirera, "MicroRNA profiling in early hypertrophic growth of the left ventricle in rats," *Biochemical and Biophysical Research Communications*, vol. 396, no. 4, pp. 989–993, 2010.

[12] X. Zhang and P. C. Schulze, "MicroRNAs in heart failure: non-coding regulators of metabolic function," *Biochimica et Biophysica Acta*, vol. 1862, no. 12, pp. 2276–2287, 2016.

[13] S. Reddy, M. Zhao, D. Q. Hu et al., "Dynamic microRNA expression during the transition from right ventricular hypertrophy to failure," *Physiological Genomics*, vol. 44, no. 10, pp. 562–575, 2012.

[14] O. Gidlof, J. G. Smith, K. Miyazu et al., "Circulating cardio-enriched microRNAs are associated with long-term prognosis following myocardial infarction," *BMC Cardiovascular Disorders*, vol. 13, no. 1, 2013.

[15] Y. Fukushima, M. Nakanishi, H. Nonogi, Y. Goto, and N. Iwai, "Assessment of plasma miRNAs in congestive heart failure," *Circulation Journal*, vol. 75, no. 2, pp. 336–340, 2011.

[16] S. K. Ucar, J. Gupta, E. Fiedler et al., "The miRNA-212/132 family regulates both cardiac hypertrophy and cardiomyocyte autophagy," *Nature Communications*, vol. 3, no. 1, p. 1078, 2012.

[17] Z. Lei, C. Wahlquist, A. H. El et al., "miR-132/212 impairs cardiomyocytes contractility in the failing heart by suppressing SERCA2a," *Frontiers in Cardiovascular Medicine*, vol. 8, article 592362, 2021.

[18] J. Bem, N. Brozko, C. Chakraborty et al., "Wnt/β-catenin signaling in brain development and mental disorders: keeping TCF7L2 in mind," *FEBS Letters*, vol. 593, no. 13, pp. 1654–1674, 2019.

[19] D. D. Yao, L. Yang, Y. Wang et al., "Geniposide promotes beta-cell regeneration and survival through regulating beta-catenin/TCF7L2 pathway," *Cell Death & Disease*, vol. 6, no. 5, article e1746, 2015.

[20] R. H. Zheng, X. J. Bai, W. W. Zhang et al., "Liraglutide attenuates cardiac remodeling and improves heart function after abdominal aortic constriction through blocking angiotensin II type 1 receptor in rats," *Drug Design, Development and Therapy*, vol. 13, pp. 2745–2757, 2019.

[21] J. Holtz, R. Studer, H. Reinecke, H. Just, and H. Drexler, "Modulation of myocardial sarcoplasmic reticulum Ca(++)-ATPase in cardiac hypertrophy by angiotensin converting enzyme?," *Basic Research in Cardiology*, vol. 87, Supplement 2, pp. 191–204, 1992.

[22] C. C. Yeh, H. Li, D. Malhotra et al., "Distinctive ERK and p38 signaling in remote and infarcted myocardium during post-MI remodeling in the mouse," *Journal of Cellular Biochemistry*, vol. 109, no. 6, pp. 1185–1191, 2010.

[23] J. K. Sinfield, A. Das, D. J. O'Regan, S. G. Ball, K. E. Porter, and N. A. Turner, "p38 MAPK alpha mediates cytokine-induced IL-6 and MMP-3 expression in human cardiac fibroblasts," *Biochemical and Biophysical Research Communications*, vol. 430, no. 1, pp. 419–424, 2013.

[24] M. S. Pillai, S. Sapna, and K. Shivakumar, "p38 MAPK regulates G1-S transition in hypoxic cardiac fibroblasts," *The International Journal of Biochemistry & Cell Biology*, vol. 43, no. 6, pp. 919–927, 2011.

[25] Q. Luo, W. Li, T. Zhao, X. Tian, Y. Liu, and X. Zhang, "Role of miR-148a in cutaneous squamous cell carcinoma by repression of MAPK pathway," *Archives of Biochemistry and Biophysics*, vol. 583, pp. 47–54, 2015.

Hindawi
Mediators of Inflammation
Volume 2022, Article ID 1478181, 10 pages
https://doi.org/10.1155/2022/1478181

Research Article

Tanshinone IIA Accomplished Protection against Radiation-Induced Cardiomyocyte Injury by Regulating the p38/p53 Pathway

Gang Wang,[1] Li Ma,[2] Bowen Wang,[3] Fentang Gao,[3] Jianfeng Li,[3] Hongyi Cai,[4] Juan Wang,[3] Tiancheng Zhang,[3] Hao Guo,[5] Ping Xie,[3] and Yi Li[6]

[1]*The First Clinical Medical College, Gansu University of Chinese Medicine, Lanzhou 730000, China*
[2]*Gansu Provincial Maternity and Child-Care Hospital, Lanzhou 730000, China*
[3]*Department of Cardiovascular Medicine, Gansu Provincial Hospital, Lanzhou 730000, China*
[4]*Department of Radiotherapy, Gansu Provincial Hospital, Lanzhou 730000, China*
[5]*School of Medicine, Xiamen University, Xiamen 361000, China*
[6]*School of Stomatology, Lanzhou University, Lanzhou 730000, China*

Correspondence should be addressed to Ping Xie; pingx189@outlook.com and Yi Li; ixk288fyk@163.com

Gang Wang and Li Ma contributed equally to this work.

Received 26 May 2022; Revised 20 July 2022; Accepted 1 August 2022; Published 22 August 2022

Academic Editor: Md Sayed Ali Sheikh

Background. Radiotherapy is one of the major strategies for treating tumors, and it inevitably causes damage to relevant tissues and organs during treatment. Radiation-induced heart disease (RIHD) refers to radiation-induced cardiovascular adverse effects caused by thoracic radiotherapy. Currently, there is no uniform standard in the treatment of RIHD. *Methods*. In our group study, by administering a dose of 4 Gy radiation, we established a radiation injured cardiomyocyte model and explored the regulatory relationship between tanshinone IIA and p38 MAPK in cardiomyocyte injury. We assessed cell damage and proliferation using clonogenic assay and lactate dehydrogenase (LDH) release assay. The measures of antioxidant activity and oxidative stress were conducted using superoxide dismutase (SOD) and reactive oxygen species (ROS). The apoptosis rate and the relative expression of apoptotic proteins were conducted using flow cytometry and western blot. To assess p38 and p53 expressions and phosphorylation levels, western blot was performed. *Results*. Experimental results suggested that tanshinone IIA restored cell proliferation in radiation-induced cardiomyocyte injury ($**P < 0.01$), and the level of LDH release decreased ($*P < 0.05$). Meanwhile, tanshinone IIA could decrease the ROS generation induced by radiation ($**P < 0.01$) and upregulate the SOD level ($**P < 0.01$). Again, tanshinone IIA reduced radiation-induced cardiomyocyte apoptosis ($**P < 0.01$). Finally, tanshinone IIA downregulated radiation-induced p38/p53 overexpression ($*** P < 0.001$). *Conclusions*. The treatment effects of tanshinone IIA against radiation-induced myocardial injury may be through the regulation of the p38/p53 pathway.

1. Introduction

Most tumor patients receive radiotherapy as a treatment for their tumors, and over half of them receive radiotherapy for their tumors [1]. Although the therapeutic effect of radiotherapy on tumors is effective, the damage of normal tissues or organs by radiation has attracted much attention [2]. Thoracic radiotherapy causes damage to the myocardium tissue, heart valves, and coronary arteries, collectively referred to as RIHD [3, 4]. The key injury mechanisms of RIHD from acute to chronic remain unanswered now [5]. Currently, there are barely options regarding the approach to the treatment of RIHD, and there are no specific drugs to prevent or treat RIHD. Therefore, the prevention and management of RIHD has become an issue to be addressed clinically, as RIHD can worsen the outcomes of cancer patients as well as the economic burden [6, 7].

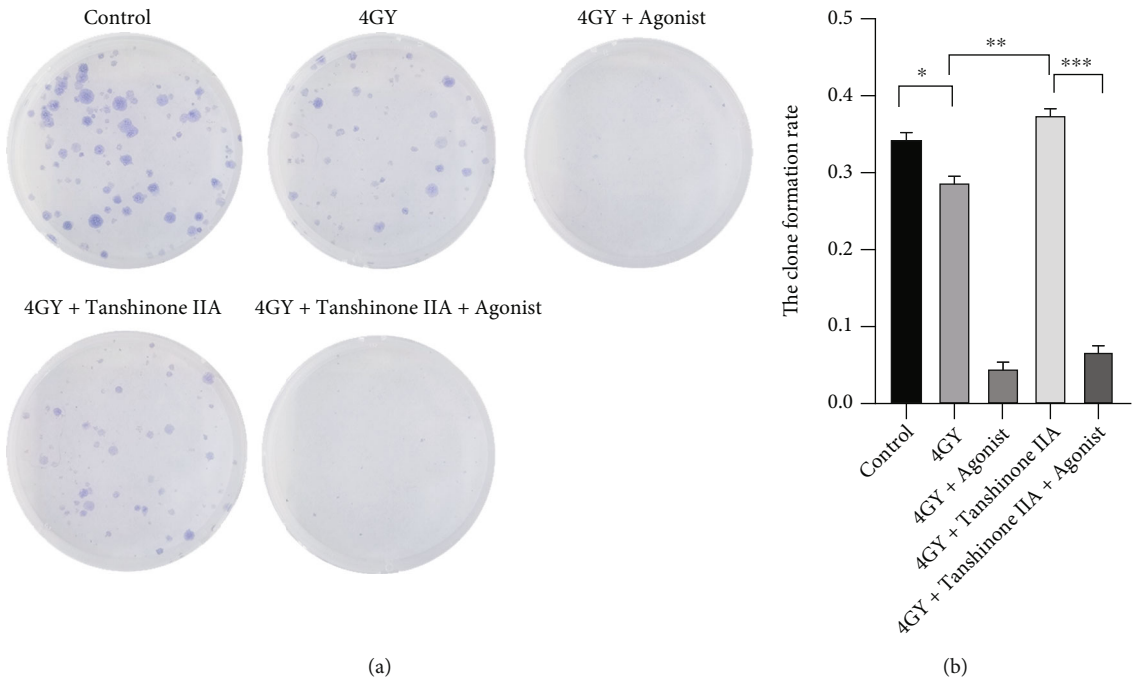

Figure 1: Effects of radiation and tanshinone IIA on cardiomyocyte proliferation. (a) The results of clonogenic assay suggested that radiation could inhibit normal cardiomyocyte growth, while tanshinone IIA could eliminate this inhibition to some extent. (b) The results of cell cloning experiments were expressed as the number of colonies of the cells. $^{***}P < 0.001$, $^{**}P < 0.01$, and $^{*}P < 0.05$.

Studies have found that ROS generated after radiation induce the destruction of intracellular macromolecules, including lipid peroxidation, enzyme inactivation with the interaction of DNA repair enzymes, and transcription factors. Damage to cells and intracellular macromolecules may lead to inflammatory responses, stress or apoptosis and necrosis, and activation of physiological mechanisms such as autophagy [4, 8, 9]. Therefore, reducing ROS production and inflammatory response is very important for treating radiation injury [10]. According to a previous study from our group, radiation causes increased apoptosis, growth inhibition, ROS secretion, p38 MAPK, and its phosphorylation in cardiomyocytes and cardiac fibroblasts, and this effect increases with radiation dose [11, 12]. P38, the most important member of the MAPK family in controlling inflammatory responses, is widespread in cells of various tissues and very important in the regulation of the oxidative stress, inflammatory responses, and apoptosis. It has been shown that p38 MAPK signaling pathway can degrade Bcl-2 and activate Bax, thereby playing a prime role in the process of apoptosis [13]. However, the p38 MAPK signaling pathway in radiation-induced cardiac injury remains unknown.

Tanshinone IIA is the main active component of Danshe. Studies have shown that tanshinone IIA has multiple biological activities, especially in antioxidative stress and attenuating inflammatory responses, and is used to treatment of heart diseases. It can improve and regulate myocardial metabolic dysfunction induced by hypoxia [14]. In addition, a protective effect of tanshinone IIA is also seen in myocardial ischemia; it could also inhibit proliferation of smooth muscle in vascular vessels and vascular intimal hyperplasia and inhibits cardiomyocyte Ca^{2+} influx [15]. According to our findings, tanshinone IIA could resist the negative effects of radiation on cardiomyocytes and cardiac fibroblasts, reduce the secretion of ROS, decrease the apoptosis of cells, and restore cell viability, thereby protecting cardiomyocytes [11, 12]. But there is no further research about the relationship between tanshinone IIA and p38 MAPK signaling pathway.

So we will continue to further investigate the role of p38/p53 signaling in RIHD by establishing a cardiomyocyte radiation injury model and the regulatory relationship between tanshinone IIA and p38/p53 pathway.

2. Materials and Methods

2.1. Culture, Radiation-Induced Injury Model, and Grouping. The H9c2 cell line was acquired from the Chinese Academy of Science (Shanghai, China). In an incubator at 37°C, 95% of the atmosphere and 5% CO_2 were used to culture the cells. DMEM (Basal Media, Shanghai, China), 10% fetal bovine serum (ABWbio, Uruguay), and double antibiotic were used to prepare the complete culture medium. When the cell number reached 80-90% culture area, the cells were used for experiments.

To simulate radiation-induced myocardial injury, H9c2 cells were irradiated with a dose of 4 Gy using the Siemens Primus high-energy linear accelerator (Siemens AG, Erlangen, Germany). For the selection of radiation dose, we referred to the results of previous studies by our group [11, 12]. After irradiation, the complete medium was replaced with tanshinone IIA (final concentration, 10 μg/mL, Shanghai First Chemical Company, Shanghai, China)

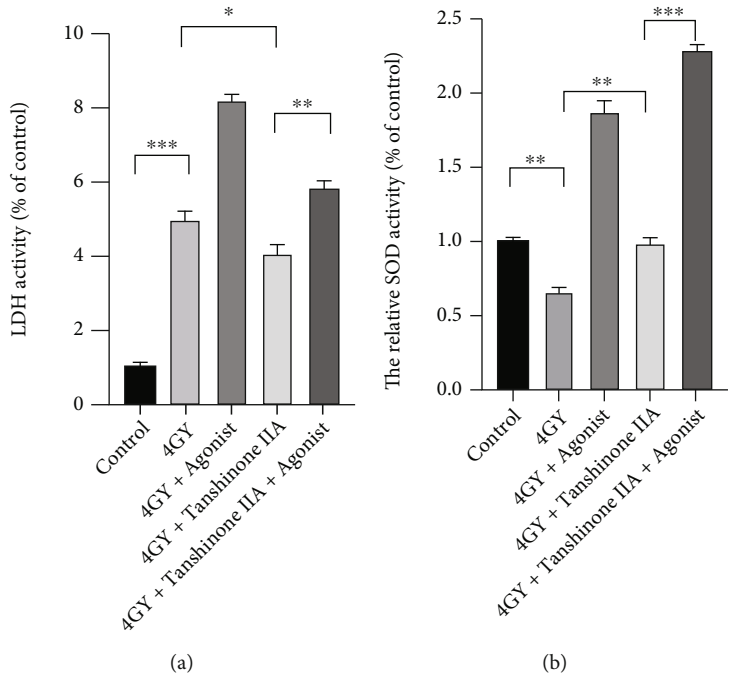

Figure 2: Radiation and tanshinone IIA effects on cardiomyocytes were detected by measuring LDH release (a) and SOD activity (b). The means ± SD are presented for each result ($n = 3$). $^{***}P < 0.001$, $^{**}P < 0.01$, and $^{*}P < 0.05$. LDH: lactate dehydrogenase; SOD: superoxide dismutase.

and p38 MAPK agonist, anisomycin (final concentration, 4 μg/mL, Cat. IA0770, Solarbio, Beijing, China). After 48 h, the cells were used in the experiment without prior change of medium.

The experimental groups were as follows: control group, 4 Gy group, 4 Gy+agonist group, 4 Gy+tanshinone IIA group, and 4 Gy+tanshinone IIA+agonist group.

2.2. Clonogenic Assay. The cells were digested with trypsin to prepare the cell suspensions and counted. 1000 cells were seeded in each 60 mm dish. After 24 h of cell adhesion, the radiation cell model was generated, and drug treatment was performed, and then, the cells were continued to be cultured for two weeks as per routine protocol. Two weeks later, after discarding old medium, the cells were fixed using methanol before staining with Giemsa staining solution (Cat. DM0002, Beijing Leagene Biotech). Finally, the number of cell colonies (≥50 cells) was counted, and the clone formation rate was calculated.

2.3. Cell Apoptosis Assay. We chose to evaluate apoptosis using the BD apoptosis detection kit (Cat. 559763, BD Pharmingen), and the experiments were performed exactly as per the instructions for use. A dose of 4 Gy was given to irradiate the cells and do the drug treatment; it was used to do experiments after 48 hours of routine culture. After making a cell suspension, 5 μL each of PE and 7-AAD reagents were added, followed by a 15 min reaction protected from light. Finally, the results were detected by flow cytometer (BD LSRFortessa) within 1 h.

2.4. LDH and SOD Assay and ROS Flow Cytometric Analysis. Cells were given an X-ray irradiation dose of 4 Gy and given drug treatment and then routinely cultured for 48 h before use in experiments. Next, proteins were extracted from the cells. SOD activity and LDH release amount were detected with kits. Cells for experiments were treated with 0.1 mmol·L^{-1} DCFH-DA. DCFH-DA can be oxidized by ROS to fluorescent DCFH. Then, ROS levels were measured by flow cytometry. We used relevant kits to accomplish each of the above assays (Nanjing Jiancheng Bioengineering Institute, Nanjing, China). Positive control and negative control were added to the grouping according to the instruction of the ROS kit. The specific groupings in the ROS experiment were as follows: negative control, positive control, control group, 4 Gy group, 4 Gy+agonist group, 4 Gy+tanshinone IIA group, and 4 Gy+tanshinone IIA+agonist group.

2.5. Western Blot Analysis. First, lysis buffer and phenylmethylsulfonyl were used to extract proteins from the cells of each group. A polyvinylidene difluoride membrane was used to capture the proteins separated by electrophoresis (SDS-PAGE). Following blocking with 5% skim milk, primary antibodies (rabbit) were incubated on the membrane. A secondary antibody (goat anti-rabbit) was then incubated at room temperature with the membrane. Finally, the membrane was visualized on an imaging system (ChemiScope 6100, Clinx Science Instruments Co., Ltd.). Rabbit antibodies for GAPDH (Cat. 10494-1-AP), Bax (Cat. 50599-2-Ig), Bcl-2 (Cat. 26593-1-AP), p38 (Cat. 14064-1-AP), p53 (Cat. 10442-1-AP), and Caspase-3 (Cat. 19677-1-AP) were purchased from the Proteintech Group (Wuhan, Hubei, China). And rabbit antibodies for

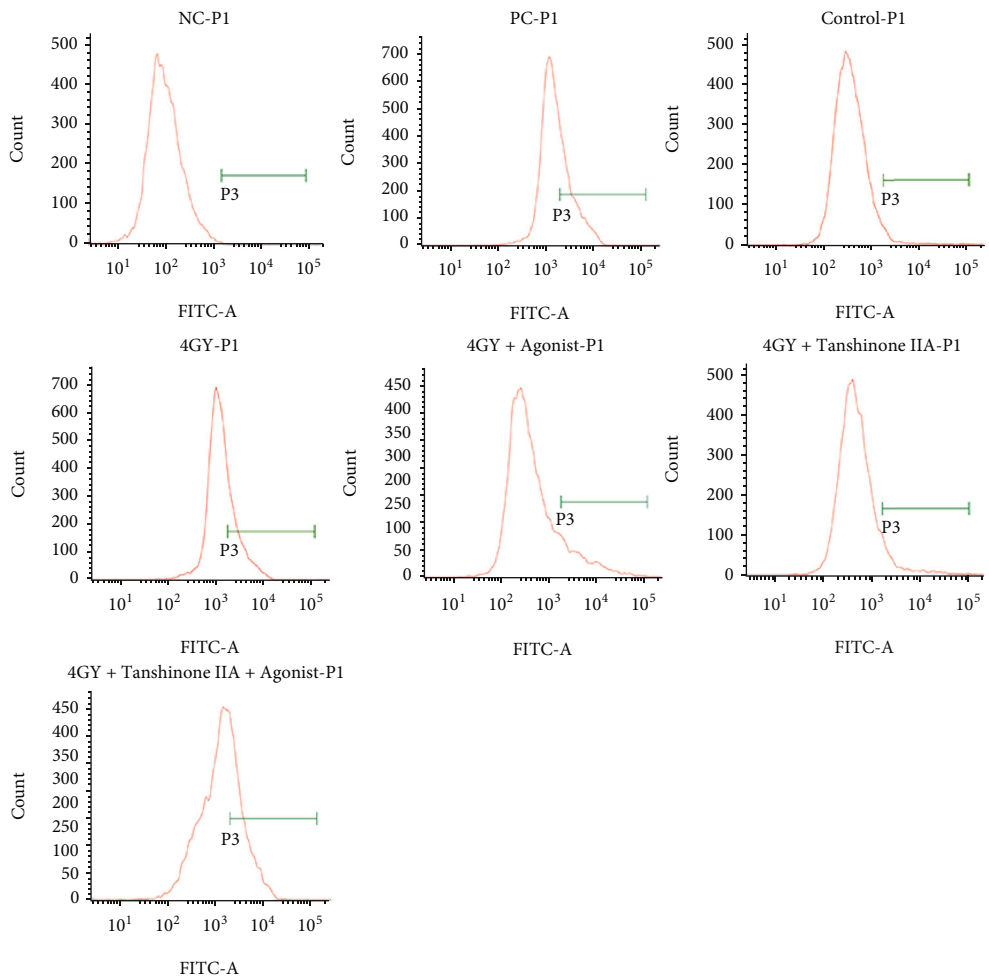

(a)

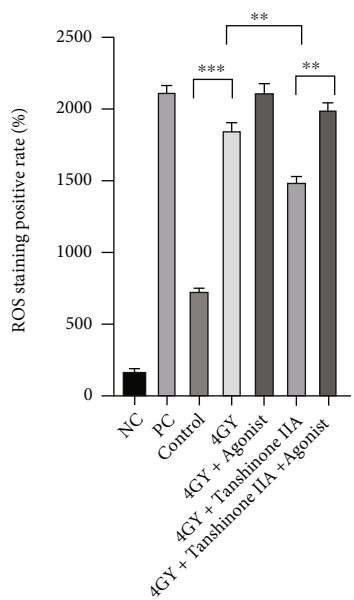

(b)

Figure 3: Effects of radiation and tanshinone IIA on oxidative stress in cardiomyocytes. (a) The ROS profile of each grouped cell was determined by flow cytometry. (b) The positive rates for ROS staining are expressed as mean ± SD. All results are presented as means ± SD ($n = 3$). $^{***}P < 0.001$ and $^{**}P < 0.01$. ROS: reactive oxygen species; NC: negative control; PC: positive control.

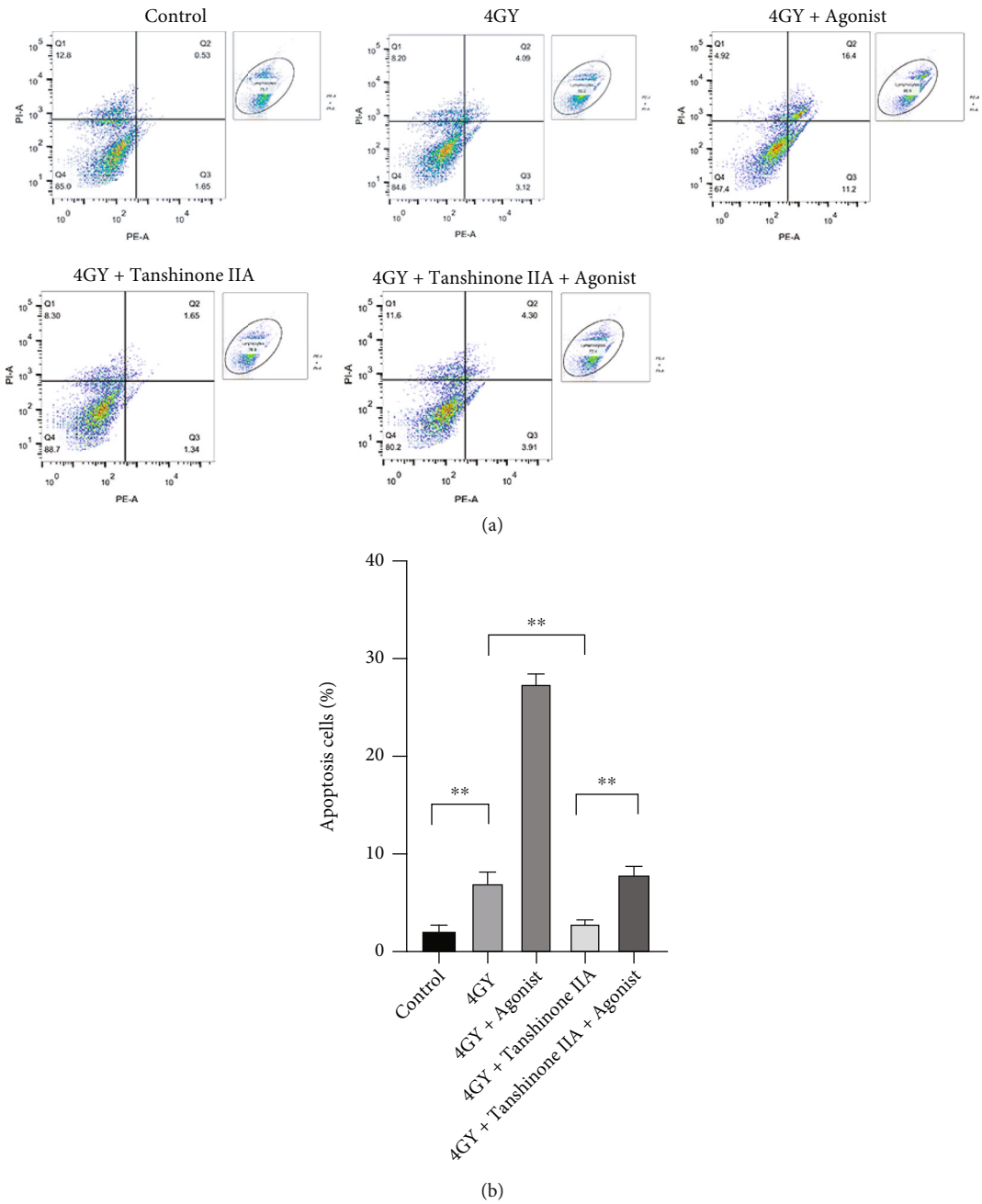

Figure 4: Effects of radiation and tanshinone IIA on cardiomyocyte apoptosis. (a) Flow cytometry was used to detect apoptosis in each group. (b) The results are expressed as mean ± SD ($n = 3$). $^{**}P < 0.01$.

p-p38 (Cat. 9211) and p-p53 (Cat. 2521) were purchased from the Cell Signaling Technology (Danvers, Massachusetts, USA). We added the tanshinone IIA group and p38 agonist group to the grouping, in order to determine the independent effects of tanshinone IIA and agonist on cardiomyocytes. The specific groupings were as follows: control group, tanshinone IIA group, agonist group, 4 Gy group, 4 Gy+agonist group, 4 Gy+tanshinone IIA group, and 4 Gy+tanshinone IIA+agonist group. To determine the gray values of the banding patterns, we used Image J (version 1.53a), and the resulting gray values were then normalized. GAPDH was used as reference.

2.6. Statistical Analysis. These results were analyzed using SPSS 20.0 (IBM Corp) and presented as mean + SD. In contrasts between two groups, one-way analysis of variance (ANOVA) was used. It was considered statistically significant when $P < 0.05$ was used.

3. Results

3.1. Tanshinone IIA Abolished Radiation-Induced Inhibition of Cardiomyocyte Proliferation. Proliferation and damage of H9C2 cells were assessed by clonogenic assay and LDH

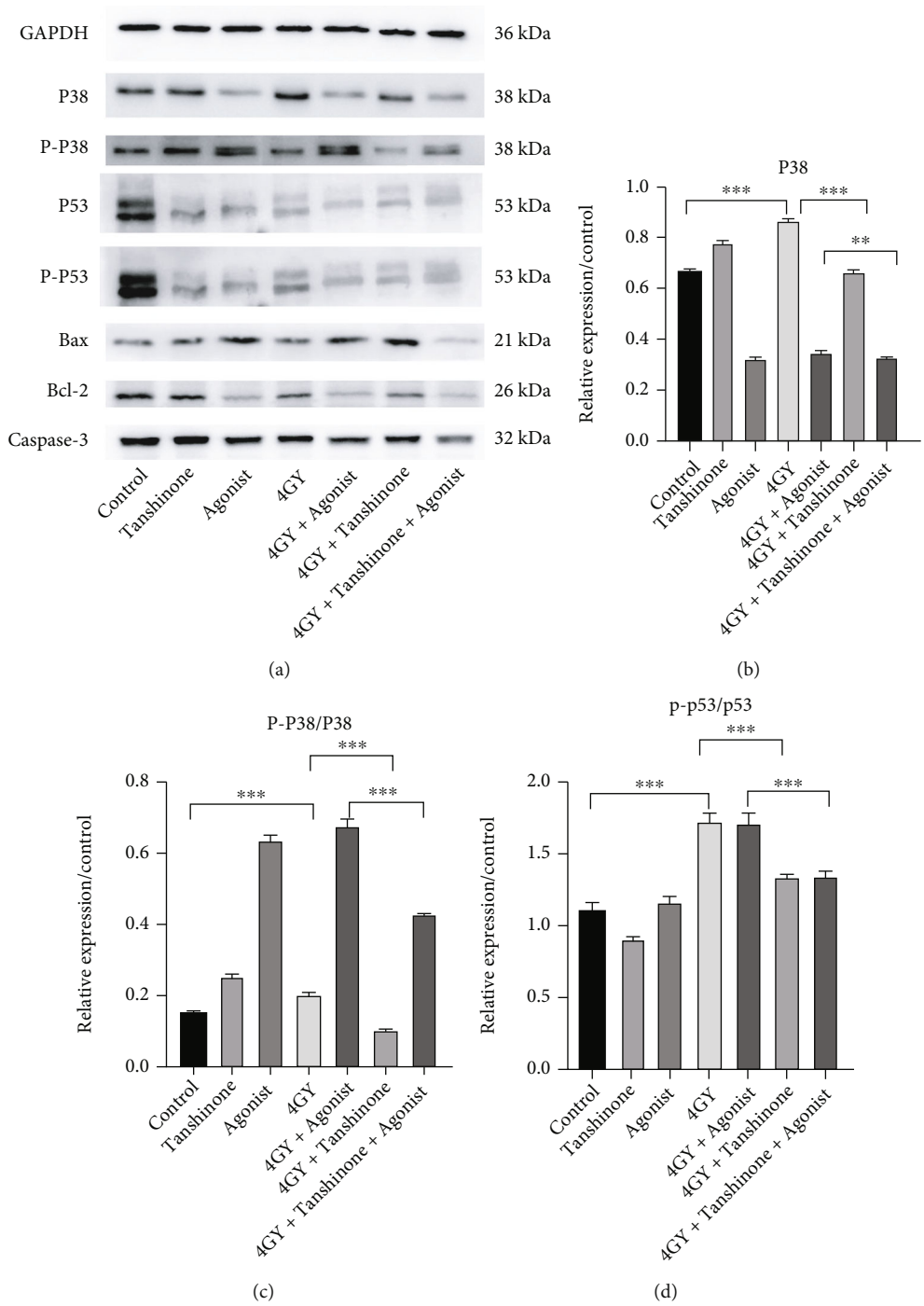

Figure 5: Continued.

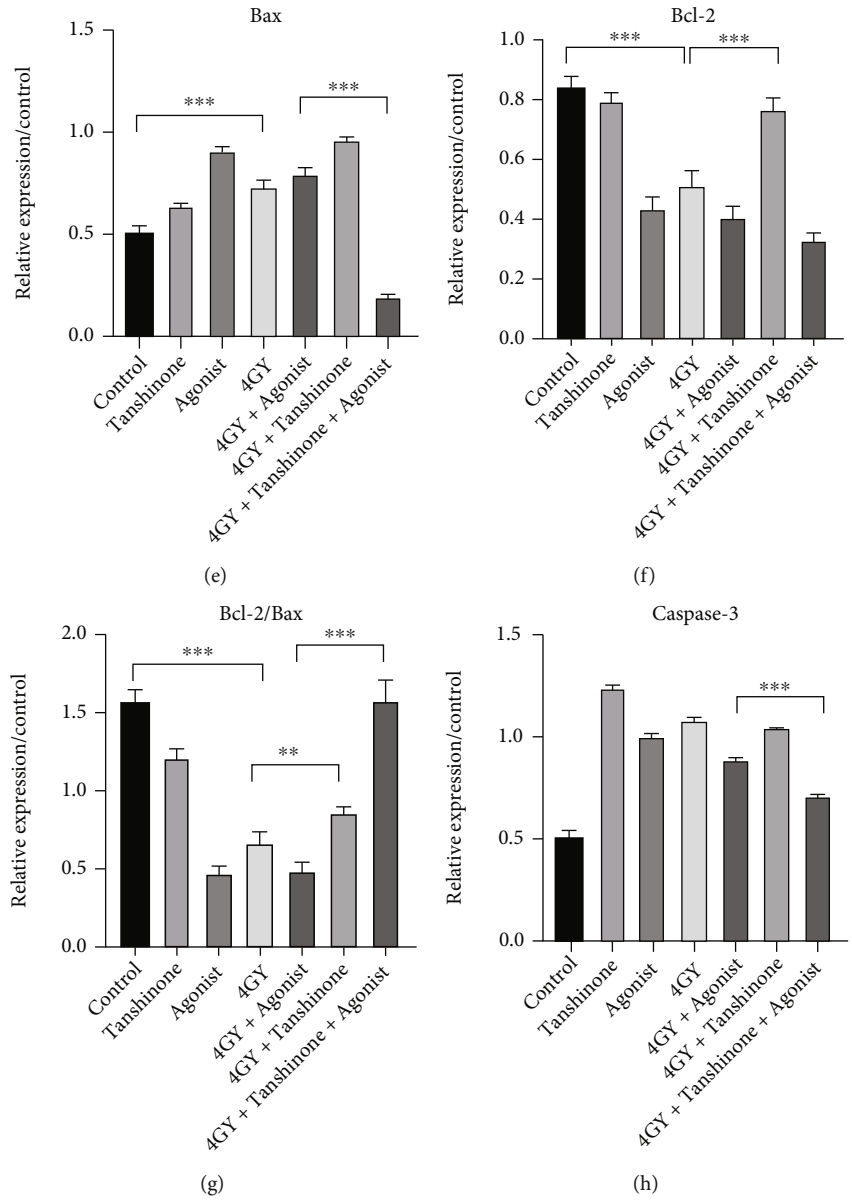

Figure 5: Expression of p38/p53 pathway related and apoptotic proteins. (a) It is a typical image of western blot. (b) P38 expression levels. (c) Ratio of p-p38/p38. (d) Ratio of p-p53/p53. (e) Bax expression levels. (f) Bcl-2 expression levels. (g) Ratio of Bcl-2/Bax. (h) Caspase-3 expression levels. GAPDH was used as reference. The results are expressed as mean ± SD. $^{***}P < 0.001$ and $^{**}P < 0.01$.

release assay, and the results are shown in Figures 1 and 2(a). Comparing the 4 Gy group to the control group, the H9C2 cell clonality rate decreased ($*P < 0.05$) while the LDH release level increased ($*** P < 0.001$). When found after treatment with tanshinone IIA, the cell clonality rate of H9C2 cells rose ($**P < 0.01$), and LDH release declined ($*P < 0.05$). It showed that tanshinone IIA inhibited radiation-induced cardiomyocyte injury while enhancing the proliferative capacity of the cells. When further administration of p38 MAPK agonist treatment, it was found that the cell clonogenic rate decreased significantly ($*** P < 0.001$), and the LDH level also increased significantly ($**P < 0.01$), suggesting that p38 MAPK aggravated the damage and inhibited cell proliferation.

3.2. Tanshinone IIA Can Reduce Radiation-Induced Oxidative Stress in Cardiomyocytes. To explore whether tanshinone IIA has the ability to exert antioxidant activity, we performed ROS and SOD activity measurements, as shown in Figures 2(b) and 3. The experimental results showed that ROS increased in the H9c2 cells ($*** P < 0.001$), while SOD decreased in the 4 Gy group ($**P < 0.01$), while LDH increased in the same way ($*** P < 0.001$). After treatment with tanshinone IIA, the antioxidant capacity of the cells clearly recovered. Tanshinone IIA increased the level of SOD ($**P < 0.01$); meanwhile, both ROS ($**P < 0.01$) and LDH ($*P < 0.05$) decreased. When further treated with p38 MAPK agonists, LDH ($**P < 0.01$), ROS ($**P < 0.01$), and SOD ($*** P < 0.001$) all rose significantly, suggesting that

p38 MAPK makes cellular oxidation and oxygen resistance become quite active, but at the same time, cellular damage is also aggravated.

3.3. Tanshinone IIA Can Decrease the Apoptosis of Cardiomyocytes Caused by Radiation. The cell apoptosis assay showed that tanshinone IIA inhibited radiation-induced cardiomyocyte apoptosis ($**P < 0.01$). However, after the use of p38 MAPK agonists, the rate of apoptosis was again significantly increased ($*** P < 0.001$). According to the results of western blot analysis, after 4 Gy irradiation, Bax expression was elevated in cardiomyocytes, and there was a significant decrease in Bcl-2 and Bcl-2/Bax levels ($*** P < 0.001$). When it was found after tanshinone IIA treatment was administered, the Bcl-2/Bax ratio was elevated ($**P < 0.01$). It showed that tanshinone IIA inhibited cell apoptosis. Finally, Bcl-2/Bax was elevated in the 4 Gy+tanshinone+agonist group ($*** P < 0.001$). The above results are shown in Figures 4 and 5.

3.4. Tanshinone IIA Downregulated Radiation-Induced p38/p53 Pathway Overexpression in Cardiomyocytes. We found that phosphorylation of p53 and p38 was overexpressed in cardiomyocytes after radiation, as compared to the control group ($*** P < 0.001$). It showed that the p38/p53 pathway was activated in radiation injury. After administration of tanshinone IIA, both p38 and p53 phosphorylation levels were downregulated, suggesting that tanshinone IIA has a regulatory effect on the p38/p53 pathway in radiation injury ($*** P < 0.001$). Comparing the 4 Gy+agonist group and 4 Gy+tanshinone IIA+agonist group revealed that tanshinone IIA could suppress the expression of p38/p53 activated by agonists ($*** P < 0.001$). The above results are shown in Figure 5.

4. Discussion

The thoracic tumor that has received radiotherapy can cause RIHD. At present, the research direction mainly focuses on inflammatory response, oxidative stress, and apoptosis [16, 17]. LDH is regarded as an indicator of cell damage. We found that in the present study, when tanshinone IIA treatment was administered to radiation injured cardiomyocytes, the cell clonogenic capacity was obviously restored, and the level of LDH decreased. This indicated that radiation-induced cardiomyocyte injury was reduced by tanshinone IIA, and the viability of the cells was restored.

For cells, antioxidation is an important self-protective mechanism that cells are able to utilize to resist damage caused by oxidants and/or electrophiles. There are many antioxidant proteins that counter the intracellular ROS, and these enzymes include thioredoxin reductase (TrxR), superoxide dismutase (SOD), catalase (CAT), and thioredoxin (TRX), among others [18]. SOD is a crucial antioxidant enzyme that guards against oxidative damage as organisms age. Therefore, the activation of intracellular SOD is crucial for the control of intracellular ROS. At present, many studies have found that radiation injury can cause abnormal elevation of ROS, which was similarly confirmed in this study, while the SOD can protect cells from oxidative stress [19, 20]. After tanshinone IIA administration, ROS decreased in cardiomyocytes, accompanied by SOD elevation, illustrating the elevation of cellular antioxidant capacity. Tanshinone IIA protected against radiation-induced cardiomyocyte injury in all of the above studies.

p38 MAPK plays important roles in cell proliferation, differentiation, inflammation, and apoptosis [21, 22]. Previous studies have shown that p38 can phosphorylate antiapoptotic proteins such as Bcl-2, MCL1, and Bclxl, thereby allowing these proteins to be degraded [23–26]. Meanwhile, p38 can phosphorylate Bax, making Bax unable to bind to Bcl-2 [27]. All the above studies can confirm the important role played by p38 in the process of apoptosis. p53 can be activated upon phosphorylation by p38 at site 46, and subsequently, another proapoptotic protein, PUMA, is activated, thereby exerting a proapoptotic effect [28–30]. In the present study, the p38/p53 pathway was activated in cardiomyocytes after radiation, whereas Bax expression increased and Bcl-2 decreased, which illustrated that p38/p53 played a role in apoptosis. When tanshinone IIA was administered, the p38/p53 expression decreased, and Bcl-2/Bax increased, and the apoptosis rate decreased. Similarly, comparing the 4 Gy+agonist group and the 4 Gy+tanshinone IIA+agonist group, we found that p38/p53 expression decreased and Bcl-2/Bax increased after administration of tanshinone IIA, which was consistent with the results of apoptosis experiment. We proved that the p38/p53 pathway was downregulated by tanshinone IIA in protecting radiation-induced myocardial injury.

In previous studies, tanshinone IIA has numerous protective effects on the myocardium. For example, tanshinone IIA can attenuate ventricular remodeling in rats with heart failure [31]. Tanshinone IIA is able to protect cardiac function by regulating angiogenesis in mice with myocardial ischemia [32]. Combined with previous studies by our group, tanshinone IIA could protect cardiomyocytes by reducing radiation-induced apoptosis through downregulation of the p38/p53 pathway. And it is predicted that p38 MAPK can be targeted for inhibition as a therapeutic approach to reduce radiation injury and provide a novel strategy to prevent and treat RIHD.

Abbreviations

7-AAD:	7-Aminoactinomycin D
ANOVA:	Analysis of variance
Bax:	B-cell lymphoma 2-associated X protein
BCA:	Bicinchoninic acid
Bcl:	B-cell lymphoma
Caspase:	Cysteinyl aspartate specific proteinase
DCFH-DA:	2,7-Dichlorodi-hydrofluorescein diacetate
DMEM:	Dulbecco's modified eagle medium
DNA:	Deoxyribonucleic acid
GAPDH:	Glyceraldehyde-3-phosphate dehydrogenase
LDH:	Lactate dehydrogenase
MAPK:	Mitogen-activated protein kinases
MCL1:	Myeloid cell leukemia 1
PE:	Phycoerythrin

PUMA: P53 upregulated modulator of apoptosis
RIHD: Radiation-induced heart disease
ROS: Reactive oxygen species
SOD: Superoxide dismutase
SPSS: Statistical Product Service Solutions.

Data Availability

All data generated or analyzed during this study are included in this published article.

Conflicts of Interest

No competing interests are declared by the authors.

Authors' Contributions

Ping Xie and Yi Li proposed, designed the entire study, and gave guidance when the experiments were performed. Gang Wang, Li Ma, and Bo-wen Wang performed the main experimental tasks and participated in the writing of the manuscript. Fentang Gao, Jianfeng Li, Juan Wang, and Tiancheng Zhang collected data, suggested, and revised the manuscript during its writing. Hongyi Cai provided and guided the use of radiological instruments and taught relevant knowledge of postradiation complications. Hao Guo did some work in the experiment. Gang Wang and Li Ma contribute equally and are co-first authors of the article. Ping Xie and Yi Li contribute equally and are cocorresponding authors of the article.

Acknowledgments

A grant from the National Natural Science Foundation of China (No. 81860047) supported this study.

References

[1] G. Delaney, S. Jacob, C. Featherstone, and M. Barton, "The role of radiotherapy in cancer treatment," *Cancer*, vol. 104, no. 6, pp. 1129–1137, 2005.

[2] M. A. Armanious, M. Homan, K. Sara, D. E. Oliver, P. A. Johnstone, and M. G. Fradley, "Cardiovascular effects of radiation therapy," *Current Problems in Cancer*, vol. 42, no. 4, pp. 433–442, 2018.

[3] P. A. Heidenreich and J. R. Kapoor, "Radiation induced heart disease: systemic disorders in heart disease," *Heart*, vol. 95, no. 3, pp. 252–258, 2009.

[4] S. Tapio, "Pathology and biology of radiation-induced cardiac disease," *Journal of Radiation Research*, vol. 57, no. 5, pp. 439–448, 2016.

[5] M. Sárközy, Z. Varga, R. Gáspár et al., "Pathomechanisms and therapeutic opportunities in radiation-induced heart disease: from bench to bedside," *Clinical Research in Cardiology*, vol. 110, pp. 507–531, 2018.

[6] Onco-Cardiology: consensus paper of the German Cardiac Society, "Onco-Cardiology: Consensus Paper of the German Cardiac Society, the German Society for Pediatric Cardiology and Congenital Heart Defects and the German Society for Hematology and Medical Oncology," *Clinical Research in Cardiology*, vol. 109, no. 10, pp. 1197–1222, 2020.

[7] M. M. Hudson, K. K. Ness, J. G. Gurney et al., "Clinical ascertainment of health outcomes among adults treated for childhood cancer," *JAMA*, vol. 309, no. 22, pp. 2371–2381, 2013.

[8] N. K. Taunk, B. G. Haffty, J. B. Kostis, and S. Goyal, "Radiation-induced heart disease: pathologic abnormalities and putative mechanisms," *Frontiers in Oncology*, vol. 5, p. 39, 2015.

[9] J. Slezak, B. Kura, P. Babal et al., "Potential markers and metabolic processes involved in the mechanism of radiation-induced heart injury," *Canadian Journal of Physiology and Pharmacology*, vol. 95, no. 10, pp. 1190–1203, 2017.

[10] E. I. Azzam, J. P. Jay-Gerin, and D. Pain, "Ionizing radiation-induced metabolic oxidative stress and prolonged cell injury," *Cancer Letters*, vol. 327, no. 1-2, pp. 48–60, 2012.

[11] Z. Dan, C. Wky, D. Yfza et al., "Sodium tanshinone IIA sulfonate prevents radiation-induced damage in primary rat cardiac fibroblasts," *Chinese Journal of Natural Medicines*, vol. 18, no. 6, pp. 436–445, 2020.

[12] W. Zhang, L. Yi, L. Rui et al., "Sodium tanshinone IIA sulfonate prevents radiation-induced toxicity in h9c2 cardiomyocytes," *Evidence-Based Complementray and Alternative Medicine*, vol. 2017, article 4537974, 13 pages, 2017.

[13] X. Z. Ao, J. P. Mei, J. H. Yu, K. A. Kang, and W. H. Jin, "Purpurogallin protects keratinocytes from damage and apoptosis induced by ultraviolet B radiation and particulate matter 2.5," *Biomolecules & Therapeutics*, vol. 27, no. 4, pp. 395–403, 2019.

[14] R. Chen, W. Chen, X. Huang, and Q. Rui, "Tanshinone IIA attenuates heart failure via inhibiting oxidative stress in myocardial infarction rats," *Molecular Medicine Reports*, vol. 23, no. 6, 2021.

[15] Q. Zhang and X. Li, "Pharmacological actions of Tanshinone II_A and sodium tanshinone II_A sulfonate," *Journal of Pediatric Pharmacy*, vol. 18, no. 2, pp. 44–46, 2012.

[16] A. E. Musa and D. Shabeeb, "Radiation-induced heart diseases: protective effects of natural products," *Medicina*, vol. 55, no. 5, p. 126, 2019.

[17] J. Spetz, J. Moslehi, and K. Sarosiek, "Radiation-induced cardiovascular toxicity: mechanisms, prevention, and treatment," *Current Treatment Options in Cardiovascular Medicine*, vol. 20, no. 4, p. 31, 2018.

[18] J. M. Tolmasoff, T. Ono, and R. G. Cutler, "Superoxide dismutase: correlation with life-span and specific metabolic rate in primate species," *Proceedings of the National Academy of Sciences*, vol. 77, no. 5, pp. 2777–2781, 1980.

[19] J. Zhu, Y. Xu, G. Ren et al., "Tanshinone IIA Sodium sulfonate regulates antioxidant system, inflammation, and endothelial dysfunction in atherosclerosis by downregulation of CLIC1," *European Journal of Pharmacology*, vol. 815, pp. 427–436, 2017.

[20] S. Ilavenil, D. H. Kim, Y.-I. Jeong et al., "Trigonelline protects the cardiocyte from hydrogen peroxide induced apoptosis in H9c2 cells," *Asian Pacific Journal of Tropical Medicine*, vol. 8, no. 4, pp. 263–268, 2015.

[21] A. R. Nebreda and A. Porras, "p38 MAP kinases: beyond the stress response," *Trends in Biochemical Sciences*, vol. 25, no. 6, pp. 257–260, 2000.

[22] E. F. Wagner and Á. R. Nebreda, "Signal integration by JNK and p38 MAPK pathways in cancer development," *Nature Reviews Cancer*, vol. 9, no. 8, pp. 537–549, 2009.

[23] I. E. Wertz, S. Kusam, C. Lam et al., "Sensitivity to antitubulin chemotherapeutics is regulated by MCL1 and FBW7," *Nature*, vol. 471, no. 7336, pp. 110–114, 2011.

[24] M. Trouillas, C. Saucourt, D. Duval et al., "Bcl2, a transcriptional target of p38alpha, is critical for neuronal commitment of mouse embryonic stem cells," *Cell Death and Differentiation*, vol. 15, no. 9, pp. 1450–1459, 2008.

[25] C. Bradham and D. R. Mcclay, "P38 MAPK in development and cancer," *Cell Cycle*, vol. 5, no. 8, pp. 824–828, 2006.

[26] J. Kale, E. J. Osterlund, and D. W. Andrews, "BCL-2 family proteins: changing partners in the dance towards death," *Cell Death and Differentiation*, vol. 25, no. 1, pp. 65–80, 2018.

[27] H. Min, G. S. Ghatnekar, A. V. Ghatnekar et al., "2-Methoxyestradiol induced Bax phosphorylation and apoptosis in human retinoblastoma cells via p38 MAPK activation," *Molecular Carcinogenesis*, vol. 51, no. 7, pp. 576–585, 2012.

[28] J. M. Solomon, R. Pasupuleti, L. Xu et al., "Inhibition of SIRT1 catalytic activity increases p53 acetylation but does not alter cell survival following DNA damage," *Molecular and Cellular Biology*, vol. 26, no. 1, pp. 28–38, 2006.

[29] D. V. Bulavin, S. Saito, M. C. Hollander et al., "Phosphorylation of human p53 by p38 kinase coordinates N-terminal phosphorylation and apoptosis in response to UV radiation," *EMBO Journal*, vol. 18, no. 23, pp. 6845–6854, 1999.

[30] P. Sridevi, M. K. Nhiayi, R. L. Setten, and J. Wang, "Persistent inhibition of ABL tyrosine kinase causes enhanced apoptotic response to TRAIL and disrupts the pro-apoptotic effect of chloroquine," *PLoS One*, vol. 8, no. 10, article e77495, 2013.

[31] X. Li, D. Xiang, Y. Shu, X. Zeng, and Y. Li, "Mitigating effect of tanshinone IIA on ventricular remodeling in rats with pressure overload-induced heart failure," *Acta Cirúrgica Brasileira*, vol. 34, no. 8, article e201900807, 2019.

[32] X. Wang and C. Wu, "Tanshinone IIA improves cardiac function via regulating miR-499-5p dependent angiogenesis in myocardial ischemic mice," *Microvascular Research*, vol. 143, article 104399, 2022.

Hindawi
Mediators of Inflammation
Volume 2022, Article ID 2185198, 13 pages
https://doi.org/10.1155/2022/2185198

Research Article

Identification of an Epigenetic Signature for Coronary Heart Disease in Postmenopausal Women's PBMC DNA

Xiao Zhong,[1] Ziguang Song,[1] Pingping Gao,[2] Mingyang Li,[1] Zhongping Ning,[2] and Xiang Song[1]

[1]*Department of Cardiology, The Fourth Hospital of Harbin Medical University, Harbin, China 150000*
[2]*Zhoupu Hospital, Shanghai University of Medicine and Health Sciences, Shanghai, China 200000*

Correspondence should be addressed to Xiang Song; song761231@sina.com

Received 20 June 2022; Revised 25 July 2022; Accepted 2 August 2022; Published 19 August 2022

Academic Editor: Md Sayed Ali Sheikh

Menopause is accompanied with an increased risk of cardiovascular disease. DNA methylation may have a significant impact on postmenopausal women's development of coronary heart disease. DNA methylation alterations in peripheral blood mononuclear cells (PBMCs) from women with coronary heart disease and healthy controls were detected using the Illumina Infinium MethylationEPIC BeadChip platform in this work. We employed Sangerbox technology and the GO and KEGG databases to further study the pathogenesis of coronary heart disease in postmenopausal women. After that, we used functional epigenetic module analysis and Cytoscape to remove the hub genes from the protein–protein interaction networks. Five genes (FOXA2, PTRD, CREB1, CTNAP2, and FBN2) were the hub genes. Lipid accumulation, endothelial cell failure, inflammatory responses, monocyte recruitment and aggregation, and other critical biological processes were all influenced by these genes. Finally, we employed methylation-specific PCR to demonstrate that FOXA2 was methylated at a high level in postmenopausal women with coronary heart disease. To better understand coronary heart disease in postmenopausal women's molecular mechanisms, our study examine the major factors contributing to the state of DNA methylation modification, which will help discover novel diagnostic tools and treatment options.

1. Introduction

Cardiovascular disease (CVD) is a leading cause of death globally [1]. The cost of treating CVD will climb as the population ages and the increase of obesity and diabetes [2]. Menopause is a time of increasing cardiovascular risk in women, and postmenopausal women have a higher risk of cardiovascular disease than men of the same age [3]. Coronary heart disease (CHD), the main type of CVD, is the leading cause of mortality in women over the age of 65, surpassing the incidence of cancer, chronic lower respiratory illness, and diabetes [4].

Apart from these discrepancies in traditional risk factors, a range of clinical conditions unique to women, such as polycystic ovary syndrome, gestational diabetes, preeclampsia, autoimmune diseases, and early menopause, could increase the risk of CHD [5].Due to a high morbidity associated with postmenopausal CHD, much emphasis has been dedicated to the disease's pathological process. A vast majority of studies have demonstrated estrogen's protective effect on the coronary arteries [6, 7]. Intuitively, estrogens appear to postpone the formation of plaques and the repercussions of coronary artery disease in women [8]. However, two studies have found no cardiovascular benefit from hormone replacement therapy (HRT) during a 6.8-year follow-up period [9, 10]. In addition, women with HRT may have had an elevated risk of coronary artery disease and nonfatal ventricular arrhythmias within the first year of treatment [9]. Compared to placebo, HRT had no favorable effects on the cardiovascular system, and estrogen therapy alone also increased the risk of stroke [11].Currently, the function of estrogen and how it affects the cardiovascular system is still unknown. While estrogen levels in premenopausal women may not be more vulnerable to cardiovascular disease than males, this is not the only contributing element; therefore, further mechanisms should be found by additional investigation.

CHD is thought to be caused by a combination of genetic and environmental factors [12]. Study on heritable changes in gene activity or function without changes in DNA sequence, known as epigenetics, is of critical importance to all disease processes [13], including in cardiovascular disease and its associated diseases [14]. In epigenetics, most DNA methylation occurs through the attachment of an extra methyl group (CH3) from S-adenosyl methionine (SAM) to the C5 position of cytosine-paired-guanine (CpG) dinucleotide sequences, leading to 5-methylcytosine (MeC) (5mC) formation, which is usually responsible for controlling tissue-specific gene expression, genomic imprinting, and the inactivation of the X chromosome [15].The DNA methyltransferases 3b (DNMT3b), 3a (DNMT3a), and 1 (DNMT1) catalyze DNA methylation, which is reversed by Tet methylcytosine dioxygenases (TET1, 2, and 3) [16].

Evidence suggests that abnormal DNA methylation may contribute to coronary heart disease. Methylation of ATP binding cassette subfamily G member 1 (ABCG1) and ATP binding cassette subfamily A member 1 (ABCA1) has been associated with coronary heart disease [17–19]. In individuals with CHD, the PCSK9 gene expression and circulating blood protein levels are linked to promoter DNA methylation [20].IL-6 promoter hypomethylation, which results in its overexpression and systemic inflammation, has been linked to an increased risk of CHD [21].Atherosclerosis, the primary pathophysiology of CHD, is an inflammatory disease, as it is well documented [22]. In research on epigenetic regulation of genes associated with atherosclerotic plaque vulnerability, the imprinted gene PLA2G7, which encodes lipoprotein-associated phospholipase A2 (Lp-PLA2), has been seen as one of the most hypomethylated genes showing the upregulated expression in response to inflammation [23]. Atherogenesis of the vascular system also may be aided by ER alpha gene methylation-associated inactivation in vascular tissue [24]. In light of what has been said so far, the relationship between CHD and DNA methylation has been studied in a number of studies; however, postmenopausal women have received less attention. Thus far, just a research by Ramos and colleagues found that postmenopausal women with lower global DNA methylation had an increased risk of cardiovascular disease [25]. The biological process that is controlled by methylation that is not right needs to be studied more. The role of epigenetic factors in the etiology of coronary artery disease in postmenopausal women needs to be looked into more.

We pooled and analyzed data from women with coronary heart disease and their equivalents, as well as data on differential DNA methylation, as part of our present work (from postmenopausal women with coronary artery disease (PC), healthy postmenopausal women (PCG), and young women (C)).The Illumina Infinium MethylationEPIC BeadChip was used to methylate the above volunteers. A total of 850 K probes were used to examine the promoter, enhancer regions, CpG island, and coding region.

2. Materials and Methods

2.1. Study Population and Sampling. This research used CHD clinical criteria to enroll four postmenopausal women with CHD, four normal postmenopausal women (using stenosis 50% cutoffs to assess whether or not they had coronary disease [26]), and four young women. Young women with a thickness of vessel intima-media thickness (IMT) of less than 1.0 mm were chosen for inclusion using Wang et al.'s [27] operation criteria. Menopause is described as the time period between the ages of 50 and 60 when menstruation ends for at least 12 months [28]. Patients who had cardiovascular and cerebrovascular diseases, such as cerebral hemorrhage, embolism, nonatherosclerotic vascular disease, myocardial infarction, cardiomyopathy, heart failure, congenital heart disease, valvular disease, diabetes, autoimmune diseases, severe liver and kidney disease, systemic infection, or any other inflammatory disease, cancer; those who have taken anti-inflammatory medicine or surgical therapy in the last 6 months; and those patients with familial hyperlipidemia, were all excluded from this study [29]. All the patients were chosen by the Department of Cardiovascular Medicine at the Zhoupu Hospital in Shanghai's Pudong New District and singed written informed permission. The hospital approved this research, and it was performed in accordance with the Declaration of Helsinki.

2.2. DNA Methylation Experiment. Following the instructions for extracting peripheral blood mononuclear cells (PBMCs), we took 8 ml of fasting peripheral blood from each research subject in the morning, from each sample, using Histopaque-1077 lymphocyte separation solution (Sigma, United States), and the experiment was completed in 4 hours. DNA was isolated from PBMCs by using the DNeasy Blood and Tissue Kit (Qiagen, Germany). The purity and concentration of DNA were estimated using Nanodrop 2000 (Thermo, Germany) and Quibt3.0. Then, 500 ng DNA of each sample was used in bisulfite convert using EZ DNA Methylation Kits (Zymo Research, United States), and the converted products were put into 850 K BeadChips in accordance with the manufacturer's guide and protocol (Illumina, United States).

2.3. Differential Methylation Position Analysis. Genome-wide DNA methylation was determined according to the manufacturer's instructions using the Illumina Infinium MethylationEPIC BeadChip (Illumina Inc., USA), which gave genome-wide coverage comprising >850 000 CpG methylation sites per sample. We selected probes with at least three beads from at least 10% of samples, non-CpG probes, multihit probes, probes situated on chromosomes X and Y, and (SNP-related probes) for future analysis. To determine the methylation level, the array data (.IDAT files) were processed in the ChAMP program of *R* (http://www.bioconductor.org/packages/release/bioc/vignettes/ChAMP/inst/doc/ChAMP.html). The beta value (β value), which was the ratio of the methylated probe intensity to the total probe intensity (sum of unmethylated and probe intensities plus constant, where is equal to 100), signified the methylation status of all probes. A DNA methylation score ranging from 0 (totally unmethylated DNA) to 1 (fully methylated DNA) (completely methylated) was used to express the β values. To account for the bias caused by the array's different bead types (peak-based correction normalization), the

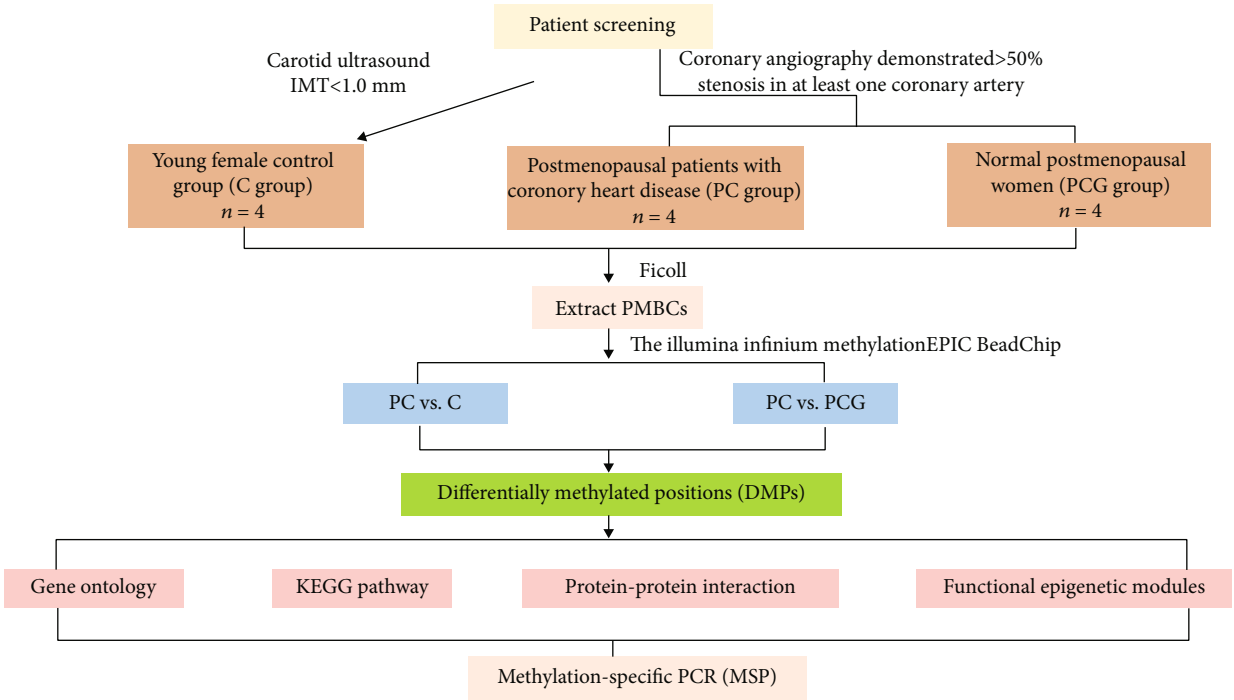

Figure 1|: Flowchart of bioinformatics analysis. DMPs: differentially methylated positions.

methylation data were normalized. Between the two groups, the average β values were compared. When the p value was lower than 0.01, $|\Delta\beta|>0.1$, differentially methylated CpG sites were detected.

2.4. Distribution Analysis of Differentially Methylated Positions (DMPs). According to 850 K array annotation, the DMPs were divided into several categories based on their distributions relative to genomic areas (3′ untranslated regions (UTR), intergenic region promoter, gene body) and CpG island regions (beach, shelf, island, or open sea). The promoter areas comprised the 5′ UTR, sections near 200 and 1500 bp of the transcription start site (TSS200, TSS1500), and the first exon.

2.5. Gene Ontology and Pathway Enrichment Analysis. We used the Sangerbox tools (http://www.sangerbox.com/tool), a free online platform for data analysis on genes related to DMPs, to conduct Gene Ontology enrichment analysis to filter overrepresented Gene Ontology words in three categories (biological processes, molecular function, and cellular component). Sangerbox methods were used to discover statistically significant enriched pathways from the Kyoto Encyclopedia of Genes and Genomes (KEGG) pathway enrichment analysis for genes associated with DMPs.

2.6. Construction of PPI Network and Related Analysis. PPI analysis was used to better understand the relationships between the two groups of genes in the development of CHD in postmenopausal women and unique biological pathways. We combined hypomethylation and hypermethylation genes to create PPI networks with minimal number of hypomethylation and hypermethylation genes. A PPI network was created using STRING 11.0 (https://string-db.org/). The cutoff threshold for the interaction score was set at 0.4. For further analysis, the findings were imported into Cytoscape 3.8.0. The hub genes were filtered using the CytoHubba software (http://apps.cytoscape.org/apps/cytohubba).

The total differential methylation site interactions were also analyzed using functional epigenetic modules (FEM, http://www.bioconductor.org/packages/3.1/bioc/vignettes/FEM/inst/doc/IntroDoFEM.pdf). The FEM method may be thought of as a functional supervised algorithm that leverages a network of gene relationships, such as a protein–protein interaction (PPI) network, to find subnetworks with a large number of genes being linked to a phenotype of interest.

2.7. Methylation-Specific Polymerase Chain Reaction (MS-PCR). MS-PCR was performed on the bisulfite-treated DNA samples using primers specific for the methylated versions of FOXA2: forward 5′-GAGGGGTAGGTTAGTTCGGT-3′ and reverse 5′-AAAATCTAACCCCTCTAACTCCG-3′ FOXA2 methylated sequence and ACTB (all six actin proteins are made by this gene. Actins are a group of proteins with a high degree of evolutionary conservation) methylation sequence, forward 5′-TGGTGATGGAGGAGGTTTAGTAAGT-3′ and reverse 5′-AACCAATAAAACCTACTCCTCCCTTAA-3′. Both versions of FOXA2 and ACTB were amplified for 35 cycles at 60°C using the Hieff Unicon® Universal TaqMan multiplex qPCR master mix (Yeasen Biotech, China). MS-PCR products were separated into aliquots and examined on a 2% agarose gel before being stained with Ethidium Bromide (Sangon Biotech, China).

2.8. Statistical Analysis. Counting and quantitative analysis was performed using ImageJ program. To evaluate whether

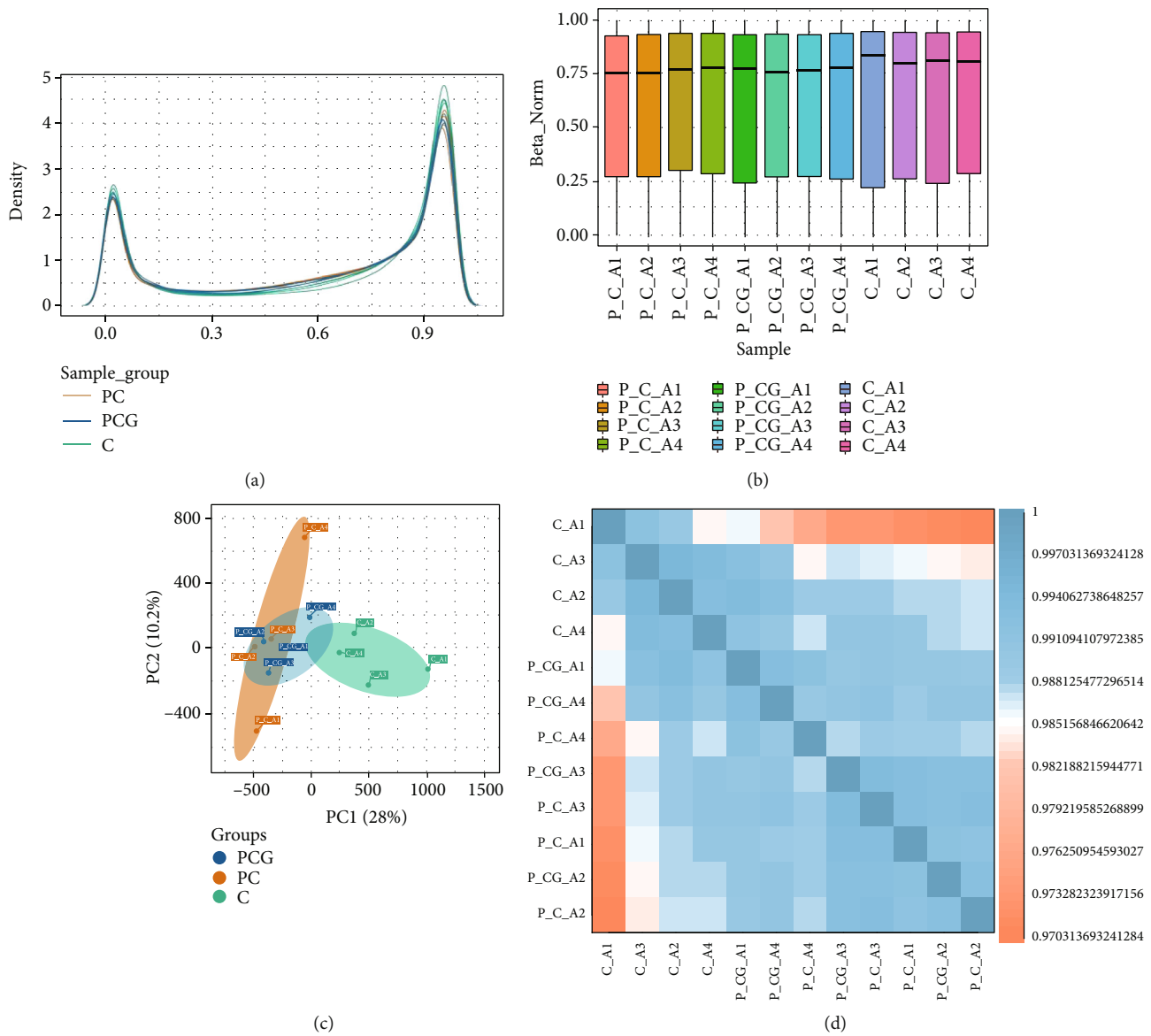

Figure 2: The methylation array data was subjected to quality control. (a) The density figure shows the distribution of the complete array probes for the PC, PCG, and C groups. (b) Boxplots of the twelve samples' β values. (c) A principal component analysis biplot of DNA methylation changes was used to highlight the data structure and sample link among the three sample groups. PC1 signifies the first principal component, whereas PC2 denotes the second main component. (d) A heat map illustrating three groupings of locations and samples that are differently methylation. The color shifts from red to blue, suggesting a strong to low correlation between the three samples.

there were statistically significant differences between the means of three separate groups, the one-way analysis of variance is utilized. The comparisons were performed using t-test and pairwise t-tests. It was statistically significant when the p value was less than 0.05. GraphPad Prism 8 (GraphPad Prism Software Inc., California) was used to correlate the analysis and visual presentation for the statistical studies.

3. Result

3.1. Quality Control of the Methylation Array Data. The flowchart of the whole analysis is shown in Figure 1. The 12 subjects' genome-wide DNA methylation patterns were produced using the Illumina Infinium MethylationEPIC BeadChip. To quantify methylation at each locus, β values were used. Preprocessing and normalization of data from postmenopausal women with coronary heart disease and control samples were performed. The density distribution of the β values revealed a characteristic bimodal distribution (Figure 2(a)), with the first peak corresponding to low or unmethylated probes with a β value near 0 and the second peak corresponding to substantially or completely methylated probes with a β value near 1.Additionally, boxplots of the 12 individuals' β value distributions were obtained (Figure 2(b)).The results of the main component analysis on the three sets of samples are shown in Figure 2(c). The gap between samples was indicative of an individual gene's methylation pattern. Thus, the PC group's gene methylation

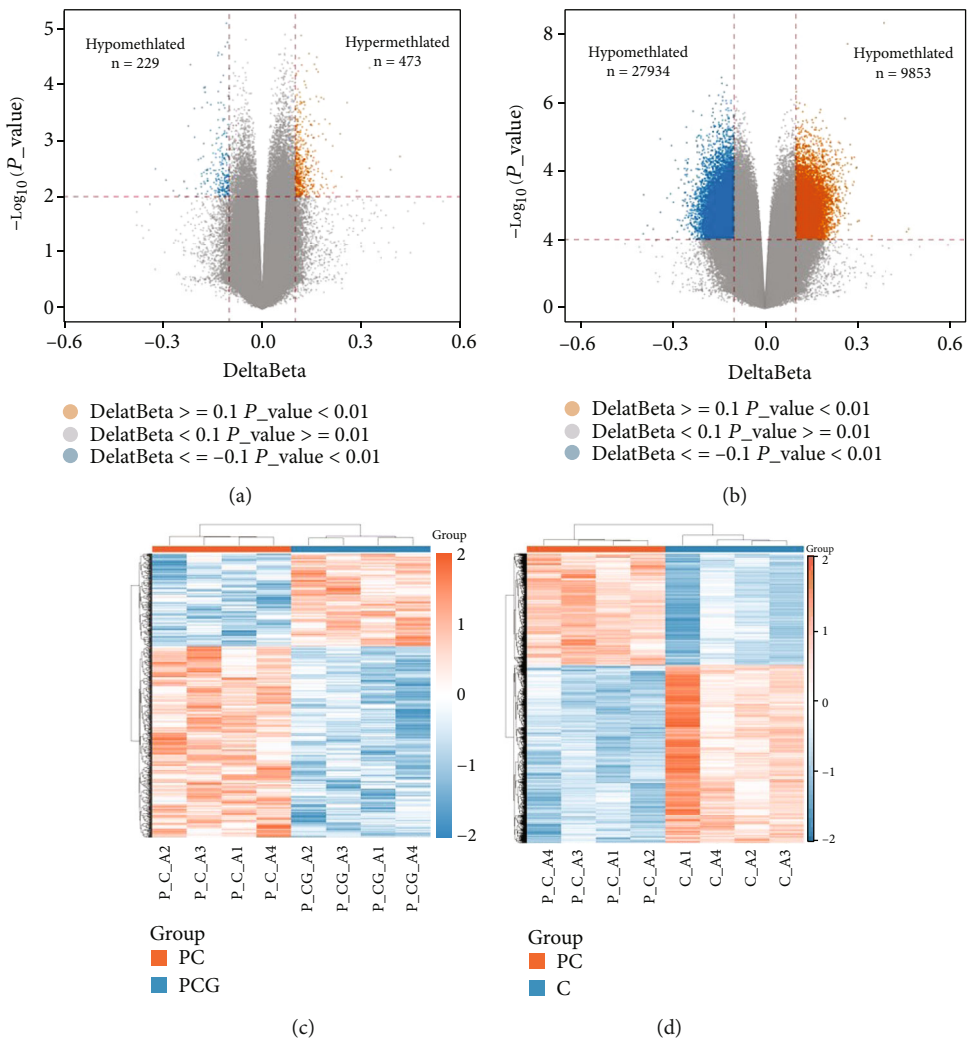

Figure 3: Methylation levels differed across groups. (a) A volcano plot of PC vs. PCG probe-level methylation. (b) A volcano plot of methylation at the probe level in PC vs. C. The graph depicts the link between the amount of the difference in values ($\Delta\beta$ values; x-axis) and the number of p values (negative log10 transformed p values; y-axis). A single probe is represented by each dot. Horizontal and vertical dashed lines represent the $p = 0.01$ and 10% methylation difference ($|\Delta\beta|$=0.1) cutoffs, respectively. Hyper- and hypomethylated DMPs are represented by orange and blue dots, respectively. (c) A heat map of the top 5000 differentially methylated CpG sites in the PC versus PCG groups. (d) Heat map of PC vs. C group's top 5000 differentially methylated CpG sites. The heat map's orange color shows loci that have been hypermethylated, while the heat map's blue color shows loci that have been hypomethylated.

profile was distinct from that of the other two control groups. A heat map of the relationships between the samples revealed that the research participants' gene methylation patterns varied (Figure 2(d)). The general distribution and concentration trend of the three data groups in the PC group and normal group were examined using the average β values of the three data groups. A heat map of the correlations among the samples and the PCA figure also supported that the sampling between groups was reasonable.

3.2. Identification of Significantly Differentially Methylated Sites. Following data preparation and quality control, 703,400 CpG sites were collected for further analysis after filtering. A total of 702 CpG sites were substantially differentially methylated with $p < 0.01$ and $|\Delta\beta|$ threshold>0.1 and comprised 473 hypermethylated and 229 hypomethylated sites in the PC group when compared to the PCG control (Figure 3(a)).Additionally, there were 37787 differential methylation sites, including 9853 hypermethylation sites and 27934 hypomethylation sites, across the PC and C groups (Figure 3(b)). Following that, we transformed the z -scores and carried out a heat map analysis on the whole set of differential methylation locations. We selected the top 5000 difference points for mapping or all mapping if the difference points were fewer than 5000. Figures 3(c) and 3(d) provide heat maps of all the substantially different methylation sites. Orange showed areas that were more hypermethylated, while blue showed areas that were less methylated. This indicated that PC patients and healthy people had different epigenetic landscapes.

3.3. Characteristics of Highly Differently Methylated Regions at the Genomic Level. We evaluated the CpG island for substantially different methylation sites in connection to

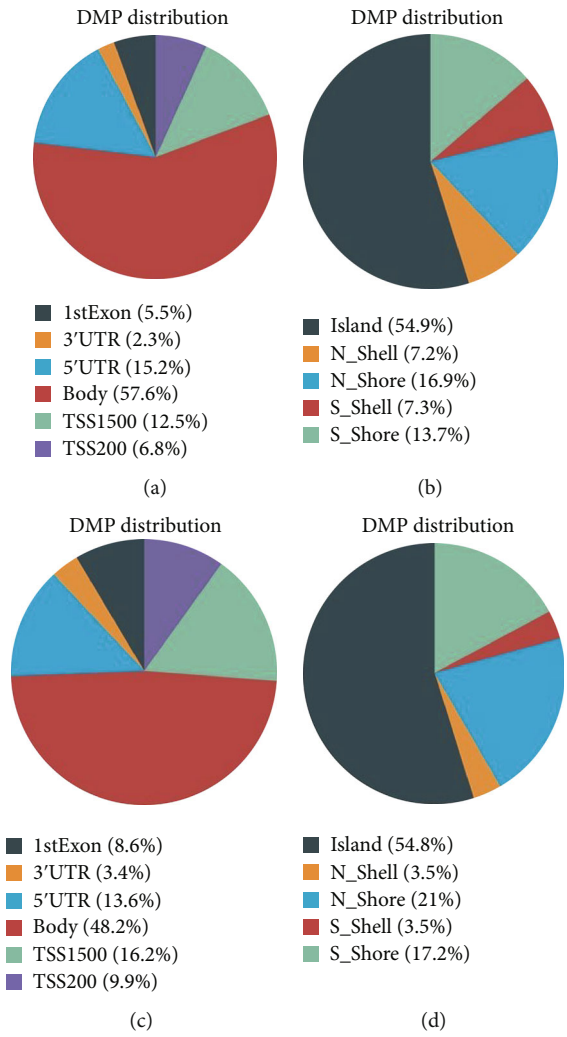

Figure 4: Differentially methylated positions are located on genomic CpG islands. (a) Distribution of methylated positions with respect to genomic regions in the PC vs. PCG group. (b) The distribution of methylated positions in the PC vs. PCG groups in relation to CpG island features. (c) Distribution of methylated positions with respect to genomic regions in the PC vs. C group. (d) The distribution of methylated positions in the PC vs. C groups in relation to CpG island features. 1stExon: first exon; TSS: transcription start site; TSS1500 and TSS200: 1500 bp and 200 bp downstream of the TSS, respectively; UTR: untranslated region. Island, probes located on CpG islands; open sea, probes not located on an island or annotated genes; shelf, probes located more than 2 k from CpG islands; and shore, probes located less than 2 kb from a CpG island.

their genomic positions. According to the CpG content, significant variations in methylated sites were identified between the PC and control groups. Figures 4(a) and 4(c) indicate the proportion of methylation in the 5/UTR, 3/UTR, transcription start site, exon, body, intergenic region, and intron for each group of postmenopausal females with CHD. The majority of substantially differentially methylated sites in postmenopausal women with coronary artery disease were located in the nonpromoter region. There was a great enrichment of DMPs situated on the CpG islands, whereas other DMPs were found in the open sea, beach, and shelf areas with low CpG island density (Figures 4(b) and 4(d).

3.4. Pathway Enrichment Analysis. We intersected the difference loci obtained from the PC vs. PCG group with the difference loci obtained from the PC against the C group and acquired a total of 365 difference loci. In addition, discrepancies between the PCG and C groups were evaluated in order to rule out the influence of age. The difference between PCG and C loci was removed from the loci listed above (Figure 5(b)). We concluded with 353 distinct loci. More notably, these sites have the same methylation trend between the PC versus PCG and PC vs. C groups. According to the different loci, 234 genes were mapped. To further comprehend the functional implications of the DMPs, we used Gene Ontology and KEGG functional enrichment analyses. The most substantially enriched biological processes were cell differentiation, cellular developmental process, and nervous system development, according to functional annotation of these genes. Transcription regulator activity, DNA-binding transcription factor activity, and RNA polymerase II-specific and DNA-binding transcription factor activity were the most notably enriched molecular functions, and synapse,

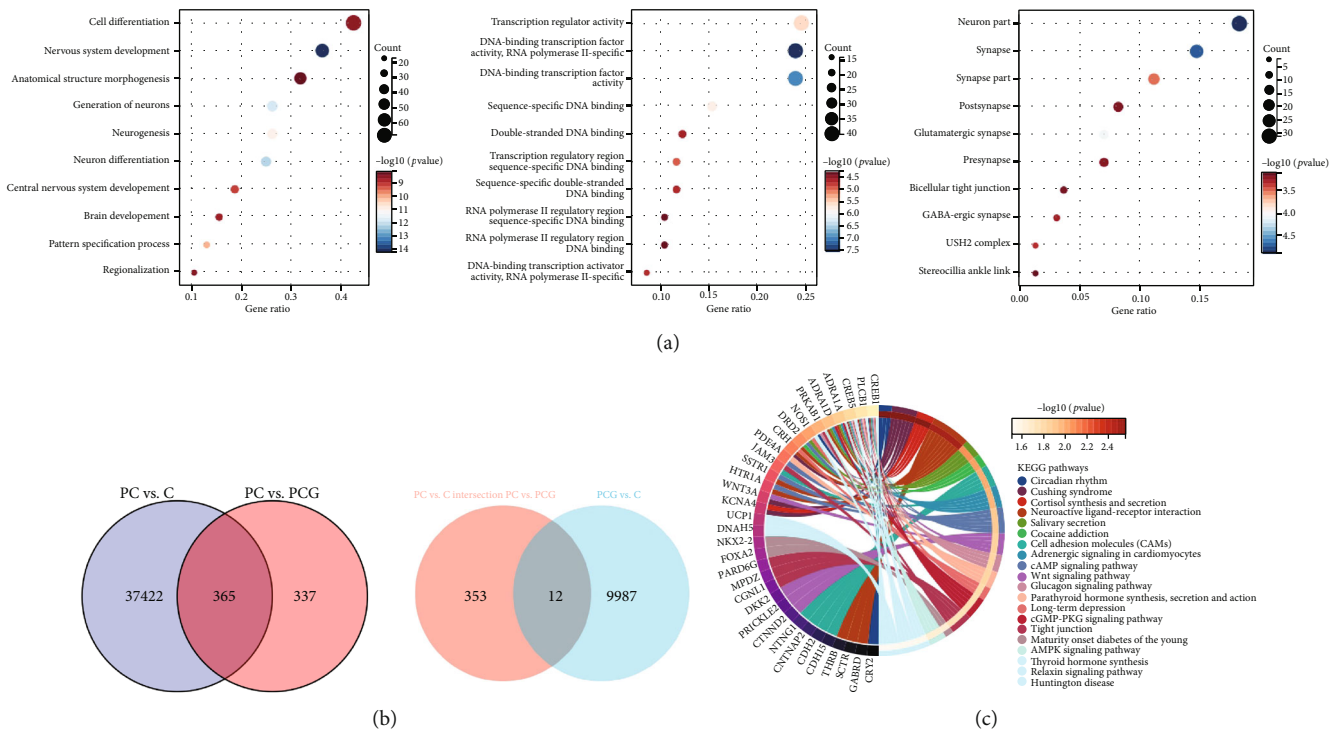

Figure 5: Analysis of differentially methylated locations (DMPs) for functional enrichment. (a) DMPs have enhanced Gene Ontology (GO) items in the categories of biological process (BP), molecular function (MF), and cell component (CC). Each category's top ten items were shown. (b) The intersection of differentially expressed loci is shown using a Venn diagram. (c) Kyoto Encyclopedia of Genes and Genomes (KEGG) pathway of DMPs. Cellular processes, environmental information processing, genetic information processing, human diseases, metabolism, and organismal systems are all subdivided into this section. The findings of the enrichment analysis for KEGG are shown in Figure 5(c). The top twenty items from each category were shown.

neuron projection, and neuronal parts were the most noticeably enriched cellular components (Figure 5(a)).

KEGG signaling network analysis was utilized to further analyze the signaling pathways associated with the differentially methylated genes between the PC and control groups. Numerous enriched KEGG pathways, including the cAMP signaling system, the Wnt signaling pathway, the cGMP-PKG signaling pathway, the AMPK signaling pathway, and adrenergic signaling in cardiomyocytes, have been implicated in postmenopausal women's coronary heart disease (Figure 5(c)).

3.5. PPI Network and Functional Epigenetic Modules. STRING identified 198 nodes and 174 edges in the PPI network. Cytoscape 3.8.0 was used to display the PPI network (Figure 6(a)), and the CytoHubba tool inside Cytoscape was used to pick the PPI network's hub node genes (Figure 6(b)). Four of the top ten hub genes identified in CytoHubba using six ranking methodologies were overlap hub genes (Figure 6(c)), including FOXA2 (forkhead box A2), CREB1 (CAMP responsive element binding protein 1), CNTNAP2 (contactin-associated protein 2), and PTPRD (protein tyrosine phosphatase receptor type D). Hypermethylation of FOXA2 and PTPRD was observed, but hypomethylation of CREB1 and CNTNAP2 was seen.

Using the FEM *R* program (http://www.bioconductor.org/packages/3.1/bioc/vignettes/FEM/inst/doc/IntroDoFEM.pdf), the FEM technique was used to further analyze the hub genes (also known as hotspots) of the methylated sites. Nine distinct functional modules were discovered in the PC versus PCG groups, and fifteen distinct functional modules were identified in the PC vs. C groups. The comparisons between the two groups included both FOXA2 and FBN2, which were notable as both of them were the module's seed genes, indicating that these genes played a critical role in the network. The network for the FOXA2 and FBN2 genes is shown in Figure 7. In comparison to control groups, FOXA2 was hypermethylated in the PC group (Figure 7(a)). Numerous members of the FOXA2 module interact with one another, including FOXA1, ABCC8, and FOXF1, all of which were hypermethylated in the PC group (Figure 7(c)). FBN2 was significantly more methylated in the PC group than in the control group (Figure 7(b)). Many members of the FBN2 module worked together, including MEGF6 and LTF, both of which were hypermethylated in the PC group (Figure 7(d)).

3.6. FOXA2 Hypermethylation Was a Possible Biomarker for Postmenopausal Coronary Heart Disease. Following confirmation by CytoHubba and FEM analysis that FOXA2 was a seed gene, MS-PCR was utilized to validate the gene's significant methylation sites. In order to develop primers, we focused on the chr20:22566821-22567055 coordinates of the methylation island in the UCSC library, where the cg16963144 site had the highest variation in chromosomal

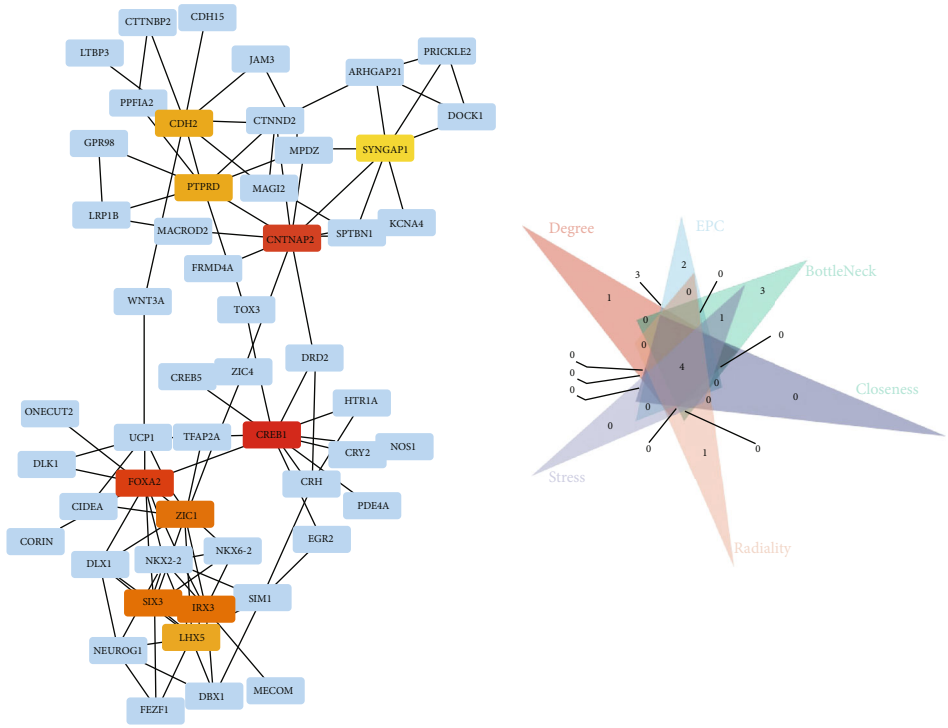

(a) (b)

The hub gene for hyper/hypo differential expressed genes ranked in CytoHubba						
Catelogy	Rank methods in cytoHubba					
	Degree	EPC	BottleNeck	Closeness	Radiality	Stress
Gene symbol top 10	CREB1	IRX3	CNTNAP2	CREB1	CNTNAP2	CNTNAP2
	FOXA2	FOXA2	CREB1	CNTNAP2	DRD2	ARHGAP21
	CNTNAP2	SIX3	DRD2	PTPRD	CREB1	RPRD1B
	IRX3	NKX2-2	FOXA2	FOXA2	PTPRD	SLC17A7
	SIX3	LHX5	PTPRD	DRD2	CRH	CREB1
	ZIC1	ZIC1	SLC17A7	CRH	TOX3	BNC2
	CDH2	CREB1	MPDZ	IRX3	FOXA2	DRD2
	PTPRD	SIM1	PPFIA2	MPDZ	MPDZ	SV2B
	LHX5	CNTNAP2	SYNGAP1	ZIC1	SLC17A7	CELF4
	SYNGAP1	PTPRD	IRX3	CDH2	CTNND2	CTNND2

(c)

Figure 6: (a) Protein-protein interaction network of differentially methylated genes (DMGs). Disconnected nodes were hidden in the network. (b) This is a Venn diagram that shows where six of the best methods in CytoHubba overlapped hub genes. (c) CytoHubba-ranked hub genes for DMGs.

coordinates. Primers were created in MethPrimer 2.0 software for the cg16963144 location using the base sequence identified in the NCBI database (Figure 8(a)). Primers for the methylation internal reference gene, ACTB, were also created (Figure 8(b)). According to Figure 9, the PC group expressed more FOXA2 methylation products than the other two groups. Subsequent semiquantitative analysis revealed that FOXA2 methylation was considerably greater in the PC group than in the PCG group ($p = 0.0380$), and it was significantly lower in the C group ($p = 0.0045$).

4. Discussion

Epigenetic changes may be crucial in regulating the gene expression in molecular pathways and cellular processes associated with the pathophysiology of postmenopausal coronary heart disease [25]. DNA was taken from four of the postmenopausal women who have coronary artery disease and eight healthy women were controls (four postmenopausal women with CHD and four young healthy women). The DNA was then sent to a lab for analysis. To detect genome-wide methylation, the Illumina Infinium MethylationEPIC BeadChip was employed. The Illumina methylation chip (the Illumina Infinium MethylationEPIC BeadChip, 850 K methylation chip) is a next-generation DNA methylation chip built on the foundation of the original 450 K methylation chip. The chip had 91% of the original 450 K methylation chip and 413745 extra sites. It completely encompasses the promoter, coding region, CpG island, and enhancer regions of a gene [30].

In this study, we found that DNA methylation was involved in the process of CHD in postmenopausal women.

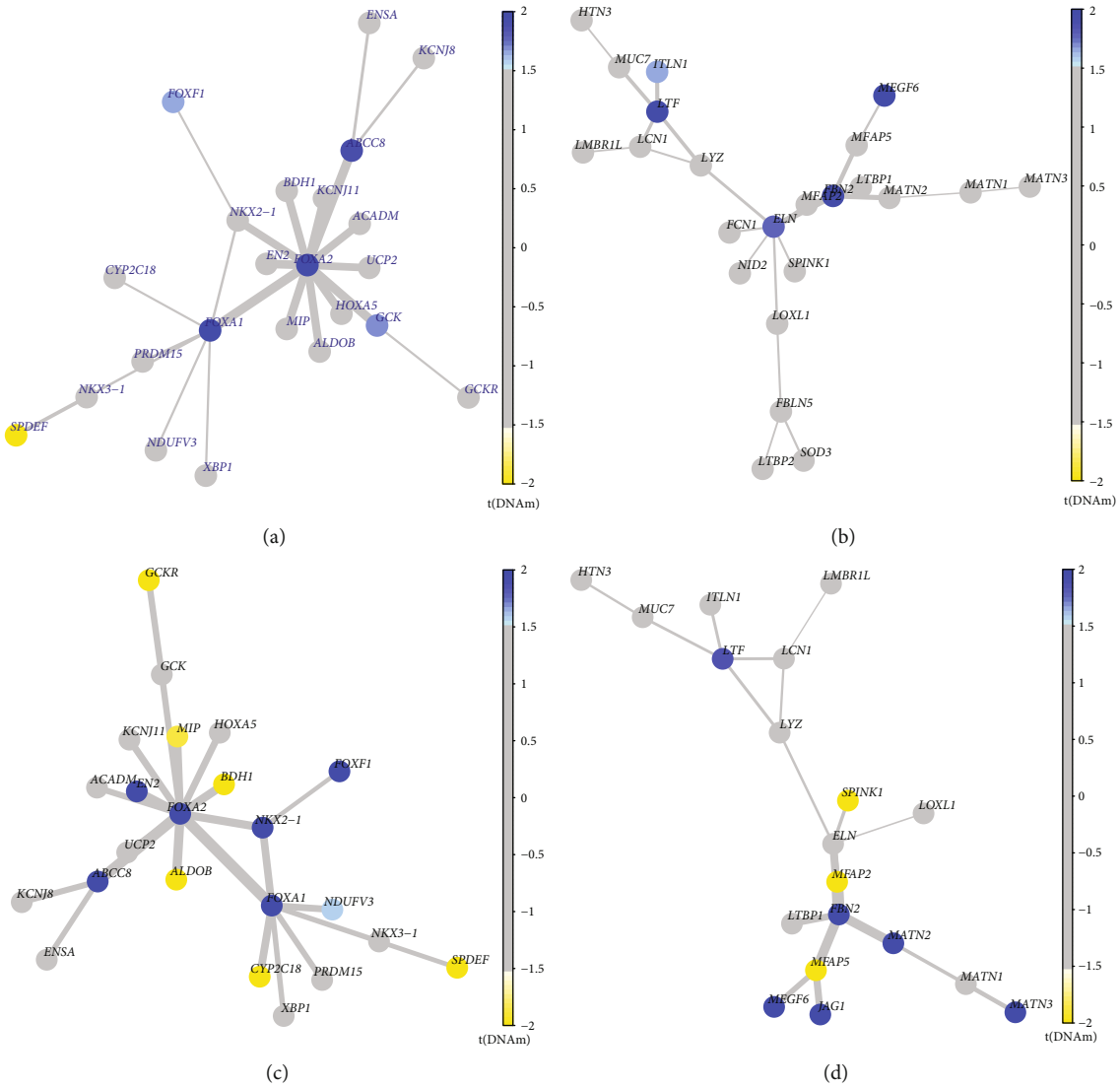

Figure 7: The core gene interaction network diagram was analyzed using a functional epigenetic module (FEM). In the FEM study, FOXA2 and FBN2 were shown to be the module's seed genes. (a) and (b) are the key gene results of PC vs PCG, while (c) and (d) represent the key gene results of PC vs. C. The protein–protein interaction (PPI) network defines the connection between each node in the diagram. The T value of differential methylation determines the node's color. It will be yellow to white if T is less than 1.5 and light blue to blue with gray in the center if it is larger than 1.5.

The intersection of different groups was obtained through comparison. Finally, 353 different loci and 234 genes were selected for subsequent enrichment analysis and screening of key genes. We used GO and KEGG pathway analyses to infer the roles of differentially methylated genes. The functional annotation of these genes revealed that the most highly enriched GO terms were cell differentiation, cellular developmental processes, and nervous system development. It had been found that macrophages, vascular smooth muscle cells, and endothelial cells were engaged in all stages of atherosclerotic lesion formation [31]. Initially, we wondered why numerous gene methylation changes regulating the nervous system were found in PBMCs in postmenopausal women with coronary heart disease. Until recently, as reported in *Nature*, the nervous system regulated the progression of atherosclerosis through local remodeling of peripheral nerve fibers [32]. Moreover, genes enriched in this pathway were related to an increased risk of coronary heart disease, such as NRG1 [33], EGR2 [34], and NOS1 [35]. However, prior studies did not take methylation modification into account, and our analysis demonstrated that the methylation levels of key genes involved in these critical regulatory processes, such as PHOX2A, HOXD10, CREB1, and MYPN, were significantly increased. As a direct outcome of our findings, we hypothesized that changes in methylation levels may influence the differential expression of functional genes in women with coronary artery disease. To our knowledge, this is the first study to probe into the methylation profile of PBMCs from women who have coronary artery disease after menopause.

According to the KEGG database, the cAMP signaling route, the Wnt signaling system, the cGMP-PKG signaling

```
  1 CCGCCGAGTGAGCGCCAGGGCGGGATTCTCCCACAAATTCAAGGTCTGTATCTCCGCGGAAGCCGTGCCTATCGGTCCCCCGAGTGCTGAAGGCTCCCAC 100
    :++:++||||||++::||||++||||||:|:::|:||||||:||||||:||||||:|:++++||||:++||::|||++||::::++||||:||||||:|:::|+
  1 TCGTCGAGTGAGCGTTAGGGCGGGATTTTTTTATAAATTTAAGGTTTGTATTTTCGCGGAAGTCGTGTTTATCGGTTTTTCGAGTGTTGAAGGTTTTTAC 100
101 GAGGGGCAGGCCAGCCCGGTGCGCCAGGGAAGGAGCTTGATGGTGTGTACGGCTACGTAGTGAACGTGGAGGTGTGCGCAGCGGAGTCAGAGGGGCTAGA 200
    +|||||:|||::||::++|||++::||||||||||:||||||||||||||++|:||++|||||||++||||||||||++:||++||||:||||||||:||||
101 GAGGGGTAGGTTAGTTCGGTGCGTTAGGGAAGGAGTTTGATGGTGTGTACGGTTACGTAGTGAACGTGGAGGTGTGCGTAGCGGAGTTAGAGGGGTTAGA 200
MF1>>>>>>>>>>>>>>>>>>>>>                                                                <<<<<<<<<<<<<<<<<<<<
201 TCCCCAGCATTTCCCACGGGGTCCCACCTAGCGCG 235
    |::::||:||||:::|++||||:::|::|||++++
201 TTTTTAGTATTTTTTACGGGGTTTTATTTAGCGCG 235
    <<<<MR1
```

(a)

CCGCCGAGTGAGCGCCAGGGCGGGATTCTCCCACAAATTCAAGGTCTGTATCTCCGCGGAAGCCGTGCCT

ATCGGTCCCCCGAGTGCTGAAGGCTCCCACGAGGGGCAGGCCAGCCCGGTGCGCCAGGGAAGGAGCTTGA

TGGTGTGTACGGCTACGTAGTGAACGTGGAGGTGTGCGCAGCGGAGTCAGAGGGGCTAGATCCCCAGCAT

TTCCCACGGGGTCCCACCTAGCGCG

(b)

Figure 8: Chr20: 22566821-22567055, corresponding sequence of methylation islands. The above figures represent the gene sequence of CHR20: 22566821-22567055. (a) represents the process of designing methylation primers after bisulfite treatment. In (b), the red font represents the flanking sequence of the 850 K methylation chip detection site (upstream and downstream 50 bp), and the yellow background represents the CG16963144 detection site. The green background shows the CG sites that are used to detect MSPs. The orange arrow shows the primer binding site.

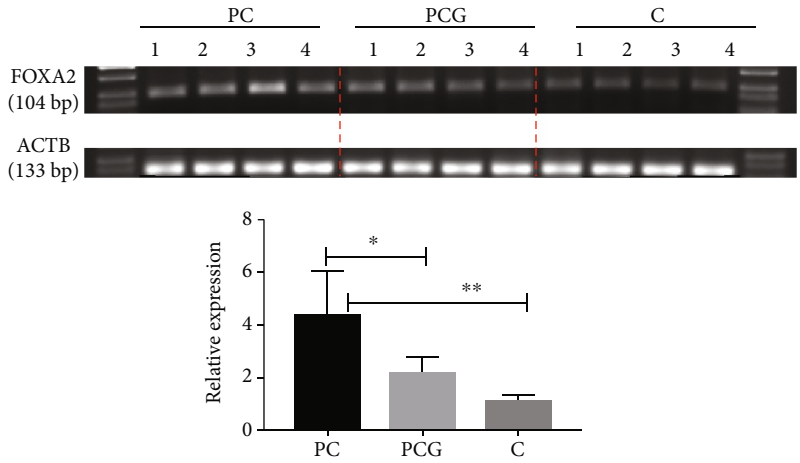

Figure 9: The FOXA2 promoter gene cg16963144 locus was expressed in three groups of patients.

pathway, and the AMPK signaling pathway all contribute significantly to the risk of coronary heart disease in postmenopausal women. The cAMP [36] and cGMP-PKG [37] signaling pathways have been implicated in the pathophysiology of coronary atherosclerosis. In the cardiovascular system, an activated AMPK signaling pathway had a protective effect [38]. The pathological process of atherosclerosis includes lipid buildup, endothelial cell failure, inflammatory responses, monocyte recruitment, and aggregation, when monocytes become tissue-resident macrophages and foam cells when they adhere to modified low-density lipoprotein. Under the intima, lipids accumulate, smooth muscle cells invade and multiply, and extracellular matrix accumulates. As a consequence of the restriction of the luminal lumen and reduced blood flow to the myocardium, chest pain, angina, and even myocardial infarction would occur. The Wnt pathway is involved in all phases of this process, from endothelial dysfunction to lipid deposition, and from early inflammation to the development of plaques [39].

CHD is the main cause of death globally, owing to the increased prevalence of CVD in postmenopausal women [40], and early prevention may help minimize morbidity and mortality. Thus, we should develop novel biomarkers to aid in the prognosis and treatment of coronary heart disease. In addition, important DNA is often methylated early in the disease, and looking for specific gene methylation that is linked to the disease has been used as a new diagnostic method. The methylation of the SEPT9 gene was the first

biological marker recognized by the FDA for detecting DNA methylation in colorectal cancer screening [41]. DNA methylation detection, which is similar to it, may also be detected in the blood and may be useful indicators for CHD in postmenopausal women. As a result, we employed FEM and the CytoHubba software to find the hub genes in the PPI networks. Finally, FOXA2 was chosen as the seed gene, and its validity was confirmed using MS-PCR. FOXA2, also known as forkhead box A2, is a protein that is encoded by the FOXA2 gene and is found in humans. Transcription factor is implicated in embryonic development, the modulation of gene expression in differentiated tissues, and the establishment of tissue-specific gene expression, among other functions. Glucose homeostasis and fat metabolism are also regulated by it [42].At the time the study was completed, no link had been found between FOXA2 and coronary atherosclerosis. This is the first time that FOXA2 gene methylation has been found in postmenopausal women with coronary heart disease.

Furthermore, FOXA2, CREB1, CNTNAP2, and PTPRD are the four of the top 10 high hub nodes in the PPI network following gene overlap.FOXA2 serves as a validation gene as described above. Among these central genes, CREB1, also known as cyclic AMP (cAMP) responsive element binding protein 1, is a human protein encoded by the CREB1 gene. Even though postmenopausal people with CHD had hypomethylation of the CERB1 gene, it was found in the gene's body, and hypomethylation of the gene's body has been linked to transcriptional suppression [43]. CREB1 is involved in the regulation of apoptosis, and its overexpression is associated with atherosclerosis. The absence of the CREB protein in VSMCs, which makes them more susceptible to activation and death, is a common pathological response to vascular injury and may contribute to plaque development [44]; CNTNAP2 plays a key role in ischemic heart disease [45] and circulating lipid levels [46]; PTPRD has an effect on the onset and progression of CHD via acting on the glycine metabolism [47]. Additionally, FEM analysis showed a critical gene, FBN2, which was methylated in the promoter area in the case group, and displayed a decreased expression. In the absence of FBN2, p38 MAPK signaling is activated in an abnormally high manner, which in turn leads to an increase in MMP activity that disrupts elastic fiber production and degrades fibronectin [48]. In humans, fibronectin stimulates the creation of the protective fibrous cap, which prevents the rupture of plaques and vascular occlusion [49]. As a result, we hypothesized that these hub genes may be implicated in the pathological process in postmenopausal women with coronary artery disease, but more functional investigations are required to confirm this.

Our study still had certain limitations that should be addressed in future research. For instance, the study used a tiny number of participants because only 12 people were included in the study. The results must be replicated in a larger sample size for confirmation. We also need to perform MS-PCR or pyrosequencing for other genes that we have identified as methylation hotspots. It also lacked experimental evidence to support that aberrant methylation affected gene expression and function in postmenopausal women with CHD. Therefore, more molecular investigations are needed to confirm our findings.

In conclusion, we discovered that interactions between differentially methylated genes with distinct roles and signaling pathways were associated with the pathophysiology of postmenopausal women with coronary heart disease. FOXA2, CREB1, CNTNAP2, PTPRD, and FBN2 were the hub genes. This work improved conceptual and biological understanding on the pathophysiology of postmenopausal women with CHD. The identified genes and pathways in postmenopausal women with CHD still required more molecular-level studies both vitro and in vivo.

Data Availability

The datasets used and/or analyzed during the current study are available from the corresponding author on reasonable request.

Conflicts of Interest

The authors declare that they have no conflicts of interest.

Acknowledgments

This study was funded by the Shanghai Pudong New District Zhoupu Hospital Foundation for Talent Introduction Program (Grant/Award Number: ZP-XK-2021B-1), 2021 Key Natural Science Programs of Shanghai Health Medical College (Grant/Award Number: SSF-21-17-01), and the Leading Personnel Training Program of Pudong New District Health and Family Planning Commission of Shanghai, China (Grant/Award Number: PWRI2021-08). Song Xiang is the host of the aforementioned projects.

Supplementary Materials

Table S1: primer sequences. *(Supplementary Materials)*

References

[1] Y. B. Somani, J. A. Pawelczyk, M. J. de Souza, P. M. Kris-Etherton, and D. N. Proctor, "Aging women and their endothelium: probing the relative role of estrogen on vasodilator function," *American Journal of Physiology. Heart and Circulatory Physiology*, vol. 317, no. 2, pp. H395–H404, 2019.

[2] D. Lin, L. Wang, S. Yan, Q. Zhang, J. H. Zhang, and A. Shao, "The Role of Oxidative Stress in Common Risk Factors and Mechanisms of Cardio- Cerebrovascular Ischemia and Depression," *Oxidative Medicine and Cellular Longevity*, vol. 2019, Article ID 2491927, 13 pages, 2019.

[3] T. Gordon, W. B. Kannel, M. C. Hjortland, and P. M. Mcnamara, "Menopause and coronary heart disease. The Framingham Study," *Annals of Internal Medicine*, vol. 89, no. 2, pp. 157–161, 1978.

[4] E. J. Benjamin, M. J. Blaha, S. E. Chiuve et al., "Heart Disease and Stroke Statistics-2017 Update: a report from the American Heart Association," *Circulation*, vol. 135, no. 10, pp. e146–e603, 2017.

[5] L. Young and L. Cho, "Unique cardiovascular risk factors in women," *Heart*, vol. 105, no. 21, pp. 1656–1660, 2019.

[6] J. R. Bell, G. B. Bernasochi, U. Varma, A. J. A. Raaijmakers, and L. M. D. Delbridge, "Sex and sex hormones in cardiac stress–mechanistic insights," *The Journal of Steroid Biochemistry and Molecular Biology*, vol. 137, pp. 124–135, 2013.

[7] M. P. Czubryt, L. Espira, L. Lamoureux, and B. Abrenica, "The role of sex in cardiac function and disease," *Canadian Journal of Physiology and Pharmacology*, vol. 84, no. 1, pp. 93–109, 2006.

[8] R. C. Christian, S. Harrington, W. D. Edwards, A. L. Oberg, and L. A. Fitzpatrick, "Estrogen status correlates with the calcium content of coronary atherosclerotic plaques in women," *The Journal of Clinical Endocrinology and Metabolism*, vol. 87, no. 3, pp. 1062–1067, 2002.

[9] D. Grady, D. Herrington, V. Bittner et al., "Cardiovascular disease outcomes during 6.8 years of hormone therapy: Heart and Estrogen/progestin Replacement Study follow-up (HERS II)," *JAMA*, vol. 288, no. 1, pp. 49–57, 2002.

[10] J. E. Rossouw, G. L. Anderson, R. L. Prentice et al., "Risks and benefits of estrogen plus progestin in healthy postmenopausal women: principal results from the Women's Health Initiative randomized controlled trial," *JAMA*, vol. 288, no. 3, pp. 321–333, 2002.

[11] D. Yang, J. Li, Z. Yuan, and X. Liu, "Effect of hormone replacement therapy on cardiovascular outcomes: a meta-analysis of randomized controlled trials," *PLoS One*, vol. 8, no. 5, article e62329, 2013.

[12] P. G. Joseph, G. Pare, and S. S. Anand, "Exploring gene-environment relationships in cardiovascular disease," *The Canadian Journal of Cardiology*, vol. 29, no. 1, pp. 37–45, 2013.

[13] L. D. Moore, T. Le, and G. Fan, "DNA methylation and its basic function," *Neuropsychopharmacology*, vol. 38, no. 1, pp. 23–38, 2013.

[14] T. F. Whayne, "Epigenetics in the development, modification, and prevention of cardiovascular disease," *Molecular Biology Reports*, vol. 42, no. 4, pp. 765–776, 2015.

[15] Y. Li, H. Zheng, Q. Wang et al., "Genome-wide analyses reveal a role of polycomb in promoting hypomethylation of DNA methylation valleys," *Genome Biology*, vol. 19, no. 1, p. 18, 2018.

[16] S. Xu, J. Pelisek, and Z. G. Jin, "Atherosclerosis is an epigenetic disease," *Trends in Endocrinology and Metabolism*, vol. 29, no. 11, pp. 739–742, 2018.

[17] V. V. Miroshnikova, A. A. Panteleeva, I. A. Pobozheva et al., "ABCA1 and ABCG1 DNA methylation in epicardial adipose tissue of patients with coronary artery disease," *BMC Cardiovascular Disorders*, vol. 21, no. 1, p. 566, 2021.

[18] F. An, C. Liu, X. Wang et al., "Effect of ABCA1 promoter methylation on premature coronary artery disease and its relationship with inflammation," *BMC Cardiovascular Disorders*, vol. 21, no. 1, p. 78, 2021.

[19] T. Infante, M. Franzese, A. Ruocco et al., "ABCA1, TCF7, NFATC1, PRKCZ, and PDGFA DNA methylation as potential epigenetic-sensitive targets in acute coronary syndrome via network analysis," *Epigenetics*, vol. 42, Supplement_1, pp. 1–17, 2021.

[20] N. Shyamala, K. K. Gundapaneni, R. K. Galimudi et al., "PCSK9 genetic (rs11591147) and epigenetic (DNA methylation) modifications associated with PCSK9 expression and serum proteins in CAD patients," *The Journal of Gene Medicine*, vol. 23, no. 8, article e3346, 2021.

[21] H. P. Zuo, Y. Y. Guo, L. Che, and X. Z. Wu, "Hypomethylation of interleukin-6 promoter is associated with the risk of coronary heart disease," *Arquivos Brasileiros de Cardiologia*, vol. 107, no. 2, pp. 131–136, 2016.

[22] R. Ross, "Atherosclerosis — an inflammatory disease," *The New England Journal of Medicine*, vol. 340, no. 2, pp. 115–126, 1999.

[23] J. Li, X. Zhang, M. Yang et al., "DNA methylome profiling reveals epigenetic regulation of lipoprotein-associated phospholipase A2 in human vulnerable atherosclerotic plaque," *Clinical Epigenetics*, vol. 13, no. 1, p. 161, 2021.

[24] W. S. Post, P. J. Goldschmidt-Clermont, C. C. Wilhide et al., "Methylation of the estrogen receptor gene is associated with aging and atherosclerosis in the cardiovascular system," *Cardiovascular Research*, vol. 43, no. 4, pp. 985–991, 1999.

[25] R. B. Ramos, V. Fabris, S. B. Lecke, M. A. Maturana, and P. M. Spritzer, "Association between global leukocyte DNA methylation and cardiovascular risk in postmenopausal women," *BMC Medical Genetics*, vol. 17, no. 1, p. 71, 2016.

[26] S. Jiangping, Z. Zhe, W. Wei et al., "Assessment of coronary artery stenosis by coronary angiography," *Circulation. Cardiovascular Interventions*, vol. 6, no. 3, pp. 262–268, 2013.

[27] X. Wang, W. Li, F. Song et al., "Carotid atherosclerosis detected by ultrasonography: a national cross-sectional study," *Journal of the American Heart Association*, vol. 7, no. 8, 2018.

[28] I. Smith, J. Robertson, L. Kilburn et al., "Long-term outcome and prognostic value of Ki67 after perioperative endocrine therapy in postmenopausal women with hormone-sensitive early breast cancer (POETIC): an open-label, multicentre, parallel-group, randomised, phase 3 trial," *The Lancet Oncology*, vol. 21, no. 11, pp. 1443–1454, 2020.

[29] J. R. Lewis, S. Radavelli-Bagatini, L. Rejnmark et al., "The effects of calcium supplementation on verified coronary heart disease hospitalization and death in postmenopausal women: a collaborative meta- analysis of randomized controlled trials," *Journal of Bone and Mineral Research*, vol. 30, no. 1, pp. 165–175, 2015.

[30] D. L. McCartney, R. M. Walker, S. W. Morris, A. M. McIntosh, D. J. Porteous, and K. L. Evans, "Identification of polymorphic and off-target probe binding sites on the Illumina Infinium MethylationEPIC BeadChip," *Genom Data*, vol. 9, pp. 22–24, 2016.

[31] A. J. Kattoor, A. Goel, and J. L. Mehta, "LOX-1: regulation, signaling and its role in atherosclerosis," *Antioxidants (Basel)*, vol. 8, no. 7, p. 218, 2019.

[32] S. K. Mohanta, L. Peng, Y. Li et al., "Neuroimmune cardiovascular interfaces control atherosclerosis," *Nature*, vol. 605, no. 7908, pp. 152–159, 2022.

[33] A. Geissler, S. Ryzhov, and D. B. Sawyer, "Neuregulins: protective and reparative growth factors in multiple forms of cardiovascular disease," *Clinical Science (London, England)*, vol. 134, no. 19, pp. 2623–2643, 2020.

[34] Y. Sun, Y. Gao, J. Sun et al., "Expression profile analysis based on DNA microarray for patients undergoing off-pump coronary artery bypass surgery," *Experimental and Therapeutic Medicine*, vol. 11, no. 3, pp. 864–872, 2016.

[35] B. Zhang, K. Zeng, R. Li et al., "Construction of the gene expression subgroups of patients with coronary artery disease

through bioinformatics approach," *Mathematical Biosciences and Engineering*, vol. 18, no. 6, pp. 8622–8640, 2021.

[36] J. Gong, C. Qiu, D. Huang, Y. Zhang, S. Yu, and C. Zeng, "Integrative functional analysis of super enhancer SNPs for coronary artery disease," *Journal of Human Genetics*, vol. 63, no. 5, pp. 627–638, 2018.

[37] X. Wu, X. Han, L. Li et al., "iTRAQ-based quantitative proteomics and target-fishing strategies reveal molecular signatures on vasodilation of compound Danshen dripping pills," *Chemico-Biological Interactions*, vol. 316, article 108923, 2020.

[38] Y. Meng, P. Ding, H. Wang et al., "Ca^{2+}/calmodulin-dependent protein kinase II inhibition reduces myocardial fatty acid uptake and oxidation after myocardial infarction," *Biochimica et Biophysica Acta - Molecular and Cell Biology of Lipids*, vol. 1867, no. 6, article 159120, 2022.

[39] Y. Liu, A. Neogi, and A. Mani, "The role of Wnt signalling in development of coronary artery disease and its risk factors," *Open Biology*, vol. 10, no. 10, article 200128, 2020.

[40] S. R. El Khoudary, B. Aggarwal, T. M. Beckie et al., "Menopause transition and cardiovascular disease risk: implications for timing of early prevention: a scientific statement from the American Heart Association," *Circulation*, vol. 142, no. 25, pp. e506–e532, 2020.

[41] L. Song, J. Jia, X. Peng, W. Xiao, and Y. Li, "The performance of the SEPT9 gene methylation assay and a comparison with other CRC screening tests: a meta-analysis," *Scientific Reports*, vol. 7, no. 1, p. 3032, 2017.

[42] A. Moreau, M. J. Vilarem, P. Maurel, and J. M. Pascussi, "Xenoreceptors CAR and PXR activation and consequences on lipid metabolism, glucose homeostasis, and inflammatory response," *Molecular Pharmaceutics*, vol. 5, no. 1, pp. 35–41, 2008.

[43] S. Costantino and F. Paneni, "The epigenome in atherosclerosis," *Handbook of Experimental Pharmacology*, vol. 270, pp. 511–535, 2022.

[44] I. E. Schauer, L. A. Knaub, M. Lloyd et al., "CREB downregulation in vascular disease: a common response to cardiovascular risk," *Arteriosclerosis, Thrombosis, and Vascular Biology*, vol. 30, no. 4, pp. 733–741, 2010.

[45] O. A. Makeeva, A. A. Sleptsov, E. V. Kulish et al., "Genomic study of cardiovascular continuum comorbidity," *Acta Naturae*, vol. 7, no. 3, pp. 89–99, 2015.

[46] T. O. Kilpeläinen, A. R. Bentley, R. Noordam et al., "Multiancestry study of blood lipid levels identifies four loci interacting with physical activity," *Nature Communications*, vol. 10, no. 1, p. 376, 2019.

[47] Q. Jia, Y. Han, P. Huang et al., "Genetic determinants of circulating glycine levels and risk of coronary artery disease," *Journal of the American Heart Association*, vol. 8, no. 10, article e011922, 2019.

[48] W. Yin, H. T. Kim, S. P. Wang et al., "Fibrillin-2 is a key mediator of smooth muscle extracellular matrix homeostasis during mouse tracheal tubulogenesis," *The European Respiratory Journal*, vol. 53, no. 3, p. 1800840, 2019.

[49] I. Rohwedder, E. Montanez, K. Beckmann et al., "Plasma fibronectin deficiency impedes atherosclerosis progression and fibrous cap formation," *EMBO Molecular Medicine*, vol. 4, no. 7, pp. 564–576, 2012.

Hindawi
Mediators of Inflammation
Volume 2022, Article ID 9661940, 10 pages
https://doi.org/10.1155/2022/9661940

Research Article

The mir-21 Inhibition Enhanced HUVEC Cellular Viability during Hypoxia-Reoxygenation Injury by Regulating PDCD4

Md Sayed Ali Sheikh

Department of Internal Medicine, College of Medicine, Jouf University, Sakaka, Saudi Arabia

Correspondence should be addressed to Md Sayed Ali Sheikh; drsheikh07@hotmail.com

Received 11 March 2022; Accepted 14 June 2022; Published 30 June 2022

Academic Editor: Daniela Caccamo

The purpose of this study was to explore the clinical value of altered plasma mir-21 expression level as a biomarker for the severity of coronary artery disease (CAD) and its molecular impact on HUVEC cellular injuries. Angiographically validated 56 patients with single-vessel CAD disease, 92 patients with double-vessel CAD, 139 complex coronary artery stenosis patients, and 56 healthy individuals ($n = 343$) were enrolled in this study. The expressions of plasma mir-21 were evidently and progressively higher while PDCD4 levels were significantly and steadily lower in single-, dual-, and multivessel occluded CAD patients than in healthy participants ($P < 0.001$). The relative expressions of mir-21 in hypoxia-reoxygenation- (HR-) exposed HUVECs were markedly upregulated, but PDCD4 concentrations were obviously downregulated as compared with normal control cells ($P < 0.001$). Moreover, altered circulatory mir-21 expression levels were able to significantly differentiate single- (AUC 0.893), double- (AUC 0.914), and multivessel stenosis CAD (AUC 0.933) patients from healthy subjects. Besides, the plasma mir-21 expressions in elderly (66-85 years) groups were remarkably higher than those in younger aged (25-45 years) subjects. Caspase-3 and ROS expression levels were remarkably elevated, but cellular viability noticeably declined in HR-induced HUVECs than in normoxic cells ($P < 0.001$). In contrast, mir-21 inhibition markedly reduced caspase-3 activity and ROS concentrations while significantly ameliorating HUVEC cellular viability in HR conditions. PDCD4 expressions in HR-exposed HUVECs were prominently decreased whereas mir-21 inhibition significantly enhanced PDCD4 levels ($P < 0.001$). Upregulated plasma mir-21 can be a valuable clinical biomarker for the detection of the severity of coronary artery stenosis patients. Elevated circulatory mir-21 concentrations have a positive correlation with aging. Inhibitory mir-21 evidently increased HUVEC cellular viability through upregulation of targeting PDCD4 and recommended a newer possible therapeutic molecule for the management of CAD patients.

1. Introduction

Atherosclerotic coronary artery disease (CAD) is the principal reason for unexpected death among adults in all ethnic groups worldwide. Due to the high incidence of unhealthy lifestyle, often poorly treated major atherosclerotic risk factors, and substantial impact of genes, by the next 10 years, approximately 12% CAD prevalence rates will be increased [1]. Early diagnosis with advanced management and also adequate control of CAD risk factors will greatly decline the CAD-associated death incidence and significantly reduced hospital admission rates and economic burden. Currently, invasive coronary angiogram (CAG) and percutaneous coronary intervention (PCI) are widely reliable clinically used techniques for the evaluation and management of ischemic coronary heart disease, respectively. However, invasive CAG has some surgical and technical complications, and it is not suitable for all the patients, especially older chronic kidney disease patients. Moreover, PCI management is also not suitable for multivessel occluded CAD patients, even in complicated left main artery (LM) CAD lesion subjects. Therefore, noninva-

sive universal early diagnostic biomarkers and newer therapeutic drugs are clinically demanded by cardiologists.

MicroRNAs (miRNAs, mirs) are highly conserved, endogenous, single-stranded, small noncoding RNAs of about 18-24 nucleotides in length that regulate gene expression via either inhibiting the translation of messenger RNAs(mRNAs) or degradation of mRNAs. In recent years, several research studies have confirmed that various miRNAs are directly regulated in the entire cardiovascular physiology and also exhibit an essential role in the many cardiovascular disease processes including CAD. Coronary artery disease usually occurred due to chronic lipid-induced atherosclerotic inflammation in the arterial wall, and several atherosclerotic-related miRNAs (mir-342-5p, mir-217, mir-126, mir-155, and mir-92a-3p) are critically involved for the formation and subsequent rupture of the coronary atherosclerotic plaque [2–4].

It has been reported that dysregulated mir-21 was essentially implicated in endothelial dysfunction, progression of early to advance atherosclerotic plaque, formation of critical coronary stenosis, and thrombus leading to acute coronary syndrome through activation of different inflammatory cells, cytokines, and signaling pathways including macrophages, tumor necrosis factor-α (TNF-α), interleukin- (IL-) 17A, IL-1β, IL-6, phosphatase and tensin homolog (PTEN), PI3K/Akt MAPK, vascular endothelial growth factor, and TLR4/NF-κB [5–9].

Programmed cell death 4 (PDCD4) protein was initially discovered as a novel upregulated gene during apoptosis, and it acts as a regulator of gene expression by the influencing translation and transcription process. It has been recently demonstrated that PDCD4 is widely expressed in myocardial cells, vascular smooth muscle cells, and endothelial cells, and PDCD4 directly regulated various inflammatory pathways including adipose inflammation, endothelial dysfunction, foam cell formation, and atherosclerosis through altering differing cytokine expressions such as interleukin-10 (IL-10), IL-17, IL-6, IL-1β, IL-8, nuclear factor-kappa B (NF-κB), tumor necrosis factor-alpha (TNF-α), and NOTCH1. Moreover, emerging evidence has shown that PDCD4 is directly involved in coronary atherosclerotic plaque formation, and its expression levels were significantly attenuated in atherosclerotic coronary artery disease [5, 10–12].

Moreover, our previous study and also some other research studies have demonstrated that circulatory mir-21 expression patterns were evidently altered in significant or insignificant coronary artery stenosis, unstable angina, and acute coronary syndrome with a strong relationship with aging [7, 8, 13, 14]. It has been explored that hypoxia-reoxygenation- (HR-) induced human umbilical vein endothelial cell (HUVEC) damage is noticeably prevented by inhibition of miR-21 expression through regulating SMAD7. Shao et al. revealed that inhibitor mir-21 prominently reduced the atherosclerotic lesion area by the RAGE/NADPH signaling pathway via regulating ADAM10 expression in the mouse model, suggesting a novel therapeutic target for the treatment of atherosclerotic disease. Another study showed that inhibitory mir-21 protects cardiomyocyte apoptosis and attenuated the infarct size in both cellular and mouse models of AMI by regulating PDCD4 expression, providing a newer therapeutic strategy for AMI treatment [15–17].

However, the association between mir-21 and PDCD4 in the severity of coronary artery lesions and HR-induced HUVEC cellular damage remains to be elucidated. The aim of the present research examined the impact of deregulated circulatory mir-21 concentrations in the categorized coronary artery stenosis patients and disclosed its molecular protective mechanisms against H/R-induced HUVEC cellular injury.

2. Materials and Methods

2.1. Study Subjects. Angiographically proven 56 single-coronary artery stenosis, 92 dual-vessel stenosis, 139 multivessel blocked CAD patients, and 56 healthy volunteers were collected between January 2016 and May 2017 from the 1st Affiliated Xiangya Hospital, Central South University. CAD was considered if coronary artery blockade was observed at ≥50% through the invasive coronary angiogram by two interventional cardiologists. Single-vessel disease is defined when one major coronary (LAD, LCX, and RCA) artery occluded, dual-vessel disease is considered when two major coronary arteries or individually blocked left main (LM) artery occluded, and multivessel lesion CAD patients were categorized when two or more than two major coronary arteries including their branches were occluded. Acute or chronic heart failure, acute coronary syndrome, stroke, implanted pacemaker or ICD, revascularization by coronary stent or open-heart surgery (CABG), cardiomyopathy, and pulmonary hypertension subjects were excluded from this study. Individuals with no history of cardiovascular diseases, chronic renal insufficiency, chronic liver, or other multisystem inflammatory disorders or malignancy were recruited as healthy participants. Prior to this study, from all the human study subjects, written informed consent was obtained, and the study was conducted by following the human research protocols in the Declaration of Helsinki. Human and cellular investigations of this study were reviewed and approved by the Ethics Committee of Xiangya Hospital, Central South University. 5 mL peripheral venous blood samples was obtained by percutaneous cubital venipuncture in EDTA-coated tubes from all the participants.

2.2. Cell Culture, Transfection, and Dual-Luciferase Reporter Gene Assay of HUVEC. The primary human umbilical vein endothelial cell line (HUVEC) was purchased from the Chinese Academy of Sciences (Shanghai, China) and cultured in 12-well plates at a density of 5×10^5 cells/well by using Dulbecco's Modified Eagle's Medium (DMEM) supplemented with 20% fetal bovine serum (FBS) in a cell incubator with maintained normoxic conditions at 37° C, 5% CO_2, and 95% air. The hypoxia-reoxygenation (HR) model was established by harvesting HUVECs in an anaerobic modular incubator containing 95% N_2, 5% CO_2, and 1% O_2, using serum and glucose-free DMEM for 12 hours; afterward, cells were reoxygenated for 6 hours in a normoxic incubator. HUVECs were transfected with has-inhibitory-

miR-21 (100 nmol/L) for inhibition, and has-inhibitory-negative control- (NC-) mir-21 (100 nmol/L) (RiboBio, Guangzhou, China) acts as an inner control by using the Lipofectamine 2000 transfection agent (Invitrogen, USA); more details are shown in our prior studies [14, 18, 19].

The luciferase reporter gene analysis technique was used to confirm the target gene of mir-21. The complementary sequence of 3′-UTR of PDCD4 was predicted with mir-21 by TargetScan (http://www.targetscan.org/). Lipofectamine 2000 reagents and has-inhibitory and negative controls-mir-21 were used for the transfection of HUVECs, and dual-luciferase gene analysis chemicals (Beyotime, Jiangsu, China) were applied for the determination of HUVEC luciferase activities normalized by Renilla and fluorescent activity was used for the measurement of their ratio.

2.3. Intracellular ROS, Caspase-3 Activity, and Cellular Viability Assays. Healthy, hypoxia-reoxygenation, and transfected HUVEC cellular ROS concentrations were demonstrated by adding the 5 μM dichlorodihydrofluorescein diacetate (DCFH-DA) solution into each 96-well black plate after proper growth of the cells and inoculated for 30 minutes at 37°C. Afterward, two times cells were cleaned by PBS, and finally, ROS values were measured using an ultraviolet SpectraMax microplate reader (Molecular Devices, Sunnyvale, CA) at the 490 nm wavelength.

Caspase-3 activities were performed by using the caspase-3 activity colorimetric kit according to the manufacturer's guidelines (Beyotime, Shanghai, China). Moreover, 100 microliters of caspase-3 substrate was added to each normal and treated 96-well plate HUVECs. All the samples were incubated at 37°C for 2 hours, and caspase-3 expression levels were evaluated through a microplate SpectraMax absorbance reader (Molecular Devices, Sunnyvale, CA) at the wavelength of 405 nm.

Cellular viability and proliferation were assessed by using CCK-8 kits (Beyotime, Shanghai, China) by following the company's protocols. The HUVECs were cultivated into 96-well plates; after proper treatment, 10 microliters of the CCK-8 reagent was mixed and inoculated at 37°C for 2 hours; then, the normal, HR, and HR plus treated HUVECs were washed twice by PBS; subsequently, cellular viability was detected at the wavelength of 450 nm by using a SpectraMax (Molecular Devices, Sunnyvale, CA) absorbance reader microplate.

2.4. Detection of miRNA and mRNA Levels. Pure RNAs were extracted with TRIzol solution from circulating human plasma, normal, HR, and HR with transfected HUVECs (Invitrogen, CA, USA). The hsa-mir-21, inhibitory and negative control- (NC-) mir-21, and internal reference miR-156a primers were designed by Guangzhou RiboBio (China). The primers of PDCD4 and endogenous reference β-actin were obtained from Shanghai (China) Biotech. Target protein primer sequences are presented in Table 1. Moreover, a total of 4 μL of pure RNA (OD: 1.8-2.2, nucleic acid concentration: 50-500 μg) was reverse-transcribed (RT) to cDNA at 42°C for 30 minutes using the Bulge-Loop miRNA-specific reverse transcription primers (RiboBio, Guangzhou, China) as per instructions of the manufacturer through the RT-PCR system (Bio-Rad, USA). Subsequently, 2 μL of cDNA was used as the template in a real-time quantitative PCR reaction by the following thermal parameters: an initial incubation at 95°C for 15 s, followed by 40 cycles of denaturation at 95°C for 5 s and annealing and extension at 60°C for 31 s. The relative expressions of mir-21 concentrations and PDCD4 levels were analyzed with Master Mix SYBR Green qRT-PCR reagents (Takara Bio, Dalian, China) through a 7300 Real-Time PCR System (Applied Biosystems, Thermo Fisher Scientific, USA.). Moreover, the RNA isolation and qRT-PCR procedures for miRNA and mRNA expressions were more discussed in our prior studies [18, 19].

2.5. Statistical Data Analysis. All the data in this study were expressed as mean ± standard deviation (SD) or SEM, and at least three independent experiments were performed for each data and analyzed through SPSS 22.0 and GraphPad Prism 8.0. To analyze the continuous variation within two groups, the 2-tailed Student t-test and the nonparametric Mann-Whitney test were performed, and for categorical variations, Fischer and the chi-square (χ^2) tests were implemented, and the differences between more than two groups were measured by one-way analysis of variance (ANOVA). The sensitivity and specificity of mir-21 as a biochemical marker were examined by the Receiver Operating Characteristic (ROC) curve analysis method. A value of $P < 0.05$ was considered to indicate a statistically significant difference.

3. Results

3.1. Baseline Clinical and Laboratory Information of All the Study Subjects. There were 56 patients (35 males, 21 females) with single-vessel blocked CAD, 92 (52 males, 40 females) patients with dual-vessel lesion CAD, 139 patients (76 males, 63 females) with multivessel occluded CAD, and 56 (28 males, 28 females) well-coordinated gender- and age-matched healthy individuals who were enrolled in this study, and their ($n = 343$) baseline clinical features are presented in Table 2. Lipid profiles (LDL, HDL, TC, and TG), serum creatinine, and C-reactive protein values were reasonably higher in multivessel CAD patients than in healthy subjects. However, other clinical information among healthy, single, dual, and complex lesion CAD subjects was not statistically significant (Table 2).

3.2. Expression of mir-21 and PDCD4 in Plasma and HUVECs. The expressions of circulating plasma mir-21 levels were progressively elevated in single-, dual-, and multivessel occluded stable CAD patients as compared with healthy individuals. The highest levels of mir-21 were found in complex-vessel lesion CAD groups compared with double- and single-vessel CAD subjects, and they were statistically significant ($P < 0.001$) (Figure 1(a)). The relative mir-21 expressions in hypoxic reoxygenation- (HR-) exposed HUVECs were significantly upregulated by 3.4-fold (29.02 ± 1.4) compared to those in normal atmospheric-cultured healthy cells (8.44 ± 0.63) ($P < 0.001$) (Figure 1(b)). The expressions of

Table 1: Primer sequences of target proteins and their relationship with mir-21 and PDCD4.

Target genes	Forward sequences (5′ to 3′)	Reverse sequences (5′ to 3′)
Hsa-miR-21	GTGCAGGGTCCGAGGT	GCCGCTAGCTTATCAGACTGATGT
Hsa-miR-156	AGGCGCCTGACAGAAGAGAGT	GTGCAGGGTCCGAGGT
Hsa-PDCD4	AGGCCGAGGTGGGCGGATCACTTGA	GCCACCATGCCTGGCTACT
Hsa-β-actin	TGACGTGGACATCCGCAAAG	CTGGAAGGTGGACAGCGAGG

(i) Position 242-249 of PDCD4: 3′-UTR-AAGUGGAAUAUUCUAAUAAGCUA. (ii) Hsa-miR-21: AGUUGUAGUCAGACUAUUCGAU. Abbreviation: Hsa: human.

Table 2: Baseline features of the study participants.

Parameters	Healthy participants ($n = 56$)	Patients with single-vessel CAD ($n = 56$)	Patients with double-vessel CAD ($n = 92$)	Patients with multivessel CAD lesion ($n = 139$)	P_1	P_2	P_3
Age (years)	57.5 ± 9.3	58.6 ± 11.7	60.4 ± 11.7	62.5 ± 12.9	0.539	0.217	0.184
Male/female	28/28	35/21	52/40	76/63	0.492	0.113	0.086
Systolic BP (mmHg)	122.3 ± 7.8	130.8 ± 10.7	131.9 ± 12.8	133.8 ± 13.5	0.089	0.326	0.251
Diastolic BP (mmHg)	75.8 ± 6.4	80.2 ± 7.9	81.6 ± 8.7	82.8 ± 8.5	0.091	0.144	0.163
Heart rate (bpm)	75.3 ± 8.6	78.7 ± 6.9	80.4 ± 9.2	81.5 ± 10.7	0.257	0.389	0.446
Body mass index (kg/m^2)	22.5 ± 5.8	23.7 ± 8.6	23.9 ± 7.4	24.1 ± 6.2	0.428	0.507	0.453
Current tobacco smoking	52% (29)	56% (31)	60% (55)	58% (81)	0.642	0.715	0.783
Lipid disorders	—	86% (48)	88% (81)	92% (128)	—	—	—
Diabetes mellitus	—	28% (16)	32% (29)	34% (47)	—	—	—
Essential hypertension	—	57% (32)	66% (61)	68% (95)	—	—	—
LDL-C (mmol/L)	2.32 ± 0.4	2.65 ± 1.2	3.2 ± 1.7	3.98 ± 1.3	0.126	0.079	<0.001
TCHO (mmol/L)	4.7 ± 0.3	5.12 ± 0.6	5.53 ± 0.4	5.76 ± 0.9	0.078	0.092	<0.001
HDL-C (mmol/L)	1.6 ± 0.9	1.03 ± 0.7	0.89 ± 0.4	0.71 ± 0.8	0.099	0.086	<0.001
TG (mmol/L)	1.29 ± 0.4	1.58 ± 0.6	1.71 ± 0.5	2.35 ± 0.9	0.084	0.065	<0.001
Serum creatinine (mg/dL)	0.78 ± 1.29	1.31 ± 1.2	1.34 ± 1.4	1.47 ± 1.5	0.122	0.096	<0.001
Left ventricular ejection fraction	59.4 ± 11.3	53.7 ± 8.6	50.9 ± 10.7	50.3 ± 11.4	0.125	0.096	0.087
C-reactive protein (mg/L)	3.7 ± 1.4	17.7 ± 10.6	23.6 ± 9.8	26.3 ± 11.2	<0.001	<0.001	<0.001

P_1: healthy controls versus single-vessel CAD groups; P_2: healthy participants and dual-vessel lesion CAD subjects; P_3: healthy volunteers and multivessel occluded CAD patients; TCHO: total cholesterol; TG: triglyceride; HDL-C: high-density lipoprotein cholesterol; LDL-C: low-density lipoprotein cholesterol.

circulating PDCD4 were gradually reduced in single-vessel stenosis and double- and multivessel occluded CAD groups as compared with healthy subjects. The lowest concentrations of PDCD4 were recorded in multivessel CAD groups as compared with those with double- and single-vessel CAD groups. Moreover, PDCD4 expressions within the different CAD disease groups were also evidently significant ($P < 0.001$) (Figure 1(c)). In HR-induced HUVECs, PDCD4 levels were markedly downregulated by 3.2-fold (11.23 ± 0.51) compared to those in control cells (3.47 ± 0.76) ($P < 0.001$) (Figure 1(d)).

3.3. Clinical Significance of Plasma mir-21 in the Grading of CAD Patients. The clinical role of circulating mir-21 to detect the severity of CAD patients was assessed through the ROC method. In single-vessel occluded CAD subjects, plasma mir-21 expressions were able to strongly discriminate from those in healthy subjects with a prominent area under the curve (AUC) of 0.893. In dual-vessel lesion CAD patients, circulating mir-21 levels were evidently separated from those in healthy participants with a significant AUC of 0.914. The plasma mir-21 concentrations in

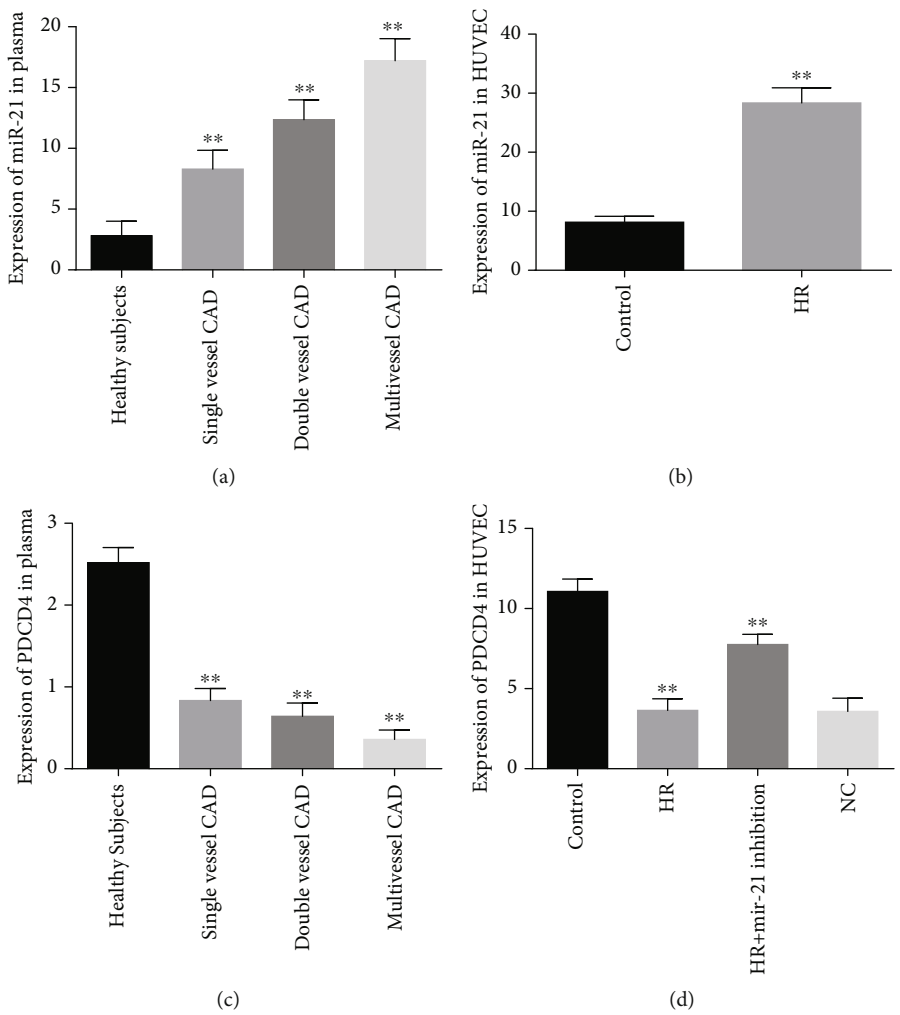

Figure 1: The expression patterns of mir-21 and PDCD4. (a) Circulating mir-21 concentrations in healthy participants versus single-, double-, and multivessel lesion CAD subjects. (b) Expression levels of mir-21 among hypoxic reoxygenation (HR) and normal control HUVECs. (c) The PDCD4 expression patterns between healthy volunteers and disease groups. (d) Comparison of PDCD4 expressions in HR-exposed and normoxic-cultured HUVECs. $^{**}P < 0.001$.

multivessel blocked CAD patients were noticeably distinguished from those in control subjects (AUC of 0.933) with high specificity and sensitivity levels. The AUC curves of plasma mir-21 were also distinctly significant and had a strong predictive power to differentiate between single-, double-, and multivessel blocked CAD patients (Figure 2). These findings suggested that upregulated plasma mir-21 has a significant clinical diagnostic role to categorize the severity of CAD patients.

3.4. Expression Profile of mir-21 in HUVECs and Luciferase Assay. The relative expressions of mir-21 were markedly upregulated in HR-exposed HUVECs as compared with healthy control cells ($P < 0.001$). In contrast, mir-21 levels were noticeably downregulated by 1.7-fold (17.32 ± 2.3) in HR-injured HUVECs transfected with inhibitory mir-21 as compared with HR-incubated HUVECs (29.02 ± 2.4), but expression profiles within negative control (NC) and HR-incubated groups were nonsignificant (Figure 3(a)). Furthermore, the current study also demonstrated that luciferase activity levels were evidently decreased in HR-incubated HUVECs by 1.8-fold (6.68 ± 1.4) compared to normoxic cells (11.84 ± 0.9), but no significant differences were observed between NC and HR groups. The inhibitory mir-21 strongly controlled luciferase activities in HR-injured HUVECs (Figure 3(b)).

3.5. The Inhibitory mir-21 Regulated PDCD4 Expression and Augmented HUVEC Survival. The relative expressions of PDCD4 levels were prominently downregulated in HR-injured HUVECs whereas they were remarkably upregulated as close to controls upon treatment with inhibitory mir-21. No obvious effects were found between NC and hypoxic-reoxygenated- (HR-) exposed HUVECs, suggesting that PDCD4 expressions were strongly regulated by inhibitory mir-21 in normal and HR-damaged HUVECs (Figure 4(a)).

In HR-exposed HUVECs, the levels of intracellular ROS were much higher than normally cultured cells while amazingly reduced by treated HR-damaged HUVECs with inhibitory mir-21. Among HR and NC groups, no significant

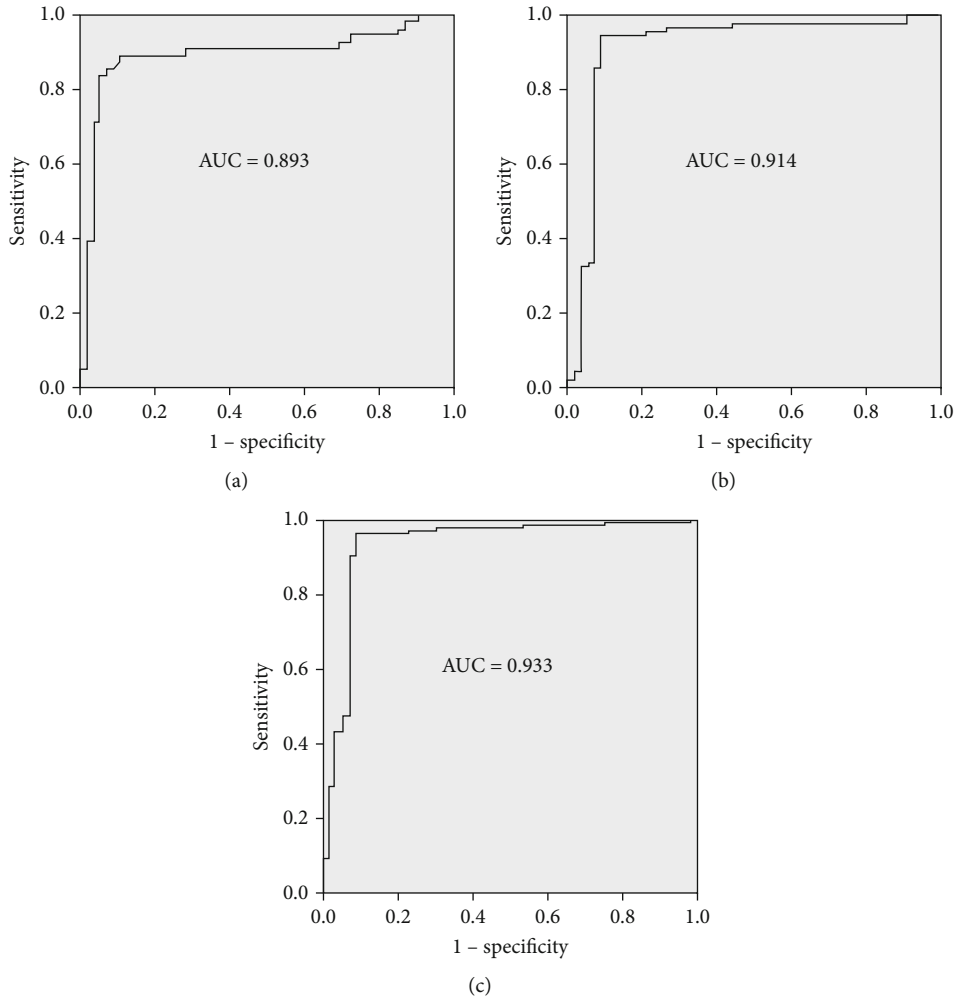

Figure 2: ROC curve analysis was used for categorizing the severity of CAD patients: (a) healthy controls and single-vessel lesion CAD (AUC 0.893); (b) dual-vessel stenosis CAD with healthy subjects (AUC 0.914); (c) healthy volunteers and multivessel blocked CAD patients (AUC 0.933).

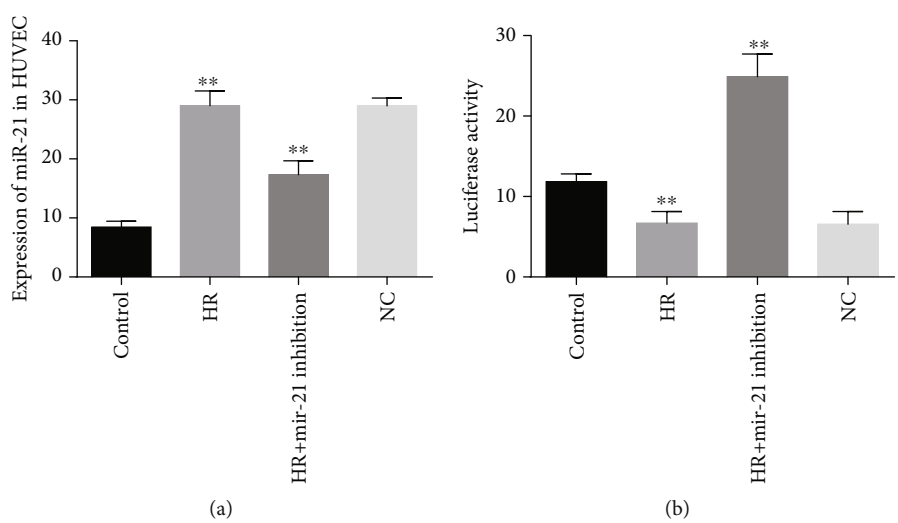

Figure 3: Expression patterns of mir-21 in HUVECs and luciferase analysis to determine the target: (a) the mir-21 expression levels in healthy and HR groups; (b) reporter gene assay luciferase expression levels in normoxic, HR, HR with transfected mir-21, and NC groups in HUVECs standardized by Renilla reniformis. $^{**}P < 0.001$.

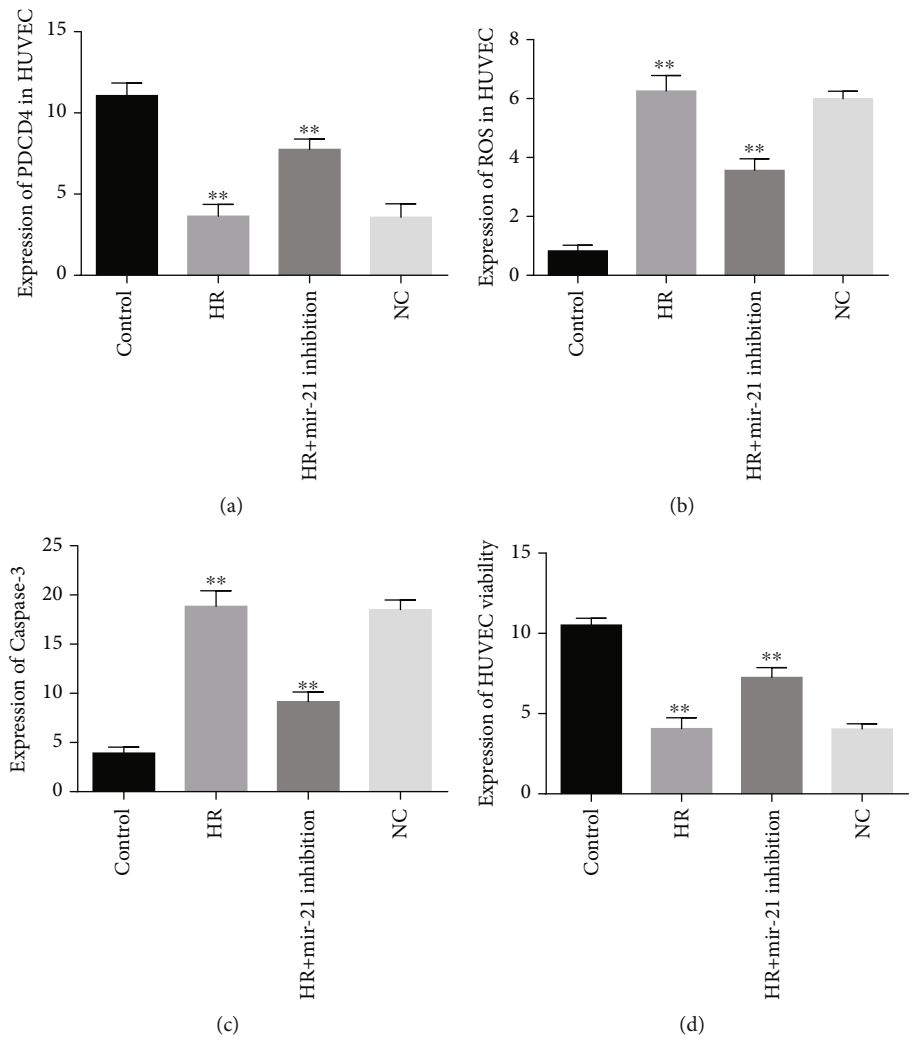

Figure 4: Effects of mir-21 inhibition on HUVECs: (a) the relative expression levels of PDCD4 in normoxic and HR cells; (b) intracellular ROS generations in normal HUVEC versus HR-injured cells; (c) caspase-3 expression between normal culture and HR-incubated cells; (d) cellular viability in HR and normal, HR and HR transfected with mir-21 inhibition, and HR and NC groups in HUVECs. $^{**}P < 0.001$.

effects were revealed on ROS expressions, indicating that inhibitory mir-21 has a major role to prevent oxidative stress-induced HUVEC cellular injures under HR situations (Figure 4(b)). Caspase-3 activities were markedly elevated in HR-exposed HUVECs than in normal cells. On the contrary, HR-induced HUVECs transfected with inhibitory mir-21 caspase-3 expressions were remarkably decreased, but the activities of caspase-3 expressions were insignificantly expressed between NC and HR, acknowledging that mir-21 inhibition is essentially involved to protect against HUVEC cellular damage in HR conditions (Figure 4(c)). The HUVEC cellular viability was significantly decreased in HR-induced groups compared to normal healthy cells. On the other hand, HR-exposed HUVECs treated with mir-21 inhibition remarkably increased cellular viability while no obvious changes were found among NC and HR groups; these findings strongly recommended that inhibitory mir-21 plays a fundamental role in cellular protection against injuries in the HR environment (Figure 4(d)).

3.6. Plasma mir-21 Expression Association with Aging and Gender. In elderly healthy subjects (66-85 years), circulatory plasma mir-21 concentrations were relatively higher than those in younger healthy participants (25-33 years) ($P < 0.001$) (Figure 5(a)). In single-, double-, and complex-vessel occluded CAD geriatric aged (66-85 years) people, the mir-21 expressions were significantly increased as compared with those in younger aged (25-33 years) people ($P < 0.001$) (Figures 5(b)–5(d)). However, in both genders among healthy and single-, dual-, and multivessel stenosis CAD groups, plasma mir-21 levels were nonsignificant ($P > 0.05$) (Figures 5(e)–5(h)). These findings indicated that upregulated mir-21 expressions have been positively and strongly correlated with aging.

4. Discussion

Promoting a healthy lifestyle and early evaluation with immediate proper treatment can significantly decline CAD

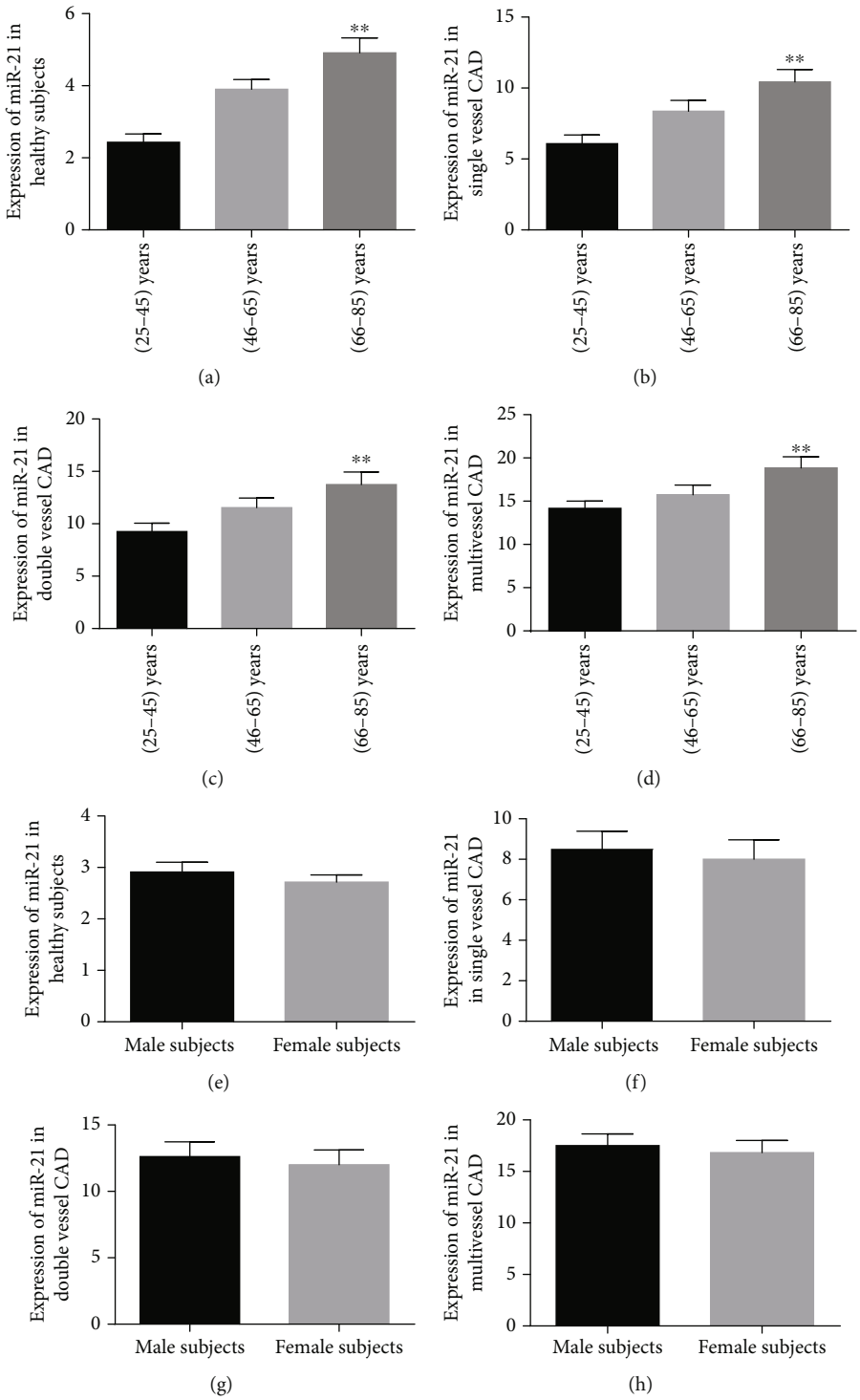

Figure 5: The relative expression of circulatory mir-21 in different aged subjects and both male and female genders: (a) the expression patterns of plasma mir-21 among healthy groups; (b) plasma mir-21 concentrations in single-vessel CAD subjects; (c) the expression of mir-21 levels in double-vessel CAD patients; (d) multivessel CAD patients' mir-21 levels; (e) healthy male and female groups' mir-21 expressions; (f) the levels of plasma mir-21 in male versus female single-vessel CAD groups; (g) the concentrations of circulatory mir-21 among male and female double-vessel stenosis CAD subjects; (h) the mir-21 levels between male and female multivessel blocked CAD patients.

death incidence. Endothelial dysfunction and various inflammatory mediators are the major molecular insights to develop atherosclerotic heart disease. Over the past two decades, accumulating evidence has elucidated that microRNA plays a vital role in regulating endothelial injury, atherosclerosis, and cellular apoptosis.

This study explored the clinical significance of mir-21 in the severity of atherosclerotic CAD patients, and it is linked with PDCD4 as well as its preventing role during HR-exposed HUVEC cellular injury. The present research study found that mir-21 expressions were obviously and steadily upregulated in the plasma of single-, double-, and complex-vessel lesion CAD patients compared to healthy control subjects. The plasma expressions of PDCD4 were progressively decreased in single-, dual-, and multivessel stenosis CAD participants compared with normal individuals. Significant or insignificant coronary stenosis subject's mir-21 concentrations were obviously higher identified by Ziba et al.'s research group [13]. Our previous stable CAD study subjects demonstrated significantly upregulated circulatory mir-21 concentrations compared to healthy subjects [14]. Moreover, the PDCD4 expression levels in the AMI rat model were evidently lower compared with those in the control groups reported by Zhou et al. [20].

The clinical significance of plasma mir-21 in the prediction of severity of CAD was evaluated by ROC curve analysis. The single-, dual-, and multivessel CAD stenosis patients were able to be significantly differentiated (AUC of 0.893, 0.914, and 0.933, respectively) from the healthy control participants, and their differences within the subgroups were statistically highly significant. These findings suggested that upregulated circulatory mir-21 can be used as a noninvasive diagnostic clinical potential marker for the detection of stenosis levels in CAD subjects, and also, similar results are reported by some clinical experiments [14, 21, 22].

The present study reported that lipid profiles and serum creatine values in multivessel CAD patients were significantly elevated compared to those in healthy controls, but difference within groups were insignificant. The C-reactive protein concentrations in single-, double-, and complex-vessel lesion CAD subjects were remarkably higher than those in healthy individuals. Our previous study also demonstrated that higher CRP levels have a strong association with stable and unstable angina patients that required further molecular studies to discover their undeveloped signaling pathways [14, 19].

This study also revealed that mir-21 expressions were evidently increased in geriatric subjects compared to younger people, suggesting a significant link with the aging process. Wang et al. and also our prior study have identified in elderly subjects remarkably elevated mir-21 and association with the cardiorenal syndrome and aging [14, 23].

It has been established that PDCD4 is crucial in regulating oxidized low-density lipoprotein (ox-LDL) metabolism, foam cell formation, coronary atherosclerosis, stress, and ischemia/reperfusion-induced cellular injuries [10–12, 24]. From our luciferase analysis experiment results, from the TargetScan database, and also from other studies, it was confirmed that PDCD4 is the direct target protein of miR-21 [20, 24, 25]. The present study detected expressions of mir-21 in HR-exposed HUVECs which were highly upregulated as compared with the control group, but there were no significant effects noted between NC and HR groups. Chang et al. also moderately supported this study [15]. Moreover, the current study demonstrated that PDCD4 expressions were evidently decreased in HR-incubated HUVECs while they were markedly elevated after transfecting with mir-21 inhibition. The intracellular production of ROS levels in HR-induced HUVECs was markedly upregulated but significantly dropped back near to normal levels after being treated with mir-21 inhibition. Caspase-3 activities in HR-cultured HUVECs were enormously elevated but noticeably reduced after transfecting with mir-21 inhibition. Zhou et al. revealed mir-21-regulated cardiomyocyte apoptosis via targeting PDCD4 which relatively supported this study [20]. Besides, the present research established that cellular viability and proliferation markedly declined in HR-induced HUVECs compared with normally cultured cells but significantly improved cellular viability after being treated with mir-21 inhibition. All these results confirmed that mir-21 inhibition can protect against HR-induced HUVEC cellular injuries and suggested a new potential therapeutic target for CAD patients.

However, the molecular relationship between mir-21 with lipid profiles and C-reactive protein was not investigated in this study and needs further studies. Additionally, this is a tertiary-level comparatively small sample size single hospital-based one ethnic population study. Therefore, different ethnic multiregional larger population-based clinical cohort experiments will be conducted in the future for the rationality of the clinical importance of circulatory miR-21 as an ideal useful early noninvasive diagnostic tool and possible therapeutic agent for the management of ischemic heart disease.

5. Conclusion

>The increased plasma mir-21 expression level could be a novel biomarker for the severity of coronary artery stenosis and correlation with aging, and mir-21 inhibition prevents HUVEC cellular injuries under hypoxia-reoxygenation insults via targeting PDCD4, suggesting a potential target for treating atherosclerotic CAD patients.

Data Availability

Data are available on request.

Conflicts of Interest

The author declares that he has no conflicts of interest.

Acknowledgments

This work was funded by the Deanship of Scientific Research at Jouf University under grant no. DSR-2021-01-03161. The author sincerely acknowledges Dr. Li fei, Dr. Xia Ke, Prof. Yang Tian Lun, and the cardiovascular unit of Xiangya Hospital for their outstanding support of this research and is also grateful to the Internal Medicine Department of Jouf University.

References

[1] C. W. Tsao, A. W. Aday, Z. I. Almarzooq et al., "Heart disease and stroke statistics-2022 update: a report from the American Heart Association," *Circulation*, vol. 145, pp. e153–e639, 2022.

[2] H. Sun, J. Feng, Y. Ma et al., "Down-regulation of microRNA-342-5p or up-regulation of Wnt3a inhibits angiogenesis and maintains atherosclerotic plaque stability in atherosclerosis mice," *Nanoscale Research Letters*, vol. 16, no. 1, p. 165, 2021.

[3] V. G. de Yébenes, A. M. Briones, I. Martos-Folgado et al., "Aging-associated miR-217 aggravates atherosclerosis and promotes cardiovascular dysfunction," *Arteriosclerosis, Thrombosis, and Vascular Biology*, vol. 40, pp. 2408–2424, 2020.

[4] S. Ghafouri-Fard, M. Gholipour, and M. Taheri, "Role of microRNAs in the pathogenesis of coronary artery disease," *Frontiers in Cardiovascular Medicine*, vol. 8, article 632392, 2021.

[5] Y. Jiang and D. Tian, "Relation of circulating lncRNA GAS5 and miR-21 with biochemical indexes, stenosis severity, and inflammatory cytokines in coronary heart disease patients," *Journal of Clinical Laboratory Analysis*, vol. 36, no. 2, article e24202, 2022.

[6] X. Pei, Y. Wen, F. Cui, Z. Yang, and Z. Xie, "lncRNA CASC7 regulates pathological progression of ox-LDL-stimulated atherosclerotic cell models via sponging miR-21 and regulating PI3K/Akt and TLR4/NF-κB signaling pathways," *Aging (Albany NY)*, vol. 13, pp. 25408–25425, 2021.

[7] H. Ling, Z. Guo, Y. Shi, L. Zhang, and C. Song, "Serum exosomal microRNA-21, microRNA-126, and PTEN are novel biomarkers for diagnosis of acute coronary syndrome," *Frontiers in Physiology*, vol. 11, p. 654, 2020.

[8] W. He, L. Zhu, H. Yu et al., "The relationship of microRNA-21 and plaque stability in acute coronary syndrome," *Medicine (Baltimore)*, vol. 98, no. 47, article e18049, 2019.

[9] F.-P. Li, D.-Q. Lin, and L.-Y. Gao, "LncRNA TUG1 promotes proliferation of vascular smooth muscle cell and atherosclerosis through regulating miRNA-21/PTEN axis," *European Review for Medical and Pharmacological Sciences*, vol. 22, no. 21, pp. 7439–7447, 2018.

[10] Y. Gao, H. Li, Y. Zhou, H. Lv, and Y. Chen, "PDCD4 expression in coronary atherosclerosis rat models and its mechanism," *Experimental and Therapeutic Medicine*, vol. 17, no. 4, pp. 3150–3154, 2019.

[11] L. Wang, Y. Jiang, X. Song et al., "Pdcd4 deficiency enhances macrophage lipoautophagy and attenuates foam cell formation and atherosclerosis in mice," *Cell Death & Disease*, vol. 7, no. 1, article e2055, 2016.

[12] J. Yang, Q. Gao, L. Wang et al., "Deficiency of programmed cell death 4 results in increased IL-10 expression by macrophages and thereby attenuates atherosclerosis in hyperlipidemic mice," *Cellular & Molecular Immunology*, vol. 13, no. 4, pp. 524–534, 2016.

[13] S. Z. Vahed, S. H. Aghaee-Bakhtiari, A. Daraei et al., "Expression pattern of miR-21, miR-25 and PTEN in peripheral blood mononuclear cells of patients with significant or insignificant coronary stenosis," *Gene*, vol. 698, pp. 170–178, 2019.

[14] M. S. A. Sheikh, "Diagnostic role of plasma microRNA-21 in stable and unstable angina patients and association with aging," *Cardiology Research and Practice*, vol. 2020, Article ID 9093151, 7 pages, 2020.

[15] C.-H. Chang, M.-C. Yen, S.-H. Liao et al., "Dual role of miR-21-mediated signaling in HUVECs and rat surgical flap under normoxia and hypoxia condition," *International Journal of Molecular Sciences*, vol. 18, p. 1917, 2017.

[16] M. Shao, M. Yu, J. Zhao et al., "miR-21-3p regulates AGE/RAGE signalling and improves diabetic atherosclerosis," *Cell Biochemistry and Function*, vol. 38, no. 7, pp. 965–975, 2020.

[17] H. Gu, Z. Liu, Y. Li et al., "Serum-derived extracellular vesicles protect against acute myocardial infarction by regulating miR-21/PDCD4 signaling pathway," *Frontiers in Physiology*, vol. 9, p. 348, 2018.

[18] M. S. A. Sheikh, U. Salma, B. Zhang, J. Chen, J. Zhuang, and P. Zhu, "Diagnostic, prognostic, and therapeutic value of circulating miRNAs in heart failure patients associated with oxidative stress," *Oxidative Medicine and Cellular Longevity*, vol. 2016, Article ID 5893064, 13 pages, 2016.

[19] M. S. A. Sheikh, A. Almaeen, A. Alduraywish et al., "Overexpression of miR-126 protects hypoxic-reoxygenation-exposed HUVEC cellular injury through regulating LRP6 expression," *Oxidative Medicine and Cellular Longevity*, vol. 2022, Article ID 3647744, 8 pages, 2022.

[20] X.-H. Zhou, H.-X. Chai, M. Bai, and Z. Zheng, "LncRNA-GAS5 regulates PDCD4 expression and mediates myocardial infarction-induced cardiomyocytes apoptosis via targeting MiR-21," *Cell Cycle*, vol. 19, no. 11, pp. 1363–1377, 2020.

[21] D. Kumar, R. Narang, V. Sreenivas et al., "Circulatory miR-133b and miR-21 as novel biomarkers in early prediction and diagnosis of coronary artery disease," *Genes*, vol. 11, p. 164, 2020.

[22] M. Sanlialp, Y. Dodurga, B. Uludag et al., "Peripheral blood mononuclear cell microRNAs in coronary artery disease," *Journal of Cellular Biochemistry*, vol. 121, no. 4, pp. 3005–3009, 2020.

[23] Y. Wang, Y. Liang, W. J. Zhao et al., "Circulating miRNA-21 as a diagnostic biomarker in elderly patients with type 2 cardiorenal syndrome," *Scientific Reports*, vol. 10, p. 4894, 2020.

[24] H. Qi, J. Zhang, Y. Shang, S. Yuan, and C. Meng, "Argon inhibits reactive oxygen species oxidative stress via the miR-21-mediated PDCD4/PTEN pathway to prevent myocardial ischemia/reperfusion injury," *Bioengineered*, vol. 12, no. 1, pp. 5529–5539, 2021.

[25] J. Xue, J. Liu, B. Xu et al., "miR-21-5p inhibits inflammation injuries in LPS-treated H9c2 cells by regulating PDCD4," *American Journal of Translational Research*, vol. 13, pp. 11450–11460, 2021.

Hindawi
Mediators of Inflammation
Volume 2022, Article ID 3101900, 10 pages
https://doi.org/10.1155/2022/3101900

Review Article

The Role of MicroRNAs in Hyperlipidemia: From Pathogenesis to Therapeutical Application

Yu Xiang,[1] Li Mao,[2] Mei-Ling Zuo,[1] Gui-Lin Song,[1,3] Li-Ming Tan,[1] and Zhong-Bao Yang[1,3]

[1]*The Affiliated Changsha Hospital of Hunan Normal University, Changsha, 410006 Hunan, China*
[2]*Department of Basic Medicine, Changsha Health Vocational College, Changsha, 410600 Hunan, China*
[3]*Institute of Emergency and Critical Care Medicine of Changsha, Changsha, China*

Correspondence should be addressed to Zhong-Bao Yang; yangzhongbao1984@163.com

Received 14 April 2022; Accepted 7 June 2022; Published 17 June 2022

Academic Editor: Agnieszka Dobrzyn

Hyperlipidemia is a common metabolic disorder with high morbidity and mortality, which brings heavy burden on social. Understanding its pathogenesis and finding its potential therapeutic targets are the focus of current research in this field. In recent years, an increasing number of studies have proved that miRNAs play vital roles in regulating lipid metabolism and were considered as promising therapeutic targets for hyperlipidemia and related diseases. It is demonstrated that miR-191, miR-222, miR-224, miR-27a, miR-378a-3p, miR-140-5p, miR-483, and miR-520d-5p were closely associated with the pathogenesis of hyperlipidemia. In this review, we provide brief overviews about advances in miRNAs in hyperlipidemia and its potential clinical application value.

1. Introduction

Hyperlipidemia is a metabolic disorder with high morbidity and high mortality, usually characterized by lipid dysfunction and oxidative stress [1]. Hyperlipidemia is one of the recognized risk factors for cardiovascular disease (CVD) [2], where elevated low-density lipoprotein cholesterol (LDL-C) is considered a major factor in the development of atherosclerosis [3] and coronary heart disease [4]. It is estimated that the reduction of LDL-C by 10 mmol/L is associated with a 22% reduction in cardiovascular mortality and incidence rate, while the triacylglycerol (TG) concentration greater than 10 mmol/L is associated with a significant increase in risk of acute pancreatitis and cardiovascular disease [5, 6]. With the increasing use of miRNA microarrays and gene expression microarrays for hyperlipidemia gene expression profiling in recent years, we have gained a deeper understanding of the molecular biological mechanisms underlying the occurrence and development of hyperlipidemia. MicroRNAs are short (~21 nucleotides) noncoding RNA molecules that play an important role in the posttranscriptional regulation of gene expression in eukaryotes [7]. miRNAs are found in most eukaryotes [8] and commonly aberrantly expressed in human diseases [9]. Many studies have shown that miRNAs are involved in the regulation of a range of human diseases, including cancer, hepatitis, and cardiovascular diseases [10–12]. miRNAs have also been found involving in the pathogenesis of many allergic diseases, including asthma, eosinophilic esophagitis, allergic rhinitis, and eczema [13–15]. miRNAs are stable in the peripheral blood circulation and exhibit good physiological properties and can tolerate different temperatures, pH, storage times, and even repeated freezing and thawing [16]. It is well demonstrated that miRNAs play an important role in lipid metabolism and are important posttranscriptional regulators of genes that related with lipid homeostasis [17]. For example, previous studies identified miRNAs, such as miR-128 and miR-144, are regulators of plasma lipoprotein and

cholesterol levels [18, 19]. Thus, discovery of specific hyperlipidemia-associated miRNAs may be a viable way to design miRNA-based therapies or obtain new prognostic markers in lipid metabolism-related diseases [20]. With the progressive research on the mechanism of small nucleic acids [21], it will greatly promote the translation of basic research into clinical practice and bring new opportunities for the development of drugs for the treatment of hyperlipidemia.

2. Hyperlipidemia

Hyperlipidemia is a disorder of lipid metabolism [22], usually with high levels of lipids in plasm because of the abnormal lipids transport and disturbed lipid metabolism [23]. Hyperlipidemia is characterized by elevated serum levels of total cholesterol (TC), triglycerides (TG), and low-density lipoprotein cholesterol (LDL-C) or reduced levels of high-density lipoprotein cholesterol (HDL-C) [24]. LDL-C is responsible for transporting fat molecules into cells, and if they are oxidized during transport, they can easily form plaques within the arterial walls, driving the progression of atherosclerosis. HDL-C helps the body to remove LDL from the arteries and brings it back to the liver to break it down, thus preventing cardiovascular disease [25, 26]. Hyperlipidemia is a serious health risk. Studies have shown that hyperlipidemia is involved in a range of diseases such as stroke, atherosclerosis, coronary heart disease, myocardial infarction, diabetes, and pancreatitis [22, 27–31] and is also closely associated with the development of neurodegenerative diseases such as Alzheimer's disease (AD) and Parkinson's disease (PD) [32]. Hyperlipidemia has a high prevalence in China, there were approximately 160 million patients with dyslipidemia in 2002, and this number is increasing [33]. In the United States, according to the 2011-2012 National Health and Nutrition Examination Survey, about 12.9% of adults over the age of 20 had excess total cholesterol [34]. More than 100 million people (about 53% of adults) have elevated LDL-C levels [35].

Hyperlipidemia can be divided into primary hyperlipidemia and secondary hyperlipidemia. Primary hyperlipidemia is characterized by a familial predisposition. Familial hypercholesterolemia (FH) is one of the most common monogenic dyslipidemias with a heterozygous prevalence of 1 : 250, which causes atherosclerosis and increases the risk of premature coronary artery disease (CAD) [36, 37]. An unhealthy diet and less physical activity are considered the most critical risk factors for hyperlipidemia [38]. Secondary hyperlipidemia is a dyslipidemia caused by other diseases, such as diabetes and hypertension. According to the Guidelines for the Prevention and Treatment of Dyslipidemia in Chinese Adults, when meeting one of the following criteria can be diagnosed as hyperlipidemia: $TC \geq 5.2$ mmol/L, $TG \geq 1.7$ mmol/L, $LDL-C \geq 3.4$ mmol/L, $non-HDL-C \geq 4.1$ mmol/L, or $HDL-C < 1.0$ mmol/L. Clinically, hyperlipidemia can be classified as hypercholesterolemia, hypertriglyceridemia, hyper-LDL-C, and mixed hyperlipidemia according to the difference of clinical indicators.

3. MicroRNAs

MicroRNAs (miRNAs) are endogenously transcribed non-coding RNAs, approximately 22 nt long, which are key regulators involving in many biological processes [39]. The first miRNA was identified in 1993 as a small RNA transcribed from the Caenorhabditis elegans lin-4 locus [40], and 7 years later, the first human miRNA let-7 was identified [41]. In humans, miRNAs involve in the expression of protein-coding genes and considered to be a complex gene expression modifier [42]. By binding to the 3′UTR of mRNA, miRNAs can posttranscriptionally inhibit mRNA translation into proteins or promote mRNA degradation [43, 44]. Based on such principles, scientists at the Sanger Institute established the microRNA Registry database to facilitate miRNAs research, later renamed miRbase in 2002 [45]. During the past decades, the number of discovered miRNAs increases year by year, and miRNAs have become a hot topic in medical research. Since miRNAs are negative regulator of genes, any change of the expression level of a certain miRNA may affect its corresponding target gene expression, even cellular homeostasis [46, 47]. Although many studies have shown changes in the expression levels of miRNAs in diseased states, their application as clinical biomarkers is still in its infancy [48, 49].

The biogenesis of miRNAs can be divided into multiple processes (Figure 1). First, synthesis of pri-miRNA is a large structure containing sequences of miRNAs and forms in the nucleus under the action of RNA polymerase II enzyme. The sequence of pri-miRNA may be an independent miRNA gene or parts of introns of protein coding for RNA polymerase II transcripts [50]. Then, the pri-miRNA transcript is cleaved in the nucleus by microprocessor, a catalytic complex composed of Drosha and Di George critical region 8 (DGCR8) [51, 52]. After that, the exportin 5 exports pre-miRNA to the cytoplasm where it is cleaved by Disher near the loop into small double-stranded RNAs [53]. This double-stranded RNA has a structure of 3′overhangs and strands that were named as guide strand and passenger strand according to their function, respectively, [54]. The guide strand, that is mature miRNA, was identified by AGO protein and forms the RNA-induced silencing complex (RISC) [55], while the passenger strand of the miRNA duplex is degraded [56, 57]. The RISC directs the miRNA to bind to its corresponding target mRNA and blocks gene expression by translational repression or mRNA degradation. This process is associated with the action of *a* about 8 nucleotides in length seed region of miRNA. The seed region will recognize the binding site of 3′UTR of mRNA by the way Watson-Crick complementary and lead to mRNA instability and finally translational repression [58, 59].

4. The Relationship between Hyperlipidemia and miRNA

It was demonstrated that miRNAs have important role in the development and progression of hyperlipidemia, which will open a new field for the study of hyperlipidemia [60].

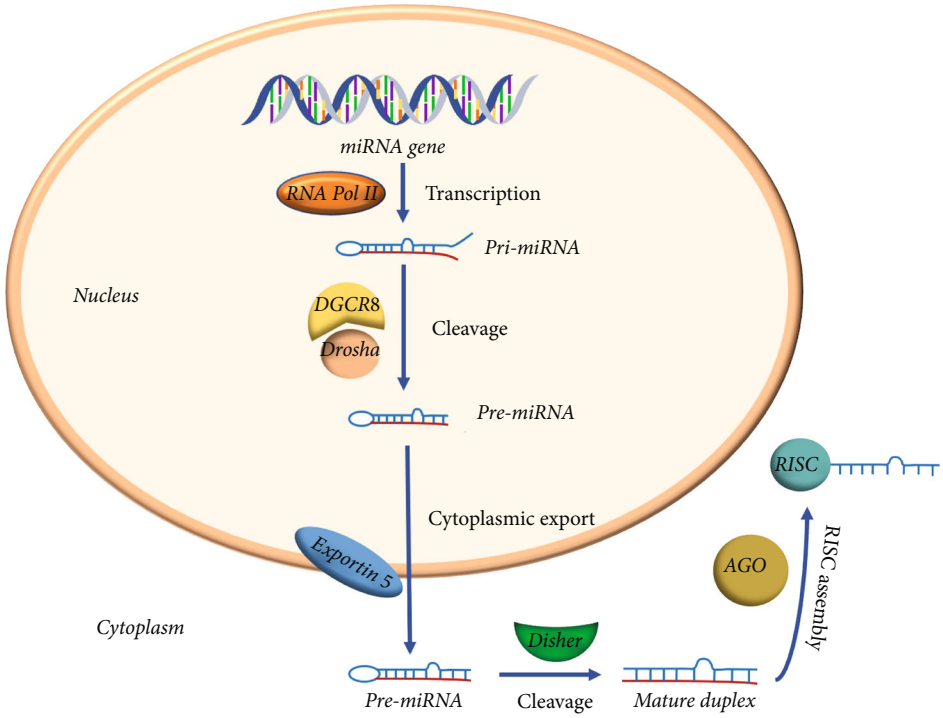

Figure 1: Overview of the miRNA biogenesis.

Several miRNAs in patients with hyperlipidemia were found undergone altered, such as miRNA-191-3p, miRNA-933, miRNA-425-3p, and miR-208a [61]. This suggested that miRNAs may involves in the pathogenesis of hyperlipidemia. In vitro and in vivo studies have revealed that miRNAs play roles in controlling plasma LDL-C by regulating the expression of LDLR, such as miR-199a and miR-140 [62, 63]. Emerging evidence demonstrates that miRNAs involve in multiple processes of hypercholesterolemia, such as lipid synthesis (miR-122), fatty acid biosynthesis (miR-33), and lipoprotein formation and secretion (miR-27a) [64]. In addition, miRNAs involve in multiple processes of HDL metabolism, from synthesis to clearance [65]. Due to the key roles of miRNAs in lipid and lipoprotein metabolism, miRNAs have been considered as new therapeutic targets for lipid metabolism diseases [66, 67]. In fact, therapies based on miR-34 and mir-122 drugs are already in phase 2 clinical trial development [68, 69]. Thus, with the proliferation of human genomic and proteomic data and new delivery vectors development, miRNAs as therapeutic agents or therapeutic targets for hyperlipidemia will become a clinical reality.

4.1. miRNA Has Important Roles in the Pathogenesis of Hyperlipidemia

4.1.1. miRNA and PCSK9. Proprotein convertase subtilisin/kexin type 9 (PCSK9) plays an important role in cholesterol metabolism by targeting LDLR [70, 71]. PCSK9 binds to LDLR on the cell surface to form the LDLR-PCSK9 complex, which hinders the endocytic recycling of LDLR for lysosomal degradation [72, 73]. This effectively reduces LDLR cell surface presentation and LDL-C endocytosis in hepatocytes, thereby increasing circulating LDL-C levels [74]. Previous studies have found that miRNAs involve in the process of formation of LDLR-PCSK9 complex, such as miR-191, miR-222, miR-224, miR-520d-5p, and miR-483, can suppress the expression of PCSK9 by directly binding to its 3′ UTR and resulting in reduction of LDL-C levels [74–76] (Figure 2). Among them, miR-483 was one of the widely studied ones. In hyperlipidemic mice and humans, serum total cholesterol and LDL-C levels were found negatively correlated with miR-483-5p levels. The overexpression of miR-483 greatly reduced serum total cholesterol and LDL-C levels in mouse. In HepG2 cells [74], the high expression of miR-483-5p significantly inhibited the PCSK9 expression and led to LDLR upregulation and enhanced LDL-C uptake. In addition, it is reported that miR-337-3p could ameliorate the elevation of plasma LDL-C in mice feed with high-fat diet by inhibiting the expression of PCSK9 [77].

4.1.2. miRNA and Sort1. In addition to the PCSK9 pathway, miRNAs, such as miR-122, miR-30c, and miR-140-5p, also have been reported to be negative regulator of some key factors in LDL-C metabolism and involve in the regulation of plasma LDL-C [78–80]. Sortilin 1 functions as an intracellular sorting receptor for apoB100 and was encoded by Sort1 gene [81]. Plasma ApoB100 levels are one of the strongest risk factors for coronary artery disease [81]. Previous studies have found that the increase of hepatic Sort1 can reduce hepatic apolipoprotein B (APOB) secretion and increase LDL catabolism, resulting in reduced plasma LDL-C and TG levels in mice [63, 82]. Emerging evidence has shown that miRNAs were involve in the expression regulation of

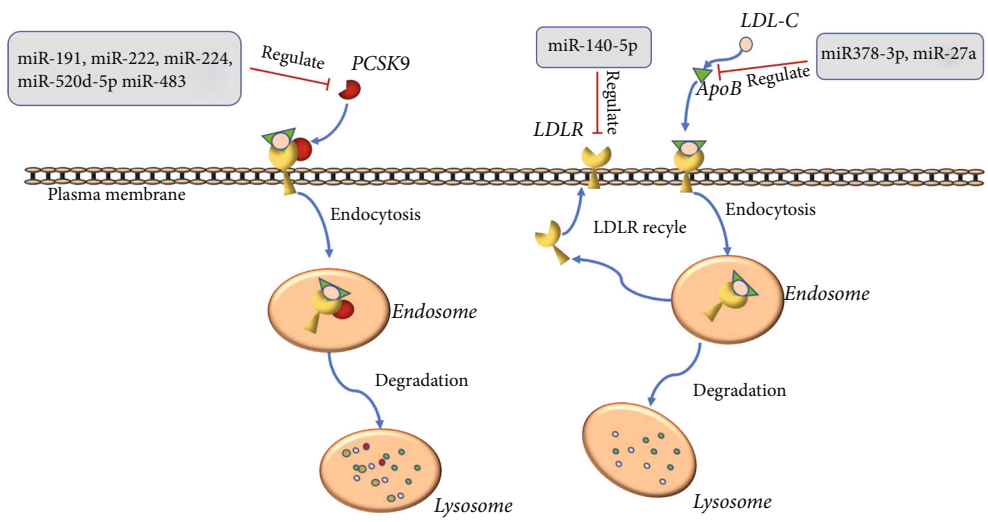

Figure 2: A schematic view of miR-mediated regulation of hyperlipidemia.

Table 1: The relationship between miRNAs, targets, and disease.

miRNAs	Target	Disease or pathophysiological process	References
miR-122, miRNA-33, and miRNA-206 miR-142a-5p	SREBP-1c	Fatty acid metabolism	[64, 117, 122]
miR-34a	PPARα	Hepatic steatosis	[109]
miR-223	NLRP3	Cholesterol metabolism	[116]
miR-128-3p	abca1, abcg1, and retinoid X receptor alpha (RXRA)	Hypercholesterolemia	[93, 94]
miR-27	(FASN), SREBP-1, SREBP-2, PPARα and PPARγ, and ApoA1, ApoB100, and ApoE3	Cholesterol metabolism	[92]
miR-33	ABCA1, ABCG1	Cholesterol metabolism	[88]
miR-337-3p, miR-191, miR-222, miR-224, miR-520d-5p, and miR-483	PCSK9	Lipid metabolism	[74–77]
miR-199a and miR-140	LDLR	Lipid metabolism	[64]

ApoB100/Sort1 axis in animals. One of the miRNAs is miR378a-3p. In the study conducted by Zhang et al., they have demonstrated that the miR378a-3p expression is significantly increased in livers of hyperlipidemic mice. By targeted inhibit Sort1 expression, miR378a-3p can stabilize ApoB100 and promote its secretion, thereby facilitate VLDL secretion in the liver and exacerbate the pathogenesis of hyperlipidemia and hypolipoproteinemia [83]. Consistently, the overexpression of miR378a-3p increased the lipid droplet size and resulted in triglyceride accumulation in mice, while knockdown decreased triglyceride accumulation [84].

4.1.3. miRNA and Cholesterol Metabolism. miRNAs also involve in cholesterol metabolism.

miR-33 was reported that it plays an important role in a variety of biological processes such as cholesterol homeostasis, HDL-cholesterol formation, and fatty acid oxidation [85]. miR-33a and miR-33b were significantly upregulated in the plasma of 28 hypercholesterolemia children compared to 25 healthy subjects, and both miRNAs were positively associated with the levels of TC and LDL-C. In the study by Price et al., they have demonstrated that inhibition of miR-33 increases HDL levels via promoting reverse cholesterol transport, and macrophage-specific loss of miR-33 decreases lipid accumulation and inflammation under hyperlipidemic conditions. This suggested that miR-33a is an important regulator of macrophage cholesterol efflux and HDL biogenesis and is a promising target for treatment of atherosclerosis [86, 87]. miR-33 also downregulates cholesterol efflux and HDL biogenesis by targeting ABC transport proteins (ABCA1: ATP-binding cassette subfamily A member 1, ABCG1: ATP-binding cassette subfamily B member 11) [88]. In a nonhuman primate model of dyslipidemia, miR-33 antagonism significantly reduced plasma VLDL-associated triglyceride levels, which was associated with the regulation of fatty acids (from synthesis to oxidation) [89].

miR-27 was demonstrated that it involves in hepatic lipid deposition, triglyceride synthesis, and lipoprotein uptake [90]. Studies have found that miR-27a can accelerate

lipolysis by releasing more glycerol and free fatty acids from adipocytes and inhibit lipid storage in cells [91]. Accumulated evidences have shown that miR-27a inhibits the expression of many lipid metabolism genes, including fatty acid synthase (FASN), SREBP-1, SREBP-2, PPARα, and PPARγ, and ApoA1, ApoB100, and ApoE3 [92]. Therefore, miR-27a is an important regulator of lipid metabolism.

miR-128-3p has important roles in cholesterol efflux. In the study by Chandra et al., they have found that anti-miR-128-3p (AM-128) treatment inhibited the expression of miR-128-3p in hypercholesterolemic mouse and resulted in a significant reduction in circulating total cholesterol levels [93]. Consistently, in vitro studies [94] have demonstrated that miR-128-3p can promote cellular cholesterol accumulation by targeted inhibiting abca1, abcg1, and retinoid X receptor alpha (RXRA) and thereby inhibition of cholesterol efflux [94]. These data suggested that inhibition of microRNA-128-3p can attenuate hypercholesterolemia in animals.

In addition, there are evidences shown that miR-96/182/183 can targeted inhibit MED1/FBXW7 in hepatocytes [95, 96], and miR-122a antagonism [97] can inhibit cholesterol synthesis and reduce plasma cholesterol levels. This suggested that these miRNAs involve in lipid synthesis.

4.2. miRNA Involves in the Pathogenesis of Other Hyperlipidemia-Related Diseases. It is reported that miR-21a [98] is one of the first identified mammalian miRNAs involved in many physiological processes and multiple diseases, and one of its most representative roles is the regulation of lipid metabolism. Previous studies shown that the expression level of miR-21a-5p is downregulated in patients diagnosed as nonalcoholic fatty liver or in mice fed with high-fat diet, and knockdown of miR-21a-5p leads to hepatic steatosis, accelerated atherosclerosis, plaque necrosis, and vascular inflammation [99]. miR-200, miR-34a, miR-217, and miR-146a were reported to be highly expressed in endothelial cell senescence characterized by uncontrolled apoptosis, severe inflammation, and reduced endothelial nitric oxide synthesis and release, which was associated with endothelial dysfunction, atherosclerosis, and its complications [100]. miRNA-153 was upregulated in the pancreas of hypertriglyceridemia (HTG) animal models and in the plasma of HTG- Acute pancreatitis (AP) patients. The increase of miR-153 worsens AP and delays pancreatic repair in LPL dysfunction-induced HTG mice and its molecular mechanism associated with the inhibition of tumor necrosis factor receptor-associated factor 3 (TRAF3) [101]. Upregulation of miR-103 will inhibit endothelial cell proliferation, promote endothelial cell DNA damage, and consequently affect inflammatory response and promote atherosclerosis. MiR29c-3p is a negative regulator of dishevelled 2 (Dvl-2), a key mediator of the wnt/β-catenin signaling pathway. By inhibiting the expression of Dvl-2, miR29c-3p plays important roles in osteoblast differentiation in the hyperlipidemic setting. For example, the high expression of miR29c-3p causes implant osseointegration deficits [102, 103]. Similarly, by negatively regulating the expression of Mafb (vmaf myofascial fibrosarcoma oncogene family protein B), miR-155-5p improves β-cell adaptation to hyperlipidemic stress and compensates for obesity-induced insulin resistance and consequently limits the progression of obesity and atherosclerosis [104].

4.3. miRNAs Have Values in Hyperlipidemia Treatment. Although PCSK9 (proprotein convertase subtilisin/kexin type 9) inhibitors (monoclonal antibody) bring a new era on hyperlipidemia treatment, however, low safety profile and high cost limit its application [105–107]. Therefore, developing new drugs for hyperlipidemia is urgent for basic and clinical study. miRNAs are promising agents for their stability, controllability, good specificity, and operation simplicity. The recent studies shown that miRNAs are negative regulator of some key factors related to lipid metabolism or cholesterol metabolism, such as SREBP-1c (sterol regulatory element-binding transcription factor 1c), PPARα, and NLRP3 (Table 1) [108–113]. Thus, miRNA as drugs or targets for hyperlipidemia therapy is theoretically possible. In fact, miRNAs as the action targets of drugs were studied broadly, such as grape seed proanthocyanidins, have an effect on the expression of miRNA-122 and miRNA-33 in rats, Averrhoa carambola free phenolic extract [114] has an effect on the expression level of miRNA-34a and miRNA-33 in db/db mice, paeonol (2′-hydroxy-4′-methoxyacetophenone, Pae) has an effect on the expression level of miRNA-223 in hyperlipidemic rats [115, 116], GNP (genipin) has an effect on the expression level of miR-142a-5p in rats [117], and diallyl trisulfide (DATS) has an effect on the miR-335 expression in obese rats [118]. In addition, even exercise has an effect on the expression of miR-21a-5p and exerts beneficial in hyperlipidemia [119, 120] [121]. Recently, therapies based on miR-34 and mir-122 drugs are already in phase 2 clinical trial development [68, 69]. These suggested that miRNAs attracted great attention by scientist and have potential values in hyperlipidemia treatment.

5. Summary and Outlook

The field of research on the use of miRNAs for hyperlipidemia is currently in its early stages. In most of the previous studies, the miRNA mimics were usually injected into target tissue sites and exert function. However, these methods cannot be used in clinic due to mimics easily be degraded by RNA enzymes in the blood. In addition, poor delivery of miRNA mimics to the target site makes it difficult to apply clinically. That is the reason why these studies of miRNAs successfully in animals cannot be translated into clinical applications [69, 123]. To overcome this above weakness of miRNAs, recently, scientists made some chemical modification of some nucleotide sequences of miRNAs to increase its stability and reduce its toxicity that it not essential for the intended function. As the advances in RNA chemical modification and delivery vector technologies have made continuously, several miRNAs have been entered into different clinical trials as therapeutic agents or therapeutic targets for human diseases. More and more studies have found that miRNAs play important roles in the pathogenesis of

hyperlipidemia via regulating some key genes of lipid metabolism and are important biomarkers or target of hyperlipidemia. Thus, people paid great attention to using miRNAs for hyperlipidemia therapy. With the depth of miRNA research on hyperlipidemia and the advance of related technologies, such as delivery technology and materials science, we believe that it will be a success that miRNAs used for hyperlipidemia therapy clinically in the near future.

Data Availability

The dataset used and/or analyzed during the current study are available from the corresponding author on reasonable request.

Conflicts of Interest

The authors declare that they have no conflict of interest.

Authors' Contributions

Yu Xiang, Mei-Ling Zuo, Li Mao, Gui-Lin Song, Li-Ming Tan, and Zhong-Bao Yang wrote the main manuscript. All authors reviewed the manuscript. Yu Xiang and Li Mao contributed equally to the work.

Acknowledgments

This work was funded by the Hunan Provincial Natural Science Foundation of China (grant No. 2020JJ5384 to Zhong-Bao Yang and grant No. 2020JJ4442 to Mei-Ling Zuo) and Changsha Science & Technology Bureau (No. kq2004153 to Zhong-Bao Yang and No. kq2004154 to Guo-Huang Hu).

References

[1] R. H. Nelson, "Hyperlipidemia as a risk factor for cardiovascular disease," *Primary Care*, vol. 40, no. 1, p. 195, 2013.

[2] J. Iqbal, A. Al Qarni, A. Hawwari, A. F. Alghanem, and G. Ahmed, "Metabolic syndrome, dyslipidemia and regulation of lipoprotein metabolism," *Current Diabetes Reviews*, vol. 14, no. 5, pp. 427–433, 2018.

[3] J. Hurtubise, K. McLellan, K. Durr, O. Onasanya, D. Nwabuko, and J. F. Ndisang, "The different facets of dyslipidemia and hypertension in atherosclerosis," *Current Atherosclerosis Reports*, vol. 18, no. 12, p. 82, 2016.

[4] V. Barrios, C. Escobar, A. F. Cicero et al., "A nutraceutical approach (Armolipid plus) to reduce total and LDL cholesterol in individuals with mild to moderate dyslipidemia: review of the clinical evidence," *Atherosclerosis. Supplements*, vol. 24, pp. 1–15, 2017.

[5] J. I. Harland, "Food combinations for cholesterol lowering," *Nutrition Research Reviews*, vol. 25, no. 2, pp. 249–266, 2012.

[6] B. G. Nordestgaard and A. Varbo, "Triglycerides and cardiovascular disease," *Lancet*, vol. 384, no. 9943, pp. 626–635, 2014.

[7] S. Paul, L. M. Ruiz-Manriquez, S. J. Ledesma-Pacheco et al., "Roles of microRNAs in chronic pediatric diseases and their use as potential biomarkers: a review," *Archives of Biochemistry and Biophysics*, vol. 699, p. 108763, 2021.

[8] M. P. Perron and P. Provost, "Protein interactions and complexes in human microRNA biogenesis and function," *Frontiers in Bioscience: a Journal and Virtual Library*, vol. 13, pp. 2537–2547, 2008.

[9] M. A. Cortez, C. Ivan, D. Valdecanas et al., "PDL1 Regulation by p53 via miR-34," *JNCI: Journal of the National Cancer Institute*, vol. 108, no. 1, 2016.

[10] M. V. Iorio and C. M. Croce, "MicroRNAdysregulation in cancer: diagnostics, monitoring and therapeutics. A comprehensive review," *EMBO Molecular Medicine*, vol. 9, no. 6, p. 852, 2017.

[11] J. Baek, S. Kang, and H. Min, "MicroRNA-targeting therapeutics for hepatitis C," *Archives of Pharmacal Research*, vol. 37, no. 3, pp. 299–305, 2014.

[12] P. Gurha, "MicroRNAs in cardiovascular disease," *Current Opinion in Cardiology*, vol. 31, no. 3, pp. 249–254, 2016.

[13] J. Weidner, S. Bartel, A. Kılıç et al., "Spotlight on microRNAs in allergy and asthma," *Allergy*, vol. 76, no. 6, pp. 1661–1678, 2021.

[14] E. Dissanayake and Y. Inoue, "MicroRNAs in allergic disease," *Current Allergy and Asthma Reports*, vol. 16, no. 9, p. 67, 2016.

[15] X. H. Zhang, Y. N. Zhang, and Z. Liu, "MicroRNA in chronic rhinosinusitis and allergic rhinitis," *Current Allergy and Asthma Reports*, vol. 14, no. 2, p. 415, 2014.

[16] J. Xu, Z. Chen, Y. Wang et al., "Several circulating miRNAs related to hyperlipidemia and atherosclerotic cardiovascular diseases," *Lipids in Health and Disease*, vol. 18, no. 1, p. 104, 2019.

[17] T. Horie, O. Baba, Y. Kuwabara et al., "MicroRNAs and lipoprotein metabolism," *Journal of Atherosclerosis and Thrombosis*, vol. 21, no. 1, pp. 17–22, 2014.

[18] L. Goedeke, A. Wagschal, C. Fernandez-Hernando, and A. M. Naar, "miRNA regulation of LDL-cholesterol metabolism," *Biochimica et Biophysica Acta (BBA)-Molecular and Cell Biology of Lipids*, vol. 1861, no. 12, pp. 2047–2052, 2016.

[19] C. M. Ramírez, N. Rotllan, A. V. Vlassov et al., "Control of cholesterol metabolism and plasma high-density lipoprotein levels by microRNA-144," *Circulation Research*, vol. 112, no. 12, pp. 1592–1601, 2013.

[20] T. Barbalata, L. Zhang, M. D. Dulceanu et al., "Regulation of microRNAs in high-fat diet induced hyperlipidemic hamsters," *Scientific Reports*, vol. 10, no. 1, pp. 1–9, 2020.

[21] M. Ogris, "Nucleic acid therapeutics: concepts for targeted delivery to solid tumors," *Therapeutic Delivery*, vol. 1, no. 1, pp. 91–107, 2010.

[22] S. S. Mogensen, K. Schmiegelow, K. Grell et al., "Hyperlipidemia is a risk factor for osteonecrosis in children and young adults with acute lymphoblastic leukemia," *Haematologica*, vol. 102, no. 5, pp. E175–E178, 2017.

[23] L. Wang, W. Zheng, J. Yang, A. Ali, and H. Qin, "Mechanism of Astragalus membranaceus alleviating acquired jyperlipidemia induced by high-fat diet through regulating lipid metabolism," *Nutrients*, vol. 14, no. 5, 2022.

[24] P. C. Li, I. J. Tsai, C. Y. Hsu et al., "Risk of hyperlipidemia in women with hysterectomy-a retrospective cohort study in Taiwan," *Scientific Reports*, vol. 8, no. 1, pp. 1–8, 2018.

[25] P. Gunness and M. J. Gidley, "Mechanisms underlying the cholesterol-lowering properties of soluble dietary fibre polysaccharides," *Food & Function*, vol. 1, no. 2, pp. 149–155, 2010.

[26] T. van der Gronde, A. Hartog, C. van Hees, H. Pellikaan, and T. Pieters, "Systematic review of the mechanisms and evidence behind the hypocholesterolaemic effects of HPMC, pectin and chitosan in animal trials," *Food Chemistry*, vol. 199, pp. 746–759, 2016.

[27] M. Pawelczyk, H. Chmielewski, B. Kaczorowska, M. Przybyla, and Z. Baj, "Platelet reactivity in patients with stroke and hyperlipidemia, GPIbα assessment," *Clinical and Applied Thrombosis/Hemostasis*, vol. 22, no. 2, pp. 166–170, 2016.

[28] Z. H. Yang, M. Pryor, A. Noguchi et al., "Dietary palmitoleic acid attenuates atherosclerosis progression and hyperlipidemia in low-density lipoprotein receptor-deficient mice," *Molecular Nutrition & Food Research*, vol. 63, no. 12, p. e1900120, 2019.

[29] W. J. Guan and G. J. Yang, "Significance of change of retinol binding protein 4 level of plasma of patients with coronary heart disease complicated with hyperlipidemia," *European Review for Medical and Pharmacological Sciences*, vol. 20, no. 19, pp. 4136–4140, 2016.

[30] L. Yan, P. Han, J. Man, Y. Tian, F. Wang, and J. Wang, "Discovery of lipid profiles of type 2 diabetes associated with hyperlipidemia using untargeted UPLC Q-TOF/MS-based lipidomics approach," *Clinica Chimica Acta*, vol. 520, pp. 53–62, 2021.

[31] F. Zhu, Y. Guan, and R. Zhang, "Inhibition of JAK2 signaling alleviates hyperlipidemia-intensified caerulin-induced acute pancreatitis in vivo," *Current Molecular Medicine*, vol. 17, no. 5, pp. 381–387, 2017.

[32] S. C. Larsson and H. S. Markus, "Does treating vascular risk factors prevent dementia and Alzheimer's disease? A systematic review and meta-analysis," *Journal of Alzheimer's Disease*, vol. 64, no. 2, pp. 657–668, 2018.

[33] M. L. Du, Q. L. Wang, J. Zhao, Y. Zhou, and F. Fang, "Investigation of serum lipid-related knowledge requirement and self-care behaviors of patients with hyperlipidemia," *Journal of Shanghai Jiaotong University*, vol. 33, no. 5, pp. 543–547, 2013.

[34] X. Wang, Y. A. Seo, and S. K. Park, "Serum selenium and non-alcoholic fatty liver disease (NAFLD) in US adults: National Health and Nutrition Examination Survey (NHANES) 2011–2016," *Environmental Research*, vol. 197, p. 111190, 2021.

[35] Y. Liu, F. Liu, L. Zhang et al., "Association between low density lipoprotein cholesterol and all-cause mortality: results from the NHANES," *Scientific Reports*, vol. 11, no. 1, pp. 1–12, 2021.

[36] A. J. Vallejo-Vaz, S. R. Kondapally Seshasai, D. Cole et al., "Familial hypercholesterolaemia: a global call to arms," *Atherosclerosis*, vol. 243, no. 1, pp. 257–259, 2015.

[37] L. E. Akioyamen, J. Genest, S. D. Shan et al., "Estimating the prevalence of heterozygous familial hypercholesterolaemia: a systematic review and meta-analysis," *BMJ Open*, vol. 7, no. 9, p. e016461, 2017.

[38] Y. Ma, W. Wang, J. Zhang et al., "Hyperlipidemia and atherosclerotic lesion development in Ldlr-deficient mice on a long-term high-fat diet," *PLoS One*, vol. 7, no. 4, article e35835, 2012.

[39] S. Rahbar, M. Pashaiasl, M. Ezzati et al., "MicroRNA-based regulatory circuit involved in sperm infertility," *Andrologia*, vol. 52, no. 1, p. e13453, 2020.

[40] R. C. Lee, R. L. Feinbaum, and V. Ambros, "The C. elegans heterochronic gene lin-4 encodes small RNAs with antisense complementarity to lin-14," *Cell*, vol. 75, no. 5, pp. 843–854, 1993.

[41] A. E. Pasquinelli, "The primary target oflet-7microRNA," *Biochemical Society Transactions*, vol. 41, no. 4, pp. 821–824, 2013.

[42] R. C. Friedman, K. K. H. Farh, C. B. Burge, and D. P. Bartel, "Most mammalian mRNAs are conserved targets of microRNAs," *Genome Research*, vol. 19, no. 1, pp. 92–105, 2009.

[43] N. Simionescu, L. S. Niculescu, G. M. Sanda, D. Margina, and A. V. Sima, "Analysis of circulating microRNAs that are specifically increased in hyperlipidemic and/or hyperglycemic sera," *Molecular Biology Reports*, vol. 41, no. 9, pp. 5765–5773, 2014.

[44] X. Lin, J. K. Zhan, Y. J. Wang et al., "Function, role, and clinical application of microRNAs in vascular aging," *BioMed Research International*, vol. 2016, Article ID 6021394, 15 pages, 2016.

[45] X. Zhong, F. Heinicke, and S. Rayner, "miRBaseMiner, a tool for investigating miRBase content," *RNA Biology*, vol. 16, no. 11, pp. 1534–1546, 2019.

[46] L. A. MacFarlane and P. R. Murphy, "MicroRNA: biogenesis, function and role in cancer," *Current Genomics*, vol. 11, no. 7, pp. 537–561, 2010.

[47] R. W. Carthew and E. J. Sontheimer, "Origins and mechanisms of miRNAs and siRNAs," *Cell*, vol. 136, no. 4, pp. 642–655, 2009.

[48] E. Bonneau, B. Neveu, E. Kostantin, G. J. Tsongalis, and V. De Guire, "How close are miRNAs from clinical practice? A perspective on the diagnostic and therapeutic market," *Ejifcc*, vol. 30, no. 2, pp. 114–127, 2019.

[49] H. Yaribeygi, S. L. Atkin, and A. Sahebkar, "Potential roles of microRNAs in redox state: an update," *Journal of Cellular Biochemistry*, vol. 120, no. 2, pp. 1679–1684, 2018.

[50] H. A. Çakmak and M. Demir, "MicroRNA and cardiovascular diseases," *Balkan Medical Journal*, vol. 37, no. 2, pp. 60–71, 2020.

[51] R. I. Gregory, K. P. Yan, G. Amuthan et al., "The microprocessor complex mediates the genesis of microRNAs," *Nature*, vol. 432, no. 7014, pp. 235–240, 2004.

[52] Y. Lee, C. Ahn, J. Han et al., "The nuclear RNase III Drosha initiates microRNA processing," *Nature*, vol. 425, no. 6956, pp. 415–419, 2003.

[53] M. Ha and V. N. Kim, "Regulation of microRNA biogenesis," *Nature Reviews. Molecular Cell Biology*, vol. 15, no. 8, pp. 509–524, 2014.

[54] C. E. Condrat, D. C. Thompson, M. G. Barbu et al., "miRNAs as biomarkers in disease: latest findings regarding their role in diagnosis and prognosis," *Cells*, vol. 9, no. 2, pp. 71–88, 2020.

[55] S. Khan, H. Ayub, T. Khan, and F. Wahid, "MicroRNA biogenesis, gene silencing mechanisms and role in breast, ovarian and prostate cancer," *Biochimie*, vol. 167, pp. 12–124, 2019.

[56] M. Xie and J. A. Steitz, "Versatile microRNA biogenesis in animals and their viruses," *RNA Biology*, vol. 11, no. 6, pp. 673–681, 2014.

[57] S. L. Romero-Cordoba, I. Salido-Guadarrama, M. Rodriguez-Dorantes, and A. Hidalgo-Miranda, "miRNA biogenesis: biological impact in the development of cancer," *Cancer Biology & Therapy*, vol. 15, no. 11, pp. 1444–1455, 2014.

[58] B. P. Lewis, I. H. Shih, M. W. Jones-Rhoades, D. P. Bartel, and C. B. Burge, "Prediction of mammalian microRNA targets," *Cell*, vol. 115, no. 7, pp. 787–798, 2003.

[59] E. C. Lai, "Micro RNAs are complementary to 3' UTR sequence motifs that mediate negative post-transcriptional regulation," *Nature Genetics*, vol. 30, no. 4, pp. 363-364, 2002.

[60] L. Zhou, S. Irani, A. Sirwi, and M. M. Hussain, "MicroRNAs regulating apolipoprotein B-containing lipoprotein production," *Biochimica et Biophysica Acta (BBA)-molecular and cell biology of lipids*, vol. 1861, no. 12, pp. 2062–2068, 2016.

[61] E. van Rooij and E. N. Olson, "MicroRNA therapeutics for cardiovascular disease: opportunities and obstacles," *Nature Reviews. Drug Discovery*, vol. 11, no. 11, pp. 860–872, 2012.

[62] B. Jamalzei, F. S. Karami Tehrani, and M. Atri, "Evaluation of LDL receptor and scavenger receptor, class B, type 1 in the malignant and benign breast tumors: the correlation with the expression of miR-199a-5p, miR-199b-5p and miR-455-5p," *Gene*, vol. 749, p. 144720, 2020.

[63] Y. Xu, J. Gao, Y. Gong et al., "Hsa-miR-140-5p down-regulates LDL receptor and attenuates LDL-C uptake in human hepatocytes," *Atherosclerosis*, vol. 297, pp. 111–119, 2020.

[64] Z. Yang, T. Cappello, and L. Wang, "Emerging role of microRNAs in lipid metabolism," *Acta Pharmaceutica Sinica B*, vol. 5, no. 2, pp. 145–150, 2015.

[65] A. Canfrán-Duque, C. M. Ramírez, L. Goedeke, C. S. Lin, and C. Fernández-Hernando, "microRNAs and HDL life cycle," *Cardiovascular Research*, vol. 103, no. 3, pp. 414–422, 2014.

[66] T. Zhang, J. Hu, X. Wang et al., "MicroRNA-378 promotes hepatic inflammation and fibrosis via modulation of the NF-κB-TNFα pathway," *Journal of Hepatology*, vol. 70, no. 1, pp. 87–96, 2019.

[67] K. Musunuru, A. Strong, M. Frank-Kamenetsky et al., "From noncoding variant to phenotype via SORT1 at the 1p13 cholesterol locus," *Nature*, vol. 466, no. 7307, pp. 714–719, 2010.

[68] Z. Qiu and Y. Dai, "Roadmap of miR-122-related clinical application from bench to bedside," *Expert Opinion on Investigational Drugs*, vol. 23, no. 3, pp. 347–355, 2014.

[69] E. van Rooij and S. Kauppinen, "Development of microRNA therapeutics is coming of age," *EMBO Molecular Medicine*, vol. 6, no. 7, pp. 851–864, 2014.

[70] B. Yerushalmi, R. J. Sokol, M. R. Narkewicz, D. Smith, J. W. Ashmead, and D. A. Wenger, "NARC-1/PCSK9 and its natural mutants: zymogen cleavage and effects on the low density lipoprotein (LDL) receptor and LDL cholesterol," *Journal of Biological Chemistry*, vol. 279, no. 47, pp. 48865–48875, 2004.

[71] J. C. Cohen, E. Boerwinkle, T. H. Mosley Jr., and H. H. Hobbs, "Sequence variations in PCSK9, low LDL, and protection against coronary heart disease," *New England Journal of Medicine*, vol. 354, no. 12, pp. 1264–1272, 2006.

[72] T. A. Lagace, D. E. Curtis, R. Garuti et al., "Secreted PCSK9 decreases the number of LDL receptors in hepatocytes and in livers of parabiotic mice," *The Journal of Clinical Investigation*, vol. 116, no. 11, pp. 2995–3005, 2006.

[73] D. W. Zhang, T. A. Lagace, R. Garuti et al., "Binding of proprotein convertase subtilisin/kexin type 9 to epidermal growth factor-like repeat A of low density lipoprotein receptor decreases receptor recycling and increases degradation," *Journal of Biological Chemistry*, vol. 282, no. 25, pp. 18602–18612, 2007.

[74] J. Dong, M. He, J. Li et al., "microRNA-483 ameliorates hypercholesterolemia by inhibiting PCSK9 production," *JCI Insight*, vol. 5, no. 23, 2020.

[75] P. Naeli, F. Mirzadeh Azad, M. Malakootian, N. G. Seidah, and S. J. Mowla, "Post-transcriptional regulation of PCSK9 by miR-191, miR-222, and miR-224," *Frontiers in Genetics*, vol. 8, p. 189, 2017.

[76] A. G. Salerno, C. van Solingen, E. Scotti et al., "LDL receptor pathway regulation by miR-224 and miR-520d," *Front Cardiovasc Medicine*, vol. 7, p. 81, 2020.

[77] X. Xu, Y. Dong, N. Ma et al., "MiR-337-3p lowers serum LDL-C level through targeting PCSK9 in hyperlipidemic mice," *Metabolism*, vol. 119, p. 154768, 2021.

[78] M. Arca, "PCSK9 inhibitors (PCSK9i), a new opportunity for cardiovascular prevention: clinical and regulatory aspects and access to therapy," *Recenti Progressi in Medicina*, vol. 110, no. 9, pp. 401–411, 2019.

[79] L. Goedeke, J. F. Aranda, and C. Fernández-Hernando, "MicroRNA regulation of lipoprotein metabolism," *Current Opinion in Lipidology*, vol. 25, no. 4, pp. 282–288, 2014.

[80] H. A. Al-Rawaf, "Circulating microRNAs and adipokines as markers of metabolic syndrome in adolescents with obesity," *Clinical Nutrition*, vol. 38, no. 5, pp. 2231–2238, 2019.

[81] J. Li, L. Bi, M. Hulke, and T. Li, "Fish oil and fenofibrate prevented phosphorylation-dependent hepatic sortilin 1 degradation in western diet-fed mice," *Journal of Biological Chemistry*, vol. 289, no. 32, pp. 22437–22449, 2014.

[82] A. Strong, Q. Ding, A. C. Edmondson et al., "Hepatic sortilin regulates both apolipoprotein B secretion and LDL catabolism," *The Journal of Clinical Investigation*, vol. 122, no. 8, pp. 2807–2816, 2012.

[83] N. Huang, J. Wang, W. Xie et al., "miR-378a-3p enhances adipogenesis by targeting mitogen-activated protein kinase 1," *Biochemical and Biophysical Research Communications*, vol. 457, no. 1, pp. 37–42, 2015.

[84] T. Zhang, H. Shi, N. Liu et al., "Activation of microRNA-378a-3p biogenesis promotes hepatic secretion of VLDL and hyperlipidemia by modulating ApoB100-Sortilin1 axis," *Theranostics*, vol. 10, no. 9, pp. 3952–3966, 2020.

[85] F. Martino, F. Carlomosti, D. Avitabile et al., "Circulating miR-33a and miR-33b are up-regulated in familial hypercholesterolaemia in paediatric age," *Clinical Science (London, England)*, vol. 129, no. 11, pp. 963–972, 2015.

[86] N. L. Price, N. Rotllan, A. Canfrán-Duque et al., "Genetic dissection of the impact of miR-33a and miR-33b during the progression of atherosclerosis," *Cell Reports*, vol. 21, no. 5, pp. 1317–1330, 2017.

[87] K. J. Rayner, F. J. Sheedy, C. C. Esau et al., "Antagonism of miR-33 in mice promotes reverse cholesterol transport and regression of atherosclerosis," *The Journal of Clinical Investigation*, vol. 121, no. 7, pp. 2921–2931, 2011.

[88] K. J. Rayner, Y. Suárez, A. Dávalos et al., "miR-33 contributes to the regulation of cholesterol homeostasis," *Science*, vol. 328, no. 5985, pp. 1570–1573, 2010.

[89] K. J. Rayner, C. C. Esau, F. N. Hussain et al., "Inhibition of miR-33a/b in non-human primates raises plasma HDL and lowers VLDL triglycerides," *Nature*, vol. 478, no. 7369, pp. 404–407, 2011.

[90] W. Xie, L. Li, M. Zhang et al., "MicroRNA-27 prevents atherosclerosis by suppressing lipoprotein lipase-induced lipid accumulation and inflammatory response in apolipoprotein E knockout mice," *PLoS One*, vol. 11, no. 6, article e0157085, 2016.

[91] L. R. Sedgeman, D. L. Michell, and K. C. Vickers, "Integrative roles of microRNAs in lipid metabolism and dyslipidemia," *Current opinion in lipidology*, vol. 30, no. 2, p. 165, 2019.

[92] F. H. Yerlikaya, U. Can, M. S. Alpaydin, and A. Aribas, "The relationship between plasma microRNAs and serum trace elements levels in primary hyperlipidemia," *Bratislavské Lekárske Listy*, vol. 120, no. 5, pp. 344–348, 2019.

[93] A. Chandra, K. Sharma, K. Pratap, V. Singh, and N. Saini, "Inhibition of microRNA-128-3p attenuates hypercholesterolemia in mouse model," *Life Sciences*, vol. 264, p. 118633, 2021.

[94] Y. K. Adlakha, S. Khanna, R. Singh, V. P. Singh, A. Agrawal, and N. Saini, "Pro-apoptotic miRNA-128-2 modulates ABCA1, ABCG1 and RXR α expression and cholesterol homeostasis," *Cell Death & Disease*, vol. 4, no. 8, article e780, 2013.

[95] L. R. Sedgeman, C. Beysen, R. M. Allen, M. A. Ramirez Solano, S. M. Turner, and K. C. Vickers, "Intestinal bile acid sequestration improves glucose control by stimulating hepatic miR-182-5p in type 2 diabetes," *American Journal of Physiology-Gastrointestinal and Liver Physiology*, vol. 315, no. 5, pp. 810–823, 2018.

[96] T. I. Jeon, R. M. Esquejo, M. Roqueta-Rivera et al., "An SREBP-responsive microRNA operon contributes to a regulatory loop for intracellular lipid homeostasis," *Cell Metabolism*, vol. 18, no. 1, pp. 51–61, 2013.

[97] J. Elmén, M. Lindow, A. Silahtaroglu et al., "Antagonism of microRNA-122 in mice by systemically administered LNA-antimiR leads to up-regulation of a large set of predicted target mRNAs in the liver," *Nucleic Acids Research*, vol. 36, no. 4, pp. 1153–1162, 2008.

[98] A. M. Krichevsky and G. Gabriely, "miR-21: a small multifaceted RNA," *Journal of Cellular and Molecular Medicine*, vol. 13, no. 1, pp. 39–53, 2009.

[99] C. Sun, F. Huang, X. Liu et al., "miR-21 regulates triglyceride and cholesterol metabolism in non-alcoholic fatty liver disease by targeting HMGCR," *International Journal of Molecular Medicine*, vol. 35, no. 3, pp. 847–853, 2015.

[100] G. Arunachalam, R. Upadhyay, H. Ding, and C. R. Triggle, "MicroRNA signature and cardiovascular dysfunction," *Journal of Cardiovascular Pharmacology*, vol. 65, no. 5, pp. 419–429, 2015.

[101] J. Dai, M. Jiang, Y. Hu et al., "Dysregulated SREBP1c/miR-153 signaling induced by hypertriglyceridemia worsens acute pancreatitis and delays tissue repair," *JCI Insight*, vol. 6, no. 2, 2021.

[102] Y. N. Lee, Y. Gao, and H. Y. Wang, "Differential mediation of the Wnt canonical pathway by mammalian dishevelleds-1, -2, and -3," *Cellular Signalling*, vol. 20, no. 2, pp. 443–452, 2008.

[103] X. Huang, Z. Wang, D. Li et al., "Study of microRNAs targeted Dvl2 on the osteoblasts differentiation of rat BMSCs in hyperlipidemia environment," *Journal of Cellular Physiology*, vol. 233, no. 9, pp. 6758–6766, 2018.

[104] M. Zhu, Y. Wei, C. Geißler et al., "Hyperlipidemia-induced microRNA-155-5p improves β-cell function by targeting-Mafb," *Diabetes*, vol. 66, no. 12, pp. 3072–3084, 2017.

[105] M. S. Sabatine, R. P. Giugliano, A. C. Keech et al., "Evolocumab and clinical outcomes in patients with cardiovascular disease," *New England Journal of Medicine*, vol. 376, no. 18, pp. 1713–1722, 2017.

[106] D. D. Waters and P. Y. Hsue, "PCSK9 inhibition to reduce cardiovascular risk," *Circulation Research*, vol. 120, no. 10, pp. 1537–1539, 2017.

[107] A. C. Burke, J. S. Dron, R. A. Hegele, and M. W. Huff, "PCSK9: regulation and target for drug development for dyslipidemia," *Annual Review of Pharmacology and Toxicology*, vol. 57, pp. 223–244, 2017.

[108] O. Cheung, P. Puri, C. Eicken et al., "Nonalcoholic steatohepatitis is associated with altered hepatic microRNA expression," *Hepatology*, vol. 48, no. 6, pp. 1810–1820, 2008.

[109] J. Ding, M. Li, X. Wan et al., "Effect of miR-34a in regulating steatosis by targeting PPARα expression in nonalcoholic fatty liver disease," *Scientific Reports*, vol. 5, no. 1, pp. 1–10, 2015.

[110] P. Ferré and F. Foufelle, "SREBP-1c transcription factor and lipid homeostasis: clinical perspective," *Hormone Research*, vol. 68, no. 2, pp. 72–82, 2007.

[111] J. Lin, R. Yang, P. T. Tarr et al., "Hyperlipidemic effects of dietary saturated fats mediated through PGC-1β coactivation of SREBP," *Cell*, vol. 120, no. 2, pp. 261–273, 2005.

[112] Z. He, C. Hu, and W. Jia, "miRNAs in non-alcoholic fatty liver disease," *Frontiers in Medicine*, vol. 10, no. 4, pp. 389–396, 2016.

[113] H. Wu, T. Zhang, F. Pan et al., "MicroRNA-206 prevents hepatosteatosis and hyperglycemia by facilitating insulin signaling and impairing lipogenesis," *Journal of Hepatology*, vol. 66, no. 4, pp. 816–824, 2017.

[114] D. Pang, L. You, L. Zhou, T. Li, B. Zheng, and R. H. Liu, "Averrhoa carambola free phenolic extract ameliorates non-alcoholic hepatic steatosis by modulating mircoRNA-34a, mircoRNA-33 and AMPK pathways in leptin receptor-deficient db/db mice," *Food & Function*, vol. 8, no. 12, pp. 4496–4507, 2017.

[115] J. Novák, V. Olejníčková, N. Tkáčová, and G. Santulli, "Mechanistic role of MicroRNAs in coupling lipid metabolism and atherosclerosis," *Advances in Experimental Medicine and Biology*, vol. 887, pp. 79–100, 2015.

[116] X. Shi, X. Xie, Y. Sun et al., "Paeonol inhibits NLRP3 mediated inflammation in rat endothelial cells by elevating hyperlipidemic rats plasma exosomal miRNA-223," *European Journal of Pharmacology*, vol. 885, p. 173473, 2020.

[117] H. Zhong, K. Chen, M. Feng et al., "Genipin alleviates high-fat diet-induced hyperlipidemia and hepatic lipid accumulation in mice via miR-142a-5p/SREBP-1c axis," *The FEBS Journal*, vol. 285, no. 3, pp. 501–517, 2018.

[118] A. Miura, A. Ikeda, M. Abe et al., "Diallyl trisulfide prevents obesity and decreases miRNA-335 expression in adipose tissue in a diet-induced obesity rat model," *Molecular Nutrition & Food Research*, vol. 65, no. 14, p. e2001199, 2021.

[119] U. P. R. Soci, T. Fernandes, N. Y. Hashimoto et al., "MicroRNAs 29 are involved in the improvement of ventricular compliance promoted by aerobic exercise training in rats," *Physiological Genomics*, vol. 43, no. 11, pp. 665–673, 2011.

[120] J. Xiao, Y. Bei, J. Liu et al., "miR-212 downregulation contributes to the protective effect of exercise against non-alcoholic fatty liver via targeting FGF-21," *Journal of Cellular and Molecular Medicine*, vol. 20, no. 2, pp. 204–216, 2016.

[121] J. Zhao, Y. Song, Y. Zeng et al., "Improvement of hyperlipidemia by aerobic exercise in mice through a regulatory effect of

miR-21a-5p on its target genes," *Scientific Reports*, vol. 11, no. 1, p. 11966, 2021.

[122] L. Baselga-Escudero, C. Bladé, A. Ribas-Latre et al., "Grape seed proanthocyanidins repress the hepatic lipid regulators miR-33 and miR-122 in rats," *Molecular Nutrition & Food Research*, vol. 56, no. 11, pp. 1636–1646, 2012.

[123] Z. Li and T. M. Rana, "Therapeutic targeting of microRNAs: current status and future challenges," *Nature Reviews. Drug Discovery*, vol. 13, no. 8, pp. 622–638, 2014.